CO$_2$ to X:

Electrochemical CO$_2$ Reduction on Metal Foam Catalysts

Inaugural dissertation
of the Faculty of Science,
University of Bern

Presented by
Kiran Kiran
from India

Supervisor: Prof. Dr. Peter Broekmann

Department of Chemistry, Biochemistry
and Pharmaceutical Sciences

CO_2 to X:

Electrochemical CO_2 Reduction on Metal Foam Catalysts

Inaugural dissertation
of the Faculty of Science,
University of Bern

Presented by
Kiran Kiran
from India

Supervisor: Prof. Dr. Peter Broekmann

Department of Chemistry, Biochemistry
and Pharmaceutical Sciences

Accepted by the Faculty of Science.

Bern, 8.11.2021

The Dean:

Prof. Dr. Zoltan Balogh

Abstract

Societal, economic, and technological advancements have collectively led to a constant increase in the atmospheric CO_2 concentration, thus giving rise to concerns about its harmful influence on the global climate. Against this backdrop, electrochemical CO_2 reduction (CO_2RR) is one particularly promising approach to alleviate the high CO_2 concentration, thereby contributing to the closing of the anthropogenic carbon cycle. This process is considered appealing as it can be operated with renewable energy sources (wind, solar, etc.). However, one of the most challenging aspects of CO_2RR is the design and fabrication of stable catalysts capable of selectively forming a specific target product at low over-potentials while remaining energetically efficient.

This thesis focused on the development of novel monometallic and binary foam catalysts. In addition to developing robust catalysts, the objective was to investigate the transformation of the catalysts under reaction conditions through *operando* techniques complemented by ex-situ techniques. These catalysts were prepared by adopting the so-called dynamic hydrogen bubble template (DHBT) deposition approach yielding metal foams and revealing porosity on various length scales. An open-cell structure of interconnected pores of various sizes on the µm length results in a primary porosity, whereas a secondary porosity was found on a nm length scale at the dendritic sidewalls of the macro-pores. In this thesis, synthesis protocols for monometallic Ag, Cu, and Bi-foams were developed and are presented. A key aspect of improved catalyst performances is the catalyst activation via thermal annealing and the subsequent reduction of the formed oxidic precursor under *operando* CO_2RR conditions. A variety of advanced *operando* techniques (XAS, XRD, and Raman) were applied to examine the oxidic precursors' potential-dependent stability and to answer the question about the extent to which the oxidic species actively participate in the electrocatalytic reaction. The Cu and the Bi foam were identified as model systems (i) for a complete oxide→metal transition prior to the CO_2RR (Cu) and (ii) for a partial oxide→metal transition during initial CO_2RR, thus indicating an active role of the oxides.

The preparation of metal foam catalysts could be further extended to bimetallic and binary alloy systems with a view to further improving the product selectivity of particular CO_2RR products targeted in this Ph.D. project (e.g. ethanol, n-propanol, formate, and carbon monoxide). Specifically, CuPd alloy and bimetallic CuAg foams were identified as superior catalysts for selective n-propanol and ethanol formation, respectively. A detailed study was undertaken on the performance of CuIn and CuSn foams in dependence on their chemical composition demonstrating characteristic concentration-dependent transitions in the resulting product distribution (e.g. from CO to formate).

Finally, the concept of metal foam electrodeposition was successfully transferred to technical support electrodes (carbon papers) which find use as gas diffusion electrodes (GDEs). This is considered an important step toward the application of this novel type of catalysts under more realistic experimental conditions.

Table of Contents

1. Motivation

1.1 The Challenge: Rising CO_2 Levels and Climate Change

The rapid increase of the carbon dioxide (CO_2) concentration in the atmosphere of our planet has resulted in an imbalance in the earth's energy system.[1] This imbalance has exerted adverse effects on the global climate, posing major challenges to all societies worldwide. For the longest time, the earth's atmosphere maintained its composition in an entirely natural way, with the main constituents of nitrogen (N_2: 78.1%), oxygen (O_2: 20.5%), and argon (Ar: 0.9%), which sum up to 99.5%.[2] The other constituents of the atmosphere include traces of CO_2, CH_4, N_2O, O_3, and water (vapor) accounting for the remaining 0.5% of the gaseous constituents of the atmosphere. These atmospheric trace gases are also known as greenhouse gases (GHGs) attributed to their capability of absorbing light in the "infrared" region radiated not only by the sun (solar radiation) but also by the earth's surface. An estimate of electromagnetic radiation emitted by matter is typically based on **Wien's displacement law** which gives the wavelength corresponding to the maximum spectral radiance of a blackbody (ideal solid) at a given temperature T.

$$\lambda_{max} = \frac{const. K}{T} = \frac{2897.7\ \mu mK}{T}$$

Assuming a temperature of ca. 5800 K of the solar surface, Wien's law predicts a maximum of the spectral radiance in the visible range at $\lambda_{max} \approx 491$ nm which indeed finds concurrence with the maximum intensity of irradiated light experimentally observed in the solar spectrum.[3] Earth's atmosphere is largely transparent (i.e., ca. 50%) towards solar radiation in the visible range. In addition, sunlight is absorbed mainly by the oceans (~ 90%) whereas the (ice-free) land and in particular polar regions contribute only to a small extent to the absorption of solar radiation (~ 10%). Herein, the light (energy) is basically transformed into heat (energy) upon absorption. Assuming a mean surface temperature of about 289 K **Wien's law predicts a maximum of Earth's spectral radiance in the infrared range ($\lambda_{max} \approx 10\ \mu m$)**. GHGs absorb the emitted infrared radiation through excitation of particular vibrational modes (e.g., the asymmetric stretch mode in the CO_2, see Figure 1.1). By returning to the initial state, the GHGs re-emit IR- radiation (energy) in a complete non-directional manner, thus implying that
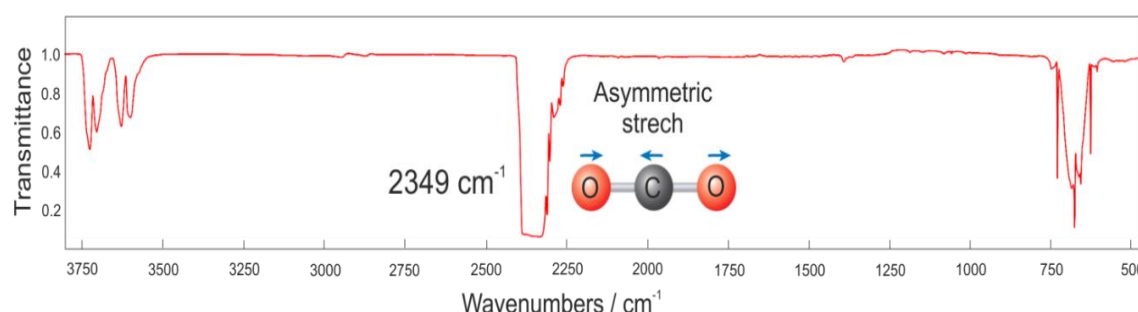
Figure 1.1. Representative IR-spectrum of gaseous CO_2 (NIST) adapted from Tghgtgpeg" 3 showing characteristic adsorption features in the "infrared" region which are assigned to the excitation of particular vibrational modes of the CO_2 molecule. The most intense band at 2349 cm⁻¹ can be assigned to the asymmetric stretching mode of the linear CO_2 molecule (i.e., a major contributor to the capability of CO_2 to absorb infrared radiation and to trap "heat").
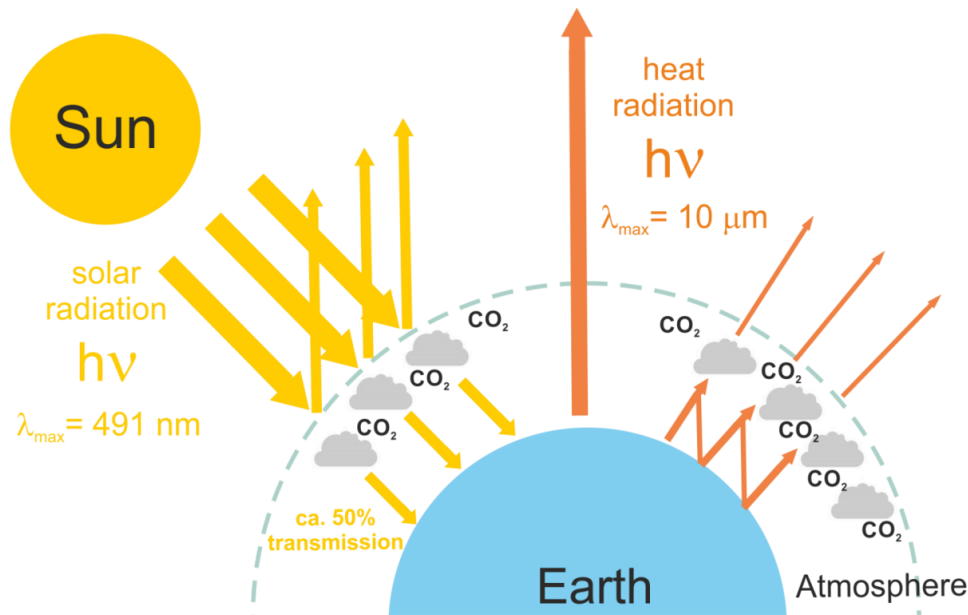
Figure 1.2. Schematic depiction of the so-called greenhouse effect. The maximum intensity of emitted radiation has been estimated based on Wien's displacement law assuming mean temperatures of 5800 K and 298 K for the solar and Earth's surface, respectively. Heat is trapped in Earth's atmosphere through the absorption of infrared radiation (emitted by the Earth's surface) by the greenhouse gases (GHGs).

a certain fraction of the IR-radiation re-emitted by the GHGs does not leave the atmosphere to escape into space (Figure 1.2). This effect is known as the so-called **greenhouse effec**t (GHE). Notably, the (natural) GHE is considered an essential prerequisite for the development of life. In the absence of any GHGs in the atmosphere, the mean temperature of the atmosphere would range from −15 °C to −21 °C, representing environmental conditions that are harmful to life.

Starting with the industrial revolution in the second half of the 18th century, the anthropogenic (non-natural) effects have led to a steady raise of the CO_2 content in our atmosphere due to the increasingly excessive **combustion of fossil fuels** [4] (namely, coal, oil, and natural gas) which serve as primary energy sources, even today. A significant percentage, i.e., 87% of today's anthropogenic CO_2 emissions originate from the burning of fossil fuels. Other main contributors are **deforestation** (in particular through fire clearance, ca. 9%) and the **large-scale production of cement** (ca. 4%).[5]Already in the year 1958, the atmospheric CO_2 content was reported to increase by 47% to a value of ca. 317 ppm (parts per million) compared to the pre-industrial era (i.e., before 1760; ca. 280 ppm).[6] Since the end of the sixties of the last century, the CO_2 content in our atmosphere has continuously been monitored via a dedicated measuring station located at the **Mauna Loa observatory** in Hawaii. This development can be attributed to the pioneering work of **Charles Keeling** (1928-2005) who developed precise analysis instruments and measurement protocols for the quantification of gaseous CO_2 in the atmosphere. The resulting curve of measured data demonstrating the steady raise in the CO_2 content over time (since 1958) is, thus named after him (→ **Keeling curve**, see Figure 1.3a). Reportedly, by 2020, the atmospheric CO_2 concentration has already reached a level of 414.5 ppm, a value which is ca. even 100 ppm above the one at the beginning of the recordings at the Mauna Loa observatory thus demonstrating the accelerated release of CO_2 into the
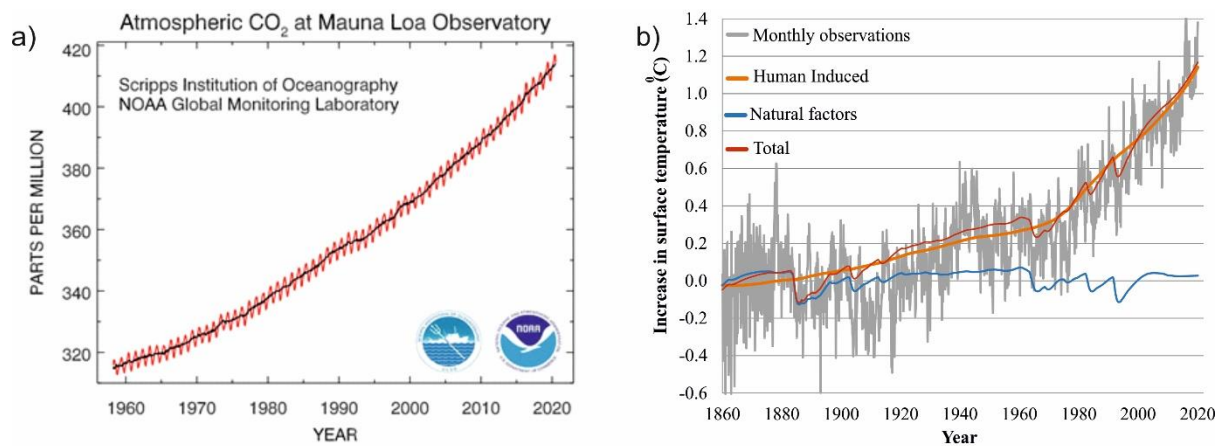
Figure 1.3. a) So-called Keeling curve measured at the Mauna Loa observatory in Hawaii demonstrating the steady increase of the atmospheric CO_2 content[7] (for details see text); b) Increase of the mean temperatures and modelling anthropogenic and non-anthropogenic contributions. Adapted from References 8-9

atmosphere by human activities. Note that the pronounced oscillations superimposed on the steady increase of the CO_2 content are due to seasonal changes of the CO_2 content in the northern hemisphere ($\rightarrow$ annual cycle of vegetation). Also, note that these oscillations are smaller in amplitude and shifted on the time scale when the southern hemisphere is considered. The increase of GHG concentrations in the atmosphere inevitably leads to a disturbance of the energy balance of our planet and in particular to global warming as a consequence of the amplified (anthropogenic) greenhouse effect. The causal relationship between an ***increased atmospheric CO_2*** concentration and ***global warming effects*** is already known to the scientific community since the end of the 19th century.

Systematic meteorological measurements carried out worldwide confirm a steady increase of the global mean temperature (atmosphere and Earth's surface, Figure 1.3b), an effect which conveys drastic consequences not only for the global climate but also for our entire ecosystem ($\rightarrow$ desertification, extreme weather events, rising sea level, etc.). It should be further noted that the **primary global warming** effect might become further amplified by **secondary effects**, e.g., in the form of an accelerated release of methane due to the unfreezing of the permafrost in the tundra of the northern hemisphere. Note that methane has a **global warming potential** that is substantially higher than the one of CO_2 as it can produce 28 times more heat per mass unit, comparatively.[10] Methane levels have also started to rise.[10] Thus, indicating a drastic (negative) impact of the accelerated climate change on the socio-economic conditions worldwide. In response to this global threat policy makers and representatives from 197 countries agreed to undertake measures in order to limit global warming to **2 °C** above the pre-industrial level ($\rightarrow$ **Paris agreement**).[11] These measures aim at transforming our societies comprising the mid- and long-term **carbon-neutral** measures—a domain which is considered a truly **intersectoral challenge** requiring **technology-driven** conversions of (i) the **energy sector**, (ii) the **industry sector**, and (iii) the **transportation sector**.

1.2 Approaches towards CO_2 fixation and valorization

To tackle the global CO_2 problem a mixture of various approaches needs to be followed and realized in parallel to keep the temperature increase below **2 °C** above pre-industrial levels. In

this context, the reduction or the **avoidance of CO_2 emissions** through the combustion of fossil fuels constitutes the highest importance. Further, several concepts and strategies are being currently explored aimed at fixing or valorising CO_2.[12-14] The latter vision considers CO_2 not solely as environmentally harmful but as an abundant carbon source that can be used for the production of valuable chemicals (→ **"CO_2 to value"** concept).[15] Irrespective of which concept of CO_2 fixation/valorization is envisaged, each of these approaches needs to start with the **capture of gaseous CO_2**.[13] Most (energy) demanding is the capture from ambient air **(direct air capture: DAC)**. As an example, *Climeworks*, a spin-off company from ETHZ, has developed and commercialized a DAC process based on amine scrubbing (see: https://climeworks.com/; Figure 1.4). Herein, the gaseous CO_2 from air is fixed by a reversible chemical reaction with primary amines (R-NH$_2$). The CO_2 is subsequently released by thermal treatment of these chemical CO_2 "filters" (→ **thermal looping**).

The limitation of this particular DAC process, at least from an economic point of view, is related to the costs of the thermal looping. As such, the pilot plants for this DAC are operated cost-efficiently in particular at sites where an excess of cheap (geo) thermal energy is available (→ Carbfix company in Iceland: https://www.carbfix.com/).[16] Concepts of **carbon" (CO_2) capture and sequestration** (**CCS**) on a particularly large scale are often based on long-term storage of CO_2, e.g. in exhausted gas fields. An appealing alternative is a geological storage approach (geo- sequestration) where the CO_2 is mineralized in basalts (or other reactive rock formations) in the form of carbonates (→ Carbfix company). [16]
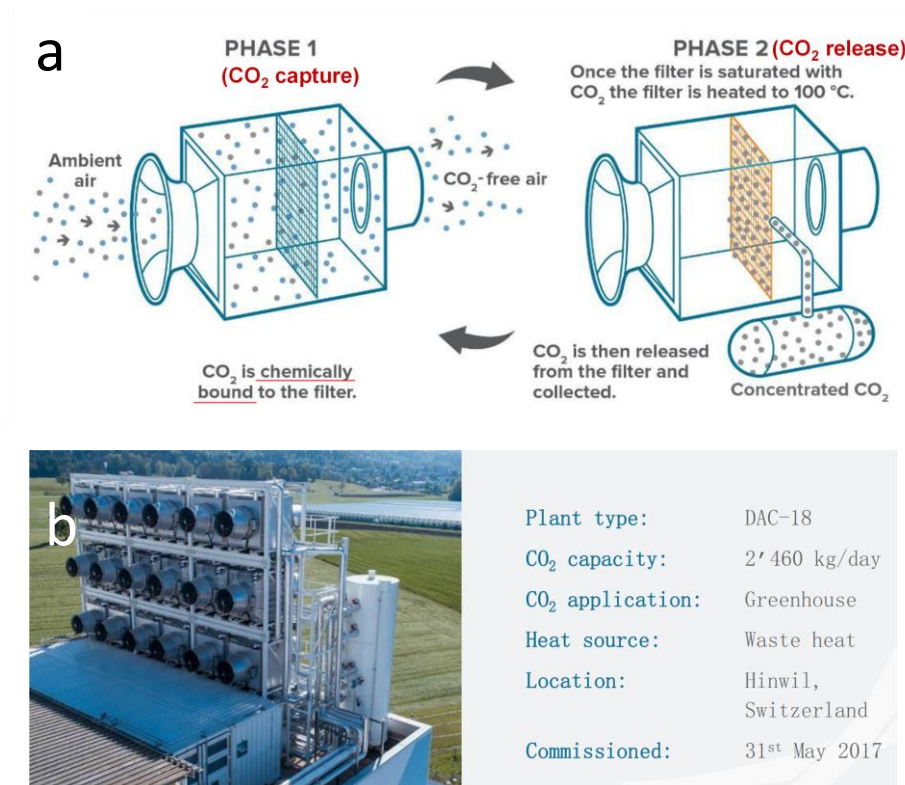
Figure 1.4. a) Schematic depicting the concept of direct air capture (DAC) based on amine scrubbing and thermal looping[17]Cxckrcdrg"xkc"kcgpug<EE"D["'6Œ; b) Picture and figures of merit of Climeworks's CO_2 capture pilot plant in Hinwil (Switzerland).[18] https://www.slideshare.net/IcelandGeothermal/c4-climeworkscapturing-CO_2-from-air.

In contrast to these storage approaches, CO_2 valorization aims at chemically transforming CO_2 into something valuable. Not only the CO_2 capture but also the required CO_2 reduction is highly energy demanding ($\rightarrow$ highly endergonic, $\Delta G > 0$), as it represents formally the reversal of the highly exergonic, ($\Delta G < 0$) combustion of the fossil energy carriers (i.e., coal, oil, and natural gas). From a sustainability point of view, any CO_2 valorization is therefore meaningful only if the energy input required for these endergonic processes originates directly or indirectly from renewable sources (i.e., solar, wind, or hydro energy).

Various concepts of chemical CO_2 conversion are being currently explored which differ in their technological readiness level (TRL).[19-20] Most mature are processes based on classical **heterogeneous catalysis** (catalytic solid/gas systems). Prime examples thereof are the production of CO from CO_2 via the reverse water-gas shift (RWGS) reaction,[21] the synthesis of methanol from CO_2,[22] and the production of renewable synthetic natural gas (SNG) through the hydrogenation of CO_2 to methane.[23] A major industrial player in this field of heterogeneous CO_2 catalysis in Switzerland is **Clariant** located in Basel. (https://www.clariant.com/en/Corporate/News/2020/07/Clariant-Catalysts-powers Ineratecrsquos-green-fuel-production-technology).[24] These processes become appealing not only because of the consumption of environmentally harmful CO_2 serving as a reactant but also due to the sustainable production of the hydrogen required for these processes, e.g. by water electrolysis fed by renewable ("green") electric power. However, processes based on biocatalytic or photocatalytic approaches can be categorized as less mature and are still on an explorative stage.[25-30]
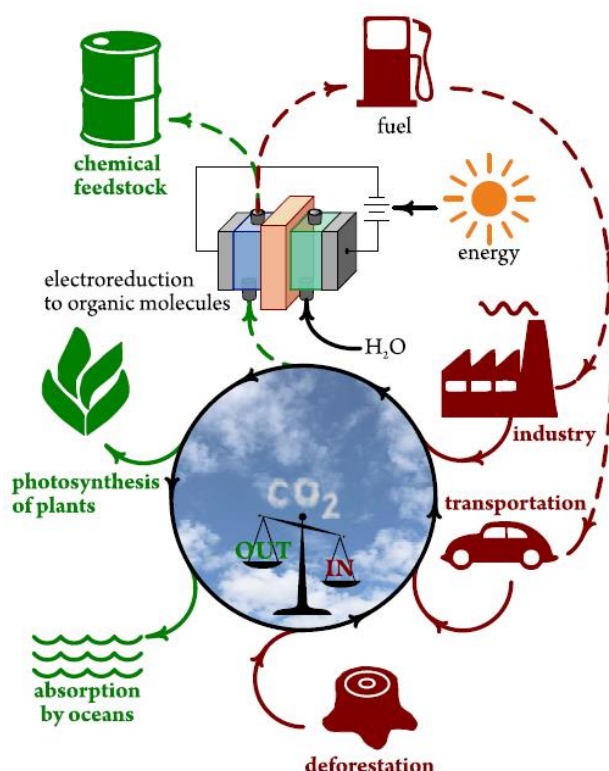
Figure 1.5. Schematic depicting the overall vision of closing the anthropogenic carbon cycle by the sustainable conversion of CO_2 into synthetic fuels or chemical feedstock (platform chemical) powered by solar energy (or wind, hydro). Adapted from Reference 31 with permission from John Wiley and Sons.

Electrochemical means of CO_2 valorization deserve, however, particular attention. This is because electrolysis can transform CO_2 *directly* into value-added products in a fully sustainable manner, though notably, provided the required electricity is generated from renewable sources (i.e., solar, wind, and hydro).[32-34] Figure 1.5 depicts the overall **vision of closing the anthropogenic carbon cycle** through the sustainable production of synthetic fuels and other valuable platform chemicals by direct H_2O/CO_2 co-electrolysis.

1.3 Assessment of possible CO_2RR target products

Depending on the catalyst material used (see discussion in section 1.4.3) the CO_2RR can yield a variety of different reaction products ranging from CO and formate to hydrocarbons (methane,[35] ethylene,[36] ethane,[37] propane[38]) and oxygenates (methanol,[39] ethanol,[40] n-propanol[41]). Even traces of aldehydes have been reported in previous studies.[42] Prior to initiating with any design of new catalyst materials, apparently it is important to identify the possible CO_2RR reaction products which are desirable also from an economic point of view. Such assessments are highly complex and their outcome strongly depends on the initial assumptions these analyses are based on (e.g. electricity costs, product efficiencies, energy efficiencies of the overall process, etc.). In collaboration with the group of Thomas Schmidt from the Paul Scherrer Institute (PSI) in Villigen (Switzerland), our research group carried out an initial assessment in 2015 for the CO_2RR.[43] The results of this analysis including estimates of the production price by electrolysis are summarized in Table 1.

Several factors are important for the decision on possible target products such as the global market size and the expected production costs in comparison to the existing mature processes in the industry. Durst et al.[43] identified, in particular, CO and formate as potential CO_2RR target products. In both cases, the electrolysis approach might become competitive to existing mature synthesis routes. In addition, the global market size for CO is particularly huge (i.e., ca. 210000 Mt year^{-1}). This is primarily because CO is a valuable platform chemical used on large scale for the production of long-chain hydrocarbons via the so-called Fischer-Tropsch process.[44] A recent process development by Siemens/Evonik ($\rightarrow$ Rheticus project)[45] already uses CO produced by CO_2 electrolysis as intermediate for the production of higher alcohols by coupling the electrolysis unit to a biotechnological fermentation unit in which anaerobe bacteria transform mixtures of CO_2/CO/H_2 into butanol and hexanol. The latter serve as ingredients for the subsequent production of fine- plastics at Evonik.[45]

The global market for formate/formic acid is much smaller (ca. 0.8 Mt year^{-1}) compared to the one for CO. Formic acid finds wide use as a preservative and antibacterial agent in livestock feed. It should be noted that the estimated production costs are already today below the current market price. What could be clearly excluded from the list of desirable target products in the study by Durst et al. are hydrocarbons like methane and ethylene.[43] In this initial assessment, C-C coupled alcohols such as ethanol and n-propanol were not included. Both oxygenates are liquid CO_2RR products (beneficial for transportation purposes) and have an extremely high energy density (e.g., n-propanol: 27.0 MJ L^{-1}) which makes them candidates that might be used in the future for temporary energy storage purposes or directly as synthetic fuels (see Figure 1.6).

Table 1. Current market price and gross margin for various EC-CO$_2$RR[43, 46]

Product	Produced by	Current market price [$ kg^{-1}]	Current production volume [Mt y^{-1}]	Production price by electrolysis [$ kg^{-1}]
H$_2$	Steam reforming, partial oxidation o methane or gasification of coal	2-4	65	4
CH$_4$	Methanogenesis or hydrogenation of CO$_2$	<0.08	2400	2-4
C$_2$H$_4$	Pyrolysis or vapocracking	0.8-105	141	1.6-3.2
CO	Boudouard reaction	0.65	210000	0.27-0.54
HCOO$^-$/ HCOOH	Hydrolysis from methyl formate and formamide or by-product of acetic acid production	0.8-1.2	0.8	0.17-0.34
CH$_3$OH	From natural gas, coal biomass, waste	0.4-0.6	100	0.70-1.4
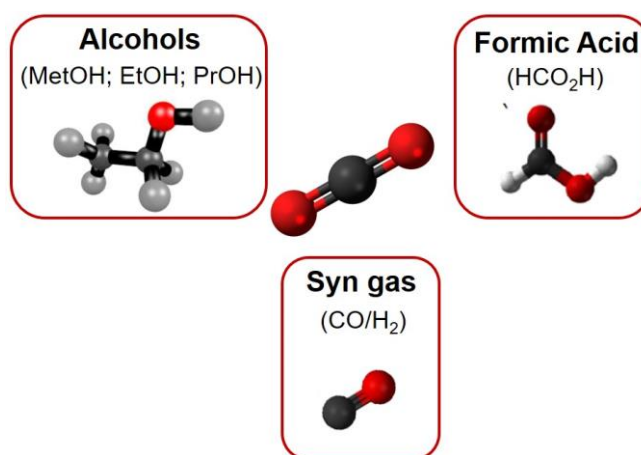
Figure 1.6 CO$_2$RR products targeted in this Ph.D. project

Based on these considerations this Ph.D. project was focussed on the CO$_2$RR catalyst development/optimization for the production of CO, formate, and higher alcohols (ethanol, n-propanol) as depicted in Figure 1.6.

1.4. Thermodynamics and Kinetics Aspects: electrochemical CO$_2$ reduction reaction

1.4.1 Thermodynamic Aspects

The discipline of chemistry that deals with the inter-relation of electrical and chemical effects are known as electrochemistry. Generally, it involves two types of processes, namely: spontaneous and non-spontaneous processes. To conduct these reactions, an electrochemical cell is required. An electrochemical cell that involves the generation of electric current as a result of the spontaneous reaction is called as galvanic or voltaic cell whereas an electrolytic cell involves the non-spontaneous reaction where an external bias is required to drive the

electrochemical reaction. An electrochemical reaction constitutes two half-cell reactions occurring at two electrodes. One of them is the oxidation (loss of electrons, at the anode) and the other one is the reduction (gain of electrons, at the cathode) occurring in two independent half-cells separated by ion exchange membrane (or salt bridge). Generally, three electrode arrangement is employed to carry out the electrochemical reaction. The electrode at which the half-cell reaction of special interest is carried out is referred to as the working electrode (WE), while the other is referred to as the counter electrode (CE). In this setup, a third electrode known as the reference electrode (RE) is utilized. Interestingly, in the case of CO_2 reduction reaction (CO_2RR), the WE is the cathode as the reduction reaction is of interest here while at the CE, an oxygen evolution reaction typically occurs (OER).

CO_2 is known to be thermodynamically stable (O=C=O) with sp hybridization of the carbon atom and delocalized ⊓ bond electrons. The C=O bond energy $E_{C=O}$ [187 (2×93.5) Kcal/mol] is much higher than the $E_{O=O}$ bond energy [116 (2×58) Kcal/mol] and the $E_{C=C}$ bond energy [145 (2×72.5) Kcal/mol].[47] Thus, in order to break the C=O double bond a substantial amount of energy is required to obtain a certain reaction rate which scales, in an electrochemical electrolysis experiment, with the applied overpotential.

The maximum of reversible work of a thermo-dynamical system at constant temperature and pressure that can be gained is represented by the change of the Gibbs free energy (under standard conditions, 298.15 K, 1 bar).

$$\Delta G° = \Delta H° - T\Delta S° \qquad (1)$$

Here, ΔH represents the enthalpy change, T is the system temperature, and ΔS refers to the entropy change. In an electrochemical system, the equation transforms for a reversible reaction at constant temperature and pressure to

$$\Delta G° = -nFE° \qquad (2)$$

where n represents the number of transferred electrons, F is the Faradays' constant (96485.33 C mol^{-1}), and $E°$ is the standard potential. The reaction becomes spontaneous when the $\Delta G°$ yields a negative value.

From thermodynamics, we know that the Gibbs free energy is related to the concentration of reactants and products (reaction quotient, Q) and can obtain the relationship between electrode potential and reaction quotient, known as the Nernst equation.

$$E = E° - \frac{RT}{nF}\ln\frac{Cr}{Co} \qquad (3)$$

where Cr/Co is the bulk concentration of Reduced and Oxidized species, $E°$ is the standard cell potential, R is the universal gas constant, and n is the number of electrons transferred.
At standard conditions the conversion of CO_2 to various products is an endergonic process, which implies that it will take a specific amount of energy to progress, depending on the intended product. Knowing the Gibbs free energy change, the corresponding standard electrode potential can be calculated. Relevant standard potentials for the OER (oxygen evolution reaction), the HER (hydrogen evolution reaction), and for the CO_2RR (CO_2 reduction reaction) products are listed in Table 2.[48]

Table 2: Half-cell reactions and corresponding standard potentials relevant to the CO_2RR. [48-49]

Reaction	n	$E°$ / V vs SHE	Product
$2H_2O \rightarrow O_2 + 4H^+ + 4e^-$	4	1.23	Oxygen
$2H^+ + 2e^- \rightarrow H_2$	2	0	Hydrogen
$CO_2 + e^- \rightarrow CO_2^{\cdot-}$	1	−1.90	CO_2 anion radical
$CO_2 + 2H^+ + 2e^- \rightarrow CO(g) + H_2O$	2	−0.10	Carbon monoxide
$CO_2 + 2H^+ + 2e^- \rightarrow HCOOH(aq)$	2	−0.20	Formic acid
$CO_2 + H_2O + 2e^- \rightarrow HCOO^- + OH^-$	2	−1.078	Formate
$CO_2 + 8H^+ + 8e^- \rightarrow CH_4 + 2H_2O$	8	0.17	Methane
$2CO_2 + 12H^+ + 12e^- \rightarrow C_2H_4 + 4H_2O$	12	0.07	Ethylene
$CO_2 + 6H^+ + 6e^- \rightarrow CH_3OH + 4H_2O$	6	0.030	Methanol
$2CO_2 + 12H^+ + 12e^- \rightarrow C_2H_5OH(aq) + 3H_2O$	12	0.085	Ethanol
$3CO_2 + 18H^+ + 18e^- \rightarrow C_3H_7OH(aq) + 5H_2O$	18	0.09	Propanol

Note that the OER is the common counter-reaction to the CO_2RR in aqueous reaction environments no matter which cell design (H-type cell, CO_2-fed flow cell) is used. According to Table 2, it is obvious that the calculated standard potentials of the CO_2RR fall within the same potential range as the one for the HER. Already from these thermodynamic considerations, the HER is inferred as a parasitic side reaction to the CO_2RR, at least when the CO_2 electrolysis is conducted in an aqueous reaction environment. However, in real electrolysis reactions, the CO_2RR is typically carried out at substantially more negative (cathodic) potentials to account for the enormous kinetic hindrance associated with the CO_2 activation. The CO_2RR is a coupled (multiple) electron/proton transfer reaction (see Table 2). This is the reason for the strong pH dependence of this electrolysis reaction.

Changes of the half-cell potential as a function of the electrolyte pH are displayed for a series of different CO_2RR products in the form of a so-called Pourbaix diagram (Figure 1.7). Note that the slope of the standard potential changes (black solid lines) is the same in most cases as the number of transferred protons and electrons is identical for these reactions (see Table 2). The formation of formate from CO_2 is an exception. The green dotted line in Figure 1.7 represents the pH-dependent change of the HER half-cell reaction. What is also important for the thermodynamic consideration of the system is the stability of the CO_2 and its reaction products in an aqueous environment. The pH-dependent stability of the carbonic acid (H_2CO_3), the bicarbonate anion (HCO_3^-), and the carbonate anion (CO_3^{2-}) are also displayed in the Pourbaix diagram (see vertical green solid lines) along with the oxidative transformation of methanol, one possible CO_2RR product (see Table 2), into the CO_2 derivatives. Thus, two important conclusions can be drawn from the diagram: (i) products of the CO_2RR, e.g., methanol, can easily be re-oxidized (at least from a thermodynamic point of view) at the anode. When considering a real electrolysis cell, a separation between catholyte and anolyte seems therefore to me mandatory thus avoiding fast re-oxidation of the formed CO_2RR products at the anode. (ii) Dissolved CO_2 is not stable at high pH values as it transforms into bicarbonate
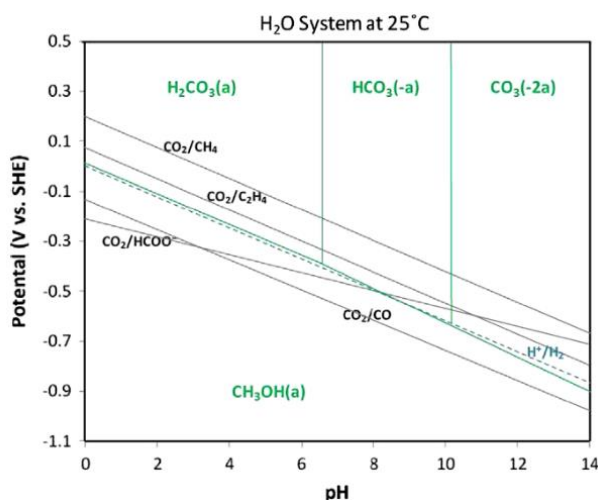
Figure 1.7. Pourbaix diagram for several cathodic and anodic reactions relevant to the CO_2 electrolysis at 25 °C (source: Hoang Le et al.)https://digitalcommons.lsu.edu/gradschool_theses/605.[72]

or carbonate under strongly alkaline conditions. Physically dissolved CO_2 is typically considered as the reactant whereas bicarbonate and carbonate are considered on most electrocatalysts as non-reactive. Therefore, it is imperative to study the changes of the solution pH during the concerted HER/CO_2RR. The parasitic HER will, at least in non-buffered systems, inevitably lead to the consumption of protons (or the production of hydroxide anions through water splitting) thereby, shifting the pH to higher values and, as a consequence of this, further decreasing the concentration of free CO_2 in the aqueous electrolyte.

1.4.2 Kinetic aspects

In addition to thermodynamics, the kinetic aspects of CO_2RR also need to be considered. Potentials closer to standard potential computed using thermodynamics considerations are required for CO_2RR, however, in practice, significant negative potentials are required as previously stated. Thermodynamics deals with the equilibrium conditions whereas kinetics comes into play when a certain reaction rate is achieved. In general, the electrode reaction can be subdivided into three steps as detailed herein: It starts with the transport of reactant species from the bulk electrolyte to the electrode (first mass transfer process), followed by the heterogeneous electron transfer at the electrode surface, and completed by the transport of the formed product species into the bulk of the electrolyte (second mass transfer process).[49]

To drive the non-spontaneous reaction, an excess of energy or overpotential ($\eta = E - E_{eq}$, it is the difference between thermodynamically determined reduction potential and experimentally applied/observed potential) is required in order to overcome the resistances or energy barriers. The total observed resistance includes the activation overpotential at the cathode ($R_{cathode}$), the barrier related to OER at the anode (R_{anode}), ohmic losses due to conduction of ion in the bulk electrolyte (R_{ions}), the resistance of the membrane ($R_{membrane}$), resistance due to gas evolution (bubble) at the cathode (due to CO and H_2)[51] and anode (OER), and the resistance associated with the cell components and contacts between these components.[52-53]

At least, upon excluding mass transfer effects on the reaction rate (at low overpotentials, low current densities) the current density is solely dependent on the applied overpotential ($\rightarrow$ pure

charge transfer control). Under these conditions, the current density/overpotential relation can be represented by the so-called Butler-Volmer (B-V) equation[49]

$$i = i_\circ[e^{-\frac{\alpha Fz}{RT}\eta} - e^{\frac{(1-\alpha)Fz}{RT}\eta}] \qquad (4)$$

where z is the number of electrons involved in the electrode reaction, F is Faraday constant, R is the universal gas constant, T is the absolute temperature in K, α is charge transfer constant or symmetry factor, a dimensionless quantity, i is the faradaic current density, $i_\circ$ is the exchange current density and η is the applied overpotential.

From Eq. 4, it can be concluded that the lower the exchange current, the higher overpotential is required for a certain current impeding the kinetics of the reaction. Limiting case scenarios are evident at lower and higher overpotential (η).

At lower η: in case of sufficiently low η, the B-V equation can be expressed as

$$i = -i_\circ \frac{Fz}{RT} \eta \qquad (5)$$

At higher η: in case of large negative or positive η, eq. 1.3 transforms into

$$\eta = \frac{RT}{z\alpha F}[\ln i_\circ - \ln i] \qquad (6)$$

Comparing it with the Tafel equation $\eta = a + b \, logi$ $\qquad (7)$

constants a and b could be determined as $a = \frac{2.3 \, RT}{z\alpha F} \, logi_\circ$ and $b = \frac{-2.3 \, RT}{z\alpha F}$. A plot of $log \, i$ vs. η, known as the Tafel plot, is useful for the determination of kinetic parameters (asymmetry factor, exchange current density).

1.4.3 Role of catalyst: Classification of metals

The very first step in the CO_2RR entails the reduction of CO_2 to CO_2^{*-} that involves a one-electron transfer to bend the linear molecule, which, in turn, requires higher overpotentials (-1.9 V vs SHE).
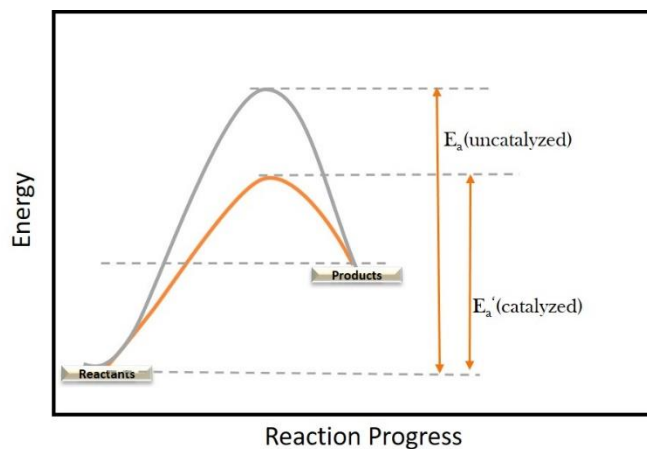
Figure 1.8 Schematic representation of the role of catalyst in the CO_2 reduction reaction depicting energy profile in case of uncatalyzed (grey line) and catalysed reaction (orange line). Catalyst provides an alternative reaction pathway accelerating the reaction.

Thus, the formation of $CO_2{}^{*-}$ radical anion is regarded as the rate-determining step (RDS) in many studies and requires a proper catalyst to lower the energy barrier while suppressing hydrogen evolution reaction (HER). A catalyst accelerates the rate of reaction by reducing the activation energy E_a ($\rightarrow$ Figure 1.8) while itself not undergoing any permanent change. In principle, chemical reactions occur faster in the presence of a catalyst because it provides an alternative reaction pathway than non-catalyzed reactions with no change in equilibrium. In other words, in a catalysed reaction, the overall reaction barrier is lowered by the catalyst, thus leading to faster conversion. It occurs by a different energetically favoured reaction pathway (Figure 1.8). In addition, the catalyst may further influence product selectivity, in scenarios where multiple products are formed. The pioneering work by Hori et al. classified monometallic catalysts into subgroups based on their selectivity towards CO_2 reduction products.[42] In Table 3, materials are listed according to the main reaction products formed at a current density of 5 mA cm^{-2}. Basically, the metallic catalysts can be divided into four major groups according to the observed product selectivity.

i)   Group 1 consisting of Pb, Tl, Hg, Cd, In, and Sn selectively produces formate.
ii)   Group 2 consisting of Ag, Au, Pd, Zn, and Ga selectively produces CO.
iii) Group 3 consisting of Ni, Fe, Pt, and Ti selectively produces hydrogen.
iv)   Group 4: Cu is the only metal producing hydrocarbons to alcohols; C-C coupling is possible.

However, this result was obtained on polycrystalline materials. Efforts have been made to develop different nanomaterials with different shapes and sizes to improve the selectivity toward a certain specified product.

Catalyst	I /mAcm^{-2}	E / V RHE	Faradaic efficiency (%)							
			H$_2$	CO	HCOO	CH$_4$	C$_2$H$_4$	EtOH	PrOH	Total
Pb	5	-1.23	5	0	97.4	0	0	0	0	102.4
Tl	5	-1.20	6.2	0	95.1	0	0	0	0	101.3
Hg	0.5	-1.11	0	0	99.5	0	0	0	0	99.5
Cd	5	-1.23	9.4	13.9	78.4	1.3	0	0	0	103
In	5	-1.15	3.3	2.1	94.9	0	0	0	0	100.3
Sn	5	-1.08	4.6	7.1	88.4	0	0	0	0	100.1
Au	5	-0.74	10.2	87.1	0.7	0	0	0	0	98
Ag	5	-0.97	12.4	81.5	0.8	0	0	0	0	94.6
Zn	5	-1.14	9.9	79.4	6.1	0	0	0	0	95.4
Pd	5	-0.80	26.2	28.3	2.8	2.9	0	0	0	60.2
Ga	5	-0.84	79	23.2	0	0	0	0	0	102
Ni	5	-1.18	88.9	0	1.4	1.8	0.1	0	0	92.4
Fe	5	-0.57	94.8	0	0	0	0	0	0	94.8
Pt	5	-0.67	95.7	0	0.1	0	0	0	0	95.8
Ti	5	-1.20	99.7	tr.	0	0	0	0	0	99.7
Cu	5	-1.04	20	1.3	9.4	33.3	25.5	5.7	3	103.5

Table 3: Transition metals grouped according to their selectivity towards CO$_2$RR products, adapted from Y. Hori et. al.[42]
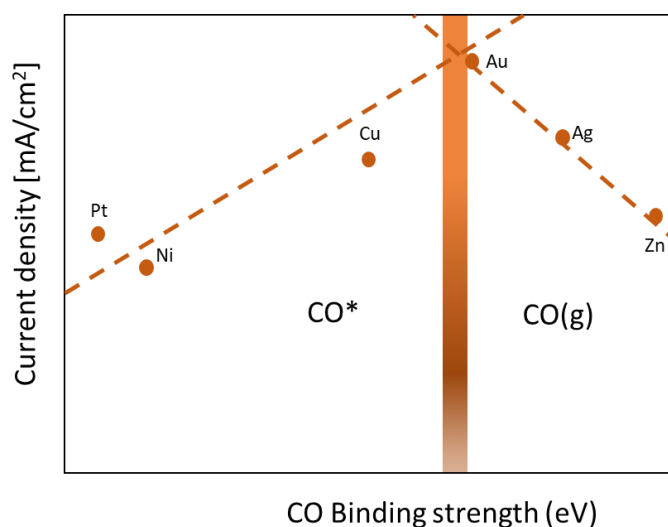
Figure 1.9 Volcano plot for some CO producing catalysts, adapted from Kuhl et al.[35]

This difference in selectivity can be rationalized based on so-called **volcano plots** that correlate the experimentally derived activity/selectivity of a given catalyst to a key descriptor of the reaction of interest. The latter is often derived from modeling / (DFT) calculations. An example from the literature is given in Figure 1.9 relating the CO_2RR current density at a given electrolysis potential to the binding strength of CO which is considered as a key intermediate for multiple CO_2RR products. According to the Sabatier principle, an effective catalyst should bind the reactant and the formed intermediates in a highly balanced manner. A binding that is too strong might lead to an irreversible poisoning (chemical degradation) of the catalyst. At the same time, in case the binding of the catalyst to the reactant is too weak, no reaction might be initiated at all. The catalysts included in the volcano plot in Figure 1.9 can be classified into three categories.

Those located on the right-hand side of the volcano maximum (e.g., Au, Ag → weak CO binding) demonstrate a high selectivity towards CO as a CO_2RR product. Due to its weak binding to the catalyst, the formed CO is easily released from the catalyst surface. Those catalysts located on the left-hand side of the volcano maximum (e.g., Ni, Pt → extremely strong CO binding) tend to get irreversibly poisoned by the CO intermediate. The main electrolysis reaction product in these cases is hydrogen. Only copper demonstrates a balanced interaction of the CO intermediate to the catalyst surface (close to the volcano maximum on the high binding energy side) thus explaining why Cu is capable to transform CO further into hydrocarbons (increased residence time of CO on the catalyst surface) and why Cu even allows the C-C coupling reactions. For the latter, a high abundance of chemisorbed CO on the catalyst surface is required.

1.4.4 CO_2RR possible reaction pathways

CO_2RR occurs at the interface between the electrode (catalyst) and electrolyte, therefore, involves three steps: CO_2 chemisorption taking place at electrode surface followed by coupled electron/proton transfer forming key intermediates and the subsequent desorption of products from the catalyst surface. As several products can be formed in CO_2RR, there are various possible pathways for obtaining a certain product. Previous literature shows that extensive
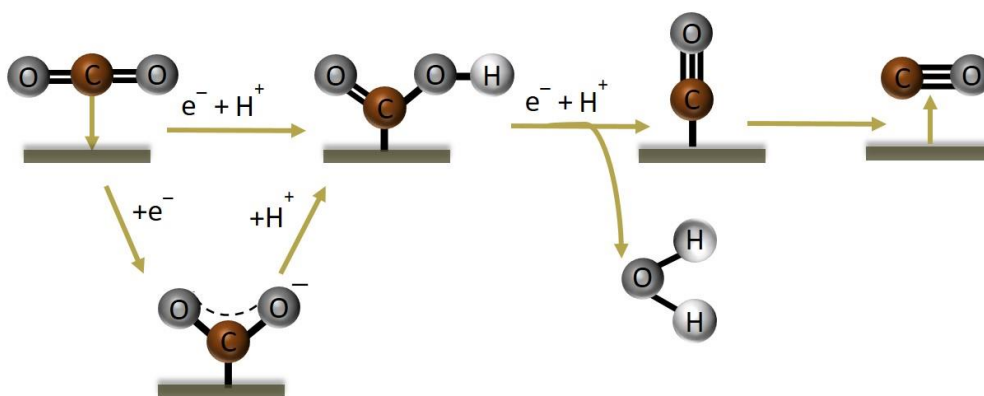
Figure 1.10 Reaction pathway for the formation of CO on a catalyst. Adapted from 'references 54-56 . One pathway could be direct conversion to *COOH (top row) and the other one is through CO_2*$^-$ (bottom).

efforts have been made to explore the mechanism of CO_2 activation and reduction.

Products such as CO, formate involving two-electron transfers are rather quite simpler and better explored than the ones involving more than two-electron transfers or complex C-C coupling (hydrocarbons and oxygenates). The reaction pathway for CO formation is depicted in Figure 1.10. CO_2 to CO conversion involves the formation of carboxyl intermediate (*COOH) via concerted proton-electron transfer. Subsequently, a second coupled proton-electron transfer (H^+/e^-) attacks the oxygen atom (OH) of carboxyl intermediate, and yielding CO and H_2O (top row of the figure). Finally, the formed CO gets desorbs from the electrode surface as explained in the previous section.[54] In this mechanism, conversion of CO_2 to form carboxyl intermediate (*COOH) and desorption of CO from the catalyst surface were assumed to be the limiting step.[57] Alternatively, another pathway suggested electron transfer that gives CO_2*$^-$ radical anion adsorbed on the surface followed by proton absorption deriving to the carboxyl intermediate (*COOH, bottom row) (i.e., Ag, Au). The formation of CO_2*$^-$ radical anion is considered a rate-determining step in the CO formation. Both of the mentioned pathways were suggested to show dependencies on pH promoting the yield of *COOH over *CO with the increase in pH or pressure.[58]

Mechanistic investigations have revealed four different reaction pathways for formate formation (Figure 1.11). The reaction route is determined by a catalyst's capacity to adsorb and desorb particular reaction intermediates. Some of the reaction intermediates involve the CO_2 insertion, an O-bond intermediate, C-bound intermediate, or bicarbonate as intermediate.[59]

CO_2 insertion into the metal-hydrogen (M-H) bond could be one of the possible mechanisms to form *HCOO intermediate and subsequently followed by *HCOO reduction to form HCOOH (Figure 1.11 top route).[55] This mechanism occurs on Pd-based catalysts.[60] Pd has a strong binding affinity towards hydrogen so that H_2 gets absorbed in the Pd lattice and the β-hydride formation takes place on the surface giving PdH_x when driven at the potentials of <0 V vs. RHE.[60] Consequently this surface hydride PdH_x will carry out the further reaction to form *HCOO from CO_2 thereby leading to the final product which is formic acid at low overpotential.[61-62]

In particular, oxophilic (non-transition) metals (e.g., Sn, In) [63-64] favor those CO_2RR reaction pathways that involve reductive CO_2 adsorption via metal-oxygen (M-O) coordination.
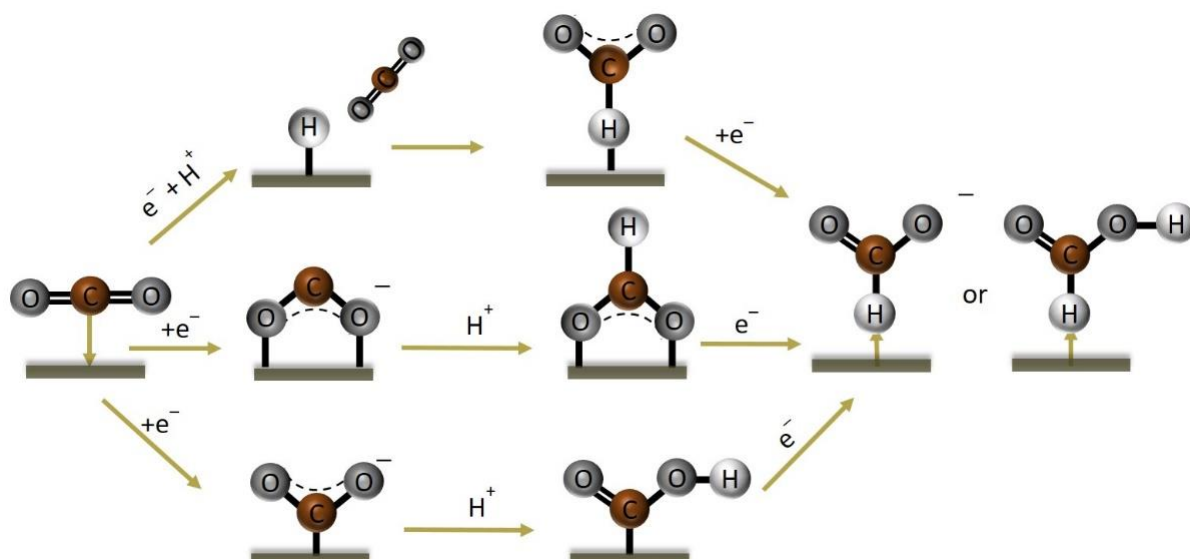
Figure 1.11 Reaction pathway for the formation of HCOO⁻ on a catalyst.Cf cr vgf "htqo "Tghgt gpegu56, 650Top row suggests the pathway via CO_2 insertion into M-H bond; the second pathway is via M-O coordination (middle row); an M-C bound pathway (bottom row) yielding formate. Formic acid can be subsequently formed via H⁺/ e⁻ transfer or depending on pH.

The first electron is transferred to CO_2 forms a weakly adsorbed CO_2^{*-} radical anion intermediate (Figure 1.11, middle route). Followed by the transfer of protons and electrons from the reaction occurring between the CO_2^{*-} radical and proton donors like water, bicarbonate, and hydronium ions which in turn form formate.[58, 60] In the M-O reaction pathway, HCOO* species emerged as the key intermediate for formate production.

When the reaction pathway involves C bound, the CO_2^{*-} radical anion gets attached by the C-atom on the catalyst surface (Figure 1.11, bottom route). Followed by the interaction of this radical anion with H⁺, it yields to adsorbed *COOH. Finally, *COOH gets reduced to HCOO⁻/HCOOH. However, the *COOH intermediate decomposes into M-H⁺ CO_2 or loses OH⁻ through a nucleophilic attack to form the M-C=O⁺ intermediate as it is unstable.[66] This mechanism is likely to happen in carbophilic catalysts (i.e., Cu- and Ru) attributed to their basic natures and because the bond formed by electron transfer from CO_2 to unoccupied metal orbitals is stabilized by back-donation from the d orbitals of the metal atom.[59]

Another pathway involves adsorbed *OH and CO_2 to form the adsorbed bicarbonate (CO_3H^*) species.[67-68] Afterward, the reaction intermediate interacts with H⁺ and receives an electron to form *HCOO and *OH. When *HCOO undergoes reduction by taking up another electron, HCOOH is readily released. Catalysts with relatively high *OH binding strengths (like Bi-Sn, $PdSnO_2$) [67, 69] are likely to show these reaction pathways. In the same vein, a recent report on Bi_xO_y reported a sub-carbonate pathway for formate.[70]

The reaction route for C1 and C2 formation with more than two electrons transfer is even more complicated. Among C1 products, CH_4 and CH_3OH formation are quite complex as it requires 8 and 6 electrons, respectively. Figure 1.12 depicts the mechanism for CH_4, CH_3OH, C_2H_4 formation. *CO is a key descriptor towards C1 and C2 formation. There are two pathways for CH_4 formation either by *HCO (middle route) or *COH (bottom route) routes. *CO can subsequently undergo hydrogenation to form *HCO, *H_2CO, and *H_3CO (methoxy). The
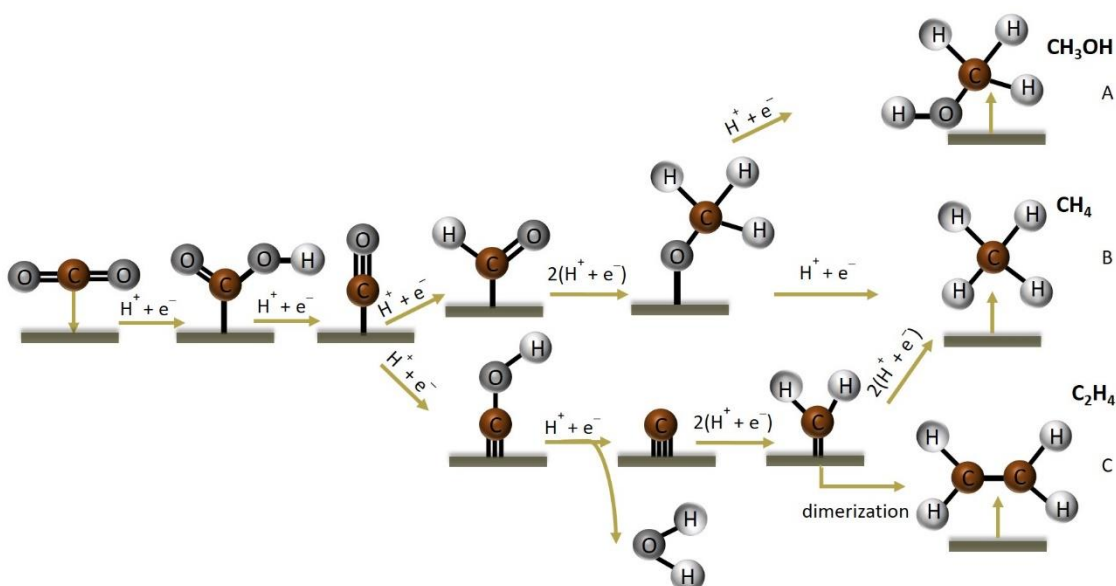
Figure 1.12 Reaction pathway for the C1 (CH₄ & CH₃OH) and C2 (C₂H₄) formation on a catalyst. Adapted from References 55-56, 71-72. Scheme A, B, and C show routes for the formation of CH₃OH, CH₄, and C₂H₄ respectively.

methoxy intermediate can be reduced to CH_4 and *O. Alternatively, *H_3CO can also further get reduced to yield methanol CH_3OH. Another possible route, as proposed, is via *COH intermediate formation which is further reduced to an adsorbed C. This surface C can further get reduced to form *CH, *CH_2, *CH_3, and finally yield CH_4. Poorly oxophilic catalyst (Au) material is seen to yield CH_3OH whereas strongly oxophilic catalyst is reported to produce CH_4. Different possible pathways have been reported in the past few decades for C2 formation by mechanistic and theoretical elucidations. For example, ethylene (C_2H_4) formation occurs via the coupling of *CH_2 species. An alternative pathway suggested dimerization of *CO which transforms to give $C_2O_2^-$, subsequently protonated to *CO-COH yielding higher carbon chain products.[55, 73]

1.4.5 Aim of the thesis

This Ph.D. thesis focuses on the development of novel high surface area catalysts for electrochemical CO_2 reduction. Novel metallic catalysts were synthesized by means of the dynamic hydrogen bubble template-assisted electrodeposition process. This method was employed to prepare monometallic and binary catalysts as well. An extensive investigation was done on the performance of the catalyst during the course of CO_2RR through various characterization tools. Additionally, the role of oxides was studied by *ex-situ* and *in-situ operando* measurements. With the aim of up-scaling the process, the deposition method was successfully transferred to the 3D substrate such as gas diffusion electrodes (GDE) which is generally used in the flow cell. Other non-aqueous systems (i.e., ionic liquids) were also explored for the CO_2 reduction process.

1.4.6 References:

(1). von Schuckmann, K.; Palmer, M. D.; Trenberth, K. E.; Cazenave, A.; Chambers, D.; Champollion, N.; Hansen, J.; Josey, S. A.; Loeb, N.; Mathieu, P. P.; Meyssignac, B.; Wild, M., An imperative to monitor Earth's energy imbalance. *Nat. Clim. Chang.* **2016,** *6* (2), 138-144.

(2). National Oceanic and Atmospheric Administration (NOAA), E. S. R. L. A. G. G. I.

(3). https://earthobservatory.nasa.gov/features/EnergyBalance/page7.php, (accessed 20 June 2021).

(4). Roser, H. R. a. M., "fossil fuel," Published online at OurWorldInData.org, 2019. [Online]. Available: https://ourworldindata.org/fossil-fuels.

(5). https://www.che-project.eu/news/main-sources-carbon-dioxide-emissions, (accessed 20 June 2021).

(6). https://www.esrl.noaa.gov/gmd/ccgg/trends/data.html, (accessed 22 June 2021).

(7). http://scrippsco2.ucsd.edu/data/atmospheric_co2/primary_mlo_co2_record, http://www.esrl.noaa.gov/gmd/ccgg/trends/(accessed 22 June 2021).

(8). Haustein, K.; Allen, M. R.; Forster, P. M.; Otto, F. E. L.; Mitchell, D. M.; Matthews, H. D.; Frame, D. J., A real-time Global Warming Index. *Sci. Rep* **2017,** *7* (1), 15417.

(9). https://globalwarmingindex.org/AWI/info_page.html, (accessed 26 March 2021).

(10). https://www.epa.gov/ghgemissions/understanding-global-warming-potentials, (accessed 20 March 2021).

(11). http://unfccc.int/files/essential_background/convention/application/pdf/english_paris_agree ment.pdf, (accessed 20 March 2021).

(12). Kondratenko, E. V.; Mul, G.; Baltrusaitis, J.; Larrazabal, G. O.; Perez-Ramirez, J., Status and perspectives of CO_2 conversion into fuels and chemicals by catalytic, photocatalytic and electrocatalytic processes. *Energy Environ. Sci.* **2013,** *6* (11), 3112-3135.

(13). Al-Mamoori, A.; Krishnamurthy, A.; Rownaghi, A. A.; Rezaei, F., Carbon Capture and Utilization Update. *Energy Technol.* **2017,** *5* (6), 834-849.

(14). Chu, S.; Majumdar, A., Opportunities and challenges for a sustainable energy future. *Nature* **2012,** *488* (7411), 294-303.

(15). Jhong, H.-R. M.; Ma, S.; Kenis, P. J. A., Electrochemical conversion of CO_2 to useful chemicals: current status, remaining challenges, and future opportunities. *Curr. Opin. Chem. Eng.* **2013,** *2* (2), 191-199.

(16). https://www.carbfix.com/, (accessed 10 June 2021).

(17). Beuttler, C.; Charles, L.; Wurzbacher, J., The Role of Direct Air Capture in Mitigation of Anthropogenic Greenhouse Gas Emissions. *Frontiers in Climate* **2019,** *1*, 10.

(18). https://climeworks.com/,https://www.slideshare.net/IcelandGeothermal/c4-climeworks-capturing-CO_2-from-air (accessed 10 June 2021).

(19). Roh, K.; Bardow, A.; Bongartz, D.; Burre, J.; Chung, W.; Deutz, S.; Han, D.; Heßelmann, M.; Kohlhaas, Y.; König, A.; Lee, J. S.; Meys, R.; Völker, S.; Wessling, M.; Lee, J. H.; Mitsos, A., Early-stage evaluation of emerging CO_2 utilization technologies at low technology readiness levels. *Green Chem.* **2020,** *22* (12), 3842-3859.

(20). Roh, K.; Al-Hunaidy, A. S.; Imran, H.; Lee, J. H., Optimization-based identification of CO_2 capture and utilization processing paths for life cycle greenhouse gas reduction and economic benefits. *AlChE J.* **2019,** *65* (7), e16580.

(21). Zhu, M.; Ge, Q.; Zhu, X., Catalytic Reduction of CO_2 to CO via Reverse Water Gas Shift Reaction: Recent Advances in the Design of Active and Selective Supported Metal Catalysts. *Trans. Tianjin Univ.* **2020,** *26* (3), 172-187.

(22). Carbon Recycling International, C. R. I., http://www.carbonrecycling.is/, (accessed 6 June 2018).

(23). Rönsch, S.; Schneider, J.; Matthischke, S.; Schlüter, M.; Götz, M.; Lefebvre, J.; Prabhakaran, P.; Bajohr, S., Review on methanation - From fundamentals to current projects. *Fuel* **2016,** *166*, 276-296. (24).https://www.clariant.com/en/Corporate/News/2020/07/Clariant-Catalysts-powers-Ineratecrsquos-green-fuel-production-technology, (accessed 12 June 2021).

(25). Deng, H.; Xu, F.; Cheng, B.; Yu, J.; Ho, W., Photocatalytic CO_2 reduction of C/ZnO nanofibers enhanced by an Ni-NiS cocatalyst. *Nanoscale* **2020,** *12* (13), 7206-7213.

(26). Zhang, S.; Yin, X.; Zheng, Y., Enhanced photocatalytic reduction of CO2 to methanol by ZnO nanoparticles deposited on ZnSe nanosheet. *Chem. Phys. Lett.* **2018,** *693*, 170-175.

(27). Wang, H.; Zhang, L.; Wang, K.; Sun, X.; Wang, W., Enhanced photocatalytic CO2 reduction to methane over WO3·0.33H2O via Mo doping. *APPL CATAL B-ENVIRON* **2019,** *243*, 771-779.

(28). Ito, R.; Akatsuka, M.; Ozawa, A.; Yamamoto, M.; Tanabe, T.; Yoshida, T., Photocatalytic Activity of Metal Oxide Supported Gallium Oxide for CO2 Reduction with Water. *Bull. Chem. Soc. Jpn.* **2020,** *93* (5), 694-700.

(29). Li, X.; Song, X.; Ma, C.; Cheng, Y.; Shen, D.; Zhang, S.; Liu, W.; Huo, P.; Wang, H., Direct Z-Scheme WO3/Graphitic Carbon Nitride Nanocomposites for the Photoreduction of CO2. *ACS Appl. Nano Mater.* **2020,** *3* (2), 1298-1306.

(30). Shehzad, N.; Tahir, M.; Johari, K.; Murugesan, T.; Hussain, M., A critical review on TiO2 based photocatalytic CO2 reduction system: Strategies to improve efficiency. *J. CO2 Util.* **2018,** *26*, 98-122.

(31). Rudnev, A. V.; Fu, Y.-C.; Gjuroski, I.; Stricker, F.; Furrer, J.; Kovács, N.; Vesztergom, S.; Broekmann, P., Transport Matters: Boosting CO2 Electroreduction in Mixtures of [BMIm][BF4]/Water by Enhanced Diffusion. *ChemPhysChem* **2017,** *18* (22), 3153-3162.

(32). Lim, R. J.; Xie, M.; Sk, M. A.; Lee, J.-M.; Fisher, A.; Wang, X.; Lim, K. H., A review on the electrochemical reduction of CO2 in fuel cells, metal electrodes and molecular catalysts. *Catal. Today* **2014,** *233*, 169-180.

(33). Kauffman, D. R.; Thakkar, J.; Siva, R.; Matranga, C.; Ohodnicki, P. R.; Zeng, C.; Jin, R., Efficient Electrochemical CO2 Conversion Powered by Renewable Energy. *ACS Appl. Mater. Interfaces* **2015,** *7* (28), 15626-15632.

(34). Bushuyev, O. S.; De Luna, P.; Dinh, C. T.; Tao, L.; Saur, G.; van de Lagemaat, J.; Kelley, S. O.; Sargent, E. H., What Should We Make with CO2 and How Can We Make It? *Joule* **2018,** *2* (5), 825-832.

(35). Kuhl, K. P.; Hatsukade, T.; Cave, E. R.; Abram, D. N.; Kibsgaard, J.; Jaramillo, T. F., Electrocatalytic Conversion of Carbon Dioxide to Methane and Methanol on Transition Metal Surfaces. *J. Am. Chem. Soc.* **2014,** *136* (40), 14107-14113.

(36). Yin, Z.; Yu, C.; Zhao, Z.; Guo, X.; Shen, M.; Li, N.; Muzzio, M.; Li, J.; Liu, H.; Lin, H.; Yin, J.; Lu, G.; Su, D.; Sun, S., Cu3N Nanocubes for Selective Electrochemical Reduction of CO2 to Ethylene. *Nano Lett.* **2019**.

(37). Chen, C. S.; Wan, J. H.; Yeo, B. S., Electrochemical Reduction of Carbon Dioxide to Ethane Using Nanostructured Cu2O-Derived Copper Catalyst and Palladium(II) Chloride. *J. Phys. Chem. C* **2015,** *119* (48), 26875-26882.

(38). Liu, Z.; Ni, Y.; Sun, T.; Zhu, W.; Liu, Z., Conversion of CO2 and H2 into propane over InZrOx and SSZ-13 composite catalyst. *J. Energy Chem.* **2021,** *54*, 111-117.

(39). Hirunsit, P.; Soodsawang, W.; Limtrakul, J., CO2 Electrochemical Reduction to Methane and Methanol on Copper-Based Alloys: Theoretical Insight. *J. Phys. Chem. C* **2015,** *119* (15), 8238-8249.

(40). Lee, S.; Park, G.; Lee, J., Importance of Ag–Cu Biphasic Boundaries for Selective Electrochemical Reduction of CO2 to Ethanol. *ACS Catal.* **2017,** *7* (12), 8594-8604.

(41). Rahaman, M.; Dutta, A.; Zanetti, A.; Broekmann, P., Electrochemical Reduction of CO2 into Multicarbon Alcohols on Activated Cu Mesh Catalysts: An Identical Location (IL) Study. *ACS Catal.* **2017,** *7* (11), 7946-7956.

(42). Hori, Y.; Wakebe, H.; Tsukamoto, T.; Koga, O., Electrocatalytic process of CO selectivity in electrochemical reduction of CO2 at metal electrodes in aqueous media. *Electrochim. Acta* **1994,** *39*, 1833-1839.

(43). Durst, J.; Rudnev, A.; Dutta, A.; Fu, Y.; Herranz, J.; Kaliginedi, V.; Kuzume, A.; Permyakova, A. A.; Paratcha, Y.; Broekmann, P.; Schmidt, T. J., Electrochemical CO2 Reduction – A Critical View on Fundamentals, Materials and Applications. *CHIMIA International Journal for Chemistry* **2015,** *69* (12), 769-776.

(44). Sunfire GmbH, S. S., https://www.sunfire.de/en/ , (accessed 9 June 2018).

(45). https://press.siemens.com/global/en/pressrelease/research-project-rheticus, (accessed 10 June 2021).

(46). kuhl, K. P., ELECTROCHEMICAL REDUCTION OF CARBON DIOXIDE ON TRANSITION METAL SURFACES.

(47). Chen, R., Novel Transition Metal-Carbon Catalysts for Carbon Monoxide Production from CO2 Electroreduction. **2018**.

(48). Nitopi, S.; Bertheussen, E.; Scott, S. B.; Liu, X.; Engstfeld, A. K.; Horch, S.; Seger, B.; Stephens, I. E. L.; Chan, K.; Hahn, C.; Nørskov, J. K.; Jaramillo, T. F.; Chorkendorff, I., Progress and Perspectives of Electrochemical CO2 Reduction on Copper in Aqueous Electrolyte. *Chem. Rev.* **2019,** *119* (12), 7610-7672.

(49). Jinli, Q.; Yuyu, L.; Jiujun, Z., Electrode Kinetics of CO Electroreduction. In *Electrochemical Reduction of Carbon Dioxide*, CRC Press: 2016.

(50). Le MTH. Electrochemical reduction of CO2to methanol. A thesis submitted tothe Graduate Faculty of the Louisiana State University and Agricultural andMechanical College, Chemical Engineering, Louisiana State University, BatonRouge, LA, USA; 2011.

(51). Faber, M. S.; Dziedzic, R.; Lukowski, M. A.; Kaiser, N. S.; Ding, Q.; Jin, S., High-Performance Electrocatalysis Using Metallic Cobalt Pyrite (CoS2) Micro- and Nanostructures. *J. Am. Chem. Soc.* **2014,** *136* (28), 10053-10061.

(52). Garg, S.; Li, M.; Weber, A. Z.; Ge, L.; Li, L.; Rudolph, V.; Wang, G.; Rufford, T. E., Advances and challenges in electrochemical CO2 reduction processes: an engineering and design perspective looking beyond new catalyst materials. *J. Mater. Chem. A* **2020,** *8* (4), 1511-1544.

(53). Zeng, K.; Zhang, D., Recent progress in alkaline water electrolysis for hydrogen production and applications. *Prog. Energy Combust. Sci.* **2010,** *36* (3), 307-326.

(54). Ma, M.; Liu, K.; Shen, J.; Kas, R.; Smith, W. A., In Situ Fabrication and Reactivation of Highly Selective and Stable Ag Catalysts for Electrochemical CO(2) Conversion. *ACS Energy Lett.* **2018,** *3* (6), 1301-1306.

(55). Kortlever, R.; Shen, J.; Schouten, K. J. P.; Calle-Vallejo, F.; Koper, M. T. M., Catalysts and Reaction Pathways for the Electrochemical Reduction of Carbon Dioxide. *J. Phys. Chem. Lett.* **2015,** *6* (20), 4073-4082.

(56). Sun, Z.; Ma, T.; Tao, H.; Fan, Q.; Han, B., Fundamentals and Challenges of Electrochemical CO2 Reduction Using Two-Dimensional Materials. *Chem* **2017,** *3* (4), 560-587.

(57). Hansen, H. A.; Varley, J. B.; Peterson, A. A.; Nørskov, J. K., Understanding Trends in the Electrocatalytic Activity of Metals and Enzymes for CO2 Reduction to CO. *J. Phys. Chem. Lett.* **2013,** *4* (3), 388-392.

(58). Chaplin, R. P. S.; Wragg, A. A., Effects of process conditions and electrode material on reaction pathways for carbon dioxide electroreduction with particular reference to formate formation. *J. Appl. Electrochem.* **2003,** *33* (12), 1107-1123.

(59). Alfath, M.; Lee, C. W., Recent Advances in the Catalyst Design and Mass Transport Control for the Electrochemical Reduction of Carbon Dioxide to Formate. *Catalysts* **2020,** *10* (8).

(60). Min, X.; Kanan, M. W., Pd-Catalyzed Electrohydrogenation of Carbon Dioxide to Formate: High Mass Activity at Low Overpotential and Identification of the Deactivation Pathway. *J. Am. Chem. Soc.* **2015,** *137* (14), 4701-4708.

(61). Podlovchenko, B. I.; Kolyadko, E. A.; Lu, S., Electroreduction of carbon dioxide on palladium electrodes at potentials higher than the reversible hydrogen potential. *J. Electroanal. Chem.* **1994,** *373* (1), 185-187.

(62). Stalder, C. J.; Chao, S.; Wrighton, M. S., Electrochemical reduction of aqueous bicarbonate to formate with high current efficiency near the thermodynamic potential at chemically derivatized electrodes. *J. Am. Chem. Soc.* **1984,** *106* (12), 3673-3675.

(63). Lee, C. W.; Hong, J. S.; Yang, K. D.; Jin, K.; Lee, J. H.; Ahn, H.-Y.; Seo, H.; Sung, N.-E.; Nam, K. T., Selective Electrochemical Production of Formate from Carbon Dioxide with Bismuth-Based Catalysts in an Aqueous Electrolyte. *ACS Catal.* **2018,** *8* (2), 931-937.

(64). Yoo, J. S.; Christensen, R.; Vegge, T.; Nørskov, J. K.; Studt, F., Theoretical Insight into the Trends that Guide the Electrochemical Reduction of Carbon Dioxide to Formic Acid. *ChemSusChem* **2016,** *9* (4), 358-363.

(65). Feaster, J. T.; Shi, C.; Cave, E. R.; Hatsukade, T.; Abram, D. N.; Kuhl, K. P.; Hahn, C.; Nørskov, J. K.; Jaramillo, T. F., Understanding Selectivity for the Electrochemical Reduction of Carbon Dioxide to Formic Acid and Carbon Monoxide on Metal Electrodes. *ACS Catal.* **2017,** *7* (7), 4822-4827.

(66). Sullivan, B. P. K., K.; Guard, H.E, Electrochemical and Electrocatalytic Reactions of Carbon Dioxide; Elsevier:Amsterdam, The Netherlands. **1993**.

(67). Wen, G.; Lee, D. U.; Ren, B.; Hassan, F. M.; Jiang, G.; Cano, Z. P.; Gostick, J.; Croiset, E.; Bai, Z.; Yang, L.; Chen, Z., Orbital Interactions in Bi-Sn Bimetallic Electrocatalysts for Highly Selective Electrochemical CO2 Reduction toward Formate Production. *Adv. Energy Mater.* **2018,** *8* (31), 1802427.

(68). Sreekanth, N.; Phani, K. L., Selective reduction of CO2 to formate through bicarbonate reduction on metal electrodes: new insights gained from SG/TC mode of SECM. *Chem. Commun.* **2014,** *50* (76), 11143-11146.

(69). Bai, X.; Chen, W.; Zhao, C.; Li, S.; Song, Y.; Ge, R.; Wei, W.; Sun, Y., Exclusive Formation of Formic Acid from CO2 Electroreduction by a Tunable Pd-Sn Alloy. *Angew. Chem. Int. Ed.* **2017,** *56* (40), 12219-12223.

(70). Dutta, A.; Zelocualtecatl Montiel, I.; Kiran, K.; Rieder, A.; Grozovski, V.; Gut, L.; Broekmann, P., A Tandem (Bi2O3 → Bimet) Catalyst for Highly Efficient ec-CO2 Conversion into Formate: Operando Raman Spectroscopic Evidence for a Reaction Pathway Change. *ACS Catal.* **2021**, 4988-5003.

(71). Nie, X.; Esopi, M. R.; Janik, M. J.; Asthagiri, A., Selectivity of CO(2) reduction on copper electrodes: the role of the kinetics of elementary steps. *Angew. Chem.* **2013,** *52* (9), 2459-2462.

(72). Zhao, K.; Liu, Y.; Quan, X.; Chen, S.; Yu, H., CO2 Electroreduction at Low Overpotential on Oxide-Derived Cu/Carbons Fabricated from Metal Organic Framework. *ACS Appl. Mater. Interfaces* **2017,** *9* (6), 5302-5311.

(73). Yang, K. D.; Lee, C. W.; Jin, K.; Im, S. W.; Nam, K. T., Current Status and Bioinspired Perspective of Electrochemical Conversion of CO2 to a Long-Chain Hydrocarbon. *J. Phys. Chem. Lett.* **2017,** *8* (2), 538-545.

2a. Result and Discussion - Monometallic and Binary Systems

2.1 CO₂ electrolysis – Complementary *operando* XRD, XAS, and Raman spectroscopy study on the stability of CuₓO foam catalysts

In this study, the aim was to evaluate the stability of oxidic copper (Cu_xO) foam catalysts via the *operando* analysis techniques during CO_2 electrolysis. As such, in this experiment based study, the potential-dependent changes of the chemical states of Cu species in the copper oxide foam catalyst were monitored through employing the advanced *operando* X-ray absorption spectroscopy (XAS), X-ray diffraction (XRD), and Raman spectroscopy. Cu and Cu based catalysts have gained significant attention particularly because of their capability to allow for C-C coupling reactions resulting in hydrocarbon and oxygenate products. Previous reports have suggested that the pre-treatment of the Cu catalyst affects not only the electrocatalytic activity but the resulting product distribution.[1-3] Most of these strategies entail the formation of an oxide layer on the catalyst surface, namely, by oxygen plasma treatment[1, 4], chemical oxidation[5], and thermal annealing[3, 6-8]. It is important to note that such formed cuprous and cupric oxides (Cu_2O or CuO) are thermodynamically unstable under harsh conditions during CO_2RR thereby leading to oxide-derived Cu catalyst. However, there is still a lack of general consensus on the stability of surface oxides and the presence of sub-surface oxygen under harsh cathodic conditions, and their specific role in the resulting product distribution. For this reason, Cu foams were first electrodeposited on conductive graphite foil and subsequently annealed at 300 °C (12 h) in the air thus yielding Cu_xO foams serving as precursors for the catalyst activations under CO_2RR conditions.

Ex-situ characterization

Cu foams show a hierarchical porous structure yielding an architecture of interconnected open cell pores with a diameter ranging from 15 to 25 µm. Figure 2.11 depicts the SEM micrographs of an as-deposited Cu foam (panel a,b) and the same foam after the process of thermal annealing (panel c,d). The walls of the pores are composed of dendritic Cu structures thus introducing a secondary porosity into the foam structure. An important outcome of our studies is that the primary macro-porosity (pores) does not get affected by the thermal annealing,

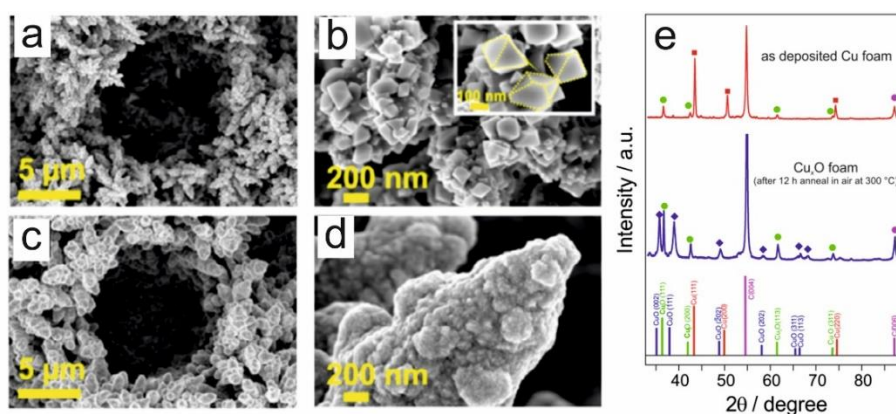**Figure 2.11.** SEM micrographs of the (a,b) as-deposited Cu foam (5 s deposition time at −3 A cm⁻²); (c,d) Thermally annealed Cu foam (300 °C, 12 h) denoted as Cu_xO foam; (e) X-ray diffractograms of the as-deposited (red) and the thermally annealed (blue) Cu foam. Readapted with permissions from Journal of Catalysis 389 (2020) 592–603. 0021-9517/©2020 Elsevier Inc. All rights reserved

whereas, the sidewalls of the pores undergo substantial structural alterations. Prior to the annealing, individual dendrites were composed of Cu nanoparticles—revealing well-defined surface facets (Figure2.11 b), and in contrast, a coalescence of the faceted nano-crystallites (Figure2.11 d) was observed after the thermal treatment. These morphological alterations can be attributed to the formation of intermixed CuO/Cu_2O composite (denoted as Cu_xO). XRD analysis further supports the presence of face centred cubic (fcc) Cu and cuprous oxide (Cu_2O) (Figure 2.11 e). The cuprous oxide, visible in the diffractogram of the as-prepared sample, can be attributed to surface-confined oxides. Note that Cu foams are prone to surface oxidation right after their emersion from the plating bath. After the thermal treatment, the diffraction peaks corresponding to metallic Cu present in the as-prepared sample have completely disappeared transforming it to the oxidic Cu_xO composite (i.e., a mixture of Cu_2O & CuO).

Product distribution

Annealed Cu foam catalysts were screened for their electrocatalytic activity by potentiostatic electrolysis experiments in the potential range from +0.07 V to −0.87 V vs. RHE. The product distribution of the CO_2 reduction reaction (CO_2RR) of the annealed Cu foam is represented in terms of partial current density (PCD) for CO_2RR products (Figure 2.12 a). CO is the primary product in low overpotential region reaching up to FE_{CO} = 28% at −0.27 V vs. RHE with j_{CO} = −0.05 mA cm^{-2} (Figure 2.12 a,b). Formate was also detected in minor amounts (ca.10 %). C2 formation started only at −0.67 V vs. RHE where FE_{C2H4} = 6% with j_{C2H4} = −0.47 mA cm^{-2} and ethane (j_{C2H6} = −0.62 mA cm^{-2}, FE_{C2H6} = 8%) were detected using the annealed catalyst. It is worth mentioning that the C1 pathway is fully blocked on the oxide-derived Cu foam catalyst (methane and methanol). The partial current density for ethanol formation increases from j_{EtOH} = −0.86 mA cm^{-2} (FE_{EtOH} = 5%) at −0.77 V vs. RHE to j_{EtOH} = −1.61 mA cm^{-2} (FE_{EtOH} = 6.7%) at −0.87 V vs. RHE (Figure 2.12c). The partial current density for n-propanol formation reaches a value of j_{PrOH} = −1.72 mA cm^{-2} (FE_{PrOH} = 7.1%) at −0.87 V vs. RHE.
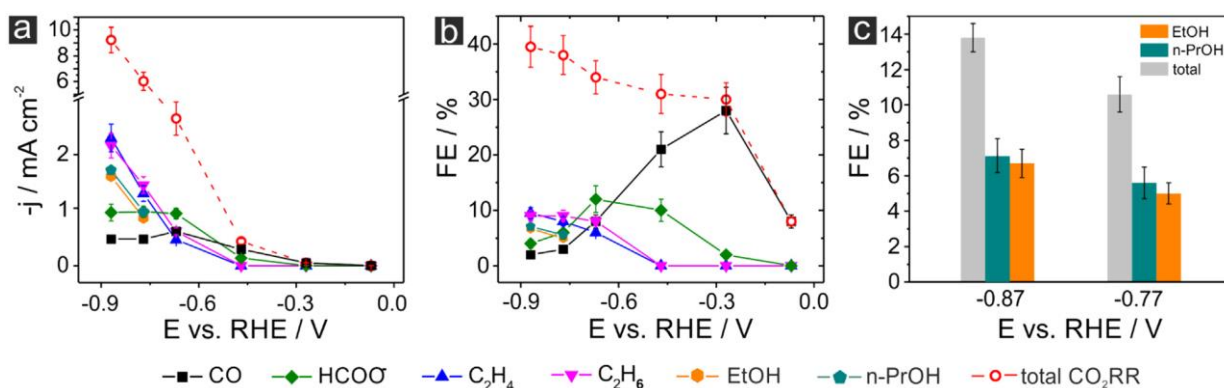
Figure 2.12. Product distribution after 1 h CO_2RR electrolysis carried out in CO_2-saturated 0.5 M $KHCO_3$ using the Cu_xO foam (300 °C, 12 h, in the air) as the catalyst; (a) CO_2RR product distribution represented as partial current densities; (b) CO_2RR product distribution represented as faradaic efficiencies (FEs); (c) Faradaic efficiencies for alcohol formation (EtOH, n-PrOH, and total alcohol efficiency) highlighted for two selected electrolysis potentials. Reprinted with permissions from Journal of Catalysis 389 (2020) 592–603. 0021-9517/© 2020 Elsevier Inc. All rights reserved

Operando analysis

To probe changes in the chemical state of copper species prior to and during CO_2RR, *operando* XAS, XRD, and Raman techniques were employed. Cu K-edge Quick-XAS measurements were conducted in CO_2-saturated 0.5 M $KHCO_3$ for both the annealed foam and as-deposited sample. Note that within the entire range of potentials applied, no significant changes in the electronic state of copper were found for the as-deposited Cu foam sample. Cu K-edge XANES (X-ray Absorption Near Edge Spectroscopy) spectra of the Cu_xO foam clearly depicts changes in the potential-dependent redox state of Cu species (Figure 2.13 a). The lowering of the Cu_xO foam mediated by the applied electrode potential is clearly seen by the trend of lowering Cu K-edge (transition) energies by applying higher negative (cathodic) potentials. Clearly, this chemical transition has already been accomplished at more positive potentials than the onset of hydrocarbon and alcohol production. Figure 2.13b depicts changes of the Cu(0), Cu(I), and Cu(II) contents in the Cu_xO foam as a function of the potential applied. According to the linear combination fitting (LCF) analysis, the Cu_xO foam at +0.6 V vs. RHE predominantly consists of Cu(II) species, which are attributed to cupric CuO, whereas only a small amount of Cu(I) (25–35 wt%) is assigned to cuprous Cu_2O. Cu(II) and Cu(I) species are in principle preserved in the range between 0 and 0.6 V vs. RHE. However, their relative abundance, changes, suggest a potential-induced shift from Cu (II) to Cu(I) prior to the reduction of the oxidic precursor to metallic Cu(0) which starts in the 'bulk' of the foam material at 0 V vs. RHE(Figure 2.13b).
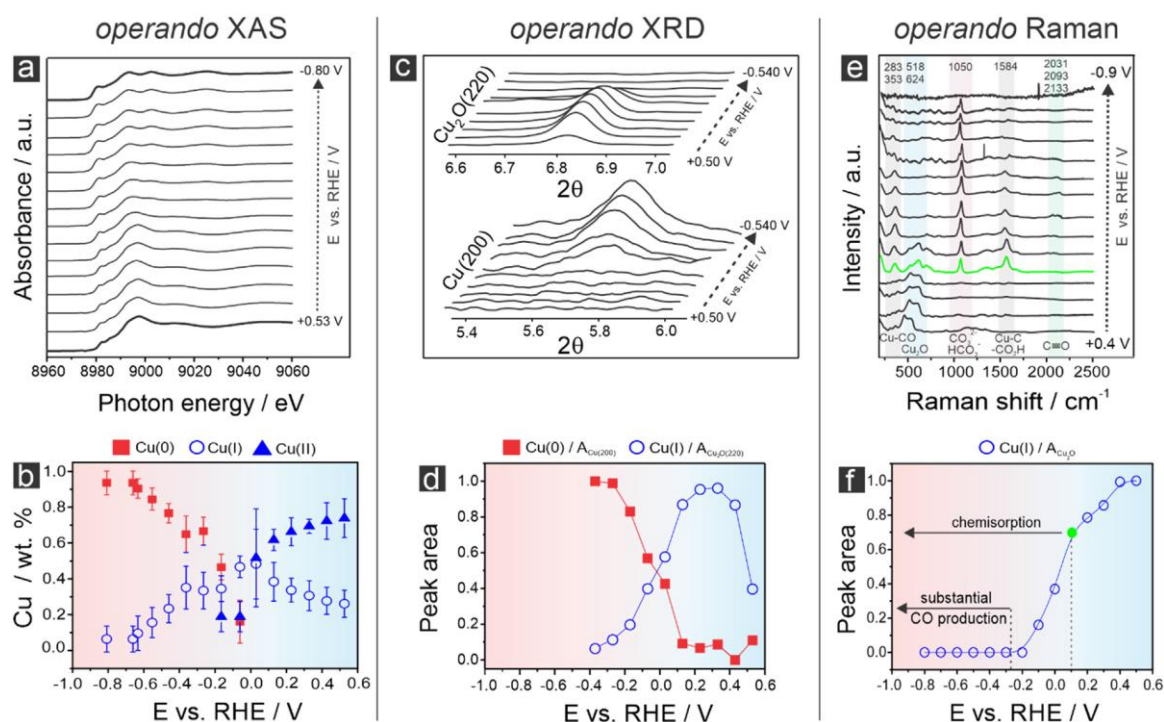
Figure 2.13. Survey of experimental *operando* results demonstrating the potential-dependent oxide-metal transition of the catalyst precursor (Cu_xO foam) in CO_2-saturated 0.5 M $KHCO_3$; (a) *Operando* XANES spectra (Cu K-edge); (b) relative content of Cu species: Cu(0), Cu(I), and Cu(II) derived from a linear combination fitting (LCF) of the XANES spectra shown in (a)); (c) *Operando* grazing-incidence X-ray diffractograms of the $Cu_2O(220)$ and Cu(200) reflections; (d) Integrated and normalized intensities of the diffractograms shown in (c); (e) Corresponding *operando* Raman spectra; (f) Integrated and normalized peak intensities of the Cu_2O related Raman peaks (518 cm^{-1} and 624 cm^{-1}) shown in (e).Reprinted with permissions from Journal of Catalysis 389 (2020)592–603. 0021-9517/©2020 Elsevier Inc. All rights reserved

Cu(II) abundance reduces to zero at potentials below 0 V vs. RHE, but Cu(I) species are present in the bulk down to −0.5 V vs. RHE. The rise in Cu(0) abundance is obviously anti-correlated with the potential-dependent drop in Cu(I) content below 0 V vs. RHE. (Figure 2.13 b). The bulk transition from the oxidic precursor to metallic Cu is accomplished at approximately −0.7 V vs. RHE.

Furthermore, the structural transition of the Cu_2O/CuO composite to the metallic fcc Cu was studied by *operando* XRD in gracing incidence geometry.[9] Figure 2.13 c presents the evolution of the Cu_2O(220) (fingerprint for the oxide precursor) and Cu(200) (fingerprint for the metallic fcc Cu) diffraction peaks. Interestingly, with the gradual shift in potentials from +0.5 V to +0.2 V vs. RHE, the integrated intensity of the Cu_2O(220) diffraction peak first increases. This trend is consistent with the hypothesis of an intermediate crystalline Cu_2O phase accumulating in the foam material during the first stage of the oxide-metal transition at the cost of the partly amorphous/crystalline CuO phase. At −0.4 V vs. RHE, the extinction of the Cu_2O associated diffraction pattern with negative going potentials is already complete (Figure 2.13 d), whereas the XAS experiment indicates the presence of Cu(I) species for potentials down to −0.8 V vs. RHE (Figure 2.13 b). This deviation in the potential dependent stability of Cu(I) species is most likely related to the intrinsic characteristics of both *operando* techniques.

On the other hand, *operando* Raman is a more surface-sensitive technique unlike the other two which are more sensitive to the bulk of the catalyst. Raman modes observed at 148 cm^{-1}, 518 cm^{-1}, and 624 cm^{-1} are ascribed to cuprous oxide species (Cu_2O), whereas peaks at 298 cm^{-1} and 346 cm^{-1} are assigned to cupric oxide.[10-12] The CuO-related vibrational modes have totally vanished from the spectrum after being exposed to the electrolyte at OCP. Only vibrational modes of cuprous oxide (Cu_2O) remain, revealing that in the early stage of the potential step experiment shown in Figure 2.13 e, the catalyst precursor surface is solely terminated by Cu(I) species. Notably, no such changes were found in the related XRD and XAS studies, indicating once more that these methods are essentially indifferent to the catalyst surface when applied to foam-type materials. The vibrational modes at 518 cm^{-1} and 624 cm^{-1} as spectroscopic fingerprints for the existence of cupric surface oxide species in the Raman spectra for quantitative investigation.

Their integrated intensities as a function of applied voltage are shown in Figure 2.13 f. The general pattern of decreasing integrated intensities with decreasing applied potentials is deemed to be qualitatively comparable to that of *operando* XRD (Figure 2.13 d). Slight differences were observed in the first stage of the oxide reduction process in the potential range of +0.5 V to +0.1 V vs. RHE, where the XRD reveals an early increase in the Cu_2O(220) associated intensities passing a maximum at +0.1 V vs. RHE (Figure 2.13d). This trend can be attributed to a temporary rise in Cu_2O concentration in the bulk of the foam material, which resulted from the partial reduction of amorphous CuO phases. It should be noted that this transformation occurred spontaneously at the surface when it came into touch with the electrolyte. Clearly, the 'surface oxide reduction' occurs faster and at somewhat more positive potentials than the comparable transition of the oxidic 'bulk phases' investigated by *operando* XAS and XRD. The disappearance of the Cu(I) in the XAS experiment (Figure 2.13 b) was delayed (on the potential scale), implying that the decrease of residual Cu(I) in the final state of the transition process

(between −0.3 and −0.6 V vs. RHE) happens from a substantially disordered state that is still identifiable by the XAS but undetectable in the XRD.

At a potential of +0.1 V vs. RHE, concerted chemisorption processes of carbonate/bicarbonate and CO_2 related species are set in (highlighted green in Figure 2.13e and f). This includes the emergence of Raman characteristics at 283 cm^{-1}/353 cm^{-1}, which are typically attributed to Cu(0)–CO vibrational modes with metallic Cu as a binding partner.[13-15] This observation led us to the conclusion that carbonate/bicarbonate and CO_2 related species preferentially chemisorb on metallic Cu domains, which co-exist at these potentials (+0.1 V vs. RHE) with surface domains of cuprous Cu_2O (Figure 2.13e). These surface-confined reactions were undetectable by the *operando* XAS and XRD at most positive applied potentials. With the potential-dependent CO_2RR product distribution shown in Figure 2.12, it is clear that when significant CO evolution occurs at applied potentials close to −0.3 V vs. RHE (Figure 2.12b), neither CuO nor Cu_2O species are detected at the catalyst surface. In the early stages of CO_2RR, the foam as a whole must be treated as a mixed metal/oxide composite.

We, therefore, conclude: All of the *operando* methods used herein indicate that the oxide is completely reduced to the Cu metallic state before the hydrocarbon and alcohol formation sets in.

2.2 A Tandem (Bi_2O_3 → Bi_{met}) catalyst for highly efficient ec-CO_2 conversion into formate: *Operando* Raman spectroscopic evidence for a reaction pathway change

Formate is one of the targeted CO_2RR products that finds use in various industrial processes. Among the formate forming catalysts, Bi- and Bi-based materials are unique, particularly because of their ability to stabilize the adsorbed CO_2 that is considered as a key intermediate in the reaction pathway towards formate formation[16-18]. Herein, we present Bi-foam catalysts prepared by the additive-assisted dynamic hydrogen bubble template (DHBT) method applied on carbon cloth (GDE) substrate which often finds use in electrolyzer systems. The electrodeposited Bi foams were further subjected to thermal annealing at 300 °C for 12 h (→ in air). Intermediate oxide species seem to play a crucial role in formate formation. However, to which extent these oxides play a role, is still unclear. To address the issue, the performance of as-prepared (*ap*) Bi/Bi_xO_y foams and the thermally annealed Bi_2O_3 foam catalysts was studied in detail.

Synthesis and ex-situ characterization
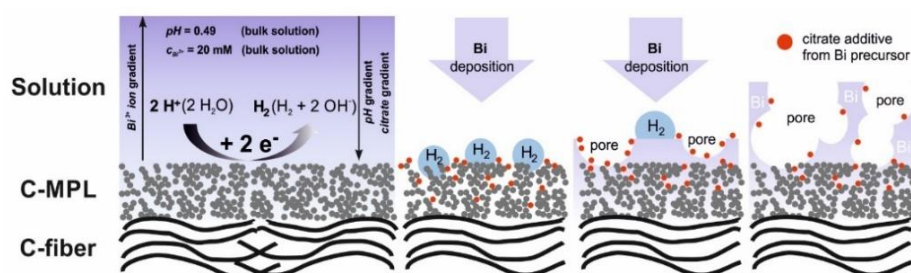
Figure 2.21. Scheme depicting the additive-assisted DHBT electrodeposition approach on the carbon cloth support (gas diffusion electrodes, GDE).[19] Reprinted with permissions from ACS Catal. 2021, 11, 4988−5003, Copyright ©2021 AmericanChemical Society

Firstly, Bi foams were deposited on planar copper (Cu) and graphite foil (C) supports. Following this, Bi foam deposition was successfully transferred to gas diffusion electrodes (GDE). The deposition mechanism involves the hydrogen evolution reaction (HER) along with the metal deposition (MD) process. Under the applied harsh conditions (-3 A cm^{-2}) in a highly acidic environment (1.5 M H$_2$SO$_4$), HER relies on the superposition of proton reduction and water splitting (Figure2.21). The so forth prepared *ap* Bi/Bi$_x$O$_y$ and annealed Bi$_x$O$_y$ deposited on Cu foil and GDE (denoted by Bi/Bi$_x$O$_y$@Cu and Bi/Bi$_x$O$_y$@GDE) were characterized by employing SEM, XRD, and XPS measurements. The thickness of the *ap* foams and the respective size distribution of the surface pores increases with elapsed deposition time.

Side-view micrographs showing the increase in thickness with the deposition time is depicted in Figure 2.22(a-d). Top- down SEM images of the four different deposition times on GDE (*ap* Bi/Bi$_x$O$_y$@GDE) are shown in Figure 2.22(e-l). The support material does not affect the dendritic nature (secondary nanoscale porosity) of pore side walls. However, the primary macroporosity was seen to experience alterations when changing the support material. This can be rationalized as the ratio of faradaic efficiencies (FE$_{H2}$/FE$_{Bi}$) and so-called "bubble break-off diameter" both depend on the choice of the support material (chemical nature and surface morphology). Generally, the pore size distribution of the Bi foam is broader and less well defined compared to the planar Cu and C foil substrates. Due to the rough surface of the GDE, the formed hydrogen bubbles tend to be more stable and further coalesce resulting in bigger surface pores compared to the planar Cu and C foil supports. Both sides of the GDE used here were coated with a microporous carbon layer (C-MPL, →Figure2.21).
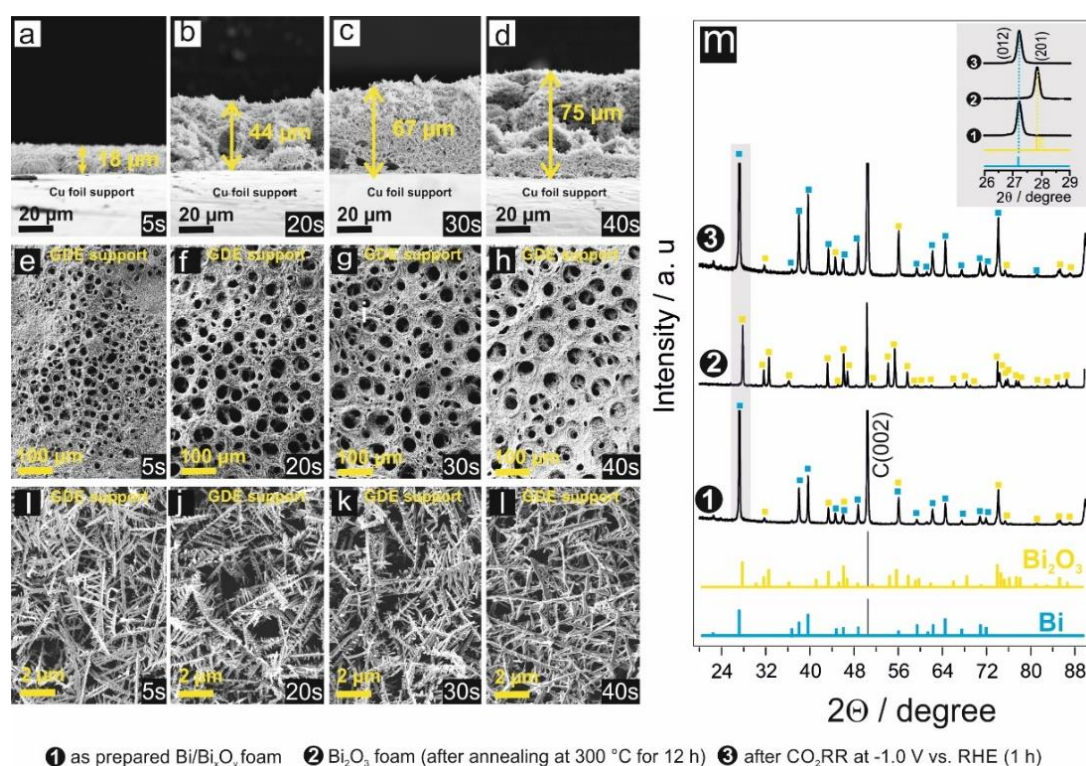
Figure 2.22. (a-d) Side-view micrographs of the with an increase in deposition time (5s, 20s, 30s, 40s) denoted as *ap* Bi/Bi$_x$O$_y$@Cu; (e-l) *ap* Bi/Bi$_x$O$_y$ foam deposited on a carbon fiber cloth support (denoted Bi/Bi$_x$O$_y$@GDE); (m) XRD inspection of the Bi foam (20 s) denoted by numbers according to their preparation stage.Readapted with permissions from ACS Catal. 2021, 11, 4988−5003, Copyright ©2021 American Chemical Society

This study was restricted to foams obtained by 20s of deposition yielding a thickness of ~44 μm (→Figure 2.22 b). XRD analysis of the Bi foams in three distinct preparation stages is shown in Figure 2.22(m). The diffraction pattern of the *ap* sample is dominated by features of polycrystalline Bi (rhombohedral crystal structure, space group P21/c denoted by no.1).[20-22] Additionally, minor contributions from α-Bi_2O_3 were observed—most likely because of the surface oxidation. The diffraction pattern of the thermally annealed sample exclusively shows the contribution from the monoclinic α-Bi_2O_3 phase. Note that this change from the *ap* sample to the thermally annealed sample can be seen in the form of color change from black (*ap* Bi/Bi_xO_y) to yellow (Bi_2O_3). Post-electrolysis XRD inspection (after 1 h at −1.0 V vs RHE in CO_2-sat. 0.5 M $KHCO_3$) suggests an electro-reduction of the α-Bi_2O_3 bulk phase back into metallic Bi.

XPS analysis shows features related to Bi(III) species (162.1 eV) with minimal contribution of Bi(0) (156.8 eV) in the *ap* catalyst. The appearance of these peaks can be assigned to photoemission from the near-surface 'bulk' of the metallic Bi foam. After the annealing, the *ap* Bi/Bi_xO_y completely transforms into fully oxidized α-Bi_2O_3, thus eliminating the contribution from Bi(0). Post-electrolysis XPS analysis of the foam sample indicates the re-appearance of satellite peaks corresponding to Bi(0). The O1s spectrum shows the presence of two different oxygen components, attributed to Bi−OH (BE (O1s) = 530.7 eV) and oxidic Bi−O species (BE (O1s) = 529.5 eV) in all of the preparation stages.

Potential dependent operando Raman spectroscopy

A deeper insight into surface oxide to metallic transitions can be studied by employing *operando* Raman spectroscopy. Three types of Raman bands were observed (i) strong Raman bands appearing at wavenumbers < 120 cm^{-1}, typically assigned to displacements of cationic-Bi(III)-entities with regard to the surrounding oxide matrix (at 119 cm^{-1})[23]; (ii) weaker bands appearing between 120 and 155 cm^{-1} due to the concerted vibrational motions of binuclear Bi-O entities[22, 24]; and vibrational modes of mononuclear −O− entities typically found at wavenumbers>155 cm^{-1} (Bi−O stretching mode at 313 cm^{-1}).[23, 25-26] Figure 2.23 (a,b) depicts potential dependent Raman spectra of Bi_2O_3 foam in Ar- saturated and CO_2 saturated
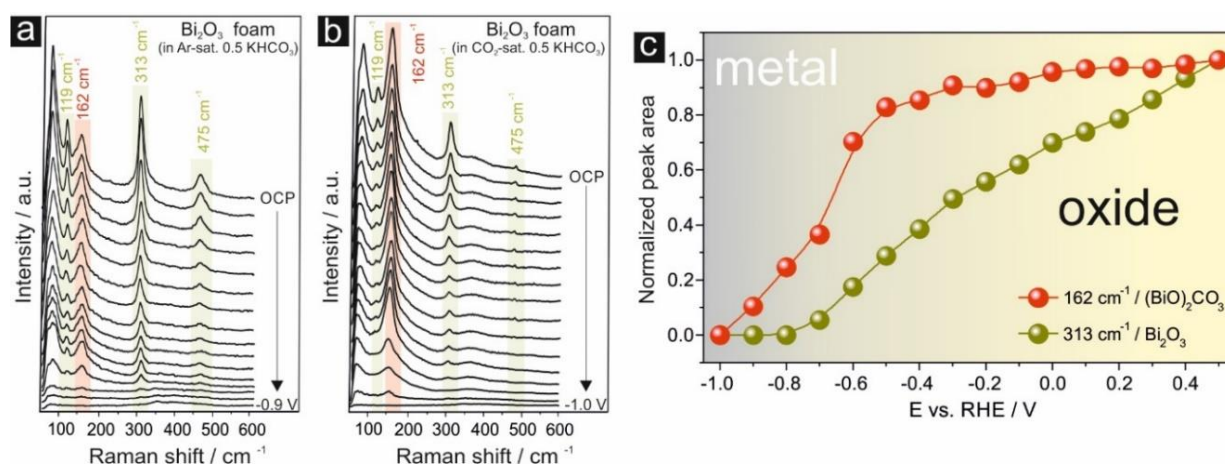
Figure 2.23. Series of potential dependent Raman spectra showing the (oxide → metal) transition of the Bi_2O_3 foam; the holding time at each potential was 3 min; (a) Ar-sat. 0.5 M $KHCO_3$ solution; (b) CO_2-sat. 0.5 M $KHCO_3$ solution; (c) Normalized integrated intensities of the Raman peaks for CO_2 saturated solution.Reprinted with permissions from ACS Catal. 2021, 11, 4988−5003, Copyright ©2021 American Chemical Society

0.5 M KHCO$_3$. All Raman features at 119, 313, and 475 cm^{-1}, attributed to the Bi$_2$O$_3$ phase are preserved in the Ar- sat. bicarbonate solution. In addition, a new strong Raman feature appears at 162 cm^{-1} (red in panel a) which is assigned to the so-called sub-carbonate species present even at the OCP through the partial surface exchange of oxidic Bi−O or Bi−OH species by Bi−CO$_3$−Bi ensembles according to Bi$_2$O$_3$ + CO$_2$ → (BiO)$_2$CO$_3$.

The formation of sub-carbonate species can be accounted by the direct adsorption of either dissolved CO$_2$ or the bicarbonate anion on the Bi$_2$O$_3$ foam. Obviously, with the gradual increase in potential (OCP of ca. +0.60 V to −0.9 V vs. RHE), both the oxide and sub-carbonate related Raman features disappear (→Figure 2.23 panel a). The intensity of sub-carbonate features at 162 cm^{-1} becomes much more pronounced in the case of CO$_2$- sat. electrolyte (→Figure 2.23-panel b) compared to Ar- sat. electrolyte. These results suggest the CO$_2$ adsorption on Bi$_2$O$_3$ prior to actual CO$_2$RR onset. Further, the pronounced intensity of sub-carbonate species suggests that this CO$_2$ embedment into the oxide precursor is not only restricted to the outermost catalyst surface but also extends into the near-surface bulk of the catalyst. Quantitatively, oxide/sub-carbonate to metal transition can be explained in terms of their normalized intensities as a function of potential (→Figure 2.23-panel c). This data suggests that the oxide to the metal transition of Bi$_2$O$_3$ foam was completed at −0.8 V vs. RHE, whereas sub-carbonate species started to decrease at −0.6 V vs. RHE, thus depicting quasi-plateau behavior. All the oxides/sub-carbonate species got completely reduced at reductive potentials of −1.0 V vs. RHE resulting in oxide sub-carbonate derived catalyst (oc-d) at more cathodic potentials.

Electrochemical characterization- CO$_2$ electrolysis

In order to test the performance of the catalyst, electrolysis experiments were conducted in a broad potential window from −0.3 V to −2.0 V vs. RHE (presented in Figure 2.24 for the *ap* Bi/Bi$_x$O$_y$, annealed Bi$_2$O$_3$, and Bi foil as reference). The product selectivity is represented in terms of the faradic efficiency (Figure 2.24 a) and the corresponding partial current density of formate is plotted in panel b of Figure 2.24. In this work, only hydrogen and formate were obtained as the main electrolysis products. The Bi foil (reference) exhibits a characteristic peak

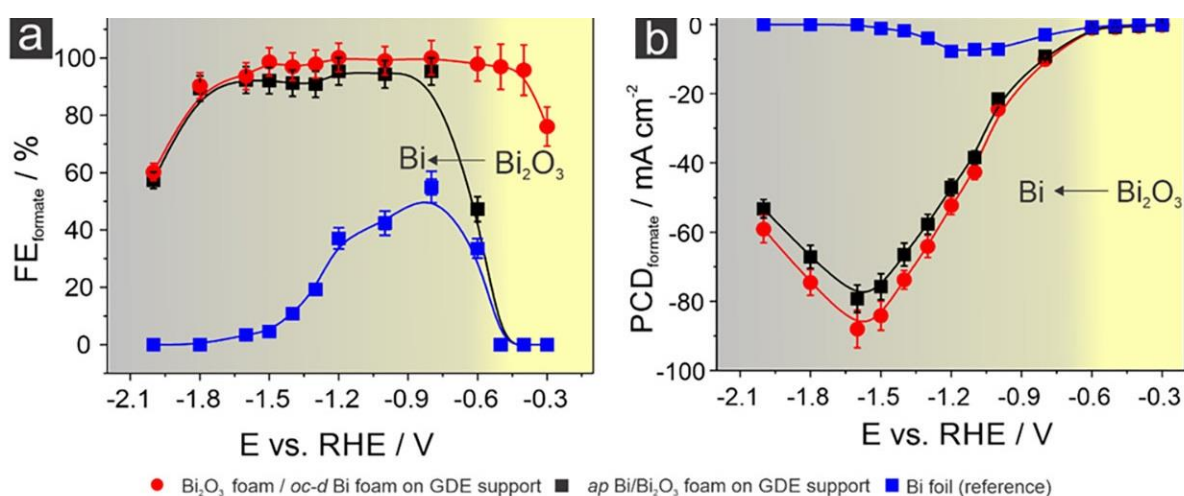**Figure 2.24.** Potential dependent product distribution of the Bi$_2$O$_3$/oc-d Bi foam, *ap* Bi/Bi$_x$O$_y$, and Bi foil in terms of (a) FE vs0E plot; (b) Partial current densities of formate vs. E.Reprinted with permissions from ACS Catal. 2021, 11, 4988−5003, Copyright ©2021 American Chemical Society

like behavior with a maximum formate efficiency of $FE_{formate}$ =55 % and PCD $_{formate}$ = − 2.92 mA cm^{-2} at −0.8 V vs. RHE. Apparently, both the *ap* Bi/Bi$_x$O$_y$ and the Bi$_2$O$_3$/oc-d Bi exhibit excellent activity for formate reaching even FEs of ∼100% within an extended plateau regime.

This plateau extends to 1100 mV (from −0.4 V to −1.5 V vs. RHE) in the case of Bi$_2$O$_3$/oc-d Bi foam whereas it is only 800 mV broad (from −0.7 V to −1.5 V vs. RHE) in the case of *ap* Bi/Bi$_x$O$_y$ foam. This difference in the potential-dependent product selectivity suggests an extra reaction formate reaction pathway on the oxide/subcarbonate/ Bi$_{met}$ composite at these low overpotentials that is not active on the *ap* Bi/Bi$_x$O$_y$ catalyst. The difference in the product selectivity can also be concluded from PCDs for polycrystalline Bi catalyst and the foam catalyst (Figure 2.24 b). The latter shows PCD$_{formate}$ reaching a value of – 88.4 mA cm^{-2} which is significantly higher compared to the planar Bi foil with PCD –7.27 mA cm^{-2} (–1.2 V vs. RHE). The *ap* foam catalyst exhibits slighter lower PCDs with maximum of –79.72 mA cm^{-2}. This trend is due to the increased electrochemically active surface area (ECSA) after the reduction of the "bulk" oxide phases. Besides product distribution and selectivity, durability is one of the most important characteristics of high-performance catalysts. To demonstrate the excellent stability of the Bi$_2$O$_3$ foam, extended electrolysis over 100 h was conducted at low (−0.6 V) and higher overpotentials (−1.0 V). At −0.6 V vs. RHE, values of FE$_{formate}$ decline only by 10% from an initial value of 97.3% to a final 89.1% whereas at high potential (−1.0 V) FE$_{formate}$ decays from 91.7% to 79.1% over 100 h of electrolysis. These results were further complemented by identical location SEM investigations demonstrating changes in the catalyst morphology during the course of CO$_2$RR.

This study demonstrates the Bi$_2$O$_3$ foam as an efficient and stable catalyst for formate production with high current densities in the half cell configuration. Experimental evidence indicates the displacement of oxidic species by carbonate species.

2b. Result and Discussion - Binary systems

2.3 An *operando* study: selectively CO formation on CuO/SnO material over gas diffusion electrodes

Porous CuSn was applied as the catalyst for promoting CO$_2$ reduction to CO. Cu, as a one-of-a-kind metal, may generate a diverse variety of products, however, it suffers from poor selectivity toward a specific product. Sn, on the other hand, creates formic acid preferentially as the major CO$_2$RR product. When neither Cu nor Sn generates CO preferentially, both were combined to yield CO as the principal product in this study. The synergistic effect in materials composed of the binary or multicomponent system plays a significant role in catalysis. This effect arises due to the chemical identities on the surface of a catalyst that helps to control reactant adsorption, activation, and product desorption to form a certain product. Herein, we explored synergistic effects in CuO/SnO catalyst for CO production. Reports have suggested that an optimum amount of Sn is needed in the Cu matrix for selective CO production.[27-29] In case, the amount of Sn is more in the catalyst, product selectivity will shift to formate rather

than forming CO. In some other studies, the role of oxide is well explained for the CuSn catalyst and claimed to be important for the path to form CO. Herein, a microporous carbon fibre cloth-based gas diffusion electrode (GDE) was used as the substrate for the preparation of CuSn electrode. The deposition bath contained 0.02 M of Cu precursor, 0.002 M of Sn precursor, 1M of sodium citrate in 1.5 M sulphuric acid (H_2SO_4) with a ratio of Cu: Sn to be 90:10. The composition was confirmed by ICP-MS and EDX.

Structural characterization

The synthesis of SnCu bimetallic foam was done by the additive assisted-DHBT method as mentioned previously in Figure 2.21. The hierarchical multilayer porous structures of the SnCu catalyst were analyzed by white light interferometer (WLI) revealing the porous structure on GDE (Figure 2.31 a) and the depth of the foam deposited. Scanning electron microscopy (SEM) revealed the porous structure (mesoporous) (Figure 2.31 b) and dendritic-like structure on the sidewalls of these pores (Figure 2.31 c). Notably, due to macro porosity, some pores experienced some variations on GDE due to the difference in 'break-off diameter' as it is a 3-D substrate compared to a planar substrate such as Cu foil. The main catalyst was achieved after annealing the as-prepared (*ap*)-Sn_9Cu_{91} at 200 °C for 12 h in the presence of air (Figure 2.31 d). The obtained thermally annealed *ann*-Sn_9Cu_{91} sample was employed for the subsequent electrolysis experiments. The morphology and pores structure did not seem to be affected by the annealing. However, changes can be seen on the nanoscale in the form of $Cu_2O@SnO_2$ nanoparticles appearing on the surface (Figure 2.31 c and d). The crystallographic analysis of *ap*-SnCu and *ann*-SnCu catalyst was carried out through XRD. Diffraction peaks corresponding to SnCu alloy were observed in (*ap*)-Sn_9Cu_{91} sample, however, after annealing alloy phases were transformed to Cu_2O (Figure 2.31 d). Note that phase segregation takes place in the Cu domains and mixed SnCu oxide phase after the annealing process. The alloy phases seem to reappear after 1 h electrolysis at −0.7 V vs. RHE.

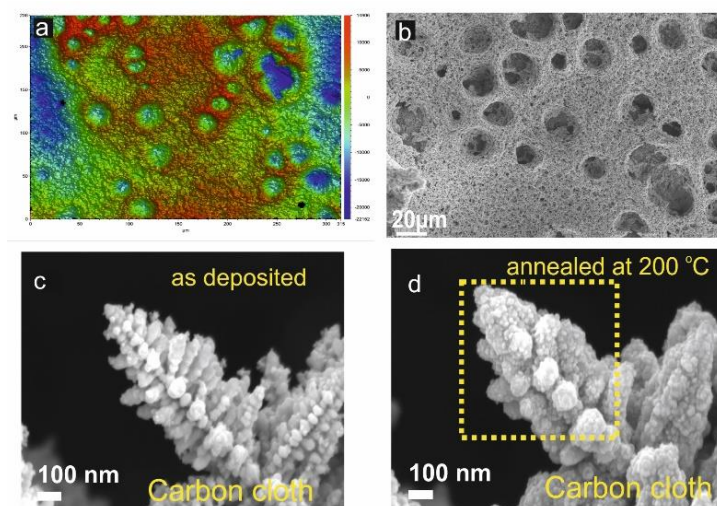**Figure 2.31.** (a) WLI image of binary alloy Sn_9Cu_{91} foam deposited for 30 s on carbon cloth (GDE); (b) Corresponding SEM micrograph of foam showing the pores uniformly distributed at the micrometer scale; Micrograph at the nanometer scale (c) for *ap*-Sn_9Cu_{91}; and (d) *ann*-Sn_9Cu_{91}

Operando Raman analysis

The stability of oxides was inspected using *operando* Raman spectroscopy. Potential dependent analysis was conducted where potential was stepped from less cathodic potential to more cathodic potentials after measuring spectra at the open circuit potential (OCP) in CO_2 saturated 0.5M $KHCO_3$ solution. Raman spectroscopic measurements were performed for the *annealed* (*ann*) Cu (Figure 2.32 a) the Sn_9Cu_{91} foams (Figure 2.32 b). The porous rough surface of CuO_x and *ann*-Sn_9Cu_{91} foam facilitates surface-enhanced Raman spectroscopy (SERS). The steady-state Raman spectra were acquired within three minutes at each potential set point for both samples (*ann*-Cu and Sn_9Cu_{91}). The peaks at 518 cm^{-1} and 624 cm^{-1} were observed at OCP and also at the applied potential at +0.4 V which corresponds to the Cu(I) oxide peak as reported in previous works.[10, 30-31] However, as the potential is swept to more cathodic potentials, the peaks are gradually decayed confirming the instability of Cu oxides prior to the onset potential for CO_2RR.[10, 26] In the case of the *ann*-Sn_9Cu_{91}, Cu(I) appeared at 518 cm^{-1} and 624 cm^{-1} at OCP while Sn(II) or Sn(IV) were not observed in Raman spectra (Figure 2.32 b) suggesting the surface of the catalyst is fully covered with Cu(I) oxides.

An additional peak started to appear at ∼ 570 cm^{-1} when the potential was just stepped from OCP to + 0.4 V (RHE) and continued to increase until a potential of −0.1 V (RHE) (Figure 2.32 b). After deconvolution of this peak, two peaks were clearly distinguished, one at ∼ 570 cm^{-1} (denoted by 4 in panel b) corresponding to A1g vibration mode of Sn^{4+} and the other at 461 cm^{-1} (denoted by 6 in panel b) can be assigned to the E1g vibration mode of Sn=O species.[32-33] Closer inspection of Figure 2.13 b reveals the peak at 570 cm^{-1} that is present in all the potential above −0.1V vs. RHE but started decay at E ≤ −0.1 V vs. RHE. The intensity of peak related to Cu(I) oxide rapidly dropped at E ≤ +0.4 V vs. RHE,
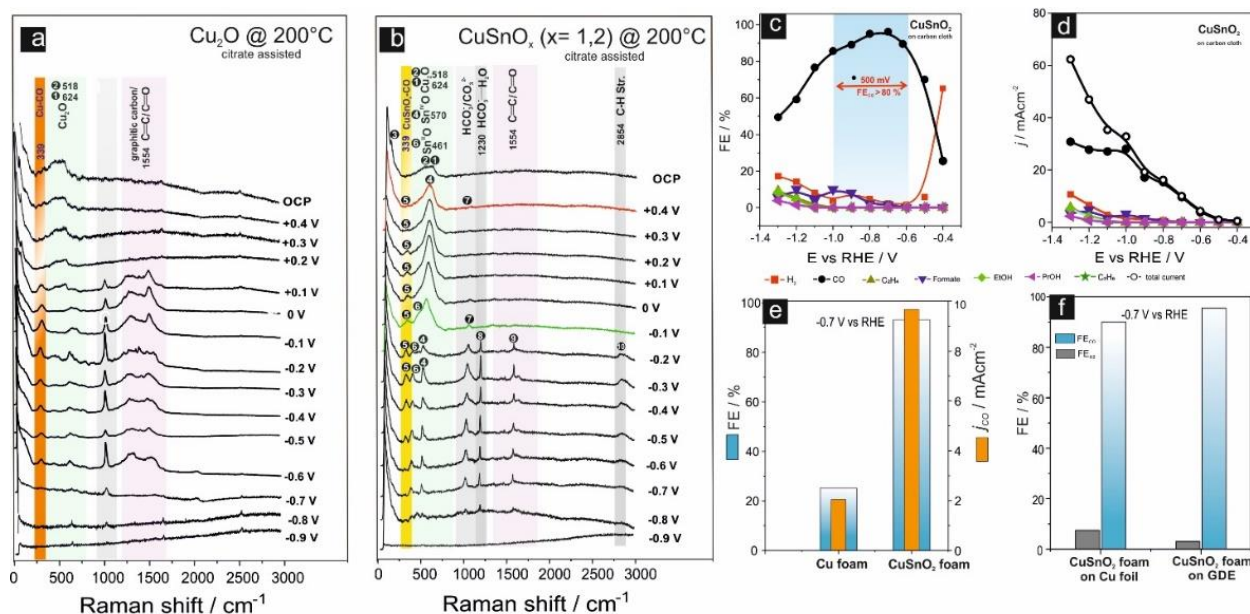
Figure 2.32. Raman analysis in the range from OCP to −0.9 V vs. RHE (a) Cu foam annealed at 200 °C; (b) $CuSnO_x$ foam at 200 °C; (c) Product analysis of *ann*-Sn_9Cu_{91} at different potentials; (d) Corresponding partial current densities and total current density as a function of potential; (e) FE_{CO} and PCD_{CO} for *ann*-Cu foam and $CuSnO_x$ at −0.7 V vs. RHE; (f) Comparison of FEs of H_2 & CO on $CuSnO_x$ on Cu foil and GDE substrate.

however, there is a possibility to camouflage under Raman peaks of SnO_2. The intensity of the Sn(IV) related peaks first increase then gradually decreases with the appearance of a Sn=O related feature, monitored at −0.1 V vs. RHE, and both oxides reduce almost ~90 % until the applied cathodic potentials at E ≤ −0.7 V. The mechanistic interpretation of CO_2 conversion to CO on the SnCu surface is still under discussion. For example, Sarfraz et.al[34] proposed the possibility of weakening the H adsorption on Cu by substitution of Sn, which consequently enhances the selectivity solely for CO. Formation of CO could be understood by the Raman spectra of *ann*-Sn_9Cu_{91} where CO absorption peak has been shown. CO absorption peak can be seen at 339 cm^{-1} in both *ann*-Cu foam & Sn_9Cu_{91}. This peak refers to chemisorbed CO species ν (Cu−CO) and is considered as a spectroscopic fingerprint for the appearance of the formation of metallic Cu state[15, 35] by partially/fully reduction of Cu_2O to Cu ($CuO_2 \rightarrow$ Cu) under reductive conditions. Interestingly, the peak related to CO absorption at 339 cm^{-1} is observed at +0.4 V vs. RHE in the case of *ann*-Sn_9Cu_{91} that is significantly positive potential than Cu foam in similar conditions, in which CO peak is observed at a later stage at +0.1 V vs. RHE (Figure 2.32 b). This shift in the potential of about 300 mV suggested the formation of CO at an early stage in *ann*-Sn_9Cu_{91} than in pure Cu. The results are well supported by product distribution, wherein gaseous products were measured by gas chromatography and formed liquid products were measured by ion chromatography.

Product analysis

Faradaic efficiency of CO (FE_{CO}) was achieved up to 90% at −0.6 V versus RHE and reached the maximum at −0.7 V vs. RHE yielding close to ~95% with a partial current density of−9.5 $mAcm^{-2}$ at the GDE substrate (Figure 2.32 c & d)**.** For a broad range of potential, FEs of CO were maintained reaching quite a high efficiency ≥ 80% with FE of H_2 staying low in the range of 5-10%. With the increase in potential, CO efficiency tends to decrease (~ 50 %) with the steady increase in H_2 reaching close to 20 % at −1.3 V vs. RHE. C2 products also started to appear with the increase in potential tending to Cu like behavior. However, efficiencies of C2 products were not as high as it shows in pure Cu. A total of ~20% C2 products (C_2H_4 ~10 %, C_2H_6 ~2 %, EtOH ~7 %, PrOH ~2.8 %) were obtained at a high potential of −1.3 V vs. RHE. Formate was also obtained with an efficiency of around 8 % yielding the total efficiency to be close to 100 %. Total current density reached more than 60 mA cm^{-2} at −1.3 V vs. RHE. For comparison, FE_{CO} and PCD_{CO} are plotted for *ann*-Cu foam and Sn_9Cu_{91} foam at −0.7 V vs. RHE. FE_{CO} on Cu foam was ~28% and PCD_{CO} was −2 $mAcm^{-2}$ which is five-fold less than in the case of *ann*-Sn_9Cu_{91} foam (Figure 2.32 e). A comparison of FEs for CO and H_2 is shown on two substrates i.e Cu foil and GDE. Importantly, FE was inferred to be comparable in both the cases (Figure 2.32 f), however, the current density was almost five times higher for *ann*-Sn_9Cu_{91}@GDE foam catalyst suggesting higher electrochemical active surface area (ECSA) on carbon cloth GDE substrate.

Identical location (IL) –SEM and long-term electrolysis experiment

The durability of the catalyst was investigated by an extended 150 h electrolysis at −0.7 V. FE_{CO} values were rather stable and maintained above 80 % for the first 90 h and decreased faster for the last 60 h with a decrease of 20-30 % reaching FE_{CO} = ~55%. The decrease in CO
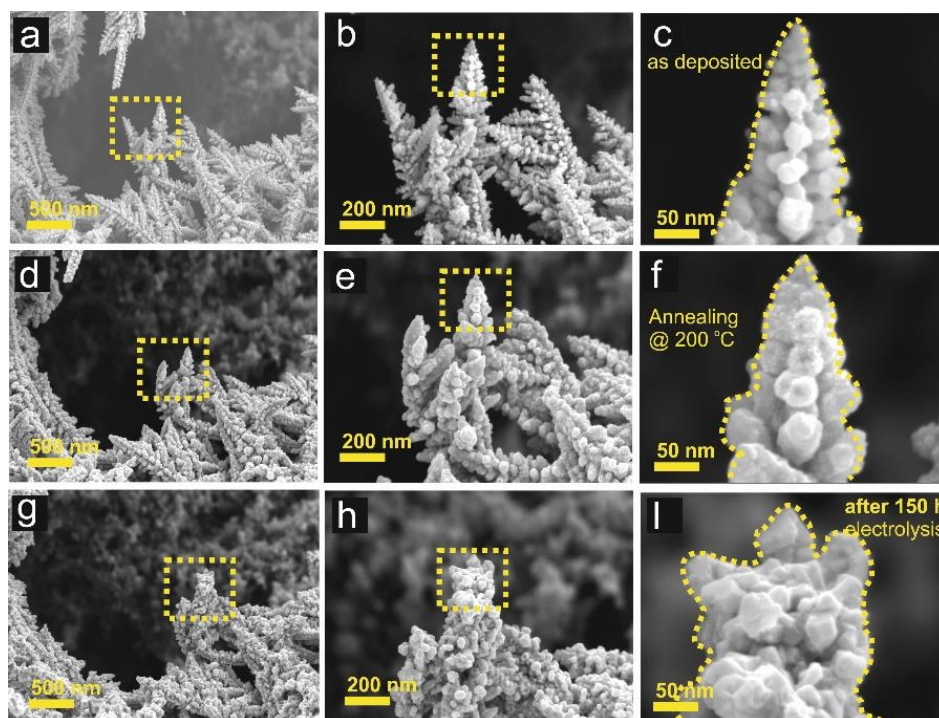
Figure 2.33. Identical location (IL)-SEM on GDE substrate (a-c) as prepared (*ap*)Sn$_9$Cu$_{91}$; (d-f) CuSnO$_x$ foam at 200 °C in air; (g-i) Long-term electrolysis of 150 h, at −0.7 V vs. RHE

selectivity was counterbalanced with the increase in H$_2$, thus, compensating for the overall total efficiency. Identical-location (IL) SEM was done at the same place before, after annealing, and after 150 h of electrolysis (Figure 2.33). After annealing, small particles seem to develop on the nanoscale (Figure 2.33 (d-f)), which after 150 h of operation in reduction conditions underwent a drastic structural change (Figure 2.33 (g-i)). Time-dependent ICP-MS analysis was done for 150 h since metal ions can get released in the electrolyte from the highly oxidic electrode surface thus causing reconstruction of the surface by re-deposition of the metal ions.

This work demonstrates the SnCu foam as an efficient CO production. *Operando* Raman spectroscopic study indicates the CO related absorption peak occurring at more positive potential in case of CuSnO$_x$ as compared to Cu$_x$O.

2.4 Selective n-propanol formation from CO$_2$ over PdCu alloy foam electrocatalysts

In this study, an alloyed PdCu catalyst was employed as the robust electro-catalyst for CO$_2$ reduction and was synthesized utilizing a DHBT-assisted deposition process. Cu is the only metal present in the periodic table that is capable to produce various hydrocarbons and oxygenates with a higher carbon chain.[36] However, Cu suffers from poor selectivity thereby causing low efficiencies toward a specific product (e.g., ethanol, propanol). An enhancement in the efficiency towards alcohol formation can be achieved by various ways such as oxidation of the catalyst, different pretreatments, morphological and structural modifications.[37-39] To achieve catalyst oxidation, thermal annealing in the air is an option to oxidize the catalyst or by supplying a controlled flow of oxygen. The formation of oxide (Cu(I) and Cu(II) oxide) on the surface is considered to be mainly responsible for catalyst activation and subsequently providing more abundant low coordinated active sites for C-C coupling forming alcohols.[8, 40] The C-C coupling or dimerization takes place in the initial stage of the CO$_2$ conversion, and as

such, the availability of sufficient chemisorbed $^*CO$ is essential for this purpose that is the key intermediate in the reaction. This can be achieved by introducing a CO producing metal to the Cu matrix. Pd is one of the CO producing catalysts.[41] One drawback of this metal is that the high affinity of Pd towards CO leads to the poisoning irrespective of the catalyst morphology thereby making it unstable for the long course of the reduction process.[42-43] This problem can be solved by co-alloying with other metals, e.g. Cu.

Herein, we prepared an alloy catalyst by introducing Pd in a small amount in the Cu matrix. The deposition bath consisted of solutions containing Cu and Pd in the ratio of 9:1 in 1.5 M H_2SO_4. The desired composition of these binary alloy materials was achieved by applying a current density of $-3A\ cm^{-2}$ for 40 s to obtain an as-prepared sample (*ap*). Thermal annealing was applied at a temperature of 200 °C for 12 h in air. After thermal annealing, this *ann*-Pd_9Cu_{91} catalyst was activated through the electrochemical reduction of this oxide surface by applying -0.65 V vs. RHE for 45 min in CO_2 saturated 0.5 M $KHCO_3$ solution resulting in phase segregated Cu- rich and Pd- rich phases as shown in the schematic (Figure 2.41c). This step is quite important in order to achieve the oxide-derived (*od*)-Pd_9Cu_{91} catalyst for alcohol formation. The optimum composition was determined with the ICP-OES (9 at% Pd and 91 at % Cu) which was in agreement with EDX data that gave comparable data of 93% of Cu and 7% of Pd. Morphological changes of the as-prepared sample (Figure 2.41a), thermally annealed, and the oxide-derived sample was studied by identical location SEM. Moreover, the structural robustness of the catalyst was also monitored by HR-SEM prior to and after 102 h
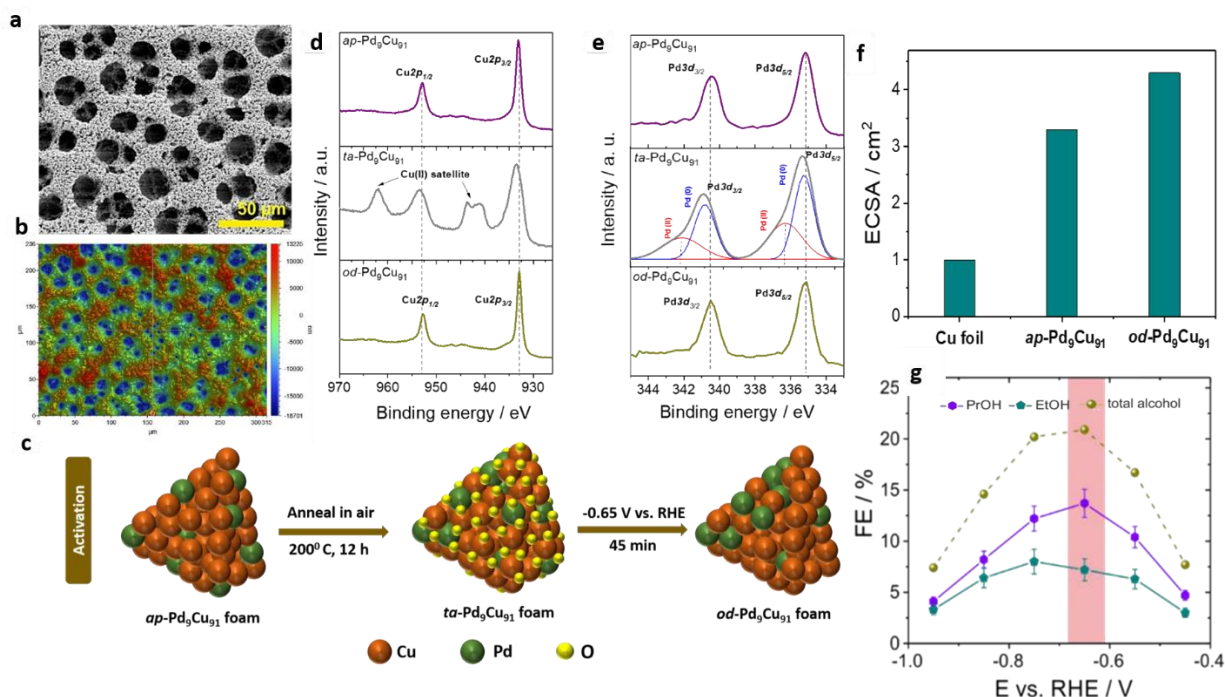
Figure 2.41. (a) SEM image of binary alloy Pd_9Cu_{91} foam deposited for the 40s; (b) corresponding white light interferometer image of foam showing the pores uniformly distributed; (c) Activation steps of *ap*-Pd_9Cu_{91} sample followed by annealing at 200 °C for 12 h in the air forming the corresponding oxides and pretreatment at -0.65V for 45 min *od*-Pd_9Cu_{91} sample which shows the phase segregation resulting into Cu-rich and Pd-rich domain; (d) XPS analysis of *ap, ann, od*-Pd_9Cu_{91} showing changes in the peak of Cu; (e) XPS analysis of *ap, ann, od*-Pd_9Cu_{91} showing changes in the peak of Pd; (f) ECSA of *od*-Pd_9Cu_{91} compared to as-prepared sample and Cu foam showing more roughness; (g) Product distribution of alcohols as a function of potentials on *od*-Pd_9Cu_{91} catalyst. Readapted from Green Chem., 2020, 22, 6497 with permission from the © The Royal Society of Chemistry 2020. All rights reserved

long-term electrolysis. The primary porosity (mesoporous structure) of the catalyst seems to stay intact whereas the second porosity (dendritic structure) at the walls of the pores seemed, however, to change at the nanoscale. The diameter of the pores was determined to be around 25 ± 2 µm from the white light interferometer (WLI) (Figure 2.41b), which is in good agreement with the mean surface diameter of 23 ± 3 µm obtained by SEM. The activation steps follow from metal to oxide formation after annealing, which, in turn is followed by reducing the oxide by pretreating it at -0.65 V for 45 minutes before conducting the electrolysis experiment.

X-ray diffraction (XRD) and X-ray photoelectron spectroscopy (XPS) studies confirmed the presence of oxide in the annealed sample and regained metal form after the reduction of oxide when cathodic potentials were applied. For conducting XRD analysis, samples were deposited on graphite foil to eliminate the contribution from the substrate. XPS analysis displays spin-orbit split Cu*2p* (Figure 2.41 panel d) and Pd*3d* (Figure 2.41 panel e) photoemissions spectra of the Pd_9Cu_{91} samples in their respective processing states. For the thermally annealed sample *ann*-Pd_9Cu_{91}, characteristic shake-up satellites were observed to appear in the Cu*2p* photoemission spectrum suggesting the presence of cupric CuO in the sample (Figure 2.41 panel d). However, the formation of cuprous oxide (Cu_2O) cannot be confirmed by XPS as binding energy for metallic Cu and Cu_2O lies in the same range (BE(*Cu2p3/2*) = ~933 eV). [44-48] The Pd*3d* peak broadened after the annealing treatment and a Pd(II) component (PdO, BE(*3d5/2*) = ~336.7 eV) was evident after peak deconvolution. Both the Cu*2p* and Pd*3d* emissions in the *od*-Pd_9Cu_{91} exhibit the same features as the metallic *ap*-Pd_9Cu_{91} sample, thus signifying the complete conversion of the intermediately formed oxide into a metallic catalyst under the applied reductive conditions (45 min at -0.65 V vs. RHE).

The instability of the oxides, under those electrochemical conditions applied for the catalyst activation (-0.65 V vs. RHE) and PrOH production was further supported by *operando* Raman spectroscopy. Notably, the Raman spectroscopy analysis is a surface sensitive technique.[49] *Operando* Raman spectra for *od*-Pd_9Cu_{91} (after pretreatment at -0.65 V vs. RHE) and *ann*-Pd_9Cu_{91} were measured in CO_2 saturated 0.5 M $KHCO_3$ electrolyte to maintain similar conditions as electrolysis experiment, where the potential is stepped from the open circuit potential (OCP) to those potentials relevant for the oxygenate production. The oxides already disappeared at 0 V vs. RHE prior to the actual onset of the CO_2RR. Notably, the chemisorption of reactants, intermediates, and products of the CO_2RR occurs only after the disappearance of the oxidic species at 0 V vs. RHE.

The roughness factor of the catalyst also changes with the morphology and the activation process. Geometric surface area is different than the actual area and one needs to determine this actual area to obtain the current density. The surface area which is mainly responsible for the activity of the catalyst is Electrochemical Active Surface Area (ECSA). The ECSA of the as-deposited, as well as the activated PdCu foam catalysts, was determined based on voltammetric measurements using di-methyl viologen as a reversible redox probe. In the *ap*-Pd_9Cu_{91} sample, sidewalls of the pores consist of a dendritic structure with nano-meter crystallites often exhibiting cube-like shapes at very high magnification. After thermal annealing, the *ann*-Pd_9Cu_{91} foam seems to change morphology by partial coalescence of the

cubic shapes dendrimers thereby completely dissolving the cubic shapes. Furthermore, morphological changes in the course of the electrochemical oxide reduction at -0.65 V vs. RHE for *od*-Pd_9Cu_{91} sample give rise to the appearance of particles (10-50 nm) on the catalyst surface. The formation of the nano-sized particles further enhanced the electrochemically active surface area (ECSA) that is four-fold than planar Cu foil (Figure 2.41 panel f).

Potentiostatic electrolysis experiments were conducted in CO_2 saturated 0.5 M $KHCO_3$ (pH 7.2) to test the catalyst efficiency using both the *ap*-Pd_9Cu_{91} and the *od*-Pd_9Cu_{91} samples. The applied electrolysis potentials ranged from -0.45 V to -0.95 V vs. RHE. A multi-catalyst approach was applied for this screening where a newly prepared catalyst was used for each screening experiment (3 h duration). The main product as a result of CO_2RR in *ap*-Pd_9Cu_{91} sample was formate reaching up to 42.7% at a low applied overpotential of -0.55 V vs. RHE. With increasing overpotentials, formate efficiencies showed a steady decrease reaching a value of $FE_{formate}$ = 12.5% at -0.95 V vs. RHE. FE of CO (FE_{CO}) was seen to observe a similar trend of decreasing efficiencies with increasing overpotentials, starting from a maximum value of FE_{CO} = 35.6% (j_{CO} = -0.52 mA cm^{-2}) at lowest applied potentials of -0.45 V vs. RHE. Low amounts of hydrocarbons were obtained, with a maximum of C2 hydrocarbon efficiency of 12.3% (FE_{C2H4} = 8.2%, FE_{C2H6} = 4.1%) at -0.75V vs. RHE.

The results were different for the *od*-Pd_9Cu_{91} catalyst reaching the total efficiency of around 80% with 20% missing (attributed to the missing oxygenates formed during the CO_2RR process). The efficiency of formate was less compared to the *ap*-Pd_9Cu_{91} sample with a maximum of 26.8 % at -0.55 V vs. RHE. Additionally, formation of hydrocarbon was preferred (FE_{C2H4} = 7.8%, FE_{C2H6} = 11.6%) at -0.75V vs. RHE. For the *od*-Pd_9Cu_{91} catalyst, both C2 (EtOH) and C3 (PrOH) alcohols were formed as CO_2RR products. A maximum selectivity of FE_{PrOH} = 13.7% (j_{PrOH} = -1.15 mA cm^{-2}) is observed at -0.65 V vs. RHE that is approximately two-fold than ethanol production, EtOH (e.g., FE_{EtOH} = 7.1% with j_{EtOH} = -0.60 mA cm^{-2}) (Figure 2.41 panel g). The onset potential of PrOH formation (-0.45 V vs. RHE) and the active potential with maximum PrOH efficiency (-0.65 V vs. RHE) are both significantly shifted towards the positive direction ($\approx$ 200 mV) in comparison to the CO_2 electrolysis reactions performed using 'pure' oxide derived copper catalysts. Additionally, catalyst durability was checked by a long-term electrolysis experiment at an optimized potential where the alcohol efficiency was highest (-0.65 V vs. RHE).

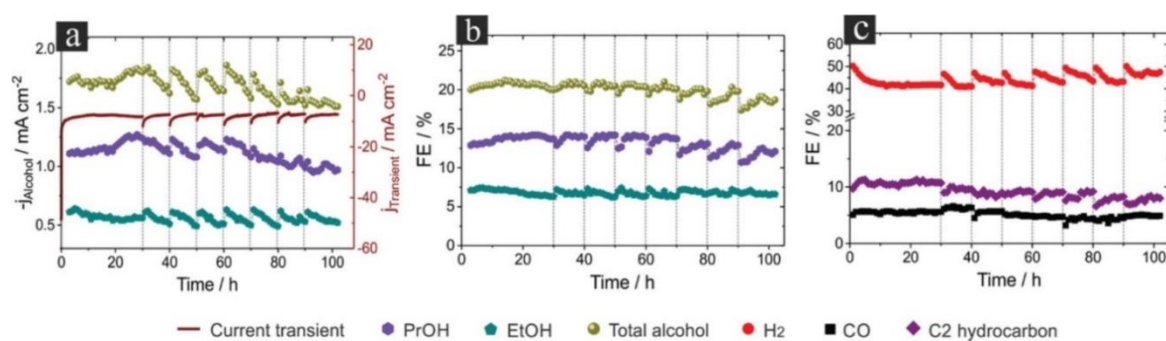**Figure 2.42.** (a) Current transient and time-dependent partial current densities of alcohols from the extended electrolysis carried out at -0.65 V vs. RHE over the *od*-Pd_9Cu_{91} sample; (b) Corresponding alcohol efficiencies; (c) Corresponding CO, H_2, and C2 hydrocarbon efficiencies.Reproduced from Green Chem., 2020, 22, 6497 with permission from the © The RoyalSociety of Chemistry 2020. All rights reserved

An electrolysis experiment of a total of 102 h (Figure 2.42) was carried out which consisted of one continuous long-term experiment of 30 h and six consecutive stressing experiments of 10 h each and one last 12 h stressing experiment. In between the stressing experiments, the catalyst was stored in milli-Q water and dried in a gentle Ar stream prior to the electrolysis experiment. The continuous-discontinuous 102 h experiments demonstrate two-fold stability with prolonged CO_2RR and switching on-off with repetitive loss of potential control. The current transient (wine curve) of 102 h of electrolysis is shown in Figure 2.42 (a).

In a steady state, the average current density of -7.5 mA cm^{-2} with $j_{Alcohol}= -1.75$ mA cm^{-2} was achieved (Figure 2.42 a). Importantly, slightly higher current densities were observed at the start of the electrolysis experiment (discontinuous) indicating the corresponding reduction of surface oxide formed while the resting time of the catalyst at OCP. Alcohol and gaseous products are presented in terms of FE (Figure 2.42 (b) & (c)). PrOH formation was achieved with an initial value of $FE_{PrOH} = 12.9\%$ to $FE_{PrOH} = 13.9\%$ during the course of 30 h of electrolysis. Alterations in the catalyst's activity towards C3 alcohol formation seem to start decreasing after 70 h of electrolysis. This decrease in FEs of PrOH and EtOH formation is anti-related with hydrogen formation, thus indicating a more significant degradation pattern in the case of stressed electrolysis in comparison to continuous electrolysis.

This contribution depicts the *ann*-PdCu foam as a robust catalyst towards propanol formation with 2 fold higher selectivity than ethanol formation at rather low overpotential.

2.5 CO_2RR to formate over porous In$_{55}$Cu$_{45}$ alloy: Suppression of HER

A high surface InCu porous catalyst was employed for the selective formate formation as a target product from CO_2RR. The post-transition metal Indium (In) is known to produce formate selectively, however, suffers from stability issue.[50-51] To address this problem, a second metal was introduced which could help to stabilize the formation of intermediates during the long-term operation. Cu was chosen as a second metal to combine due to its relatively low cost and higher availability. One benefit of such a two-component catalyst system could be the increase of CO_2RR selectivity toward a certain target product that is predominantly or exclusively formed on one of the catalyst constituents. This work presents an In$_{55}$Cu$_{45}$ alloy foam catalyst with dendrimers in the sidewalls of pores. This notation for the alloyed catalyst was determined as in the bulk by the use of the ICP-OES analysis technique. Pure In deposited under similar conditions has a completely different morphology compared to the dendrimers. This change in the morphology gives rise to higher ECSA which grow in the following sequence: In@Cu (1.5 cm^2) < In$_{55}$Cu$_{45}$@Cu (2.7 cm^2) < Cu-foam@Cu (3.6 cm^2).

White light interferometer (WLI) was used to get an idea about the thickness of the sample and the average thickness was found to be 19 ± 1 µm, whereas the corresponding cross-sectional SEM inspection revealed a slight increase in the thickness (20 to 23 µm) of the catalyst. This is simply because the WLI does not probe the catalyst completely down to Cu foil support. XRD analysis was done to understand the crystalline structure of the material. The In$_{55}$Cu$_{45}$ catalyst showed peaks corresponding to the alloyed peak (In$_x$Cu$_y$) revealing the formation of
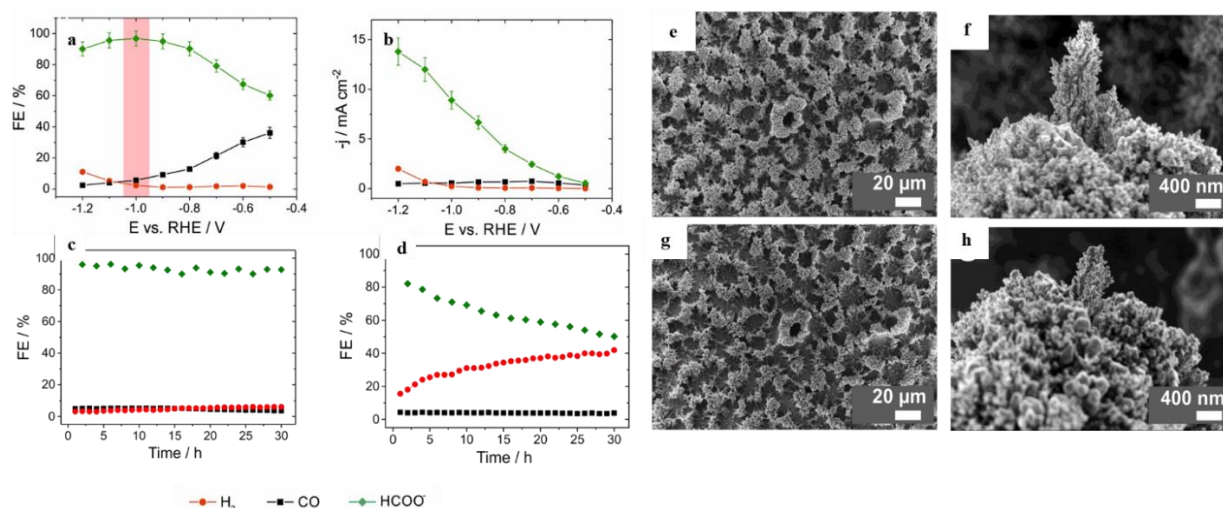
Figure 2.51. (a) Potentiostatic product analysis of $In_{55}Cu_{45}$ catalyst; (b) Corresponding partial current densities of H_2, CO, $HCOO^-$ normalized to the geometric surface area; (c) FEs of respective CO_2RR products a function of time at −1.0 V in long term operation of 30 h; (d) Long term operation at −1.0 V for pure In deposited under similar conditions; (e, f) SEM images of $In_{55}Cu_{45}$ catalyst prior to electrolysis; (g, h) Identical location SEM images of $In_{55}Cu_{45}$ catalyst after 30 h of electrolysis at −1.0 V.Readapted with permissions from ACS Appl. Mater. Interfaces 2021, 13, 35677−35688.Copyright ©2021 American Chemical Society.

alloy in XRD analyses of material. Interestingly, there is no indication in the diffractograms of the presence of (surface) oxides that are reported for pure (as-prepared) Cu foams.[6] It can be assumed that the oxidic skin on the ap-$In_{55}Cu_{45}$ alloy is either too thin or in a largely amorphous state to be probed by XRD, which is sensitive only to phases with sufficient long-range transitional order. XPS analysis, which is more surface sensitive was able to probe a thin oxidic layer on the ap-$In_{55}Cu_{45}$ alloy. In the case of Cu, Cu (0), and Cu (I) peak was obtained in the XPS spectra but due to their similar binding energy, it is hard to discern between metallic Cu and Cu (I). Indium, however, showed two broad peaks for $In3d_{3/2}$ and $In3d_{5/2}$ corresponding to In (0) and In (III) components on the surface. The In (III) corresponds to the thin oxide layer, whereas the In(0)-related photoemission most likely resulted from contributions of the metallic $In_{55}Cu_{45}$ bulk.

Electrochemical characterization of the catalyst was done utilizing the CO_2 electrolysis under reductive conditions in the potential range from −0.5 V to −1.2 V vs. RHE. For every potential, a new catalyst was used for a 1 h electrolysis experiment each (so-called multi-catalyst approach). Starting from −0.5 V, FE for formate was 60.2% which started to increase with more negative overpotentials (Figure 2.51 a). FE of formate reached a maximum at −1.0 V with 96.8% and decreased slightly up to 90% at −1.2 V vs. RHE which is rather a high overpotential. Most strikingly, parasitic HER remains almost fully suppressed in the entire range of potentials studied herein. CO production as a minor product was evident at low overpotential reaching 36.1% at −0.5 V, decreases with increase in overpotentials and rise in formate efficiencies. Partial Current density (PCD), normalized to the geometric surface area, is presented as a function of applied potential (Figure 2.51 b) and the PCD for formate reached up to −14 $mAcm^{-2}$ at the highest applied potential (−1.2 V vs. RHE). At the optimum potential of −1.0 V vs. RHE, where the FE for formate reached the maximum value, PCD for formate was observed as high as −8.9 $mAcm^{-2}$.

To check the stability of the catalyst, a continuous long-term operation of 30 h was conducted at the best potential (-1.0 V) for formate production. FE of formate was found to never decrease below 90% and maintained an average value of 94.2 ± 2.1 % (Figure 2.51 c). The catalyst activity of the *ap*-In$_{55}$Cu$_{45}$ foam was compared with the In film deposited in the same conditions and at the same potential of -1.0 V vs. RHE. Initially, for long-term (30 h) conditions, the FE of formate was around 82% with the H$_2$ efficiency of 15% which started to increase with time, finally reaching up to 42%. On the other hand, formate started to decrease leaving the efficiency to only ~50% at the end of 30 h showing degradation in the performance of pure In catalyst (Figure 2.51 d). Structural and morphological analysis during this long-term operation was done by IL-SEM. Both macroporosity and dendritic structures of the material (*ap*-In$_{55}$Cu$_{45}$) did not show significant changes before and after 30 h of electrolysis (Figure 2.51 (e-h)) thereby supporting the long-term catalytic stability.

Structure alterations by ICP-MS

The partially oxidized catalyst undergoes further alterations when exposed to the electrolyte at OCP and subsequently under reductive conditions. Oxide reduction not only affects the surface of the catalyst but also can alter the electrolyte to which the catalyst is exposed. Releasing of metal ions preferentially occurs upon reduction of formed oxides and can cause the rearrangement of the catalyst surface by redepositing during the CO$_2$RR. This can be done by ICP-MS measurement. Time-dependent ICP-MS analysis of In and Cu content in the electrolyte for two extreme potentials (-0.5 V and -1.2 V vs. RHE) is given in Figure 2.52. Both the metal ion concentration (In and Cu ion) showed a rapid increase within the initial 5 to 10 min of exposure to the electrolyte before a (quasi) plateau was reached. Because of the continual bubbling of CO$_2$ gas through the catholyte during electrolysis, the liberated metal ions are easily disseminated (diluted) throughout the whole electrolyte volume when the oxide reduction is complete. The dissolving properties were affected by the electrolysis potential used. At the lowest applied overpotentials (0.5 V vs. RHE), the Cu component of the oxidic skin dissolves preferentially into the electrolyte, while the In content of the electrolyte remains relatively low (Figure 2.52 a). This is most likely due to the In(III)/In's greater negative standard potential ($E^0(\text{In}^{3+}/\text{In}^0) = -0.34$ V vs. SHE). Under these experimental settings, the reduction of indium oxide is expected to be significantly slower and incomplete.
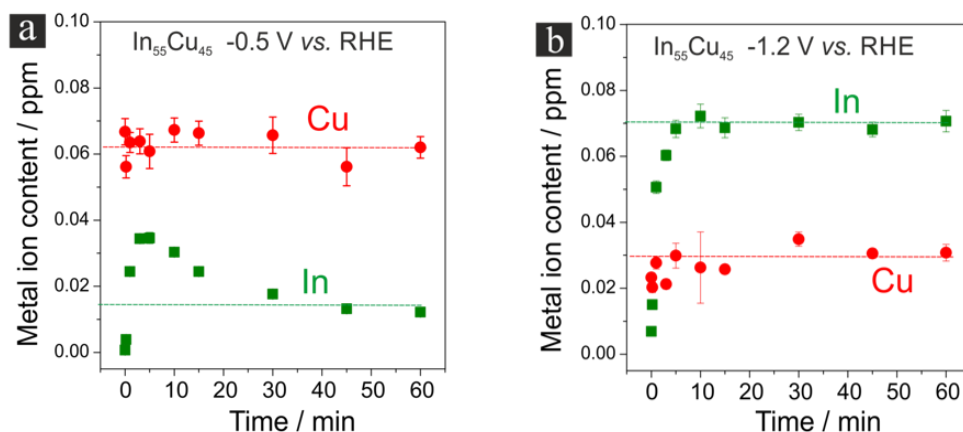
Figure 2.52. Time-dependent ICP-MS of the metal ion content in CO$_2$- sat. 0.5 M KHCO$_3$ (a) at -0.5 V vs. RHE; (b) at -1.2 V vs. RHE. 0.5 ml of electrolyte was taken out for the mentioned time-interval for 1 h. Reprinted with permissions from ACS Appl. Mater. Interfaces 2021, 13, 35677−35688,Copyright ©2021American Chemical Society.

Surprisingly, at the highest applied potentials (1.2 V vs. RHE), the condition was reversed. Notably, In is preferentially dissolved following surface oxide reduction, whilst the Cu concentration in solution stays relatively low (Figure 2.52 b).

Transfer of the catalyst to technical GDE substrates

The *ap*-In$_{55}$Cu$_{45}$ alloy foam was then further transferred to technical support (GDE). Important to note that when the electrolyte comes in touch with the carbon fabric, it seeps into the uppermost layers of the carbon microporous layer (C-MPL) of the GDE support to some extent. Correspondingly, the catalyst deposition at the MPL's outermost region is advantageous because it increases the overall adhesion (wetting) of the porous metallic catalyst deposit onto the carbon substrate. To demonstrate the performance of the In$_{55}$Cu$_{45}$@GDE catalyst, a 1hr electrolysis from CO$_2$-sat. 0.5 M KHCO$_3$ solution at −1.0 V vs. RHE was performed and compared to data obtained for the In$_{55}$Cu$_{45}$@Cu catalyst (Figure 2.53). The remarkable selectivity toward formate was found to remain substantially unchanged (Figure 2.53 a). However, as compared to the In$_{55}$Cu$_{45}$@Cu, FE$_{CO}$ was somewhat higher (15%). It is worth noting that the GDE support had a larger surface area than the Cu foil. During electrodeposition, this increased roughness is transmitted to the In$_{55}$Cu$_{45}$ catalyst layer. Improved total and partial CO$_2$RR current densities were obtained, with PCD$_{formate}$ ≈ −30 mA cm^{-2} at −1.0 V vs. RHE (Figure 2.53 b).
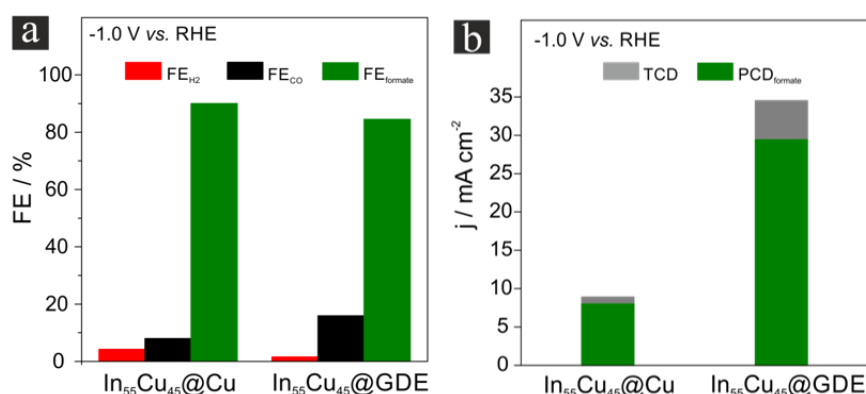
Figure 2.53. Comparison of the performance using the In$_{55}$Cu$_{45}$@Cu and the In$_{55}$Cu$_{45}$@GDE as the catalyst at −1.0 V vs. RHE for 1 h in CO$_2$-sat. 0.5 KHCO$_3$ solution in terms of (a) Product distribution as FE; (b) Corresponding total (TCD), and partial (PCD) current densities normalized to the geometric surface area of the support.Reprinted with permissions from ACS Appl. Mater. Interfaces 2021, 13, 35677−35688, Copyright ©2021 American Chemical Society.

This work showed excellent electrocatalytic performance toward formate production, with FE$_{formate}$ values never falling below 90% within the extended (400 mV) potential window (−0.8 to −1.2 V *vs.* RHE) and exhibiting long-term stability

2.6 References:

(1). Gao, D.; Zegkinoglou, I.; Divins, N. J.; Scholten, F.; Sinev, I.; Grosse, P.; Roldan Cuenya, B., Plasma-Activated Copper Nanocube Catalysts for Efficient Carbon Dioxide Electroreduction to Hydrocarbons and Alcohols. *ACS Nano* **2017,** *11* (5), 4825-4831.

(2). Li, C. W.; Kanan, M. W., CO_2 Reduction at Low Overpotential on Cu Electrodes Resulting from the Reduction of Thick Cu_2O Films. *J. Am. Chem. Soc.* **2012,** *134* (17), 7231-7234.

(3). Frese, K. W., Electrochemical Reduction of CO_2 at Intentionally Oxidized Copper Electrodes. *J. Electrochem. Soc.* **1991,** *138* (11), 3338-3344.

(4). Mistry, H.; Varela, A. S.; Bonifacio, C. S.; Zegkinoglou, I.; Sinev, I.; Choi, Y. W.; Kisslinger, K.; Stach, E. A.; Yang, J. C.; Strasser, P.; Cuenya, B. R., Highly selective plasma-activated copper catalysts for carbon dioxide reduction to ethylene. *Nat. Commun.* **2016,** *7.*

(5). Le, M.; Ren, M.; Zhang, Z.; Sprunger, P. T.; Kurtz, R. L.; Flake, J. C., Electrochemical Reduction of CO_2 to CH_3OH at Copper Oxide Surfaces. *J. Electrochem. Soc.* **2011,** *158* (5), E45.

(6). Dutta, A.; Rahaman, M.; Luedi, N. C.; Mohos, M.; Broekmann, P., Morphology Matters: Tuning the Product Distribution of CO_2 Electroreduction on Oxide-Derived Cu Foam Catalysts. *ACS Catal.* **2016,** *6* (6), 3804-3814.

(7). Kas, R.; Kortlever, R.; Milbrat, A.; Koper, M. T. M.; Mul, G.; Baltrusaitis, J., Electrochemical CO_2 reduction on Cu_2O-derived copper nanoparticles: Controlling the catalytic selectivity of hydrocarbons. *PCCP* **2014,** *16* (24), 12194-12201.

(8). Li, C. W.; Ciston, J.; Kanan, M. W., Electroreduction of carbon monoxide to liquid fuel on oxide-derived nanocrystalline copper. *Nature* **2014,** *508,* 504.

(9). T. Kondo, T. M., K. Uosaki,, In situ SXS and XAFS measurements ofelectrochemical interface, in: C.S.S.R. Kumar (Ed.), X-ray and NeutronTechniques for Nanomaterials Characterization, Springer, Berlin Heidelberg,Berlin, Heidelberg, **2016,** pp. 367–449.

(10). Jiang, S.; Klingan, K.; Pasquini, C.; Dau, H., New aspects of operando Raman spectroscopy applied to electrochemical CO_2 reduction on Cu foams. *J. Chem. Phys.* **2018,** *150* (4), 041718.

(11). Deng, Y.; Handoko, A. D.; Du, Y.; Xi, S.; Yeo, B. S., In Situ Raman Spectroscopy of Copper and Copper Oxide Surfaces during Electrochemical Oxygen Evolution Reaction: Identification of CuIII Oxides as Catalytically Active Species. *ACS Catal.* **2016,** *6* (4), 2473-2481.

(12). Balkanski, M.; Nusimovici, M. A.; Reydellet, J., First order Raman spectrum of Cu_2O. *Solid State Commun.* **1969,** *7* (11), 815-818.

(13). Oda, I.; Ogasawara, H.; Ito, M., Carbon monoxide adsorption on copper and silver electrodes during carbon dioxide electroreduction studied by infrared reflection absorption spectroscopy and surface-enhanced Raman spectroscopy. *Langmuir* **1996,** *12* (4), 1094-1097.

(14). Akemann, W.; Otto, A., The effect of atomic scale surface disorder on bonding and activation of adsorbates: vibrational properties of CO and CO_2 on copper. *Surf. Sci.* **1993,** *287-288,* 104-109.

(15). Akemann, W.; Otto, A., Vibrational modes of CO adsorbed on disordered copper films. *J. Raman Spectrosc.* **1991,** *22* (12), 797-803.

(16). Su, P.; Xu, W.; Qiu, Y.; Zhang, T.; Li, X.; Zhang, H., Ultrathin Bismuth Nanosheets as a Highly Efficient CO_2 Reduction Electrocatalyst. *ChemSusChem* **2018,** *11* (5), 848-853.

(17). Han, N.; Wang, Y.; Yang, H.; Deng, J.; Wu, J.; Li, Y.; Li, Y., Ultrathin bismuth nanosheets from in situ topotactic transformation for selective electrocatalytic CO_2 reduction to formate. *Nat. Commun.* **2018,** *9* (1), 1320.

(18). Zhang, H.; Ma, Y.; Quan, F.; Huang, J.; Jia, F.; Zhang, L., Selective electro-reduction of CO_2 to formate on nanostructured Bi from reduction of BiOCl nanosheets. *Electrochem. Commun.* **2014,** *46,* 63-66.

(19). Dutta, A.; Zelocualtecatl Montiel, I.; Kiran, K.; Rieder, A.; Grozovski, V.; Gut, L.; Broekmann, P., A Tandem ($Bi_2O_3 \rightarrow Bi_{met}$) Catalyst for Highly Efficient ec- CO_2 Conversion into Formate: Operando Raman Spectroscopic Evidence for a Reaction Pathway Change. *ACS Catal.* **2021,** 4988-5003.

(20). Pereira, A. L. J.; Errandonea, D.; Beltrán, A.; Gracia, L.; Gomis, O.; Sans, J. A.; García-Domene, B.; Miquel-Veyrat, A.; Manjón, F. J.; Muñoz, A.; Popescu, C., Structural study of α-Bi_2O_3 under pressure. *J. Phys.: Condens. Matter* **2013,** *25* (47), 475402.

(21). Kumar, P.; Singh, J.; C Pandey, A., Rational low temperature synthesis and structural investigations of ultrathin bismuth nanosheets. *RSC Adv.* **2013,** *3* (7), 2313-2317.

(22). Harwig, H. A., On the Structure of Bismuthsesquioxide: The α, β, γ, and δ-phase. *Z. Anorg. Allg. Chem.* **1978,** *444* (1), 151-166.

(23). Betsch, R. J.; White, W. B., Vibrational spectra of bismuth oxide and the sillenite-structure bismuth oxide derivatives. *Spectrochim. Acta A: Mol. Spectrosc.* **1978,** *34* (5), 505-514.

(24). Ho, C.-H.; Chan, C.-H.; Huang, Y.-S.; Tien, L.-C.; Chao, L.-C., The study of optical band edge property of bismuth oxide nanowires α-Bi_2O_3. *Opt. Express* **2013,** *21* (10), 11965-11972.

(25). Steele, J. A.; Lewis, R. A., In situ micro-Raman studies of laser-induced bismuth oxidation reveals metastability of β-Bi_2O_3 microislands. *Opt. Mater. Express* **2014,** *4* (10), 2133-2142.

(26). Dutta, A.; Montiel, I. Z.; Erni, R.; Kiran, K.; Rahaman, M.; Drnec, J.; Broekmann, P., Activation of bimetallic AgCu foam electrocatalysts for ethanol formation from CO_2 by selective Cu oxidation/reduction. *Nano Energy* **2020,** *68*, 104331.

(27). Zeng, J.; Bejtka, K.; Ju, W.; Castellino, M.; Chiodoni, A.; Sacco, A.; Farkhondehfal, M. A.; Hernández, S.; Rentsch, D.; Battaglia, C.; Pirri, C. F., Advanced Cu-Sn foam for selectively converting CO_2 to CO in aqueous solution. *Appl. Catal. B: Environmental* **2018,** *236*, 475-482.

(28). Li, Q.; Fu, J.; Zhu, W.; Chen, Z.; Shen, B.; Wu, L.; Xi, Z.; Wang, T.; Lu, G.; Zhu, J.-j.; Sun, S., Tuning Sn-Catalysis for Electrochemical Reduction of CO_2 to CO via the Core/Shell Cu/SnO_2 Structure. *J. Am. Chem. Soc.* **2017,** *139* (12), 4290-4293.

(29). Sarfraz, S.; Garcia-Esparza, A. T.; Jedidi, A.; Cavallo, L.; Takanabe, K., Cu–Sn Bimetallic Catalyst for Selective Aqueous Electroreduction of CO_2 to CO. *ACS Catal.* **2016,** *6* (5), 2842-2851.

(30). Balkanski, M.; Nusimovici, M. A.; Reydellet, J., First order Raman spectrum of Cu_2O. *Solid State Commun.* **1969,** *7* (11), 815-818.

(31). Deng, Y.; Handoko, A. D.; Du, Y.; Xi, S.; Yeo, B. S., In Situ Raman Spectroscopy of Copper and Copper Oxide Surfaces during Electrochemical Oxygen Evolution Reaction: Identification of CuIII Oxides as Catalytically Active Species. *ACS Catal.* **2016,** *6* (4), 2473-2481.

(32). Diéguez, A.; Romano-Rodríguez, A.; Vilà, A.; Morante, J. R., The complete Raman spectrum of nanometric SnO_2 particles. *J. Appl. Phys.* **2001,** *90* (3), 1550-1557.

(33). Eifert, B.; Becker, M.; Reindl, C. T.; Giar, M.; Zheng, L.; Polity, A.; He, Y.; Heiliger, C.; Klar, P. J., Raman studies of the intermediate tin-oxide phase. *Phys. Rev. Mater.* **2017,** *1* (1), 014602.

(34). Sarfraz, S.; Garcia-Esparza, A. T.; Jedidi, A.; Cavallo, L.; Takanabe, K., Cu–Sn Bimetallic Catalyst for Selective Aqueous Electroreduction of CO_2 to CO. *ACS Catal.* **2016,** *6* (5), 2842-2851.

(35). Dutta, A.; Rahaman, M.; Hecker, B.; Drnec, J.; Kiran, K.; Zelocualtecatl Montiel, I.; Jochen Weber, D.; Zanetti, A.; Cedeño López, A.; Martens, I.; Broekmann, P.; Oezaslan, M., CO_2 electrolysis – Complementary operando XRD, XAS and Raman spectroscopy study on the stability of Cu_xO foam catalysts. *J. Catal.* **2020,** *389*, 592-603.

(36). Hori, Y.; Wakebe, H.; Tsukamoto, T.; Koga, O., Electrocatalytic process of CO selectivity in electrochemical reduction of CO_2 at metal electrodes in aqueous media. *Electrochim. Acta* **1994,** *39*, 1833-1839.

(37). Rahaman, M.; Dutta, A.; Zanetti, A.; Broekmann, P., Electrochemical Reduction of CO_2 into Multicarbon Alcohols on Activated Cu Mesh Catalysts: An Identical Location (IL) Study. *ACS Catal.* **2017,** *7* (11), 7946-7956.

(38). Zhuang, T.-T.; Pang, Y.; Liang, Z.-Q.; Wang, Z.; Li, Y.; Tan, C.-S.; Li, J.; Dinh, C. T.; Luna, P.; Hsieh, P.-L.; Burdyny, T.; Li, H.-H.; Liu, M.; Wang, Y.; Li, F.; Proppe, A.; Johnston, A.; Nam, D.-H.; Wu, Z.; H. Sargent, E., Copper nanocavities confine intermediates for efficient electrosynthesis of C3 alcohol fuels from carbon monoxide. *Nat. Catal.* **2018**.

(39). Kim, T.; Kargar, A.; Luo, Y.; Mohammed, R.; Martinez-Loran, E.; Ganapathi, A.; Shah, P.; Fenning, D. P., Enhancing C2–C3 Production from CO_2 on Copper Electrocatalysts via a Potential-Dependent Mesostructure. *ACS Appl. Energy Mater.* **2018,** *1* (5), 1965-1972.

(40). Verdaguer-Casadevall, A.; Li, C. W.; Johansson, T. P.; Scott, S. B.; McKeown, J. T.; Kumar, M.; Stephens, I. E. L.; Kanan, M. W.; Chorkendorff, I., Probing the Active Surface Sites for CO Reduction on Oxide-Derived Copper Electrocatalysts. *J. Am. Chem. Soc.* **2015,** *137* (31), 9808-9811.

(41). Gao, D.; Zhou, H.; Wang, J.; Miao, S.; Yang, F.; Wang, G.; Wang, J.; Bao, X., Size-dependent electrocatalytic reduction of CO_2 over Pd nanoparticles. *J. Am. Chem. Soc.* **2015,** *137* (13), 4288-91.

(42). Min, X.; Kanan, M. W., Pd-Catalyzed Electrohydrogenation of Carbon Dioxide to Formate: High Mass Activity at Low Overpotential and Identification of the Deactivation Pathway. *J. Am. Chem. Soc.* **2015,** *137* (14), 4701-4708.

(43). Rahaman, M.; Dutta, A.; Broekmann, P., Size-Dependent Activity of Palladium Nanoparticles: Efficient Conversion of CO_2 into Formate at Low Overpotentials. *ChemSusChem* **2017,** *10* (8), 1733-1741.

(44). Dutta, A.; Rahaman, M.; Mohos, M.; Zanetti, A.; Broekmann, P., Electrochemical CO_2 Conversion Using Skeleton (Sponge) Type of Cu Catalysts. *ACS Catal.* **2017,** *7* (8), 5431-5437.

(45). Wu, C.-K.; Yin, M.; O'Brien, S.; Koberstein, J. T., Quantitative Analysis of Copper Oxide Nanoparticle Composition and Structure by X-ray Photoelectron Spectroscopy. *Chem. Mater.* **2006,** *18* (25), 6054-6058.

(46). Miller, A. C.; Simmons, G. W., Copper by XPS. *Surf. Sci. Spectra* **1993,** *2* (1), 55-60.

(47). Rupp, H.; Weser, U., X-ray photoelectron spectroscopy of copper(II), copper(I), and mixed valence systems. *Bioinorg. Chem.* **1976,** *6* (1), 45-59.

(48). Wu, C.-K.; Yin, M.; O'Brien, S.; Koberstein, J. T., Quantitative Analysis of Copper Oxide Nanoparticle Composition and Structure by X-ray Photoelectron Spectroscopy. *Chem. Mater.* **2006,** *18* (25), 6054-6058.

(49). Dutta, A.; Rahaman, M.; Hecker, B.; Drnec, J.; Kiran, K.; Zelocualtecatl Montiel, I.; Jochen Weber, D.; Zanetti, A.; Cedeño López, A.; Martens, I.; Broekmann, P.; Oezaslan, M., CO_2 electrolysis – Complementary operando XRD, XAS and Raman spectroscopy study on the stability of Cu_xO foam catalysts. *J. Catal* **2020,** *389*, 592-603.

(50). Bohlen, B.; Wastl, D.; Radomski, J.; Sieber, V.; Vieira, L., Electrochemical CO_2 reduction to formate on indium catalysts prepared by electrodeposition in deep eutectic solvents. *Electrochem. commun* **2020,** *110*, 106597.

(51). Luo, W.; Xie, W.; Li, M.; Zhang, J.; Züttel, A., 3D hierarchical porous indium catalyst for highly efficient electroreduction of CO_2 *J. Mater. Chem. A* **2019,** *7* (9), 4505-4515.

3. Results from other projects

In addition to the aqueous systems, other reaction environments such as ionic liquids were also explored for the CO_2RR in this thesis. Ionic Liquids (ILs) have received special attention as the alternative electrolyte to the conventional aqueous systems in the electrochemical reduction of CO_2. Primary properties of ILs include enhanced solubility of CO_2, ability to suppress hydrogen evolution reaction (HER) and wide potential window. Pioneering endeavours in this field have revealed the use of room temperature ionic liquid (RTIL), [EMIm][BF4] (1-ethyl-3-methyl-imidazolium tetra fluoroborate) with the combination of Ag as working electrode for CO_2RR can appreciably lower the CO_2RR overpotential. ILs when combined with the water reportedly subdue parasitic HER. The comprehensive study of different metal electrodes altogether of thirteen different electrodes comprising of Platinum (Pt), Palladium (Pd), Silver (Ag), Gold (Au), Bismuth (Bi), Tin (Sn), Nickel (Ni), Molybdenum (Mo), Iron (Fe), Zinc (Zn), Copper (Cu) and Glassy carbon (GC) with combination of ionic liquid was explored. Metal electrodes were divided into three major groups depending on the activity towards CO_2RR. First group comprised of metals (Pt, Pd, Ni, Fe, Mo & GC) shows negligible or no activity towards CO_2RR. Second group was comprised of Cu, Zn, Bi, Pb, Au which are moderately active metals for CO_2 reduction in IL. The third group of metals, Sn and Ag were found to be most active for CO_2RR. Effect of cation and anion of IL was also explored in the study. High surface area catalyst obtained by DHBT method were also explored in Ionic liquid. Ag foam catalysts, when combined with 1-butyl-3-methylimidazolium tetrafluoroborate ([BMIm][BF4]) ionic liquid exhibits preferable electrocatalytic performance towards CO production reaching upto $FE_{CO} = \sim100\%$ within the broad potential window of ~400 mV and a shift in onset potential towards more positive was observed. A secondary enhancement for the CO_2RR was observed from the addition of water (20% mole fraction) to the [BMIm][BF$_4$] electrolyte resulting into furhter shifting of CO_2RR onset.

4. Conclusion and Outlook

High surface area catalysts, primarily in H-type configuration, were developed and used in the CO_2RR. A range of different products was obtained from these large surface area catalysts ranging from CO, COOH, C_2H_5OH, and C_3H_7OH. Previous studies have shown that pre-treating the catalyst influences not only the electrocatalytic activity but also the product distribution. One method for increasing catalytic activity and selectivity is to form oxide, however, the significance and stability of oxide in CO_2RR are not well understood. In the case of monometallic oxidic Cu foam, the stability of oxide was evaluated utilizing *operando* XAS, XRD, and Raman techniques. The fact that the oxide was fully reduced to metallic Cu prior to the production of hydrocarbons and alcohols was a significant finding in this work. Another mono-metallic foam (Bi) catalyst demonstrates higher stability when it is subjected to form Bi_2O_3. Bi_2O_3 was found to be an efficient and stable catalyst for formate production with FEs reaching up to ~100% within an extended potential window (~1100 mV) compared to the *ap* Bi/Bi_xO_y. Experimental investigations have suggested the formation of sub-carbonate species at low overpotentials indicating the alternate reaction mechanism (through sub-carbonate).

Following this approach, bimetallic/alloyed catalysts were developed. More specifically, Cu was combined with the other metals such as Pd, In, and Sn. The combination of Cu with Pd resulted in the formation of propanol with an efficiency of $FE_{PrOH} = 13.7\%$, which was 2 times higher than ethanol formation $FE_{EtOH} = 7.1\%$. The overpotential required for propanol generation was -0.65 V vs. RHE, which is significantly lower than for pure Cu foam. It is important to note that the as-prepared sample showed no alcohol formation. To obtain the catalyst, a two-step treatment was performed, followed by thermal annealing in air at 200 °C to obtain the thermally annealed sample, and subsequent reduction of the oxide at -0.65 V for 45 min, resulting in an oxide-derived catalyst that was subsequently used in electrolysis. A long-term analysis (100 h) was carried out to monitor the catalyst performance during continuous operation and subsequent loading experiments by switching the potential on and off. Formate was obtained as the main product when Cu was combined with In to give the composition of $In_{55}Cu_{45}$. FE of formate was obtained by 97% at -1.0 V vs. RHE and by 90% for a wide potential window from -0.8 V to -1.2 V vs. RHE.

This process of deposition was successfully transferred to 3d substrates such as gas diffusion electrode (GDE) as used in flow cell. An optimum amount of Sn was introduced into the Cu lattice, resulting in $Cu_{91}Sn_9$ with a lower Sn content for the formation of CO, and with further annealing, the CuO/SnO catalyst was prepared. CO was prepared with nearly 95% efficiency at -0.7 V vs. RHE with a potential window of 500 mV for more than 85% of the production of CO. *Operando* characterizations are very important to study the oxide reduction to a metallic state particularly under reductive conditions. *Operando* Raman spectroscopic analysis was performed to investigate the role of oxide in CO production when none of the components produced CO catalyst. The degradation of the catalyst was studied after 150 h of operation. Simultaneously, IL -SEM was performed in order to observe structural changes for the respective steps used for catalyst production.

Certainly, the avenues to improvement remain open, notwithstanding the progress that already made in this area. On the same lines, one of the topics that has to be thoroughly investigated is the reason for the catalyst's deterioration. Several characterisation technologies may be used to study the structural and morphological scales at the nanoscale range, for example, IL-SEM and IL-TEM. Another critical component would be to garner mechanistic insight in order to analyse the intermediates created during the reaction, as well as to investigate the role of oxide and construct a reaction mechanism. *Operando* techniques are useful to identify the intermediates formed during the reaction and the role of the oxides, e.g., *operando* IR, *in-situ* Raman, *operando* EXAFS (Extended X-ray absorption fine structure). Moreover, to scale up the process, the future goal would be to use the catalysts in a flow cell configuration. Some of the key issues with this setup are flooding of the electrolyte and catalyst stability. During CO_2RR, H_2 is also formed as a result of the parasitic reaction that occurs, which again proves to be a problem for long-term operation. An inverted rotating disk (IRDE) electrode could be one of the interesting ways to deal with this problem, as in this configuration the electrode surface is turned upside down to get rid of the H_2 bubble that forms on the surface of the electrode.

5. Publications

5.1. Enhanced electrocatalytic CO formation from CO$_2$ on nanostructured silver foam electrodes in ionic liquid/water mixtures

Authors: Alexander V. Rudnev, Kiran Kiran, Alena Cedeño López, Abhijit Dutta, Ilche Gjuroski, Julien Furrer, Peter Broekmann

Highlights: This contribution comprises of nanostructured silver foam electrocatalyst for the electrochemical CO$_2$ reduction reaction (CO$_2$RR) in 1-butyl-3-methylimidazolium tetrafluoroborate [Bmim][BF$_4$] ionic liquid. The Ag foam electrocatalyst shifts the onset of CO$_2$ electroreduction by 220 mV to less negative potentials as compared to a polished Ag foil electrode. Furthermore, addition of water in moderate amounts (mole fraction of 20 %) significantly leads in lowering the overpotential (120 mV), thus enhancing electrocatalytic activity towards CO formation. Identical location scanning electron microscopy further provides the support of structural stability of Ag foam catalyst.

Contribution: I was involved in the fabrication of the catalyst and investigated the overall performance of the catalyst using electrochemical methods. Furthermore, the physical characterization of the catalyst was carried out. I was involved in data analysis and writing some parts of the paper

Enhanced electrocatalytic CO formation from CO_2 on nanostructured silver foam electrodes in ionic liquid/water mixtures

Alexander V. Rudnev [a, b, *], Kiran Kiran [a], Alena Cedeño López [a], Abhijit Dutta [a], Ilche Gjuroski [a], Julien Furrer [a], Peter Broekmann [a, **]

[a] Department of Chemistry and Biochemistry, University of Bern, Freiestrasse 3, 3012, Bern, Switzerland
[b] A.N. Frumkin Institute of Physical Chemistry and Electrochemistry, Russian Academy of Sciences, Leninskii pr. 31, 119071, Moscow, Russia

ABSTRACT

We employ a novel type of nanostructured silver foam electrocatalyst to the electrochemical CO_2 reduction reaction (CO_2RR) in 1-butyl-3-methylimidazolium tetrafluoroborate ([Bmim][BF_4]) ionic liquid. The Ag catalyst is prepared from an aqueous electroplating bath by means of an additive-assisted electrodeposition approach, yielding macro-porous Ag foams. The pore sidewalls are composed of Ag nanoneedles having diameters of ~50−100 nm and lengths that can exceed 1 μm. We demonstrate that, when combined with the [Bmim][BF_4] electrolyte, this Ag electrocatalyst significantly shifts the onset of CO_2 electroreduction by ~220 mV to less negative potentials as compared to a polished Ag foil electrode. The addition of moderate amounts of water (optimum water mole fraction of 20%) to the pure [Bmim][BF_4] electrolyte leads to a further ~120 mV decrease in the CO_2RR overpotential. The combination of the Ag foam catalyst with the [Bmim][BF_4]/water mixture results in a ~300 mV wide potential window where CO is selectively produced with Faraday efficiencies >94%. The structural stability of the catalyst is supported by identical location scanning electron microscopy.

© 2019 Elsevier Ltd. All rights reserved.

1. Introduction

Since the industrial revolution, the consumption of fossil fuels has steadily increased, which, in turn, can be regarded as one of the major origins of today's environmental problems [1]. The most challenging one among them is certainly the global warming which has its primary origin in the continuous rise of the atmospheric carbon dioxide (CO_2) content which already reaches a level of >400 ppm [2]. This is why the CO_2 problem has received considerable attention worldwide, not only in the scientific community. As a result, a number of different approaches have been proposed for CO_2 capture [3], sequestration [4], and its conversion into value added products with the aim at contributing to a future closing of the anthropogenic CO_2 cycle [5−7]. The electrochemical reduction of CO_2 (hereinafter referred to as CO_2RR) deserves particular

attention [8] since it can convert CO_2 into high energy density fuels [7] (e.g., methanol [9,10], ethanol [11−14], and n-propanol [12,14]) and various chemical feedstock compounds (e.g., formate [12,15], ethylene [11,14,16] and CO [17−19]) by using a surplus of electricity originating from renewable wind, solar or hydro sources (so-called power to value approach) [12,20]. Among these valuable target products, CO is particularly promising due to the strong demand from the chemical industry [20] as primary reactant of the so-called Fisher-Tropsch process [21].

However, to become economically feasible, the CO_2RR must meet various criteria such as (i) high CO_2 conversion rates, (ii) a high product selectivity, (iii) a high energy efficiency, and (iv) a high catalyst durability [20]. In particular when using aqueous electrolyte media, the competing parasitic hydrogen evolution reaction (HER) significantly reduces the efficiency of CO_2 conversion. To avoid HER, room temperature ionic liquids (ILs) have been proposed as alternative electrolytes to common aqueous systems [22,23], particularly due to their unique physico-chemical properties, such as nearly zero vapor pressure (therefore considered as green solvents) [24], a wide stability potential window of up to 5 V [25], a relatively high electric conductivity [26], and a high affinity

towards CO_2 absorption [27]. It has also been reported that ILs can suppress the parasitic HER even in diluted IL/water mixtures [28,29]. Among the ILs studied so far, imidazolium-based ILs belong to the most promising and therefore most widely studied ones, also because of their extra electrocatalytic properties [30]. The presence of imidazolium based ILs can significantly reduce the CO_2RR over-potential [29,31], e.g. when combined with Ag catalysts. Imidazolium cations can therefore be considered as effective CO_2RR co-catalysts [32].

Of high importance to the overall activity of the CO_2RR catalysts is the abundance of low-coordinated reaction sites on the catalyst surface. This is why metallic nanomaterials (e.g. Ag [33–36], Cu [37], Au [38,39], Pd [40], and Zn [41]) have received considerable attention [42] with Ag being the most selective one towards CO formation [43]. Besides the wet chemical synthesis of nanoparticles [44,45] (NPs) and nanowires [45] (NWs) various nanostructuring approaches have been proposed [46] including, but not restricted to, catalyst activation through repetitive cycles of electro-anodization/electro-of Ag substrates [34,35], O_2 plasma treatment followed by the electroreduction of the formed surface-confined oxides [19], and the selective dealloying of Ag based bimetallic precursors, e.g. Ag-Al alloys [42]. Often, these activated and nano-structured Ag catalysts are superior over conventional Ag-NP and Ag-NW type of catalysts in terms of efficiencies and partial currents at a given applied overpotential [47].

In this work, we introduce a novel type of porous and nano-structured Ag foam catalysts [48] which demonstrates superior electrocatalytic performance in CO formation when combined with 1-butyl-3-methylimidazolium tetrafluoroborate (denoted herein-after as [BMIm][BF$_4$]) ionic liquid. [BMIm][BF$_4$] has similar excellent properties as [EMIm][BF$_4$] (EMIm = the 1-ethyl-3-methyl-imida-zolium cation), which is considered as the benchmark RTIL co-catalyst [29]. Electronanofoaming of metals [49,50] is a fast, experimentally robust approach towards high-surface area CO_2RR catalysts [37,48,51] and therefore a promising alternative to the wet chemical synthesis of nanomaterials and to the activation/nano-structuring of the respective bulk materials [16]. Since it is not only the CO_2RR activity itself which defines the overall catalyst perfor-mance, but also the stability of the combined catalyst/electrolyte system, we apply herein NMR spectroscopy and so-called identical location microscopy techniques [12,52,53] to elaborate under which experimental conditions the combined catalyst/IL system remains stable against structural and compositional degradation.

2. Experimental

2.1. Chemicals

The ionic liquid 1-butyl-3-methyl-imidazolium tetra-fluoroborate [BMIm][BF4] was purchased from Merck (high purity grade, >99%) and used without any further purification. The water content was measured by NMR spectroscopy to be ~0.2% of mole fraction. A calculated volume of Milli-Q water (R > 18.2 MΩ, TOC < 3 ppb) was added to the IL to obtain 20% water mole fraction. pH of the IL was changed from ~6.4 to 6.2 after addition of 20% water.

2.2. Electrochemistry

Cyclic voltammetry was performed using a PGSTAT30 poten-tiostat (Autolab, Netherlands) and a custom-designed single-compartment glass cell. The cell was equipped with a gas inlet/outlet, enabling atmospheric control (Ar or CO_2). The cell used for the experiment and all other glassware were cleaned in hot 25% nitric acid (Grogg-Chemie AG) followed by several heating-rinsing

cycles (3 times) with Milli-Q water (R > 18.2 MΩ, TOC < 3 ppm). Cleaned components used were dried in an oven at 105 °C over-night. A volume of 1.6 mL of IL was added to the glass cell in a glove box under N_2 atmosphere (N50, Carbagas). The sealed cell was then transferred to the ambient atmosphere and the solution was first purged with Ar (~30 min) for oxygen removal followed by CO_2 saturation (~40 min). Voltammograms were recorded in both Ar- and CO_2-saturated electrolytes at a potential sweep rate of dE/dt = 0.5 V s^{-1}.

As working electrodes (WEs), we used an Ag foil (99.9%, 0.25 mm thickness, Sigma Aldrich) and an electrodeposited Ag foam catalyst. Prior to the measurements, the Ag foil was me-chanically polished with 1 μm Alumina paste on a polishing cloth, ultrasonicated for about 1 min, rinsed with Milli-Q water and then dried in a gentle stream of Ar gas. A leakless Ag/AgCl$_{3M}$ (eDAQ) electrode served as a reference (RE) and a platinized Pt foil was used as a counter electrode (CE). Prior to use, the electrodeposited Ag foam (WE) and the Ag|AgCl$_{3M}$ (RE) were dried in a gentle Ar stream and afterwards transferred into the IL containing electrol-ysis cell. Automatic IR compensation was applied for the voltam-metric measurements after measurement of the solution resistance by the positive feedback approach. The measured current was normalized to the geometric surface area.

2.3. Preparation of Ag foam catalysts

Firstly, a ~4 × 4 mm^2 sized Ag foil (99.9%, 0.125 mm thickness, Mateck, Jülich, Germany) was mechanically polished on polishing cloth using 1 μm Alumina slurry (Buehler), followed by ultra-sonication for about 1 min and extensive rinsing with Milli-Q water before the sample was dried in a gentle Ar stream. The Ag elec-trodeposition on the Ag foil substrate was adopted from the dy-namic hydrogen bubble template method [37,48–50]. The metal foaming process results from of the superposition of the HER (proton reduction, water splitting) taking place under such harsh experimental conditions and the metal deposition (Scheme S1) [48]. The Ag deposition was carried out under galvanostatic con-ditions (nominal current density of J = −3 A cm^{-2} for 20 s). The aqueous plating bath contained 0.02 M Ag$_2$SO$_4$ (Sigma-Aldrich, purity ≥99.5%), 0.1 M trisodium citrate dihydrate (ACS grade >99.7%, Merck), and 1.5 M H$_2$SO$_4$ (ACS grade, Sigma-Aldrich). Before use, the plating bath was ultrasonicated until all precursor salts were dissolved. A Pt foil (15 × 15 mm^2) and Ag/AgCl$_{3M}$ glass electrode (with double-junction system, Metrohm) were used as counter (CE) and reference electrode (RE), respectively. The dis-tance between working and counter electrode was 3.5 cm (face-to-face WE/CE geometry). After deposition, the formed Ag foam was thoroughly rinsed with Milli-Q water, dried in a gentle Ar stream and kept in a glovebox under N_2 atmosphere.

2.4. Online gas chromatography analysis

Gas chromatography (GC) analysis was carried out in an H-type cell with catholyte (the IL) and anolyte (0.5 M H$_2$SO$_4$, prepared from KHCO$_3$, ≥99.95%, Sigma Aldrich and Milli-Q water) compartments separated by a polymer membrane (Nafion 117, Sigma-Aldrich). During electrolysis, the catholyte was continuously stirred by magnetic agitation to facilitate the CO_2 mass transport towards the cathode. Potentiostatic control was provided by a PGSTAT128 N (Metrohm Autolab) instrument. The headspace of the catholyte compartment was continuously purged with CO_2 gas, thereby transporting volatile reaction products from the electrochemical cell into the sampling loops of the online gas chromatograph (SRI Instruments). The Faraday efficiency (FE) for a given gaseous product was obtained by normalizing the partial current density for

a given reaction product to the total current density [54]:

$$FE(\%) = \frac{I_i}{I_{total}} 100\% \qquad (1)$$

$$I_i = \frac{c_i \cdot v \cdot F \cdot z}{10^6 \cdot V_m} \qquad (2)$$

I_i represents the partial current for the conversion of CO_2 into product i, c_i the volume fraction of the products measured via on-line GC using an independent calibration standard gas (Carbagas), z is the number of electrons involved in the reaction to form a particular product, F is the Faraday constant (96485 C mol^{-1}), v is the flow rate [L s^{-1}], V_m represents the molar volume, I_{total} refers to the total current at the time of measurement. Gas products were analyzed online during steady-state potentiostatic CO_2 electrolysis. For further details we refer to SI (Section 5).

2.5. NMR spectroscopy

NMR data were recorded on a Bruker Avance IIIHD spectrometer operating at the nominal proton frequency of 400 MHz, equipped with a dual direct broadband 5 mm probehead (SmartProbe©) with an additional z-gradient coil. All 1D and 2D NMR measurements were carried out at room temperature (298 K). Topspin (versions 3.2 and 3.5, Bruker BioSpin GmbH) software was used to process the NMR data. The quantitative ^{1}H NMR spectra were recorded using a standard one-pulse experiment (zg30 pulse sequence from the Bruker pulse-program library). Typically, 8 transients were acquired over a spectral width of 20 ppm, with a data size of 64 k points, and a relaxation delay of 30 s. Quantitative ^{13}C NMR spectroscopy data were measured with 8 transients into 128 k data points over a width of 200 ppm by using a classical one-pulse experiment with inverse-gated ^{1}H decoupling (zgig pulse sequence from the Bruker pulse-program library). A relaxation delay of 180 s was applied between the transients (the ^{13}C T_1 relaxation time of CO_2 amounts 35 s). Quantitative ^{19}F NMR spectra were measured with 32 transients over a spectral width of 200 ppm, with a data size of 256 k. A specific antiring sequence ("aring" from the Bruker pulse-program library) to flatten the baseline was used. The relaxation delay was 6 s.

2.6. Identical location scanning electron microscopy and energy dispersive x-ray spectroscopy (EDX)

SEM imaging and EDX analyses were carried out by means of a Hitachi S-3000 N Scanning Electron Microscope and a Noran SIX NSS200 energy-dispersive X-ray spectrometer, respectively. High-resolution SEM (HR-SEM) and identical location images were recorded using a field emission scanning electron microscope DSM 982 Gemini (Zeiss) by applying an accelerating voltage of 5 kV at a working distance of 9–11 mm. For the identical location imaging, reference point was made with the help of marker to get the same location before and after electrolysis.

2.7. White light interferometry

The surface morphology of the prepared Ag foam electrodes was analyzed by means of a white light interferometer (Contour GT, Bruker).

2.8. X-ray diffraction

The crystallinity of the Ag catalyst was studied by means of powder XRD techniques. An STOE Stadi P system with a Cu Kα radiation source ($\lambda = 0.1540$ nm, 40 mA) generated at 40 keV was used. XRD spectra were recorded in reflection mode (Bragg-Brentano geometry) between 10 and 90° 2θ in steps of 1° min^{-1}. To exclude Ag diffraction peaks originating from the Ag foil substrate, the silver foam was deposited onto a graphite substrate (99.8%, Alfa Aesar, 0.13 mm thickness) for this measurement. The obtained XRD pattern were analyzed and compared to JCPDS (Joint Committee on Powder Diffraction standards) for Ag, Ag_2O, and AgO.

3. Results and discussion

3.1. Structural characterization

The microscopic investigation of the electrodeposited Ag catalyst (Fig. 1) shows a metal foam with an open-cell architecture of interconnected macro-pores (denoted as *primary* porosity [48]) having dimensions in the μm range: pore diameters range from 10 μm to 50 μm. As known from electrodeposited Cu foams [37,50] this Ag foam also reveals a distinct gradient in the pore diameter
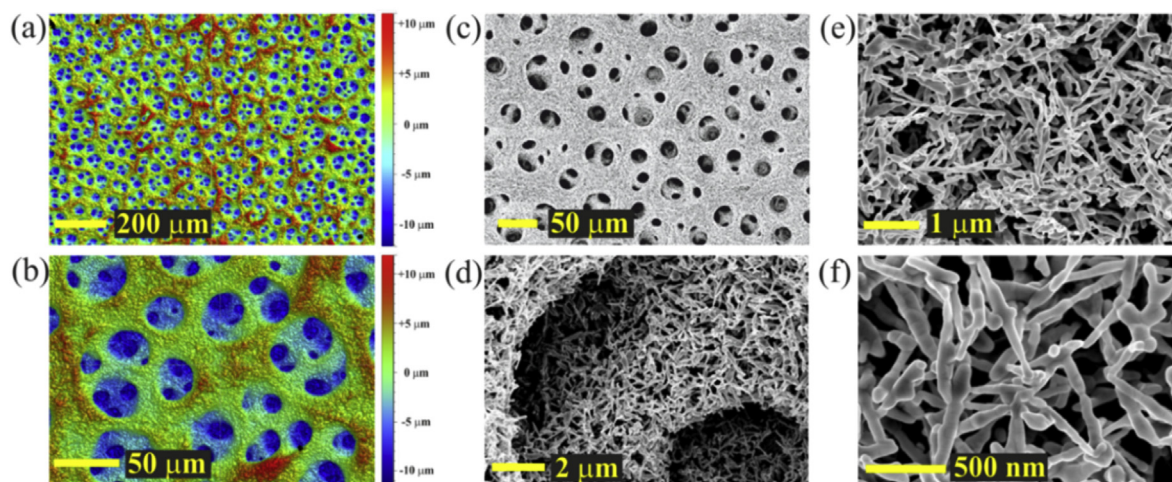

Fig. 1. (a)–(b) White-light interferometric characterization of the primary macro-porosity of the Ag foam; (c)–(f) SEM characterization of the Ag foam showing both the macro-porosity (panel c) and the meso-porosity of the pore side-walls of a nm length scale (panels e–f).

along the surface normal with the smallest pores close to the Ag foil substrate level and the largest ones at the outer-most surface of the foam. This characteristic can be rationalized in terms of a dynamic hydrogen bubble template (DHBT) [37,48–50] with initially smaller H_2-gas bubbles that tend to coalesce to larger ones in the course of the concerted electrodeposition/HER process. It is the increased residence time of the gas bubbles on the evolving foam surface which also increases the so-called bubble break-off diameter d_0 and thereby the surface pore diameter [48,55–57]. Such multilevel characteristics of the Ag foam can be deduced from white light interferometry inspection in panels a and b of Fig. 1 as well as from the SEM image shown in panel c. The interferometry introduces an extra depth resolution into the morphological characterization and allows for an estimation of the thickness/depth of the Ag foam of ~22 μm assuming that the deepest pores reach the substrate level. A closer SEM inspection reveals that the pore sidewalls of the Ag foam are not compact but composed of loosely agglomerated Ag nanoneedles (Ag-NNs) having diameters ranging from 50 to 100 nm and lengths that can even exceed 1 μm (Fig. 1c−e). The particular anisotropy of the Ag-NNs in the pore sidewalls results from the citrate additive action during the electroplating (see Scheme S1) which serves as a surface active surfactant and complexing agent for Ag^+ ions impacting the nucleation and growth behaviour of the Ag deposit [48]. Note that Ag foams deposited under similar experimental conditions but in the absence of the citrate additive are composed of more isotropic Ag-NPs [48]. Ag foils were used as reference catalysts for the characterization of the CO_2RR performance on the Ag foam. SEM and white light interferometry indicate a comparably flat Ag foil surface (Fig. S1).

The XRD analysis of the Ag foam reveals dominant fcc diffraction pattern of polycrystalline Ag bulk material as expected from the random distribution of the needle-like Ag crystallites in the pore side-walls (Fig. S2). Only minor traces of an oxidic Ag phases are visible in the XRD spectrum at 2θ values below 38°, thus confirming the lack of 3D translational order of the surface confined oxide phases [48]. The polycrystalline Ag foil shows a somewhat anomalous texturing with relative peak intensities of I(111): I(200): I(220) = 1 : 0.79: 4.76 which differ from regular polycrystalline Ag samples (I(111): I(200): I(220) = 1 : 0.4: 0.15). EDX data demonstrate high-purity Ag foam deposit (Fig. S3). Electrochemical characterization of the Ag foam electrode in an aqueous solution demonstrates the presence of (110) and (111) surface domains (Fig. S4).

3.2. Electrochemical characterization

The dotted curves in Fig. 2a display the voltammograms of the Ag foam and the foil substrate in the Ar-saturated [BMIm][BF4] electrolyte. The exponential increase in the cathodic current observed at potentials < −1.84 V for the Ag foil and < −1.71 V for the Ag foam has to be attributed to the massive reductive degradation of the [BMIm]$^+$ cations [58]. Interestingly, the IL decomposition starts in case of the Ag foam at more positive potentials as compared to the Ag foil (see also Fig. S5). Obviously, the Ag foam promotes the [BMIm]$^+$ decomposition more effectively than the planar Ag foil.

Characteristic changes in the voltammetric responses occur, when the electrolytes are saturated with CO_2 (solid lines in Fig. 2a). The most prominent difference to the measurements in the CO_2-free and Ar-saturated environment concerns the appearance of an irreversible cathodic peak which has to be assigned the electrochemical reduction of CO_2 in the IL. The peak-like behaviour in the voltammetric responses points to a CO_2RR which becomes, at a certain rate of reaction, limited by the CO_2 mass transport [28]. One can see that the highly porous Ag foam displays an only moderately
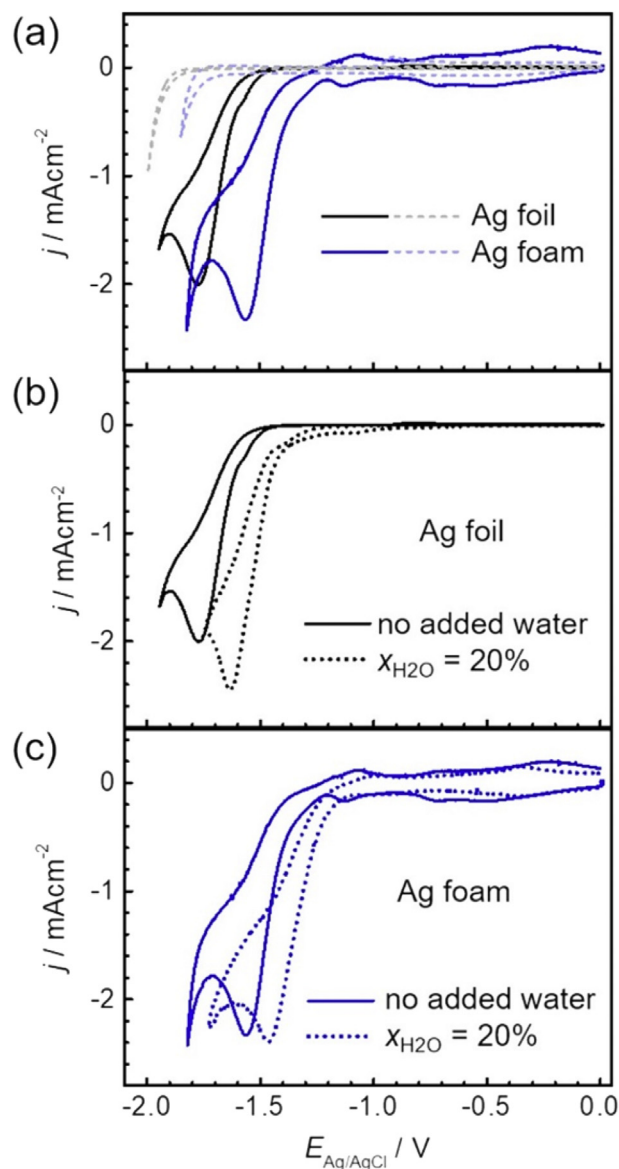
Fig. 2. CVs comparing the electrocatalytic activity of the Ag foam and the Ag foil reference: (a) CVs in the Ar- and CO_2-saturated [BMIm][BF4] (dashed and solid lines, respectively); (b) CVs of the Ag foil in CO_2-saturated [BMIm][BF4] with and without water; (c) CVs of the Ag foam in CO_2-saturated [BMIm][BF4] with and without water. Potential sweep rate: 0.05 V^{-1}.

larger CO_2RR peak as compared to the Ag foil electrode. It clearly demonstrates that the overall CO_2RR rates are not further increased on the high-surface area metal foam catalyst, when, at higher overpotentials, the reaction gets controlled by the reactant mass transfer. A primary enhancement of the CO_2RR is related to an increased electrocatalytic activity of the Ag foam itself. Both the CO_2RR onset (−1.33 V and −1.55 V for the foam and foil, respectively, as defined at −0.2 mAcm^{-2} after correction for capacitive currents) and the CO_2 reduction peak maximum are shifted by ~200 mV towards lower overpotentials when compared to the Ag foil reference system. A similar enhanced electrocatalytic activity of electrodeposited Ag foams towards CO production at particularly low overpotentials has recently been reported by Dutta el al [48]. for CO_2-saturated aqueous bicarbonate electrolytes and rationalized by an improved binding strength of the *CO (the asterisk * refers to an adsorption state) on the highly anisotropic Ag-NNs. This

has been deduced from an almost quantitative suppression of the HER at low overpotentials in the aqueous electrolyte [48] which substantially differs from the characteristics of common Ag foil catalysts showing a peak-like behaviour in aqueous media for the FE_{CO} in the respective FE_{CO} vs E plots [59,60]. We assign the improved electrocatalytic performance of the novel Ag foam for the particular anisotropy of NNs the foam is composed of (Fig. 1, see also discussion of electroactive surface area in SI, Section 3 and Fig. S6).

A secondary enhancement of the CO_2RR results from the addition of water (20% mole fraction) to the [BMIm][BF$_4$] electrolyte (panels b and c of Fig. 2). The CO_2RR onset and the CO_2 reduction peak maximum are further upward shifted by 120 mV for the Ag-foam and 140 mV for the Ag foil with respect to the water-free case. This water-mediated enhancement of the CO_2RR is observed for both the Ag foam and the Ag foil reference system and is therefore independent on the catalyst material used. It is important to note that this extra shift of the CO_2RR onset potential is not related to an undesired change in Ag/AgCl$_{3M}$ reference potential upon water addition. A ferrocene/ferrocenium (Fc/Fc$^+$) redox couple has been used to confirm the stability the Ag/AgCl$_{3M}$ reference electrode in ILs. As seen in Fig. S7 the shift of the Fc/Fc$^+$ formal potential is only ~10 mV upon addition of 20% water. The extra enhancement of the CO_2RR upon water addition may be explained by increasing proton availability near electrode surface, which facilitate the reaction of CO_2 reduction (eq. (3)):

$$CO_2 + 2e^- + 2H^+ \rightarrow CO + H_2O \tag{3}$$

Also, a water-mediated acceleration of the CO_2 diffusional transport in the IL needs to be taken into account. By using advanced pulse gradient spin echo (PGSE) NMR techniques we recently demonstrated that the presence of water could, within a certain concentration range, lead to an increase of the CO_2 diffusion constant without compromising the excellent CO_2 solubility in the IL [28]. For the pure (as-received) [BMIm][BF$_4$] electrolyte we determine a CO_2 diffusion constant of $D_{CO2} = 1.66 \times 10^{-10}\,m^2\,s^{-1}$. A residual water content (mole fraction) of $x_{H2O} = 2 \cdot x\ 10^{-4}$ was determined by NMR. The addition of extra water ($x_{H2O} = 0.18$) resulted in an increase in the diffusion constant to $D_{CO2} = 2.41 \times 10^{-10}\,m^2\,s^{-1}$ (see details in SI and Fig. S8). A water mole fraction of 20% was chosen based on recent investigations on water effects on CO_2RR from ILs [28]. At this water concentration the anodic shift of the CO_2RR onset potential is nearly maximized without considerable contributions from the HER, which starts to dominate the product distribution at high water contents ($x_{H2O} \geq 50\%$).

We notice that the magnitude of CO_2RR peaks expressed in current density, normalized to geometric area, is rather similar for Ag-foil and Ag-foam electrodes, although the surface roughness of the latter is certainly higher than that of the foil electrode (Fig. 1). Thus, increasing the electrode surface area by nanostructuring and/or increasing porosity does not necessarily result in a higher diffusion-limited current of CO_2RR, at least in viscous media such as ILs (see also discussion of electroactive surface area in SI, Section 3). This observation can be rationalized by a slow diffusion of CO_2 into pores and gaps between nanoneedles and the fact that the CO_2RR occurs mostly on the topmost electroactive sites of the Ag foam catalyst.

3.3. CO_2RR online product analysis

For the quantification of the CO_2RR products by means of online gas-chromatography we applied a so-called single catalyst approach [48], where one single catalyst was used for the entire potential dependent electrolysis campaign (Fig. 3, the FE values are

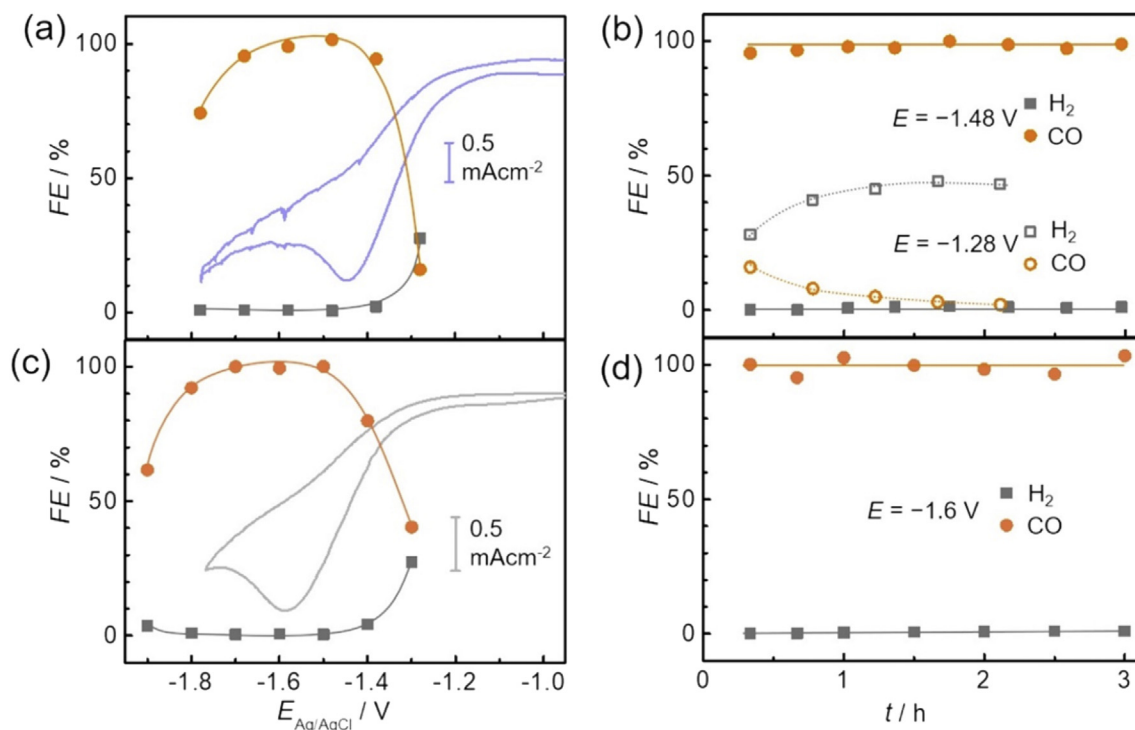**Fig. 3.** (a, c) FE vs E plots for the potentiostatic CO_2RR on the Ag foam (a) and Ag foil (c) catalysts in CO_2-saturated [BMIm][BF$_4$] + 20% water; for comparison purposes the respective CVs in the CO_2-saturated ILs are shown. (b, d) Long-term potentiostatic CO_2RR experiments on the Ag foam (b) and Ag foil (d) in the same solution (the electrolysis potentials are indicated at the plots).

also given in Tables S1–S4). In this standard approach, the CO$_2$RR was carried out for 20 min in the [BMIm][BF$_4$]/water mixture at a given electrolysis potential before the headspace was analyzed for the volatile electrolysis products. Only two gaseous products, CO and H$_2$, were detected. Fig. 3a shows the resulting CO$_2$RR product distribution obtained for the Ag foam catalyst represented as *FE vs E* plot. For comparison purposes the CV of the Ag foam measured in the two-compartment electrolysis cell is superimposed on the respective FE data. The respective current transients are given in the SI file (Fig. S10). The *FE vs E* can be subdivided into three characteristic sections. At potentials >−1.3 V (Fig. 3a), the product distribution shows comparably low efficiencies values of 16% for CO, but noticeable contributions from the HER (FE$_{H2}$ = ~44%). At lowest overpotentials the parasitic HER is obviously well competitive with regard to the targeted CO$_2$RR. FE$_{CO}$ and FE$_{H2}$ values are both strongly depending on the electrolysis time at these low overpotentials as demonstrated by the extended electrolysis experiment presented in Fig. 3b ($E = -1.28$ V). After a transient non-steady-state period of about 1 h, FE$_{CO}$ and FE$_{H2}$ values reach both plateaus in the *FE vs t* plot at ~5% and 47%, respectively. The decrease in FE with time at low overpotential seems to be due to poisoning the active Ag foam surface at extended electrolysis times. It is evident that the sum of partial FEs does not reach 100% in this low overpotential regime at any electrolysis time (Fig. 3b and Table S2). It can therefore be hypothesized that a further cathodic process, e.g. an IL degradation, substantially contributes to the total reduction current in this potential regime. A first experimental hint for such an extra IL degradation pathway at particularly low overpotentials comes from the observation that the prolonged CO$_2$RR in the [BMIm][BF$_4$]/water mixture already leads at −1.28 V to the appearance of a yellowish color of the afore colorless IL (Fig. S11a). The scheme in Fig. 4a depicts the proposed reaction mechanism for these low overpotentials, which involves the formation of carbene intermediates from the [BMIm] cation, their subsequent reaction with CO$_2$ to a carboxylate (or other) species and the production of hydrogen. The formation of carboxylate was proposed previously as a side product during CO$_2$RR on a lead electrode in water-free 1-ethyl-3-methylimidazolium bis(trifluoromethylsulfonyl)imide IL dissolved in acetonitrile [61]. Nevertheless, apparently, rather a low concentration of IL decomposition products even after 3 h of electrolysis did not allow us detecting these products by NMR (Fig. S13).

In this scenario, it might not only the reductive water splitting in the [BMIm][BF$_4$]/water mixture, which contributes to the observed HER, but also the reductive H abstraction from the [BMIm]$^+$ cation

in the presence of CO$_2$. H$_2$ can be detected also in the CO$_2$-saturated and water-free [BMIm][BF$_4$] electrolyte, but on a lower level (Fig. S12), thus supporting the hypothesis on an additional IL degradation pathway operative at low overpotentials.

A further (minor) source for parasitic HER can be HF, which forms in the course of partial hydrolysis of BF$_4^-$ anions in the presence of water [62]. ^{19}F NMR spectroscopy of the [BMIm][BF$_4$]+ H$_2$O sample carried out after the electrolysis reveals an additional minor ^{19}F resonance (Fig. S13) attributed to a product of the [BF$_4$]$^-$ hydrolysis [62].

At medium potentials, in the range from −1.38 V to −1.68 V, the CO efficiency reaches a stable ~300 mV wide plateau where the FE$_{CO}$ values never fall below 94% (CO$_2$RR-CO regime) whereas the FE$_{H2}$ values never exceed 2%. At potentials close to the pronounced CO$_2$ reduction peak in the CV, the CO efficiency reaches a maximum value of ~100%. The corresponding time-resolved product analysis carried out at potentials close to the maximum of the CO$_2$ reduction peak (−1.48 V in Fig. 3b) shows (i) no delayed catalyst conditioning in the early stage of electrolysis and (ii) no catalyst and IL degradation upon prolonged CO$_2$RR with FE$_{CO}$ values never falling below 95% (see also Table S2). In full agreement with these considerations also the color of the IL remains unchanged upon prolonged electrolysis (Fig. S11b). Obviously, the predominant CO formation prevents IL degradation in this medium potential regime. The overpotentials are sufficiently high to allow for the rapid formation of the CO$_2^{\bullet-}$ intermediates on the Ag surface in the presence of the [BMIm]$^+$ co-catalyst followed by the transformation into CO and its release from the catalyst (see reaction scheme in Fig. 4b) in accordance with [31,61].

Below −1.68 V the FE$_{CO}$ starts to drop down, interestingly without corresponding increase in the H$_2$ efficiencies. This observation can be rationalized by the onset of a massive reductive IL degradation which becomes superimposed on the CO$_2$RR thereby decreasing the overall CO Faraday efficiency. This argumentation is in full agreement with the voltammetric data (Figs. 2c and 3a) showing the onset of a further cathodic process below −1.68 V after passing the CO$_2$-related reduction peak at −1.45 V. Note that the IL degradation pathway at high overpotentials is different from the one described at low overpotentials (Fig. 3a). The FE$_{H2}$ values which remain on a low level at $E < -1.68$ V indicate that no reductive H abstraction (carbene formation) is involved in this IL degradation process. Also, the color change upon electrolysis is less severe at these high overpotentials than observed for the low overpotential degradation pathway (Fig. S11c). We also notice that the addition of
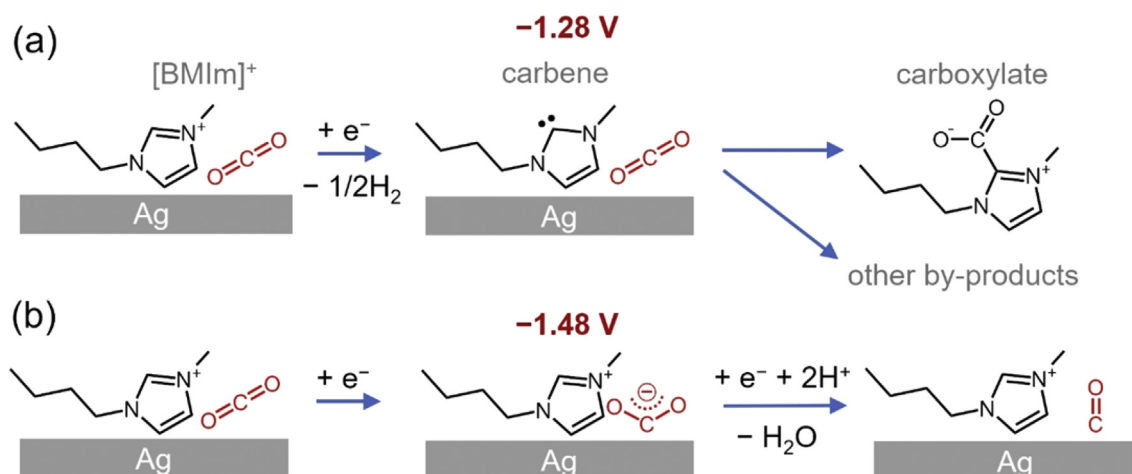

Fig. 4. Scheme demonstrating the proposed reaction mechanism at low (−1.28 V vs Ag/AgCl) and high (−1.48 V vs Ag/AgCl) overpotentials, respectively.
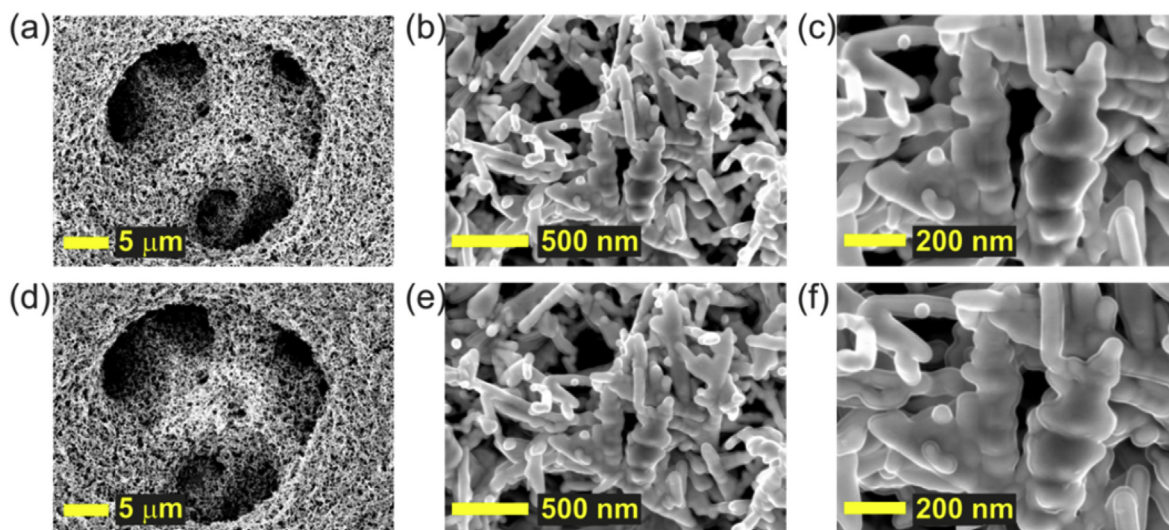
Fig. 5. Identical location (IL) investigation of the Ag foam catalyst prior (a—c) and after 5 h of CO$_2$ electrolysis (d—f) at −1.55 V.

water (20%) to the IL leads to the less negative onset of the IL degradation: e.g. for the Ag-foam electrode, −1.80 V in the absence of water and −1.68 V with $x_{H2O} = 20\%$ (cf. Fig. 3a and Fig. S12). On the other hand, the CO$_2$RR onset shifts by 140 mV upon water addition (see also Fig. 2c), which preserves the wide region of stable CO production without IL decomposition. Recently, Schmid et al. [63] reported severe decomposition of 1-ethyl-3-methylimidazolium trifluoromethanesulfonate IL in the presence of 50% water due to an increase in local pH. However, such decomposition took place at high current densities (50 mAcm^{-2} and higher) by employing flow cell and a gas-diffusion electrode. The same authors did not observe the IL decomposition at a moderate CO$_2$RR current density (~6 mAcm^{-2}) and overpotential [63,64], which agrees well with our results.

To further support our hypothesis of an improved electro-catalytic activity of the Ag foam as concluded from the voltammetric experiments (Fig. 2), the corresponding potential-dependent (Fig. 3c) and time-resolved (Fig. 3d) electrolysis was conducted using the Ag foil as a reference catalyst. The data show qualitatively the same electrolysis characteristics as the Ag foam including the three sections in the *FE vs E* plot (low→ mixed HER/ CO$_2$RR-CO/IL degradation; medium→ CO$_2$RR-CO; high→ mixed IL degradation/CO$_2$RR-CO). However, the ~300 mV wide plateau of the FE$_{CO}$ is shifted to more negative potentials with respect to the Ag foam, thus, confirming the enhanced CO$_2$RR activity of the Ag foam concluded from the CV data in Fig. 2.

3.4. Identical location SEM analysis

The stability of the Ag foam electrocatalyst is further confirmed by so-called identical location investigations [12,52] performed prior and after a 5 h lasting CO$_2$RR at −1.55 V (Fig. 5; current transient and FE$_{CO}$ are presented in Fig. S14). Neither the primary macro-porosity nor the secondary micro-porosity of the pore side walls is affected by the prolonged CO$_2$RR (Fig. 5). Moreover, no visible electrochemical and morphological degradation of Ag nanoneedles is observed. This finding confirms a high stability of the foam catalyst in the IL during CO$_2$ electrolysis.

4. Conclusions

We employed a novel Ag foam type of catalysts composed of Ag

nanoneedles for the electrochemical conversion of CO$_2$ into CO from ionic liquid solutions. The catalyst was prepared by a versatile galvanostatic deposition approach utilizing high current densities (−3 A cm^{-2}) and an aqueous Ag(I) solution as silver source, yielding macro-porous Ag foams with pore diameters ranging from 10 μm to 50 μm. The pore sidewalls are composed of Ag nanoneedles (Ag-NNs) having diameters of ~50−100 nm and lengths that can exceed 1 μm. The loosely packing of the Ag-NNs in the pore sidewalls introduces a secondary meso-porosity into the catalyst system. The obtained Ag foam catalyst significantly decreased the required cathodic potential for CO$_2$RR by about 220 mV compared to the Ag foil reference system.

The addition of moderate amounts of water (20% mole fraction, optimized conditions) to the [BMIm][BF$_4$] ionic liquid leads to the further ~120 mV decrease in the CO$_2$RR onset potential. CO$_2$RR product analysis confirmed for the [BMIm][BF$_4$]/water mixture an anodically shifted 300 mV broad potential plateau, where the CO efficiency reaches almost 100%. Both prolonged electrolysis experiments in the CO forming region and identical location SEM imaging confirmed a superior electrochemical and structural stability of the Ag foam catalyst.

Thus, in the combination with nanostructured Ag catalysts IL-based electrolyte solution provide rather low overpotentials of CO$_2$RR, selective product formation, the suppression of parasitic HER as well as electrolyte and catalyst stability. However, the problem of high viscosity of ILs and slow CO$_2$ mass transport should be considered, and possible solutions for this problem should be further investigated.

Appendix A. Supplementary data

Supplementary data to this article can be found online at https://doi.org/10.1016/j.electacta.2019.03.102.

References

[1] T.R. Karl, K.E. Trenberth, Modern global climate change, Science 302 (2003) 1719–1723.

[2] National Oceanic and Atmospheric Administration, https://www.noaa.gov/.

[3] H. Yang, Z. Xu, M. Fan, R. Gupta, R.B. Slimane, A.E. Bland, I. Wright, Progress in carbon dioxide separation and capture: a review, J. Environ. Sci. 20 (2008) 14–27.

[4] M. Mikkelsen, M. Jorgensen, F.C. Krebs, The teraton challenge. A review of fixation and transformation of carbon dioxide, Energy Environ. Sci. 3 (2010) 43–81.

[5] H.-R.M. Jhong, S. Ma, P.J.A. Kenis, Electrochemical conversion of CO_2 to useful chemicals: current status, remaining challenges, and future opportunities, Current Opinion in Chem. Eng. 2 (2013) 191–199.

[6] J.-P. Jones, G.K.S. Prakash, G.A. Olah, Electrochemical CO_2 reduction: recent advances and current trends, Isr. J. Chem. 54 (2014) 1451–1466.

[7] G. Centi, S. Perathoner, Opportunities and prospects in the chemical recycling of carbon dioxide to fuels, Catal. Today 148 (2009) 191–205.

[8] A.M. Appel, J.E. Bercaw, A.B. Bocarsly, H. Dobbek, D.L. DuBois, M. Dupuis, J.G. Ferry, E. Fujita, R. Hille, P.J.A. Kenis, C.A. Kerfeld, R.H. Morris, C.H.F. Peden, A.R. Portis, S.W. Ragsdale, T.B. Rauchfuss, J.N.H. Reek, L.C. Seefeldt, R.K. Thauer, G.L. Waldrop, Frontiers, opportunities, and challenges in biochemical and chemical catalysis of CO_2 fixation, Chem. Rev. 113 (2013) 6621–6658.

[9] K.W. Frese, S. Leach, Electrochemical reduction of carbon dioxide to methane, methanol, and CO on Ru electrodes, J. Electrochem. Soc. 132 (1985) 259–260.

[10] K.P. Kuhl, T. Hatsukade, E.R. Cave, D.N. Abram, J. Kibsgaard, T.F. Jaramillo, Electrocatalytic conversion of carbon dioxide to methane and methanol on transition metal surfaces, J. Am. Chem. Soc. 136 (2014) 14107–14113.

[11] Y. Hori, A. Murata, R. Takahashi, S. Suzuki, Enhanced formation of ethylene and alcohols at ambient temperature and pressure in electrochemical reduction of carbon dioxide at a copper electrode, J. Chem. Soc., Chem. Commun. (1988) 17–19.

[12] M. Rahaman, A. Dutta, A. Zanetti, P. Broekmann, Electrochemical reduction of CO_2 into multicarbon alcohols on activated Cu mesh catalysts: an identical location (IL) study, ACS Catal. 7 (2017) 7946–7956.

[13] S. Ma, M. Sadakiyo, R. Luo, M. Heima, M. Yamauchi, P.J.A. Kenis, One-step electrosynthesis of ethylene and ethanol from CO_2 in an alkaline electrolyzer, J. Power Sources 301 (2016) 219–228.

[14] D. Ren, Y. Deng, A.D. Handoko, C.S. Chen, S. Malkhandi, B.S. Yeo, Selective electrochemical reduction of carbon dioxide to ethylene and ethanol on copper(I) oxide catalysts, ACS Catal. 5 (2015) 2814–2821.

[15] A. Dutta, A. Kuzume, M. Rahaman, S. Vesztergom, P. Broekmann, Monitoring the chemical state of catalysts for CO_2 electroreduction: an in operando study, ACS Catal. 5 (2015) 7498–7502.

[16] H. Mistry, A.S. Varela, C.S. Bonifacio, I. Zegkinoglou, I. Sinev, Y.-W. Choi, K. Kisslinger, E.A. Stach, J.C. Yang, P. Strasser, B.R. Cuenya, Highly selective plasma-activated copper catalysts for carbon dioxide reduction to ethylene, Nat. Commun. 7 (2016) 12123.

[17] Y. Hori, K. Kikuchi, S. Suzuki, Production of CO and CH_4 in electrochemical reduction of CO_2 at metal-electrodes in aqueous hydrogencarbonate solution, Chem. Lett. (1985) 1695–1698.

[18] C. Delacourt, J. Newman, Mathematical modeling of CO_2 reduction to CO in aqueous electrolytes: II. Study of an electrolysis cell making syngas (CO + H_2) from CO_2 and H_2O reduction at room temperature, J. Electrochem. Soc. 157 (2010) B1911–B1926.

[19] H. Mistry, Y.W. Choi, A. Bagger, F. Scholten, C.S. Bonifacio, I. Sinev, N.J. Divins, I. Zegkinoglou, H.S. Jeon, K. Kisslinger, E.A. Stach, J.C. Yang, J. Rossmeisl, B.R. Cuenya, Enhanced carbon dioxide electroreduction to carbon monoxide over defect-rich plasma-activated silver catalysts, Angew. Chem. Int. Ed. 56 (2017) 11394–11398.

[20] J. Durst, A. Rudnev, A. Dutta, Y. Fu, J. Herranz, V. Kaliginedi, A. Kuzume, A.A. Permyakova, Y. Paratcha, P. Broekmann, T.J. Schmidt, Electrochemical CO_2 reduction - a critical view on fundamentals, materials and applications, CHI-MIA Int. J. Chem. 69 (2015) 769–776.

[21] M. Samavati, M. Santarelli, A. Martin, V. Nemanova, Production of synthetic fischer–tropsch diesel from renewables: thermoeconomic and environmental analysis, Energy Fuels 32 (2018) 1744–1753.

[22] M. Alvarez-Guerra, J. Albo, E. Alvarez-Guerra, A. Irabien, Ionic liquids in the electrochemical valorisation of CO_2, Energy Environ. Sci. 8 (2015) 2574–2599.

[23] H.-K. Lim, H. Kim, The mechanism of room-temperature ionic-liquid-based electrochemical CO_2 reduction: a review, Molecules 22 (2017) 536.

[24] J. Ranke, S. Stolte, R. Störmann, J. Arning, B. Jastorff, Design of sustainable chemical Products – The example of ionic liquids, Chem. Rev. 107 (2007) 2183–2206.

[25] S. Kazemiabnavi, Z. Zhang, K. Thornton, S. Banerjee, Electrochemical stability window of imidazolium-based ionic liquids as electrolytes for lithium batteries, J. Phys. Chem. B 120 (2016) 5691–5702.

[26] M.V. Fedorov, A.A. Kornyshev, Ionic liquids at electrified interfaces, Chem. Rev. 114 (2014) 2978–3036.

[27] M. Ramdin, T.W. de Loos, T.J.H. Vlugt, State-of-the-Art of CO_2 capture with ionic liquids, Ind. Eng. Chem. Res. 51 (2012) 8149–8177.

[28] A.V. Rudnev, Y.-C. Fu, I. Gjuroski, F. Stricker, J. Furrer, N. Kovács, S. Vesztergom, P. Broekmann, Transport matters: boosting CO_2 electroreduction in mixtures of [BMIm][BF_4]/water by enhanced diffusion, ChemPhysChem 18 (2017) 3153–3162.

[29] B.A. Rosen, A. Salehi-Khojin, M.R. Thorson, W. Zhu, D.T. Whipple, P.J.A. Kenis, R.I. Masel, Ionic liquid–mediated selective conversion of CO_2 to CO at low overpotentials, Science 334 (2011) 643–644.

[30] L. Aldous, A. Khan, M.M. Hossain, C. Zhao, CHAPTER 8 Electrocatalysis in Ionic Liquids, Catalysis in Ionic Liquids: from Catalyst Synthesis to Application, The Royal Society of Chemistry, 2014, pp. 433–473.

[31] G.P.S. Lau, M. Schreier, D. Vasilyev, R. Scopelliti, M. Grätzel, P.J. Dyson, New insights into the role of imidazolium-based promoters for the electro-reduction of CO_2 on a silver electrode, J. Am. Chem. Soc. 138 (2016) 7820–7823.

[32] S.-F. Zhao, M. Horne, A.M. Bond, J. Zhang, Is the imidazolium cation a unique promoter for electrocatalytic reduction of carbon dioxide? J. Phys. Chem. C 120 (2016) 23989–24001.

[33] S. Liu, H. Tao, L. Zeng, Q. Liu, Z. Xu, Q. Liu, J.-L. Luo, Shape-dependent electrocatalytic reduction of CO_2 to CO on triangular silver nanoplates, J. Am. Chem. Soc. 139 (2017) 2160–2163.

[34] Y.-C. Hsieh, S.D. Senanayake, Y. Zhang, W. Xu, D.E. Polyansky, Effect of chloride anions on the synthesis and enhanced catalytic activity of silver nanocoral electrodes for CO_2 electroreduction, ACS Catal. 5 (2015) 5349–5356.

[35] M. Ma, B.J. Trześniewski, J. Xie, W.A. Smith, Selective and efficient reduction of carbon dioxide to carbon monoxide on oxide-derived nanostructured silver electrocatalysts, Angew. Chem. Int. Ed. 55 (2016) 9748–9752.

[36] J. Rosen, G.S. Hutchings, Q. Lu, S. Rivera, Y. Zhou, D.G. Vlachos, F. Jiao, Mechanistic insights into the electrochemical reduction of CO_2 to CO on nanostructured Ag surfaces, ACS Catal. 5 (2015) 4293–4299.

[37] A. Dutta, M. Rahaman, N.C. Luedi, M. Mohos, P. Broekmann, Morphology matters: tuning the product distribution of CO_2 electroreduction on oxide-derived Cu foam catalysts, ACS Catal. 6 (2016) 3804–3814.

[38] J. Kim, J.T. Song, H. Ryoo, J.-G. Kim, S.-Y. Chung, J. Oh, Morphology-controlled Au nanostructures for efficient and selective electrochemical CO_2 reduction, J. Mater. Chem. (2018).

[39] Y. Chen, C.W. Li, M.W. Kanan, Aqueous CO_2 reduction at very low overpotential on oxide-derived Au nanoparticles, J. Am. Chem. Soc. 134 (2012) 19969–19972.

[40] D. Gao, H. Zhou, F. Cai, J. Wang, G. Wang, X. Bao, Pd-containing nanostructures for electrochemical CO_2 reduction reaction, ACS Catal. 8 (2018) 1510–1519.

[41] J. Rosen, G.S. Hutchings, Q. Lu, R.V. Forest, A. Moore, F. Jiao, Electrodeposited Zn dendrites with enhanced CO selectivity for electrocatalytic CO_2 reduction, ACS Catal. 5 (2015) 4586–4591.

[42] Q. Lu, J. Rosen, F. Jiao, Nanostructured metallic electrocatalysts for carbon dioxide reduction, ChemCatChem 7 (2015) 38–47.

[43] Y. Hori, Electrochemical CO_2 reduction on metal electrodes, in: C.G. Vayenas, R.E. White, M.E. Gamboa-Aldeco (Eds.), Modern Aspects of Electrochemistry, Springer, New York, 2008, pp. 89–189.

[44] Y. Sun, Y. Xia, Shape-controlled synthesis of gold and silver nanoparticles, Science 298 (2002) 2176–2179.

[45] C.J. Murphy, T.K. Sau, A.M. Gole, C.J. Orendorff, J. Gao, L. Gou, S.E. Hunyadi, T. Li, Anisotropic metal Nanoparticles: synthesis, assembly, and optical applications, J. Phys. Chem. B 109 (2005) 13857–13870.

[46] F. Li, D.R. MacFarlane, J. Zhang, Recent advances in the nanoengineering of electrocatalysts for CO_2 reduction, Nanoscale 10 (2018) 6235–6260.

[47] Q. Lu, J. Rosen, Y. Zhou, G.S. Hutchings, Y.C. Kimmel, J.G. Chen, F. Jiao, A selective and efficient electrocatalyst for carbon dioxide reduction, Nat. Commun. 5 (2014).

[48] A. Dutta, C.E. Morstein, M. Rahaman, A. Cedeño López, P. Broekmann, Beyond copper in CO_2 electrolysis: effective hydrocarbon production on silver-nanofoam catalysts, ACS Catal. 8 (2018) 8357–8368.

[49] H.-C. Shin, J. Dong, M. Liu, Porous tin oxides prepared using an anodic oxidation process, Adv. Mater. 16 (2004) 237–240.

[50] H.-C. Shin, M. Liu, Copper foam structures with highly porous nanostructured walls, Chem. Mater. 16 (2004) 5460–5464.

[51] A. Dutta, M. Rahaman, M. Mohos, A. Zanetti, P. Broekmann, Electrochemical CO_2 conversion using skeleton (sponge) type of Cu catalysts, ACS Catal. 7 (2017) 5431–5437.

[52] K.J.J. Mayrhofer, S.J. Ashton, J.C. Meier, G.K.H. Wiberg, M. Hanzlik, M. Arenz, Non-destructive transmission electron microscopy study of catalyst degradation under electrochemical treatment, J. Power Sources 185 (2008) 734–739.

[53] K.J.J. Mayrhofer, J.C. Meier, S.J. Ashton, G.K.H. Wiberg, F. Kraus, M. Hanzlik, M. Arenz, Fuel cell catalyst degradation on the nanoscale, Electrochem. Commun. 10 (2008) 1144–1147.

[54] A.V. Rudnev, Online chromatographic detection, in: K. Wandelt (Ed.), Encyclopedia of Interfacial Chemistry, Elsevier, Oxford, 2018, pp. 321–325.

[55] H. Vogt, R.J. Balzer, The bubble coverage of gas-evolving electrodes in stagnant electrolytes, Electrochim. Acta 50 (2005) 2073–2079.

[56] W. Fritz, Maximum volume of vapor bubbles, Phys. Z. 36 (1935) 379–384.

[57] N.D. Nikolić, G. Branković, M.G. Pavlović, K.I. Popov, The effect of hydrogen co-deposition on the morphology of copper electrodeposits. II. Correlation

between the properties of electrolytic solutions and the quantity of evolved hydrogen, J. Electroanal. Chem. 621 (2008) 13–21.

[58] M.C. Kroon, W. Buijs, C.J. Peters, G.-J. Witkamp, Decomposition of ionic liquids in electrochemical processing, Green Chem. 8 (2006) 241–245.

[59] T. Hatsukade, K.P. Kuhl, E.R. Cave, D.N. Abram, T.F. Jaramillo, Insights into the electrocatalytic reduction of CO_2 on metallic silver surfaces, Phys. Chem. Chem. Phys. 16 (2014) 13814–13819.

[60] R. Daiyan, X. Lu, Y.H. Ng, R. Amal, Highly selective conversion of CO_2 to CO achieved by a three-dimensional porous silver electrocatalyst, Chemistry 2 (2017) 879–884.

[61] L. Sun, G.K. Ramesha, P.V. Kamat, J.F. Brennecke, Switching the reaction course of electrochemical CO_2 reduction with ionic liquids, Langmuir 30 (2014)

6302–6308.

[62] M.G. Freire, C.M.S.S. Neves, I.M. Marrucho, J.A.P. Coutinho, A.M. Fernandes, Hydrolysis of tetrafluoroborate and hexafluorophosphate counter ions in imidazolium-based ionic liquids, J. Phys. Chem. A 114 (2010) 3744–3749.

[63] S.S. Neubauer, B. Schmid, C. Reller, D.M. Guldi, G. Schmid, Alkalinity initiated decomposition of mediating imidazolium ions in high current density CO_2 electrolysis, ChemElectroChem 4 (2017) 160–167.

[64] S.S. Neubauer, R.K. Krause, B. Schmid, D.M. Guldi, G. Schmid, Overpotentials and Faraday efficiencies in CO_2 electrocatalysis–the impact of 1-ethyl-3-methylimidazolium trifluoromethanesulfonate, Adv. Energy Mater. 6 (2016) 1502231.

5.2. Activation of bimetallic AgCu foam electrocatalysts for ethanol formation from CO$_2$ by selective Cu oxidation/reduction

Authors: Abhijit Dutta, Ivan Zelocualtecatl Montiel, Rolf Erni, Kiran Kiran, Motiar Rahaman, Jakub Drnec, Peter Broekmann

Highlights: This report displays the performance of bimetallic AgCu metal foams toward ethanol production with an optimum composition of 15% Ag and 85% Cu produced via electrodeposition. The performance of as deposited Ag$_{15}$Cu$_{85}$ is compared to that of annealed catalyst. CO and C$_2$H$_4$ are preferentially formed at low and high overpotentials in case of as deposited sample. When subjected to thermal annealing, as deposited sample transforms to oxidic AgCu$_x$O leading to oxide-derived (OD) bimetallic Ag$_{15}$Cu$_{85}$ catalyst upon reduction of oxidic precursor. Interestingly, this OD leads to the ethanol formation with an efficiency of 33.7% with partial current density of -8.67 mA cm^{-2} at -1.0 V vs RHE. This result was explained by means of the CO spillover concept.

Contribution: I was involved in the morphological analysis of the catalyst by SEM. I assisted Abhijit Dutta, the first author of the paper, in the performance analysis of the foam catalyst.

Full paper

Activation of bimetallic AgCu foam electrocatalysts for ethanol formation from CO_2 by selective Cu oxidation/reduction
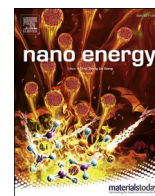
Abhijit Dutta [a,*,1], Iván Zelocualtecatl Montiel [a,1], Rolf Erni [b], Kiran Kiran [a], Motiar Rahaman [a], Jakub Drnec [c], Peter Broekmann [a,**]

[a] Department of Chemistry and Biochemistry, University of Bern, Freiestrasse 3, Bern, 3012, Switzerland
[b] Electron Microscopy Center, Swiss Federal Laboratories for Materials Science and Technology (EMPA), Überlandstrasse 129, 8600, Dübendorf, Switzerland
[c] European Synchrotron Radiation Facility (ESRF), 71 Avenue des Martyrs, 38000, Grenoble, France

A B S T R A C T

Bimetallic AgCu metal foams (15 at% Ag, 85 at% Cu) have been synthesized by means of an additive-assisted electrodeposition process using the dynamic hydrogen bubble template approach. Ag and Cu remain fully phase-segregated in the as deposited bimetallic foam exhibiting a high degree of dispersion of pure nm-sized Ag domains embedded in the Cu matrix. An activation of this bimetallic material towards ethanol formation is achieved by thermal annealing of the as deposited foam under mild conditions (200 °C for 12 h). Such annealing quantitatively transforms the Cu in the bimetallic system into a mixture of crystalline Cu_2O and amorphous CuO whereas the Ag remains in its metallic state due to the thermal instability of Ag_2O above temperatures of 180 °C. The selective oxidation of Cu in the bimetallic $Ag_{15}Cu_{85}$ catalyst goes along with an enrichment of Cu oxides on the surface of the formed mixed $AgCu_xO$ foam.

Both *operando* X-ray diffraction and *operando* Raman spectroscopy demonstrate, however, that the oxide reduction is completed before the electrochemical CO_2 reduction sets in. The thus formed oxide-derived (OD) bimetallic $Ag_{15}Cu_{85}$ foam catalyst shows high selectivity towards alcohol formation with Faradaic efficiencies of $FE_{EtOH} = 33.7\%$ and $FE_{n\text{-}PrOH} = 6.9\%$ at −1.0 V and −0.9 V vs RHE, respectively. Extended electrolysis experiments (100 h) indicate a superior degradation resistance of the oxide-derived bimetallic catalyst which is ascribed to the effective suppression of the C1 hydrocarbon reaction pathway thus avoiding irreversible carbon contaminations appearing in particular during methane production.

1. Introduction

In recent years, the electrochemical conversion of environmentally harmful CO_2 into products of higher value is considered a promising and technologically feasible approach to mitigate the increase of atmospheric CO_2 [1–3] which reaches already levels above 410 ppm [4]. Because of this global threat, a paradigm shift currently drives both the energy and mobility sectors away from fossil-based (coal, oil, and natural gas) towards renewables (hydro, wind, and solar) energy sources. The chemistry sector follows this trend which will surely affect entire production chains of most commodity and fine chemicals. This so-called 'energy transition' can therefore be considered as a truly intersectorial challenge which calls for new transsectorial strategies. Several

technologies including capture [5] and sequestration [6] have already been devised in order to reduce levels of CO_2 in the atmosphere. Amongst these, CO_2 reduction by electrochemical means [7] deserves particular attention as it can transform CO_2 directly back into synthetic fuels (so-called e-fuels) or other platform chemicals of high value [1,2]. In particular the electrochemical co-electrolysis of water and CO_2 has a great potential to directly interlink the energy sector to the chemistry sector (see 'Rheticus' process as a prime example thereof) [8]. The CO_2 reduction reaction might become not only economically feasible in the future but also truly sustainable, in particular when the surplus of renewables originating from solar radiation, wind power, and hydro sources is used as energy input to drive this electrochemical CO_2 conversion. This so-called 'power to value' concept might, in future, become
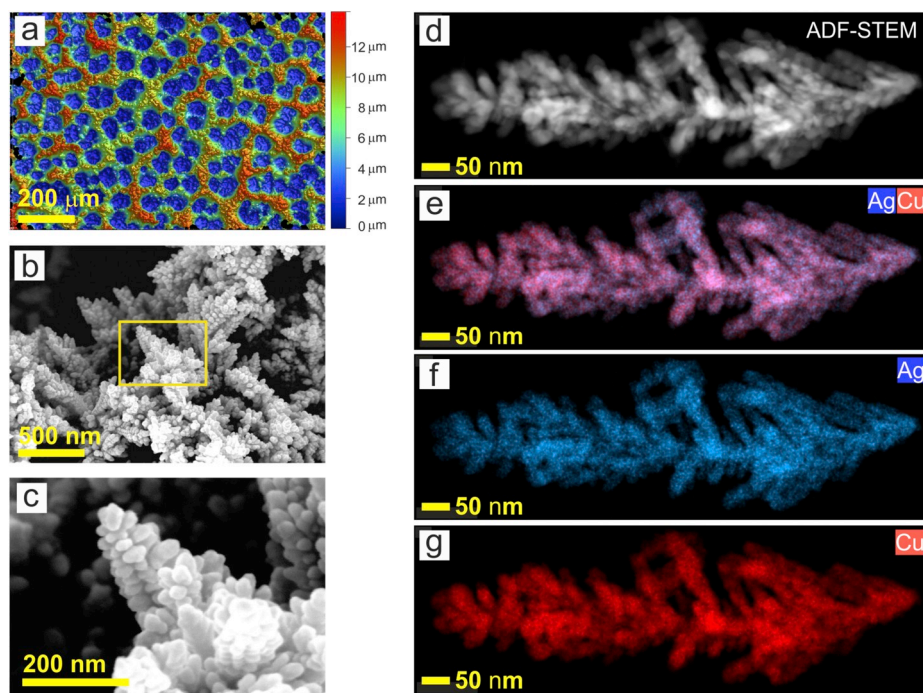
Fig. 1. Morphological and compositional analysis of the as deposited $Ag_{15}Cu_{85}$ foam deposited on a Cu foil substrate. a) White-light interferometric image of the bimetallic foam; b) and c) SEM analysis; d) ADF-STEM analysis of an individual dendrite; e) EDX mapping of the dendrite (Ag, Cu); f) spatial distribution of the Ag component; g) spatial distribution of the Cu component.

one important element among others contributing to the closing of the anthropogenic carbon cycle [3,9,10].

This electrocatalytic process typically relies on the oxidative splitting of water (OER: Oxygen Evolution Reaction) and the reductive conversion of CO_2 (CO_2RR: CO_2 Reduction Reaction). Oxygen (O_2) is the only product that can form on the anode side when using aqueous environments, irrespective of which anode material is used (e.g., RuO_2, IrO_2, or FeNi based systems) [11,12]. However, a variety of different CO_2RR products are typically produced on the cathode side [7], ranging from formate [13–15], carbon monoxide (CO) [16–27], saturated and non-saturated hydrocarbons (e.g. methane [16,20,28], ethylene [29–32]) to oxygenates of various chain length and energy density (e.g., methanol [20,28,33], ethanol [29,34,35], and n-propanol [34,36]). The specific CO_2RR product distribution is mainly governed by chemical nature [7], the structure, and the morphology [30] of the electrocatalyst. Cu stands out in the group of monometallic CO_2RR catalysts [7] as it is capable to produce hydrocarbons [7,16,37–41] and oxygenates [32–35] of variable C–C chain length.

In particular, the multi-hydrocarbon and oxygenate formation from CO_2 typically requires the balanced interaction between catalyst active sites and chemisorbed *CO (Sabatier principle), the latter being considered as the key intermediate in the CO_2RR. Such balance guarantees a sufficiently high abundance and residence time of the *CO at the reactive sites as mechanistic pre-requisites to undergo further C–C coupling and reductive hydrogenation reactions [42]. For several CO_2RR catalysts, Kuhl et al. [28] derived a Volcano like interrelation between the *CO binding strength and experimentally determined CO_2RR current densities at −0.8 V vs RHE. Au and Ag were found on the low binding energy side of the volcano curve, rationalizing the facile release of the formed CO as main product when the CO_2RR is carried out over Ag and Au. Cu was found on the high binding energy side next to the volcano maximum with the right balance of the *CO binding strength to prevent irreversible poisoning of the catalyst (e.g., as in case of Pd [13,15]) but allowing for C–C coupling reactions.

One major drawback of the Cu catalysts is, however, their poor product selectivity [7]. One recently discussed experimental concept

towards improved selectivity of C–C coupled hydrocarbons (e.g., ethylene) is based on the use of bimetallic materials consisting of a CO producer (e.g., Ag, Au, or Zn) and the C–C coupler (Cu) [29,43–46]. A high abundance of CO is achieved, e.g. through selective CO_2RR on the Ag component in the bimetallic system. CO is subsequently transported to Cu sites in close proximity that are active for the C–C coupling. Short diffusion paths from Ag to Cu on the catalyst surface are essential for this 'CO spillover' concept. Further, CO_2RR efficiencies are per se improved when using AgCu bimetallics as the Ag reveals an intrinsically higher overpotential for the parasitic hydrogen evolution reaction (HER). It is the high surface concentration of chemisorbed *CO which leads to a further suppression of the HER by blocking surface sites, at least within a certain range of potentials applied [44].

In this present study, we further develop this approach by selectively activating the Cu component in the bimetallic AgCu system for alcohol formation. This can be achieved by thermal annealing, which leads to the selective formation of Cu oxides, whereas the Ag remains in its metallic state. Electroreduction of the formed oxidic Cu precursor under CO_2RR conditions transforms the bimetallic AgCu system into a C–C coupling and alcohol forming catalyst. The latter is denoted in the following as oxide-derived (OD) $Ag_{15}Cu_{85}$.

A combination of *operando* Raman spectroscopy and X-ray diffraction is used, along with TEM, STEM and so-called identical location (*IL*)-SEM imaging, to probe compositional and structural changes of the catalyst which go along with its activation for alcohol production.

For the preparation of model catalysts we apply the so-called dynamic hydrogen bubble template approach, originally developed for the electrodeposition of monometallic metal foams [47,48], to the bimetallic AgCu system [27]. Also we will show that the use of complexing plating additives (e.g., citrate) plays a vital role for the required dispersion of the Ag in the Cu matrix.
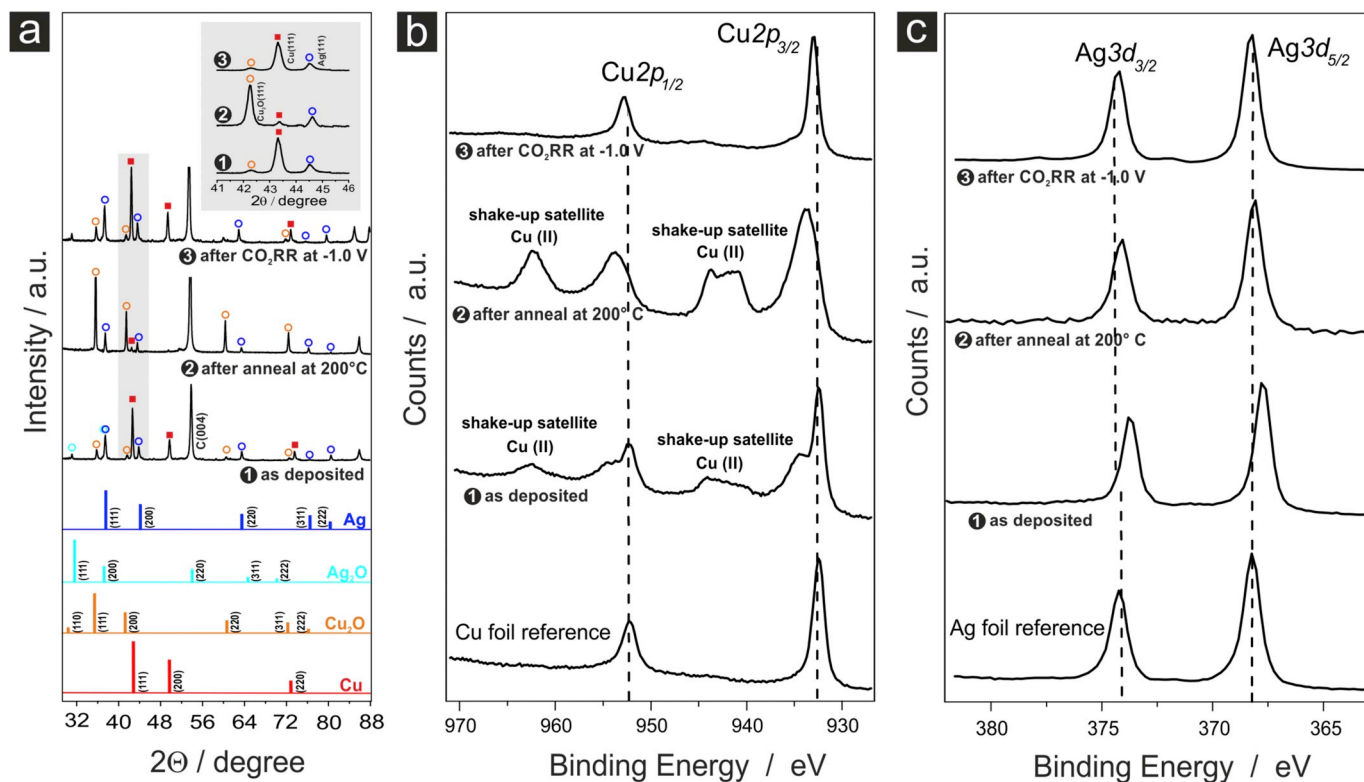
Fig. 2. a) *Ex situ* XRD analysis of the as deposited $Ag_{15}Cu_{85}$ foam, the annealed foam (12 h at 200 °C), and the OD-$Ag_{15}Cu_{85}$ (after 1 h CO_2RR at −1.0 V vs RHE); b) and c) Corresponding XPS analysis of the bimetallic foam.
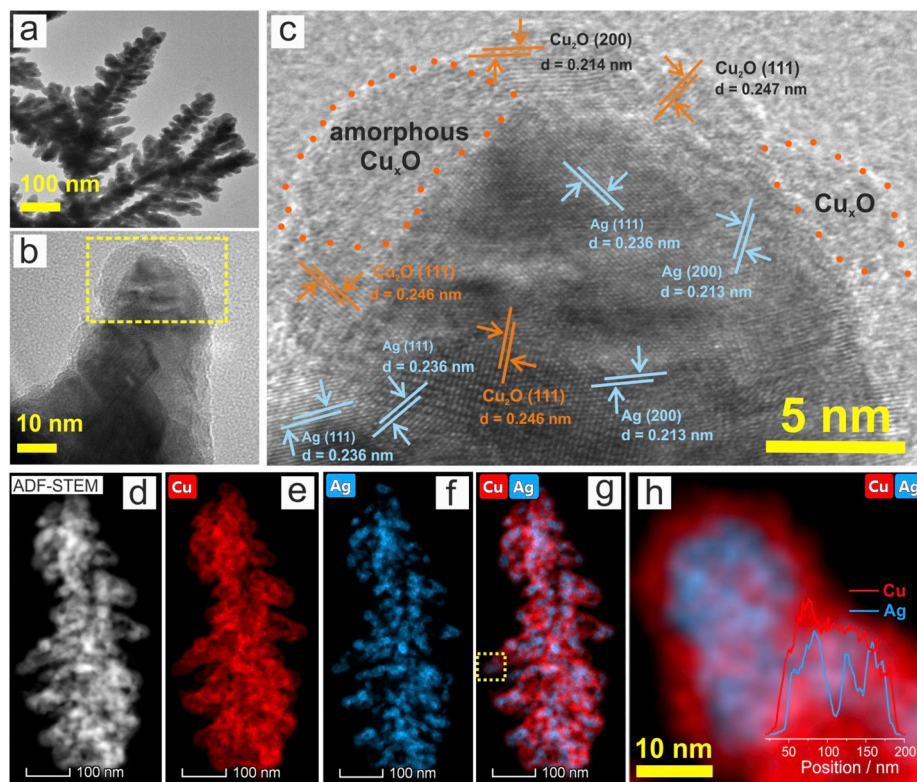
Fig. 3. Structural and compositional analysis of the thermally annealed $Ag_{15}Cu_{85}$ (12 h at 200 °C) foam; a) - c) HR-TEM micrographs of the thermally annealed $Ag_{15}Cu_{85}$ foam; d) ADF-STEM micrograph of the annealed $Ag_{15}Cu_{85}$ foam; e) – h) EDX mapping of an isolated dendrite of the annealed $Ag_{15}Cu_{85}$ foam. The yellow square in panel g highlights the section shown in panel h. The inset in panel h depicts one-dimensional line-scans over the feature (exhibited from panel g).
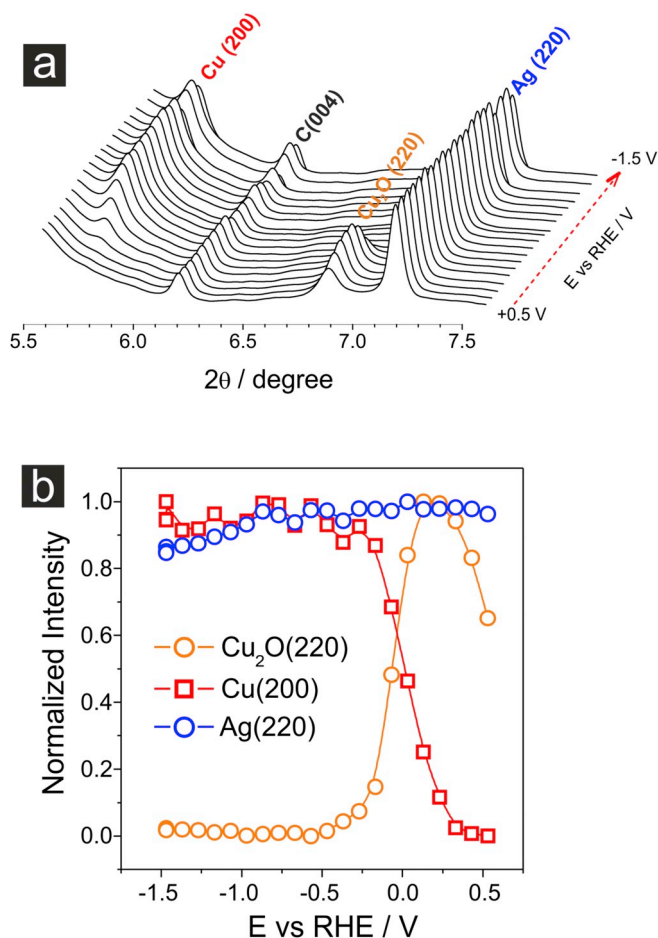
Fig. 4. *Operando* XRD experiment demonstrating the electro-reduction of Cu_2O in the annealed $Ag_{15}Cu_{85}$ foam as function of the applied electrode potential; a) Potential dependent XRD spectra; b) Integrated and normalized intensities derived from spectra shown in panel a (orange: integrated intensity of the Cu_2O (220) peak; red: integrated intensity of the Cu (200) peak; blue: integrated intensity of the Ag (220) peak).

2. Results and discussion

2.1. Synthesis and activation of the $Ag_{15}Cu_{85}$ foam catalyst

The as deposited $Ag_{15}Cu_{85}$ foam - The bimetallic $Ag_{15}Cu_{85}$ foam catalyst (this notation refers to the bulk composition derived from the ICP-OES analysis, see Table S1) has been electrodeposited on a Cu foil substrate at $j = -3$ A cm^{-2} (20 s) using a plating bath containing 1.5 M H_2SO_4, 20 mM $CuSO_4$, 2 mM Ag_2SO_4, and 0.1 M $Na_3C_6H_5O_7$. Key to this process is the hydrogen evolution reaction (HER, secondary process) that is superimposed on the metal deposition (primary process) when such high cathodic current densities are applied [30,47,48]. Hydrogen bubbles, which appear on the cathode during the massive HER, thereby serve as transient geometric template for the metal foaming process [30, 47,48]. Proton consumption and water splitting (OH$^-$ formation) lead to the appearance of pronounced *pH* gradients at the interface thus resulting into the deprotonation of the citric acid (10^{-1} M tri-sodium citrate di-hydrate) in the reaction boundary layer [18]. The formed citrate tends to chemisorb on the cathode thus altering the nucleation and growth characteristics of the emerging foam deposit [18]. In addition, citrate anions undergo fast chelating reactions with the Ag$^+$ and Cu^{2+} cations in the near electrode surface reaction boundary layer [18]. It can therefore be assumed that the actual deposition process occurs from a complexed metal ion solution produced *in situ* in the near surface electrolyte (see schematic in Fig. S1) [18]. In this present study, we

restrict ourselves to the discussion of one particular composition of the bimetallic AgCu foam catalyst containing 15 at% Ag and 85 at% Cu. Detailed compositional studies of this kind of catalysts are hampered by the fact that any changes of the bath composition (e.g., the Ag$^+$: Cu^{2+} ion ratio or the citrate additive concentration) will inevitably affect the Faradaic efficiencies of hydrogen production and metal deposition [27]. As a consequence of that not only the chemical composition of the deposit is altered but also its morphology on various length scales [27]. Compositional and morphological effects (e.g., pore size distribution, morphology of the pore side-walls) can therefore not be studied independently from each other when applying the dynamic hydrogen bubble approach [48] to these bimetallic systems.

Fig. 1 shows representative white-light interferometry (panel a) and SEM micrographs (panels b and c) of the as deposited $Ag_{15}Cu_{85}$ foam which resembles in appearance to the pure Cu foams with their multi-level 3D architecture of interconnected pores [30,48,49]. A cross-sectional SEM inspection reveals a thickness of ~18 μm (see Fig. S2) of the as deposited $Ag_{15}Cu_{85}$ foam. A similar bimetallic AgCu foam has recently been reported by Kottakat et al. [27] which has, however, been deposited from an additive-free plating bath and showed therefore different structural and morphological characteristics compared to the one discussed herein. The mean outermost surface pore diameter of the $Ag_{15}Cu_{85}$ foam discussed herein amounts to ~25 μm. Note that these metal foams typically reveal a gradient in pore size along the surface normal due to the coalescence of hydrogen bubbles in the course of the metal deposition [30,48]. Similar to the pure Cu metal foams deposited from an additive-free Cu plating bath [30,48,49], also the sidewalls of the bimetallic $Ag_{15}Cu_{85}$ foam reveal a dendritic nature with individual dendrites composed of AgCu particles having dimensions of <50 nm (panel c). Note that individual dendrites in the pure Cu foams deposited from additive-free plating baths are composed of shaped Cu crystallites showing preferential (111) and (100) facets on their surface [49]. No such texturing is, however, visible on the bimetallic $Ag_{15}Cu_{85}$ foam. Also note that pure Cu catalysts deposited under identical plating conditions (current density and plating time) in the presence of the citrate additive do not show a well-developed foam morphology at all (Fig. S3) thus demonstrating that the presence of the citrate not only impacts the nucleation and growth of the metal deposition process but also the formation and release of the hydrogen bubbles from the electrode.

The correlation between the catalyst morphology and its composition has been achieved by means of ADF-STEM imaging (Fig. 1d) combined with EDX mapping, the latter providing information on the spatial distribution of Cu and Ag, respectively (Fig. 1e–g). The EDX analysis confirms that the electrodeposition approach yields bimetallic foams with a high degree of dispersion of Ag in the Cu matrix, which is considered as a crucial prerequisite for the intended CO 'spillover' concept [50]. The presence of the citric acid additive in the plating bath is found to be essential to yield a bimetallic catalyst material where the nm-sized Ag and Cu domains form a maximum of phase boundaries. By contrast, the respective metal foam deposited in the absence of citric acid resembles more a physical mixture of loosely packed Ag and Cu particles (see Fig. S4).

Activation of the $Ag_{15}Cu_{85}$ foam: ex situ XRD and XPS analysis - An activation of the as deposited $Ag_{15}Cu_{85}$ foam for the selective formation of ethanol from CO_2 requires a further treatment which is typically based on an oxidation of the catalyst material. Both thermal annealing [34,49,51–55] and the exposure of Cu-based catalysts to oxygen plasma [40,56,57] have already been demonstrated to be beneficial for the formation of oxidic catalyst precursors which, under CO$_2$RR conditions, reductively transform into their metallic form thereby creating those reactive sites which are actually active towards C–C coupling and the formation of alcohols [34]. In addition, the C1 hydrocarbon (methane) reaction pathway gets effectively suppressed by this oxidation/reduction cycle [34]. This side effect of the thermal treatment has been found to be particularly beneficial for the degradation stability of the
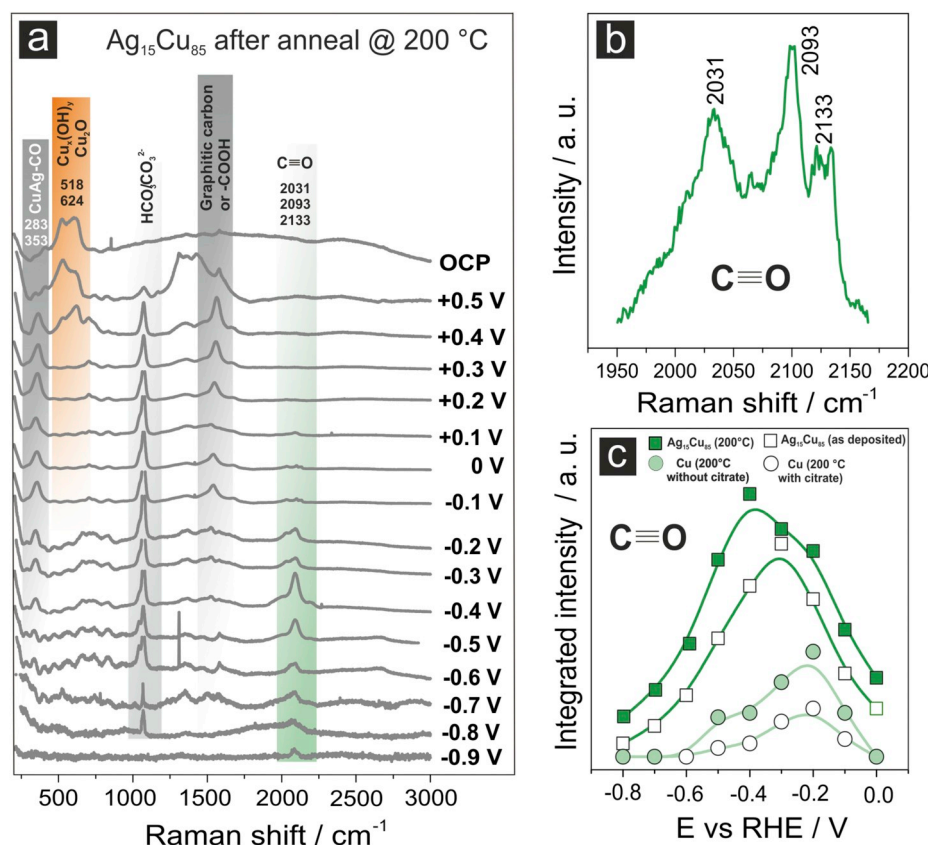
Fig. 5. a) Representative *Operando* Raman spectra of the thermally annealed $Ag_{15}Cu_{85}$ foam (12 h at 200 °C) as function of the applied electrode potential; b) Enlarged section of the operando Raman spectrum of the thermally annealed sample at −0.2 V vs RHE focusing on the intramolecular stretching mode of chemisorbed CO demonstrating three different adsorption sites; c) Integrated intensities of Raman peaks assigned to the intramolecular CO stretching modes. For comparison purposes also the results for the as deposited $Ag_{15}Cu_{85}$ foam and for the pure Cu catalysts (deposited in the presence and absence of citrate and thermally annealed at 200 °C for 12 h) are presented.

CO_2RR catalysts [34]. The formation of methane via the coupled C1/C2 reaction pathway [34,58] typically involves an undesired and irreversible carbonization of the catalyst surface [59–61].

A mild thermal annealing treatment in air at 200 °C was applied for 12 h to the as deposited $Ag_{15}Cu_{85}$ foam. Fig. 2a depicts representative diffraction patterns of the as deposited $Ag_{15}Cu_{85}$ foam, the thermally annealed one, and the catalyst after 1 h of CO_2RR at −1.0 V vs RHE (OD-$Ag_{15}Cu_{85}$ foam). For the sake of interpretability also the respective JCPDS reference data for *fcc* Cu, fcc Ag, Cu_2O and Ag_2O are presented (see also Table S1). From the XRD analysis, it can be concluded that the as deposited $Ag_{15}Cu_{85}$ foam is composed of pure Cu and Ag phases with minor contributions originating from Cu_2O and Ag_2O. Qualitatively similar diffraction patterns of bimetallic CuAg thin films were recently reported by Clark et al. also showing peaks coinciding with those of pure *fcc* Ag and Cu [44]. In the latter case, a small contribution from an AgCu surface alloying was observed. In the present case there are, however, no experimental hints in the XRD analysis for any alloying (see Table S1) in agreement with recent results by Kottakat et al. [27]. These different experimental observations can be rationalized by the particular preparation route of AgCu film formation used by Clark et al. which actually facilitates AgCu surface alloy formation [44]. The phase-segregation of Cu and Ag is indeed expected as the respective binary phase diagram indicates an immiscibility of Ag and Cu for a wide range of temperatures and compositions relevant to this study [50]. Minor oxidic components visible in the diffractogram of the as deposited sample might originate in particular at the surface of the deposit after its emersion from the metal ion containing plating bath and the subsequent drying procedure in air [30,49].

Thermal annealing in air at 200 °C partly transforms the Cu into crystalline Cu_2O whereas the diffraction pattern of metallic Cu almost disappears. Diffraction patterns of crystalline Ag_2O are not detected due to thermal instability of the Ag_2O which decomposes at temperatures above 180 °C [62]. From the XRD analysis it can be concluded that the thermally annealed $Ag_{15}Cu_{85}$ is a mixed metal/oxide ($AgCu_xO$) composite material.

As expected, the post-electrolysis XRD analysis reveals again major contributions from metallic Cu and Ag whereas the oxidic components have almost been disappeared (see also the inset in Fig. 2a). Only trace amounts of crystalline Cu_2O can be detected which have likely been formed on the catalyst surface after the CO_2 electrolysis during exposure of the catalyst to air.

As the XRD experiment is only sensitive to bulk phases revealing long-range translational order, complementary XPS analysis has been applied being more sensitive to the chemical state of the catalyst surface. Panels b and c of Fig. 2 depict Cu2p and Ag3d core level emissions of the bimetallic catalyst material representing different stages of its preparation and use. As reference, also XPS spectra of pure Ag and Cu foil samples are provided. Obviously, Cu(II) species are already present on the as deposited foam.

This can be deduced from the satellite features on the high binding energy side of the Cu(0)/Cu(I) related Cu2p emission. In addition, characteristic shake-up features are visible in the XPS spectrum of the as deposited sample, thus further confirming the presence of Cu(II). Cu(II) related XPS features might originate from residuals of the complexed Cu (II) precursors which were trapped inside the metal foam after its emersion from the plating bath. Note that Cu foams deposited from a non-complexed (citric acid free) solution do not show these characteristic Cu(II) features in the XPS (Fig. S5) [49]. Further, the annealed $Ag_{15}Cu_{85}$ foam sample contains Cu(I) and Cu(II) species which, in this case, can be assigned to oxidic Cu as product of the thermal treatment [49]. The annealing temperature of 200 °C is, however, not high enough to induce sufficient translational order in the formed CuO phase to be detected in the XRD (Fig. 2a) in full agreement with the literature [49]. After the electrolysis, the sample contains metallic Cu as well as minor amounts of cuprous and cupric oxides. The latter can be attributed to the post-electrolysis re-oxidation of the sample when exposed to air in
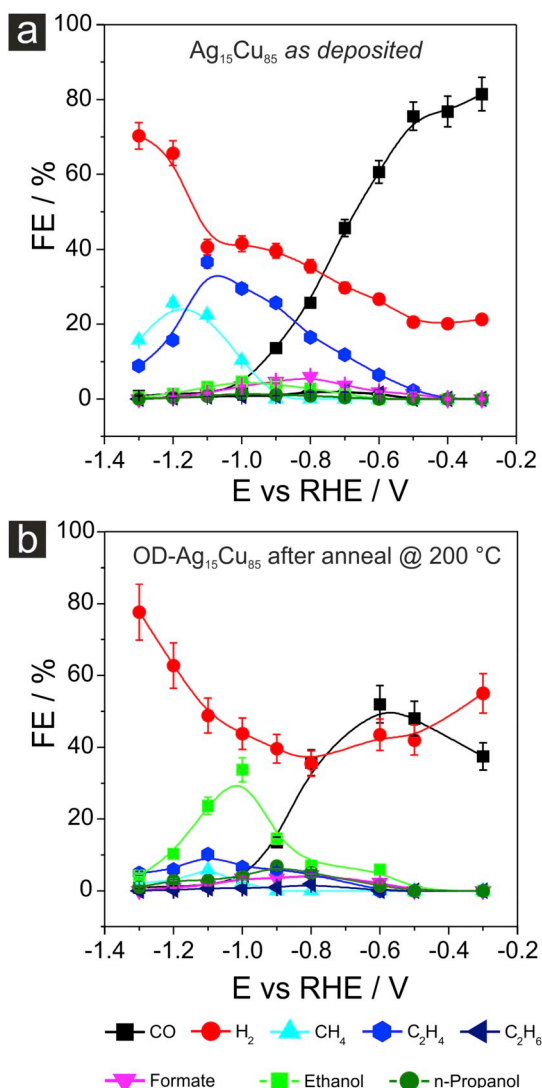
Fig. 6. Potential dependent CO_2RR product distribution for (a) the as deposited $Ag_{15}Cu_{85}$ foam and (b) the (oxide-derived) OD-$Ag_{15}Cu_{85}$ foam catalyst after the annealing at 200 °C.

agreement with the XRD analysis.

Also the Ag$3d_{5/2}$ core level emissions of the $Ag_{15}Cu_{85}$ foam (panel c) confirm our *ex situ* XRD analysis. After electrodeposition of the $Ag_{15}Cu_{85}$ foam both Ag(0) and Ag(I) species are observed in the XPS. For instance, the Ag$3d_{5/2}$ peak at BE = 367.9 eV is downward-shifted by ΔBE $\approx$0.3 eV with respect to the Ag reference (BE(Ag$3d_{5/2}$) = 368.2 eV thus indicating the presence of Ag(I) species. One possible origin of the Ag(I) might be residual Ag(I) complexes trapped inside the metal foam after the deposition. Note that similar Ag(I) features appear in the photoemission spectra of pure Ag metal foams deposited from a citrate containing plating bath [18]. In accordance with the XRD analysis, the Ag$3d$ core level emission of the annealed $Ag_{15}Cu_{85}$ foam does not show any contribution of Ag(I). This once more confirms the thermal instability of the Ag_2O phase and the AgCu_xO composite nature after its annealing at 200 °C. For the discussion of the CO_2RR product distribution (see below) it is important to note that the relative abundance of Cu and Ag on the catalyst surface differs from the respective bulk composition determined by ICP-OES and further changes in the course of the thermal oxidation/*ec* reduction treatment as evidenced by the quantitative analysis of the Cu$2p$ and the Ag$3d$ core level emissions. Their integrated intensities (I_{Cu2p}:I_{Ag3d}) change from 62:38 (as deposited) to 91:9 (annealed at 200 °C) and 77:23 (after 1 h CO_2RR at −1.0 V vs RHE). In particular the

surface of the annealed foam sample seems to be substantially enriched by (oxidic) Cu. Basis for this quantification was the XPS data set presented in Fig. S6.

This scenario becomes further supported by a combined HR-TEM and ADF-STEM inspection of the annealed $Ag_{15}Cu_{85}$ foam sample (Fig. 3) providing information of the spatial distribution of the metallic Ag and oxidic Cu_xO domains in the bimetallic foam. From the HR-TEM image in Fig. 3c it can be seen that the surface of the dendrite is composed of amorphous Cu_xO and crystalline Cu_2O whereas metallic Ag is found predominantly in the interior of the dendrite (see also the EDX analysis in Fig. 3h). Diameters of the Cu_xO and the metallic Ag domains in the composite are in the range of 4–8 nm. Spatially resolved EDX analysis combined with ADF-STEM imaging (Fig. 3) confirms a uniform dispersion of nm-sized Ag and Cu_xO domains in the bulk of the dendrite as already concluded from the EDX analysis of the as deposited sample (Fig. 1).

Activation of the $Ag_{15}Cu_{85}$ foam: operando XRD and Raman spectroscopic analysis - Applying cathodic electrode potentials relevant for the CO_2RR leads to further structural and compositional changes in the mixed metal-oxide foam involving in particular the electro-reduction of the cupric and cuprous oxides. These compositional changes can be probed under reactive conditions by means of the *operando* XRD technique using characteristic diffraction features of the crystalline Cu_2O as fingerprint for the presence of oxidic copper (Fig. 4a). Fig. 4b depicts the normalized intensities of the (220) diffraction peak of Cu_2O as well as intensities of the Ag and Cu related to (220) and (200) reflections, respectively, as a function of the applied electrode potential. Again, crystalline CuO was not detectable in the XRD due to its amorphous state (see also Fig. 3c). The intensity of Cu_2O related diffraction peaks first increase when going from +0.5 V to +0.25 V vs RHE before dropping down to zero at potentials < −0.5 V vs RHE. Such initial rise in the normalized intensity of the Cu_2O related diffraction peaks can be attributed to the reduction of amorphous CuO to metallic Cu which proceeds via crystalline Cu_2O as an intermediate. In general, the decrease of the Cu_2O related diffraction intensity at potentials < +0.25 V vs RHE is anti-correlated to the raise in the integrated peak intensity of the metallic Cu. Fig. 4 suggests that the reduction of the oxidic Cu 'precursor' is already completed before the CO_2RR sets in ($\approx$-0.3 V vs RHE). The normalized intensity of the Ag related (220) peak remains constant, at least in the potential range relevant for the Cu oxide-metal transition (+0.5 V vs RHE to −0.5 V vs RHE). A certain decrease in the integrated intensity is, however, observed at potentials < −1.0 V vs RHE. One possible explanation might be a preferential leaching of the Ag component under CO_2RR/HER conditions.

Operando Raman spectroscopy further supports the conclusion on the metal-oxide transition occurring at potentials more anodic than the CO_2RR onset. Not only is this technique more sensitive to the chemical state of the catalyst surface than the XRD, it is in addition suitable to probe chemisorbed intermediates of the CO_2RR [27]. Fig. 5a shows a series of potential dependent steady-state Raman spectra covering a potential window from the open circuit potential (OCP) down to −0.9 V vs RHE. According to the literature, the vibrational modes observed at 518 and 624 cm^{-1} originate from $Cu_x(OH)_y$ and Cu_2O species at the catalyst surface [63]. Their peak intensities drop down to zero already at potentials < +0.2 V vs RHE (Fig. 5a). This value is even more positive than the oxide-metal transition probed by the *operando* XRD (Fig. 4). Differences in the observed oxide-metal transition potential might be related to technique specific. Also note that neither the *operando* XRD nor the *operando* Raman spectroscopy can exclude the presence of traces of so-called sub-surface oxygen after completion of the potential-induced oxide-metal transition [64].

CO stretching modes of chemisorbed carbon monoxide appear in the *operando* Raman spectra at applied potentials < +0.1 V vs RHE. The discernable Raman peaks at 2031 cm^{-2}, 2093 cm^{-2}, and 2133 cm^{-2} (Fig. 5b) are due to different adsorption sites of CO chemisorbed either on metallic Cu or on Ag of the $Ag_{15}Cu_{85}$ foam [65,66]. A clear
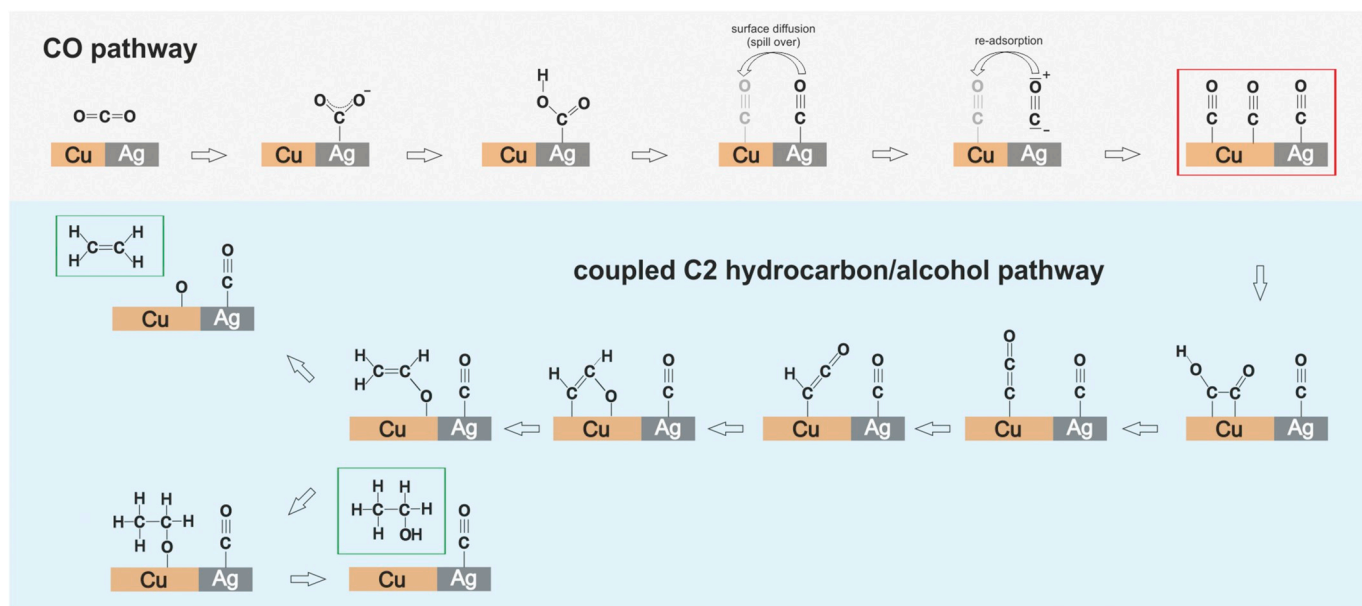
Fig. 7. Proposed reaction scheme illustrating the coupling of the CO pathway and the C2 hydrocarbon/alcohol reaction pathways.

improvement of the bimetallic $Ag_{15}Cu_{85}$ foam with regard to pure Cu catalysts is a higher abundance of chemisorbed CO at more cathodic potentials (Fig. 5c, Fig. S7). Note that the peak maximum of the integrated peak intensity of the CO stretching mode is shifted by ~200 mV towards more cathodic potentials in case of the thermally annealed $Ag_{15}Cu_{85}$ foam. A similar increased abundance of chemisorbed CO is observed for the as deposited $Ag_{15}Cu_{85}$ foam (Fig. 5c). This characteristic feature of the bimetallic $Ag_{15}Cu_{85}$ foams can be regarded as beneficial for the ethylene and the alcohol formation which require both a high abundance of chemisorbed CO on the catalyst surface [67]. The stabilization of chemisorbed CO on the catalyst surface under CO_2RR conditions can be regarded as crucial mechanistic prerequisite for any

Fig. 8. a) Current density/time transient curve of the 100 h lasting catalyst stressing experiment at −1.0 V vs RHE (note the electrolysis current is normalized to the geometric surface area); b) Corresponding CO_2RR product distribution focusing on the alcohols (ethanol and n-propanol).

further improvement of the ethanol efficiency.

2.2. Electrochemical performance of the $Ag_{15}Cu_{85}$ foam catalysts

The electrocatalytic performance of the $Ag_{15}Cu_{85}$ foam has been evaluated by means of potential dependent electrolysis experiments (1 h duration) from CO_2-saturated 0.5 M $KHCO_3$ electrolytes (pH = 7.2). Results of these electrolysis experiments are shown in Fig. 6a for as deposited $Ag_{15}Cu_{85}$ foam. In principle, the potential dependent product distribution can be subdivided into three distinct potential regimes. In the range from −0.3 to −0.7 V vs RHE CO is the predominant CO_2RR product reaching a maximum Faradaic efficiency of FE_{CO} = 81.45% (Table S2) at −0.3 V, which corresponds to a partial CO current density of j_{CO} = - 0.24 mA cm^{-2} (Table S3). It can be assumed that it is the Ag component in the as deposited $Ag_{15}Cu_{85}$ foam catalyst on which the CO_2RR preferentially takes place at these low overpotentials. This bimetallic catalyst outperforms pure Cu catalysts in terms of CO production at low overpotentials. One reason might be related to the almost quantitative suppression of the formate production (Fig. 6a, Table S2) which is typically produced over pure Cu electrocatalysts at these conditions (e.g. $FE_{formate}$ = 49.2% at −0.7 V vs RHE [34]). Comparably high efficiencies of formate formation are also observed for pure Cu catalysts deposited in the presence of citrate additives (see Fig. S3 and Fig. S8 in supplementary information).

A similar effect of suppressed formate production has recently been discussed by Kottakat et al. for electrodeposited bimetallic AgCu foams [27]. In this latter case a maximum CO efficiency of $\sim FE_{CO}$ = 58.4% at −0.6 V vs RHE was reported [27]. Highest CO efficiencies at particularly low overpotentials similar to those reported herein were so far reported only for pure Au [68] or Ag [69] electrocatalysts. An example related to this present work is the pure Ag foam electrocatalyst also deposited from a citrate-containing plaiting bath [18]. In this latter case the FE_{CO} values did not fall below 90% within a 800 mV broad potential window ranging from −0.3 to −1.2 V vs RHE [18]. It should be emphasized, however, that the bimetallic AgCu foams are superior over the pure Ag catalyst in terms of Ag mass activity [27].

In the present case the FE_{CO} values start to drop down at potentials < −0.5 V vs RHE not only because of the HER which becomes more favored with increasing cathodic potentials, but also because of the C1 (methane) and C2 (ethylene, ethane) hydrocarbon pathways which are opened at potentials < −0.4 V and < −0.9 V vs RHE, respectively. The
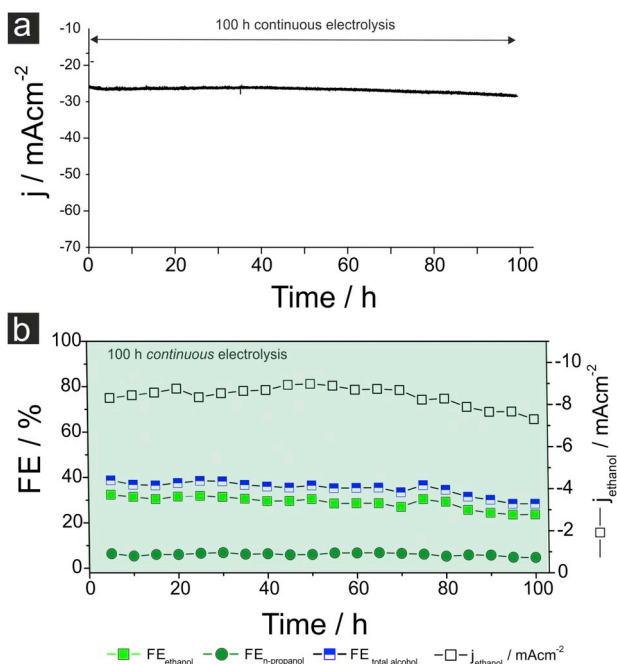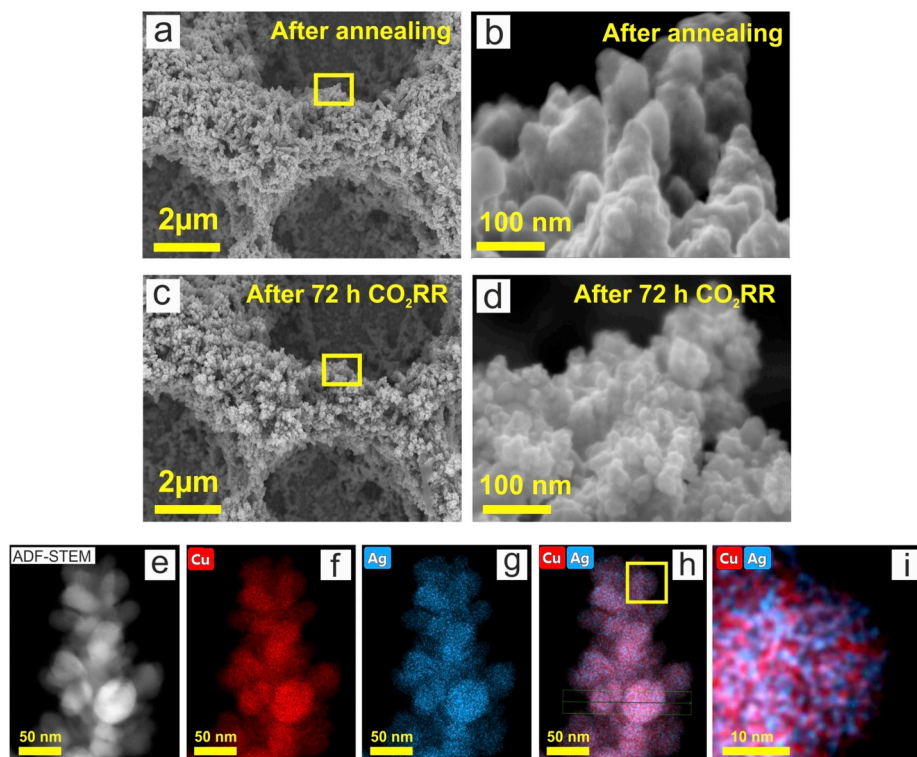
Fig. 9. a) – d) Identical location (IL) SEM analysis of the catalyst before (panel a and b) and after (panel c and d) 72 h CO_2RR at -1.0 V vs RHE; e) – i) ADF-STEM micrograph and EDX mapping of a single dendrite after CO_2RR at -1.0 V vs. RHE. The yellow square in panel h highlights the section shown in panel i.

ethylene efficiency reaches its maximum of $FE_{C2H4} = 36.56\%$ ($j_{C2H4} = -11.32$ mA cm^{-2}) at -1.1 V vs RHE. These efficiencies are comparable to those reported for Cu nano-foams [70] or Cu nano-cubes with (100) surface orientation [71,72]. Table S4 provides an overview on the best performing Cu-based catalysts for ethylene production. Interesting to note is that, in contrast to pure Cu foams [30], the C_2H_6 formation remains on a low level on the bimetallic catalyst within the entire potential range studied herein never exceeding 1% (Table S2).

As known from polycrystalline Cu electrocatalysts [73], methane production sets in at slightly higher overpotentials as compared to ethylene reaching on as deposited $Ag_{15}Cu_{85}$ a maximum of $FE_{CH4} = 25.6\%$ at -1.2 V vs RHE (Fig. 6a). C2 and C3 alcohol formation is negligible on the as deposited $Ag_{15}Cu_{85}$ foam. The n-propanol efficiencies never exceed 1% whereas a maximum ethanol efficiency of $FE_{EtOH} = 4.6\%$ ($j_{EtOH} = -1.11$ mA cm^{-2}) is obtained at -1.0 V vs RHE. The second characteristic potential regime in the product CO_2RR distribution (<-0.7 V vs RHE) is obviously dominated by the Cu component in the as deposited $Ag_{15}Cu_{85}$ foam with its capability of enabling C–C coupling reactions. It can be assumed that the C–C coupling reaction benefits from the high abundance of CO inside the porous catalyst. Due to the small domain sizes of the metallic components of the as deposited $Ag_{15}Cu_{85}$ foam (Fig. 1, see also below discussion on Fig. 9i) the CO intermediate is rapidly transported from the Ag (CO producer) to the Cu domains (C–C coupler) either by surface diffusion ('spillover') or by diffusion through the liquid electrolyte phase inside the pores of the bimetallic foam (re-adsorption of trapped CO).

In principle, this basic concept holds true also for the thermally annealed (oxide-derived) $Ag_{15}Cu_{85}$ foam (Fig. 6b). The C1 and C2 hydrocarbon pathways are, however, substantially suppressed on the OD-$Ag_{15}Cu_{85}$ foam (Table S5). A maximum value of only $FE_{C_2H_4} = 10.2\%$ ($j_{C2H4} = -3.1$ mA cm^{-2}) is observed at -1.1 V vs RHE. Instead, ethanol is the predominant CO_2RR product at electrolysis potentials < -0.8 V vs RHE reaching a maximum value of $FE_{EtOH} = 33.7\%$ ($j_{EtOH} = -8.67$ mA cm^{-2}) at -1.0 V vs RHE. Important to note is that the efficiency for n–propanol formation remains on a low level (e.g., $FE_{n-PrOH} = 6.9\%$, j_{n-} $_{PrOH} = -1.8$ mA cm^{-2} at -0.9 V vs RHE) thus pointing to a catalyst which is selective towards C2 alcohol formation (Table S5 and Table S6). Rahaman et al. recently reported a high alcohol efficiency for thermally annealed dendritic Cu of $FE_{alcohol} = 24.8\%$ ($j_{alcohol} = -7.73$ mA cm^{-2}) at -1.0 V vs RHE [34]. The alcohol selectivity itself was, however, poor with almost equivalent efficiencies for ethanol and n-propanol [34].

The OD-$Ag_{15}Cu_{85}$ is currently among the best performing catalysts for the production of higher alcohols (an overview is provided in Table S7 and Table S8).

A certain drawback of the thermal annealing of the $Ag_{15}Cu_{85}$ foam is the decrease of the Ag (CO producer) content at the catalyst surface in the course of the thermal oxidation/ec reduction treatment (see discussion of the XPS data). This structural and compositional alteration of the catalyst surface becomes apparent also from the CO_2RR product distribution, in particular in the low overpotential regime ranging from -0.3 V to -0.8 V vs RHE (Fig. 6b). In comparison to the as deposited sample (Fig. 6a) the Faradaic yield of CO production is substantially lower for the oxide-derived catalyst at lowest overpotentials, e.g. at -0.3 V vs RHE ($FE_{CO} = 37.4\%$ instead of $FE_{CO} = 81.45\%$ (as deposited)) and slightly lower at medium overpotentials, e.g. at -0.6 V vs RHE ($FE_{CO} = 52.0\%$ instead of $FE_{CO} = 60.7\%$ (as deposited)). However, the Ag content on the catalyst surface after the reduction of the oxides seems to be sufficient to substantially improve the total alcohol efficiency $FE_{alcohol}$ compared to pure Cu foams (see also discussion of Fig. 9).

Fig. 7 summarizes the suggested mechanism of alcohol formation on the bimetallic AgCu catalyst surface which is consistent with published models on alcohol formation on Cu [34]. CO forms selectively on the Ag domains and is subsequently transported to the Cu via surface diffusion ('spillover') or alternatively via CO transport through the solution phase (desorption/re-adsorption). Besides the increased abundance of CO intermediates it is the stabilization of the chemisorbed *CO on the catalyst surface which further directs the CO_2RR towards C–C coupling and alcohol formation. This stabilization is deduced from the potential dependent integrated intensity of the CO stretching mode (Fig. 5c). Its maximum is downward-shifted on the potential scale in case of the

$Ag_{15}Cu_{85}$ foam compared to the pure Cu foam (Fig. 5c). Note that the Raman experiment does not allow for a direct comparison of the CO surface concentration on the pure Cu and the $Ag_{15}Cu_{85}$ foam due to differences in the surface morphology (e.g. roughness) and chemical composition of both catalyst materials.

2.3. Stability of the annealed $Ag_{15}Cu_{85}$ foam catalyst

Besides the CO_2RR product selectivity and activity, it is the long term stability of the catalyst which defines its overall performance. Therefore, long term CO_2 electrolysis experiments were performed at −1.0 V vs RHE corresponding to the maximum ethanol efficiency in the potential dependent screening experiment (Fig. 6b). Fig. 8 depicts the current/time transient curve (panel a) and the corresponding *FE/PCD vs t* plot (panel b) of a 100 h continuous electrolysis experiment. The partial current density (PCD) for ethanol formation drops down slightly from −8.4 mA/cm^2 to −7.3 mA/cm^2 thus pointing to an excellent degradation stability of the bimetallic catalyst. Note that, when the electrolysis is carried out in a discontinuous fashion, the degradation process proceeds faster (see discussion on Fig. S9 in the supplementary information).

Structural and compositional changes upon catalyst activation via the precursor reduction and the CO_2 electrolysis itself become apparent from identical location IL-SEM analyses of the $Ag_{15}Cu_{85}$ foam in Fig. 9 after anneal at 200 °C (panel a–b) and after 72 h of continuous CO_2 electrolysis (panel c–d). The electroreduction of the precursor and the CO_2 electrolysis at −1.0 V vs RHE leaves the mesoscopic pore structure on the μm scale fully unaffected (panel a and c) similar to what is known from Cu and Ag foams [18,30]. Distinct structural changes are, however, visible on the nm length scale (panel b and d). After the 72 h of electrolysis (panel d) smaller particles have been evolved, most likely in the initial stage of the electrolysis where the CO_2RR is superimposed on the Cu oxide reduction (see e.g. Fig. 4). Similar morphological changes become apparent from an extended IL-analysis of the catalyst carried out at discontinuous operation mode (Fig. S10 in the supplementary information).

Combined ADF-STEM imaging and EDX mapping (Fig. 9) clearly indicate a high degree of dispersion of Ag and Cu domains. The preferential segregation of Cu in the form of cuprous and cupric oxides has disappeared under CO_2RR conditions in full agreement also with the XPS analysis.

3. Conclusions

Bimetallic $Ag_{15}Cu_{85}$ foam catalysts have been produced by means of an additive (citrate) assisted electrodeposition approach utilizing the dynamic hydrogen bubble template approach. Whereas the as deposited catalyst is selective towards CO at particularly low overpotentials (FE_{CO} = 81.45%, j_{CO} = −0.24 mA cm^{-2} at −0.3 V vs RHE) and towards C_2H_4 at higher overpotentials (FE_{C2H4} = 36.56%, j_{C2H4} = - 11.32 mA cm^{-2} at −1.1 V vs RHE) an activation of the catalyst for selective alcohol formation is achieved by thermal annealing of the $Ag_{15}Cu_{85}$ at 200 °C for 12 h. This treatment leads to a metal/oxide composite material consisting of metallic Ag and oxidized Cu (denoted as $AgCu_xO$ foam), the latter being accumulated at the surface of the foam. Electroreduction of the oxidic components in the $AgCu_xO$ precursor leads to an oxide-derived (OD) bimetallic AgCu catalyst which outperforms in terms of ethanol selectivity (FE_{EtOH} = 33.7%, j_{EtOH} = −8.67 mA cm^{-2} at −1.0 V vs RHE) and durability (100 h).

A key feature of the OD-$Ag_{15}Cu_{85}$ foam catalyst is the high dispersion of nm-sized domains of metallic Ag (CO producer) and Cu (C–C coupler, alcohol former) in the bimetallic catalyst thus allowing for a facile transport of the CO intermediate to those Cu surface sites that are particularly active for C–C coupling and ethanol formation (CO spillover concept). The excellent performance of the OD-$Ag_{15}Cu_{85}$ foam catalyst is due to the synergistic effects of an increased CO abundance at higher overpotentials and the selective activation of the Cu component by the

oxide formation and its electroreduction under CO_2RR conditions.

Operando Raman spectroscopy and X-ray diffraction both clearly demonstrate that the activation (electro-reduction) of the annealed $Ag_{15}Cu_{85}$ foam is completed before the CO_2RR sets in.

4. Experimental section

4.1. Chemical and materials

Cu foils were purchased from Alfa Aesar (thickness 0.25 mm, purity ≥ 99.95%) and cut into pieces having dimensions of ~8 mm × 22 mm. Prior to the electrodeposition of the CuAg foam, Cu foils were subjected to an electropolishing treatment in ortho-phosphoric acid (50w%, ACS grade, SigmaAldrich) using a two-electrode arrangement. A graphite foil thereby served as counter (cathode) and the Cu foil as working electrodes (anode), respectively. A constant potential difference of 2.0 V was applied between both electrodes for the duration of 2 min. During the electropolishing treatment, the Cu foil was gently moved in the phosphoric acid solution to remove oxygen bubbles formed upon electrode polarization on the Cu. The resulting surface morphology was characterized by means of atomic force microscopy (AFM, NanoSurf, see Fig. S11 in the supplementary information).

4.2. Electrolyte solutions

The standard plating bath for the bimetallic AgCu foam deposition was composed of 1.5 M H_2SO_4 (prepared from 96% H_2SO_4, ACS grade, Sigma-Aldrich) serving as supporting electrolyte, 20 mM $CuSO_4$ (Fluka), 2 mM Ag_2SO_4 (Sigma Aldrich, purity ≥ 99.5%), and 0.1 M $Na_3C_6H_5O_7 \cdot 2H_2O$ (tri-sodium citrate di-hydrate, >99.7%, Merck). For comparison purposes AgCu electroplating experiments were performed also in the additive-free bath. Furthermore also pure Cu catalysts were deposited from a plating bath in the absence of Ag containing 1.5 M H_2SO_4 (ACS grade, Sigma-Aldrich) and 20 mM $CuSO_4$ (Fluka). This deposition was carried out in the presence and the absence of 0.1 M $Na_3C_6H_5O_7 \cdot 2H_2O$ (tri-sodium citrate di-hydrate, >99.7%, Merck). See the *operando* Raman results in Fig. 5c and SEM images in Fig. S3 in the supplementary information.

The electrochemically active surface area (denoted hereinafter as ECSA) was estimated by means of cyclic voltammetry (CV) using dimethyl viologen dichloride ($DMVCl_2$) as reversible redox-probe following a protocol described previously [30]. Scan-rate dependent CVs were measured in aqueous 1 M Na_2SO_4 (ACS grade, Sigma-Aldrich) solution containing 10 mM $DMVCl_2$ (Sigma-Aldrich). The estimated ECSA of the bimetallic AgCu foams (as deposited) used herein amounts to 2.66 cm^{-2} (referring to 1 cm^{-2} geometric surface area). Note that the ECSA further increases to 4.45 cm^{-2} after the thermal annealing. For details of the ECSA determination see Fig. S12 in the supplementary information.

All CO_2RR experiments were carried out in 0.5 M $KHCO_3$ (ACS grade, Sigma-Aldrich) electrolyte solutions saturated with CO_2 gas (99.999%, Carbagas, Switzerland). For blank experiments the same electrolyte was saturated with inert Ar gas.

4.3. Electrochemical experiments

The AgCu foam deposition was carried out in a glass-beaker containing 100 mL of the plating solution. For the galvanostatic deposition process, a nominal current density of j = −3.0 A cm^{-2} (referred to the geometric surface area of the Cu foil support electrode) was applied for 20 s. The three-electrode arrangement consisted of a leakless $Ag/AgCl_{3M}$ reference electrode (RE, EDAQ), a bright Pt-foil (15 mm × 5 mm) serving as counter electrode (CE), and the Cu foil (substrate of the bimetallic AgCu foam) catalysts serving as working electrode (WE). The electrodeposition was performed in a face-to-face configuration (WE-CE) as indicated in Fig. S13 in the supplementary information. Note that

the deposited bimetallic foam is sufficiently thick (>15 μm) so that any contribution from the substrate to the resulting CO_2RR product distribution is excluded.

Electrodeposited bimetallic AgCu and the pure Cu foams were further activated by thermal annealing in air at 200 °C for 12 h using a tube furnace (GERO Hochtemperaturofen GmbH, Germany).

All voltammetric and CO_2RR electrolysis experiments were carried out in a custom-built, air-tight glass-cell (H-type) described elsewhere [30].

Possible chloride ion cross-contaminations in the working electrolytes originating from the $Ag/AgCl_{3M}$ reference electrode were monitored and excluded by ion exchange (IC) chromatography (Metrohm). Technical details of the CO_2RR product analysis based on online gaschromatography and ion exchange (IC) chromatography were described elsewhere [30].

All potentials given herein are iR-corrected and referenced to the reversible hydrogen electrode (RHE) by using the following equation:

$$E_{RHE} (V) = E_{Ag/AgCl(3M)} (V) + 0.210 V + (0.059 V \times pH)$$

4.4. Structural and compositional characterization

For the XRD analysis an STOE Stadi P system with a Cu Kα radiation source (λ = 0.1540 nm, 40 mA) operated at 40 keV was used. XRD spectra were recorded in reflection mode (Bragg-Brentano geometry) in steps of $1° min^{-1}$ with 2θ values ranging from 0 to 90°. To exclude Cu diffraction peaks originating from the Cu foil support, the bimetallic foam was deposited onto a graphite substrate (99.8%, Alfa Aesar, 0.13 mm thickness). The obtained XRD patterns were analyzed and compared to JCPDS (Joint Committee on Powder Diffraction standards) data of polycrystalline Ag, Ag_2O, AgO, Cu, Cu_2O, and CuO (File No. 04–0783, 43–0997, 43–1038, 04–0836, 05–0667, 41–0254).

Elemental analysis of the bimetallic foams was carried out by means of inductively coupled plasma optical emission spectrometry (Agilent 5110 inductively coupled plasma optical emission spectrometry (ICP-OES)).

X-ray photoelectron spectroscopy (XPS) studies were carried out using a PHI VersaProbeII scanning XPS micro-probe (Physical Instruments AG, Germany) equipped with a monochromatic Al Kα X-ray source operated at 24.8 W with a spot size of 100 μm. Peak positions were referenced to the carbon C1s peak at 285.5 eV and curve fitting was performed using the Casa-XPS software.

The morphology of the bimetallic foams was characterized by means of Scanning Electron Microscopy (SEM) and Energy-Dispersive X-ray spectroscopy (EDX) using a Hitachi S-3000 N Scanning Electron Microscope and a Noran SIX NSS200 energy-dispersive X-ray spectrometer. For the high-resolution identical location IL-SEM imaging a Zeiss DSM 982 instrument was used. In addition the mesoscopic surface morphology of the bimetallic AgCu foam was analyzed by means of a white light interferometry (Contour GT, Bruker).

For the transmission electron microscopy (TEM), the $Ag_{15}Cu_{85}$ catalyst was dispersed on a carbon coated TEM Au grid (200 mesh) after initial electrodeposition on a Cu foil substrate, followed by dispersion in absolute ethanol. For the HR-TEM imaging an FEI Tecnai F2 instrument was used with an accelerating voltage of 200 kV. Annular dark-field scanning transmission electron microscopy (ADF-STEM) in combination with EDX measurements were carried out using a FEI Titan Themis operated at 300 kV equipped with a SuperEDX detector.

4.5. Operando Raman spectroscopy

Raman spectroscopic measurements were performed using a Lab-RAM HR800 confocal microscope (Horiba Jobin Yvon). A large working distance objective lens (50 times magnification, 8 mm focal length) has been applied with a numerical aperture of 0.1 in order to focus a diodepumped solid-state laser beam (excitation wavelength 632 nm, power 3 mW) on the sample. The Raman signal was collected in backscattering geometry using a home-made spectro-electrochemical cell (see Fig. S14 in the supplementary information) [74,75].

4.6. Operando X-ray diffraction (XRD)

Operando XRD experiments (see Fig. S15 in the supplementary information) were performed at the European Synchrotron Radiation Facility ID31 high energy beamline. The 69 keV monochromatic X-ray beam was focused to the size of $5 \times 20 \ \mu m^2$ (vertical x horizontal) at the sample position. The 2D XRD patterns were collected with a Dectris Pilatus 2 M CdTe detector. A custom made PEEK electrochemical cell consists of a Pt counter electrode, an Ag/AgCl (3 M KCl) reference electrode (EDAQ) and the sample working electrode supported on carbon paper electrically connected with an Au wire. The measurements were performed in CO_2-saturated 0.5 M $KHCO_3$ electrolyte and in grazing incidence geometry. The sample was first measured at OCP after the electrolyte was introduced to the cell and then at subsequently decreasing potentials in steps of 0.1 V. The resting time at each potential before the measurement was 2 min. The raw 2D diffraction patterns were radially integrated to the final 1D patterns using the pyFAI package [76]. The 1D patterns were further analyzed by integrating the characteristic peak intensities and fitting the Gaussian function to determine the FWHM.

Declaration of competing interest

No conflict of interest exists.

Acknowledgements

Appendix A. Supplementary data

Supplementary data to this article can be found online at https://doi.org/10.1016/j.nanoen.2019.104331.

References

[1] D.T. Whipple, P.J.A. Kenis, Prospects of CO_2 utilization via direct heterogeneous electrochemical reduction, J. Phys. Chem. Lett. 1 (2010) 3451–3458.

[2] A.M. Appel, J.E. Bercaw, A.B. Bocarsly, H. Dobbek, D.L. DuBois, M. Dupuis, J. G. Ferry, E. Fujita, R. Hille, P.J.A. Kenis, C.A. Kerfeld, R.H. Morris, C.H.F. Peden, A. R. Portis, S.W. Ragsdale, T.B. Rauchfuss, J.N.H. Reek, L.C. Seefeldt, R.K. Thauer, G. L. Waldrop, Frontiers, opportunities, and challenges in biochemical and chemical catalysis of CO_2 fixation, Chem. Rev. 113 (2013) 6621–6658.

[3] H.-R.M. Jhong, S. Ma, P.J.A. Kenis, Electrochemical conversion of CO_2 to useful chemicals: current status, remaining challenges, and future opportunities, Curr. Opin. Chem. Eng. 2 (2013) 191–199.

[4] National oceanic and atmospheric administration. https://www.noaa.gov/.

[5] H. Yang, Z. Xu, M. Fan, R. Gupta, R.B. Slimane, A.E. Bland, I. Wright, Progress in carbon dioxide separation and capture: a review, J. Environ. Sci. 20 (2008) 14–27.

[6] M. Mikkelsen, M. Jørgensen, F.C. Krebs, The teraton challenge. A review of fixation and transformation of carbon dioxide, Energy Environ. Sci. 3 (2010) 43–81.

[7] Y. Hori, in: R.E.W.C.G. Vayenas, M.E. Gamboa-Aldeco (Eds.), Modern Aspects of Electrochemistry, Springer, New York, 2008, pp. 89–189.

[8] T. Haas, R. Krause, R. Weber, M. Demler, G. Schmid, Technical photosynthesis involving CO_2 electrolysis and fermentation, Nat. Catal. 1 (2018) 32–39.

[9] J.-P. Jones, G.K.S. Prakash, G.A. Olah, Electrochemical CO_2 reduction: recent advances and current trends, Isr. J. Chem. 54 (2014) 1451–1466.

[10] G. Centi, S. Perathoner, Opportunities and prospects in the chemical recycling of carbon dioxide to fuels, Catal. Today 148 (2009) 191–205.

[11] S. Cherevko, S. Geiger, O. Kasian, N. Kulyk, J.-P. Grote, A. Savan, B.R. Shrestha, S. Merzlikin, B. Breitbach, A. Ludwig, K.J.J. Mayrhofer, Oxygen and hydrogen

evolution reactions on Ru, RuO$_2$, Ir, and IrO$_2$ thin film electrodes in acidic and alkaline electrolytes: a comparative study on activity and stability, Catal. Today 262 (2016) 170–180.

[12] M. Görlin, M. Gliech, J.F. de Araújo, S. Dresp, A. Bergmann, P. Strasser, Dynamical changes of a Ni-Fe oxide water splitting catalyst investigated at different pH, Catal. Today 262 (2016) 65–73.

[13] M. Rahaman, A. Dutta, P. Broekmann, Size-dependent activity of palladium nanoparticles: efficient conversion of CO$_2$ into formate at low overpotentials, ChemSusChem 10 (2017) 1733–1741.

[14] A. Dutta, A. Kuzume, M. Rahaman, S. Vesztergom, P. Broekmann, Monitoring the chemical state of catalysts for CO$_2$ electroreduction: an in operando study, ACS Catal. 5 (2015) 7498–7502.

[15] X.Q. Min, M.W. Kanan, Pd-catalyzed electrohydrogenation of carbon dioxide to formate: high mass activity at low overpotential and identification of the deactivation pathway, J. Am. Chem. Soc. 137 (2015) 4701–4708.

[16] Y. Hori, K. Kikuchi, S. Suzuki, Production of CO and CH$_4$ in electrochemical reduction of CO$_2$ at metal-electrodes in aqueous hydrogencarbonate solution, Chem. Lett. (1985) 1695–1698.

[17] S. Ma, Y. Lan, G.M.J. Perez, S. Moniri, P.J.A. Kenis Silver, Supported on titania as an active catalyst for electrochemical carbon dioxide reduction, ChemSusChem 7 (2014) 866–874.

[18] A. Dutta, C.E. Morstein, M. Rahaman, A. Cedeño López, P. Broekmann, Beyond copper in CO$_2$ electrolysis: effective hydrocarbon production on silver-nanofoam catalysts, ACS Catal. (2018) 8357–8368.

[19] S. Liu, H. Tao, L. Zeng, Q. Liu, Z. Xu, Q. Liu, J.-L. Luo, Shape-dependent electrocatalytic reduction of CO$_2$ to CO on triangular silver nanoplates, J. Am. Chem. Soc. 139 (2017) 2160–2163.

[20] K.W. Frese, S. Leach, Electrochemical reduction of carbon dioxide to methane, methanol, and CO on Ru electrodes, J. Electrochem. Soc. 132 (1985) 259–260.

[21] T. Hatsukade, K.P. Kuhl, E.R. Cave, D.N. Abram, T.F. Jaramillo, Insights into the electrocatalytic reduction of CO$_2$ on metallic silver surfaces, Phys. Chem. Chem. Phys. 16 (2014) 13814–13819.

[22] N. Hoshi, M. Kato, Y. Hori, Electrochemical reduction of CO$_2$ on single crystal electrodes of silver Ag(111), Ag(100) and Ag(110), J. Electroanal. Chem. 440 (1997) 283–286.

[23] H. Mistry, Y.W. Choi, A. Bagger, F. Scholten, C.S. Bonifacio, I. Sinev, N.J. Divins, I. Zegkinoglou, H.S. Jeon, K. Kisslinger, E.A. Stach, J.C. Yang, J. Rossmeisl, B. R. Cuenya, Enhanced carbon dioxide electroreduction to carbon monoxide over defect-rich plasma-activated silver catalysts, Angew. Chem. Int. Ed. 56 (2017) 11394–11398.

[24] Y. Hori, H. Wakebe, T. Tsukamoto, O. Koga, Electrocatalytic process of CO selectivity in electrochemical reduction of CO$_2$ at metal electrodes in aqueous media, Electrochim. Acta 39 (1994) 1833–1839.

[25] M. Li, J.J. Wang, P. Li, K. Chang, C.L. Li, T. Wang, B. Jiang, H.B. Zhang, H.M. Liu, Y. Yamauchi, N. Umezawa, J.H. Ye, Mesoporous palladium-copper bimetallic electrodes for selective electrocatalytic reduction of aqueous CO$_2$ to CO, J. Mater. Chem. 4 (2016) 4776–4782.

[26] S. Verma, X. Lu, S. Ma, R.I. Masel, P.J.A. Kenis, The effect of electrolyte composition on the electroreduction of CO$_2$ to CO on Ag based gas diffusion electrodes, Phys. Chem. Chem. Phys. 18 (2016) 7075–7084.

[27] T. Kottakkat, K. Klingan, S. Jiang, Z.P. Jovanov, V.H. Davies, G.A.M. El-Nagar, H. Dau, C. Roth, Electrodeposited AgCu foam catalysts for enhanced reduction of CO$_2$ to CO, ACS Appl. Mater. Interfaces 11 (2019) 14734–14744.

[28] K.P. Kuhl, T. Hatsukade, E.R. Cave, D.N. Abram, J. Kibsgaard, T.F. Jaramillo, Electrocatalytic conversion of carbon dioxide to methane and methanol on transition metal surfaces, J. Am. Chem. Soc. 136 (2014) 14107–14113.

[29] T.T.H. Hoang, S. Verma, S. Ma, T.T. Fister, J. Timoshenko, A.I. Frenkel, P.J. A. Kenis, A.A. Gewirth, Nanoporous copper–silver alloys by additive-controlled electrodeposition for the selective electroreduction of CO$_2$ to ethylene and ethanol, J. Am. Chem. Soc. 140 (2018) 5791–5797.

[30] A. Dutta, M. Rahaman, N.C. Luedi, M. Mohos, P. Broekmann, Morphology matters: tuning the product distribution of CO$_2$ electroreduction on oxide-derived Cu foam catalysts, ACS Catal. 6 (2016) 3804–3814.

[31] Y. Hori, A. Murata, R. Takahashi, S. Suzuki, Enhanced formation of ethylene and alcohols at ambient temperature and pressure in electrochemcial reduction of carbon dioxide at a copper electrode, J. Chem. Soc., Chem. Commun. (1988) 17–19.

[32] D. Ren, Y. Deng, A.D. Handoko, C.S. Chen, S. Malkhandi, B.S. Yeo, Selective electrochemical reduction of carbon dioxide to ethylene and ethanol on copper(I) oxide catalysts, ACS Catal. 5 (2015) 2814–2821.

[33] J. Albo, A. Irabien, Cu$_2$O-loaded gas diffusion electrodes for the continuous electrochemical reduction of CO$_2$ to methanol, J. Catal. 343 (2016) 232–239.

[34] M. Rahaman, A. Dutta, A. Zanetti, P. Broekmann, Electrochemical reduction of CO$_2$ into multicarbon alcohols on activated Cu mesh catalysts: an identical location (IL) study, ACS Catal. 7 (2017) 7946–7956.

[35] S. Ma, M. Sadakiyo, R. Luo, M. Heima, M. Yamauchi, P.J.A. Kenis, One-step electrosynthesis of ethylene and ethanol from CO$_2$ in an alkaline electrolyzer, J. Power Sources 301 (2016) 219–228.

[36] D. Ren, N.T. Wong, A.D. Handoko, Y. Huang, B.S. Yeo, Mechanistic insights into the enhanced activity and stability of agglomerated Cu nanocrystals for the electrochemical reduction of carbon dioxide to n-propanol, J. Phys. Chem. Lett. 7 (2016) 20–24.

[37] Y. Hori, I. Takahashi, O. Koga, N. Hoshi, selective formation of C2 compounds from electrochemical reduction of CO$_2$ at a series of copper single crystal electrodes, J. Phys. Chem. B 106 (2002) 15–17.

[38] Y. Hori, I. Takahashi, O. Koga, N. Hoshi, Electrochemical reduction of carbon dioxide at various series of copper single crystal electrodes, J. Mol. Catal. A Chem. 199 (2003) 39–47.

[39] Y. Hori, R. Takahashi, Y. Yoshinami, A. Murata, Electrochemical reduction of CO at a copper electrode, J. Phys. Chem. B 101 (1997) 7075–7081.

[40] H. Mistry, A.S. Varela, C.S. Bonifacio, I. Zegkinoglou, I. Sinev, Y.W. Choi, K. Kisslinger, E.A. Stach, J.C. Yang, P. Strasser, B.R. Cuenya, Highly selective plasma-activated copper catalysts for carbon dioxide reduction to ethylene, Nat. Commun. 7 (2016).

[41] R. Reske, H. Mistry, F. Behafarid, B. Roldan Cuenya, P. Strasser, Particle size effects in the catalytic electroreduction of CO$_2$ on Cu nanoparticles, J. Am. Chem. Soc. 136 (2014) 6978–6986.

[42] A.A. Peterson, F. Abild-Pedersen, F. Studt, J. Rossmeisl, J.K. Norskov, How copper catalyzes the electroreduction of carbon dioxide into hydrocarbon fuels, Energy Environ. Sci. 3 (2010) 1311–1315.

[43] Z.-Y. Chang, S.-J. Huo, J.-M. He, J.-H. Fang, Facile synthesis of Cu–Ag bimetallic electrocatalyst with prior C2 products at lower overpotential for CO$_2$ electrochemical reduction, Surf. Interfaces 6 (2017) 116–121.

[44] E.L. Clark, C. Hahn, T.F. Jaramillo, A.T. Bell, Electrochemical CO$_2$ reduction over compressively strained CuAg surface alloys with enhanced multi-carbon oxygenate selectivity, J. Am. Chem. Soc. 139 (2017) 15848–15857.

[45] J. Huang, J. Mensi, E. Oveisi, V. Mantella, R. Buonsanti, Structural sensitivities in bimetallic catalysts for electrochemical CO$_2$ reduction revealed by Ag–Cu nanodimers, J. Am. Chem. Soc. 141 (2019) 2490–2499.

[46] D. Ren, B.S.-H. Ang, B.S. Yeo, Tuning the selectivity of carbon dioxide electroreduction toward ethanol on oxide-derived CuxZn catalysts, ACS Catal. 6 (2016) 8239–8247.

[47] H.C. Shin, J. Dong, M. Liu, Porous tin oxides prepared using an anodic oxidation process, Adv. Mater. 16 (2004) 237–240.

[48] H.C. Shin, M. Liu, Copper foam structures with highly porous nanostructured walls, Chem. Mater. 16 (2004) 5460–5464.

[49] A. Dutta, M. Rahaman, M. Mohos, A. Zanetti, P. Broekmann, Electrochemical CO$_2$ conversion using skeleton (sponge) type of Cu catalysts, ACS Catal. 7 (2017) 5431–5437.

[50] E.L. Clark, A.T. Bell, Electrochemical reduction of CO$_2$ over phase segregated cuag bimetallic electrodes with enhanced oxygenate selectivity by CO spillover, Meet. Abstr. (2016). MA2016-02 3339-3339.

[51] K.W. Frese, Electrochemical reduction of CO$_2$ at intentionally oxidized copper electrodes, J. Electrochem. Soc. 138 (1991) 3338–3344.

[52] A. Verdaguer-Casadevall, C.W. Li, T.P. Johansson, S.B. Scott, J.T. McKeown, M. Kumar, I.E.L. Stephens, M.W. Kanan, I. Chorkendorff, Probing the active surface sites for CO reduction on oxide-derived copper electrocatalysts, J. Am. Chem. Soc. 137 (2015) 9808–9811.

[53] C.W. Li, J. Ciston, M.W. Kanan, Electroreduction of carbon monoxide to liquid fuel on oxide-derived nanocrystalline copper, Nature 508 (2014) 504–507.

[54] C.W. Li, M.W. Kanan, CO$_2$ reduction at low overpotential on Cu electrodes resulting from the reduction of thick Cu$_2$O films, J. Am. Chem. Soc. 134 (2012) 7231–7234.

[55] R. Kas, R. Kortlever, A. Milbrat, M.T.M. Koper, G. Mul, J. Baltrusaitis, Electrochemical CO$_2$ reduction on Cu$_2$O-derived copper nanoparticles: controlling the catalytic selectivity of hydrocarbons, Phys. Chem. Chem. Phys. 16 (2014) 12194–12201.

[56] D. Gao, F. Scholten, B. Roldan Cuenya, Improved CO$_2$ electroreduction performance on plasma-activated Cu catalysts via electrolyte design: halide effect, ACS Catal. 7 (2017) 5112–5120.

[57] D. Gao, I. Zegkinoglou, N.J. Divins, F. Scholten, I. Sinev, P. Grosse, B. Roldan Cuenya, Plasma-activated copper nanocube catalysts for efficient carbon dioxide electroreduction to hydrocarbons and alcohols, ACS Nano 11 (2017) 4825–4831.

[58] R. Kortlever, J. Shen, K.J.P. Schouten, F. Calle-Vallejo, M.T.M. Koper, Catalysts and reaction pathways for the electrochemical reduction of carbon dioxide, J. Phys. Chem. Lett. 6 (2015) 4073–4082.

[59] Y. Hori, A. Murata, R. Takahashi, formation of hydrocarbons in the electrochemical reduction of carbon dioxide at a copper electrode in aqueous solution, J. Chem. Soc., Faraday Trans. 1 85 (1989) 2309–2326.

[60] S.A. Akhade, W. Luo, X. Nie, N.J. Bernstein, A. Asthagiri, M.J. Janik, Poisoning effect of adsorbed CO during CO$_2$ electroreduction on late transition metals, Phys. Chem. Chem. Phys. 16 (2014) 20429–20435.

[61] D.W. Dewulf, T. Jin, A.J. Bard, Electrochemical and surface studies of carbon-dioxide reduction to methane and ethylene at copper electrodes in aqueous-solutions, J. Electrochem. Soc. 136 (1989) 1686–1691.

[62] J.F. Weaver, G.B. Hoflund, Surface characterization study of the thermal decomposition of Ag$_2$O, Chem. Mater. 6 (1994) 1693–1699.

[63] S. Jiang, K. Klingan, C. Pasquini, H. Dau, New aspects of operando Raman spectroscopy applied to electrochemical CO$_2$ reduction on Cu foams, J. Chem. Phys. 150 (2018), 041718.

[64] A. Eilert, F. Cavalca, F.S. Roberts, J. Osterwalder, C. Liu, M. Favaro, E.J. Crumlin, H. Ogasawara, D. Friebel, L.G.M. Pettersson, A. Nilsson, Subsurface oxygen in oxide-derived copper electrocatalysts for carbon dioxide reduction, J. Phys. Chem. Lett. 8 (2017) 285–290.

[65] Y. Ichinohe, T. Wadayama, A. Hatta, Electrochemical reduction of CO$_2$ on silver as probed by surface-enhanced Raman scattering, J. Raman Spectrosc. 26 (1995) 335–340.

[66] K.G. Schmitt, A.A. Gewirth, In situ surface-enhanced Raman spectroscopy of the electrochemical reduction of carbon dioxide on silver with 3,5-diamino-1,2,4-triazole, J. Phys. Chem. C 118 (2014) 17567–17576.

[67] X. Nie, M.R. Esopi, M.J. Janik, A. Asthagiri, Selectivity of CO_2 reduction on copper electrodes: the role of the kinetics of elementary steps, Angew. Chem. Int. Ed. 52 (2013) 2459–2462.

[68] S. Verma, Y. Hamasaki, C. Kim, W. Huang, S. Lu, H.-R.M. Jhong, A.A. Gewirth, T. Fujigaya, N. Nakashima, P.J.A. Kenis, Insights into the low overpotential electroreduction of CO_2 to CO on a supported gold catalyst in an alkaline flow electrolyzer, ACS Energy Lett. 3 (2018) 193–198.

[69] Q. Lu, J. Rosen, Y. Zhou, G.S. Hutchings, Y.C. Kimmel, J.G. Chen, F. Jiao, A selective and efficient electrocatalyst for carbon dioxide reduction, Nat. Commun. 5 (2014) 3242.

[70] S. Sen, D. Liu, G.T.R. Palmore, Electrochemical reduction of CO_2 at copper nanofoams, ACS Catal. 4 (2014) 3091–3095.

[71] J. Huang, N. Hörmann, E. Oveisi, A. Loiudice, G.L. De Gregorio, O. Andreussi, N. Marzari, R. Buonsanti, Potential-induced nanoclustering of metallic catalysts during electrochemical CO_2 reduction, Nat. Commun. 9 (2018) 3117.

[72] A. Loiudice, P. Lobaccaro, E.A. Kamali, T. Thao, B.H. Huang, J.W. Ager, R. Buonsanti, Tailoring copper nanocrystals towards C2 products in electrochemical CO_2 reduction, Angew. Chem. Int. Ed. 55 (2016) 5789–5792.

[73] K.P. Kuhl, E.R. Cave, D.N. Abram, T.F. Jaramillo, New insights into the electrochemical reduction of carbon dioxide on metallic copper surfaces, Energy Environ. Sci. 5 (2012) 7050–7059.

[74] A. Kuzume, A. Dutta, S. Vesztergom, P. Broekmann, Operando Raman spectroscopy: studies on the reactivity and stability of SnO_2 nanoparticles during electrochemical CO_2 reduction reaction, in: K. Wandelt (Ed.), Encyclopedia of Interfacial Chemistry,Surface Science and Electrochemistry, Elsevier, Amsterdam, 2018, pp. 217–226.

[75] A. Dutta, A. Kuzume, V. Kaliginedi, M. Rahaman, I. Sinev, M. Ahmadi, B.R. Cuenya, S. Vesztergom, P. Broekmann, Probing the chemical state of tin oxide NP catalysts during CO_2 electroreduction: a complementary operando approach, Nano Energy 53 (2018) 828–840.

[76] G. Ashiotis, A. Deschildre, Z. Nawaz, J.P. Wright, D. Karkoulis, F.E. Picca, J. Kieffer, The fast azimuthal integration Python library: pyFAI, J. Appl. Crystallogr. 48 (2015) 510–519.

Dr. Abhijit Dutta obtained his PhD degree in chemistry from the Indian Institute of Engineering Science and Technology, Kolkata. During his PhD study, his research mainly focused on the development of Pt and Pd based nanostructured for the application to Fuel cell such as alcohol electro oxidation, hydrogen oxidation and oxygen reduction reaction. He worked as a post-doctoral fellow at the National University of Singapore, Singapore. In 2015 he joined the interfacial electro-chemistry group of Prof. Peter Broekmann at University of Bern, Switzerland, where he focuses on the development of various operando spectroscopies (Raman, XAS, and XRD) to characterize novel electrocatalysts for the selective conversion of CO_2 to value-added products.

Iván Zelocualtecatl Montiel received his B.S and M.Sc. in Chemistry from Meritorious Autonomus University of Puebla (BUAP) in 2013 and 2016, respectively. He is currently a Ph.D. candidate in the Department of Chemistry and Biochemistry at University of Bern under the supervision of Prof. Dr. Peter Broekmann. His research interest is focused on the development of novel catalyst for the CO_2 electroreduction.

Dr. Rolf Erni received his doctoral degree from the Swiss Federal Institute of Technology Zurich (ETH Zurich) in the Institute of Applied Physics. He carried out postdoctoral studies at the University of California, Davisand at the National Center for Electron Microscopy (NCEM), Lawrence Berkeley National Laboratory. He then joined FEI Company as an application specialist and senior system engineer. Before returning to NCEM as a staff scientist, he spent a period of time as a faculty member at the EMAT Institute of the University of Antwerp. Rolf Erni is now head of the Electron Microscopy Center at Empa. His research interests cover various topics in electron microscopy, such as diffraction physics, ultra-high resolution and low-voltage (scanning) transmission electron microscopy as well as valence electron energy-loss spectroscopy (VEELS).
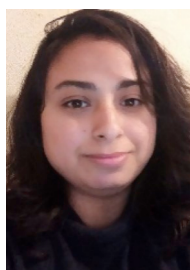
Kiran Kiran received her M.Sc in Physics from Maharshi Dayanand University (M.D.U) India in 2015. She is currently pursuing her Ph.D. at the Department of Chemistry and Biochemistry at University of Bern under the supervision of Prof. Peter Broekmann. Her research interests is focused on the synthesis of novel electrocatalyst for CO_2RR.

Dr. Motiar Rahaman received his M.Sc. in chemistry (2013) from the Indian Institute of Technology Madras, India. He obtained his PhD (2018) on the electrochemical conversion of CO_2 into value-added products from the University of Bern (group of Peter Broekmann). Currently he works as a post-doctoral fellow at the University of Cambridge (UK).

Dr. Jakub Drnec obtained his PhD degree at University of Victoria, Canada, in the field of surface electrochemistry. He is a beamline scientist at European Synchrotron (ESRF) in Grenoble (France), developing new high energy X-rays experimental techniques to study materials for energy conversion and storage. His main goal is to probe materials in their working environment in order to better understand their functioning. His current projects involve operando investigations of fuel cells and batteries, fundamental studies of electrocatalyst's degradation and structure-activity relationships, and development of operando electrochemical cells and data analysis routines.

Prof. Dr. Peter Broekmann obtained his M.Sc. in chemistry (1998) and a PhD (2000) from the University of Bonn. After a post-doctoral stay at the University of Twente (The Netherlands) in 2001, he became project leader at the Institute of Physical Chemistry in Bonn. Since 2008 he holds a lecturer position for electrochemistry at the University of Bern (Switzerland). His research is focused on metal deposition processes for semiconductor and electrocatalysis applications.

5.3. Inverted RDE(iRDE) as Novel Test Bed for Studies on Additive-Assisted Metal Deposition under Gas-Evolution Conditions

Authors: Pavel Moreno-García, Vitali Grozovski, María de Jesús Gálvez Vázquez, Nisarga Mysuru, Kiran Kiran, Noé.mi Kovács, Yuhui Hou, Soma Vesztergom, and Peter Broekmann

Highlights: Due to the intrinsic complications of the water/Co system, the creation of electrochemical Co-connections is more difficult than that of Cu interconnections. Using sweep voltammetry and galvanostatic electrolysis linked to online gas chromatography analysis, the effect of a model redox-active suppressor additive on the electrochemical deposition of cobalt is studied. Minor quantities of the additive added to the conventional Co-based virgin make-up solution considerably reduces the pace and efficiency of Co deposition, favoring instead the competitive hydrogen evolution process under particular experimental circumstances. A custom designed hermetically sealed inverted RDE (iRDE) instrument was used in this work.

Contributed: I assisted the first author, Pavel Moreno-García of the manuscript, in performing the SEM analysis of the Co sample deposited on Pt RDE.

Inverted RDE (iRDE) as Novel Test Bed for Studies on Additive-Assisted Metal Deposition under Gas-Evolution Conditions

Pavel Moreno-García,[1,z] **Vitali Grozovski,**[1] **María de Jesús Gálvez Vázquez,**[1]
Nisarga Mysuru,[1] **Kiran Kiran,**[1] **Noémi Kovács,**[1,2] **Yuhui Hou,**[1] **Soma Vesztergom,**[1,2] **and**
Peter Broekmann[1,*,z]

[1]*Department of Chemistry and Biochemistry, University of Bern, Switzerland*
[2]*Department of Physical Chemistry, Eötvös Loránd University, Budapest 1117, Hungary*

The development of Co interconnects by electrochemical means is more challenging than that of Cu interconnects not only due to the ever decreasing critical feature dimensions but also to intrinsic complications of the water/Co system, as Co electrodeposition processes are inevitably plagued by the competing hydrogen evolution reaction (HER). We present herein a novel custom-made inverted RDE instrument, particularly suitable for studying additive-assisted metal deposition processes that are accompanied by HER or any other gas evolving side reactions. We investigate the influence of a model redox-active suppressor additive on the electrochemical deposition of cobalt by means of linear sweep voltammetry and galvanostatic electrolysis coupled to online gas chromatography analysis. We find that under specific experimental conditions, addition of minor amounts of the additive to the standard Co-based virgin make-up solution significantly decreases the rate and efficiency of Co deposition, and favours instead the competing HER. Moreover, we identify and quantify the reductive conversion of the additive that accompanies the primary metal deposition process. Importantly, our approach complements standard screening Co plating studies as it succeeds to directly deconvolve the overall process into its three individual components, namely the metal ion reduction, the HER and the additive activation process.
© 2020 The Electrochemical Society ("ECS"). Published on behalf of ECS by IOP Publishing Limited. [DOI: 10.1149/1945-7111/ab7984]

For the last two decades, the manufacture of state-of-the-art back-end-of-line (BEOL) interconnect structures has been based on Cu electrodeposition processes.[1,2] However, the critical dimension of such structures has currently approached the electron mean free path (MFP) of copper, introducing new challenges to the continuous scaling of interconnects for the 7 nm technology node and beyond.[3–5] Reports on shorter MFP metals (e.g., Ni, Co, Mo, and Ru) that are less prone to resistance scaling effects keep promise to continue downsizing device dimensions.[3,6–12] Similarly to what was done for copper, the electrochemical screening of additive-assisted cobalt plating processes for cutting-edge interconnects is based on rotating disc electrode (RDE) approaches.[13–17] Nonetheless, the manufacture of Co interconnects by wet methods is found to be more challenging than it was in the case of Cu, not only due to the ever decreasing critical feature dimensions but also due to the intrinsic complications of the water/Co system. Co electrodeposition processes, carried out from aqueous plating baths, are unavoidably accompanied by the hydrogen evolution reaction (HER). The standard reduction potential of Co^{2+} to metallic Co lies 280 mV more negative than that of H^+ to H_2.[16,18,19] This implies that, unlike Cu, a complete description of the Co electroplating process requires quantification of the parasitic gas evolving process. Obviously, the realization of gas analysis coupled to RDE experiments is challenging, since it requires a hermetic sealing of the cell around rotating elements and the implementation of gas analysis techniques, e.g., gas chromatography (GC). Additionally, a fraction of the electrochemically generated gas bubbles typically adheres to the surface of both the RDE working electrode and its embedding shaft, preventing them from reaching the solution-gas interface. This partial shielding of active electrode sites by bubble retention at the RDE tip undermines the accuracy of the electrochemical measurements and hinders quantitative analysis of the gaseous products collected from the headspace of an electrochemical reactor. Therefore, we present here an inverted RDE (iRDE) cell design, coupled to GC for the first time, that helps overcoming these technical limitations.[20] Note that although alternative iRDE-based investigations have been

previously reported demonstrating that the analytical equations of mass and charge transfer valid for the conventional RDE also comply with the proposed iRDEs, no quantitative analysis of electrochemically generated gaseous products was carried out in these cells.[21–27] Our home-developed instrument features important assets: *i*) it is amenable to the same mathematical treatment as standard (downward facing) RDEs; *ii*) it can be operated air-tight and coupled to online GC; and *iii*) due to its upward facing design, the electrode surface is less prone to blockage by any formed gas bubbles.

In this paper we investigate the influence of a model redox-active suppressor additive on the electrochemical deposition of cobalt by means of linear sweep voltammetry and galvanostatic electrolysis, coupled to an online detection of gaseous products by gas chromatography. We find that the addition of minor amounts (60 ppm) of the model suppressor additive to the standard Co-based virgin make-up solution (VMS) significantly decreases the efficiency of Co deposition and favours the competing hydrogen evolution reaction instead, when lower current densities than those corresponding to the limiting current density value of H^+ reduction are applied. In addition, we are able to identify and quantify a reductive conversion of the additive that comes along with the deposition process. Importantly, as schematically depicted in Fig. 1, our approach complements standard screening Co plating studies because it succeeds to deconvolve the overall process into its individual components, e.g., Co^{2+} reduction to metallic Co, HER and reductive additive activation.

Experimental

$CoSO_4·7H_2O$ (ReagentPlus, $\geqslant$ 99%) and H_3BO_3 (ReagentPlus, 99.97%) were purchased from Sigma-Aldrich. H_2SO_4 (96% Suprapure) was purchased from Merck. The VMS cobalt plating solution (50 mM $CoSO_4·7H_2O$, 0.5 M H_3BO_3, adjusted to pH 2.5 by H_2SO_4 addition) was prepared with as-received chemicals and Milli-Q water (18.2 MΩ cm, TOC ⩽ 5 ppb, Millipore).[15,18] The electrolyte was deoxygenated by Ar bubbling (99.9999%, Carbagas, Switzerland) through the solution for 20 min prior to the measurements. All electrochemical measurements were performed at room temperature by a potentiostat/galvanostat system (Metrohm Autolab

*Electrochemical Society Member.
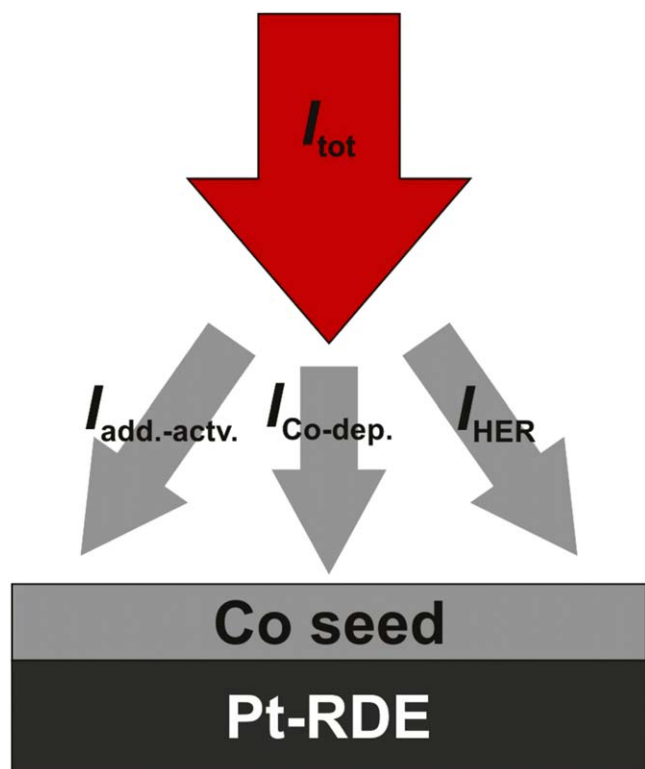zE-mail: pavel.moreno@dcb.unibe.ch; peter.broekmann@dcb.unibe.ch

Figure 1. Scheme representing the deconvolution of the overall cathodic process into its individual components by the *i*RDE&GC approach.

128 N, The Netherlands) in a three electrode configuration using a custom-made H-type glass cell fitted on top of the *i*RDE. Ionic conductivity between the two cell compartments was achieved via a proton exchange membrane (Nafion 117, Sigma-Aldrich). A leakless Ag/AgCl$_{3M}$ electrode (Metrohm, Switzerland) and a Pt wire (99.99% MaTeck) were used as reference and counter electrode, respectively. The support working electrode for Co deposition was a 5 mm diameter, 4 mm thick Pt disk purchased from MaTeck. The electrode was pressed and embedded into the home-made polytetrafluoroethylene (PTFE) shaft of the *i*RDE setup. Prior to the electrochemical measurements, the electrode was first polished on a polishing cloth (Buehler) to a mirror finish with 0.05 μm alumina particles (Micropolish, Buehler) and thoroughly rinsed by Milli-Q water. The Pt surface was then covered for 1 min by a drop of fresh piranha solution followed by rinsing with Milli-Q water. Finally the surface was electrochemically polished in 1 M H$_2$SO$_4$ by sequential oxidation/reduction at ±4 V, respectively, for 30 s each, and the surface was then rinsed and protected by a droplet of Milli-Q water.

All electrochemical investigations were carried out on Co-seeded Pt electrodes. The seed was deposited at −10 mA cm^{-2} and 100 rpm for 25 s.

The ohmic resistance of the solution was determined by means of electrochemical impedance spectroscopy (EIS) at various applied sample potentials where no electrochemical reactions take place. The applied potentials for linear sweep voltammetry and galvanostatic Co electrodeposition accounted for the *IR* drop accordingly.

The Co current efficiencies (FE_{Co}) in galvanostatic electrodeposition measurements were determined by integrating the current of anodic dissolution experiments of the respective Co layers at $E =$ 0.5 V vs Ag|AgCl$_{3M}$. The Co seed contribution was taken into account (subtracted) for the efficiency determination. Gaseous products generated during Co deposition from the HER (or any other side reaction) were analyzed by online gas chromatography (GC, SRI Instruments Multi-Gas Analyzer #3) hermetically connected to the *i*RDE. The continuous flow of Ar through the electrolysis cell during Co deposition carried the volatile reaction

products from the headspace of the *i*RDE cell ensemble into the sampling loops of the gas chromatograph. The partial current density j_i of any gaseous product is calculated using Eq. 1:

$$j_i = x_i n_i F \cdot v_m \quad [1]$$

where x_i represents the volume fraction of product i measured via online GC using an independent calibration standard gas (Carbagas, Switzerland), n_i the number of electrons involved in the electrochemical reaction to form it (here 2 for H$_2$ evolution), F the Faraday constant (96485.3 C mol^{-1}) and v_m the molar Ar gas flow rate measured by a universal flowmeter (7000 GC flowmeter by Ellutia) at the exit of the electrochemical cell. The partial current density for the produced H$_2$ was normalized to the total current density thus providing the faradaic efficiency of H$_2$ production (FE_{H2}).

To demonstrate the usefulness of our *i*RDE&GC approach for additive-assisted metal deposition screening investigations, dedicated linear sweep voltammetric and galvanostatic deposition experiments employing VMS plating baths containing 60 ppm of a model suppressing additive were also carried out. The additive-carrying VMS solution is denoted as VMS-ADD hereafter.

Ex situ SEM-EDS analyses of the *i*RDE working electrodes at different stages of the Co electrodeposition were performed using a Zeiss instrument (Gemini 450 SEM, Germany). The recorded SEM images were acquired at 3 kV, 3.4–3.6 mm and 100 pA as accelerating voltage, working distance and current. The corresponding applied values for the EDS investigations were 18 kV, 8.5 mm and 300 pA. These results are shown in Fig. S1 (available online at stacks. iop.org/JES/167/042503/mmedia) of the Supplementary Information file.

Results and Discussion

***i*RDE and cell assembly.**—In this section we provide a brief description of the custom-made *i*RDE&GC setup. Detailed description of the instrument can be found in Ref. 20. The hermetically tight *i*RDE cell consists of two separable compartments made of modified 80 ml round borosilicate glass flasks (see upper part in Fig. 2A). Reference electrode, counter electrode and gas input and outlet necks with custom winding are attached hermetically to the flasks by custom-made polytetrafluoroethylene (PTFE) caps and O-ring fittings. Physical connection between compartments is provided by a Nafion proton exchange membrane separating catholyte from anolyte. Both compartments are provided with gas inputs and outlets via PTFE caps to feed Ar gas to the cell and chromatograph, respectively. The main features of the *i*RDE setup are shown in Fig. 2. The contacting part (*b*, *b'*) of the *i*RDE with the glass cell is machined of polyoxymethylene polymer (POM). It provides rigid connection to the RDE rotator (AFMSRCE from Pine, not shown) and bears a cone joint to fit the outer socket of the *i*RDE cell (size 29/32, ground glass joint standard). The rotation momentum is transferred by a modified RDE shaft (*a*, *a'*) that fits the MSR rotator. It bears two ceramic sleeves (*q*) that pass through radial shaft seals (*k*). A pressure chamber (*l*) confined between the radial shaft seals is fed by N$_2$ or Ar gas (99.999% Carbagas Switzerland) through a lateral pressuring gas inlet (*j*) to enforce a constant pressure of 0.2–0.4 bar above the ambient pressure. Note that the enforced pressure inside the gland chamber (*l*) has no influence on the inner part of the electrochemical cell. It simply ensures that the electrolyte contained by the working cell compartment (*c*) does not leak through the seal surrounding the upper rotating ceramic fitting (*q*). The pressurized chamber is a single POM tube fixed in the main housing. The latter also holds both radial shaft seals in place. The shaft exact coaxial position is maintained by a ball bearing (*m*) situated in the upper part of the pressure chamber. The radial shaft seals are made of high quality Vitton rubber and operate oil/grease-free. Note that the upper seal (*k*) comes in contact with the solution in the *i*RDE cell compartment. The RDE working electrode is pressed into a lab made PTFE holder (*n*), which is fitted into the upper ceramic sleeve.
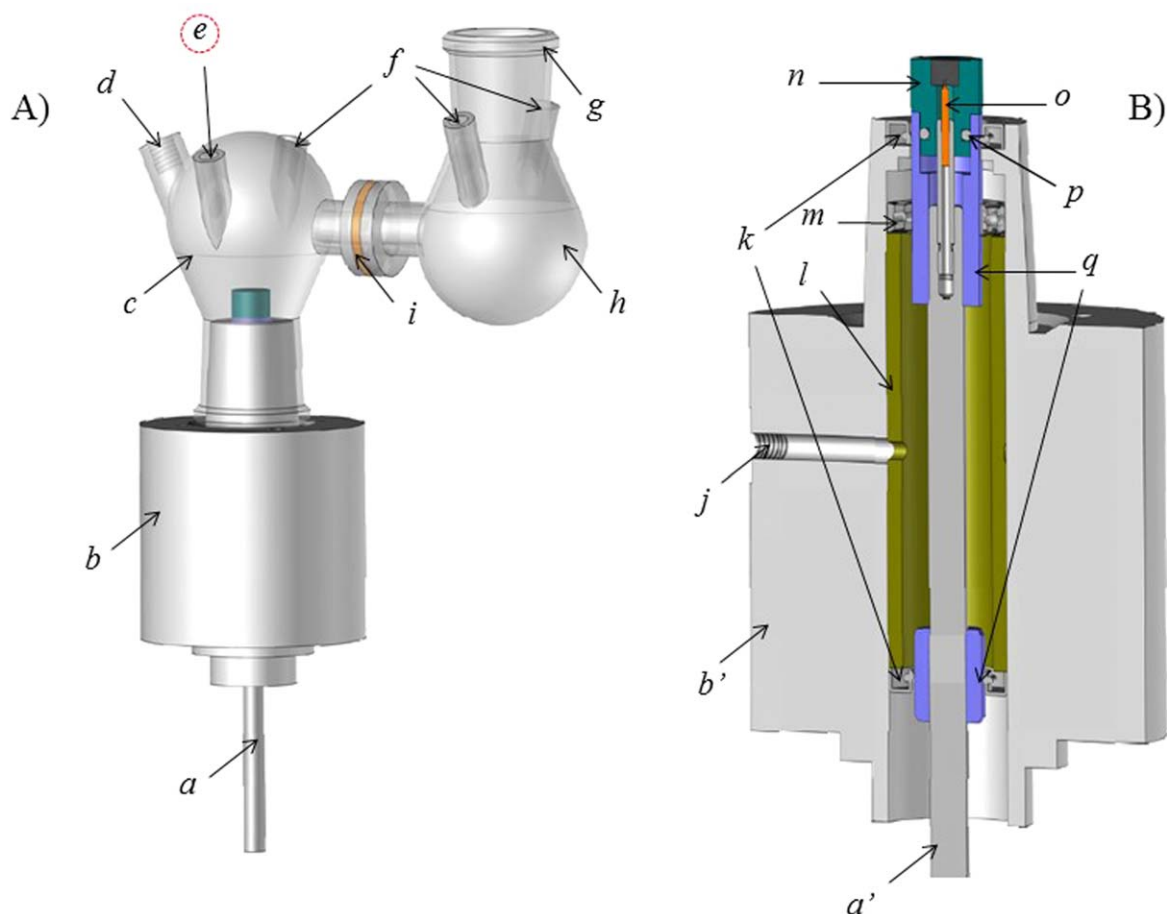
Figure 2. Schematic representation of the (A) H-type cell mounted on the *i*RDE assembly and (B) cross-section of the *i*RDE setup. Components of the design are *a/a'*: rotating shaft; *b/b'*: *i*RDE housing; *c*: working cell compartment; *d*: reference electrode inlet; *e*: purging gas outlet for GC analysis; *f*: purging gas inlet/outlet; *g*: counter electrode inlet; *h*: counter cell compartment; *i*: H^+ exchange membrane; *j*: pressurized gas inlet; *k*: radial shaft seals; *l*: pressurized gland chamber; *m*: ball bearing; *n*: PTFE *i*RDE tip with embedded electrode; *o*: spring contact node; *p*: PTFE tip groove for O-ring fitting; *q*: ceramic fittings.

Tightness between the RDE holder and the upper ceramic sleeve is maintained by an O-ring placed in the groove of the PTFE holder (*p*). The spring contact from the shaft (*o*) provides the electrical contact for the working electrode. The whole system is maintenance friendly and the radial shaft sealings can be straightforwardly exchanged once they are worn out.

Quantification of Co and H₂ current efficiencies by iRDE&GC during galvanostatic deposition.—Figure 3 displays an overview of the *i*RDE&GC-based metal deposition approach that we introduce to quantitatively describe the overall electrochemical process. Similarly to superconformal Co deposition on patterned wafers, the plating studies are performed on Co-seeded supports to match the experimental conditions of metal interconnect manufacture as closely as possible.[13–15,17] Prior to Co layer deposition, a thin Co seed was

deposited from the additive-free VMS solution at –10 mA cm^{-2} and 100 rpm for 25 s. This condition ensures high Co deposition efficiencies necessary to yield a compact, homogeneous Co seed layer on the Pt-RDE support without the interference of generated bubbles. Figures S1A–S1B show typical SEM characterization of a Pt-*i*RDE working electrode before and after Co seed deposition. The corresponding EDS spectra displayed in Figs. S1F–S1G reveal the presence of the thin Co layer on top of the underlying Pt support that forms upon electrochemical deposition. This seed layer was then anodically dissolved back into the plating bath at 0.5 V vs Ag/AgCl$_{3M}$. This seed deposition/dissolution procedure was applied three times to estimate the average Co seed current efficiency from the respective Q_{diss}/Q_{dep} ratios before every Co bulk deposition experiment was carried out (Figs. 3A–3B). A typical example of such calculation is displayed in Fig. S2. Based on a significant
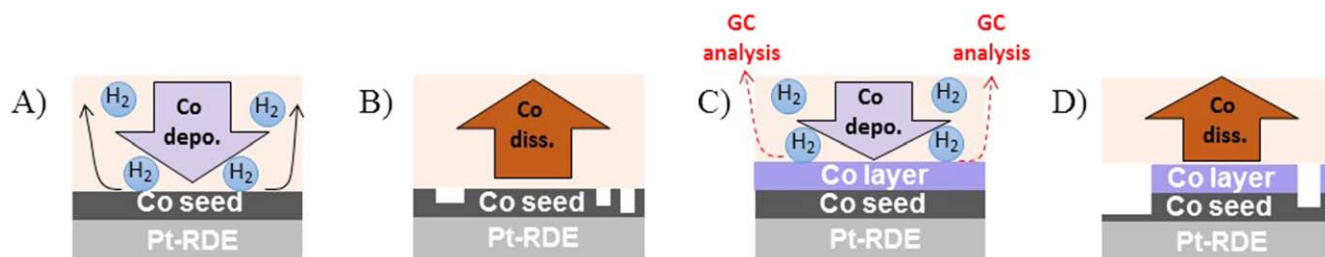

Figure 3. Schematic representation of the iRDE&GC approach for quantification of the galvanostatic Co deposition and accompanying HER efficiencies: (A) galvanostatic Co seed deposition on rotating Pt disk support; (B) anodic Co seed dissolution; (C) galvanostatic Co layer deposition on Co-seeded Pt – *i*RDE and simultaneous analysis of gaseous products by online gas chromatography; (D) Anodic dissolution of the whole Co deposit.

amount of iterations, the Co seed deposition efficiency was found to be (72.6 ± 4.8) %. The high current efficiency and morphological homogeneity of the deposited seed layer are due to the applied current density being higher than the expected mass transport limiting current for proton reduction under the applied conditions. Additionally, the electrogenerated bubbles do not interfere with the metal deposition and straightforwardly detach from the solid liquid interface due to the upward facing configuration of the iRDE and the applied rotation. Next, galvanostatic Co layer deposition was performed on a freshly seeded support at selected current density, angular frequency and deposition time. Simultaneously, electrogenerated gaseous products (here H_2) were analyzed at selected time intervals by the coupled gas chromatograph as soon as the layer deposition set in (Fig. 3C). Once the desired layer was achieved, the electrodeposited Co was anodically dissolved back into the VMS solution (Fig. 3D). Finally, the Co layer current efficiency was determined analogously to the case of the seed, this time by subtracting the charge corresponding to the seed dissolution. Addition of FE_{Co} and FE_{H2} thus renders quantitative description of the whole process (additive-free case). Note that direct assessment of the parasitic HER contribution by a dedicated method is usually missing, and its introduction to metal deposition studies enables unequivocal confirmation of the electrochemical data.

We exemplarily demonstrate the above-mentioned strategy for Co deposition through galvanostatic experiments conducted at a rotation rate of 900 rpm and lasting for different times at current density values of either -5 or -10 mA cm^{-2}. These values lie close but at opposite sides of the expected mass transport limited current density (ca.—8.1 mA cm^{-2}, based on the Levich equation) for H$^+$ reduction at a pH of 2.5 and a rotation rate of 900 rpm.[28] They lie, however, considerably below the corresponding limiting current for Co^{2+} reduction (ca. -42 mA cm^{-2}).[29] Note that the selection of higher applied rotational frequencies for Co bulk deposition obeys to the fact that the FE_{H2} increases with ω. The increased partial current density of proton reduction enabled accurate quantification of electrogenerated hydrogen by online GC analysis at shorter times. An upcoming publication will address the effect of pH, applied current densities and rotation rates on the overall Co deposition

process in more detail. Figures 4A and 4D show the corresponding measured Co current efficiencies (FE_{Co}) as a function of the applied deposition time. For the experiments performed with $j = -5$ mA cm^{-2}, at deposition times shorter than 5 min, the FE_{Co} amounted to $\sim$30%. When longer electrolysis (5 min $\leqslant t \leqslant$ 60 min) were carried out the FE_{Co} values rose up to 39.8% $\pm$ 1.3% and stayed rather constant, regardless of the specific duration. The experiments at $j = -10$ mA cm^{-2} show significantly larger FE_{Co} values clustering at 64.7 $\pm$ 2.6%. Corresponding analysis of the electrogenerated hydrogen accompanying the deposition was carried out at times just before the single depositions were stopped. Additionally, FE_{H2} values were also determined for the longer electrolysis ($t \geqslant$ 16.5 min) in sequential intervals of 7 min starting at 9.5 min. This dwell time corresponds to the shortest period a whole GC run for H_2 detection takes. Figures 4B and 4E summarize the GC results. The displayed FE_{H2} vs t dependencies show that an initiation period of about 15 min is required to achieve quantitative determination of the HER contribution to the whole process: the reason for this latitude is that the electrogenerated hydrogen needs a certain time to fill the cell headspace and the GC loops. This is an intrinsic limitation of the iRDE&GC approach that may not be fully circumvented but can to some extent be improved by, e.g., increasing the surface area of the working electrode and/or decreasing the volume of the electrochemical cell. The plot clearly shows that once this conditioning period is elapsed, the actual FE_{H2} values reach a constant value of 58.5% $\pm$ 1.4% or 35.5 $\pm$ 1.9% for the current densities of -5 or -10 mA cm^{-2}, respectively. The experimental summary displayed in panels C and F fully describe the overall electrochemical process and enable the deconvolution of the current density into two components: one corresponding to the primary Co deposition, the other to the parasitic HER. The total faradaic efficiencies reach 99.6 $\pm$ 1.2% and 99.8 $\pm$ 1.1% for both experiments with applied current densities of -5 and -10 mA cm^{-2}, respectively, within (15 $\leqslant t \leqslant$ 60) min. It is noteworthy that our approach enables direct insight into the gas evolution component of the electrochemical process, which is typically inferred from the electrochemical data. In the following section we demonstrate that this feature proves particularly useful for additive-assisted Co electrodeposition studies where a third
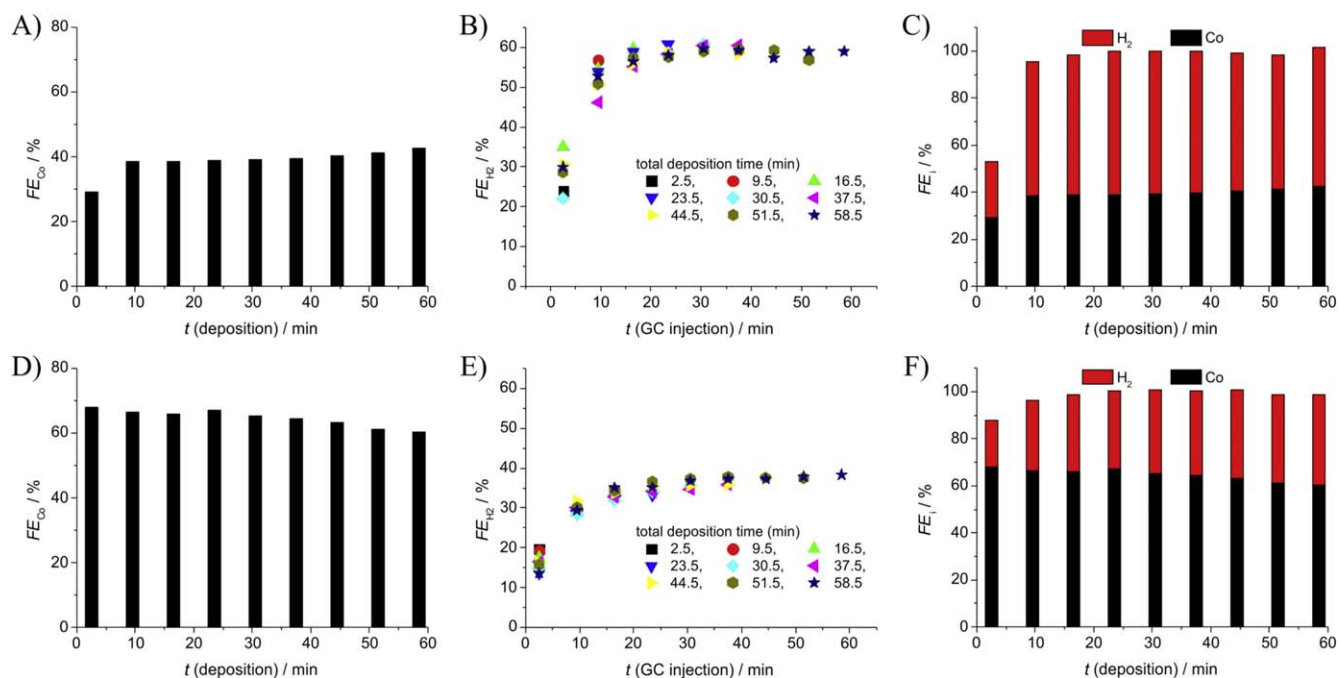

Figure 4. (A) and (D) Co current efficiencies of galvanostatic Co plating from additive-free VMS electrolyte on Co-seeded Pt - iRDEs at a rotation rate of 900 rpm, as a function of the total deposition time, at current densities of -5 mA cm^{-2} (A) and -10 mA cm^{-2} (D). Corresponding FE_{H2} values calculated from coupled online GC measurements at all applied GC injection times are shown in (B) and (E). Panels (C) and (F) summarize the FE survey at $j = -5$ mA cm^{-2} (C) and $j = -10$ mA cm^{-2} (F).

constituent (additive activation) needs to be taken into account for the complete description of the process.

Influence of a model suppressing additive on Co electrodeposition.—In this section we demonstrate how the *i*RDE&GC hyphenation can be used for advanced screening studies on additive-assisted Co plating. Figure 5A shows a comparison of linear sweep voltammograms (LSVs) recorded in a bare VMS plating bath and in a bath where the model suppressing additive was added to the VMS in a 60 ppm final concentration. Both LSVs were independently acquired with *IR* drop compensation on Co-seeded Pt *i*RDE electrodes at a sweep rate of 10 mV s^{-1} and a rotation rate of 900 rpm. From the data it is obvious that the action of the model additive at the Co surface significantly slows down the kinetics of the electrochemical process as compared to the additive-free experiment (e.g., the potential required to reach $j = -5$ mA cm^{-2} is shifted by ∼250 mV in the cathodic direction when the additive is present). Further support for the inhibiting characteristics of the test additive on the Co deposition is exemplarily provided by the potential transients displayed in Fig. 5B. These were recorded during galvanostatic deposition experiments lasting 60 min at a current density of -10 mA cm^{-2} and a rotation rate of 900 rpm in VMS (green) and VMS-ADD (blue) plating baths. Besides a slight instability of the potential in the early stage of the deposition (first 5 min), both potential transients attain steady-state during the time span of the experiment. However, the attained potential values are about 350 mV more negative in the additive-containing electrolyte, which qualitatively correlates with the LSV results.

To discern the effect of the additive on the kinetics of both Co deposition and HER, similar analysis as shown for the additive-free experiment in Fig. 4 was performed with a VMS-ADD plating bath

at -5 and -10 mA cm^{-2} current densities; these results are shown in Figs. 5C and 5D. Note that for this experiment the FE_{Co} values were determined via anodic dissolution only at the end of the deposition. The plots are built assuming that the Co current efficiency is independent of the deposition time at $(5 \leqslant t \leqslant 60)$ min as it was found in the case of the experiments where no additive was used (Figs. 4A and 4D). It is clearly noticeable for the experiment carried out at $j = -5$ mA cm^{-2} that the Faradaic efficiencies of both Co deposition and HER are severely affected by the action of the test additive under reactive conditions. Compared to the experiment in pristine VMS, the FE_{Co} is significantly diminished by roughly a factor 8 (see Figs. 4A and 5C). The opposite trend is observed for FE_{H2} which rises to values about 74.2%. The situation is somewhat different when instead of -5 mA cm^{-2}, we apply a current density of -10 mA cm^{-2}. In this case, although both FE_{Co} and FE_{H2} are diminished, compared to their respective values measured in additive-free VMS, their intrinsic ratios remain much closer to the additive-free case (compare Figs. 4F and 5D). The observed difference between the $j = -5$ mA cm^{-2} and $j = -10$ mA cm^{-2} case can be explained by taking into consideration the limiting current value of HER expected in the pH = 2.5 solution (ca. -8.1 mA cm^{-2}). It seems that in case of applied current densities higher than this value, the additive—in the absence of free H$^+$ ions in the boundary layer—exerts a much smaller "boosting effect" on H$^+$ reduction.

Interestingly, regardless of the applied current density, summation of the FE_{Co} and FE_{H2} values measured in VMS-ADD solutions falls short of the 100% Faradaic efficiency, which was not the case in the additive-free case (see Figs. 4C and 4F). In general, the Faradaic efficiencies obtained from VMS-ADD solutions lack 14%–22% (Figs. 5C–5D). This deficit hints that a reductive conversion of the
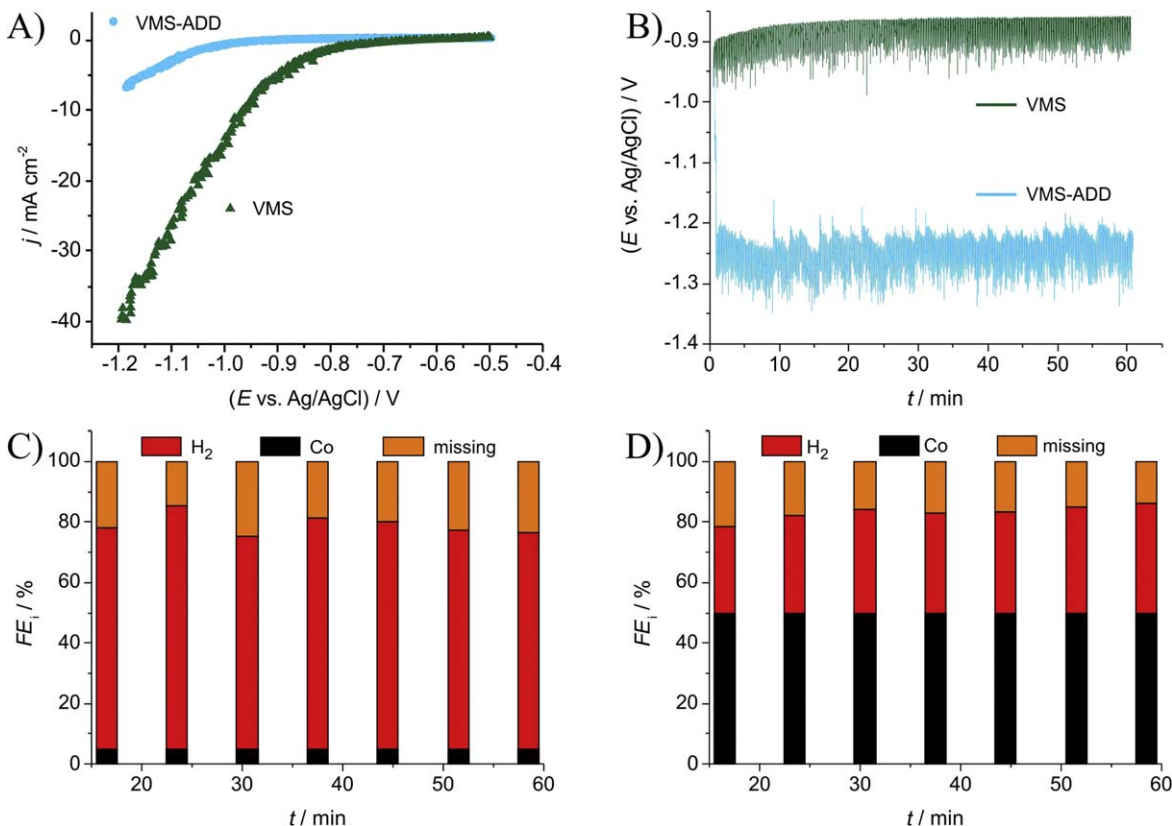

Figure 5. (A) Linear sweep voltammograms recorded on a Co-seeded Pt - *i*RDEs in VMS (green) and VMS-ADD (blue) solutions at a sweep rate of 10 mV s^{-1} and a rotation rate of 900 rpm. Automatic *IR* compensation was applied. (B) Potential transients corresponding to galvanostatic Co depositions at $j = -10$ mA cm^{-2} in VMS (green) and VMS-ADD (60 ppm, blue) solutions. (C) and (D) Faradaic efficiencies of Co deposition (black) and H$_2$ generation (red) from 1 h galvanostatic deposition experiments at current densities of -5, respectively -10 m A cm^{-2} from a VMS-ADD electrolyte. The FE_{H2} values are calculated from coupled online GC measurements.

suppressor additive, concomitant with the metal deposition and HER, may take place under the applied experimental conditions. This demonstrates that the relatively minor concentration of the additive in the plating bath further decreases in the bath as the Co^{2+} reduction and HER proceed. Table S1 displays the calculated amount of Co^{2+} and precursor additive consumed upon 1 h electrolysis at -5 and -10 mA cm^{-2} and 900 rpm based on Faraday's law of electrolysis and the partial Faraday efficiencies displayed in Figs. 5C–5D. These data show that after 1 h electrolysis the concentration of the precursor additive diminishes by less than 10% relative to the initial value. Note that the *i*RDE&GC approach is required to account for this extra *FE* deficit that standard electrochemical methods often fail to recognize, ascribing Co Faradaic efficiency losses to H_2 generation alone.[16] In this respect it is interesting to note, for example, that the blue LSV in Fig. 5A shows no hint of reductive conversion of the suppressor additive.

We suggest that the unique capability of our approach to break down the overall process into its individual components, e.g., metal deposition, HER and possible additive conversion should be exploited in future screening of additive-assisted superconformal filling investigations.

Conclusions

We present the design and operation of a custom-made hermetically sealed inverted RDE (*i*RDE) instrument coupled to gas chromatography for quantitative analysis of gas evolving processes. We demonstrate that the setup is a useful test bed particularly suitable for additive-assisted metal deposition studies that are plagued by the HER or any other gas evolving side process. Particularly, we investigate the influence of a model redox-active suppressor additive on the electrochemical deposition of cobalt by means of linear sweep voltammetry and galvanostatic electrolysis coupled to simultaneous online gas analysis by GC. We find that addition of minor amounts (60 ppm) of the additive to the standard Co-based virgin make up solution significantly decreases the rate and efficiency of Co deposition and favours those of the competing hydrogen evolution under specific experimental conditions. Importantly, we are able to identify and quantify reductive conversion of the additive that comes along with the metal deposition process. We suggest that more attention should be devoted to this aspect, which is usually neglected or scarcely studied. Investigations providing such information could add useful insights into plating bath stability. Finally, we propose that the developed *i*RDE&GC approach builds on existing additive-assisted electroplating approaches because it enables unambiguous dissection of the overall process into its individual components, e.g., M^{n+} reduction to elemental M^0, HER and potential additive conversion.

Acknowledgments

ORCID

Pavel Moreno-García https://orcid.org/0000-0002-6827-787X
María de Jesús Gálvez Vázquez https://orcid.org/0000-0002-0416-6556
Noémi Kovács https://orcid.org/0000-0002-7112-3396
Soma Vesztergom https://orcid.org/0000-0001-7052-4553
Peter Broekmann https://orcid.org/0000-0002-6287-1042

References

1. P. C. Andricacos, *The Electrochemical Society Interface*, **7**, 23 (1998).
2. P. C. Andricacos, *The Electrochemical Society Interface*, **8**, 32 (1988).
3. Q. Huang, T. W. Lyons, and W. D. Sides, *J. Electrochem. Soc.*, **163**, D715 (2016).
4. K. Barmak, A. Darbal, K. J. Ganesh, P. J. Ferreira, J. M. Rickman, T. Sun, B. Yao, A. P. Warren, and K. R. Coffey, *J. Vac. Sci. Technol. A*, **32**, 061503 (2014).
5. D. Josell, S. H. Brongersma, and Z. Tőkei, *Annu. Rev. Mater. Res.*, **39**, 231 (2009).
6. D. Gall, *J. Appl. Phys.*, **119**, 085101 (2016).
7. K. Sankaran, S. Clima, M. Mees, and G. Pourtois, *ECS J. Solid State Sci. Technol.*, **4**, N3127 (2015).
8. C. H. Lee, J. E. Bonevich, J. E. Davies, and T. P. Moffat, *J. Electrochem. Soc.*, **156**, D301 (2009).
9. R. N. Akolkar, F. Gstrein, and D. J. Zierath, Pat.US2012/0153483 A1 (2012).
10. J. S. Chawla et al., *Proc. IEEE IITC/AMC*, p. 63 (2016).
11. J. Kelly et al., "Experimental study of nanoscale Co damascene BEOL interconnect structures." *IEEE/AMC*, San Jose, California, p. 40 (2016).
12. C. Auth et al., "A 10 nm high performance and low-power CMOS technology featuring 3rd generation FinFET transistors, Self-Aligned Quad Patterning, contact over active gate and cobalt local interconnects." *IEEE/IEDM*, San Francisco, California, p. 1 (2017).
13. D. Josell, M. Silva, and T. P. Moffat, *J. Electrochem. Soc.*, **163**, D809 (2016).
14. M. A. Rigsby, L. J. Brogan, N. V. Doubina, Y. Liu, E. C. Opocensky, T. A. Spurlin, J. Zhou, and J. D. Reid, *ECS Trans.*, **80**, 767 (2017).
15. J. Wu, F. Wafula, S. Branagan, H. Suzuki, and J. van Eisden, *J. Electrochem. Soc.*, **166**, D3136 (2019).
16. O. E. Kongstein, G. M. Haarberg, and J. Thonstad, *J. Electrochem. Soc.*, **157**, D335 (2010).
17. F. Wafula, J. Wu, S. Branagan, H. Suzuki, A. Gracias, and J. V. Eisden, *IEEE IITC*, 123 (2018).
18. M. A. Rigsby, L. J. Brogan, N. V. Doubina, Y. Liu, E. C. Opocensky, T. A. Spurlin, J. Zhou, and J. D. Reid, *J. Electrochem. Soc.*, **166**, D3167 (2018).
19. O. E. Kongstein, G. M. Haarberg, and J. Thonstad, *J. Appl. Electrochem.*, **37**, 669 (2007).
20. P. Moreno-García, N. Kovács, V. Grozovski, M. D. J. Gálvez-Vázquez, S. Vesztergom, and P. Broekmann, *Anal. Chem.* (2020).
21. A. D. Zdunek and J. R. Selman, *J. Electrochem. Soc.*, **139**, 2549 (1992).
22. P. E. Bradley and D. Landolt, *J. Electrochem. Soc.*, **144**, L145 (1997).
23. P. M. M. C. Bressers and J. J. Kelly, *J. Electrochem. Soc.*, **142**, L114 (1995).
24. E. J. Podlaha, A. Bögli, C. Bonhôte, and D. Landolt, *J. Appl. Electrochem.*, **27**, 805 (1997).
25. H. Van Parys, E. Tourwé, T. Breugelmans, M. Depauw, J. Deconinck, and A. Hubin, *J. Electroanal. Chem.*, **622**, 44 (2008).
26. T. Nierhaus, H. Van Parys, S. Dehaeck, J. van Beeck, H. Deconinck, J. Deconinck, and A. Hubin, *J. Electrochem. Soc.*, **156**, P139 (2009).
27. H. Van Parys, E. Tourwé, M. Depauw, T. Breugelmans, J. Deconinck, and A. Hubin, *WIT Trans. Eng. Sci.*, **54**, 183 (2007).
28. G. K. H. Wiberg and M. Arenz, *Electrochim. Acta*, **158**, 13 (2015).
29. C. Q. Cui, S. P. Jiang, and A. C. C. Tseung, *J. Electrochem. Soc.*, **137**, 3418 (1990).

5.4. Specific Cation Adsorption: Exploring Synergistic Effects on CO_2 Electroreduction in Ionic Liquids

Authors: Alexander V. Rudnev, Kiran Kiran, and Peter Broekmann

Highlights: Ionic liquids (ILs) have gained popularity as potential solvents for the electrochemical conversion of CO_2 into value-added products. CO_2 reduction reactions can be co-catalyzed by ILs (in particular when Ag is applied as the primary metallic electrocatalyst) The activity of the electrode/IL combinations towards CO_2 reduction is investigated here. The precise adsorption of the IL cation on the electrode is critical to the Ionic liquid action. This contribution presents a comprehensive study of thirteen electrode materials in three different ILs with combination of cation and anion. Based on the synergistic interaction of the electrodes with ILs, three classes of electrodes were identified depending on their activity towards CO_2RR.

Contribution: I was involved in the electrochemical characterization of the electrode materials by means of cyclic voltammetry (CV), linear sweep voltammetry (LSV), and product quantification.

JOHN WILEY AND SONS LICENSE
TERMS AND CONDITIONS

Nov 23, 2021

This Agreement between University of Bern -- Kiran Kiran ("You") and John Wiley and Sons ("John Wiley and Sons") consists of your license details and the terms and conditions provided by John Wiley and Sons and Copyright Clearance Center.

License Number	5194710971193
License date	Nov 23, 2021
Licensed Content Publisher	John Wiley and Sons
Licensed Content Publication	ChemElectroChem
Licensed Content Title	Specific Cation Adsorption: Exploring Synergistic Effects on CO_2 Electroreduction in Ionic Liquids
Licensed Content Author	Peter Broekmann, Kiran Kiran, Alexander V. Rudnev
Licensed Content Date	Apr 20, 2020
Licensed Content Volume	7
Licensed Content Issue	8
Licensed Content Pages	7
Type of use	Dissertation/Thesis
Requestor type	Author of this Wiley article

Format	Print and electronic
Portion	Full article
Will you be translating?	No
Title	Dr
Institution name	University of Bern
Expected presentation date	Nov 2021
Requestor Location	University of Bern Freiestrasse 3 University of Bern Bern, other Switzerland Attn: University of Bern
Publisher Tax ID	EU826007151
Total	0.00 USD

Terms and Conditions

TERMS AND CONDITIONS

this Agreement by you.

- You shall indemnify, defend and hold harmless WILEY, its Licensors and their respective directors, officers, agents and employees, from and against any actual or threatened claims, demands, causes of action or proceedings arising from any breach of this Agreement by you.

- IN NO EVENT SHALL WILEY OR ITS LICENSORS BE LIABLE TO YOU OR ANY OTHER PARTY OR ANY OTHER PERSON OR ENTITY FOR ANY SPECIAL, CONSEQUENTIAL, INCIDENTAL, INDIRECT, EXEMPLARY OR PUNITIVE DAMAGES, HOWEVER CAUSED, ARISING OUT OF OR IN CONNECTION WITH THE DOWNLOADING, PROVISIONING, VIEWING OR USE OF THE MATERIALS REGARDLESS OF THE FORM OF ACTION, WHETHER FOR BREACH OF CONTRACT, BREACH OF WARRANTY, TORT, NEGLIGENCE, INFRINGEMENT OR OTHERWISE (INCLUDING, WITHOUT LIMITATION, DAMAGES BASED ON LOSS OF PROFITS, DATA, FILES, USE, BUSINESS OPPORTUNITY OR CLAIMS OF THIRD PARTIES), AND WHETHER OR NOT THE PARTY HAS BEEN ADVISED OF THE POSSIBILITY OF SUCH DAMAGES. THIS LIMITATION SHALL APPLY NOTWITHSTANDING ANY FAILURE OF ESSENTIAL PURPOSE OF ANY LIMITED REMEDY PROVIDED HEREIN.

- Should any provision of this Agreement be held by a court of competent jurisdiction to be illegal, invalid, or unenforceable, that provision shall be deemed amended to achieve as nearly as possible the same economic effect as the original provision, and the legality, validity and enforceability of the remaining provisions of this Agreement shall not be affected or impaired thereby.

- The failure of either party to enforce any term or condition of this Agreement shall not constitute a waiver of either party's right to enforce each and every term and condition of this Agreement. No breach under this agreement shall be deemed waived or excused by either party unless such waiver or consent is in writing signed by the party granting such waiver or consent. The waiver by or consent of a party to a breach of any provision of this Agreement shall not operate or be construed as a waiver of or consent to any other or subsequent breach by such other party.

- This Agreement may not be assigned (including by operation of law or otherwise) by you without WILEY's prior written consent.

- Any fee required for this permission shall be non-refundable after thirty (30) days from receipt by the CCC.

- These terms and conditions together with CCC's Billing and Payment terms and conditions (which are incorporated herein) form the entire agreement between you and WILEY concerning this licensing transaction and (in the absence of fraud) supersedes all prior agreements and representations of the parties, oral or written. This Agreement may not be amended except in writing signed by both parties. This Agreement shall be binding upon and inure to the benefit of the parties' successors, legal representatives, and authorized assigns.

- In the event of any conflict between your obligations established by these terms and conditions and those established by CCC's Billing and Payment terms and conditions, these terms and conditions shall prevail.

- WILEY expressly reserves all rights not specifically granted in the combination of (i) the license details provided by you and accepted in the course of this licensing transaction, (ii) these terms and conditions and (iii) CCC's Billing and Payment terms and conditions.

- This Agreement will be void if the Type of Use, Format, Circulation, or Requestor Type was misrepresented during the licensing process.

- This Agreement shall be governed by and construed in accordance with the laws of the State of New York, USA, without regards to such state's conflict of law rules. Any legal action, suit or proceeding arising out of or relating to these Terms and Conditions or the breach thereof shall be instituted in a court of competent jurisdiction in New York County in the State of New York in the United States of America and each party hereby consents and submits to the personal jurisdiction of such court, waives any objection to venue in such court and consents to service of process by registered or certified mail, return receipt requested, at the last known address of such party.

WILEY OPEN ACCESS TERMS AND CONDITIONS

Wiley Publishes Open Access Articles in fully Open Access Journals and in Subscription journals offering Online Open. Although most of the fully Open Access journals publish open access articles under the terms of the Creative Commons Attribution (CC BY) License only, the subscription journals and a few of the Open Access Journals offer a choice of Creative Commons Licenses. The license type is clearly identified on the article.

The Creative Commons Attribution License

The Creative Commons Attribution License (CC-BY) allows users to copy, distribute and transmit an article, adapt the article and make commercial use of the article. The CC-BY license permits commercial and non-

Creative Commons Attribution Non-Commercial License

The Creative Commons Attribution Non-Commercial (CC-BY-NC)License permits use, distribution and reproduction in any medium, provided the original work is properly cited and is not used for commercial purposes.(see below)

Creative Commons Attribution-Non-Commercial-NoDerivs License

The Creative Commons Attribution Non-Commercial-NoDerivs License (CC-BY-NC-ND) permits use, distribution and reproduction in any medium, provided the original work is properly cited, is not used for commercial purposes and no modifications or adaptations are made. (see below)

Use by commercial "for-profit" organizations

Use of Wiley Open Access articles for commercial, promotional, or marketing purposes requires further explicit permission from Wiley and will be subject to a fee.

Further details can be found on Wiley Online Library http://olabout.wiley.com/WileyCDA /Section/id-410895.html

Other Terms and Conditions:

v1.10 Last updated September 2015

Questions? customercare@copyright.com or +1-855-239-3415 (toll free in the US) or +1-978-646-2777.

ChemElectroChem

Articles
doi.org/10.1002/celc.202000223

Chemistry Europe
European Chemical
Societies Publishing

Specific Cation Adsorption: Exploring Synergistic Effects on CO₂ Electroreduction in Ionic Liquids

Alexander V. Rudnev,*[a, b] Kiran Kiran,[a] and Peter Broekmann*[a]

Ionic liquids (ILs) have gained attention as promising solvents as reaction media for the electrochemical conversion of CO_2 into valued-added products. ILs can co-catalyze the CO_2 reduction reaction (CO₂RR), in particular, when Ag is applied as the primary metallic electrocatalyst. To broaden this co-catalysis concept, we conducted a comprehensive study of a range of electrode materials exposed to three ILs, which differed in the chemical nature of their anions and cations. Here, we examine the activity of the electrode/IL combinations toward the CO₂RR based on cyclic voltammetry data. The voltammetric experi-ments are complemented by gas chromatography analysis of the products, demonstrating that CO is the main product for most of the electrode/IL combinations. Our results demonstrate that the specific adsorption of the IL cation on the electrode plays a crucial role in the co-catalytic effect of the ILs. Based on our analysis, we identify three classes of electrode materials, which differ in their synergistic interaction with the IL cations and their resulting CO₂RR activity. The key criterion for this classification is the extent to which the CO₂RR is superimposed on the reductive decomposition of the ILs.

1. Introduction

Significant attention has been paid to room temperature ionic liquids (ILs) as electrolyte media for the electrochemical CO_2 reduction reaction (CO₂RR).[1] ILs are known to lower the required CO₂RR overpotential, which clearly indicates an IL-mediated co-catalytic effect.[2–3] This enhanced electrocatalytic activity was first rationalized on the basis of a change in the reaction pathway, as compared to that in an aqueous environment. In early work on this topic,[2] it was hypothesized that the mechanistic origin of the experimentally observed decrease in the CO₂RR overpotential involved the formation of CO_2-imidazolium intermediate complexes. However, it has also been reported that this co-catalytic effect is not limited to imidazo-lium-type ILs but extends to ILs bearing cationic structure motifs, such as pyrrolidium, ammonium, and phosphonium functional groups.[4] Moreover, this co-catalysis concept was recently shown to be applicable to choline chloride-based deep eutectic solvents as well.[5]

The co-catalysis concept was further refined by Lau et al.,[6] who applied a series of imidazolium-based ILs with different substitution patterns at their C2-position. Based on a compar-ison of voltammetric responses, the authors proposed that the electrostatic stabilization of the $CO_2^{•-}$ radical anion, which is an intermediate in the CO₂RR, by IL cations adsorbed on the Ag electrode surface was the origin for the co-catalytic effect, rather than the formation of intermediate CO_2-imidazolium complexes.[6] Despite several attempts to rationalize the IL-mediated co-catalytic effect in the CO₂RR, the underlying catalytic mechanism is not yet fully understood. The majority of the studies published in this field have utilized Ag materials of varying morphology (planar surfaces, nanoparticles, nanowires, metal foams, etc.) as primary CO₂RR catalysts in ILs, whereas other electrode materials have scarcely been studied.[2–14]

Herein, we present a comprehensive study of thirteen electrode materials, including Pt, Pd, Ag, Au, Bi, Pb, Sn, Ni, Mo, Fe, Zn, Cu, and glassy carbon (GC), in three ILs, which differ in the chemical nature of their anion and cation (Figure 1). The activity of the electrode materials toward the CO₂RR is examined by comparing cyclic voltammetry data recorded in Ar- and CO₂-saturated ILs. We demonstrate that IL cation adsorption on an electrode surface plays a crucial role in the overall co-catalytic effect of ILs. Therefore, we consider this adsorption phenomenon to be *specific cation adsorption* because only particular combinations of electrode materials and IL cations enhance the CO₂RR activity.

2. Results and Discussion

Figure 2 provides an overview of the voltammograms measured in Ar- and CO₂-saturated [BMIm][BF₄], [BMIm][TFSI], and [BMP] [TFSI]. In the absence of CO₂, the voltammetric responses of

[a] Dr. A. V. Rudnev, K. Kiran, Prof. P. Broekmann
Department of Chemistry and Biochemistry
University of Bern
Freiestrasse 3, CH-3012 Bern, Switzerland
E-mail: rudnev@dcb.unibe.ch
peter.broekmann@dcb.unibe.ch
[b] Dr. A. V. Rudnev
A.N. Frumkin Institute of Physical Chemistry and Electrochemistry
Russian Academy of Sciences
Leninskii pr. 31, Moscow 119071, Russia
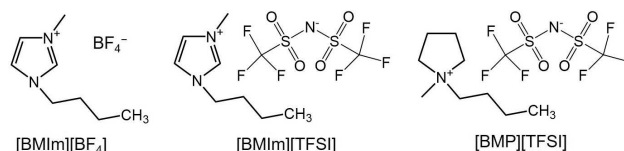
Figure 1. Chemical structure of the ILs studied herein.

ChemElectroChem

Articles
doi.org/10.1002/celc.202000223

Chemistry Europe
European Chemical
Societies Publishing
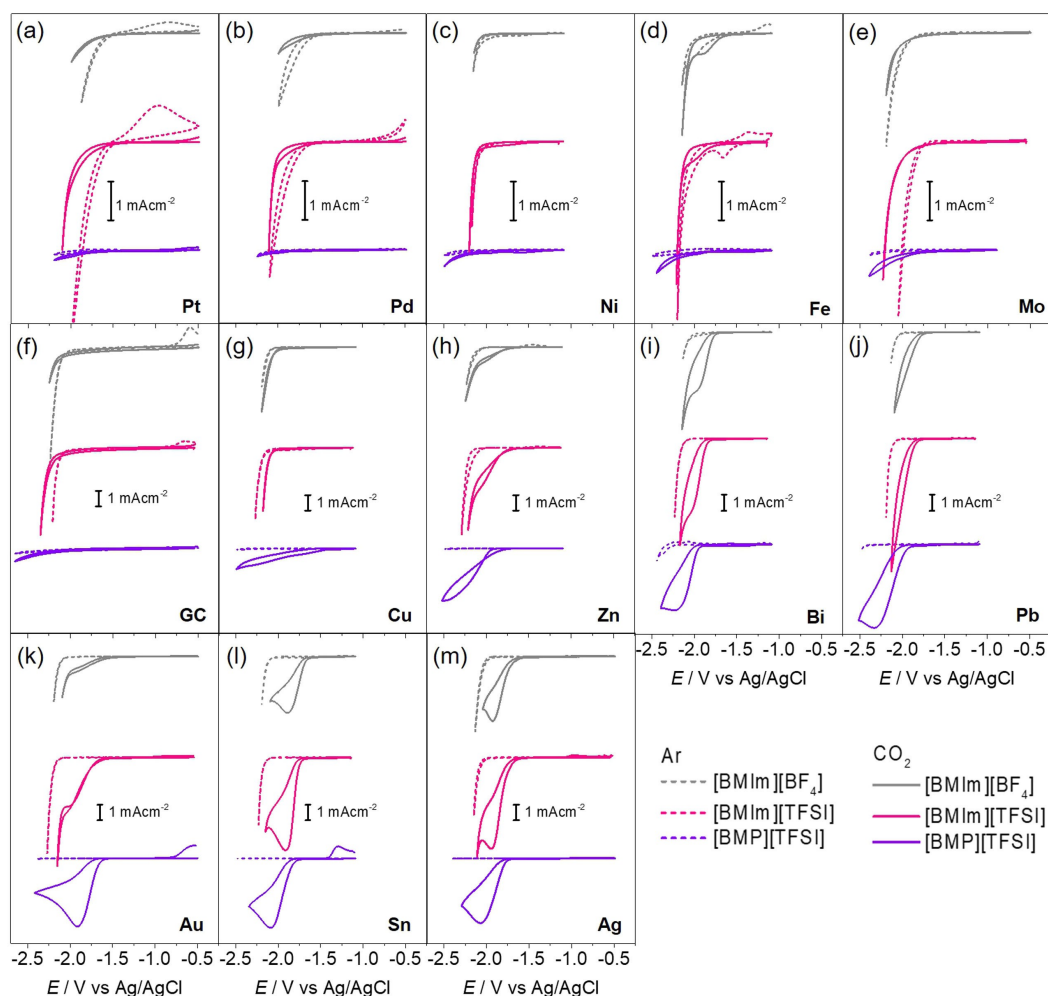
Figure 2. The CVs recorded in Ar- and CO_2-saturated ILs (dashed and solid lines, respectively) by employing different working electrode materials. Scan rate is 0.05 Vs^{-1}.

[BMIm][BF$_4$] and [BMIm][TFSI] consistently show a sharp increase in the cathodic current at potentials less than −1.80 V. In full accordance with the literature, this cathodic process must be assigned to the reductive decomposition of the [BMIm]$^+$ cations.[14–15] The onset potential of [BMIm]$^+$ reduction (see the onset potential values in Table 1) is only marginally affected by the chemical nature of the corresponding counter anion but varies significantly based on the electrode material used. Obviously, Pt significantly accelerates the [BMIm]$^+$ degradation (onset potential of ca. −1.70 V, Table1) as compared with the

Table 1. Onset potentials of IL degradation or CO$_2$RR estimated at $j = -0.5$ mA cm^{-2} (with correction for double layer charging currents).

Electrode	Ar-saturated, E (−0.5 mA cm^{-2}) [V]			CO$_2$-saturated, E (−0.5 mA cm^{-2}) [V]		
	[BMIm][BF$_4$]	[BMIm][TFSI]	[BMP][TFSI]	[BMIm][BF$_4$]	[BMIm][TFSI]	[BMP][TFSI]
Pt	−1.699	−1.638	< −2.190	−1.916	−1.856	< −2.190
Pd	−1.754	−1.824	< −2.245	−1.992	−1.898	< −2.245
Ni	−2.111	−2.100	< −2.490	−2.143	−2.132	< −2.490
Fe	−1.967	−1.956	< −2.490	−1.936	−2.035	< −2.445
Mo	−1.996	−1.842	< −2.390	−2.089	−2.010	< −2.390
GC	−2.104	−2.112	< −2.645	−2.125	−2.136	< −2.645
Cu	−2.118	−2.175	< −2.490	−2.064	−2.101	−1.894
Zn	−2.151	−2.197	< −2.490	−1.895	−1.842	−2.007
Bi	−2.072	−2.141	−2.358	−1.795	−1.868	−1.894
Pb	−2.082	−2.119	< −2.470	−1.817	−1.863	−1.976
Au	−2.121	−2.175	< −2.390	−1.752	−1.723	−1.672
Sn	−2.140	−2.165	< −2.490	−1.694	−1.751	−1.842
Ag	−2.019	−2.062	< −2.390	−1.707	−1.710	−1.802

ChemElectroChem

Articles
doi.org/10.1002/celc.202000223

**Chemistry
Europe**
European Chemical
Societies Publishing

other electrode materials under investigation. One interesting observation is that in comparison to $[BMIm]^+$, the $[BMP]^+$ cation appears to be more resistant to reductive decomposition, as evidenced by its corresponding onset potentials, which are typically less than -2.20 V for the range of electrode materials studied. Again, the Pt electrode is observed to catalyze the IL cation degradation most effectively (onset potential of -2.19 V). The extended potential window observed for the $[BMP][TFSI]$ is, as we discuss below, beneficial for the CO_2RR.

Saturation of the ILs with CO_2 leads to significant changes in the voltammetric responses, which indicates that the extra cathodic processes are associated with the CO_2RR. A group of six electrode materials (Pt, Pd, Ni, Fe, Mo, and GC) shows minimal catalytic activity toward the CO_2RR in the ILs (Figure 2a–f). This result is consistent with that of similar electrolysis experiments carried out in an aqueous environment.[16] At least for Pt, Ni, Fe, and Mo, this observation can be rationalized, in accordance with similar considerations for aqueous systems, by the concept of electrode poisoning through irreversible chemisorption of *CO (the asterisk * indicates an adsorption state), which generally forms as the prevalent CO_2RR product in ILs in the absence of water. Chemisorbed *CO species tend to sterically block the catalytically active sites on the electrode surface. In full agreement with this reasoning, the reductive decomposition of the ILs is hindered when CO_2 is present in the electrolyte (Figure 2a–f and Table 1). The onset potentials for the reductive IL decomposition are negatively shifted in the CO_2 containing ILs. It can be hypothesized that the presence of chemisorbed *CO also hinders the adsorption of the $[BMIm]^+$ cation and its subsequent degradation. The Pt electrode in $[BMIm][BF_4]$ and $[BMIm][TFSI]$ is a prime example: the cathodic current density of 0.5 mA cm^{-2} is reached at potential values that are ~200 mV more negative in the CO_2-saturated ILs as compared to the Ar-saturated ILs (Table 1). In the case of the $[BMP][TFSI]$, there is a minor increase in cathodic currents at $E < -2.00$ V (Figure 2a–f), likely due to a slow CO_2RR.

A second group of moderately active materials includes Cu, Zn, Bi, Pb, and Au and is characterized by the (partial) superposition of the CO_2RR and IL degradation processes (Figure 2g–k). In the CO_2-saturated ILs, the onset of cathodic processes is significantly shifted toward less negative potentials, as compared to the respective CO_2-free cases. Except for Cu, all of these metals display a pronounced cathodic wave in the forward (negative direction) scans of the CVs when CO_2 is

present in the electrolyte. Therefore, this peak-like feature can be ascribed to the CO_2RR process, which is limited by the diffusional CO_2 transport when a certain reaction rate (current density) is surpassed. When either $[BMIm][BF_4]$ or $[BMIm][TFSI]$ is used as the electrolyte, these CO_2RR-related features overlap with the faradaic processes associated with the reductive IL decomposition, which is, in contrast to the CO_2RR, not limited by mass transfer at any potential. The potential window of the $[BMP][TFSI]$ IL is significantly broader than that of the $[BMIm]^+$-based ILs (compare the CVs in pure ILs in Figure 2, Table 1). For this reason, the CO_2RR-related current peaks are most clearly discernible in the case of $[BMP][TFSI]$, in particular when Bi, Pb, and Au are used as the primary electrocatalyst.

For the third group of metals, Ag (the benchmark catalyst) and Sn, all CO_2RR-related cathodic features in the CVs are clearly separated from the onset of the IL degradation processes and represent well-defined cathodic peaks in the three ILs (Figure 2l,m). The absence of CO_2RR interference with IL degradation is also supported by the linear dependence of the CO_2RR cathodic peak current densities on the square-root of the applied sweep rate, which is typical for a diffusion-limited process.[17–18] An example of this characteristic is shown for the Ag catalyst in Figure 3.

For several electrodes Pt, Pd, Fe, GC, Au, Sn, one could observe an increase in anodic current density (in some cases, anodic peak can be seen) on the reverse scans of the CVs (Figure 2). These anodic features can be related to oxidation of CO_2RR products (in CO_2-saturated ILs) and/or of the products of IL reductive degradation, which may also include molecular hydrogen.

The specific impact of the ILs on the CO_2RR is highlighted in Figure 4, in which the CVs of Sn, Au, and the Ag benchmark are compared. Specifically, by comparing the CVs in $[BMIm][BF_4]$ and $[BMIm][TFSI]$ (same cation but different anions), one can see that the IL anions do not severely affect the CO_2RR onset potential (Figure 4): e.g., for the Ag electrode, the CO_2RR onset potentials are -1.707 and -1.710 V in $[BMIm][BF_4]$ and $[BMIm][TFSI]$, respectively (see also Table 1). However, IL anions significantly alter the resulting CO_2RR peak current density in the order of $[BMIm][BF_4] \leq [BMP][TFSI] \ll [BMIm][TFSI]$ (Figure 4a): e.g., in the case of Ag, j_p is -4.16, -4.32, and -5.89 mA cm^{-2}, respectively. Changes in the peak current densities are directly correlated with the CO_2 transport characteristics in the respective IL, which depend on the CO_2 solubility

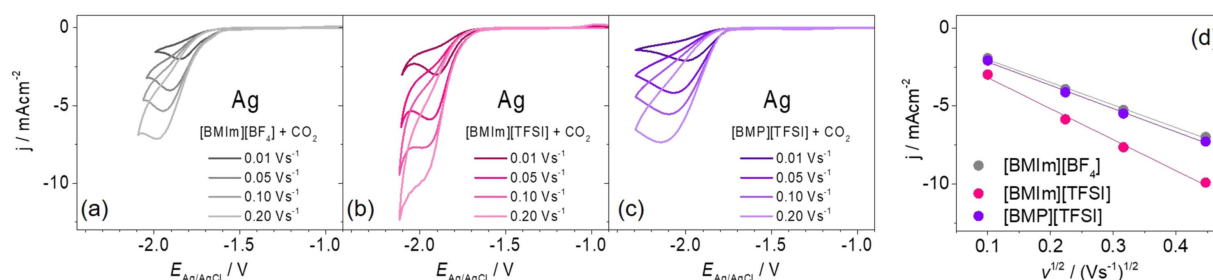**Figure 3.** Cyclic voltammograms of Ag measured at different sweep rates (indicated in the graphs) in a) $[BMIm][BF_4]$, b) $[BMIm][TFSI]$, c) $[BMP][TFSI]$. d) The peak current densities at different sweep rates show a linear dependence on the square-root of the sweep rate.

ChemElectroChem
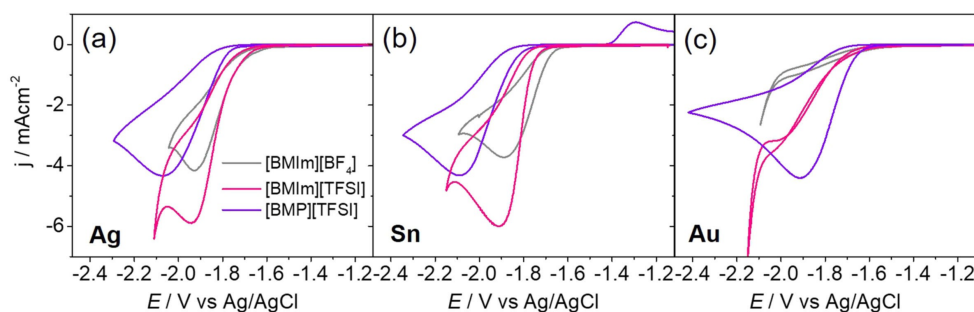
Articles
doi.org/10.1002/celc.202000223

Chemistry Europe
European Chemical
Societies Publishing

Figure 4. Comparison of the CV fragments in CO_2-saturated ILs for the a) Ag, b) Sn, and c) Au electrodes. Scan rate is 0.05 Vs^{-1}.

and the CO_2 diffusion rate. The latter is determined by the (kinematic) viscosity of the IL (according to Stokes-Einstein equation, see also Ref. [17]). According to the literature, the solubility of CO_2 is almost identical for all three ILs, at least at room temperature and atmospheric pressure. CO_2 saturation concentrations of 0.101 mol L^{-1}, 0.100 mol L^{-1}, and 0.098 mol L^{-1} were previously measured for [BMIm][BF$_4$],[17] [BMIm][TFSI],[19] and [BMP][TFSI],[20] respectively. From these results, it can be concluded that the observed differences in the peak current densities are due to variations among the (kinematic) viscosities of the ILs. The observed trend in peak current densities agrees well with the decrease in the viscosity from 0.109 Pa s for [BMIm][BF$_4$][21–22] to 0.077 Pa s for [BMP][TFSI][23] and 0.050 Pa s for [BMIm][TFSI].[23] Indeed, the latter IL shows the highest peak current density and the lowest viscosity (Figure 4a,b).

It should be noted that when Au is used as the primary catalyst material, a well-defined CO_2RR peak develops only in [BMP][TFSI] and not in [BMIm][BF$_4$] and [BMIm][TFSI] (Figure 4c). Although the onset potentials for the CO_2RR are comparably low in the latter cases (−1.752 and −1.723 V, respectively), the further increase in the CO_2 reduction rate is significantly less pronounced, as compared with the cases of Sn and Ag (Figure 4). Further, in the case of Au, a well-defined diffusion-limited reduction peak does not develop prior to the onset of [BMIm]$^+$ reduction. In agreement with the literature,[24–25] the overall slower reaction kinetics on Au can be associated with the extraordinarily high affinity of the [BMIm]$^+$ cations for Au and their resulting strong chemisorption on the electrode surface, which (partially) blocks reactive surface sites and thus limits the CO_2RR.

Due to the co-catalytic properties of IL cations, their nature has a significant influence on the CO_2RR onset potential. When comparing the results for Ag and Sn (Table 1, Figure 4a,b), it becomes evident that the CO_2RR onset is negatively shifted by ~100 mV in [BMP][TFSI] with respect to the corresponding onset in either [BMIm][BF$_4$] or [BMIm][TFSI]. Because the cation ([BMIm]$^+$) is the same in the latter cases, the onset voltages are also similar. It can be assumed that the origin of this negative shift in the CO_2RR onset potential is due to a reduced capability of the [BMP]$^+$ cation to stabilize the $CO_2^{\bullet-}$ radical anion at the electrode surface, which is the key intermediate of the CO_2RR. This reasoning is in agreement with previous studies discussing the surface-confined electrostatic stabilization of the $CO_2^{\bullet-}$

radical anion, which crucially depends on the core structure of the IL cation and its particular substitution pattern.[3,6]

Our study also demonstrates that the co-catalytic effect is not solely an inherent characteristic of the IL cation but also depends crucially on the chemical nature of the primary metallic catalyst. We found that the observed trend in the co-catalytic activity of [BMIm]$^+$ > [BMP]$^+$, as observed for Ag and Sn, is opposite that for Au. For Au in the [BMP][TFSI] IL, the CO_2RR onset potential is −1.672 V, which is less negative than in either [BMIm][BF$_4$] (−1.752 V) or [BMIm][TFSI] (−1.723 V) (Figure 4, Table 1). Again, it can be argued that the strong chemisorption of the [BMIm]$^+$ cation on the Au blocks the catalytically active sites that would otherwise be available for CO_2RR on the Au electrode. An optimal co-catalytic effect requires a more balanced interaction of the IL cation with the electrode surface, which would still allow for electrostatic coupling with the $CO_2^{\bullet-}$ radical anion on the electrode surface. Furthermore, a recent density functional theory study predicted significant charge transfer from a single crystalline Au(111) model catalyst to the IL cation, thus also affecting the charge transfer kinetics of the CO_2RR.[26] In general, this charge transfer effect is expected to depend on both the chemical nature of the primary metallic electrocatalyst and that of the IL cation.

The voltammetric data are further complemented by online gas chromatography (GC) analysis of the gaseous products, confirming that CO is the prevalent CO_2RR product in these ILs (Table 2), at least for the primary electrocatalysts that show an activity toward CO_2RR in the corresponding CV measurements (Figure 3). CO is formed according to Reaction (1):

$$CO_2 + 2H^+ + 2e^- \rightarrow CO + H_2O \tag{1}$$
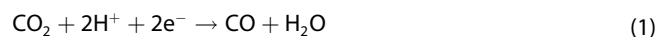
The primary source of the required protons is the anolyte (0.5 M H_2SO_4) separated from the IL-containing catholyte by a proton-conductive Nafion membrane. A secondary source of the protons might be the IL itself. Deprotonation in the course of the CO_2RR represents one possible reaction pathway, among others, of IL degradation.[14]

The Ag (benchmark) electrocatalyst demonstrates the highest faradaic efficiencies of FE$_{CO}$ > 97%, regardless of IL composition. Similar to the aqueous reaction environment,[16] Au also performs well as a CO producer in the ILs, reaching high values of FE$_{CO}$ = 99% in the [BMP][TFSI] (Table 2). In the imidazolium-

Table 2. Faradaic efficiency (FE) for CO and H_2 production in potentiostatic electrolysis at potential E (given in the table), corresponding approximately to the position of the cathodic peak on the CV or curve bend (just prior to intensive reductive decomposition of the ILs).

Electrode	[BMIm][BF$_4$]			[BMIm][TFSI]			[BMP][TFSI]		
	FE$_{CO}$ [%]	FE$_{H2}$ [%]	E [V]	FE$_{CO}$ [%]	FE$_{H2}$ [%]	E [V]	FE$_{CO}$ [%]	FE$_{H2}$ [%]	E [V]
Ag	99.7	0.0	−1.84	97.8	0.0	−1.90	99.5	0.3	−2.10
Sn	79.9	0.8	−1.84	68.0	0.4	−1.85	69.2	0.9	−2.09
Au	66.4	1.3	−1.98	69.2	2.8	−1.94	98.9	0.0	−1.90
Pb	34.2	0.3	−2.00	53.1	0.0	−2.00	46.4	0.1	−2.12
Zn	65.0	3.9	−1.98	84.6	7.2	−1.89	97.1	0.1	−2.05
Bi	58.6	1.4	−1.92	42.4	2.1	−1.97	62.0	2.2	−2.12
Cu[a]	12.9	4.3	−2.10	22.7	22.2	−2.10	17.0	18.1	−2.20

[a] In addition to CO and H_2, C2 and C3 gaseous products were detected during CO_2 electrolysis on Cu with the total FE of these products less than 5%.

type ILs, FE$_{CO}$ did not exceed 70% on Au, probably, due to the parallel reaction of [BMIm]$^+$ reductive decomposition (see the CVs in Figure 4c).

CO efficiencies range from 68 to 80% when Sn is used as the primary electrocatalyst material, whereas the FE$_{H2}$ values remain less than 1% in all three ILs studied (Table 2). This might be an indication that non-volatile CO_2RR products are also forming, in addition to CO (the main product) and traces of H_2, when a more positive electrolysis potential is applied relative to the onset of reductive IL degradation. From previous studies in aqueous environments, it is known that Sn and Sn-based catalysts yield formate as a major CO_2RR product.[16,27] Therefore, we cannot exclude the possibility that formate is formed as a CO_2RR by-product when using the Sn catalyst in the ILs. This fact would account for the lack of a FE to compensate for 100% (Table 2). The same argument holds for Pb in [BMIm][BF$_4$] and [BMIm][TFSI].

In regard to the group of primary electrode materials that show a moderate activity toward CO_2RR, which includes Zn, Bi, and Cu, the formation of CO is typically superimposed on the onset of reductive IL degradation. In the cases of the largely inactive electrocatalysts, which include Pt, Pd, Ni, Co, and GC, the main cathodic process is the reductive decomposition of the IL, as already concluded from the CV measurements. A prime example of this class of materials, Pt in [BMIm][TFSI], yields only FE$_{CO}$ < 0.7%, in contrast to FE$_{H2}$ = 67.5%, at an applied electrolysis potential of −2.00 V. In the latter case, the main source for the hydrogen is the IL itself. A further indication pointing to significant IL degradation is the readily apparent color change upon electrolysis at −2.00 V (Figure S1).

3. Conclusions

Based on our combined voltammetric and potentiostatic CO_2 electrolysis experiments, we identify three major groups of primary CO_2RR electrocatalyst materials for IL applications: (i) the first group of electrode materials includes Pt, Pd, Ni, Fe, Mo, and GC, which are largely inactive with regard to the CO_2RR within the stability window of the studied ILs. IL degradation is the prevalent cathodic process. (ii) The second group of moderately active materials includes Cu, Zn, Bi, Pb, and Au and is characterized by the superposition of the CO_2RR and IL degradation processes. (iii) Only in the cases of Ag and Sn are the CO_2RR and reductive IL degradation processes clearly separated from each other on the potential scale due to the low CO_2RR overpotentials on both electrocatalysts.

Overall electrocatalytic activity is the result of a synergistic effect of the choice of electrode material and IL cation, which serves as a co-catalyst. To achieve co-catalytic action of the IL cation, a balanced chemisorption process is required. This chemisorption can be denoted as a specific adsorption process because this phenomenon depends on the chemical nature of both the electrode and the IL cation. The IL counter anions do not have any direct influence on the overall electrocatalytic performance of the electrode/IL combination. However, the chemical nature of the anion determines the IL (kinematic) viscosity and, as a result, affects the maximal diffusion-limited CO_2RR current density.

The voltammetric results are complemented by online gas chromatography analysis of the gaseous electrolysis products, showing that CO is the main product in CO_2RR in ILs for most of the electrode materials studied here.

Experimental Section

ILs

1-Butyl-3-methylimidazolium tetrafluoroborate ([BMIm][BF$_4$], > 99%, high purity grade, H_2O < 100 ppm) and 1-butyl-1-methylpyrrolidinium bis(trifluoromethylsulfonyl)imide ([BMP][TFSI], > 99%, high purity grade, H_2O < 100 ppm) were purchased from Merck and used without further purification. 1-Butyl-3-methylimidazolium bis(trifluoromethylsulfonyl)imide ([BMIm][TFSI], > 99.5%, H_2O < 500 ppm) was purchased from Solvionic and then was further dried prior to use via a combined thermal (70 °C) and vacuum treatment. In all three cases, the water content was less than the detection limit of the ^{1}H-NMR analysis (Figure S2), suggesting that the actual residual water content of each neat IL was less than 200 ppm.

NMR Spectroscopy

NMR data were recorded using a Bruker AVANCE IIIHD spectrometer operating at the nominal proton frequency of 400 MHz, equipped with a dual direct broadband 5-mm probehead (SmartProbe©) with an additional z-gradient coil. The quantitative ^{1}H-NMR spectra were recorded at room temperature (298 K) using a

standard one-pulse experiment (zg30 pulse sequence from the Bruker pulse-program library). Typically, 8 transients were acquired over a spectral width of 20 ppm, with a data size of 64 k points, and a relaxation delay of 30 s.

Electrochemical Measurements

Cyclic voltammetry measurements were carried out in a custom-designed, single-compartment glass cell equipped with an inlet and outlet for the gas supply (either Ar or CO_2) (Figure S3a). All electrochemical experiments were performed using an Autolab PGSTAT302 N instrument (Metrohm, Netherlands). Glassware and Teflon parts were cleaned in hot 25% HNO_3 prior to use followed by several boiling/rinsing cycles, each with Milli-Q water (R > 18.2 MΩ, TOC < 3 ppb). All parts were dried overnight in an oven at a temperature of 105 °C. Measurements were carried out at a temperature of 23 ± 2 °C. Polycrystalline Pt, Pd, Mo, Ni, Fe, Zn, Cu, Bi, Au, Ag, Sn, and Pb foils (99.99%, Goodfellow) of either 0.10 or 0.25 mm thickness were used for the working electrodes such that the electrodes would have geometric surface areas in the range of 0.25 to 0.35 cm². The glassy carbon (GC) electrode was purchased from BASi. The GC disc (3 mm in diameter) was embedded in a solvent-resistant PCTFE polymer body.

Prior to the measurements, all electrodes were polished with suspensions containing 1-μm alumina particles (Bühler AG), followed by ultrasonication, thorough rinsing with Milli-Q water, and drying in a gentle stream of Ar gas. A leakless Ag|AgCl$_{3.4M}$ (eDAQ) electrode and a Pt foil (~2 cm² geometric surface area) were used as the reference and the counter electrodes, respectively. The neat ILs were added to the glass cell in a dedicated glovebox under a protective nitrogen gas atmosphere (N60, Carbagas). Prior to the measurements, all electrolyte solutions were deaerated by purging with either Ar (N50, Carbagas) or CO_2 gas (N48, Carbagas) for 30 min. During each measurement, a continuous flow of the respective gas was established above the IL electrolyte solution. Automatic IR compensation was applied for the voltammetric measurements after measuring the solution resistance by means of the positive feedback approach. The measured currents were normalized to the geometric surface area of the electrode used.

CO$_2$RR Product Analysis

The CO_2RR product distribution was obtained in a headspace analysis of the formed gases by using online gas-chromatography (GC) in the course of potentiostatic electrolysis. The GC run was always started 20 min after the beginning of the electrolysis process to ensure the equilibration of gas concentrations in the headspace. For the electrolysis experiments, the catholyte (corresponding IL) and analyte (0.5 M H_2SO_4, Suprapur®, Merck) compartments were separated by a polymer membrane (Nafion 117, Chemours) in an H-type cell (Figure S3b). The headspace of the catholyte compartment was continuously purged with CO_2 gas at the flow rate of 15 mL/min, thereby transporting the volatile reaction products (e.g., CO and H_2) of the electrolysis process from the headspace into the sampling loops of the gas chromatograph (SRI Instruments). An 80–100 mesh column (HayeSep D) was employed for the separation, and TCD and FID (equipped with a methanizer) were used as the detectors. The faradaic efficiency for a given gaseous product was determined by Equations (2) and (3):

$$FE(\%) = I(i)/I(total) \cdot 100\% \qquad (2)$$

$$I(i) = x_i\, n_i\, F\, v_m \qquad (3)$$

where $I(i)$ is the partial current for the conversion of CO_2 to the product i, $I(total)$ is the measured current density, x_i represents the volume fraction of the products measured via online GC using an independent calibration standard gas (Carbagas), n_i is the number of electrons involved into the reduction reaction to form a particular product, v_m represents the molar CO_2 gas flow rate, and F is the Faraday constant. Gas aliquots were analyzed after 20 min of CO_2 electrolysis.

Conflict of Interest

The authors declare no conflict of interest.

Keywords: CO_2 electroreduction · ionic liquids · co-catalysis · cation adsorption · intermediate stabilization

[1] Y. Chen, T. Mu, *Green Chem.* **2019**, *21*, 2544–2574.
[2] B. A. Rosen, A. Salehi-Khojin, M. R. Thorson, W. Zhu, D. T. Whipple, P. J. A. Kenis, R. I. Masel, *Science* **2011**, *334*, 643–644.
[3] D. Vasilyev, E. Shirzadi, A. V. Rudnev, P. Broekmann, P. J. Dyson, *ACS Applied Energy Materials* **2018**, *1*, 5124–5128.
[4] S.-F. Zhao, M. Horne, A. M. Bond, J. Zhang, *J. Phys. Chem. C* **2016**, *120*, 23989–24001.
[5] D. V. Vasilyev, A. V. Rudnev, P. Broekmann, P. J. Dyson, *ChemSusChem* **2019**, *12*, 1635–1639.
[6] G. P. S. Lau, M. Schreier, D. Vasilyev, R. Scopelliti, M. Grätzel, P. J. Dyson, *J. Am. Chem. Soc.* **2016**, *138*, 7820–7823.
[7] A. Atifi, D. W. Boyce, J. L. DiMeglio, J. Rosenthal, *ACS Catal.* **2018**, *8*, 2857–2863.
[8] F. Zhou, S. Liu, B. Yang, P. Wang, A. S. Alshammari, Y. Deng, *Electrochem. Commun.* **2015**, *55*, 43–46.
[9] A. Salehi-Khojin, H.-R. M. Jhong, B. A. Rosen, W. Zhu, S. Ma, P. J. A. Kenis, R. I. Masel, *J. Phys. Chem. C* **2013**, *117*, 1627–1632.
[10] Q. Feng, S. Liu, X. Wang, G. Jin, *Appl. Surf. Sci.* **2012**, *258*, 5005–5009.
[11] J. L. DiMeglio, J. Rosenthal, *J. Am. Chem. Soc.* **2013**, *135*, 8798–8801.
[12] H.-K. Lim, Y. Kwon, H. S. Kim, J. Jeon, Y.-H. Kim, J.-A. Lim, B.-S. Kim, J. Choi, H. Kim, *ACS Catal.* **2018**, *8*, 2420–2427.
[13] Y. Fu, M. R. Ehrenburg, P. Broekmann, A. V. Rudnev, *ChemElectroChem* **2018**, *5*, 748–752.
[14] A. V. Rudnev, K. Kiran, A. Cedeño López, A. Dutta, I. Gjuroski, J. Furrer, P. Broekmann, *Electrochim. Acta* **2019**, *306*, 245–253.
[15] M. C. Kroon, W. Buijs, C. J. Peters, G.-J. Witkamp, *Green Chem.* **2006**, *8*, 241–245.
[16] Y. Hori, H. Wakebe, T. Tsukamoto, O. Koga, *Electrochim. Acta* **1994**, *39*, 1833–1839.
[17] A. V. Rudnev, Y.-C. Fu, I. Gjuroski, F. Stricker, J. Furrer, N. Kovács, S. Vesztergom, P. Broekmann, *ChemPhysChem* **2017**, *18*, 3153–3162.
[18] I. Reche, I. Gallardo, G. Guirado, *Phys. Chem. Chem. Phys.* **2015**, *17*, 2339–2343.
[19] M. Gonzalez-Miquel, J. Bedia, C. Abrusci, J. Palomar, F. Rodriguez, *J. Phys. Chem. B* **2013**, *117*, 3398–3406.
[20] T. Turnaoglu, D. L. Minnick, A. R. C. Morais, D. L. Baek, R. V. Fox, A. M. Scurto, M. B. Shiflett, *J. Chem. Eng. Data* **2019**, *64*, 4668–4678.
[21] J. Jacquemin, P. Husson, A. A. H. Padua, V. Majer, *Green Chem.* **2006**, *8*, 172–180.

[22] H. F. D. Almeida, J. N. Canongia Lopes, L. P. N. Rebelo, J. A. P. Coutinho, M. G. Freire, I. M. Marrucho, *J. Chem. Eng. Data* **2016**, *61*, 2828–2843.

[23] M. Vranes, S. Dozic, V. Djeric, S. Gadzuric, *J. Chem. Eng. Data* **2012**, *57*, 1072–1077.

[24] Y. Fu, A. V. Rudnev, *Curr. Opin. Electrochem.* **2017**, *1*, 59–65.

[25] A. V. Rudnev, M. R. Ehrenburg, E. B. Molodkina, A. Abdelrahman, M. Arenz, P. Broekmann, T. Jacob, *ChemElectroChem* **2020**, *7*, 501–508.

[26] S. Kamalakannan, M. Prakash, G. Chambaud, M. Hochlaf, *ACS Omega* **2018**, *3*, 18039–18051.

[27] A. Dutta, A. Kuzume, M. Rahaman, S. Vesztergom, P. Broekmann, *ACS Catal.* **2015**, *5*, 7498–7502.

5.5. *CO₂ electrolysis – Complementary operando XRD, XAS and Raman spectroscopy study on the stability of CuₓO foam catalysts*

Authors: Abhijit Dutta, Motiar Rahaman, Burkhard Hecker, Jakub Drnec, Kiran Kiran, Ivan Zelocualtecatl Montiel, Daniel Jochen Weber, Alberto Zanetti, Alena Cedeño López, Isaac Martens, Peter Broekmann, Mehtap Oezaslan

Highlights: C2 and C3 products are one of the important and desired commodity fuel as a result of CO_2 reduction. Copper oxide were studied here as a promising catalyst for higher carbon products formation. Advanced operando techniques were employed to investigate the stability of oxides during the potential dependent electrolysis experiment. The key finding of this work was this complementary approach of bulk and surface sensitive techniques, demonstrating the reduction of Cu_xO foam into Cu metallic form before the hydrocarbon and alcohol formation starts.

Contribution: I assisted the first author of the article analyzing the catalyst electrochemically for product quantification and took part in the potential dependent analysis of the Cu_xO catalyst during beam time at the SLS in Villigen.

CO_2 electrolysis – Complementary *operando* XRD, XAS and Raman spectroscopy study on the stability of Cu_xO foam catalysts

Abhijit Dutta [a],*,[1], Motiar Rahaman [a],[1], Burkhard Hecker [b], Jakub Drnec [c], Kiran Kiran [a], Ivan Zelocualtecatl Montiel [a], Daniel Jochen Weber [b,d], Alberto Zanetti [a], Alena Cedeño López [a], Isaac Martens [c], Peter Broekmann [a],*, Mehtap Oezaslan [b,d],*

[a] Department of Chemistry and Biochemistry, University of Bern, Freiestrasse 3, Bern 3012, Switzerland
[b] Department of Chemistry, University of Oldenburg, 26111 Oldenburg, Germany
[c] European Synchrotron Radiation Facility, 38000 Grenoble, France
[d] Technical Electrocatalysis Laboratory, Institute of Technical Chemistry, Technical University of Braunschweig, 38106 Braunschweig, Germany

A B S T R A C T

Copper oxides have recently emerged as promising precursor catalyst materials demonstrating enhanced reactivity and selectivity towards C2 and C3 products like ethylene, ethanol, and n-propanol generated from the direct electro-reduction reaction of CO_2 (denoted as CO_2RR). Advanced *operando* X-ray absorption spectroscopy (XAS), X-ray diffraction (XRD) and Raman spectroscopy were employed to probe the potential-dependent changes of the chemical states of Cu species in the Cu oxide foams (referred to as Cu_xO) before and during the CO_2RR. This complementary and holistic approach of 'bulk'- and surface-sensitive techniques demonstrates that the electro-reduction of Cu_xO foams into metallic Cu is completed before hydrocarbon (e.g., ethylene, ethane) and alcohol (e.g., ethanol, n-propanol) formation sets in. There are, however, substantial differences in the potential dependence of the oxide reduction when comparing the 'bulk' with the respective 'surface' processes. Only in the very initial stage of the CO_2RR, the reduction of the Cu oxide precursor species is temporarily superimposed on the production of CO and H_2. Complementary identical location (IL) SEM analysis of the Cu_xO foams prior to and after the CO_2RR reveals a significant alteration in the surface morphology caused by the appearance of smaller Cu nanoparticles formed by the reduction process of Cu_xO species.

© 2020 Elsevier Inc. All rights reserved.

1. Introduction

The energy supply of modern society does still rely to a large extent on the combustion of fossil fuels (coal, oil, and gas) being the major source for the drastic increase of the CO_2 content in the atmosphere. Today, there is a general consensus within the scientific community that this raises in the atmospheric CO_2 concentration, already exceeding a level of 400 ppm [1], is the physical origin of global warming, one of the major threats to humankind. Clearly, a paradigm shift is required in the energy sector, also known as the 'energy transition' [2,3]. However, such a shift from fossil fuels towards more sustainable energy sources (wind, solar, and hydro) will heavily affect the entire chemistry sector as well. For instance, fossil feedstocks (e.g., natural gas) stand at the begin-

ning of product and supply chains in the chemical industry. Therefore, the chemical sector will have to follow the energy sector in its transition from fossil to renewables, denoted the 'chemistry transition' [4]. Among the technological approaches that are currently under evaluation, electrochemical conversion processes stand out as they can convert CO_2 directly into the desired 'eco'-fuels or chemical feedstocks by using the surplus of renewable electricity from solar and wind plants. Not only might this approach contribute to the desired closing of the anthropogenic carbon cycle, it also provides means of storing intermittently produced excess electricity in the form of chemical energy which is considered as a key element of the 'energy transition'.

Most electrochemical CO_2 conversions are, however, still immature, very costly and short-lived. This is mainly due to insufficient electrocatalysts which need substantial improvements in terms of (i) (energy) efficiency, (ii) product selectivity (faradaic efficiency), (iii) material costs, and (iv) longterm durability. In the context of the electrochemical reduction of CO_2 (denoted hereinafter as CO_2-RR) copper-based catalysts have attracted particular attention over

the last decades as they can convert CO_2 directly into C-C coupled hydrocarbons [5–13] and alcohols [7,10,13–20] Previous studies have demonstrated that the pre-treatment of Cu-based catalysts is of eminent importance not only for their overall electrocatalytic activity but also for the resulting CO_2RR product distribution [21–23]. The fabrication of Cu catalysts for the CO_2RR often starts with the (electro-)synthesis of precursor materials where copper is present in an oxidized state (+1 or +2). An ultimate activation of these Cu oxide-based precursor materials is often achieved in the electrochemical environment prior to or during the CO_2RR [13,17,24–30].

Various approaches towards precursor synthesis and catalyst activation have been reported including but not restricted to electrode anodization [16], electropolishing [31], and cathodic electrodeposition processes [11,12,17]. Most successful strategies rely on the formation of a thin oxide layer on the respective catalyst surface, e.g. by chemical oxidation [16], thermal annealing treatments [11,21,24,25] or by exposure to oxygen plasma [22,32]. It should be pointed out that such formed cuprous or cupric oxides (Cu_2O or CuO) are thermodynamically unstable under such harsh cathodic conditions relevant to the CO_2RR, thus leading to so-called oxide-derived (OD) Cu catalysts [33]. However, massively precipitated cuprous/cupric oxides result in reduced electric conductivity, which might lead in some cases to the kinetic stabilization of the oxidic catalyst precursor phases even under reductive conditions. Effects such as the embedment of oxygen species into the forming metallic Cu matrix during oxide reduction are controversially discussed in the literature [22,34–36]. To date, there is no ultimate consensus achieved on the potential-dependent stability of surface and sub-surface oxide/oxygen species and their specific role for the CO_2RR [30,32,37–39].

To shine light on the question how stable cuprous and cupric oxides are under electrochemical conditions prior to and during the CO_2RR, we applied a set of highly complementary techniques ranging from ex situ (before and after electrolysis) chemical (XPS) and morphological (identical location (IL)-SEM) analyses to advanced operando XAS (X-ray absorption spectroscopy), XRD (X-ray diffraction), and more surface-sensitive Raman spectroscopy approaches. The unique combination of complementary operando techniques combined with various levels of structural and chemical information allows discriminating the different transient phenomena of the electro-reduction of Cu oxide species. This is a crucial pre-requisite for the interpretation of faradaic efficiency data derived from potential-dependent CO_2RR product analyses. As model system of choice we used Cu foams that were electrodeposited on a conductive carbon support and transformed into their corresponding Cu_xO bulk phases by means of a thermal annealing treatment in air at 300 °C (12 h) [12,17,40,41].

2. Experimental section

2.1. Chemicals

$KHCO_3$ (Sigma-Aldrich, ACS grade), $CuSO_4\cdot5\ H_2O$ (Sigma-Aldrich, ACS grade), H_2SO_4 (Sigma-Aldrich, ACS grade), and Milli-Q water (Millipore, 18.2 MΩ cm, 4 ppb of total organic carbon) were used for the preparation of solutions without further purification.

2.2. Electrodeposition of porous Cu/CuₓO foams

Cu foams were electrodeposited onto activated carbon foil substrates (0.25 mm thick, 99.8%, Alfa Aesar, Germany) using the dynamic hydrogen bubble template approach [11,17,42–44]. Prior to the Cu electrodeposition, the carbon foils were activated by a thermal treatment at 550 °C for 12 h in air, followed by a cleaning

step in an acetone/water mixture (volume ratio of 1:1) and subsequent drying at 100 °C for 1 h. The geometric surface area (A_{geo}) of the carbon foil, exposed to the plating bath, was 1 cm^2. The activated carbon foil was then immersed into a Cu plating bath containing 0.2 M $CuSO_4\cdot5\ H_2O$ and 1.5 M H_2SO_4. The Cu plating was carried out in a 250 mL glass beaker with a Cu plate (5 cm × 5 cm) and a leak-less double-junction Ag/AgCl(3 M KCl, Metrohm) serving as the counter and reference electrode, respectively [11,40,44,45]. For the galvanostatic deposition process, a current density of j = −3.0 A cm^{-2} (normalized to the geometric surface area of the carbon support) was applied for the duration of 5 s. After the electrodeposition, all Cu foam samples were thoroughly rinsed with Milli-Q water and subsequently dried in a gentle Ar gas stream (99.999%, Carbagas, Switzerland). The electrodeposited Cu foams were further subjected to a thermal annealing treatment in air for 12 h at a temperature of 300 °C using a tube furnace (GERO, GmbH, Germany).

2.3. Ex situ material characterization

The crystal structure of the electrodeposited and annealed Cu foams was investigated by means of powder XRD (Bruker D8) with Cu Kα radiation (λ = 0.1540 nm) operated at 40 mA and 40 kV. Scans were recorded at a rate of 1° min^{-1} for 2θ values between 20 and 90°. The obtained XRD patterns of the electrodeposited and annealed Cu foams were analyzed and compared to JCPD (Joint Committee on Powder Diffraction) standards (Cu_2O: 050667, CuO: 410254, and polycrystalline Cu: 040836) [46,47].

Ex situ X-ray photoelectron spectroscopy (XPS) studies were carried out using a PHI VersaProbeII scanning XPS micro-probe (Physical Instruments AG, Germany) equipped with a monochromatic Al Kα X-ray source operated at 24.8 W with a spot size of 100 μm. Peak positions were referenced to the carbon C1s peak at 284.5 eV. A graphite foil served as the reference material. The peak deconvolution and fitting of the XPS spectra were performed using the Casa-XPS software. After completion of the electrolysis reactions, all samples were stored under Ar gas atmosphere prior to the XPS analysis.

The morphology of the Cu foams was characterized by means of scanning electron microscopy (SEM). For the high-resolution SEM imaging a Zeiss DSM 982 instrument was used (working distance of 8 mm).

2.4. CO₂RR and product analysis

Potentiostatic CO_2RR experiments were performed in an airtight H-type glass cell using a classical three electrode configuration. A leakless miniature Ag/AgCl(3 M KCl, EDAQ) electrode served as the reference electrode and was checked with a leakless double junction Ag/AgCl(3 M KCl, Metrohm) master reference electrode prior to each experiment. A 18 mm × 7 mm Pt foil (0.1 mm of thickness, 99.95%, Alfa Aesar) served as the counter electrode. Prior to its use the Pt foil was treated by flame annealing. The two compartments of the glass cell were separated by a cation exchange membrane (Nafion 117, Sigma Aldrich). Both the cathode and the anode compartments were filled with 30 mL of 0.5 M $KHCO_3$ solution. Prior to the electrolysis the solutions were purged with CO_2 (99.999%, Carbagas, Switzerland) for at least 30 min. The pH of the CO_2-saturated 0.5 M $KHCO_3$ solution was 7.2.

All electrochemical measurements (galvanostatic Cu deposition, cyclic voltammetry and potentiostatic CO_2RR experiments) were carried out using a potentiostat/galvanostat (Metrohm Autolab 128 N, The Netherlands). Automatic iR compensation (∼85%, the exact value was determined by the positive feedback technique) was applied during these measurements, following the determination of the cell resistance by electrochemical impedance spec-

troscopy (EIS) or alternatively by the current interrupt method; both methods provide similar results of the cell resistance. For the sake of comparability and to eliminate the pH dependency, all potentials measured versus Ag/AgCl(3 M KCl) were converted to the reversible hydrogen electrode (RHE) scale using Eq. (1):

$$E_{RHE}(V) = E_{Ag/AgCl(3M)}(V) + 0.210V + (0.059V \times pH) \qquad (1)$$

The headspace gas of the cathode compartment was vented with CO_2 to transport gaseous electrolysis products into the sampling loop of the gas chromatograph (GC 8610C, SRI Instruments). Online headspace GC measurements (detection of volatile products, e.g. H_2, CO, C_2H_4, C_2H_6) were conducted every 20 min at each potential step. The total duration of each electrolysis reactions was 1 h. The GC was equipped with two packed Hayesep D columns. Argon (99.9999%, Carbagas, Switzerland) served as the carrier gas. A flame ionization detector (FID) coupled to a methanizer was used for the quantification of all gaseous CO_2RR products, whereas a thermal conductivity detector (TCD) was applied for the quantitative hydrogen detection. The partial current density for a given gaseous product was determined using the Eq. (2):

$$j(i) = x_i \cdot n_i \cdot F \cdot v_m \qquad (2)$$

where x_i represents the volume fraction of each product measured via online GC using an independent calibration standard gas (Carbagas, Switzerland); n_i is the number of electrons involved into the reduction reaction to form a particular product; v_m represents the molar CO_2 flow rate; and F – the Faraday constant. The partial current density for a given reaction product was normalized to the total current density to estimate the faradaic efficiency (FE) for a given reaction product.

Non-volatile products (e.g. alcohols) were quantified by a second FID detector. After the electrolysis, 2 μL aliquot of the electrolyte solution was injected into a second Haysep D column equipped with a pre-column to prevent the electrolyte salt entering into the main column (post-electrolysis alcohol detection). Other liquid products (e.g. formate) were detected and quantified by means of ion exchange chromatography (IC, Metrohm Advanced Modular Ion Chromatograph: L-7100 pump, Metrosep A Supp 7– 250 column, conductivity detector). Electrolyte aliquots were diluted 20 times with Milli-Q water before injection into the IC instrument (post-electrolysis formate detection).

Note that all (partial) current densities given in the paper were normalized with respect to the geometric surface area of the electrode (A = 1 cm²). The surrace roughness factors (RF) of the as prepared (RF = 1.54) and the oxide-derived Cu foams (RF = 1.8) were determined by means of voltammetric measurements in an inert 0.1 M $HClO_4$ electrolyte (determination of the double layer capacitance). In a further attempt, the electrochemically active surface area (ECSA) was determined by the viologen method [11,48,49] using di-methyl viologen as a reversible redox probe (see supplementary file). Scan-rate dependent cyclic voltammograms (CVs) were recorded in aqueous solution containing 1 M Na_2SO_4 (ACS grade, Sigma-Aldrich) and 10 mM $DMVCl_2$ (Sigma-Aldrich). The estimated ECSA of the 'as prepared' Cu foam was 3.68 cm² (referring to 1 cm² geometric surface area). It is important to note that the ECSA of the Cu foam was further increased to 4.89 cm² after the thermal annealing treatment and the subsequent 1 h electrolysis at −0.9 V vs RHE. Partial current densities of the CO_2RR were also normalized to the ECSA (see supplementary file).

2.5. Operando Quick-X-ray absorption spectroscopy (Quick-XAS)

Quick-XAS investigations were performed at the SuperXAS (X10DA) beamline, Swiss Light Source (SLS), Switzerland. The storage ring was operated at 2.4 GeV and 400 mA. A home-made spectro-electrochemical flow cell was used for the measurements

(Fig. S1). The classical three-electrode configuration consisted of the Cu foam as the working electrode, an Au foil served as the counter and a non-leakage Ag/AgCl (3 M KCl, EDAQ) was used as the reference electrode. All potentials were corrected for the ohmic iR drop. The basic design of the spectro-electrochemical flow-cell was published elsewhere [50]. For the Quick-XAS experiments at the Cu K-edge, the cell was adjusted in a way that the electrolyte thickness in the X-ray window was about 1 mm and the porous Cu foam was only 30–40 μm thick to obtain sufficient signal-to-noise ratio in the transmission mode. XAS experiments were carried out in CO_2-saturated 0.5 M $KHCO_3$ electrolyte solution (pH = 7.2) in the potential range from +0.8 V to −0.9 V vs. RHE. A syringe pump was used to establish a constant flow of CO_2-saturated electrolyte through the spectro-electrochemical cell. For the potential-dependent Quick-XAS measurements, a fast oscillating channel cut crystal monochromator with a frequency of 40 Hz (~40 scans per second) was employed. The ionization chambers for the detection of incident (I_0) and transmitted (I_1 and I_2) X-ray radiation were filled with N_2. IFEFFIT software suite [51] was used for the data processing which included the background subtraction, edge step normalization and conversion of the energy units (eV) to photoelectron wave vector k units (Å⁻¹) by assigning the photoelectron energy origin, E_0, corresponding to k = 0, to the first inflection point of the absorption edge. The resulting $\chi(k)$ functions were weighted with k^2 to compensate for the dampening of the XAS amplitude with increasing k. Linear combination fitting (LCF) analysis of the X-ray absorption near edge structure (XANES) spectra at the Cu K-edge was performed to establish the contribution of different chemical Cu species based on the reference spectra of Cu foil, Cu_2O and CuO. In addition, the extended X-ray absorption fine structure (EXAFS) spectra were Fourier-transformed to obtain pseudo radial structure functions (RSFs). The amplitude reduction factor (S_0^2) was obtained from the fit of the EXAFS spectrum of a Cu foil to be 0.78. Using the ARTEMIS software [51], the coordination number (N), interatomic bond length (R), mean squared bond length disorder (σ^2), and correction to the energy origin (ΔE_0), together with its error bars were established for Cu-Cu and Cu-O scattering pairs by fitting theoretical EXAFS signals to the data in R-space.

2.6. Operando X-ray diffraction (XRD)

Operando XRD experiments were performed at ID31 high energy beamline of the European Synchrotron Radiation Facility (ESRF). The X-ray beam was mono-chromatized with a Laue-Laue monochromator to the energy of 69 keV and focused to the size of 5 × 20 μm² (vertical × horizontal) at the sample position. The 2D XRD patterns were collected with a Dectris Pilatus 2 M CdTe detector. A custom made PEEK electrochemical flow cell [41,52] was used for the experiments (Fig. S2). The cell consists of a Pt wire serving as the counter electrode, a Ag/AgCl (3 M KCl, EDAQ) as the reference electrode and an oxidized Cu foam sample supported on carbon paper electrically connected with Au wire as the working electrode. The measurements were performed in grazing incidence geometry, incidence angle less than 1°, in CO_2-saturated 0.5 M $KHCO_3$ electrolyte. A continuous flow of fresh CO_2-saturated electrolyte solution through the spectro-electrochemical cell avoids any undesired accumulation of soluble Cu species in the investigated X-ray window. The sample was first measured at OCP and then the potentials were changed from +0.5 V to −0.5 V vs. RHE by applying potential steps of 100 mV. The resting time at each potential before the measurement was around 2 min and 15 s. The cell resistance was measured by the current-interrupt method. Potentials were corrected manually after the measurements. The raw 2D diffraction patterns were radially integrated using the pyFAI software package [53]. All reflections were normalized tak-

ing into the account different electron densities of the crystalline structures, such that they can be compared on an absolute scale. The initial powder pattern at OCP was subtracted from following data to correct for the complex background signal from the cell and substrate material.

2.7. Operando Raman spectroscopy

Raman spectra were collected by a LabRAM HR800 confocal microscope (Horiba Jobin Yvon) [54]. Calibration was performed using a silicon wafer standard (520.6 cm^{-1}). Raman spectroscopy was performed using a working distance of 8 mm between the objective lens (LMPLFLN from Olympus, 50X magnification) and the sample with a numerical aperture of 0.1 in order to focus a diode-pumped solid-state laser beam (excitation wavelength 633 nm, power 3 mW) on the sample. The Raman signal was collected in a back-scattering geometry using a lab-made spectro-electrochemical cell made of Kel-F (Fig. S3) [54–57]. For *operando* Raman experiments, the air-annealed Cu foam was electrodeposited on an activated carbon foil and placed on glassy carbon (3 mm diameter) support. A Ag/AgCl (3 M KCl, EDAQ) and a Au ring served as the reference and counter electrode, respectively. CO$_2$-saturated 0.5 M KHCO$_3$ solution was used as the electrolyte. A μ-Autolab III (EcoChemie) potentiostat was used for the electrochemical Raman measurements. The ohmic drop was determined using the positive feedback technique and compensated during the measurement. Steady-state Raman spectra were acquired after five minutes at each potential set point (from +0.5 V to −0.9 V vs. RHE, applied potential steps of 100 mV).

3. Results

3.1. Ex situ characterization of as deposited and annealed Cu foam catalysts

Fig. 1 shows white light interferometry (panel a) and SEM images of the Cu foam prior to (panels b-d) and after (panels e–g) the annealing treatment at 300 °C (12 h in air). A hierarchical pore structure was formed on the activated carbon foil support as a result of the Cu electrodeposition process that was superimposed on the vigorous hydrogen evolution reaction (HER) [11,12,44]. Fig. S4 in the supplementary file demonstrates the basic principle of the hydrogen bubble assisted metal foam electrodeposition. A Cu electrodeposition at -3.0 A cm^{-2} for 5s yielded a two-level foam architecture of interconnected open-cell pores with surface pore diameters ranging from 15 to 25 μm and a total foam thickness of approximately 30–43 μm, assuming that the deepest pores reach the carbon foil substrate (Fig. 1a, see also Fig. S5). These results are further corroborated by the side-view SEM

inspection of the as deposited Cu foam showing a foam thickness of ∼43 μm (Fig. S5j).

The mean pore diameter and foam thickness slightly deviate from those values for Cu foams supported on a Cu wafer substrate reported by Dutta et al. [11]. This is due to faradaic efficiencies of Cu deposition and the competing HER which are slightly different on the previously used Cu wafer substrate. Carbon was used as the support material in the present study to avoid any undesired contribution of the Cu wafer support to Cu related signals in the *operando* XAS and XRD experiments.

Important to note is that the thermal annealing does not affect the primary macro-porosity of the Cu foam (Fig. S6). In contrast to that, the secondary meso-porosity of the pore side-walls and particularly their dendritic fine structure undergoes substantial structural and compositional alterations during the annealing process. Prior to such thermal treatment, individual dendrites are composed of faceted Cu nanoparticles as evidenced by the high-
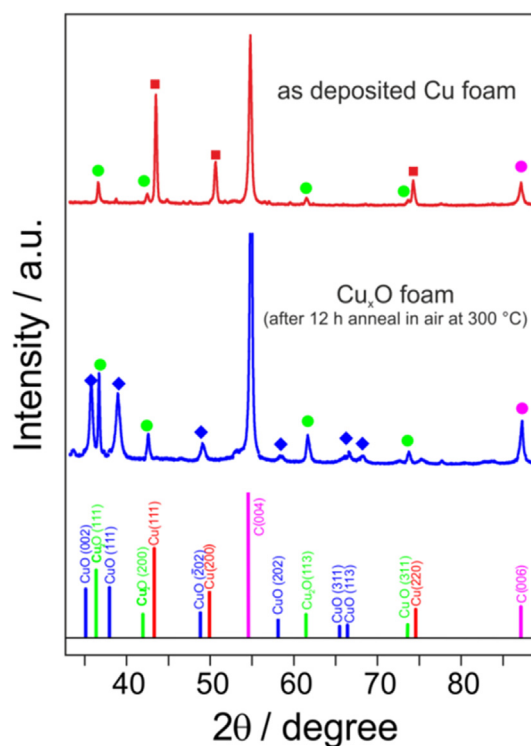
Fig. 2. X-ray diffractograms of the as deposited (red) and the thermally annealed (blue) Cu foam (300 °C, 12 h, in air). For comparison purposes the corresponding JCPDS reference data is indicated (Cu$_2$O: 050667, CuO: 410254, and polycrystalline Cu: 040836).
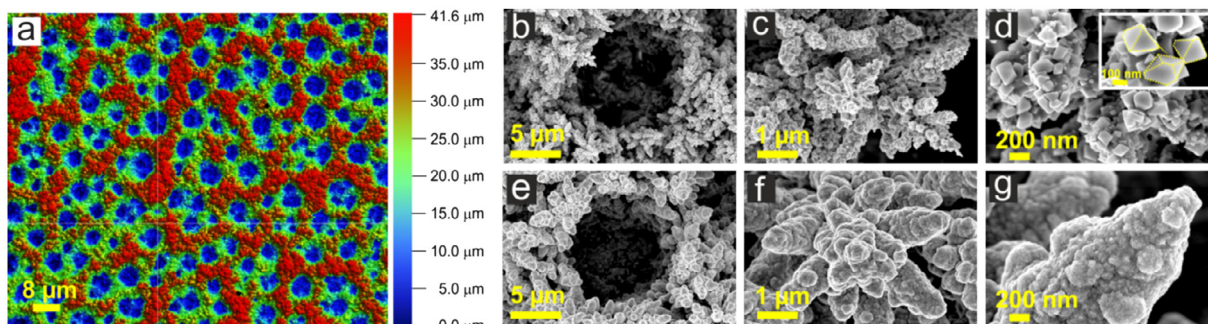
Fig. 1. (a) White-light interferometric characterization of the as deposited Cu foam (5 s deposition time at −3 A cm^{-2}); (b–d) SEM micrographs of the as deposited Cu foam; (e-g) SEM micrographs of the thermally annealed Cu foam (300 °C, 12 h, in air) denoted as Cu$_x$O foam.
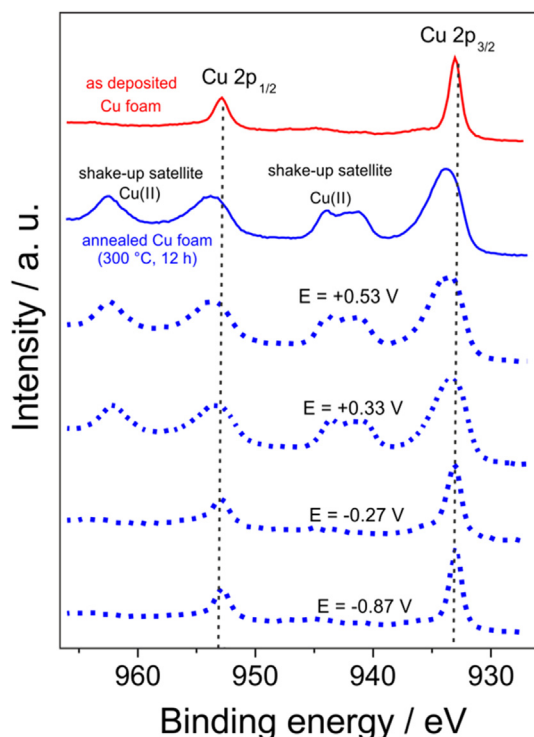
Fig. 3. XPS spectra (Cu$2p$ emission) of the Cu/Cu$_x$O foams. The red curve represents the as deposited foam sample, the blue curve shows the Cu$2p$ emission of the thermally annealed one (300 °C, 12 h, in air). The blue dotted spectra represent post-electrolysis XPS measurements carried out after 1 h potentiostatic electrolysis in CO$_2$ saturated 0.5 M KHCO$_3$ solution. The respective electrolysis potentials vs. RHE are indicated.

minor contribution originating from crystalline cuprous oxide (Cu$_2$O). Note that electrodeposited metal foams are prone to surface oxidation right after their emersion from the respective Cu plating bath and exposure to air [11,12]. All diffraction features related to metallic Cu have disappeared after the 12 h annealing treatment at 300 °C in air. Obviously, the as deposited metallic Cu foam has completely been transformed by the applied thermal treatment into an oxidic Cu$_x$O composite (mixture of Cu$_2$O and CuO). Note that thicker Cu foams deposited under similar experimental conditions (current density, metal ion concentration in solution), but using more extended deposition times, remain partly metallic in their interior upon annealing at 300 °C for 12 h in air as reported by Dutta et al. [12].

Complementary surface-sensitive XPS analysis of the as deposited Cu foam shows the spin-orbit split photoemissions of metallic Cu and cuprous oxide with binding energies (BE) of Cu$2p_{3/2}$ = 932.9 eV (FWHM = 1.26 eV) and Cu$2p_{1/2}$ = 952.6 eV (Fig. 3). Note that the XPS cannot discriminate between Cu(I) and Cu(0) species [12,58–60]. Thermal annealing at 300 °C leads to an up-ward shift of the Cu related photoemissions which goes along with a peak broadening and the appearance of characteristic shake-up satellites. These observations are clearly pointing to the presence of cupric oxide (CuO) at the surface of the Cu$_x$O foam [12]. The Cu$2p_{3/2}$ peak can be de-convoluted by considering two components with binding energies (peak maxima) at 932.8 eV and 933.7 eV which are assigned to Cu(I) and Cu(II), respectively (Fig. S7). The assignment of the photo-emission at 932.8 eV to Cu(I) species is based on the *ex situ* XRD data showing no experimental evidence for the presence of metallic Cu after the thermal treatment (Fig. 2). The deconvolution of both components (Fig. S7) yields a relative abundance of 68 at% Cu(I) as Cu$_2$O and 32 at% Cu(II) as CuO. Note that these values do not necessarily represent the bulk composition of the annealed Cu foam (Cu$_x$O) as the XPS is a surface-sensitive technique.

3.2. CO$_2$RR product analysis

To probe the performance of the annealed Cu foams, a dedicated campaign of potentiostatic electrolysis experiments (1 h duration) was carried out in the potential range from +0.07 V vs. RHE to −0.87 V vs. RHE. Note that a so-called multi-catalyst approach [61] was applied. A freshly prepared catalyst was used for each individual electrolysis experiment. Fig. 4 shows the CO$_2$RR product analysis derived from the thermally annealed Cu (Cu$_x$O) foam catalyst (see also Tables S1 and S2). For comparison purposes, the respective results of the as deposited Cu foam are presented in

resolution SEM micrograph (see inset in Figs. 1d and S5g–i). The annealing of the Cu foam at 300 °C induces the coalescence of the faceted nano-crystallites leaving non-textured dendrites behind (Figs. 1g, S6g–i). These morphological alterations taking place on the meso-scale result from the formation of intermixed CuO/Cu$_2$O phases (denoted hereinafter as Cu$_x$O) which involve the concerted mass transport of oxygen and copper into and out of the pristine crystalline dendrite structure.

This scenario becomes further supported by the corresponding *ex situ* XRD analysis presented in Fig. 2. As expected, XRD patterns of the as deposited Cu foam show all characteristic diffraction features of polycrystalline face-centered cubic (fcc) Cu and in addition

Fig. 4. Product distribution after 1 h CO$_2$RR electrolysis carried out in CO$_2$-saturated 0.5 M KHCO$_3$ using the Cu$_x$O foam (300 °C, 12 h, in air) as the catalyst; (a) CO$_2$RR product distribution represented as partial current densities; (b) CO$_2$RR product distribution represented as faradaic efficiencies (FEs); (c) Faradaic efficiencies for alcohol formation (EtOH, n-PrOH, and total alcohol efficiency) highlighted for two selected electrolysis potentials.

Fig. S8 (see also Tabled S3 and S4). The product distribution of the CO_2RR carried out over the as deposited Cu foam (Fig. S8) shows qualitatively the same trends as previously reported for other Cu foam electrocatalysts [11]. CO is the main CO_2RR product in the low overpotential regime reaching a maximum of faradaic efficiency (FE) of CO, FF_{CO} = 19% (j_{CO} = −0.18 mA cm^{-2}) at −0.47 V vs. RHE. The hydrocarbon pathways are opened at electrolysis potentials more neagtive than −0.8 V vs RHE. A characteristic feature of the electrodeposited Cu foam catalysts is the full suppression of the C1 (methane) reaction pathway [11]. A C2 hydrocarbon efficiency of 20% is yielded at −0.77 V vs. RHE (see Table S3) with a slight preference towards C_2H_6 (FE_{C2H6} = 11%). The unusual appearance of ethane as CO_2RR product has previously been rationalized on the basis of particular intermediate trapping effects inside the pores of the Cu foam electrocatalysts [11] facilitating in particular the re-adsorption of ethylene on the catalyst surface and its subsequent reductive hydrogenation. It should be noted that the faradaic efficiencies yielded for ethane and ethylene are lower as compared to the ones previously reported by Dutta et al. [11]. Both the total CO_2RR efficiency and the ratio of ethylene/ethane formation were, however, shown to be strongly depending on the (surface) pore size distribution and catalyst film thickness (controlled by the deposition time). Note that the Cu foams used herein were optimized with regard to the *operando* investigations (see below) in terms of film thickness and not with regard to the CO_2RR product distribution. A much smaller film thickness was chosen in the present study (see Fig. S5) as compared to the conditions yielding optimum CO_2RR efficiencies [11].

In Fig. 4a, the potential dependent product analysis of the CO_2-RR carried out over the oxide-derived Cu foam is represented in terms of partial current densities whereas in panel b the corresponding faradaic efficiencies (FEs) are shown. Minor CO_2RR activity towards CO starts already at −0.07 V vs. RHE. The partial current density for CO remains, however, on an extremely low level of only j_{CO} = −4 μA cm^{-2} (FE_{CO} = 8%) close to the detection limit in the GC analysis (Fig. 4). Changing the electrolysis potential to −0.27 V vs. RHE let the CO partial current increase by about one order of magnitude to j_{CO} = −0.05 mA cm^{-2} (FE_{CO} = 28%). This potential is identified as on-set of substantial CO evolution (see also discussion of Fig. 5f below). In addition, minor amounts of formate were detected ($j_{formate}$ = −4 μA cm^{-2}, $FE_{formate}$ = 2%). At −0.47 V vs. RHE the total CO_2RR current density has already raised to −0.44 mA cm^{-2}. The only CO_2RR products are CO (j_{CO} = −0.3 mA cm^{-2}, FE_{co} = 21%) and formate ($j_{formate}$ = −0.14 mA cm^{-2}, $FE_{formate}$ = 10%) again. At electrolysis potentials more negative than −0.6 V the hydrocarbon pathway is activated, thus leading to a further increase of the total CO_2RR current density to j_{CO2RR} = −2.65 mA cm^{-2} at −0.67 V. At this electrolysis potential ethylene (j_{C2H4} = −0.47 mA cm^{-2}, FE_{C2H4} = 6%) and ethane (j_{C2H6} = −0.62 mA cm^{-2}, FE_{C2H6} = 8%) were detected. The total CO_2-RR efficiency shows a constantly increasing trend in the potential range studied, and reaches a value of ~40% at −0.87 V vs. RHE (Fig. 4b).

In agreement with previous studies, the thermal annealing activates the Cu catalyst for C2 and C3 oxygenate production (Fig. 4). Note that no methanol production was observed in the product analysis. As already observed for the hydrocarbons, the C1 alcohol
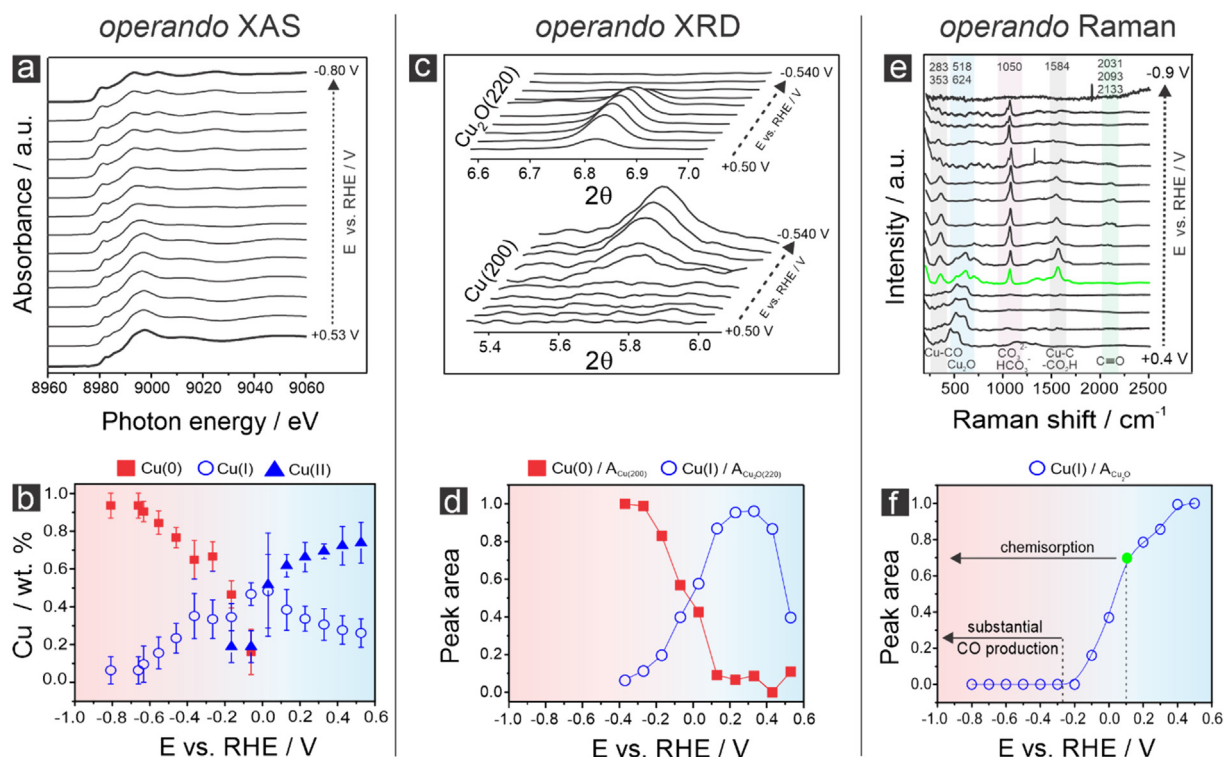
Fig. 5. Survey of experimental *operando* results demonstrating the potential-dependent oxide-metal transition of the catalyst precursor (Cu$_x$O foam). (a) Potential-dependent *operando* XANES spectra (Cu K-edge) of the thermally annealed Cu foam (Cu$_x$O) in CO_2-saturated 0.5 M KHCO$_3$; (b) Potential-dependent composition of the Cu$_x$O foam (relative content of Cu species: Cu(0), Cu(I), and Cu(II) derived from a linear combination fitting (LCF) of the XANES spectra shown in (a)); (c) Potential-dependent *operando* grazing-incidence X-ray diffractograms of the Cu$_2$O(220) and Cu(200) reflections; (d) Integrated and normalized intensities of the diffractograms shown in (c); (e) Corresponding potential-dependent *operando* Raman spectra; (f) Integrated and normalized peak intensities of the Cu$_2$O related Raman peaks (518 cm^{-1} and 624 cm^{-1}) shown in (e), the peak areas were normalized with respect to the most intense peaks at most positive electrode potentials. The red and blue colours in panel b, d, and f indicate the transition from the oxide to the metallic state of Cu.

pathway is fully blocked on the oxide-derived Cu foam catalyst. The partial current density for ethanol formation increases from j_{EtOH} = −0.86 mA cm^{-2} (FE$_{EtOH}$ = 5%) at −0.77 V vs. RHE to j_{EtOH} = −1.61 mA cm^{-2} (FE$_{EtOH}$ = 6.7%) at −0.87 V vs. RHE (Fig. 4c). The partial current density for n-propanol formation reaches a value of j_{PrOH} = −1.72 mA cm^{-2} (j_{PrOH} = 7.1%) at −0.87 V (Fig. 4c). All current densities discussed herein were normalized to the geometric surface area of the carbon support. Corresponding FE and partial current density (PDC) data normalized to the electrochemically active surface (ECSA, Fig. S13), determined by the viologen method, is provided in the supporting information (see Fig. S14 and Tables S5 and S6).

3.3. Post electrolysis XPS inspection

After completion of the 1 h lasting electrolysis, the used foam samples were transferred to an airtight and Ar containing (99.9999%, Carbagas, Switzerland) sample container to minimize further oxidation when exposed to air prior to the XPS inspection. CuO related photoemission features are clearly visible in the XPS spectra down to applied electrolysis potentials of +0.33 V vs. RHE (Fig. 3). Holding the potential for 1 h at −0.27 V is already sufficient to let all CuO related features disappear from the XPS spectrum which shows only characteristics of metallic Cu similar to the as deposited Cu foam. Note that the potential range where the reduction process of cupric and cuprous oxides is observed is fully consistent with thermodynamic predictions [33,62]. Our post electrolysis XPS results suggest that the surface of the thermally formed Cu oxides is already reduced at very low cathodic potentials, where only minimal traces of CO could be detected during CO$_2$RR (Fig. 4). Substantial CO$_2$RR activity on the thermally annealed Cu foam catalysts was observed only at potentials below −0.3 V vs. RHE, where the surface oxide layers are entirely transformed into metallic Cu. Therefore, the active catalyst for the CO$_2$RR can be indeed denoted as oxide-derived (OD) [11,12,21,23]. It should be noted, however, that these results do not exclude the presence of residual traces of sub-surface oxygen [22,32,34,35,37,38]. Its concentration might, however, be below the XPS detection limit.

3.4. Identical location (IL)-SEM study

The thermally induced formation of oxide phases from the metallic precursors and their subsequent electrochemical reduction back to the metallic state go along with changes in the morphology of the deposit, thus often considered as an important factor of the desired catalyst activation process [17]. To probe these morphological alterations, identical location (IL) SEM analysis was applied to the Cu foam catalysts in their different chemical states. Panels a–d in Fig. S9 represent the as deposited Cu foam whereas panels e-h show the corresponding Cu$_x$O foam obtained by the 12 h thermal annealing at 300 °C in air. In addition, panels i-l depict the metallic OD-Cu foam after the 1 h CO$_2$RR at −0.67 V vs. RHE. The primary macro-porosity of the Cu foam catalyst remains unaffected by the thermal treatment and the subsequent electrochemical reduction of the oxide phases under CO$_2$RR conditions. This observation demonstrates the structural benefits and robustness of the self-assembled Cu foam catalysts. Changes occur, however, on a smaller length scale starting with the disappearance of the facetted crystallites as a result of the thermal annealing and followed by a grain coarsening process upon the electrochemical reduction of the thermally formed oxides under CO$_2$RR conditions. A more fissured and rough surface appears along with a high density of nm-sized spherical Cu particles (Fig. S9l). Similar changes have recently been reported for dendritic Cu deposited on Cu mesh supports by Rahaman et al. [17]. This oxide-derived (OD)-Cu, which only forms under *operando* conditions, needs to

be considered as the actual catalyst for the CO$_2$RR being active for hydrocarbon and alcohol production.

3.5. Operando Quick X-ray absorption spectroscopy (Quick-XAS)

To probe changes in the chemical state of copper before and during CO$_2$RR, Cu K-edge Quick-XAS measurements were carried out in CO$_2$-saturated 0.5 M KHCO$_3$ for both the annealed foam (Figs. 5a, b, S10, and 6) and the as deposited one (Fig. S11). Note that no substantial changes in the electronic state of copper were observed for the as deposited Cu foam sample within the entire range of potentials applied (Fig. S11). Changes in the potential-dependent Cu K-edge XANES (X-ray Absorption Near Edge Spectroscopy) spectra of the Cu$_x$O foam can clearly be attributed to potential-dependent redox state changes of Cu species (Fig. 5a). For instance, the observed shifts of the transition energy are due to changes of the ion charges and their potential-dependent redox-state (8984.3 eV, 8981.1 eV and 8979.7 eV for CuO, Cu$_2$O and Cu, respectively). The trend of decreasing Cu K-edge (transition) energies by applying more cathodic potentials is clearly pointing to the reduction of the Cu$_x$O foam mediated by the
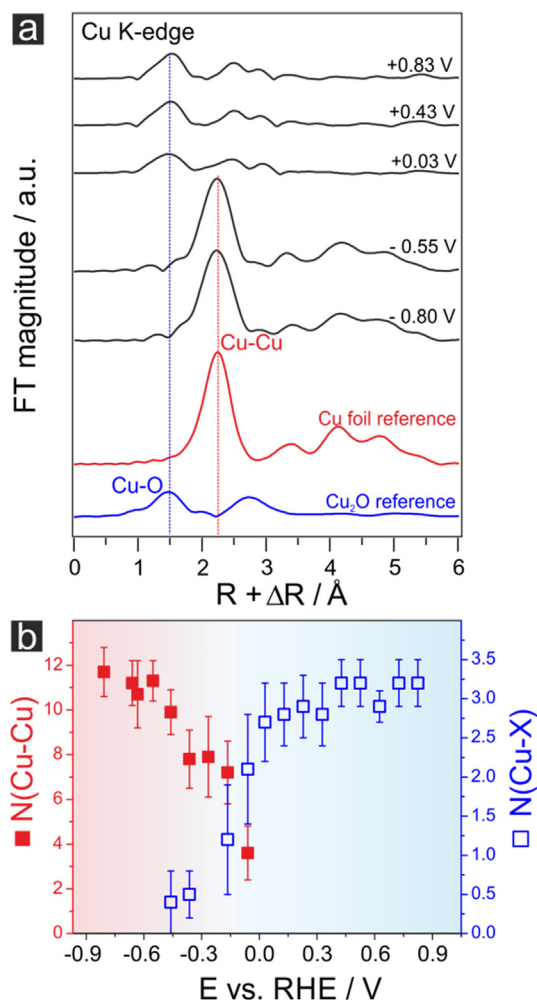
Fig. 6. (a) Changes of the Fourier-transform magnitudes of the k^2-weighted EXAFS data at the Cu K-edge as function of the applied potential for the Cu$_x$O foam. For comparison purposes also the EXAFS reference spectra for Cu$_2$O (blue) and metallic Cu (red) are provided; (b) Dynamic behavior of the partial coordination numbers for Cu-Cu and Cu-X (X = O or C) scattering pairs as function of the applied potential. The red and blue colours in panel b indicate the transition from the oxide to the metallic state of the oxidized copper. See also Table S7.

applied electrode potential. Obviously this chemical transition is already completed at potentials more positive than the onset of substantial hydrocarbon and alcohol formation (Fig. 4), which is in full agreement with the post electrolysis XPS analysis (Fig. 3).

A linear combination fitting (LCF) analysis was applied to the XANES data. Cu K-edge XANES spectra of the Cu foil, Cu_2O and CuO served as references for the LCF analysis. Note that the quality of the reference spectra used substantially influences the accuracy of the LCF analysis. As a result of this fitting, Fig. 5b shows changes of the Cu(0), Cu(I), and Cu(II) contents in the Cu_xO foam as a function of the potential applied. The LCF analysis suggests that the Cu_xO foam at + 0.6 V vs. RHE predominantly consists of Cu(II) species, assigned to cupric CuO, whereas only a lower Cu(I) content was observed (25–35 wt%). The latter is assigned to cuprous Cu_2O. Note that this Cu(I)/Cu(II) ratio is different from that derived from the more surface sensitive post electrolysis XPS inspection (Figs. 3, S7). When gradually changing the potential to more cathodic values, Cu(II) and Cu(I) species are in principle retained in the range between 0 and 0.6 V vs. RHE. Their relative abundance change, thus pointing to a potential-induced transition from Cu(II) to Cu(I) prior to the reduction of the oxidic precursor to metallic Cu(0) which starts in the 'bulk' of the foam material at 0 V vs. RHE. At potentials below 0 V vs. RHE the Cu(II) abundance drops down to zero, whereas Cu(I) species are present in the bulk down to potentials of −0.5 V vs. RHE. The potential-dependent decrease of the Cu(I) content below 0 V vs. RHE is clearly anti-correlated to the increase of the Cu(0) abundance (Fig. 5b). The transition from the oxidic precursor to metallic Cu in the bulk is completed at about −0.7 V vs. RHE.

Further, the Fourier-transformed k^2-weighted EXAFS spectra for the electrodeposited and annealed Cu foams as a function of the applied potential are illustrated in Figs. 6 and S10. From the EXAFS data, the coordination number (N), the interatomic bond length (R), the mean squared bond length disorder (σ^2), and correction to the energy origin (ΔE_0) for the Cu-Cu and Cu-O scattering pairs were derived and listed in Tables S7 and S8. Fig. 6a displays a representative set of EXAFS spectra of the Cu_xO foam. For comparison the reference spectra for metallic Cu (foil) and Cu_2O are also provided. Results of the analysis are displayed in Fig. 6b showing changes of the Cu-X (X = O, C) and Cu-Cu coordination numbers as function of the potential applied. Due to the scattering properties of light elements, it is impossible to distinguish between Cu-O and Cu-C by EXAFS. A very minor contribution from Cu-C coordination to the overall EXAFS signal might result from the appearance of chemisorbed CO_2RR intermediates adsorbed via the carbon to the Cu catalyst surface (see Discussion section below). At the applied potential of +0.8 V vs. RHE the mean (averaged) coordination number (N) for Cu-X is 3.2 ± 0.2 in agreement with the assumption of an oxidic foam material (catalyst precursor) that is composed of a Cu_2O/CuO mixture. Note that for an annealing temperature of 300 °C, applied for the preparation of the Cu_xO foam, the Cu_2O is expected to be crystalline (space group of Pn-3 m with a coordination number N(Cu-O) = 4 in the first shell), whereas the CuO remains largely in an amorphous state [11,12,17]. Substantially higher annealing temperatures are typically required to yield a fully crystalline CuO phase than for crystalline Cu_2O. In the potential range between +0.8 V and 0 V vs. RHE the mean coordination number N(Cu-X) drops down moderately. A substantial alteration occurs, however, at potentials below 0 V vs. RHE, which involves the appearance of metallic Cu (see also Figs. 3 and 5b). In the very initial stage of this transition, the metallic Cu is highly under-coordinated. Values of the N(Cu-Cu) start from 3.6 ± 1.2 at 0 V vs. RHE and gradually approach the target value of 12 for a face-centered cubic (fcc) bulk copper at highest cathodic potentials applied herein (e.g., N(Cu-Cu) = 11.7 ± 1.1 at −0.8 V vs. RHE).

3.6. Operando X-ray diffraction (XRD)

To further study the structural transition of the Cu_2O/CuO composite to the metallic fcc Cu we applied operando XRD in a gracing incidence geometry [63]. For the survey in Fig. 5c we restrict ourselves on the evolution of the $Cu_2O(220)$ (fingerprint for the oxide precursor) and Cu(200) (fingerprint for the metallic fcc Cu) diffraction peaks. Their noise to signal ratio was most appropriate for the quantitative analysis. Interestingly, the integrated intensity of the $Cu_2O(220)$ diffraction peak first increases when going from +0.5 V to +0.2 V vs. RHE. This trend is consistent with the assumption of an intermediate crystalline Cu_2O phase which accumulates in the initial stage of the oxide-metal transition in the foam material on the expense of the partially amorphous/crystalline CuO phase. A qualitatively similar trend of increasing Cu(I) content was observed in the corresponding XAS experiment (Fig. 5b). However, the disappearance of the Cu_2O related diffraction pattern with negative going potentials is already completed at −0.4 V vs. RHE, whereas the XAS experiment indicates the presence of Cu(I) species for potentials down to −0.8 V vs. RHE. These deviations in the particular potential-dependence of the Cu(I)(XAS)/Cu$_2$O(XRD) stability regime are most likely related to the intrinsic characteristics of both operando techniques (see Discussion section below). Our XRD results are in full agreement with the work by Ahn et al. also demonstrating the disappearance of copper oxide species prior to the CO_2RR onset [64]. An important finding of the XRD analysis concerns the average size of the coherent domains for Cu_2O and fcc Cu calculated on the basis of the Scherrer formula. The mean crystallite size of the Cu_2O in the range between 0 V and 0.7 V vs. RHE is 13.3 nm whereas a mean crystallite size drops down to 6.7 nm when the fcc Cu has formed below −0.2 V vs. RHE. This large shift of the mean domain size cannot solely be rationalized by changes of the unit-cell volume during the oxide-metal transition. The identical location (IL)-SEM analysis demonstrates morphological changes on the nm length-scale upon oxide reduction involving the appearance of smaller nanoparticles on the dendritic foam structure. In general, the reduction of the oxidic precursor typically leads to an increase of the electrochemically active surface area (ECSA, see also Figs. S12 and S13) [11,12,41,49,61]. Such change in the micro- and nano-structure upon reduction of the oxidic precursor is most likely the origin of the different performances of Cu nanomaterials prepared from similar precursors. These effects are also known from other types of catalyst materials, e.g. those used for the oxygen reduction reaction (ORR) [65–67]. Not only is the ECSA affected by these morphological alteration but also the density of low-coordinated surface sites and the grain boundary density are altered, explain changes in the overall catalytic activity and product selectivity for the CO_2RR.

3.7. Operando Raman spectroscopy

Whereas XRD and XAS are techniques which are both sensitive to the bulk of the catalyst material, the operando Raman spectroscopy provides additional and highly valuable insights into chemical state changes of the catalyst surface. In addition, chemisorption phenomena of CO_2RR intermediates become accessible thereby providing insights into the CO_2RR reaction mechanism [68]. The highly porous nature of the foam material might further facilitate the Raman experiment due to the SERS (Surface Enhanced Raman Spectroscopy) effect, at least when the Cu_xO precursor has been (partially) transformed to its metallic state [69].

In the potential-dependent Raman experiment (shown in Fig. 5e) the potential applied was started at the open circuit potential (OCP) followed by a stepwise change of the potential from +0.5 V vs. RHE to −0.8 V vs. RHE. Note that a significant change
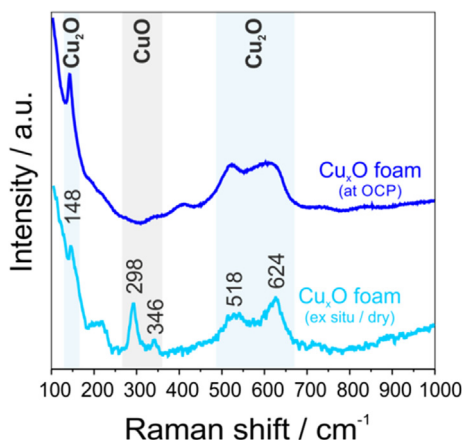
Fig. 7. Raman spectra of the Cu$_x$O foam (after annealing of the as deposited Cu foam at 300 °C, 12 h, in air). The bright blue spectrum (bottom) represents the dry Cu$_x$O foam (ex situ) whereas the blue one (top) shows the Cu$_x$O foam exposed to the CO$_2$-saturated 0.5 M KHCO$_3$ solution under OCP conditions (OCP = +0.504 V vs. RHE; see also Fig. S15).

in the surface condition takes already place, when the Cu$_x$O foam is brought into the contact with the CO$_2$-saturated 0.5 M KHCO$_3$ electrolyte solution under OCP conditions. This pronounced surface effect is highlighted in Fig. 7 comparing the Raman spectrum of the dry Cu$_x$O foam sample with the one measured under steady-state conditions at the OCP. Raman modes observed at 148 cm^{-1}, 518 cm^{-1}, and 624 cm^{-1} are ascribed to cuprous oxide species (Cu$_2$O), whereas peaks at 298 cm^{-1} and 346 cm^{-1} have to be assigned to cupric oxide [40,70,71]. After exposure to the electrolyte at OCP, the CuO related vibrational modes have completely disappeared from the spectrum. Only vibrational modes of the cuprous oxide (Cu$_2$O) are left thus demonstrating that the catalyst precursor surface is exclusively terminated by Cu(I) species in the initial stage of the potential step experiment presented in Fig. 5e. Note that no alteration of this kind were observed in the corresponding XRD and XAS experiments confirming once more that these techniques are largely insensitive to the catalyst surface, when applied to foam type of materials. These materials exhibit a large and dominating contribution of the bulk to the XRD and XAS signals. For the quantitative analysis of the Raman spectra we focused on the vibrational modes at 518 cm^{-1} and 624 cm^{-1} as spectroscopic fingerprints for the presence of cupric surface oxide species. Their integrated intensities are displayed in Fig. 5f as function of the applied potential. The overall trend of decreasing integrated intensities with decreasing applied potentials is qualitatively similar to the one derived from the *operando* XRD (Fig. 5d). Slight deviations concern, however, the initial stage of the oxide reduction process in the potential range from +0.5 V to +0.1 V vs. RHE, where the XRD shows an initial increase of the Cu$_2$O(220) related intensities passing a maximum at +0.1 V vs. RHE (Fig. 5d). The latter trend has been ascribed to the transient increase of the Cu$_2$O content in the bulk of the foam material, originating from the partial reduction of the amorphous CuO phases. Note that this transition occurs spontaneously at the surface when brought into contact to the electrolyte (Fig. 7). Obviously the 'surface oxide reduction' proceeds faster and at slightly more positive potentials than the corresponding transition of the oxidic 'bulk phases' probed by operando XAS and XRD. Delayed (on the potential scale) is in particular the disappearance of the Cu(I) in the XAS experiment (Fig. 5b) suggesting that the reduction of residual Cu(I) in the final state of the transition process (between −0.3 and −0.6 V vs. RHE) occurs from a largely disordered state which is still detectable by the XAS but invisible in the XRD.

Operando Raman spectroscopy provides not only insights into the chemical state of the catalyst (precursor) surface but also on the appearance and disappearance of chemisorbed intermediates associated to the CO$_2$RR. Raman modes observed at 283 cm^{-1}/253 cm^{-1}, 1050 cm^{-1}, 1584 cm^{-1} and 2031 cm^{-1}/2093 cm^{-1}/2133 cm^{-1} can be, in full agreement to the literature, assigned to CO$_{ads}$, HCO$_{ads}^{-2}$ and HCOOH$_{ads}$ species [71,72]. These intermediates start to appear only from potentials of +0.2 V vs. RHE on (see green highlighted spectrum in Fig. 5e), where a certain fraction of the surface Cu$_2$O has already been disappeared from the surface (see also Discussion section below for further information on the Raman spectroscopy's results).
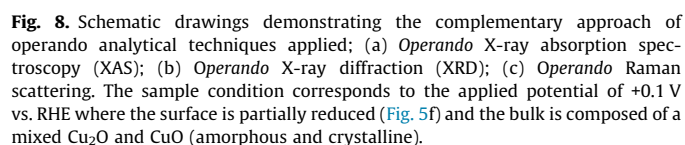
4. Discussion

Understanding the activation of oxidic precursor catalyst materials for the CO$_2$RR requires the application of highly complementary *operando* techniques. Fig. 8 demonstrates the basic working principles of the approaches applied herein. It further indicates their particular strengths and weaknesses for the analysis of the potential-mediated oxide-metal transition which is considered essential for the activation process of the oxidic Cu$_x$O precursor in particular when alcohols are targeted as CO$_2$RR products.

The XAS technique (XANES, EXAFS) is sensitive to the bulk of the catalyst (precursor) material and provides valuable information on the oxidation state and related coordination number changes which go along with the electrochemical reduction of the Cu$_x$O foam. Although considered as high-surface area catalysts, Cu foams exhibit a more unfavorable volume (bulk) to surface ratio as compared to nanoparticulate catalyst materials. This is why the XAS data acquired from the Cu$_x$O electro-reduction predominantly originate from the bulk with rather minor contribution from the surface of the oxide/metal foam (see Fig. S10). A clear strength of the XAS is, however, related to its capability of probing oxidation state changes even when (partially) amorphous phases are involved. This is particularly important for those structurally demanding samples where the crystalline oxide phases are not fully developed [12], e.g. in the case of the Cu$_x$O foam discussed herein. It has been demonstrated that oxide-metal transitions may occur via non-crystalline intermediate states, particularly in their final stage (see 'delayed' Cu(I) disappearance in Fig. 5b (XAS) compared to Fig. 5d (XRD)). This is why XAS is superior to all other techniques used herein in determining the ultimate completion of the (bulk) oxide-metal transition [11,12,41].

Operando XRD is highly complementary to the XAS technique as it allows monitoring changes in the crystal structure which often go along with the oxidation state alterations. In this present case, XRD could identify the crystalline Cu$_2$O as an intermediate phase whose abundance temporarily increases in the bulk phase during the Cu$_x$O reduction process (Fig. 5d) in full accordance with the XAS (Fig. 5b). Particularly valuable is the comparison of the XAS and XRD data in the highly cathodic potential regime suggesting the persistence of structurally disordered Cu$_2$O (and therefore not visible in the XRD, see Fig. 5d) at potentials more negative than those expected from the structure-sensitive XRD.

More sensitive to the very initial stage of the oxide-metal transition is the *operando* Raman spectroscopy (Figs. 5e, f and 7). *Operando* Raman spectroscopy probes predominantly the surface of the Cu/Cu$_x$O foams with little contributions from the near surface bulk regime.

Structural alterations already occur when the Cu$_x$O is exposed to electrolyte under OCP conditions. The presence of cupric oxide (CuO) at the surface of the dry sample has been confirmed by both ex situ XPS (Fig. 3) and Raman spectroscopy (Fig. 7). It instantaneously disappears from the outermost surface of the Cu$_x$O foam

Fig. 8. Schematic drawings demonstrating the complementary approach of operando analytical techniques applied; (a) *Operando* X-ray absorption spectroscopy (XAS); (b) O*perando* X-ray diffraction (XRD); (c) O*perando* Raman scattering. The sample condition corresponds to the applied potential of +0.1 V vs. RHE where the surface is partially reduced (Fig. 5f) and the bulk is composed of a mixed Cu_2O and CuO (amorphous and crystalline).

when brought into contact with the electrolyte phase, whereas the Cu(II) → Cu(I) transition is completed in the bulk material only at potentials more negative than −0.2 V vs. RHE (Fig. 5b and d). Note that the Raman spectroscopy does not detect any CuO related vibrational modes at the OCP (Fig. 7) and at any applied potential (Fig. 5e), whereas the *operando* XAS clearly proves CuO as the main constituent of the Cu_xO foam material in the potential range between +0.6 and +0.1 V vs. RHE (Fig. 5b). This experimental observation clearly indicates that, under the given experimental conditions, the Raman spectroscopy has a highly limited probing depth making it to a surface sensitive technique with little or even negligible contributions from the 'bulk' material.

The comparison of the *operando* techniques applied (Fig. 5) clearly points to a huge difference in the potential-dependent surface phase behavior and corresponding structural and compositional transitions in the respective 3D volume of the foam material. Based on our comprehensive analysis, we conclude that all compositional and redox state changes in the bulk of the Cu_xO foam are 'delayed' on the potential scale compared to corresponding processes taking place at the oxide precursor surface which is in contact to the electrolyte solution.

Generally, the disappearance of the Cu_2O is anti-correlated to the appearance of metallic Cu (see Fig. 5b).

According to the *operando* Raman spectroscopy, concerted chemisorption phenomena of carbonate/bicarbonate and CO_2 related species set in at a potential of +0.1 V vs. RHE (highlighted green in Fig. 5e and f). This also involves the appearance of Raman features at 283 cm^{-1}/353 cm^{-1} that are commonly ascribed to Cu (0)–CO vibrational modes involving metallic Cu as binding partner [72–74]. This particular feature in the Raman spectrum can therefore be considered as a clear spectroscopic fingerprint for the appearance of metallic Cu. Raman features of the adsorbed species might be further enhanced by the SERS effect originating from the appearance of metallic domains on the foam surface (Fig. 5e, highlighted green).

Important to note is that all Raman features not related to the oxides (Cu_2O: 148 cm^{-1}, 518 cm^{-1}, and 624 cm^{-1}; CuO: 298 cm^{-1} and 346 cm^{-1}) appear along with the ones at 283 cm^{-1}/353 cm^{-1} (Cu fingerprint). This observation let us conclude that the chemisorption of carbonate/bicarbonate and CO_2 related species takes preferentially place on metallic Cu domains that obviously co-exist already at these potentials (+0.1 V vs. RHE) with surface domains of cuprous Cu_2O (Fig. 5e). These surface-confined processes at most positive applied potentials remain invisible for the *operando* XAS and XRD.

When comparing the acquired *operando* Raman data (Fig. 5f), which reflect those surface properties most relevant for the electrocatalytic activity of the Cu foam, with the potential-dependent CO_2RR product distribution in Fig. 4, it becomes evident that neither CuO nor Cu_2O species are detectable at the catalyst surface when substantial CO evolution sets in at applied potentials close to −0.3 V vs. RHE (Fig. 4b). Note, however, that the overall oxide reduction process in the bulk is not yet completed under these experimental conditions (Fig. 5b and 5d). The foam as a whole needs at these potentials to be considered as a mixed metal/oxide composite in the very initial stage of CO_2RR. The question, whether and if yes to which extent, the remaining oxide domains in the bulk of the foam catalyst actively participate in the initial CO_2RR, cannot be ultimately answered herein. What becomes, however, obvious from the comprehensive survey of the applied *operando* techniques (Fig. 5) is that both hydrocarbon formation and alcohol production take place on an activated Cu foam catalysts where the oxidic species have completely disappeared not only from the surface but

also from the bulk of the foam material. These findings are in full agreement with the work by Mandal et al. [29].

Note that the *operando* XAS and Raman measurements were not extended to potentials more negative than -0.8 vs. RHE (potential range of hydrocarbon and alcohol formation) as it is rather unlikely that oxidic species re-appear under these extremely cathodic conditions.

5. Conclusion

We applied herein a set of highly complementary *operando* techniques sensitive to potential-dependent alteration of oxidic precursor materials used for the electrochemical reduction of CO_2 into value-added products such as hydrocarbons and higher alcohols.

Our analyses strongly suggest that the overall oxide-metal transition commences at the oxidic precursor surface. When brought into contact with the CO_2-saturated solution cupric oxide (CuO) species spontaneously disappear from the surface leaving a Cu_2O enriched interface behind as starting point for further potential-mediated surface transformations. *Operando* Raman spectroscopy further indicates that chemisorption phenomena of CO_2 related species preferentially occurs on metallic Cu and not on oxidic Cu species.

Particularly valuable is the comparison with the bulk-sensitive XAS and XRD techniques which both indicate oxide-metal transitions that are 'delayed' on the potential scale with respect to what is observed in the surface-sensitive Raman spectroscopy. The in-depth analysis of XAS and XRD data further revealed that the ultimate formation of metallic Cu at most cathode potentials applied herein occurs from Cu_2O lacking long-range transitional order. XRD showed the disappearance of crystalline Cu_2O before completion of the $Cu(I) \rightarrow Cu(0)$ transition as probed by the XAS.

All three *operando* techniques applied herein consistently prove, however, that the oxides are entirely reduced to the metallic state of Cu before the production of hydrocarbons and alcohols sets in.

This study demonstrates that a complementary approach of *operando* investigations is required to derive a complete view on the potential induced metal-oxide transition required to activate the Cu catalyst in particular towards alcohol formation.

Declaration of Competing Interest

The authors declare that they have no known competing financial interests or personal relationships that could have appeared to influence the work reported in this paper.

Acknowledgement

Appendix A. Supplementary material

Supplementary data to this article can be found online at https://doi.org/10.1016/j.jcat.2020.06.024.

References

[1] G.M.D. Earth System Research Laboratory, https://www.esrl.noaa.gov/gmd/ccgg/trends/, in, Earth System Research Laboratory, Global Monitoring Division, https://www.esrl.noaa.gov/gmd/ccgg/trends/, 2018.

[2] N. Kittner, F. Lill, D.M. Kammen, Energy storage deployment and innovation for the clean energy transition, Nat. Energy 2 (2017) 17125.

[3] B.D. Solomon, K. Krishna, The coming sustainable energy transition: History, strategies, and outlook, Energy Policy 39 (2011) 7422–7431.

[4] Change is in the air, Nat. Catalysis, 1 (2018) 93-93.

[5] M.G. Kibria, C.-T. Dinh, A. Seifitokaldani, P. De Luna, T. Burdyny, R. Quintero-Bermudez, M.B. Ross, O.S. Bushuyev, F.P. García de Arquer, P. Yang, D. Sinton, E.H. Sargent, A surface reconstruction route to high productivity and selectivity in CO_2 electroreduction toward C2+ hydrocarbons, Adv. Mater. 30 (2018) 1804867.

[6] Y. Zhou, F. Che, M. Liu, C. Zou, Z. Liang, P. De Luna, H. Yuan, J. Li, Z. Wang, H. Xie, H. Li, P. Chen, E. Bladt, R. Quintero-Bermudez, T.-K. Sham, S. Bals, J. Hofkens, D. Sinton, G. Chen, E.H. Sargent, Dopant-induced electron localization drives CO_2 reduction to C2 hydrocarbons, Nat. Chem. 10 (2018) 974–980.

[7] Y. Hori, A. Murata, R. Takahashi, Formation of hydrocarbons in the electrochemical reduction of carbon dioxide at a copper electrode in aqueous solution, J. Chem. Soc., Faraday Trans. 1: Phys. Chem. Condens. Phases 85 (1989) 2309–2326.

[8] Y. Hori, A. Murata, R. Takahashi, S. Suzuki, Enhanced formation of ethylene and alcohols at ambient temperature and pressure in electrochemical reduction of carbon dioxide at a copper electrode, J. Chem. Soc., Chem. Commun. (1988) 17–19.

[9] Y. Hori, K. Kikuchi, S. Suzuki, Production of CO and CH_4 in electrochemical reduction of CO_2 at metal electrodes in aqueous hydrogencarbonate solution, Chem. Lett. 14 (1985) 1695–1698.

[10] S. Ma, M. Sadakiyo, R. Luo, M. Heima, M. Yamauchi, P.J.A. Kenis, One-step electrosynthesis of ethylene and ethanol from CO_2 in an alkaline electrolyzer, J. Power Sources 301 (2016) 219–228.

[11] A. Dutta, M. Rahaman, N.C. Luedi, M. Mohos, P. Broekmann, Morphology matters: tuning the product distribution of CO_2 electroreduction on oxide-derived Cu foam catalysts, ACS Catal. 6 (2016) 3804–3814.

[12] A. Dutta, M. Rahaman, M. Mohos, A. Zanetti, P. Broekmann, Electrochemical CO_2 conversion using skeleton (sponge) type of Cu catalysts, ACS Catal. 7 (2017) 5431–5437.

[13] R.M. Arán-Ais, F. Scholten, S. Kunze, R. Rizo, B. Roldan Cuenya, The role of in situ generated morphological motifs and Cu(i) species in C2+ product selectivity during CO_2 pulsed electroreduction, Nat. Energy 5 (2020) 317–325.

[14] K.W. Frese, S. Leach, Electrochemical reduction of carbon dioxide to methane, methanol, and CO on Ru electrodes, J. Electrochem. Soc. 132 (1985) 259–260.

[15] K.P. Kuhl, T. Hatsukade, E.R. Cave, D.N. Abram, J. Kibsgaard, T.F. Jaramillo, Electrocatalytic conversion of carbon dioxide to methane and methanol on transition metal surfaces, J. Am. Chem. Soc. 136 (2014) 14107–14113.

[16] M. Le, M. Ren, Z. Zhang, P.T. Sprunger, R.L. Kurtz, J.C. Flake, Electrochemical reduction of CO_2 to CH_3OH at copper oxide surfaces, J. Electrochem. Soc. 158 (2011) E45.

[17] M. Rahaman, A. Dutta, A. Zanetti, P. Broekmann, Electrochemical reduction of CO_2 into multicarbon alcohols on activated Cu mesh catalysts: an identical location (IL) study, ACS Catal. 7 (2017) 7946–7956.

[18] D. Ren, N.T. Wong, A.D. Handoko, Y. Huang, B.S. Yeo, Mechanistic insights into the enhanced activity and stability of agglomerated Cu nanocrystals for the electrochemical reduction of carbon dioxide to n-propanol, J. Phys. Chem. Lett. 7 (2016) 20–24.

[19] K. Zhao, Y. Liu, X. Quan, S. Chen, H. Yu, CO2 electroreduction at low overpotential on oxide-derived Cu/carbons fabricated from metal organic framework, ACS Appl. Mater. Interfaces 9 (2017) 5302–5311.

[20] Y.C. Li, Z. Wang, T. Yuan, D.-H. Nam, M. Luo, J. Wicks, B. Chen, J. Li, F. Li, F.P.G. de Arquer, Y. Wang, C.-T. Dinh, O. Voznyy, D. Sinton, E.H. Sargent, Binding site diversity promotes CO_2 electroreduction to ethanol, J. Am. Chem. Soc. 141 (2019) 8584–8591.

[21] K.W. Frese, Electrochemical reduction of CO_2 at intentionally oxidized copper electrodes, J. Electrochem. Soc. 138 (1991) 3338–3344.

[22] D. Gao, I. Zegkinoglou, N.J. Divins, F. Scholten, I. Sinev, P. Grosse, B. Roldan Cuenya, Plasma-activated copper nanocube catalysts for efficient carbon dioxide electroreduction to hydrocarbons and alcohols, ACS Nano 11 (2017) 4825–4831.

[23] C.W. Li, M.W. Kanan, CO_2 reduction at low overpotential on Cu electrodes resulting from the reduction of thick Cu_2O films, J. Am. Chem. Soc. 134 (2012) 7231–7234.

[24] R. Kas, R. Kortlever, A. Milbrat, M.T.M. Koper, G. Mul, J. Baltrusaitis, Electrochemical CO_2 reduction on Cu_2O-derived copper nanoparticles: controlling the catalytic selectivity of hydrocarbons, PCCP 16 (2014) 12194–12201.

[25] C.W. Li, J. Ciston, M.W. Kanan, Electroreduction of carbon monoxide to liquid fuel on oxide-derived nanocrystalline copper, Nature 508 (2014) 504–507.

[26] M. Ma, K. Djanashvili, W.A. Smith, Selective electrochemical reduction of CO$_2$ to CO on CuO-derived Cu nanowires, PCCP 17 (2015) 20861–20867.

[27] D. Ren, Y. Deng, A.D. Handoko, C.S. Chen, S. Malkhandi, B.S. Yeo, Selective electrochemical reduction of carbon dioxide to ethylene and ethanol on copper (I) oxide catalysts, ACS Catal. 5 (2015) 2814–2821.

[28] F.S. Roberts, K.P. Kuhl, A. Nilsson, High selectivity for ethylene from carbon dioxide reduction over copper nanocube electrocatalysts, Angew. Chem. Int. Ed. 54 (2015) 5179–5182.

[29] L. Mandal, K.R. Yang, M.R. Motapothula, D. Ren, P. Lobaccaro, A. Patra, M. Sherburne, V.S. Batista, B.S. Yeo, J.W. Ager, J. Martin, T. Venkatesan, Investigating the role of copper oxide in electrochemical CO$_2$ reduction in real time, ACS Appl. Mater. Interfaces 10 (2018) 8574–8584.

[30] Y. Lum, J.W. Ager, Stability of residual oxides in oxide-derived copper catalysts for electrochemical CO$_2$ reduction investigated with 18O labeling, Angew. Chem. Int. Ed. 57 (2018) 551–554.

[31] W. Tang, A.A. Peterson, A.S. Varela, Z.P. Jovanov, L. Bech, W.J. Durand, S. Dahl, J. K. Nørskov, I. Chorkendorff, The importance of surface morphology in controlling the selectivity of polycrystalline copper for CO$_2$ electroreduction, PCCP 14 (2012) 76–81.

[32] H. Mistry, A.S. Varela, C.S. Bonifacio, I. Zegkinoglou, I. Sinev, Y.-W. Choi, K. Kisslinger, E.A. Stach, J.C. Yang, P. Strasser, B.R. Cuenya, Highly selective plasma-activated copper catalysts for carbon dioxide reduction to ethylene, Nat. Commun. 7 (2016) 12123.

[33] B. Beverskog, I. Puigdomenech, Revised Pourbaix diagrams for copper at 25 to 300°C, J. Electrochem. Soc. 144 (1997) 3476–3483.

[34] F. Cavalca, R. Ferragut, S. Aghion, A. Eilert, O. Diaz-Morales, C. Liu, A.L. Koh, T. W. Hansen, L.G.M. Pettersson, A. Nilsson, Nature and distribution of stable subsurface oxygen in copper electrodes during electrochemical CO$_2$ reduction, J. Phys. Chem. C 121 (2017) 25003–25009.

[35] A. Eilert, F. Cavalca, F.S. Roberts, J. Osterwalder, C. Liu, M. Favaro, E.J. Crumlin, H. Ogasawara, D. Friebel, L.G.M. Pettersson, A. Nilsson, Subsurface oxygen in oxide-derived copper electrocatalysts for carbon dioxide reduction, J. Phys. Chem. Lett. 8 (2017) 285–290.

[36] H. Mistry, R. Reske, Z. Zeng, Z.-J. Zhao, J. Greeley, P. Strasser, B.R. Cuenya, Exceptional size-dependent activity enhancement in the electroreduction of CO$_2$ over Au nanoparticles, J. Am. Chem. Soc. 136 (2014) 16473–16476.

[37] M. Fields, X. Hong, J.K. Nørskov, K. Chan, Role of subsurface oxygen on Cu surfaces for CO$_2$ electrochemical reduction, J. Phys. Chem. C 122 (2018) 16209–16215.

[38] A.J. Garza, A.T. Bell, M. Head-Gordon, Is subsurface oxygen necessary for the electrochemical reduction of CO$_2$ on copper?, J Phys. Chem. Lett. 9 (2018) 601–606.

[39] P. Grosse, D. Gao, F. Scholten, I. Sinev, H. Mistry, B. Roldan Cuenya, Dynamic changes in the structure, chemical state and catalytic selectivity of Cu nanocubes during CO$_2$ electroreduction: size and support effects, Angew. Chem. Int. Ed. 57 (2018) 6192–6197.

[40] M. Balkanski, M.A. Nusimovici, J. Reydellet, First order Raman spectrum of Cu$_2$O, Solid State Commun. 7 (1969) 815–818.

[41] A. Dutta, I.Z. Montiel, R. Erni, K. Kiran, M. Rahaman, J. Drnec, P. Broekmann, Activation of bimetallic AgCu foam electrocatalysts for ethanol formation from CO$_2$ by selective Cu oxidation/reduction, Nano Energy 68 (2020) 104331.

[42] A. Abbas, M. Ullah, Q. Ali, I. Zahid, S. Abbas, X. Wang, An overview of CO$_2$ electroreduction into hydrocarbons and liquid fuels on nanostructured copper catalysts, Green Chem. Lett. Rev. 9 (2016) 166–178.

[43] H.C. Shin, J. Dong, M. Liu, Porous tin oxides prepared using an anodic oxidation process, Adv. Mater. 16 (2004) 237–240.

[44] H.-C. Shin, M. Liu, Copper foam structures with highly porous nanostructured walls, Chem. Mater. 16 (2004) 5460–5464.

[45] H.C. Shin, J. Dong, M. Liu, Nanoporous structures prepared by an electrochemical deposition process, Adv. Mater. 15 (2003) 1610–1614.

[46] R. Jenkins, Profile data acquisition for the JCPDS-ICDD database s, Aust. J. Phys. 41 (1988) 145–154.

[47] R. Jenkins, T.G. Fawcett, D.K. Smith, J.W. Visser, M.C. Morris, L.K. Frevel, JCPDS — international centre for diffraction data sample preparation methods in X-ray powder diffraction, Powder Diffr. 1 (2013) 51–63.

[48] H.-J. Kim, W.S. Jeon, Y.H. Ko, K. Kim, Inclusion of methylviologen in cucurbit[7] uril, PNAS 99 (2002) 5007.

[49] S. Sen, D. Liu, G.T.R. Palmore, Electrochemical reduction of CO$_2$ at copper nanofoams, ACS Catal. 4 (2014) 3091–3095.

[50] T. Binninger, E. Fabbri, A. Patru, M. Garganourakis, J. Han, D.F. Abbott, O. Sereda, R. Kötz, A. Menzel, M. Nachtegaal, T.J. Schmidt, Electrochemical Flow-Cell Setup for In Situ X-ray Investigations, J. Electrochem. Soc. 163 (2016) H906–H912.

[51] M. Newville, IFEFFIT: interactive XAFS analysis and FEFF fitting, J. Synchrotron Radiat. 8 (2001) 322–324.

[52] I. Martens, R. Chattot, M. Rasola, M.V. Blanco, V. Honkimäki, D. Bizzotto, D.P. Wilkinson, J. Drnec, Probing the dynamics of platinum surface oxides in fuel cell catalyst layers using in situ X-ray diffraction, ACS Appl. Energy Mater. 2 (2019) 7772–7780.

[53] G. Ashiotis, A. Deschildre, Z. Nawaz, J. Wright, D. Karkoulis, F. Picca, J. Kieffer, The fast azimuthal integration Python library: PyFAI, J. Appl. Crystallogr. 48 (2015).

[54] A. Dutta, A. Kuzume, S. Rahaman, S. Vesztergom, P. Broekmann, Monitoring the chemical state of catalysts for CO2 electroreduction: an in operando study, ACS Catal. 5 (2015) 7498–7502.

[55] V. Stancovski, S. Badilescu, In situ Raman spectroscopic–electrochemical studies of lithium-ion battery materials: a historical overview, J. Appl. Electrochem. 44 (2014) 23–43.

[56] A. Dutta, A. Kuzume, V. Kaliginedi, M. Rahaman, I. Sinev, M. Ahmadi, B. Roldán Cuenya, S. Vesztergom, P. Broekmann, Probing the chemical state of tin oxide NP catalysts during CO$_2$ electroreduction: a complementary operando approach, Nano Energy 53 (2018) 828–840.

[57] A. Kuzume, A. Dutta, S. Vesztergom, P. Broekmann, Operando Raman Spectroscopy: Studies on the Reactivity and Stability of SnO2 Nanoparticles During Electrochemical CO2 Reduction Reaction, in: K. Wandelt (Ed.) Encyclopedia of Interfacial Chemistry, Elsevier, Oxford, Encyclopedia of Interfacial Chemistry,Surface Science and Electrochemistry, Elsevier, Amsterdam, 2018, pp. 217–2262018, pp. 217-226.

[58] A.C. Miller, G.W. Simmons, Copper by XPS, Surf. Sci. Spectra 2 (1993) 55–60.

[59] H. Rupp, U. Weser, X-ray photoelectron spectroscopy of copper(II), copper(I), and mixed valence systems, Bioinorg. Chem. 6 (1976) 45–59.

[60] C.-K. Wu, M. Yin, S. O'Brien, J.T. Koberstein, Quantitative analysis of copper oxide nanoparticle composition and structure by X-ray photoelectron spectroscopy, Chem. Mater. 18 (2006) 6054–6058.

[61] A. Dutta, C.E. Morstein, M. Rahaman, A. Cedeño López, P. Broekmann, Beyond copper in CO2 electrolysis: effective hydrocarbon production on silver-nanofoam catalysts, ACS Catal. 8 (2018) 8357–8368.

[62] N. Ibl, Atlas d'équilibres électrochimiques à 25 °C. Von M. Pourbaix, unter Mitwirkung zahlreicher Fachgelehrter. Verlag: Gauthier-Villars & Cie., Paris 1963. 1. Aufl., 644 S., zahlr. Abb., geb. NF 140.—, Angew. Chem., 76 (1964) 444-444.

[63] T. Kondo, T. Masuda, K. Uosaki, In situ SXS and XAFS measurements of electrochemical interface, in: C.S.S.R. Kumar (Ed.), X-ray and Neutron Techniques for Nanomaterials Characterization, Springer, Berlin Heidelberg, Berlin, Heidelberg, 2016, pp. 367–449.

[64] S. Ahn, K. Klyukin, R.J. Wakeham, J.A. Rudd, A.R. Lewis, S. Alexander, F. Carla, V. Alexandrov, E. Andreoli, Poly-amide modified copper foam electrodes for enhanced electrochemical reduction of carbon dioxide, ACS Catal. 8 (2018) 4132–4142.

[65] R. Chattot, T. Asset, P. Bordet, J. Drnec, L. Dubau, F. Maillard, Beyond strain and ligand effects: microstrain-induced enhancement of the oxygen reduction reaction kinetics on various PtNi/C nanostructures, ACS Catal. 7 (2017) 398–408.

[66] R. Chattot, O. Le Bacq, V. Beermann, S. Kühl, J. Herranz, S. Henning, L. Kühn, T. Asset, L. Guétaz, G. Renou, J. Drnec, P. Bordet, A. Pasturel, A. Eychmüller, T.J. Schmidt, P. Strasser, L. Dubau, F. Maillard, Surface distortion as a unifying concept and descriptor in oxygen reduction reaction electrocatalysis, Nat. Mater. 17 (2018) 827–833.

[67] L. Dubau, J. Nelayah, S. Moldovan, O. Ersen, P. Bordet, J. Drnec, T. Asset, R. Chattot, F. Maillard, Defects do catalysis: CO monolayer oxidation and oxygen reduction reaction on hollow PtNi/C nanoparticles, ACS Catal. 6 (2016) 4673–4684.

[68] X. Chang, A. Malkani, X. Yang, B. Xu, Mechanistic insights into electroreductive C-C coupling between CO and acetaldehyde into multicarbon products, J. Am. Chem. Soc. 142 (2020) 2975–2983.

[69] M. Fleischmann, P.J. Hendra, A.J. McQuillan, Raman spectra from electrode surfaces, J. Chem. Soc., Chem. Commun. (1973) 80–81.

[70] Y. Deng, A.D. Handoko, Y. Du, S. Xi, B.S. Yeo, In Situ Raman spectroscopy of copper and copper oxide surfaces during electrochemical oxygen evolution reaction: identification of CuIII oxides as catalytically active species, ACS Catal. 6 (2016) 2473–2481.

[71] S. Jiang, K. Klingan, C. Pasquini, H. Dau, New aspects of operando Raman spectroscopy applied to electrochemical CO$_2$ reduction on Cu foams, J. Chem. Phys 150 (2018) 041718.

[72] W. Akemann, A. Otto, The effect of atomic scale surface disorder on bonding and activation of adsorbates: vibrational properties of CO and CO$_2$ on copper, Surf. Sci. 287–288 (1993) 104–109.

[73] I. Oda, H. Ogasawara, M. Ito, Carbon monoxide adsorption on copper and silver electrodes during carbon dioxide electroreduction studied by infrared reflection absorption spectroscopy and surface-enhanced Raman spectroscopy, Langmuir 12 (1996) 1094–1097.

[74] W. Akemann, A. Otto, Vibrational modes of CO adsorbed on disordered copper films, J. Raman Spectrosc. 22 (1991) 797–803.

5.6. Selective n-propanol formation from CO_2 over degradation-resistant activated PdCu alloy foam electrocatalysts

Authors: Motiar Rahaman[Δ], Kiran Kiran[Δ], Ivan Zelocualtecatl Montiel, Vitali Grozovski, Abhijit Dutta, and Peter Broekmann

Δ These authors contributed equally to this work.

Highlights: Binary PdCu catalyst was employed as an electrocatalyst for CO_2 reduction to *n*-propanol formation (PrOH) with two fold higher selectivity than ethanol (EtOH) formation at relatively low overpotential (− 0.65 V vs RHE). In addition to the selectivity, the catalyst demonstrates the excellent long term stability during CO_2 electrolysis experiment of 102 h composed of continuous and discontinuous electrolysis experiment. The as deposited was activated by two step process (i) first by thermal annealing (200 °C for 12 h in air), completely transforming to oxidic catalyst, and followed (ii) subsequently by reduction of oxidic precursor by pre-treating it at (− 0.65 V vs RHE) for 45 min transforming it to Pd-rich and Cu-rich domains. Stable C3 alcohol formation is rationalized by the fact that the C1 hydrocarbon (methane) formation is completely suppressed.

Contribution: I prepared the catalyst and investigated the performance of the catalyst. I studied the stability of the catalyst via long-term CO_2 electrolysis experiments. I was involved in physical and electrochemical characterization of the catalyst. I contributed in the ICP-MS measurement to inspect the amount of metal ions released in the electrolyte upon oxide reduction.

Check for updates

Selective *n*-propanol formation from CO₂ over degradation-resistant activated PdCu alloy foam electrocatalysts†

Motiar Rahaman, [iD] *‡§ Kiran Kiran,‡ Ivan Zelocualtecatl Montiel, Vitali Grozovski, Abhijit Dutta [iD] * and Peter Broekmann [iD] *

We present a novel, foam-type, high surface area electrocatalyst for the CO₂ reduction reaction (CO₂RR) that is not only highly selective toward *n*-propanol (PrOH) formation (FE$_{PrOH}$ = 13.7%, j_{PrOH} = −1.15 mA cm$^{−2}$) at relatively low overpotentials (−0.65 V *vs.* RHE) but also demonstrates an excellent long-term stability during CO₂ electrolysis experiments of 102 h in duration. A dynamic hydrogen bubble template approach is applied to electrodeposit a binary PdCu alloy foam yielding a nominal bulk composition of 9 at% Pd and 91 at% Cu (denoted as Pd₉Cu₉₁). The material is further modified by means of thermal annealing (12 h at 200 °C in air), which completely transforms the as-prepared metallic Pd₉Cu₉₁ alloy foam into its oxidic state. The ultimate catalyst activation is achieved by subsequent reduction (at −0.65 V *vs.* RHE for 45 min) of the oxidic precursors (composite of Cu₂O, CuO, and CuPdO₃) into metallic state, as indicated by *operando* Raman spectroscopy. Identical location scanning electron microscopy (IL-SEM) analysis, carried out prior to and after the activation treatments, demonstrates significant morphological alterations of the Pd₉Cu₉₁ foam on the nm length scale, which go along with a phase segregation into nm-range Pd-rich and Cu-rich domains that helps to increase the PrOH selectivity. Time-dependent ICP-MS analyses of the electrolyte solution, carried out during the catalyst activation, demonstrate preferential (rapid) Cu dissolution followed by (slow) Cu redeposition on the catalyst surface. These processes are found to be superimposed on the actual oxide reduction. A two-fold selectivity of PrOH was observed over ethanol (EtOH). The excellent long-term stability of the activated Pd₉Cu₉₁ foam catalyst is rationalized by the full suppression of the C1 hydrocarbon (methane) pathway. The improved product selectivity towards the highly valuable C3 alcohol is rationalized by an efficient and concerted spillover of chemisorbed carbon monoxide (*CO) and atomic hydrogen (*H) species from the Pd-rich domains to the activated Cu-rich domains of the oxide-derived Pd₉Cu₉₁ foam catalyst where the C–C coupling and subsequent hydrogenation processes take place to form the targeted oxygenate product.

Introduction

The electrochemical conversion of CO₂ into high energy density fuels or valuable chemicals is considered a promising approach for mitigating anthropogenic contributions to the steadily increasing CO₂ content (currently ∼410 ppm) of our atmosphere.[1–4] This so-called *power-to-X* concept becomes particularly appealing when the surplus of renewable electric energy from hydro, solar, or wind sources is used to power the highly endergonic CO₂ conversion process. Catalysts are needed for this electrochemical transformation not only to accelerate the kinetically hindered CO₂ reduction reaction (CO₂RR) but also to guide the process towards the desired reaction products.[5,6] Recent studies have demonstrated that, not only the chemical nature of the catalyst but also its morphology at various length scales which dictates the resulting CO₂RR product distribution.[7,8]

Among the various catalysts studied thus far, Cu stands out as the only mono-metallic material that can produce multiple hydrocarbons and oxygenates of various chain lengths from CO₂.[9–14] Higher alcohols are particularly desirable due to their high volumetric energy density (*e.g. n*-propanol: 27.0 MJ L$^{−1}$). They can be considered synthetic energy carriers of high

Department of Chemistry and Biochemistry, University of Bern, Freiestrasse 3, 3012 Bern, Switzerland. E-mail: mr820@cam.ac.uk, abhijit.dutta@dcb.unibe.ch, peter.broekmann@dcb.unibe.ch

†Electronic supplementary information (ESI) available. See DOI: 10.1039/d0gc01636e

‡These authors contributed equally to this work.

§Current address: Department of Chemistry, University of Cambridge, Lensfield Road, CB2 1EW Cambridge, UK.

added-value that are essential for the so-called energy transition.[9,11,15–21]

In early related studies, Hori *et al.* observed the formation of *n*-propanol on Cu foil.[22] However, the reported faradaic efficiency was rather low (FE_{PrOH} = 3.0% at −1.44 V *vs.* NHE). In principle, an improvement of the selectivity towards alcohols can be achieved by a partial or complete oxidation of the Cu catalyst prior to the CO_2 electrolysis. The formed cuprous and cupric oxides are considered to be precursors of the active catalyst material and, under the harsh experimental conditions commonly applied for the CO_2RR, typically undergo rapid electroreduction thereby accomplishing catalyst activation and the formation of the low-coordinated sites that are required for C–C coupling and subsequent alcohol formation.[23–25]

As an example, Rahaman *et al.* reported improved efficiencies of ethanol (EtOH) and *n*-propanol (PrOH) formation of FE_{EtOH} = 10.4% and FE_{PrOH} = 13.1%, respectively, at −0.90 V *vs.* RHE on oxide-derived dendritic Cu catalysts.[26] A similar mixture of EtOH and PrOH was obtained by Ren *et al.* with Cu nanocrystal agglomerates (FE_{PrOH} = 10.6% and FE_{EtOH} = 7.7% at −0.85 V *vs.* RHE).[27] Activation by plasma treatment also yields a slightly higher selectivity towards the C2 alcohol (FE_{EtOH} = 17% and FE_{PrOH} = 8.1% at −0.95 V *vs.* RHE).[28] To date, the highest reported PrOH efficiency still do not exceed 15% (FE_{EtOH} = 13% and FE_{PrOH} = 15% at −0.95 V *vs.* RHE).[29] So there is much room to improve the PrOH selectivity.

One crucial requirement for the production of higher alcohols is the sufficient abundance of chemisorbed carbon monoxide (*CO, the asterisk refers to an adsorbed state) which forms as a key intermediate in the course of the CO_2RR.[30] The further stabilization of *CO on the catalytically active surface is particularly important as the CO dimerization (C–C coupling) process ideally takes place in an early stage of alcohol formation.

Attempting to further increase the product selectivity towards C2 or C3 oxygenates therefore, often relies on the addition of a second catalyst component to the activated Cu (C–C coupler, alcohol producer), which selectively produces CO (CO producer).[31] Obvious candidates for the CO forming catalysts, according to the CO_2RR catalyst classification scheme introduced by Hori *et al.*, are Zn, Ag, Au, and Pd.[22] Pd nanoparticles have recently been employed to produce CO at medium overpotentials with a high selectivity reaching FE_{CO} values of ~90%.[32] However, one particular drawback of Pd as the CO-producing component is related to its comparably high affinity for CO chemisorption, which can lead to irreversible catalyst poisoning in the course of extended CO_2 electrolyses as demonstrated in several studies.[33,34] One promising approach for tackling the shortcoming of this CO_2RR catalyst is based on the co-alloying of Pd, *e.g.*, with Cu. This approach is known to reduce the binding strength of *CO to the catalyst sites[35,36] with the result that CO can be released more easily from the catalyst during extended electrolyses thus preventing any irreversible poisoning of the catalyst by strong CO chemisorption.[37] At the same time, co-alloying Pd with Cu introduces the required C–C coupling component and, if further

activated, the actual 'alcohol forming phases' to the catalytic system. A further beneficial role of the Pd, embedded into the Cu matrix of the binary alloy, is associated to the required hydrogenation reaction of the C–C coupled reaction intermediates. This is due to the moderate hydrogen adsorption energy of the *H reactant on the Pd in combination with its facile transfer to the adjacent Cu sites where the actual hydrogenation reaction of the C–C coupled intermediated is supposed to take place.[38]

In this study, we apply the so-called dynamic hydrogen bubble template approach[7,39,40] to form binary high surface area alloy catalysts containing Cu and Pd as the major and minor components, respectively. This approach was originally developed by Shin *et al.* for mono-metallic Cu[40] and Sn[39] systems, based on the superposition of the metal electroplating (primary process) by a massive hydrogen evolution reaction (HER, secondary process) at high cathodic current densities of up to −3 A $cm^{−2}$. H_2 bubbles, which evolve at the cathode surface due to the rigorous HER, act as a temporary geometric template for the metal foaming process.[7,8,39–42]

In particular when C–C coupled alcohols are targeted as the CO_2RR product, it is mandatory to further activate the Cu component prior to the actual CO_2RR, *e.g.* by oxidation.[26] For this purpose we applied a thermal annealing treatment (200 °C for 12 h in air) to the as-deposited homogeneous alloy foam, which resulted in significant morphological and compositional changes of the material, a process that can be probed by so-called identical location scanning electron microscopy (IL-SEM) imaging. The catalyst pretreatment was completed by applying −0.65 V *vs.* RHE cathodic potentials that transforms the oxides into a phase-separated metallic catalyst (oxide-derived) which is essential for multicarbon alcohol formation. A maximum efficiency of 13.7 ± 0.8% PrOH (j_{PrOH} = −1.15 mA $cm^{−2}$) was obtained by this approach at relatively low overpotentials of −0.65 V *vs.* RHE, with only 7.1 ± 0.3% of EtOH (j_{EtOH} = −0.60 mA $cm^{−2}$) as a minor oxygenate product, providing a remarkable C3 alcohol selectivity that was two times higher than the respective C2 alcohol yield.

Extended catalyst stressing experiments of >100 h in duration demonstrate a superior degradation stability of the binary CuPd alloy foam catalyst with average total faradaic efficiencies of alcohol formation never decreasing to values less than 18%. More importantly, the high PrOH selectivity is also maintained during the extended electrolyses experiments.

Experimental

Materials and chemicals

The Cu foil (99.99% pure) was purchased from Goodfellow (initial dimension 10 cm × 10 cm) and cut into pieces measuring 8 mm × 25 mm. The Cu foils served as substrates for catalyst preparation by means of hydrogen bubble assisted alloy electrodeposition. Na_2PdCl_4 (Sigma Aldrich, 99.99%) and

$CuSO_4 \cdot 5H_2O$ (Sigma Aldrich, 99.99%) served as metal precursors for the plating step. $KHCO_3$ (ACS grade) and K_2SO_4 (ACS grade) were purchased from Sigma Aldrich. ACS grade H_2SO_4 (Sigma) was used to prepare the plating bath. All chemicals were used without further purification. Milli-Q water (Millipore, 18.2 MΩ cm, 4 ppb of total organic carbon content) was used for the preparation of all solutions.

Catalyst preparation

Prior to alloy electrodeposition the Cu foil substrate was electropolished in 50% phosphoric acid (ACS grade, Sigma Aldrich) to remove the native oxide layer from its surface. For this pre-treatment step, a two electrode arrangement that consisted of a graphite foil and the Cu foil serving as cathode and anode, respectively, was used. A potential difference of 2.0 V was applied for 2 min. After electropolishing, the Cu foil was thoroughly rinsed in Milli-Q water, subsequently sonicated in ethanol for 15 min, and finally dried in air before use.

To obtain a well-defined geometric surface area of 1 cm^2 the Cu foil substrate was masked with an insulating PTFE tape. Unless otherwise stated, alloy deposition was carried out using a plating bath containing Na_2PdCl_4 and $CuSO_4 \cdot 5H_2O$ metal ion sources (1:9 ratio, 25 mM) in 1.5 M H_2SO_4 electrolyte (pH ~ 0.5). A three-electrode arrangement, consisting of a Pt foil (4 cm × 3 cm, counter electrode), an Ag/AgCl$_{3M}$ reference electrode (Metrohm), and the Cu foil substrate serving as the working electrode, was used for electrodeposition. A constant current density of −3 A cm^{-2} was applied for 40 s. After deposition, the formed metal foams were gently rinsed with Milli-Q water to remove excess electrolyte.

For the majority of the CO_2 electrolysis experiments the PdCu foam catalyst were further activated by 12 h of thermal annealing in air at a temperature of 200 °C using a tube furnace (GERO, GmbH, Germany). Catalyst activation was completed by an electrochemical reduction of the formed oxidic precursor in CO_2-saturated 0.5 M $KHCO_3$ solution for 45 min at an applied potential of −0.65 V vs. RHE. The individual steps of the catalyst preparation and activation procedure are schematically shown in Fig. 1.

The electrochemically active surface area (ECSA) of the as-deposited as well as the activated PdCu foam catalysts was determined based on voltammetric measurements using dimethyl viologen as a reversible redox probe. This procedure has been described in detail elsewhere.[7]

CO_2 electrolysis experiments

All electrochemical measurements were carried out using a potentiostat/galvanostat (Metrohm Autolab 128N, The Netherlands). Prior to the electrolysis experiments, the cell resistance was measured by means of impedance spectroscopy. All potentials reported herein are iR-corrected. The CO_2RR was carried out at room temperature using a custom-made H-type glass cell where the two compartments were separated by a cation exchange membrane (Nafion 117, Electrochem, USA). Aqueous 0.5 M $KHCO_3$ solution was used as electrolyte. A leak-less Ag/AgCl$_{3M}$ (EDAQ) served as the reference electrode, a Pt foil (15 mm × 5 mm, 99.95%, Alfa Aesar) was used as the counter (anode), and the CuPd foam catalyst served as the working electrode (cathode). Prior to commencing CO_2 electrolysis, both the anolyte and the catholyte were purged with CO_2 (99.9999%, Carbagas, Switzerland) at a flow rate of ~30 mL min^{-1} at least for 30 min. During the electrolysis, the catholyte was constantly purged with CO_2 at a flow rate of ~13 mL min^{-1}.

For the sake of comparability, all potentials, recorded versus the Ag/AgCl$_{3M}$ electrode, were converted to the reversible hydrogen electrode (RHE) scale using the following equation:

$$E_{RHE} \ (V) = E_{Ag/AgCl_{3M}} \ (V) + 0.210 \ V + (0.0591 \ V \times pH)$$

The quantification of the gaseous and non-gaseous reaction products by means of gas-chromatography and ion-exchange chromatography is described elsewhere.[7,26]
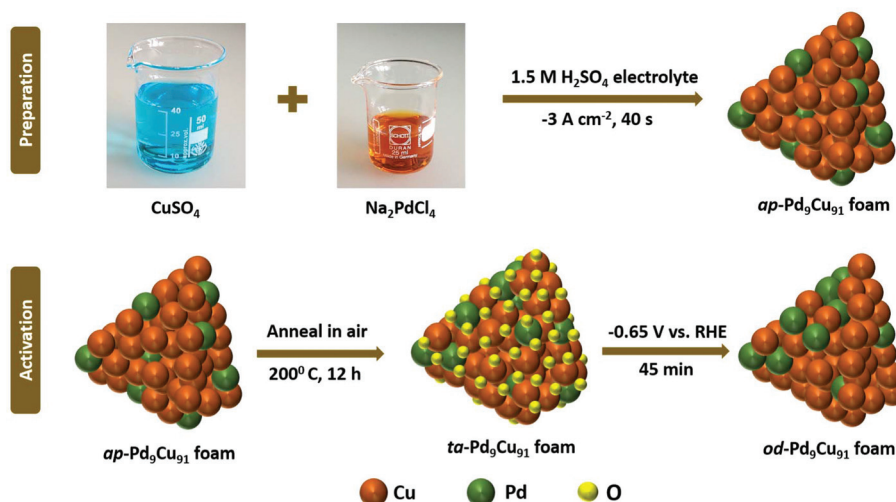

Fig. 1 Scheme illustrating individual preparation and activation steps of the Pd_9Cu_{91} catalyst.

According to the post-electrolysis inductively coupled plasma optical emission spectroscopy (ICP-OES) and X-ray photoelectron spectroscopy (XPS) measurements, Pt was detected neither in the separated catholyte compartment nor on the catalyst surface. Any interference of Pt dissolution at the anode during electrolysis can thus be excluded.

X-ray diffraction (XRD) analysis

XRD analyses of the as-prepared (*ap*), thermally annealed (*ta*), and oxide-derived (*od*) PdCu catalysts were carried out by means of powder XRD (Bruker D8) using CuKα radiation (λ = 0.1540 nm, 40 mA) generated at 40 keV. Scans were recorded at 1° min^{-1} for 2θ values ranging from 20 to 90°. The obtained XRD patterns were analyzed and compared with JCPD (Joint Committee on Powder Diffraction) standards for different pure metals, bimetallic alloy materials (Cu, Pd, and CuPd alloy) and corresponding oxide phases (CuO, Cu_2O, $CuPdO_3$). An activated graphite foil was used as the substrate for all XRD analyses to avoid undesirable contributions of the substrate to the XRD pattern of the PdCu alloy sample of interest.

Scanning electron microscopy (SEM) and energy-dispersive X-ray spectroscopy (EDX)

The morphology and composition of the as-prepared and oxide-derived CuPd catalysts were studied by means of a FE Zeiss DSM 982 SEM instrument equipped with a Noran SIX NSS200 energy dispersive X-ray spectrometer.

X-ray photoelectron spectroscopy

XPS studies were performed by means of Al-Kα radiation sources which was operated at 150 W with an Omicron Multiprobe (Omicron Nano Technology) spectrometer coupled to an EA 125 (Omicron) hemi-spherical analyzer. C 1s peak was used as reference and the fitting was performed using CasaXPS software. Note that, the samples were used for the XPS analyses without any further modifications (*e.g.* metal sputtering).

High resolution transmission electron microscopy (HR-TEM) and high-angle annular dark-field scanning transmission electron microscopy (HAADF-STEM)

HR-TEM and HAADF-STEM were carried out by a Thermo Scientific Talos F200X G2 TEM (FEI, operating voltage 200 kV). For these measurements, the catalyst materials were gently removed from the Cu foil substrate, dispersed in ethanol by sonication, and subsequently drop-casted on a carbon coated Ni grid (300 mesh).

Inductively coupled plasma optical emission spectrometry (ICP-OES) and inductively coupled plasma mass spectrometry (ICP-MS)

The bulk elemental composition has been studied by ICP-OES analysis (Thermo Scientific iCAP 7400 ICP-OES DUO). The PdCu metal foams have been dissolved in 30% HNO_3 for ICP-OES analysis. The time-dependent monitoring of the electrolyte chemical composition (metal content) has been carried out using a NexION 2000 ICP-MS instrument (PerkinElmer).

Operando Raman spectroscopy

Details of the *operando* Raman spectroscopy have been described elsewhere.[43] The spectroscopic analysis was conducted by means of a LabRAM HR800 confocal microscope (Horiba Jobin Yvon). Spectral data were collected with Lab Space 3.0 software. A large working distance objective lens (50× magnification, 8 mm focal length) was applied with a numerical aperture of 0.1 in order to focus a diode-pumped solid-state laser beam (excitation wavelength 633 nm, DPSS laser, power 3 mW) on the sample and collect the incident and scattered laser light. A home-made spectro-electrochemical cell made of Kel-F was used for the spectro-electrochemical experiments. The spectro-electrochemical cell consisted of a Ag/AgCl reference (EDAQ) electrode whereas a Au-wire served as the counter electrode. A μ-Autolab III (EcoChemie) potentiostat was used for the electrochemical measurements. Raman spectra were collected in the spectral range of 100–2500 cm^{-1}. For the data acquisition during the potentiostatic experiments, the holding time was 120 s at each applied electrolysis potential.

Results and discussion

Characterization of the catalyst

The PdCu alloy foam, used herein for the CO_2RR experiments, contains a nominal composition of 9 at% Pd (minor component) and 91 at% Cu (major matrix component) and thus named as Pd_9Cu_{91}. This 'integral' bulk composition was determined on the basis of quantitative ICP-OES measurements. EDX analysis, which is more sensitive to the near-surface region of the catalyst and thus is a more spatially-confined method, yielded, however, comparable results of 7 at% Pd and 93 at% Cu (see Fig. S1, ESI†). Note, however, that the EDX analysis is only semi-quantitative and that chemical composition of the outermost surface and the near-surface 'bulk' region of the deposit might slightly deviate from that of the bulk material. In the following we denote the catalysts analyzed herein according to their stage of preparation/activation as *ap*-Pd_9Cu_{91} (as-prepared), *ta*-Pd_9Cu_{91} (thermally-annealed), and *od*-Pd_9Cu_{91} (oxide-derived). This notation assumes that thermal annealing and the subsequent electrochemical (*ec*) reduction of the oxidic precursor don't lead substantial changes in the integral 'bulk' composition of the foam material. This assumption is in agreement with ICP-OES analyses of *ap*-Pd_9Cu_{91} and *od*-Pd_9Cu_{91} samples which provide similar % of Pd and Cu as bulk compositions of the materials. The term 'oxide-derived' (*od*) refers to the state of the annealed catalyst after the electrochemical pretreatment (45 min at −0.65 V *vs.* RHE in CO_2-saturated 0.5 M $KHCO_3$ solution, pH 7.2), assuming that it represents the stable metallic state under reactive conditions during the CO_2RR experiments.

Fig. 1 depicts the individual preparation and activation steps of the bimetallic Pd_9Cu_{91} catalyst used throughout this study.

Fig. 2 shows a collection of representative identical location (IL)-SEM micrographs of the ap-Pd_9Cu_{91} (panels a–d), the ta-Pd_9Cu_{91} (panels e–h), and the od-Pd_9Cu_{91} sample (panels i–l), demonstrating morphological alterations of the as-prepared alloy foam that are due to thermal annealing treatment and the subsequent electrochemical reduction of the oxidic catalyst precursor. The SEM images (panel a) reveal a three-dimensional architecture of meso-pores (primary porosity) with a mean surface diameter of 23 ± 3 μm. This value corresponds well to the respective depth of the topmost meso-pores of 25 ± 2 μm, as determined by white-light interferometry analysis (Fig. S2, ESI†). As it can be seen, the porosity on the μm length scale neither changes upon thermal annealing (panel e) nor upon oxide reduction (panel i). Due to their dendritic nature, the sidewalls of the 3D foam structure reveal a secondary porosity on the nanometer length scale that is, in contrast to the meso-pores, significantly affected by the combined thermal and electrochemical catalyst pre-treatment. One prominent feature of the ap-Pd_9Cu_{91} is the presence of textured nanometer-sized (~50 nm) crystallites that often exhibit a cubic shape ((100) texture, $e.g.$, see Fig. 2, panel d). SEM results of as-prepared pure Cu and pure Pd foams are also shown in Fig. S3 (ESI†). The cubic-shaped crystallites (in ap-Pd_9Cu_{91}) completely disappear upon thermal treatment due to the partial coalescence of the fine dendritic features that compose the pore sidewalls (Fig. 2, panel h). The ta-Pd_9Cu_{91} foam undergoes further morphological changes in the course of the electrochemical oxide reduction at −0.65 V $vs.$ RHE. Under these reductive conditions, nm-sized (10–50 nm) particles appear on the catalyst surface, further increasing the electrochemically active surface area (ECSA) upon

catalyst activation (see Fig. S4, ESI†). Similar morphological alterations, as demonstrated in Fig. 2, have also been reported for the activation of dendritic Cu and can be rationalized by the significant migration of oxygen and Cu associated with oxide precursors formation (thermal annealing) and their subsequent electroreduction.[26]

The IL-SEM analysis results are further supported by the complementary $ex\ situ$ XRD analysis of the metallic and oxidic foams, as presented in Fig. 3. For comparison purposes, XRD data of pure Cu and Pd metallic foams are included in Fig. 3a. A comparison of the three diffractograms confirms the co-alloying of Pd and Cu in the ap-Pd_9Cu_{91} sample. The (111), (200), and (220) diffraction peaks of the face centered cubic (fcc) ap-Pd_9Cu_{91} sample appear at 2θ values of 42.73°, 49.74°, and 73.18°, which reside between the corresponding peaks reported for Cu (43.3°, 50.4°, and 74.1°; JCPDS: 85-1326) and Pd (40.2°, 46.8°, and 68.3°; JCPDS: 87-0638). The intense diffraction feature at $2\theta \sim 56°$ corresponds to the C(004) diffraction of the graphite foil support on which the metal foams were deposited for XRD inspection.

Fig. 3b demonstrates alterations in the crystal structure of the ap-Pd_9Cu_{91} that are associated with the thermal treatment and the subsequent oxide reduction. Clearly, all diffraction features of the fcc ap-Pd_9Cu_{91} sample disappear after thermal annealing (see diffractogram of ta-Pd_9Cu_{91}), indicating the transformation of the metallic alloy into an oxidic form, which obviously affects not only the catalyst surface but the entire 'bulk' of the alloy foam. Note that this oxidation process causes a partial phase segregation into domains of copper oxide(s) and a mixed PdCu oxide phase. The Cu_2O (200) and CuO (111) diffraction peaks appear at $2\theta = 40.9°$ (JCPDS: 74-1230) and at $2\theta = 38.76°$ (JCPDS: 80-1268), respectively. The
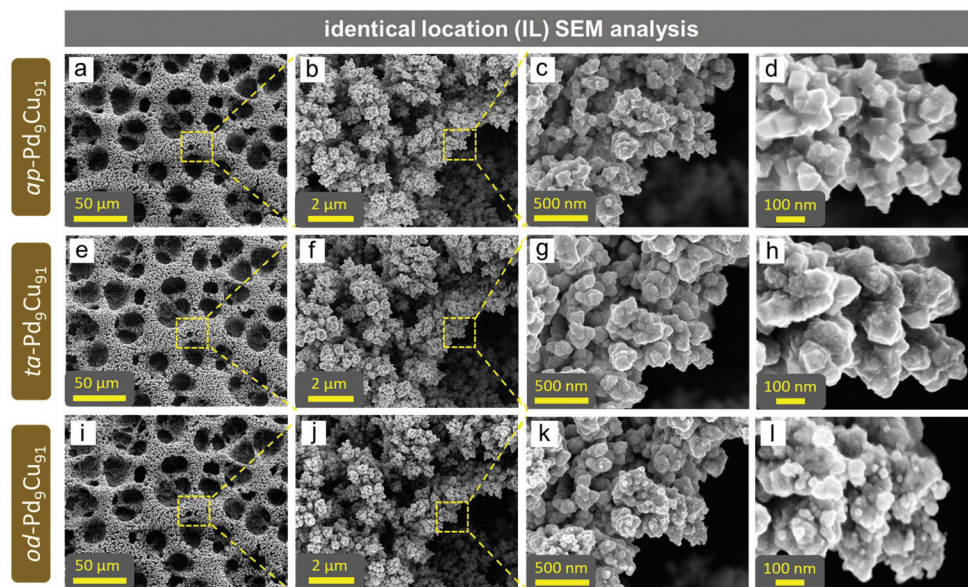

Fig. 2 Identical location (IL) SEM analysis of the co-alloyed foam catalyst depending on the processing stage; (a)–(d) as-prepared (ap) alloy foam; (e)–(h) thermally annealed (ta) alloy foam (200° C, 12 h, in air); (i)–(l) oxide-derived (od) alloy foam (after ec pretreatment at −0.65 V $vs.$ RHE for 45 min).
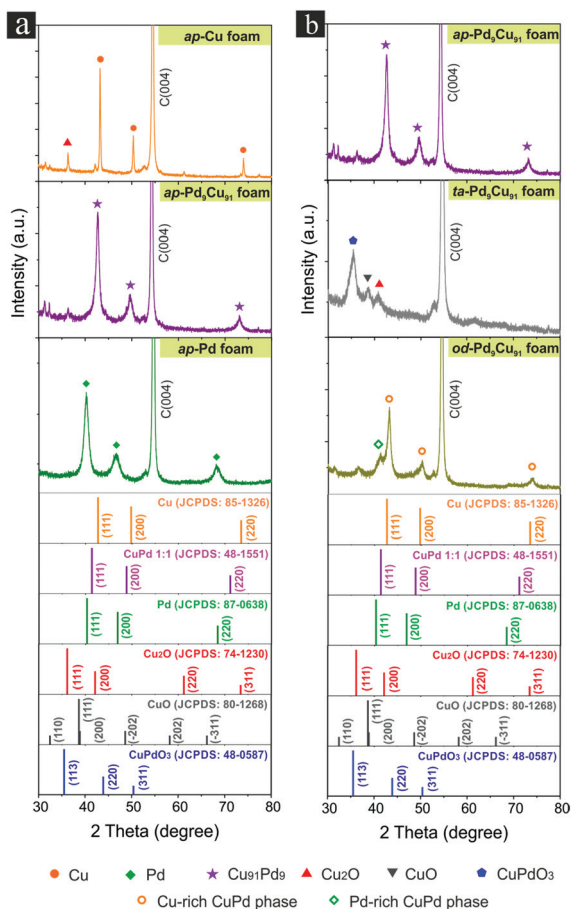
Fig. 3 (a) X-ray diffraction pattern of the as-prepared (*ap*) pure Cu, pure Pd, and the Pd$_9$Cu$_{91}$ foam samples. (b) X-ray diffraction pattern of the Pd$_9$Cu$_{91}$ sample depending on the processing stage (as-prepared (*ap*), thermally annealed (*ta*), and oxide-derived (*od*)). Standard diffraction peaks and their corresponding JCPDS files are shown.

mixed CuPdO$_3$ oxide phase was identified *via* its (113) diffraction peak at $2\theta = 35.32°$ (JCPDS: 48-0587).

Under reductive conditions, applied during the electrochemical part of the catalyst pre-treatment, these oxide phases are thermodynamically unstable and undergo rapid compositional and structural transitions back into their metallic state. Thus, there is no indication for the presence of any oxide phase with long-range transitional order after the electrochemical treatment (see diffractogram of the *od*-Pd$_9$Cu$_{91}$ sample in Fig. 3b). However, the partial phase segregation, initially started after thermal annealing treatment, is retained after the subsequent oxide reduction. As a consequence, a Cu-rich phase is formed which exhibits a Cu-like diffraction pattern with (111) plane at $2\theta = 43.18°$ (JCPDS for Cu: 85-1326). Besides this major Cu-enriched phase, a second Pd-rich alloy phase develops, as deduced from the shift of the main (111) diffraction peak from 42.73° (*ap*-Pd$_9$Cu$_{91}$) to 41.34° (*od*-Pd$_9$Cu$_{91}$). An expansion of the crystal lattice towards the fcc Pd thus confirms enrichment by Pd (JCPDS for Pd: 87-0638) in the second phase (see Fig. 3).

The (metal → oxide → metal) transitions, observed in the XRD patterns, are also in full agreement with a complementary XPS analysis presented in Fig. S5 (ESI†), which shows the spin–orbit split Cu 2p (panel a) and Pd 3d (panel b) photoemissions of the Pd$_9$Cu$_{91}$ samples in their respective processing states. The appearance of characteristic shake-up satellites in the Cu 2p photoemission spectrum after thermal treatment indicates the presence of cupric CuO in the *ta*-Pd$_9$Cu$_{91}$ sample. It should be noted, however, that XPS cannot discriminate between metallic Cu and cuprous oxide (Cu$_2$O) as both phases exhibit the same binding energy of BE(Cu 2p$_{3/2}$) = ~933 eV.[44] The Pd 3d peak broadened after the annealing treatment and a Pd(II) component (PdO, BE(3d$_{5/2}$) = ~336.7 eV) was evident after peak deconvolution (Fig. S5, ESI†). After completion of the electrochemical pre-treatment, both the Cu 2p and Pd 3d emissions in the *od*-Pd$_9$Cu$_{91}$ exhibit the same features as the metallic *ap*-Pd$_9$Cu$_{91}$ sample, thus indicating the complete conversion of the intermediately formed oxide into a metallic catalyst under the applied reductive conditions (45 min at −0.65 V *vs.* RHE). Survey XPS analysis further proves that there is no contamination of other metals on the catalyst surface (Fig. S6, ESI†).

Operando Raman spectroscopy (Fig. 4) further confirms the instability of the oxides, formed during thermal annealing of the alloy foam, under those electrochemical conditions applied for the catalyst activation (−0.65 V *vs.* RHE) and PrOH production (see below discussion of Fig. 7 and 8). Note the Raman spectroscopic experiment probes to some extent the bulk but in particular the surface conditions of the catalyst material.[45] Fig. 4a shows the potential-dependent evolution of *operando* Raman spectra for *od*-Pd$_9$Cu$_{91}$ in CO$_2$ saturated 0.5 M KHCO$_3$ electrolyte where the potential is stepped from the open circuit potential (OCP) to those potentials relevant for the oxygenate production. Raman features at 518 cm^{-1} and 624 cm^{-1} are typically assigned to the presence of cuprous oxides.[45–47] It becomes obvious that the oxides have already disappeared at 0 V *vs.* RHE prior to the actual onset of the CO$_2$RR which in full agreement with previous results on pure Cu foam catalysts.[31,45] Important to note is that the chemisorption of reactants, intermediate and products of the CO$_2$RR starts only after the disappearance of the oxidic species from the catalyst surface at 0 V *vs.* RHE (Fig. 4a). The Raman features at 283 cm^{-1} and 353 cm^{-1} (Fig. 4a, inset) can be assigned to the restricted rotational and vibrational modes of chemisorbed CO (*CO) on the binary PdCu catalyst which forms as key intermediate for the oxygenate products formation on Cu-based catalysts.[45]

Fig. 4b directly compares to the electrochemical part of the catalyst pre-treatment protocol where the potential is stepped from the OCP directly to −0.65 V *vs.* RHE using a *ta*-Pd$_9$Cu$_{91}$ sample. Within a few minutes (time needed to record the Raman spectrum) the oxide features have completely disappeared under the applied cathodic potential.

As suggested by the XRD data (Fig. 3), the consecutive (metal → oxide → metal) transitions leads to a phase segregation into Cu-rich and Pd-enriched domains. This hypothesis
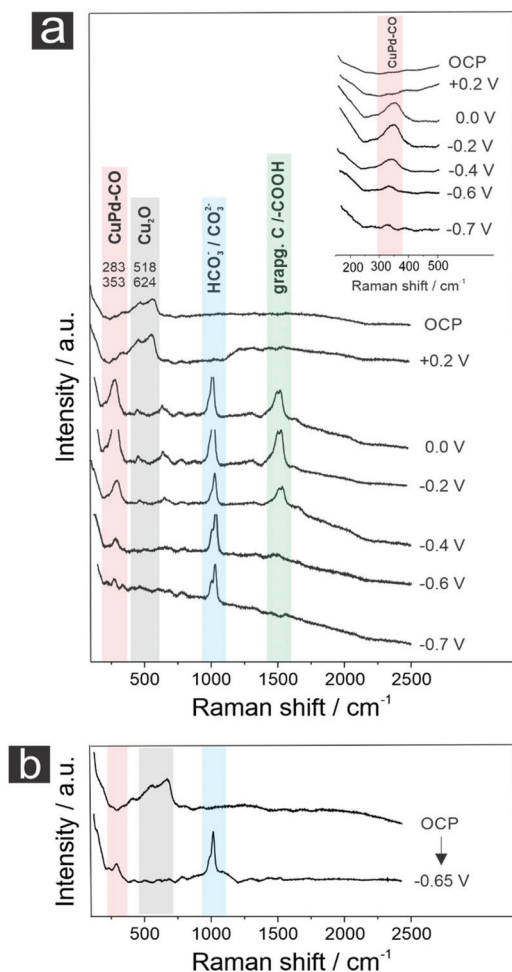
Fig. 4 (a) Potential-dependent *operando* Raman spectra of the *od*-Pd$_9$Cu$_{91}$ foam sample in the CO$_2$-saturated 0.5 M KHCO$_3$ electrolyte starting at the OCP, inset is showing zoomed PdCu−CO adsorption features; (b) *operando* Raman spectra corresponding to the catalyst activation procedure by stepping the potential from the OCP to −0.65 V *vs.* RHE using a *ta*-Pd$_9$Cu$_{91}$.

is further experimentally corroborated by combined TEM, HR-TEM, HAADF, and STEM-EDX analyses of the *ap*-Pd$_9$Cu$_{91}$ (a–d) and the *od*-Pd$_9$Cu$_{91}$ (e–h) sample, presented in Fig. 5. HR-TEM analysis identifies almost pure Cu domains in the dendrites of the foam after electrochemical oxide reduction (Fig. 5, panel f). Local changes in the chemical composition (Pd/Cu ratio) as a consequence of the oxidation/reduction treatment are further corroborated by the spatially-resolved STEM-EDX maps shown in panels d and h of Fig. 5. Three spots, indicated by the yellow frames (panel d), were analyzed in more detail by means of STEM-EDX. The EDX spot analysis reveals a chemical composition of 9 at% Pd and 91 at% Cu (scattering of ± 0.5%) which is in excellent agreement with the bulk composition of the *ap*-Pd$_9$Cu$_{91}$ sample determined on the basis of ICP-OES analysis. Visual inspection of the STEM-EDX mapping (panel d) confirms the homogeneous distribution of the Pd (minor component) in the Cu matrix prior to the catalyst activation treatment.

In total 10 different spots were analyzed by the STEM-EDX for their chemical composition on the *od*-Pd$_9$Cu$_{91}$ sample (Fig. 5, panel h). Two different kinds of surface domains can be distinguished on the catalyst surface as indicated by the black and green frames, respectively. Those regions, highlighted by the black frames, indicate Cu-rich domains with a mean chemical composition of ∼2 at% Pd and 98 at% Cu (± 1% scattering) which can be found predominantly at the center of the dendritic features. Regions indicated by the green frames represent a PdCu alloy which is substantially enriched by Pd. The respective EDX analysis reveals a mean composition of ∼22 at% Pd and 78 at% Cu (± 5% scattering). These Pd-enriched domains are preferentially observed at the outermost periphery of the dendritic features of the alloy foam. To demonstrate the reproducibility of the proposed preparation and activation procedure respective repetition experiments are presented in Fig. S7 (ESI†) demonstrating a similar phase segregation phenomenon as shown in Fig. 5.
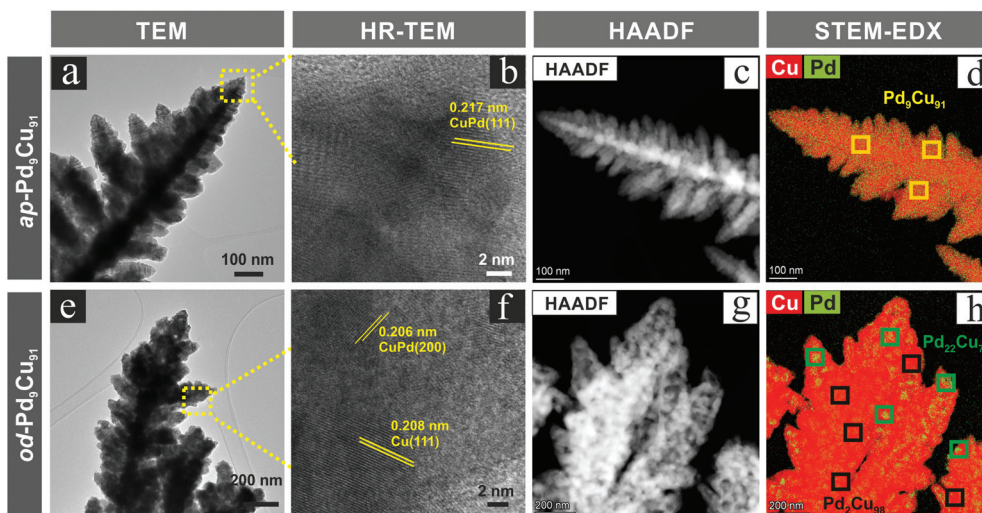

Fig. 5 (a)−(d) TEM, HR-TEM, HAADF and elemental STEM-EDX analysis of the *ap*-Pd$_9$Cu$_{91}$ sample; (e)−(h) TEM, HR-TEM, HAADF and STEM-EDX analysis of the *od*-Pd$_9$Cu$_{91}$ sample (after annealing (12 h at 200 °C in air) and *ec* pre-treatment (45 min at −0.65 V *vs.* RHE)).

Not only the initial thermal annealing contributes to the observed phase segregation (see Fig. 3) of the ap-Pd$_9$Cu$_{91}$ catalyst but also its further activation under potential control. This can be concluded from complementary time-dependent ICP-MS analyses of the electrolyte solution during the oxide reduction reaction at −0.65 V $vs.$ RHE. Form the work by Mayrhofer et $al.$[48,49] it is known that a release of metal ions from an oxidized electrode surface into the bulk of the electrolyte preferentially takes place upon oxide reduction. The same phenomenon can be observed in the present case for the reductive activation of the ta-Pd$_9$Cu$_{91}$ foam catalyst. Fig. 6 depicts the time-dependent change of the Cu and Pd content in the CO$_2$-saturated electrolyte during the electrolysis at −0.65 V $vs.$ RHE. Also for the experiment shown in Fig. 6, the potential was stepped right after the sample immersion into electrolyte from the OCP to −0.65 V $vs.$ RHE. It has, however, to be noted that already the contact of the ta-Pd$_9$Cu$_{91}$ sample to the electrolyte at OCP leads to a certain release of Cu components into the solution phase (c_{Cu} = 0.3 mg L^{-1} prior to the potential step to −0.65 V $vs.$ RHE). This dissolution process is accelerated during the first minutes (<30 min) of the oxide-reduction which is superimposed on the electrolysis reaction (HER, CO$_2$RR). The Cu content in the solution reaches a maximum of 0.54 mg L^{-1} at t = 5 min before it slowly drops down as a function of time. This experiment clearly demonstrates that the 45 min lasting catalyst pre-treatment at −0.65 V $vs.$ RHE involves both (i) the initial dissolution and (ii) the subsequent partial re-deposition of Cu material on the alloy surface from the electrolyte phase. The applied potential of −0.65 V $vs.$ RHE
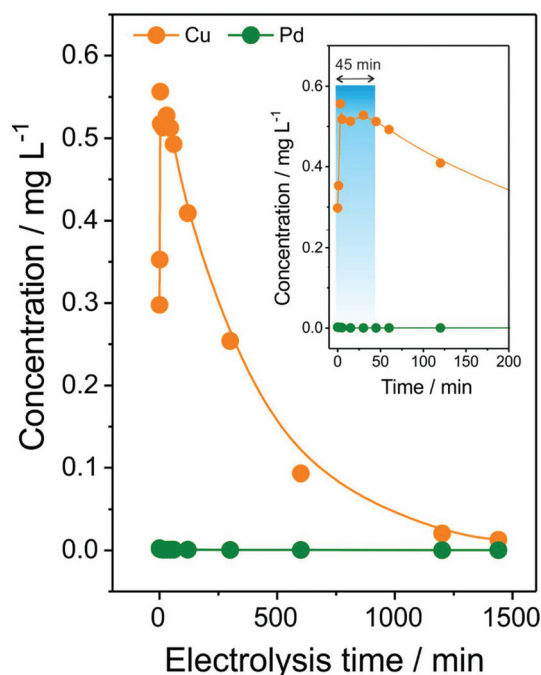
is well below the respective reversible Nernst potential for Cu deposition/dissolution. Interestingly these sequential dissolution and re-deposition processes are selective with regard to the less noble Cu component of the binary alloy whereas the minor Pd component is not affected by the oxide reduction. The Pd content in the solution phase remains almost 0 ppm over the entire analysis time.

Electrochemical performance

Systematic catalyst performance testing was carried out by potentiostatic electrolysis experiments in CO$_2$ saturated 0.5 M KHCO$_3$ (pH 7.2) using both the ap-Pd$_9$Cu$_{91}$ and the od-Pd$_9$Cu$_{91}$ samples. The applied electrolysis potentials ranged from −0.45 V to −0.95 V $vs.$ RHE. A multi-catalyst approach has been applied for this screening where a newly-prepared catalyst was used for each screening experiment (3 h duration). Fig. 7a depicts the potential (E) dependent evolution of the product distribution (faradaic efficiency (FE)), represented as a plot of FE vs E for the ap-Pd$_9$Cu$_{91}$ sample.

Formate is the main CO$_2$RR product at low applied overpotentials reaching a maximum faradaic efficiency of FE$_{formate}$ = 42.7% ($j_{formate}$ = −1.2 mA cm^{-2}) at −0.55 V $vs.$ RHE. Both pure Pd and PdCu alloys have already been identified as excellent catalysts showing high efficiencies towards formate production at particularly low overpotentials.[33,34,37] In the present case, the formate efficiency steadily decreases with increasing overpotentials reaching a value of FE$_{formate}$ = 12.5% at −0.95 V $vs.$ RHE (see Table S1, ESI†). A similar trend is also observed for CO, starting from a maximum value of FE$_{CO}$ = 35.6% (j_{CO} = −0.52 mA cm^{-2}) at lowest applied potentials of −0.45 V $vs.$ RHE.[37,50] Within the entire window of applied electrolysis potentials, hydrocarbon formation remains at a relatively low level and reaches a maximum C2 hydrocarbon efficiency of FE$_{C2}$ = 12.3% (FE$_{C_2H_4}$ = 8.2%, FE$_{C_2H_6}$ = 4.1%) at −0.75 V $vs.$ RHE. The sum of the FE values detected by online (headspace) gas-chromatography (for CO, H$_2$, C$_2$H$_4$, and C$_2$H$_6$ detection) and post-electrolysis ion-exchange chromatography (for formate detection) reaches close to 100% irrespective of the applied electrolysis potential and thus demonstrating that all relevant major products were covered by this analysis approach. The result is obviously different when the CO$_2$RR is carried out over the od-Pd$_9$Cu$_{91}$ catalyst, for which as much as 20% appears to be missing in the balance of total faradaic efficiencies (Fig. 7b). The reason for this discrepancy is due to the appearance of oxygenates as major CO$_2$RR products. The results are depicted in panels c and d of Fig. 7. Both C2 (EtOH) and C3 (PrOH) alcohols form as CO$_2$RR products, however, with a clear preference for PrOH. A maximum selectivity of FE$_{PrOH}$ = 13.7% (j_{PrOH} = −1.15 mA cm^{-2}) is observed at −0.65 V $vs.$ RHE (Table S2, ESI†). The onset potential of PrOH formation (−0.45 V $vs.$ RHE) and the electrolysis potential of maximum PrOH efficiency (−0.65 V $vs.$ RHE) are both significantly shifted towards the positive direction (≈200 mV) in comparison to the CO$_2$ electrolysis reactions carried out over 'pure' oxide-derived copper catalysts (Fig. S8, ESI†).[9,26,27] The presented potential-dependent product distribution clearly
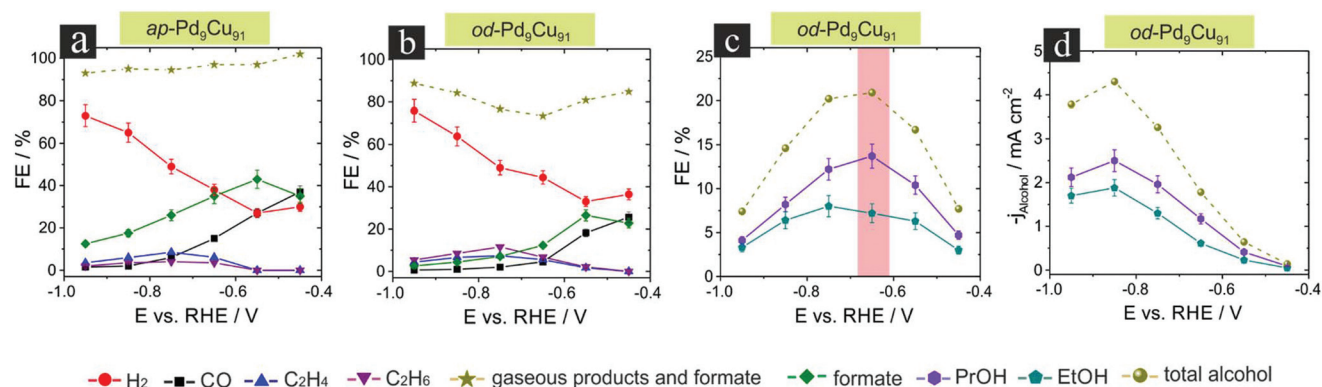

Fig. 6 Time-dependent ICP-MS analysis of the CO$_2$-saturated 0.5 M KHCO$_3$ solution during the CO$_2$RR at −0.65 V $vs.$ RHE starting with the ta-Pd$_9$Cu$_{91}$ foam as the catalyst. The inset highlights the first 200 min of the electrolysis.

Fig. 7 (a) Product distribution of the electrolyses (3 h) carried out over the *ap*-Pd$_9$Cu$_{91}$ sample. (b) Product distribution of the electrolyses (3 h) carried out over the *od*-Pd$_9$Cu$_{91}$ sample. (c) Alcohol efficiencies derived from the electrolysis carried out over the *od*-Pd$_9$Cu$_{91}$ sample. (d) Partial current densities of multicarbon alcohols.

demonstrates the beneficial catalytic effect of the co-alloyed Pd particularly in regard to the C3 alcohol formation (see discussion of the proposed reaction mechanism in Fig. 9 below). In contrast, the EtOH efficiency remains at a comparably low level (*e.g.*, FE$_{EtOH}$ = 7.1% with j_{EtOH} = −0.60 mA cm^{-2}). Under these optimum electrolysis conditions, the PrOH efficiency is actually twice as high as that for EtOH. A representative GC chromatogram is provided in Fig. S9 (ESI†). In both the FE *vs. E* and the *j vs. E* plots, the trends of EtOH follow the ones for PrOH but at a significantly lower level. In contrast, previous studies indicated either similar FE values for PrOH and EtOH under optimized experimental conditions or a higher selectivity towards EtOH (see Table S3 for a comparison data, ESI†).[26–29] Note that the maximum faradaic efficiency (FE$_{PrOH}$) and the optimum rate of production (j_{PrOH}) are obtained at different electrolysis potentials. The maximum partial current density for PrOH production, j_{PrOH} = −2.50 mA cm^{-2}, was observed at −0.85 V *vs.* RHE where the FE$_{PrOH}$ was 8.2% (Table S4, ESI†).

To demonstrate the excellent stability of the novel PdCu foam catalyst against degradation, extended CO$_2$ electrolysis experiments were performed at an applied potential of −0.65 V *vs.* RHE using *od*-Pd$_9$Cu$_{91}$ as the catalyst. Gaseous and liquid (PrOH, EtOH) products were quantified in intervals of 1 h for a total duration of 102 h (Fig. 8). The electrolyses consisted of an initial continuous section (first 30 h) and an extra sequence of discontinuous electrolysis experiments of variable duration (six 10 h and one 12 h experiments). The potential control was switched off after each electrolysis experiment, and the catalyst was stored in pure Milli-Q water at the open circuit potential (OCP) before the next electrolysis was started. The main purpose of these continuous-discontinuous, long-term experiments was to demonstrate whether the catalyst could be successfully stored for long time periods and reused whenever necessary. This long-term experiment actually represents a two-fold stressing of the catalyst achieved by (i) the prolonged CO$_2$RR itself and (ii) the repetitive loss of potential control in combination with the storage of catalyst in an aqueous environment (Milli-Q water) at the OCP. Fig. 8a shows the current transient (wine curve) of the

102 h of electrolyses. The average steady state current density reached −7.5 mA cm^{-2}. Slightly higher current densities were observed at the beginning of the individual electrolysis experiments (discontinuous 10/12 h section), likely corresponding to the reduction of surface oxides formed during the resting time when the catalyst was kept at the OCP in Milli-Q water. Irrespective of the applied interruptions the resulting steady-state current density remained largely stable over the entire period of 102 h. This can be considered as a first experimental indication for an excellent structural and compositional stability of the catalyst. As already argued for pure Cu catalysts, one important factor contributing to the chemical stability of the catalyst is the successful total suppression of the C1 hydrocarbon pathway.[26]

Methane production was identified as the mechanistic origin of an irreversible poisoning of the Cu surface with chemisorbed carbon species. In the present case, the absence of methane as one of the CO$_2$RR products can also be considered beneficial for the observed long-term stability of the catalyst. During the first 30 h of continuous electrolysis, both the partial current density (panel a) and the corresponding faradaic efficiency (panel b) of PrOH formation increase with elapsing electrolysis time, from an initial value of j_{PrOH} = −1.11 mA cm^{-2} (FE$_{PrOH}$ = 12.9%) to j_{PrOH} = −1.25 mA cm^{-2} (FE$_{PrOH}$ = 13.9%). This trend is consistent with a slight decrease of the EtOH selectivity and the respective rate of production with time. However, the overall alcohol production rate does increase within the first 30 h period of the electrolysis reaction, thus proving that a continuous electrolysis does not cause any significant loss of catalytic performance, in particular with regard to the targeted C3 alcohol formation. Alterations in the catalyst's CO$_2$RR activity appear to be more complex when the sequence of discontinuous electrolyses is applied. The initial reduction of the surface oxide species, which likely formed during the resting period under the OCP conditions, leads to a temporary increase in the overall current density as well as partial currents of both PrOH and EtOH (panel a) right after restarting of the electrolysis which, however, steadily drops down in the further course of the reaction. However, in the first four 10 h discontinuous electrolyses, FE$_{PrOH}$ reaches a
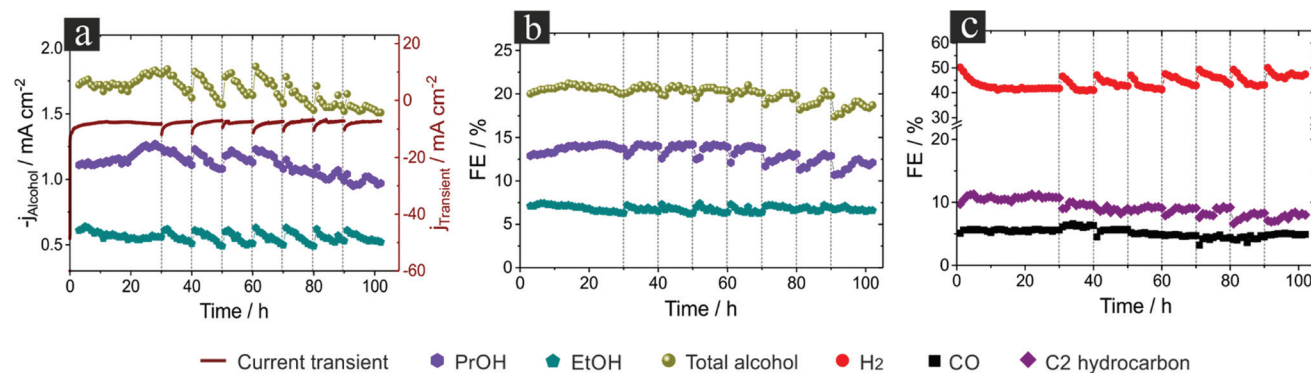
Fig. 8 (a) Current transient and time-dependent partial current densities of alcohols from the extended electrolysis carried out at −0.65 V vs. RHE over the od-Pd_9Cu_{91} sample; (b) corresponding alcohol efficiencies; (c) corresponding CO, H_2 and C2 hydrocarbon efficiencies. This set of long term experiments shows that we could store the catalyst for long time and reuse it when necessary.

steady state value of ~13.4 ± 0.9% after approximately 4 h of electrolysis time, keeping the low FE_{EtOH} of ~6.8 ± 0.3% and thus maintaining the steady PrOH selectivity until nearly 70 h (Fig. 8b). After that time, FE_{PrOH} starts to decrease slightly, which affects the PrOH selectivity. This result demonstrates that repetitive switching between the off and on state of electrolysis leads to a more significant degradation pattern than the (initial) continuous electrolysis experiment. CO and C2 hydrocarbon efficiencies decreased slightly with time whereas FE_{H_2} increased with time (see panel c of Fig. 8). Combined HAADF, STEM-EDX, and SEM analyses confirm that the compositional and structural characteristics of the od-Pd_9Cu_{91} catalyst are preserved even after prolonged electrolysis at −0.65 V vs. RHE (Fig. S10 and S11, ESI†).

Mechanistic explanation

The experimental data presented herein can be considered as a prime example of a CO_2RR catalyst material that undergoes significant structural and compositional changes during the activation stage of subsequent thermal and electrochemical pre-treatment thereby creating those electrocatalytically active sites that govern the resulting product distribution. The design of our catalyst is based on the combination of a *CO and *H forming component with a C–C coupler and alcohol-former component, which follows the similar concept of recently published bimetallic AgCu catalysts for selective ethanol production where the ethanol selectivity was rationalized by a spillover effect and the improved abundance of CO as the key intermediate of C–C coupled CO_2RR products in comparison to pristine Cu.[31,51,52] According to Dutta et al., segregated domains of pure Ag take over the role of the CO formation whereas the Cu, activated by thermal annealing prior to the CO_2RR, transforms the formed CO into ethanol with a high selectivity, reaching FE_{EtOH} = 33.7% at −1.0 V vs. RHE.[31] Due to the limited miscibility of Ag and Cu, efficient phase segregation is easily achieved during the initial foam electrodeposition stage.[31,53] In contrast, Pd and Cu show a strong tendency towards co-alloying, thus resulting in a rather homogeneous distribution of the Pd in the Cu matrix

of the as-prepared foam (Fig. 5, panels b and d). In our PdCu alloy foam, the spatial separation into *CO and *H forming and C–C coupling (alcohol forming) domains does not occur in the initial electroplating step but rather in the sequential activation steps of oxide formation and their subsequent electrochemical reduction (Fig. 1, 3 and 5). The thermally annealed Pd_9Cu_{91} foam consists of copper oxides (CuO, Cu_2O) and a mixed PdCu oxide phase ($CuPdO_3$, see Fig. 3). Subsequent electro-reduction of these oxide phases forms the phase separated Cu-rich and Pd-rich metallic domains. Kenis et al. also discussed the effect of phase separation in a bimetallic PdCu catalyst where ethylene and ethanol were produced from CO_2RR on phase-separated bimetallic PdCu nanoparticles.[54]

The domain of a Pd-rich PdCu alloy, formed after the electrochemical oxide reduction, can take over the role of the *CO and *H former (see Fig. 3 and 5h). Recent studies have already shown that both pure Pd and PdCu alloys are promising CO_2RR catalysts with excellent selectivity towards formate particularly at low overpotentials[33,34,37] (see also Fig. 7a) and towards CO at medium and high overpotentials.[32] However, pure Pd catalysts suffer from strong CO chemisorption, which leads to an irreversible poisoning of the active sites in the course of the CO_2RR.[33,34] One possible approach to tackling this challenge is to co-alloy the Pd with a second transition metal that exhibits CO_2RR activity in its own pure state but has a lower affinity towards CO adsorption/absorption in comparison to pure Pd.

A number of bimetallic systems have already been reported as CO_2RR catalysts including PdAu,[55] PdNi,[56] and PdCu.[57,58] Among these, copper is the most promising candidate for such a co-alloying approach because it shows a moderate binding strength towards CO, and allows for the C–C coupling reaction, towards oxygenate formation.[9,10,59] In this case, the C–C coupling role is taken over by Cu-rich PdCu domains (Fig. 3, 5h, and Fig. S7, ESI†).

Fig. 9 summarizes the proposed mechanism of C3 alcohol formation on the od-Pd_9Cu_{91} catalyst surface. *CO and *H form preferentially on the Pd-rich PdCu domains and they are
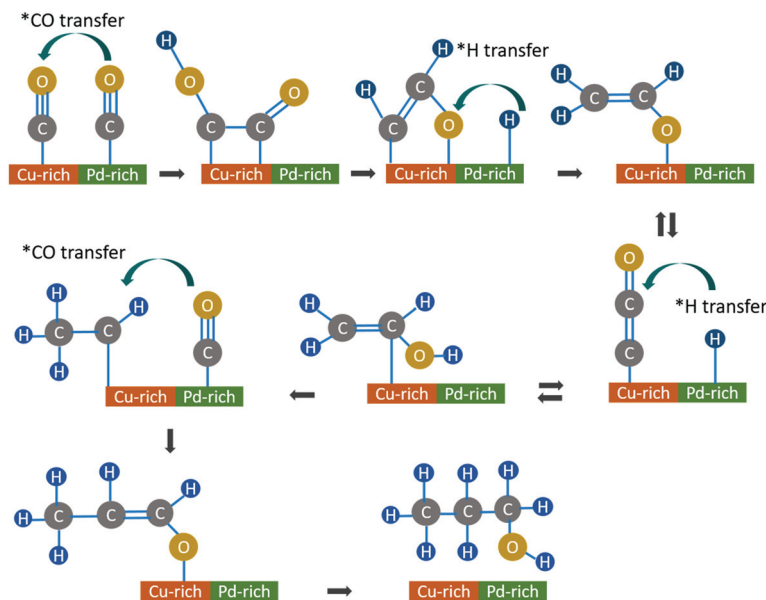
Fig. 9 Proposed reaction scheme for *n*-propanol formation from CO_2 over a phase-separated *od*-Pd_9Cu_{91} catalyst.

subsequently transported to the Cu-rich domain *via* surface diffusion or, alternatively, *via* CO and H transport through the solution phase (coupled desorption and re-adsorption processes). Besides the increased abundance of *CO and *H intermediates, it is the stabilization of the chemisorbed *CO on the catalyst surface and the efficient *H-transfer for the hydrogenation of the C–C coupled intermediates further direct the CO_2RR towards multicarbon alcohol formation.[38] This stabilization is achieved by the presence of Pd-rich domains next to the Cu-rich domains, which help to bind *CO and *H intermediates stronger than pure Cu.[10,60] *Operando* Raman spectroscopy provides a proof of *CO adsorption on the catalyst surface as it shows clear bands at 283 cm^{-1} and 353 cm^{-1} which can be assigned to the chemisorbed *CO (Fig. 4a, inset). EtOH formation most likely proceeds *via* a combined C2 hydrocarbon–oxygenate pathway, as discussed by Nie *et al.* and Kortlever *et al.*[61,62] In addition, another *CO further binds to the stabilized C2 intermediate to form the key-intermediate of PrOH, which is the adsorbed C3 aldehyde species (*CH_3CHCHO).[9] Additional control experiments in Ar-saturated CO_2-free 0.5 M K_2SO_4 electrolyte using CH_3CH_2CHO as the reactant demonstrated that PrOH can be obtained from the respective C3 aldehyde (see Fig. S12, ESI†) under similar electrochemical conditions.

Conclusions

A novel PdCu alloy electrocatalyst was prepared by means of a hydrogen bubble-assisted foam deposition process. The Pd (minor component, 9 at%) was homogeneously dispersed in the Cu matrix (major component, 91 at%) of the as-prepared alloy foam sample.

The basic bimetallic catalyst concept, followed herein, is based on the combination of a *CO and *H forming catalyst component and a second component, active for C–C coupling and subsequent alcohol formation. Additional catalyst activation, involving the thermal annealing of the *ap*-Pd_9Cu_{91} foam at 200 °C (12 h in air) and the subsequent reduction of the formed oxidic precursor under electrochemical conditions (at −0.65 V *vs.* RHE, 45 min), led to segregation into Pd-rich and Cu-rich domains which took over the role of *CO, *H-producer and C–C coupler (alcohol producer), respectively.

Highly selective *n*-propanol formation was observed (FE_{PrOH} = 13.7%, j_{PrOH} = −1.15 mA cm^{-2}) over ethanol (FE_{EtOH} = 7.1%, j_{EtOH} = −0.60 mA cm^{-2}) at −0.65 V *vs.* RHE, which led the selectivity of the C3 alcohol over the C2 alcohol by a factor of two. Key to the extraordinary performance of the oxide-derived *od*-Pd_9Cu_{91} foam catalyst was the complete suppression of methane formation (C1 hydrocarbon pathway). Extended CO_2 electrolyses, carried out for 102 h in a combined continuous and discontinuous mode, demonstrated rather stable PrOH selectivity and efficiencies that did not decrease during the continuously performed electrolysis but eventually were affected by the repetitive (intended) loss of potential control during the discontinuously performed catalyst stressing experiments. The continuous–discontinuous electrolyses indicated that the catalyst could be stored for long time and then used again when necessary.

Future work will focus on the transfer of these promising electrocatalysts to flow-cell electrolyzer with the aim of studying the catalyst degradation characteristics under well-defined mass transport conditions at elevated current densities relevant to industrial applications.

Conflicts of interest

The authors declare no competing financial interest.

Acknowledgements

References

1 *Nat. Catal.*, 2018, **1**, 93.

2 H.-R. M. Jhong, S. Ma and P. J. A. Kenis, *Curr. Opin. Chem. Eng.*, 2013, **2**, 191–199.

3 J.-P. Jones, G. K. S. Prakash and G. A. Olah, *Isr. J. Chem.*, 2014, **54**, 1451–1466.

4 J. Durst, A. Rudnev, A. Dutta, Y. Fu, J. Herranz, V. Kaliginedi, A. Kuzume, A. A. Permyakova, Y. Paratcha, P. Broekmann and T. J. Schmidt, *Chimia*, 2015, **69**, 769–776.

5 Y. Hori, in *Modern Aspects Electrochem.*, Springer, New York, 2008, pp. 89–189.

6 A. J. Martín, G. O. Larrazábal and J. Pérez-Ramírez, *Green Chem.*, 2015, **17**, 5114–5130.

7 A. Dutta, M. Rahaman, N. C. Luedi, M. Mohos and P. Broekmann, *ACS Catal.*, 2016, **6**, 3804–3814.

8 A. Dutta, C. E. Morstein, M. Rahaman, A. Cedeño López and P. Broekmann, *ACS Catal.*, 2018, **8**, 8357–8368.

9 K. P. Kuhl, E. R. Cave, D. N. Abram and T. F. Jaramillo, *Energy Environ. Sci.*, 2012, **5**, 7050–7059.

10 K. P. Kuhl, T. Hatsukade, E. R. Cave, D. N. Abram, J. Kibsgaard and T. F. Jaramillo, *J. Am. Chem. Soc.*, 2014, **136**, 14107–14113.

11 S. Nitopi, E. Bertheussen, S. B. Scott, X. Liu, A. K. Engstfeld, S. Horch, B. Seger, I. E. L. Stephens, K. Chan, C. Hahn, J. K. Nørskov, T. F. Jaramillo and I. Chorkendorff, *Chem. Rev.*, 2019, **119**, 7610–7672.

12 M. Gattrell, N. Gupta and A. Co, *J. Electroanal. Chem.*, 2006, **594**, 1–19.

13 W. Ma, S. Xie, T. Liu, Q. Fan, J. Ye, F. Sun, Z. Jiang, Q. Zhang, J. Cheng and Y. Wang, *Nat. Catal.*, 2020, **3**, 478–487.

14 C. Guo, P. He, R. Cui, Q. Shen, N. Yang and G. Zhao, *Adv. Energy Mater.*, 2019, **9**, 1900364.

15 Y. Hori, A. Murata and R. Takahashi, *J. Chem. Soc., Faraday Trans. 1*, 1989, **85**, 2309–2326.

16 S. Kaneco, K. Iiba, N.-H. Hiei, K. Ohta, T. Mizuno and T. Suzuki, *Electrochim. Acta*, 1999, **44**, 4701–4706.

17 O. A. Baturina, Q. Lu, M. A. Padilla, L. Xin, W. Li, A. Serov, K. Artyushkova, P. Atanassov, F. Xu, A. Epshteyn, T. Brintlinger, M. Schuette and G. E. Collins, *ACS Catal.*, 2014, **4**, 3682–3695.

18 C.-T. Dinh, T. Burdyny, M. G. Kibria, A. Seifitokaldani, C. M. Gabardo, F. P. García de Arquer, A. Kiani, J. P. Edwards, P. De Luna, O. S. Bushuyev, C. Zou, R. Quintero-Bermudez, Y. Pang, D. Sinton and E. H. Sargent, *Science*, 2018, **360**, 783–787.

19 C. Costentin, M. Robert and J.-M. Saveant, *Chem. Soc. Rev.*, 2013, **42**, 2423–2436.

20 G. Keerthiga, B. Viswanathan and R. Chetty, *Catal. Today*, 2015, **245**, 68–73.

21 J. Lee and Y. Tak, *Electrochim. Acta*, 2001, **46**, 3015–3022.

22 Y. Hori, H. Wakebe, T. Tsukamoto and O. Koga, *Electrochim. Acta*, 1994, **39**, 1833–1839.

23 C. W. Li, J. Ciston and M. W. Kanan, *Nature*, 2014, **508**, 504–507.

24 A. Verdaguer-Casadevall, C. W. Li, T. P. Johansson, S. B. Scott, J. T. McKeown, M. Kumar, I. E. L. Stephens, M. W. Kanan and I. Chorkendorff, *J. Am. Chem. Soc.*, 2015, **137**, 9808–9811.

25 Y. Lum, B. Yue, P. Lobaccaro, A. T. Bell and J. W. Ager, *J. Phys. Chem. C*, 2017, **121**, 14191–14203.

26 M. Rahaman, A. Dutta, A. Zanetti and P. Broekmann, *ACS Catal.*, 2017, **7**, 7946–7956.

27 D. Ren, N. T. Wong, A. D. Handoko, Y. Huang and B. S. Yeo, *J. Phys. Chem. Lett.*, 2016, **7**, 20–24.

28 D. Gao, I. Zegkinoglou, N. J. Divins, F. Scholten, I. Sinev, P. Grosse and B. Roldan Cuenya, *ACS Nano*, 2017, **11**, 4825–4831.

29 K. Jiang, R. B. Sandberg, A. J. Akey, X. Liu, D. C. Bell, J. K. Nørskov, K. Chan and H. Wang, *Nat. Catal.*, 2018, **1**, 111–119.

30 K. J. P. Schouten, Y. Kwon, C. J. M. van der Ham, Z. Qin and M. T. M. Koper, *Chem. Sci.*, 2011, **2**, 1902–1909.

31 A. Dutta, I. Z. Montiel, R. Erni, K. Kiran, M. Rahaman, J. Drnec and P. Broekmann, *Nano Energy*, 2020, **68**, 104331.

32 D. F. Gao, H. Zhou, J. Wang, S. Miao, F. Yang, G. X. Wang, J. G. Wang and X. H. Bao, *J. Am. Chem. Soc.*, 2015, **137**, 4288–4291.

33 X. Q. Min and M. W. Kanan, *J. Am. Chem. Soc.*, 2015, **137**, 4701–4708.

34 M. Rahaman, A. Dutta and P. Broekmann, *ChemSusChem*, 2017, **10**, 1733–1741.

35 J. Ko, H. Kwon, H. Kang, B. K. Kim and J. W. Han, *Phys. Chem. Chem. Phys.*, 2015, **17**, 3123–3130.

36 S. Sakong, C. Mosch and A. Gross, *Phys. Chem. Chem. Phys.*, 2007, **9**, 2216–2225.

37 Y. Hou, R. Erni, R. Widmer, M. Rahaman, H. Guo, R. Fasel, P. Moreno-García, Y. Zhang and P. Broekmann, *ChemElectroChem*, 2019, **6**, 3189–3198.

38 J. Li, A. Xu, F. Li, Z. Wang, C. Zou, C. M. Gabardo, Y. Wang, A. Ozden, Y. Xu, D.-H. Nam, Y. Lum, J. Wicks, B. Chen, Z. Wang, J. Chen, Y. Wen, T. Zhuang, M. Luo, X. Du, T.-K. Sham, B. Zhang, E. H. Sargent and D. Sinton, *Nat. Commun.*, 2020, **11**, 3685.

39 H. C. Shin, J. Dong and M. Liu, *Adv. Mater.*, 2004, **16**, 237–240.

40 H. C. Shin and M. Liu, *Chem. Mater.*, 2004, **16**, 5460–5464.

41 A. Dutta, M. Rahaman, M. Mohos, A. Zanetti and P. Broekmann, *ACS Catal.*, 2017, **7**, 5431–5437.

42 A. V. Rudnev, K. Kiran, A. Cedeño López, A. Dutta, I. Gjuroski, J. Furrer and P. Broekmann, *Electrochim. Acta*, 2019, **306**, 245–253.

43 A. Dutta, A. Kuzume, M. Rahaman, S. Vesztergom and P. Broekmann, *ACS Catal.*, 2015, **5**, 7498–7502.

44 C. K. Wu, M. Yin, S. O'Brien and J. T. Koberstein, *Chem. Mater.*, 2006, **18**, 6054–6058.

45 A. Dutta, M. Rahaman, B. Hecker, J. Drnec, K. Kiran, I. Zelocualtecatl Montiel, D. Jochen Weber, A. Zanetti, A. Cedeño López, I. Martens, P. Broekmann and M. Oezaslan, *J. Catal.*, 2020, **389**, 592–603.

46 H. Y. H. Chan, C. G. Takoudis and M. J. Weaver, *J. Phys. Chem. B*, 1999, **103**, 357–365.

47 Y. Deng, A. D. Handoko, Y. Du, S. Xi and B. S. Yeo, *ACS Catal.*, 2016, **6**, 2473–2481.

48 S. Cherevko, T. Reier, A. R. Zeradjanin, Z. Pawolek, P. Strasser and K. J. J. Mayrhofer, *Electrochem. Commun.*, 2014, **48**, 81–85.

49 M. Löffler, P. Khanipour, N. Kulyk, K. J. J. Mayrhofer and I. Katsounaros, *ACS Catal.*, 2020, **10**, 6735–6740.

50 R. Cui, Q. Shen, C. Guo, B. Tang, N. Yang and G. Zhao, *Appl. Catal., B*, 2020, **261**, 118253.

51 J. Gao, H. Zhang, X. Guo, J. Luo, S. M. Zakeeruddin, D. Ren and M. Grätzel, *J. Am. Chem. Soc.*, 2019, **141**, 18704–18714.

52 Y. C. Li, Z. Wang, T. Yuan, D.-H. Nam, M. Luo, J. Wicks, B. Chen, J. Li, F. Li, F. P. G. de Arquer, Y. Wang, C.-T. Dinh, O. Voznyy, D. Sinton and E. H. Sargent, *J. Am. Chem. Soc.*, 2019, **141**, 8584–8591.

53 T. Kottakkat, K. Klingan, S. Jiang, Z. P. Jovanov, V. H. Davies, G. A. M. El-Nagar, H. Dau and C. Roth, *ACS Appl. Mater. Interfaces*, 2019, **11**, 14734–14744.

54 S. Ma, M. Sadakiyo, M. Heima, R. Luo, R. T. Haasch, J. I. Gold, M. Yamauchi and P. J. A. Kenis, *J. Am. Chem. Soc.*, 2017, **139**, 47–50.

55 R. Kortlever, I. Peters, C. Balemans, R. Kas, Y. Kwon, G. Mul and M. T. M. Koper, *Chem. Commun.*, 2016, **52**, 10229–10232.

56 S. W. Kim, M. Park, H. Kim, K. J. Yoon, J. W. Son, J. H. Lee, B. K. Kim and J. Hong, *Appl. Catal., B*, 2017, **200**, 265–273.

57 T. Takashima, T. Suzuki and H. Irie, *Electrochim. Acta*, 2017, **229**, 415–421.

58 Z. Yin, D. Gao, S. Yao, B. Zhao, F. Cai, L. Lin, P. Tang, P. Zhai, G. Wang, D. Ma and X. Bao, *Nano Energy*, 2016, **27**, 35–43.

59 D. Raciti, K. J. Livi and C. Wang, *Nano Lett.*, 2015, **15**, 6829–6835.

60 S. Zhu, B. Jiang, W.-B. Cai and M. Shao, *J. Am. Chem. Soc.*, 2017, **139**, 15664–15667.

61 X. Nie, M. R. Esopi, M. J. Janik and A. Asthagiri, *Angew. Chem., Int. Ed.*, 2013, **52**, 2459–2462.

62 R. Kortlever, J. Shen, K. J. Schouten, F. Calle-Vallejo and M. T. Koper, *J. Phys. Chem. Lett.*, 2015, **6**, 4073–4082.

5.7. *Hydrogen Bubble Templated Metal Foams as Efficient Catalysts of CO_2 Electroreduction*

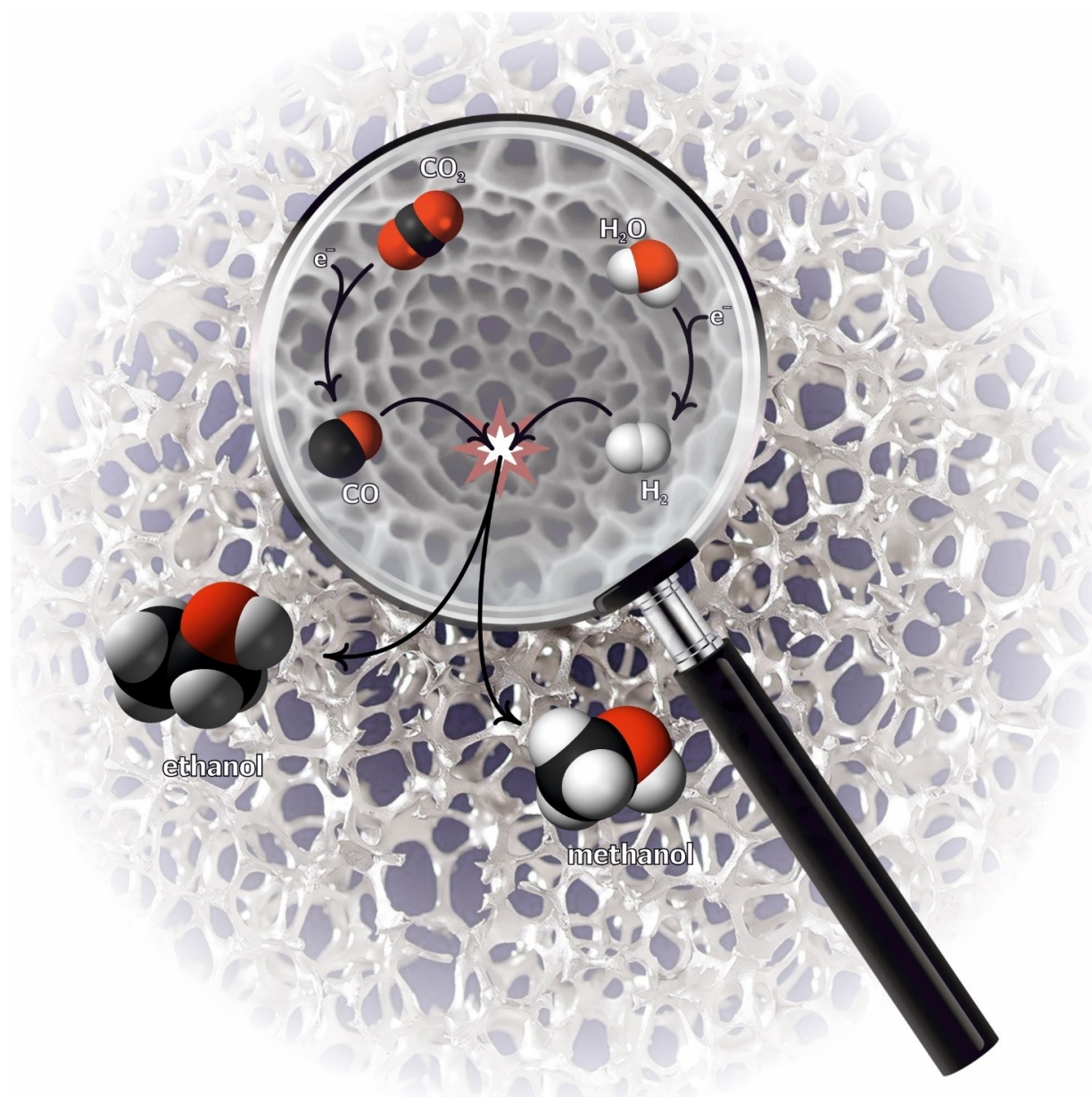**Authors:** Soma Vesztergom, Abhijit Dutta, Motiar Rahaman, Kiran Kiran, Ivan Zelocualtecatl Montiel, and Peter Broekmann

Highlights: This work summarizes brief description of several recipes for the deposition of metal foams including mono metallic Sn, Pb, Cu, Ag, Zn and bimetallic foams as well. Factors affecting the porous structure of the material obtained as a result of the dynamic hydrogen bubble template (DHBT) assisted method are discussed herein. Hierarchical 3d structures are shown to harbour reactions due to entrapment of the key intermediates.

Contribution: I was involved in the electrochemical measurements and physical characterization of the monometallic Cu foam, Ag foam and binary foam catalysts for the CO_2 reduction process.

Hydrogen Bubble Templated Metal Foams as Efficient Catalysts of CO₂ Electroreduction

Soma Vesztergom,*[a, b] Abhijit Dutta,[a] Motiar Rahaman,[a] Kiran Kiran,[a] Iván Zelocualtecatl Montiel,[a] and Peter Broekmann*[a]

ChemCatChem

Reviews
doi.org/10.1002/cctc.202001145

Chemistry Europe
European Chemical
Societies Publishing

The creation of open porous structures with an extremely high surface area is of great technological relevance. The electrochemical deposition of metal foams around co-generated hydrogen bubbles that act as templates for the deposition is a promising, cheap and simple approach to the fabrication of new electrocatalyst materials. Metal foams obtained by dynamic hydrogen bubble templating (DHBT) offer an intrinsically high electrical conductance with an open porous structure that enables the fast transport of gases and liquids. As an additional benefit, the confined space within the pores of DHBT metal foams may act as small reactors that can harbour reactions not possible at an open electrode interface. The number, distribution, and size of the pores can be fine-tuned by an appropriate choice of the electrolysis parameters so that metal foam catalysts prepared by the DHBT technique meet certain requirements. In this paper, we review the preparation of certain metal foams, and their applications as catalysts for the electrochemical reduction of CO_2.

1. Introduction

The rising concentration of atmospheric carbon dioxide (CO_2) and its consequences on climate and related societal changes present a major challenge to humankind, necessitating the development of industries with a zero, or possibly negative, CO_2 footprint.[1] Electrochemical technologies provide an attractive solution to the problem, where electrons preferably gained from a renewable energy source can be used to turn CO_2 into value-added products.[2] Technologies already exist to achieve this goal, although their operation is still far from perfect. A key factor of developing CO_2 electrolysis technologies was, and probably still remains, the invention of new catalytic electrode materials. The application of proper catalysts can ensure higher yield and also a tailored selectivity toward the formation of certain sought-after products.

At recent technological levels, the most desired products of CO_2 electroreduction are syngas (a mixture of CO and H_2); C_2 hydrocarbons (primarily, C_2H_4); short carbon chain alcohols (like methanol, ethanol or propanol); and formate or formic acid. The formation of other products by electrochemical CO_2 reduction (e.g., that of methane) would also be possible, but considering current market prices, the above aims are the ones that remain economically viable.[3]

Electrocatalysis plays a central role in lowering the energy barrier and thereby increasing the yield and decreasing the cost of CO_2 electroreduction, and in assuring that the reaction results in the desired product. Many efforts have thus been made to improve the performance of electrocatalysts, such as increasing the surface area, improving the intrinsic activity of the active sites, and manipulating the transport of reactants and products to and from the electrode surface.[4] Among these methods, the fabrication of three-dimensional porous structures (i.e., metal foams[5]) and the application of these as electrode materials was proven to be an attractive way to improve electrocatalytic performance.[6]

The application of metal foams as electrocatalysts is advantageous, as self-standing foams can directly be employed as working electrodes, often without the need of additional mechanical support. They offer a large surface area that is not only accessible to reactants, but also enables fast, multi-dimensional electron transport pathways.[6,7] Also, metal foams can act as a support for other catalysts, rendering the application of conductive binders, like Nafion, unnecessary in catalyst design.

According to IUPAC,[8] "a foam is a dispersion in which a large proportion of gas by volume in the form of gas bubbles, is dispersed in a liquid, solid or gel." Foams can either be open-cell or closed-cell structured; for the purposes of electrocatalysis, foams with open-cell structures are the most useful.[9] Several non-electrochemical[10] and electrochemical[9] methods have been described for the preparation of metal foams, mainly including selective dissolution,[11–14] templating,[15,16] combustion,[17,18] and the sol-gel method.[19,20] Synthesis and characterization strategies of noble metal foams prepared by these methods, as well as their application for electrocatalysis purposes, were recently reviewed in detail by the Eychmüller group[9,20] and by Zhu et al.[6] A relatively newly developed, yet very promising method of the preparation of metal foams namely, dynamic hydrogen bubble templated (DHBT) electrodeposition[22] was, however, not addressed in these works. The aim of this survey is to fill this gap, and to review, in details, the use of DHBT for the preparation of metal foams that can be used, primarily, as electrocatalysts for CO_2 reduction.

2. DHBT Based Preparation of Metal Foams

2.1. General Considerations

When electrodepositing noble (e.g., Au, Pt, Ag, Cu), or especially base metals (e.g., Zn, Co, Fe, Ni) from solutions of their salts, concurrent hydrogen evolution is usually considered as a major problem that causes ramification of the deposited metal layer and accounts for often undesired changes in its mechanical and

[a] Dr. S. Vesztergom, Dr. A. Dutta, Dr. M. Rahaman, K. Kiran,
I. Zelocualtecatl Montiel, Prof. P. Broekmann
Department of Chemistry and Biochemistry
University of Bern
Freiestraße 3
Bern 3012 (Switzerland)
E-mail: peter.broekmann@dcb.unibe.ch
vesztergom@chem.elte.hu

[b] Dr. S. Vesztergom
Department of Physical Chemistry
Eötvös Loránd University
Pázmány Péter sétány 1/A
Budapest 1117 (Hungary)

ChemCatChem

Reviews
doi.org/10.1002/cctc.202001145

Chemistry Europe
European Chemical
Societies Publishing

optical properties, sometimes impairing the entire process.[26] Dynamic hydrogen bubble templating (DHBT) serves as a glaring counter-example, where the loss of some current due to hydrogen evolution is turned to a benefit, as the formed hydrogen bubbles aid the creation of spongy, high surface area metal foams that can be extremely useful for the purposes of electrocatalysis.

The co-generation of hydrogen along with metal deposition, in order to create high surface area electrode materials, has been part of the arsenal of electrochemists for quite some time now; *e.g.*, this was the method used for the creation of platinum black in the original recipe of Lummer and Kurlbaum[23] and of Kohlrausch[24] (Figure 1). Starting with the advent of the 21st century, the method experienced a boom, as it turned out to be quite useful for the creation of high surface area electrocatalyst materials – not necessarily platinum based ones. Among recent works directed at the development of tailored electrocatalyst materials using the DHBT method, the works of Chialvo and Marozzi,[27,28] Shin *et al.*,[29,30] Nikolić *et al.*,[31–36] Cherevko *et al.*,[37–43] as well as the works of the Bhargava group,[44–47] including a review[22] deserve further attention.

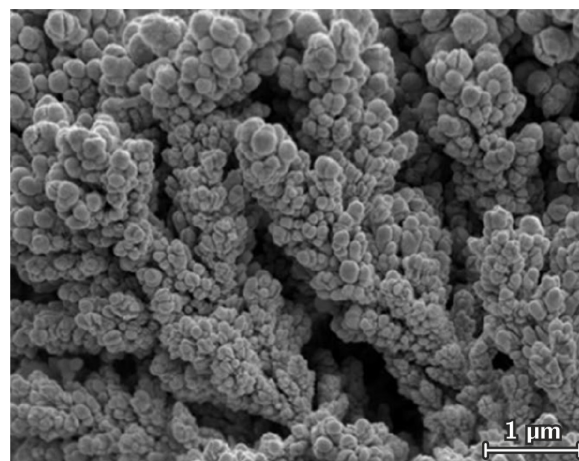In principle, there are two processes underlying the DHBT method that play a crucial role in the fabrication of metal

Figure 1. Scanning electron micrograph of platinum black, electrochemically deposited on a Pt surface from a hexachloroplatinate solution, using the recipe of Lummer and Kurlbaum[23] modified by Kohlrausch.[24] Reproduced from Ref. 25 with the permission of Nature.

foams. One is Reaction (R1), the deposition of the metal from a solution of its salt:

$$Me^{z+} + ze^{-} \rightarrow Me \qquad (R1)$$

Soma Vesztergom obtained his M.Sc. (2010) and Ph.D. (2014) degrees in chemistry at Eötvös Loránd University of Budapest, Hungary. He was a post-doctoral researcher in Peter Broekmann's group at the University of Bern for a year (2014) and is a regular collaborator of this group since then. His research primarily focuses on instrumental developments in electrochemistry and on the modelling of electrocatalytic processes. Currently, he is an assistant professor at Eötvös Loránd University in Budapest.

Abhijit Dutta obtained his Ph.D in chemistry from the Indian Institute of Engineering Science and Technology, Kolkata. He worked as a post-doctoral fellow at the National University of Singapore. Afterwards, he joined the interfacial electrochemistry group of Peter Broekmann at the University of Bern, Switzerland. His research is focused on the development of various operando spectroscopies (Raman, XAS, and XRD) to characterize novel electrocatalysts for the selective conversion of CO$_2$ to value-added products.

Motiar Rahaman obtained his M.Sc. degree in chemistry at the Indian Institute of Technology Madras, Chennai (2013) and his Ph.D. (2018) at the University of Bern. The topic of his Ph.D. thesis was the electrochemical conversion of CO$_2$ into value-added products. Currently he is a post-doctoral researcher at the University of Cambridge.
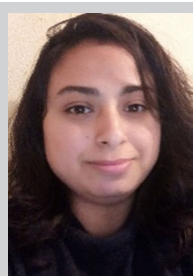
Kiran obtained her M.Sc. degree in physics at the Maharshi Dayanand University in Rohtak, India, in 2015 and currently pursues a Ph.D. in Peter Broekmann's research group at the University of Bern. Her primary research interests are in the preparation of nanomaterials and the application of these as catalysts for CO$_2$ electroreduction.

Ivan Zelocualtecatl Montiel received his B.Sc. and M.Sc. in Chemistry from the Meritorious Autonomus University of Puebla, Mexico, in 2013 and 2016, respectively. He is currently a Ph.D. candidate in the Department of Chemistry and Biochemistry at the University of Bern, under the supervision of Prof. Dr. Peter Broekmann. His research interest is focused on the development of novel catalysts for CO$_2$ electroreduction.

Peter Broekmann obtained his M.Sc. in chemistry (1998) and a Ph.D. (2000) from the University of Bonn, Germany. After a post-doctoral stay in 2001 at the University of Twente he became project leader at the Institute of Physical Chemistry in Bonn. Since 2008, Prof. Dr. Broekmann is lecturer for electrochemistry at the University of Bern (Switzerland). His research focuses on metal deposition processes for semiconductor and electrocatalysis applications.

ChemCatChem

Reviews
doi.org/10.1002/cctc.202001145

**Chemistry
Europe**
European Chemical
Societies Publishing

The other is the hydrogen evolution reaction (HER) that in an acidic solution is supposed to proceed by Reaction (R2),

$$H^+ + e^- \rightarrow \frac{1}{2}H_2 \qquad \text{(R2)}$$

while in solutions of pH > 7, the primary source of hydrogen is the electroreduction of water itself:

$$H_2O + e^- \rightarrow \frac{1}{2}H_2 + OH^- \qquad \text{(R3)}$$

Although for the preparation of metal foams using the DHBT technique, usually acidic solutions are applied, it has to be noted that under harsh cathodic conditions the surroundings of the electrode surface quickly get depleted in H^+, in which case direct water reduction, Reaction (R3), cannot be ignored.[48]

The fundamental idea of DHBT is that the H_2 bubbles generated in Reactions (R2) and (R3) disrupt the growth of the metal layer, acting as a dynamic template for the electrodeposition process. Micropores in the submicron range and macropores in the 10–100 μm size range are formed as a result of the growth of metal around small or coalesced bubbles generated on the surface, blowing up the specific surface area.[22]

When applying the DHBT method, high cathodic overpotentials are used, so that the rates of Reactions (R1) and (R2)–(R3) become comparable and decisive for the obtained foam structure. Apart from the reaction rates, however, other factors such as the nucleation, growth and detachment of the surface-generated bubbles, the intensive stirring and the related convective effects caused by bubble formation, the local alkalination of the near-electrode solution layers and its consequences on the chemistry of metal deposition, complex formation, the action of additives, etc. may also determine the surface morphology of the deposited foam. Below, we give a summary of these effects.

2.2. Mechanistic Aspects

In an excellent work, Nikolić[35] treats DHBT following Winand's classification of metals,[49] and shows contrary to previous claims[51] that metals from all three Winand groups can be obtained in three dimensional foam forms under the appropriate electrodeposition conditions. According to Winand, metals can be classed in the following three groups (Figure 2): *i.)* normal metals (such as Cd, Zn, Sn, Ag) that are characterized by low melting points, high $(j_{0,dep} > 100 \text{ A cm}^{-2})$ exchange current densities of metal deposition and low catalytic activities for hydrogen evolution; *ii.)* intermediate metals (such as Au, Cu and Ag, if in the case of Ag, deposition occurs from the solution of a complex and not of free Ag^+ ions) that are characterized by moderate melting points, intermediate $(1 \text{ A cm}^{-2} \leq j_{0,dep} \leq 100 \text{ A cm}^{-2})$ exchange current densities of metal deposition and relatively low catalytic activities for hydrogen evolution; and *iii.)*
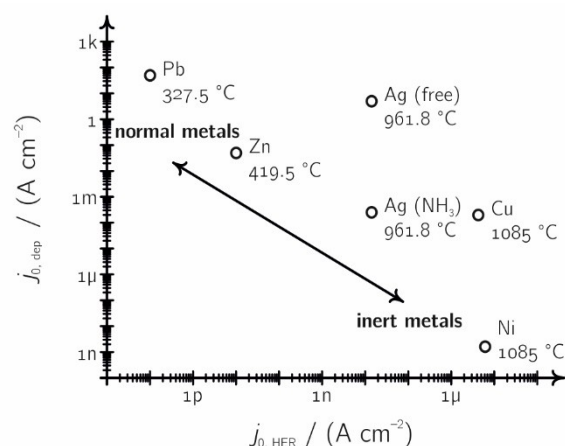

Figure 2. According to Winand,[49] metals can be classed into three groups (normal, intermediate and inert) based on their $j_{0,dep}$ deposition exchange current densities and melting points. In his treatise on DHBT,[35] Nikolić extends Winand's original classification[49] based on the $j_{0,HER}$ exchange current density of HER. The graph shown here was created using data obtained from Refs. 50 and 36.

inert metals (such as Fe, Ni, Co, Pt, Cr, Mn) that have high melting points, low $(j_{0,dep} < 1 \text{ A cm}^{-2})$ exchange current densities of metal deposition and relatively high catalytic activities for hydrogen evolution.

In case of each three metal groups, the success of DHBT in creating metal foams depends on whether on the given metal, hydrogen is forming large enough bubbles (that is mostly a question of nucleation and growth kinetics and of surface thermodynamics) and on whether the rate of metal deposition is high enough to allow deposited dendritic metal structures to overgrow a hydrogen bubble, before it leaves the electrode surface.

As shown by Popov et al.,[53] in case of metals with low or moderate $j_{0,dep}$ values, dendrite formation is possible only if the deposition overpotential η exceeds a minimum initiation overpotential

$$\eta_{ini} = -\frac{RT}{zF}\frac{j_{lim,dep}}{j_{0,dep}} \qquad (1)$$

where $j_{lim,dep}$ is the effective limiting current density of metal deposition. Note that the value of $j_{lim,dep}$ strongly depends on the prevailing hydrodynamic conditions and the vigorous mixing of the near-electrode solution caused by HER.

While for metal depositions in quiescent systems, the thickness of the diffusion layer of metal ions can (over time) extend to even a few hundreds of micrometers, it was shown that for quickly gas evolving electrodes (volumetric gas evolution rate normalized to surface area: $100 \text{ cm}^3 \text{ min}^{-1}$, corresponding to hydrogen evolution occurring with a current density of about 5 A cm^{-2}), the diffusion layer becomes only a few micrometers thick and the coverage of the surface by gas bubbles can exceed 30%.[54] Thus, at electrodes that evolve hydrogen at a high rate, due to the decrease of the diffusion

layer thickness and the corresponding increase of $j_{lim,dep}$, the "effective overpotential" (a term coined by Nikolić *et al.*[31]) may be lower than what is required for efficient dendrite formation.

What was said above is nicely demonstrated in Ref. 31 for the deposition of honeycomb-like copper foams on plane copper substrates from an aqueous solution containing 0.10 mol dm^{-3} CuSO$_4$ and 0.50 mol dm^{-3} H$_2$SO$_4$. In Figure 3 we can observe the following: *i.)* that at $\eta = -0.550$ V, a value that falls inside the limiting current density of copper deposition where no hydrogen evolution takes place, cauliflower-like agglomerates of copper grains were formed; *ii.)* that at $\eta = -0.700$ V, just outside the limiting current region of copper deposition, where the Faradaic efficiency of HER is only about 5%, branch-like three dimensional dendrites are formed; and finally *iii.)* that at $\eta = -0.800$ or -1.000 V, holes formed of detached hydrogen bubbles surrounded by cauliflower-like agglomerates of copper grains are seen.

It is important to note with respect to the depositions occurring at high overpotentials that the number of holes formed at -1.000 V is larger than that at -0.800 V, which is due to the higher Faradaic efficiency of hydrogen evolution (almost 50% at -1.000 V and about 30% at -0.800 V). As communi-

cated by Nikolić *et al.* elsewhere,[32] the critical Faradaic efficiency that hydrogen evolution should achieve in order to create hydrodynamic conditions that favour foam formation is 10% for copper depositing baths with a CuSO$_4$ concentration of 0.15 mol dm^{-3} and less, in 0.5 mol dm^{-3} H$_2$SO$_4$.

2.3. Creating Metal Foams with Hierarchic Porosity: The Effect of Deposition Time

As shown in Figure 4, at the initial stages (after the first 10 seconds) of the potentiostatic preparation of copper foams ($\eta = -1.000$ V, $c_{CuSO4} = 0.1$ mol dm^{-3}, $c_{H2SO4} = 0.5$ mol dm^{-3}), nucleation sites of H$_2$ bubbles and surrounding agglomerates of copper grains are already visible. Hydrogen evolution is initiated at irregularities of the surface, where small bubbles are formed, grow to a certain size and are then detached. The higher the current density, the more nucleation sites become active, and also the rate of growth of the bubbles increases. While at lower current densities, only the surface irregularities are active, at higher current densities bubbles are also formed on the more homogeneous parts of the surface.[56] After
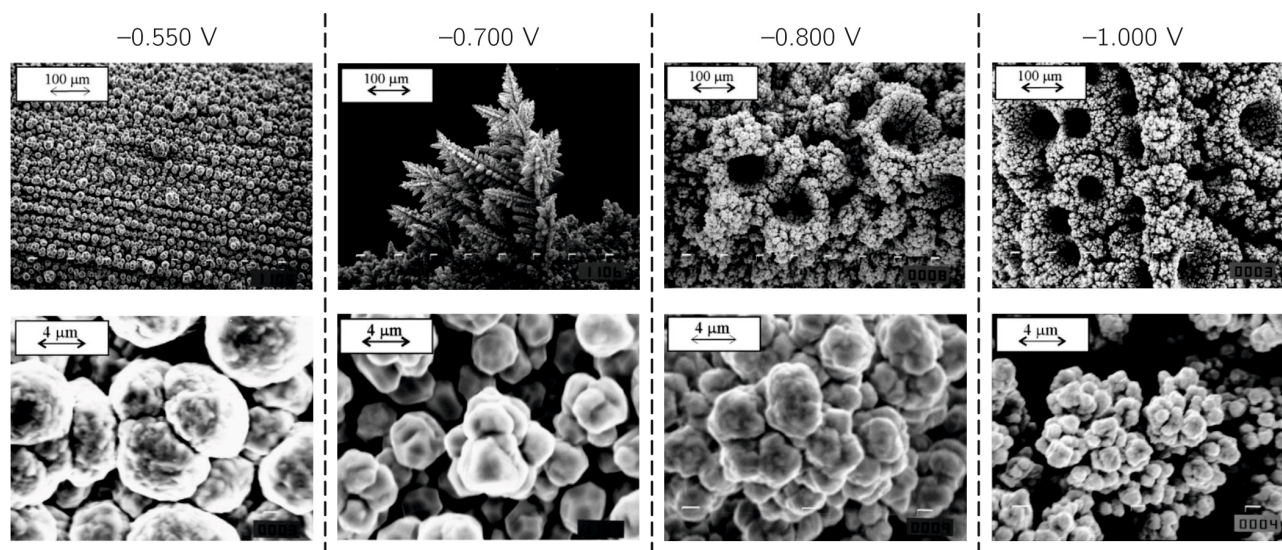

Figure 3. Morphologies of Cu deposits obtained after 60 s of potentiostatic electrolysis, at different values of the deposition overpotential from an aqueous solution containing 0.10 mol dm^{-3} CuSO$_4$ and 0.50 mol dm^{-3} H$_2$SO$_4$. Reproduced from Ref. 31 with the permission of Elsevier.
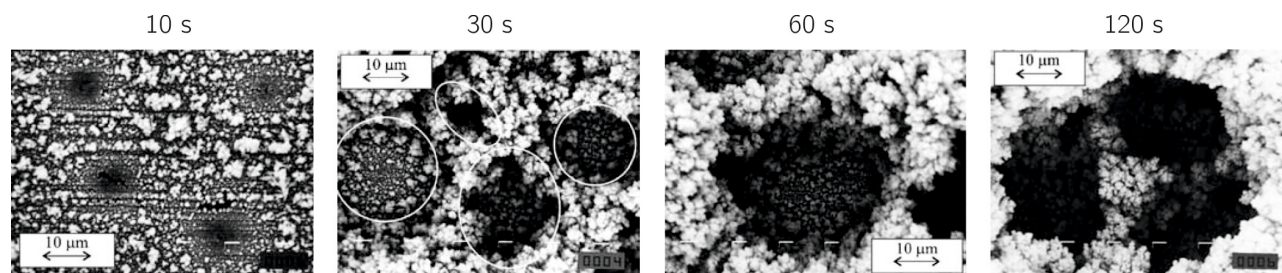

Figure 4. Morphologies of Cu deposits obtained after different times of potentiostatic electrolysis at a deposition overpotential of -1.000 V, from an aqueous solution containing 0.10 mol dm^{-3} CuSO$_4$ and 0.50 mol dm^{-3} H$_2$SO$_4$. Reproduced from Ref. 34 with the permission of Springer.

ChemCatChem

Reviews
doi.org/10.1002/cctc.202001145

Chemistry Europe
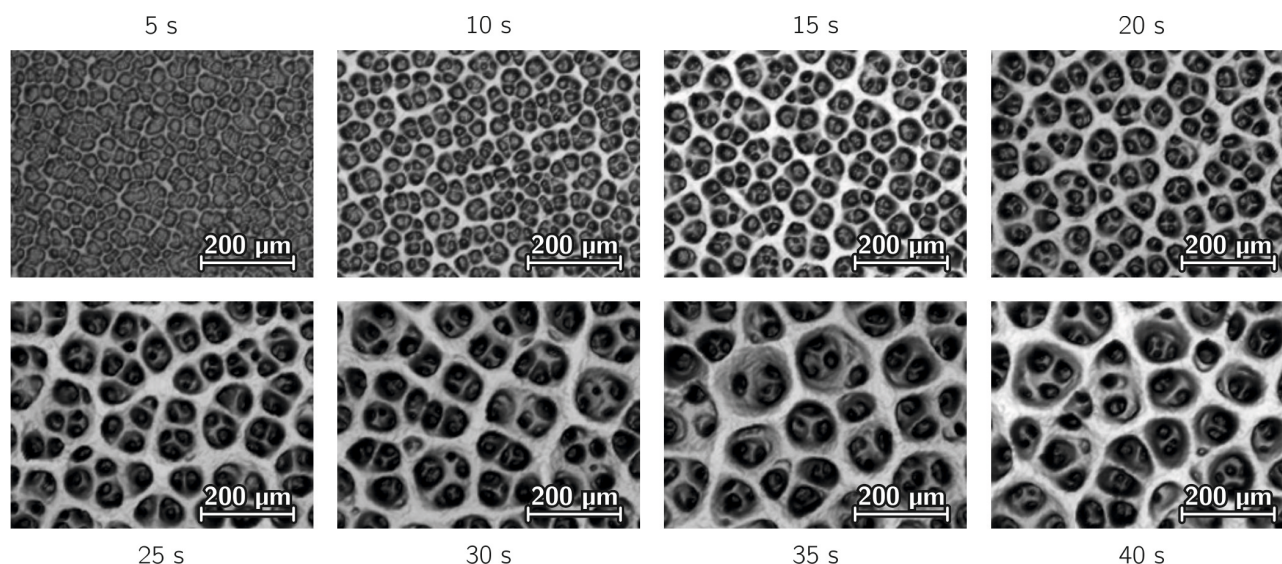European Chemical
Societies Publishing

Figure 5. Morphologies of Cu deposits obtained after different times of galvanostatic electrolysis at $-2.0\,A\,cm^{-2}$, from an aqueous solution containing $0.20\,mol\,dm^{-3}\,CuSO_4$ and $1.0\,mol\,dm^{-3}\,H_2SO_4$. Reproduced from Ref. 52 with permission of The Electrochemical Society.

30 seconds of potentiostatic electrolysis (Figure 4) we can notice that the deposited copper grows around the hydrogen bubbles that remained adherent to the surface, forming regular (circle-shaped) and irregular (from top view, ellipse shaped) cavities. As shown in Figure 5, an even more pronounced hierarchy is achieved if instead of potentiostatic control, we apply galvanostatic electrodeposition of foamed copper.[52]

As evident in Figures 3 and 4, the deposited metal foams exhibit two types of porosity: they show macropores, formed by the larger, coalesced bubbles; and micropores (porosities within the walls of the macropores) that are created as channels by the vigorous formation of small hydrogen bubbles over the copper dendrites.[34] As the electrolysis proceeds, the size of the macropores tends to increase, yielding a hierarchically structured foam deposit that has a bigger number of small pores close to the substrate, and fewer but bigger-sized pores close to the solution interface (Figures 6 and 7). This graded structure is ideally suited for the preparation of electrocatalyst materials with pore sizes specifically tuned by the selection of appropriate deposition times.[30]

2.4. Further Factors Affecting Foam Structure

As pointed out by Nikolić,[35] the formation of porous structures is possible for metals of all three Winand classes, provided that the deposition overpotential that is either directly applied or established as a result of galvanostatic polarization, exceeds the minimum initiation overpotential η_{ini}, defined by Equation (1), and that at this overpotential, hydrogen production is already vigorous.

Intensive hydrogen evolution will then have two effects: *i.)* that due to stirring the near-electrode solution, it decreases the thickness of the diffusion layer, increasing the limiting current
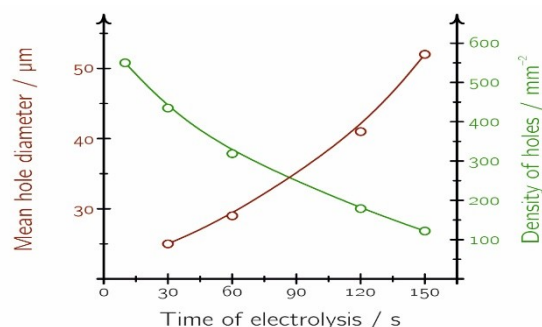

Figure 6. The size and number of H_2 bubble templated holes in Cu deposits obtained at a deposition overpotential of $-1.000\,V$, from an aqueous solution containing $0.10\,mol\,dm^{-3}\,CuSO_4$ and $0.50\,mol\,dm^{-3}\,H_2SO_4$ are anti-correlated as the deposition proceeds. Graph created using data from Ref. 34.
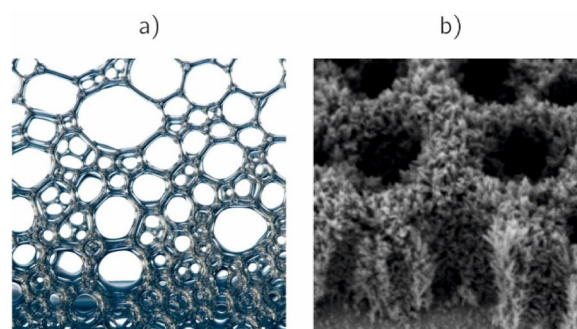

Figure 7. a) Illustration of the hierarchical porosity of metal foams and b) cross-sectional scanning electron micrographs of a potentiostatically obtained Cu foam deposit, reproduced from Ref. 30 with permission of the American Chemical Society.

ChemCatChem

Reviews
doi.org/10.1002/cctc.202001145

Chemistry Europe
European Chemical
Societies Publishing

density $j_{lim,dep}$ of metal deposition; and *ii.)* that due to the at least, temporal adherence of the bubbles to the surface, it will increase the effective current density. In case θ denotes the ratio of the surface (in a time average) blocked by bubbles, the effective current density will be $1/(1-\theta)$ times bigger than the current density applied (that is the current normalized by the geometric surface area).[57]

When preparing metal foams, one must keep in mind that exchange current densities found in the literature (like those plotted in Figure 2) are concentration dependent quantities and values found in literature are usually (but not always) normalized to a unity concentration of the metal or H^+ ions in the bulk solution (for metal deposition and HER, respectively). Thus, the overall electrolyte composition will have a strong effect on determining actual hydrogen evolution/metal deposition current ratios.[58] When preparing metal foams from noble metals, *e.g.*, from silver,[38] gold[40] or palladium salts,[43] a larger metal salt concentration in the bath may be required than, for example, when depositing normal metals such as Sn or Pb, or even intermediate metals like Cu.

The success of metal foams preparation lies however not only in whether the right current densities for metal deposition and hydrogen evolution are achieved. The morphology of the deposit, especially on the macroscale, will be determined by the maximum size that H_2 bubbles formed during the electrolysis can reach before breaking off the surface, and also by the rate at which bubble growth occurs (Figure 8).[55,59]

The break-off diameter d was found to depend on the partial current density of hydrogen evolution j_{HER} according to the empirical formula

$$d = d_0 \ (1 + a \ j_{HER})^b \qquad (2)$$

where the constants $a \approx 0.2 \ m^2 A^{-1}$ and $b \approx 0.45$ were determined by Vogt and Balzer[57] by fitting to experimental data; note that these constant values may be significantly different, depending on the system studied.

The parameter d_0 in Equation (2) is the break-off diameter in a current-free case, the value of which can be estimated by using a simplified form of the Fritz equation:[60]

$$d_0 = 1.20 \, \vartheta \sqrt{\frac{\gamma}{g \, \rho}} \qquad (3)$$

where g is the gravitational acceleration, ϑ denotes the contact angle of the bubble on the electrode surface, ρ is the density of the solution, and γ is the interfacial stress of the gas/liquid interface. Both the contact angle ϑ and the surface tension γ

may vary as function of the applied electrode potential (and/or current),[61] as well as near-surface variations of the viscosity of the solution[62] may affect both the break-off diameter and the trajectory of bubbles leaving the electrode surface.

Additives affecting the surface energetics (either the solid/liquid or the gas/liquid interfacial stress, for example by preferential adsorption on one or both of these interfaces) may have a significant impact on both the macro- and the micro-porosity of the obtained deposit.[30] For example cationic surfactants like cetyltrimethylammonium bromide (CTAB), when used as additives in copper deposition baths, were shown to suppress the collision among hydrogen bubbles by specifically adsorbing on the gas/liquid interface. This leads to a mild rate of hydrogen evolution and smaller hydrogen bubbles, thus resulting in a smaller pore structure.[63] Eventually, it was also shown that CTAB can also be used to fine-tune the hydro-phobicity of DHBT-deposited copper foams.[64]

Another important factor that has an effect on the structure of the finally obtained deposit is the concentration and form of available H^+ sources present in the depositing solutions. This parameter is probably even more important than the pH, which is only related to the concentration of free H^+ ions in the bulk solution. During intensive hydrogen evolution, however, when the near-electrode solution region gets alkalinated, additional H^+ sources such as NH_4^+ or citric acid can act as buffers, providing an excess amount of H^+ as a reactant supply for HER. Naturally, at large negative applied overpotentials or currents, even the direct reduction of H_2O can serve as means of HER. While in this case it is the autoprotolysis reaction of water that has to be taken into account to describe HER current densities,[48] for buffered systems additional (buffer) equilibria must be considered.[58]

Near-surface alkalination may have an adverse effect on the nature of the obtained deposits; *e.g.*, it can lead to the formation of hydroxides of the metal to be deposited.[64] While the application of buffers as bath components may successfully circumvent this effect, one also has to consider that some buffer components (especially due to complex formation) may also have other, indirect effects on the foam deposition process. For example, in case NH_4^+ ions are used as a buffer, the NH_3 molecules formed in the (alkaline) near-surface layers of the electrolyte solutions may act as complexing agents for the deposited metal, hindering its deposition. Although some experimental results do confirm this assumption,[38] the possibilities of complex formation are only scarcely treated in the literature of DHBT metal foam deposition.[22]
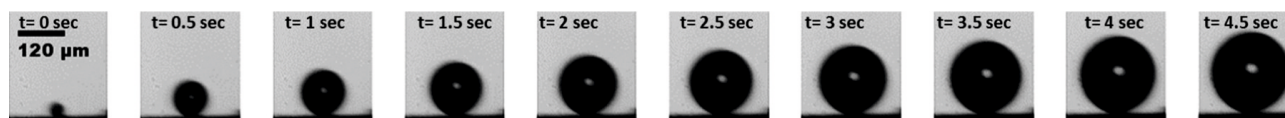

Figure 8. Sequence of images illustrating hydrogen bubble growth on an electrode surface at 60 mA cm^{-2} current density for HER. Reproduced from Ref. 55 with the permission of Elsevier.

ChemCatChem

Reviews
doi.org/10.1002/cctc.202001145

Chemistry
Europe
European Chemical
Societies Publishing

2.5. Technical Challenges of DHBT Metal Foam Deposition

Although it is rarely mentioned in literature, one technical challenge that needs to be addressed with respect to DHBT metal foam deposition is the extreme high current that these methods require. Depositing hydrogen bubble templated metal foams necessitates the use of current densities in the range of 1 to 10 A cm^{-2} (normalization is meant to the geometric surface area of the sample). This means that already in lab-scale experiments, the standard instrumentation (galvanostat/potentiostat) is to be equipped with current boosters. As standard boosters usually allow the control of currents up to 20 A, up-scaling may require specialized instruments as well. When using such high currents, secondary effects (such as that of Joule heat and *IR*-drop) should not be ignored, well-chosen cell geometries must be applied, and measures for electric shock protection must be taken.

3. Some Metal Foams Prepared by DHBT, with Potential Application in the Electroreduction of CO$_2$

Metals suited for catalysing electrochemical CO$_2$ reduction are usually those where hydrogen evolution proceeds only at high overpotentials. These metals can exhibit a relatively broad range of potentials where CO$_2$ reduction may already occur, while water splitting still remains relatively suppressed. These metals belong, according to Winand's classification, to the group of normal or intermediate metals. A non-exhaustive list includes pure metals such as Sn,[66,67] Pb,[68] Zn,[69,70] Bi,[71] Ag[72–74] and Cu,[75–78] as well as bimetallic systems where Sn foams are deposited on Cu surfaces[79–84] or when smoothly dispersed Ag and Cu form one bimetallic foam structure.[85,86] In what follows, we summarize the DHBT-assisted preparation strategies of these metal foams, as well as some important aspects of CO$_2$ reduction occurring on them.

3.1. Sn Foams (Pure)

Sn is a prime example of normal metals having a low melting point, little activity for HER and high activity for metal deposition. Although on a Cu substrate, Sn foams were deposited relatively early by Shin *et al.*,[29] from a bath that contained 0.15 mol dm^{-3} SnSO$_4$ dissolved in 1.5 mol dm^{-3} H$_2$SO$_4$. By applying galvanostatic deposition at a (geometric surface area normalised) current density of -3 A cm^{-2} for 5 to 20 seconds, 100 to 300 μm thick deposits with surface pores of 100 to 400 μm diameter were obtained (Figure 9). The foam walls of Sn were composed of relatively long and dense, straight dendritic particles. The apparent microporosity (that is, the microscopic porosity of the walls of bigger pores) described in the same work by Shin *et al.*[29] for Cu, was not seen in the case of Sn, probably as a result of the suppressed electrocatalytic activity of Sn towards HER (Figure 2).
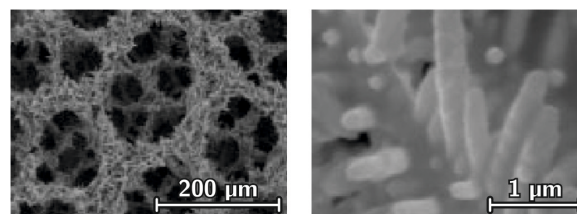

Figure 9. Scanning electron micrographs of a Sn foam deposited on a Cu substrate from a bath that contained 0.15 mol dm^{-3} SnSO$_4$ dissolved in 1.5 mol dm^{-3} H$_2$SO$_4$ by galvanostatic electrolysis at -3 A cm^{-2} nominal current density, lasting 5 seconds. Reproduced from Ref. 29, with the permission of Wiley.

Using a Sn instead of a Cu substrate, and SnCl$_2$ instead of SnSO$_4$ as a metal source bath component, deposits with qualities similar to those shown in Figure 9 were obtained by Du *et al.*[67] and were used for the electroreduction of CO$_2$. They showed that compared to planar Sn electrodes, Sn foams can deliver a higher yield and better selectivity for the production of formate. In a CO$_2$-saturated 0.1 mol dm^{-3} NaHCO$_3$ solution, the maximum Faradaic efficiency of formate production could reach above 90% at a current density of about 23.5 mA cm^{-2} ($E = -1.9$ V vs. SCE), which are among the highest reported to date under ambient conditions (H-type cell, aqueous solution, atmospheric pressure and room temperature).[67]

This improved production rate of formate can be attributed to the high surface area and porous structure. Moreover, Du *et al.*[67] demonstrated a high stability of their Sn foam catalyst; namely, the Faradaic efficiency remained unchanged during 16 hours of electrolysis. What cannot be inferred from Ref. 67 is, however, whether the outstanding tendencies towards the production of formate had any relation to the oxidation state of the Sn foam electrode. That oxide remnants on Sn catalysts have a guiding role in the production of formate has long been known,[66,87–89] and that surface oxidation promotes formate production (on the account of CO formation) was proven also for the case of large surface area Sn dendrites, the surface oxidation of which was induced by heating in air.[66]

3.2. Sn Foams (Deposited on Cu)

While reports on the use of pure Sn foams clearly point out that the large surface area of these foams lead to both a higher catalytic activity and an increased selectivity towards the production of formate,[66,67] the picture is not this clear in the case of foams composed of Sn deposited on top of Cu substrates (that is, Sn@Cu foams).

While browsing the literature, we can find works that advocate Sn@Cu foams for their excellent selectivity ($>90\%$) towards formate production,[79,81,82] while for some other researchers,[83,84] Sn@Cu foams seem to be of more value if the selectivity towards CO production is higher (again, $>90\%$). A comparison of two Sn foams deposited on Cu, with markedly different selectivities, is shown in Figure 10.
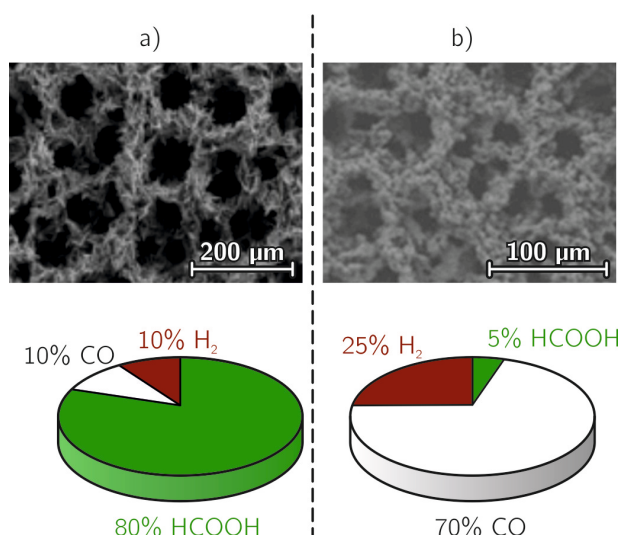
Figure 10. Sn foams deposited on a Cu substrate by a) Qin *et al.*[81] and by b) Li *et al.*[84] Scanning electron micrographs, reproduced from Ref. 81 with the permission of Elsevier and from Ref. 84 with that of MDPI, show similar surface morphologies, yet the product distribution is markedly different, as determined for potentiostatic electrolyses at -1.0 V *vs.* RHE in 0.1 mol dm^{-3} CO$_2$-saturated KHCO$_3$ solutions.

It is expected that also in case of these systems, the surface oxidation state of Sn particles has a pivotal role in determining selectivity. It was found, for example, by Li *et al.*[84] that the surface of Sn foams deposited on Cu substrates often contains SnO$_2$. We presume that stannic (or for that matter stannous) oxide domains in Sn foams may either be incorporated in the foam structure due to the local alkalination of the electrode as a result of DHBT deposition, or that even the entire foam surface may get partly oxidised after the foam is emerged from the depositing bath, and dried in air. Either way, it was found that these electrodes exhibit an SnO$_x$ coverage-dependent catalysis – *i.e.*, a shift from CO selectivity to HCOOH selectivity with increasing SnO$_2$ coverage.[84]

We assume that in case of Sn@Cu systems, bimetallic corrosion effects may account for that some electrocatalytically active SnO$_x$ particles may survive the reductive conditions of CO$_2$ electrolysis. This may explain that, as shown in Figure 10, in some Sn@Cu foams the selectivity of formate production is preserved.

3.3. Pb Foams

According to Winand's classification, Pb also belongs to the group of normal metals.[49] The preparation method of Pb foams was described by Cherevko *et al.*,[41] using perchloric acid both as a supporting electrolyte and an H$^+$ source. Deposition occurred on a Pt substrate from a solution containing 0.01 mol dm^{-3} PbClO$_4$ and 0.01–1.8 mol dm^{-3} HClO$_4$, under potentiostatic control at -2 V vs. Ag | AgCl. Good porous structures were only obtained above a HClO$_4$ concentration of 0.6 mol dm^{-3} (Figure 11). From a bath with a HClO$_4$ concen-
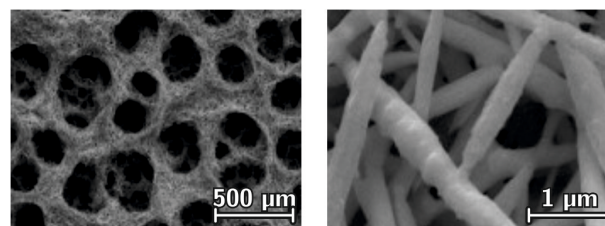

Figure 11. Scanning electron micrographs of a Pb foam deposited on a Pt substrate from a bath that contained 0.01 mol dm^{-3} PbClO$_4$ dissolved in 0.6 mol dm^{-3} HClO$_4$ by potentiostatic electrolysis lasting 2 seconds at -2 V *vs.* Ag | AgCl. Reproduced from Ref. 41, with the permission of Elsevier.

tration of 0.6 mol dm^{-3}, deposited Pb layers exhibited pore sizes of about 300 μm. The walls of the pores showed a microstructure consisting of 200–300 nm diameter wires at lower perchloric acid concentrations, while at higher concentrations (>0.9 mol dm^{-3}) the Pb wires were either partially or fully covered by granular particles.

The above procedure was adapted by Wang *et al.*[68] in order to obtain Pb foams applicable for the electroreduction of CO$_2$. They showed that the porous Pb foam had a better electrocatalytic performance for the production of formate than a Pb plate: at 5 °C, the highest recorded Faradaic efficiency of formate production was 96.8% at an applied potential of -1.7 V vs. SCE in a 0.5 mol dm^{-3} KHCO$_3$ solution saturated by CO$_2$. In another study, Fan *et al.*[90] have shown that the selectivity towards formate seems to correlate with the proportion of surface sites with the (100) orientation.

3.4. Zn Foams

While also belonging to the normal group of metals, reports about the electrodeposition of Zn foams are recent. In the work of Luo *et al.*,[69] Zn foams were deposited on a Cu mesh from solutions containing 0.1 mol dm^{-3} ZnSO$_4$ and 1.5 mol dm^{-3} (NH$_4$)$_2$SO$_4$. They applied a current density of -1 A cm^{-2} for 30 seconds in order to obtain the deposited Zn foam shown by the micrographs of Figure 12. These reveal macropores with an average diameter of 30 μm and micropores with a diameter
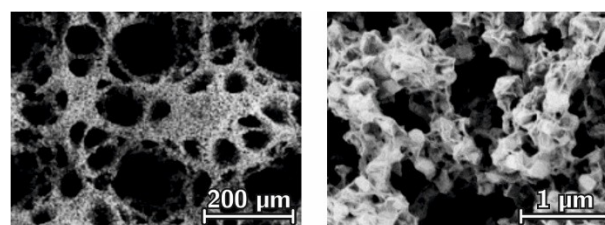

Figure 12. Scanning electron micrographs of a Zn foam deposited on a Pt substrate from a bath that contained 0.1 mol dm^{-3} ZnSO$_4$ dissolved in 1.5 mol dm^{-3} (NH$_4$)$_2$SO$_4$ by galvanostatic electrolysis at -3 A cm^{-2} nominal current density, lasting 5 seconds. Reproduced from Ref. 69, with permission of the American Chemical Society.

ChemCatChem

Reviews
doi.org/10.1002/cctc.202001145

Chemistry
Europe
European Chemical
Societies Publishing

smaller than 2 μm, the latter formed as channels of the leaving, smaller H_2 bubbles.

Luo et al.[69] investigated the electroreduction of CO_2 on their highly porous Zn foam (Figure 12), and found a remarkably high Faradaic efficiency of 95% towards the formation of CO at $E = -0.95$ V vs. RHE, where the current density was about -27 mA cm^{-2}, in a CO_2-purged 0.1 mol dm^{-3} $KHCO_3$ electrolyte. They argued that above the overall increase of the surface area, the Zn foam also offers a large number of active surface sites (compared to Zn foils) that play a decisive role in improving the catalytic activity. At the same time, the high local pH induced by the porous structure of Zn results in an enhanced CO selectivity because of suppressed H_2 evolution. Luo et al.[69] also transformed their Zn foam into a gas diffusion electrode, achieving a current density of 200 mA cm^{-2} for the reduction of CO_2 and an 84% Faradaic efficiency for CO production at -0.64 V in a flow-cell reactor.

In another work,[70] we also developed a Zn-based alloy foam catalyst by the application of DHBT, using copper ions as a foaming agent and thereby obtaining an alloy with 6 atomic % copper content. We detected a >90% Faradaic efficiency for CO production at -0.95 V vs. RHE in CO_2-purged 0.5 mol dm^{-3} $KHCO_3$. The high efficiency was ascribed to the combination of high density of low coordinated active sites and preferential Zn(101) over Zn(002) texturing,[70] and we pointed out by means of X-ray photoelectron spectroscopy investigations that the actual catalyst material is shaped upon reduction of an oxide/hydroxide-terminating surface, under CO_2 electrolysis conditions. In Ref. 70 we have also shown that intentional stressing by oxidation at ambient conditions proves to be beneficial for further activation of the catalyst.

3.5. Ag Foams

Silver is usually also considered a normal metal according to Winand's classification[49] but as long as silver is deposited not from a simple Ag^+ solution but from a solution of its complexes, it is usually treated as an intermediate metal.[35]

The first reports on the DHBT fabrication of silver foams originate from Cherevko et al.,[37,38] and these occurred from a thiocyanate complex solution of silver. The foam structure shown in Figure 13 was obtained by potentiostatic deposition at -3 V vs. Ag | AgCl lasting 30 seconds. For this deposition, Cherevko et al.[38] used a Pt substrate and a bath containing
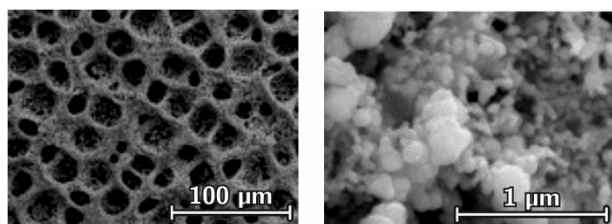
0.01 mol dm^{-3} Ag_2SO_4, 1.5 mol dm^{-3} KSCN acting as a complexing agent, 0.75 mol dm^{-3} NH_4Cl, and 0.01 mol dm^{-3} sodium citrate. NH_4Cl acted as an H^+ source and the authors found that a minimum threshold concentration of >0.5 mol dm^{-3} of NH_4Cl is required for the deposit to show a foamy structure. A decrease in the diameter (from 45 to about 20 μm) and wall thickness of the surface pores, as well as an increase of the number of formed holes with increasing concentrations of NH_4Cl was observed. The authors found[38] that the microscale morphology of the formed Ag deposits changes, from exhibiting nanosized dendrites in case of foams deposited at low NH_4Cl concentrations towards small particle agglomerates, deposited from baths with higher NH_4Cl content.

As for the preparation of silver foams from normal (i.e., noncomplexed) solutions, reports are relatively recent. In Ref. 72 we used a silver foil substrate and a bath containing 0.02 mol dm^{-3} Ag_2SO_4, 1.5 mol dm^{-3} H_2SO_4 and 0.1 mol dm^{-3} sodium citrate. Note that while the bulk of the solution was acidic enough not to allow complexation of silver by citrate, in the heavily alkaline near-electrode solution region, chelation of silver ions may occur. Silver foams obtained from citrate containing and citrate-free baths are compared in Figure 14. The thickness of the deposited foams is around 17 μm. Compared to the citrate-free deposition process, Ag foams deposited in the presence of citrate show a more uniform macroporosity with an open-cell architecture of interconnected pores. The average diameter of the macropores is significantly smaller, compared to deposits obtained from a citrate-free solution (Figure 14). This is probably related to the effect of citrate, decreasing the stress of the liquid/gas interface (cf. to Equation (3)). As expected, the inclusion of citrate in the depositing bath formulation does not only impact the obtained
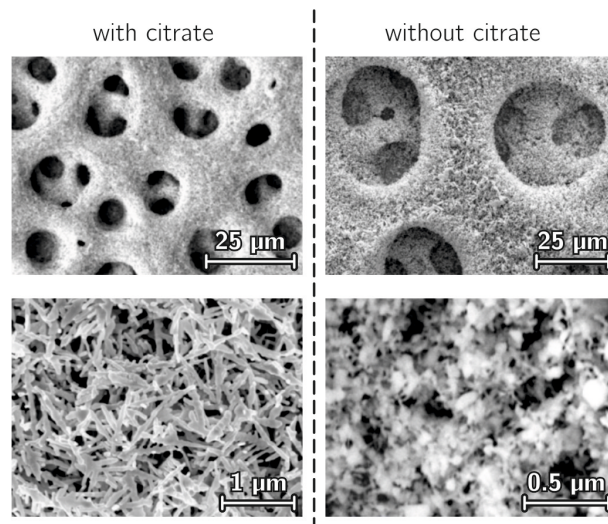

Figure 13. Scanning electron micrographs of an Ag foam deposited on a Pt substrate from a bath that contained 0.01 mol dm^{-3} Ag_2SO_4,

with citrate   without citrate

Figure 14. Scanning electron micrographs of an Ag foam deposited on an Ag substrate from a bath composed of 0.02 mol dm^{-3} Ag_2SO_4 and 1.5 mol dm^{-3} H_2SO_4. The effect of adding sodium citrate to the bath in a 0.1 mol dm^{-3} concentration can clearly be seen. Galvanostatic depositions with a nominal current density of -3 A cm^{-2}, lasting 20 seconds, were carried out in both cases. Reproduced from Ref. 72, with permission of the American Chemical Society.

ChemCatChem | Reviews
doi.org/10.1002/cctc.202001145

Chemistry
Europe
European Chemical
Societies Publishing

foam morphology, but also its catalytic activity towards CO_2 electroreduction. Especially in terms of long-term stability, the multiporous Ag foams deposited from citrate containing baths perform better than the ones prepared from citrate-free depositing solutions.[72]

Silver foams deposited from a citrate-containing solution were used as electrocatasysts for CO_2 reduction. Potentiostatic electrolyses in CO_2-saturated 0.5 $mol\,dm^{-3}$ $KHCO_3$ solutions were carried out in a hermetically tight H-type cell, and the partial current densities corresponding to the formation of each products were determined by means of on-line gas chromatography.[91] The potential of using silver foams as electrocatalyst materials becomes evident by comparing the catalytic properties of foams to those of a plain silver plate, as in Figure 15.[72]

There are two features of DHBT-deposited silver foams that become immediately apparent in Figure 15: *i.)* that the silver foam produces CO with a much higher activity and over a considerably broader potential region, compared to a simple silver plate; and *ii.)* that due to the foam-like structure, the diversity of products is increased, and especially at high negative potentials, some rather significant amounts of hydrocarbons (primarily methane and ethylene) are also formed. While the former feature casts the silver foam catalyst described in Ref. 72 one of the best Ag-based CO forming catalysts reported so far in the literature for aqueous environments, the latter feature deserves attention because the formation of hydrocarbons was reported before only on Cu-based electrode materials, while Ag is traditionally considered a strictly CO-forming catalyst.[92] Note here that, as proven by control experiments in Ref. 72, the colourful product palette shown in Figure 15b is not due to artefacts caused by citrate that was applied as an additive to the deposition bath.

As shown in Figure 15b, some $-20\ \mu A\ cm^{-2}$ partial current of CO formation can already be detected at the potential of -0.3 V *vs.* RHE, while the onset potential of CO_2 reduction is about 300 mV more negative on planar silver surfaces. Note that onset potentials as low as -0.3 V *vs.* RHE were so far only reported for gold nano-needle catalysts.[93] As the potential is set to more and more cathodic values, the overall current density rises, with CO remaining the only or at least the majority reaction product, down until -0.8, respectively to -1.2 V.

At potentials less cathodic than -0.8 V *vs.* RHE, not even hydrogen evolution is observed, unlike the case of plain surface silver electrodes, at which HER competes with CO_2 reduction even at low overpotentials. As a result, the CO-selectivity of the silver foam prepared in Ref. 72 is not peak-like as is the case of planar silver electrodes, but it remains constantly above 90% over a more than 900 mV broad potential range.

This superior selectivity towards the formation of CO was not met by other silver foam catalysts reported in the literature,[73,74] in particular because of differences of the foam structure at the nanoscale. In Ref. 72 we hypothesized that the highly anisotropic, needle-like structures seen in Figure 14, obtained so far only by citrate-assisted deposition, may account for the superior selectivity towards CO production by increasing the bonding strength of adsorbed CO to the catalyst surface. For example, on commercially available silver foam electrodes with grain-like microstructure, the Faradaic efficiency of CO production is generally lower, although the potential regime of CO formation is still broader than that on pristine silver plates.[74]

Another hint that underlines the pivotal role of adsorbed CO played in the mechanism is the formation of C_1 (methane) and, to some extent, C_2 (ethylene) hydrocarbons, which also necessitates an adsorbed CO intermediate.[94] Of course, apart
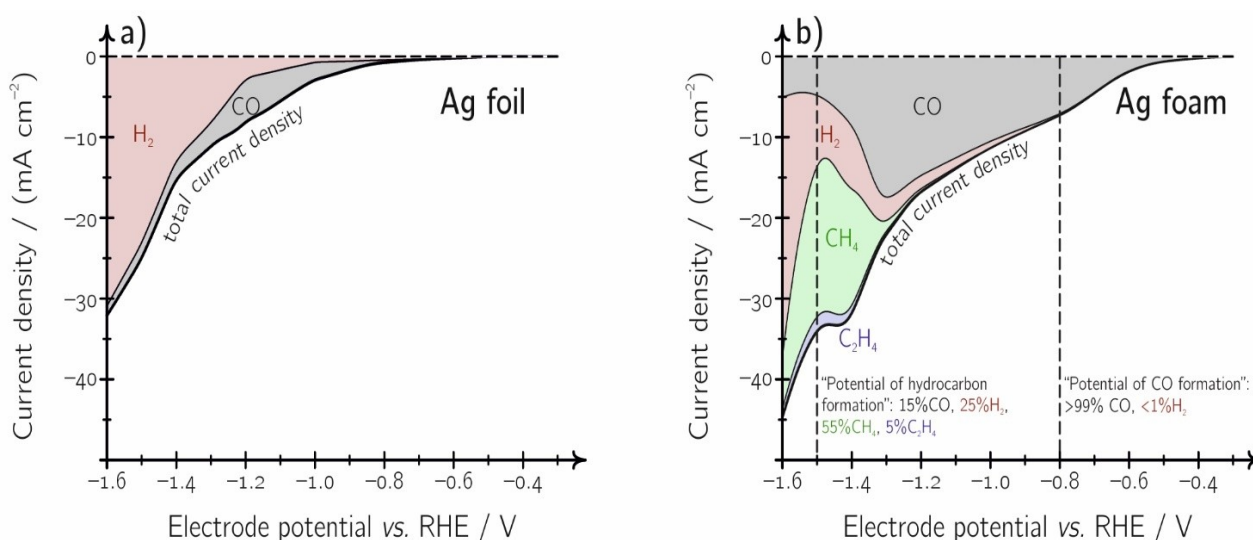

Figure 15. Polarization curves (interpolated) of a) a silver plate and b) the silver foam deposited from a citrate containing solution, shown in Figure 14. Electrolyses were carried out at distinct potentials in a CO_2-saturated 0.5 $mol\,dm^{-3}$ $KHCO_3$ solution, and the product distribution was determined by online gas chromatography. Colour-shaded areas show the distribution of reaction products. Currents were normalized to the geometric (nominal) surface area of the electrodes. The graphs were prepared using data from Ref. 72.

ChemCatChem

Reviews
doi.org/10.1002/cctc.202001145

**Chemistry
Europe**
European Chemical
Societies Publishing

from the higher bonding energy of adsorbed CO, and the longer residence time of surface-bound CO caused thereby, for the effective formation of hydrocarbons relatively intense H$^+$ reduction is also required to take place, so that surface-bound H atoms and CO molecules can effectively react.

From this point of view, the confinement of the reaction scenery to the small (macro)pores seems to be of primary importance. The hierarchical structure of the silver foam can make sure that potential intermediates (such as surface-bound CO or H$_2$) may not easily leave the electrode surface (and become a product), but instead get entrapped in the pores, at least for some time, having a higher chance to recombine.

The effect of confinement is illustrated by Figure 16a, showing a cavity of diameter d in contact with its surroundings through an opening of diameter a and length L. By theoretical studies on the random walk of a particle inside this cavity, it was shown by Berezhkovskii et al.[95] that the τ_{res} characteristic time of residence (i.e., the average time a molecule would spend inside the void before diffusing out through the neck) can well be approximated using the simple formula

a)

b)

Figure 16. a) A spherical cavity of diameter d, connected to its surroundings by a neck with length L and diameter a. b) Simulated motion of a particle inside a spherical segment. After formed, the particle leaves the surface of the cavity and begins to traject, hitting in this case, four times the cavity wall before eventually leaving the void.

$$T_{res} = \frac{2d^3}{3a^2}\frac{L}{D} \tag{4}$$

where D denotes the diffusion coefficient of the molecule.

Further taking into account that the characteristic time between two molecule-to-wall collisions can well be approximated as

$$T_{coll} = \frac{d^2}{6\,D} \tag{5}$$

it can be assumed that an average molecule, after born and before leaving the void, collides

$$N_{coll} = \frac{T_{res}}{T_{coll}} = \frac{4dL}{a^2} \tag{6}$$

times to the surface of the cavity. Using the arbitrary (but, based on the morphology shown for example in Figure 14, not unrealistic) parameter set of $d = 50$ μm, $a = 25$ μm, $L = 50$ μm and $D = 5 \cdot 10^{-6}$ cm^2 s^{-1}, we get to a residence time of about 13 seconds, during which a formed molecule would impact about 16 times the wall of the cavity, having ample opportunity to re-adsorb, and act further as an intermediate.

As seen in Equations (4) and (6), the characteristic residence time and the mean collision number increases with the L length of the neck that separates the cavity from its surroundings. This hints to that the confinement effect in case of deep-buried cavities is bigger. For near-surface cavities (for which $L \approx 0$), another work of Berezhkovskii et al.[96] provides the formula

$$T_{res} = \frac{d^3\pi}{12aD} \tag{7}$$

for the residence time, from which an average collision number

$$N_{coll} = \frac{d\pi}{2a} \tag{8}$$

follows. Using the above-mentioned parameters, the obtained residence time and collision number are about an order of magnitude smaller compared to when the escape occurs through a finite length neck. The concept is further illustrated by Figure 16b, showing the presumed Langevin trajectory[97] of a particle being formed and moving inside a void, before leaving it through an opening.

Although the above arguments are very simple and rather qualitative in nature, they well explain the effect of small-scale confinement on electrocatalytic processes. It is assumed that the above "multi-collision" effect is what lies behind the possibility of the formation of C$_2$ products on Ag foams, and a similar argument is often used for explaining CO$_2$ electro-reduction mechanisms on-going on Cu electrodes, allowing even the formation of C$_3$ products.[98]

One has to note, however, that the Ag foam catalyst described in Ref. 72, although it is one of the most excellent
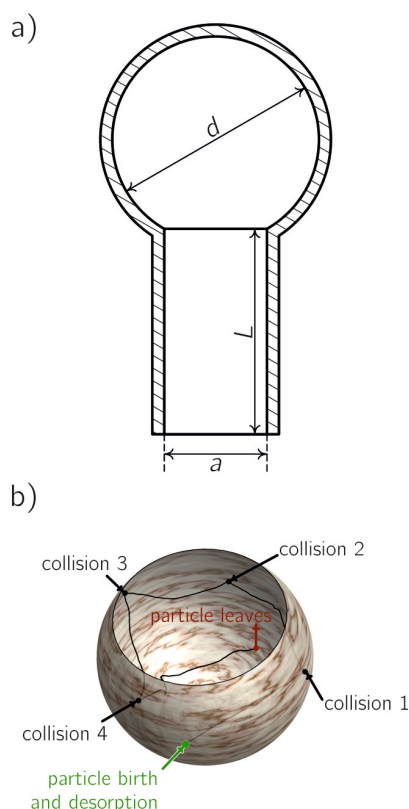
catalyst material for CO production, is not the ideal playground for hydrocarbon formation. While it was observed that when operated on a long run at potentials of CO formation (see Figure 15b) the catalyst performs well without any significant degradation effects, as electrolyses are carried out at more negative potentials to form hydrocarbons, the performance of the catalyst decreases over time. This probably has to do with the poisoning of the silver foam by the formed methane, and can also be related to a mechanical degradation caused by the intensive gas evolution observed during long-lasting electrolyses.

In order to study degradation effects, we used identical location scanning electron microscopy[99] in Ref. 72. Figure 17 demonstrates degradation suffered by silver foams over long times of electrolyses at potentials where hydrocarbons are formed. Note here also, that long-lasting electrolysis at CO-forming potential does not cause any visible degradation of the catalyst.

From point of view of future applications of Ag foams in CO-producing electrolyzers, it also seems important in particular for future studies to fine-tune the foam preparation procedure in the direction of obtaining well-structured foams on sub-strates that are more challenging than a plain Ag foil. Deposition on gas diffusion electrodes (GDEs) seems to be a logical first step of up-scaling attempts. During our pilot studies in this direction, we found that the Ag foam preparation recipe mentioned before (and described in details in Ref. 72) needs further improvement, as it yields a less well-defined foam structure when we apply it for the deposition of Ag foams on GDEs (compare Figure 18a to Figure 14). Nonetheless, even though there is obviously space for further development, Ag foams on GDEs exhibit a superior activity towards CO formation, as shown by results of our recent (yet unpublished) investigations (Figure 18b).

3.6. Cu Foams

As opposed to silver and to the other metals discussed above, copper is usually considered as the only metal where the formation of C_1 (methane and methanol), C_2 (ethylene and ethyl-alcohol), or even C_3 products (propyl-alcohol) is possible, even if the applied catalyst is not of a foam structure.[92]

Several studies were conducted in the past with the aim of understanding the selectivity of Cu catalysts towards the formation of certain products.[75–78,94,100–107] These studies all
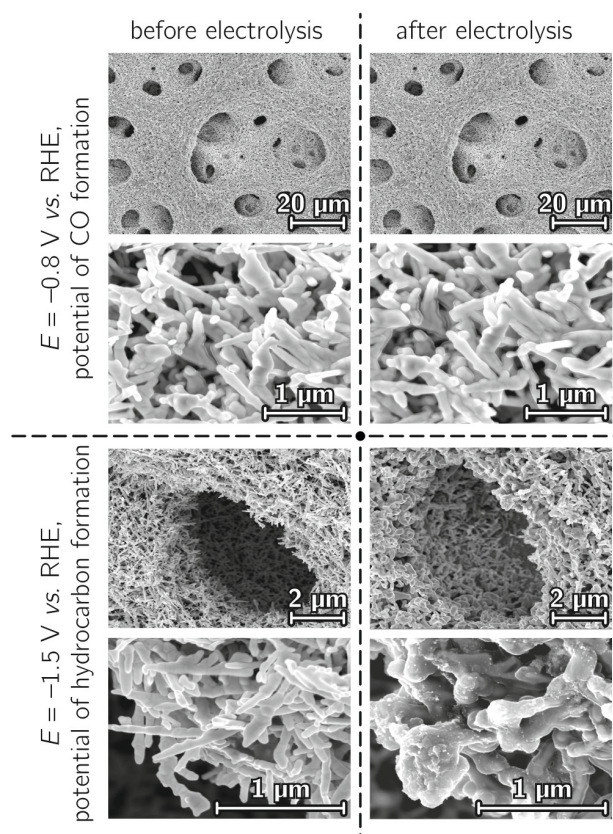
Figure 17. Scanning electron micrographs recorded at identical locations of an Ag foam catalyst, before and after being used for some hours for the electroreduction of CO_2. Mild potentials, where only CO is formed, cause no significant damage; however, long-time polarization in the range of extreme negative potentials where hydrocarbons are formed causes visible degradation, especially on the nanoscale.
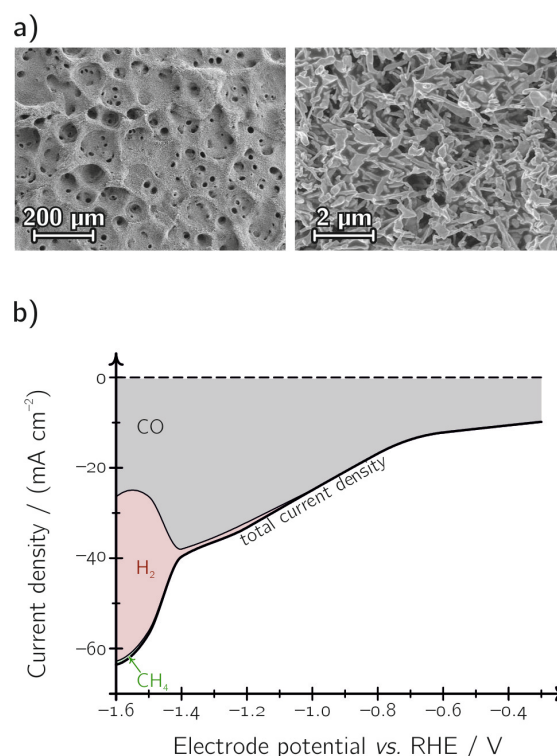
Figure 18. a) Scanning electron micrographs of a silver foam deposited by 20 s electrolysis using the recipe described in Ref. 72 onto a Sigracet 39 BC gas diffusion electrode (Fuel Cell Store). b) Interpolated product distribution and total current density plot measured on the GDE by electrolyses carried out in an H-type cell at distinct potentials in a CO_2-saturated 0.5 mol dm^{-3} $KHCO_3$ solution. (Unpublished data)

ChemCatChem

Reviews
doi.org/10.1002/cctc.202001145

**Chemistry
Europe**
European Chemical
Societies Publishing

underline the importance of the bonding strength between the catalyst surface and the $\cdot CO_2^-$ radical anion that, following a coupled H^+/e^- (alternatively, direct adsorbed H) transfer, forms surface-bound CO, which acts as a second key intermediate.[75] By contrast to some other metals previously mentioned in this study, copper can bond CO strongly enough to allow its further reduction to C_1, C_2 or even to C_3 products. Both experimental[100] and theoretical investigations[104] indicate that C—C coupling is more probable on (100) oriented copper surfaces while the C_1 pathway is preferential on the (111) surface.[75] As a result, significant effort (relying on the use of sputtering and electropolishing,[103] as well as electrodeposition and anodization techniques[108]) has recently been devoted to find possibilities of tuning Cu surfaces towards the right (preferably, C_2) selectivity. Amongst these approaches, the oxidation of the copper surface,[105–107] yielding weekly coordinated structures, seems to be the most promising. Note here, however, that the thus obtained catalysts should not be referred to as copper oxide, but rather as oxide derived (OD) copper catalysts, since under the heavily cathodic operating conditions, the copper oxide is instantaneously reduced to an elementary Cu state.

In a recent paper,[75] we combined the activation of Cu catalysts via the reduction of its surface oxide with the DHBT-based foam deposition approach first developed by Shin et al.[30] We thus produced mesoporous, large surface area copper foams, shown in Figure 19. Several procedures for the potentiostatic (Figures 3 and 4) and galvanostatic (Figure 5) means of copper foam preparation were reported by the works of Nikolić et al.[31–36] and of Zhang et al.[52] These works, and the mechanistic description of copper foam deposition described therein, were reviewed here in the section before.

For purposes of CO_2 electrolysis, our group used galvanostatic deposition (nominal current density: $-3\ A\,cm^{-2}$) to deposit black copper foams on a Cu wafer substrate from a bath that contained $0.2\ mol\,dm^{-3}$ $CuSO_4$ and $1.5\ mol\,dm^{-3}$ H_2SO_4. As seen in Figure 19, deposits with a hierarchical macroporosity were obtained, with macropore sizes growing as a function of deposition time. The thus prepared Cu foams underwent a fast surface oxidation, following emersion from the plating bath. We demonstrated that these OD Cu foam catalysts show a superior selectivity toward C_2 product formation at particularly low overpotentials.[75]

In Figure 20 the electrocatalytic properties of the copper foam deposited with a 20 s deposition time are compared to those of a planar Cu wafer. Both surfaces exhibit a clear preference for hydrocarbon formation, in combination with a significantly reduced preference for formate production. Whereas on the Cu wafer methane is the primary product, the C_2 pathway seems to prevail on the Cu foam catalyst, with the C_1 pathway suppressed to such extent that not even traces of methane formation are detected.

The preference of OD Cu foams towards the C_2 pathway can probably be explained by two, synergistic effects: *i.)* that the OD Cu surface is composed more of (100) oriented (open) facets[75] and *ii.)* that due to the porous structure (confinement), key intermediates of the C_2 pathway may be entrapped and get readsorbed inside the catalyst pores. The latter effect is demonstrated by Figure 21, showing an anti-correlated variation of the Faradaic efficiencies of C_2 products and that of CO, as a function of the surface pore size of the copper foam catalyst.

With regard to the microscopic structure of the OD copper foam catalysts, we note that while thermal annealing can aid in the oxidation of the foam surface (and by altering the surface morphology, it may result in FE variations), the thus formed oxide is almost immediately reduced to elementary copper under the harsh cathodic conditions applied for CO_2 electrolysis, and has thus no role in the CO_2 reduction mechanism. The
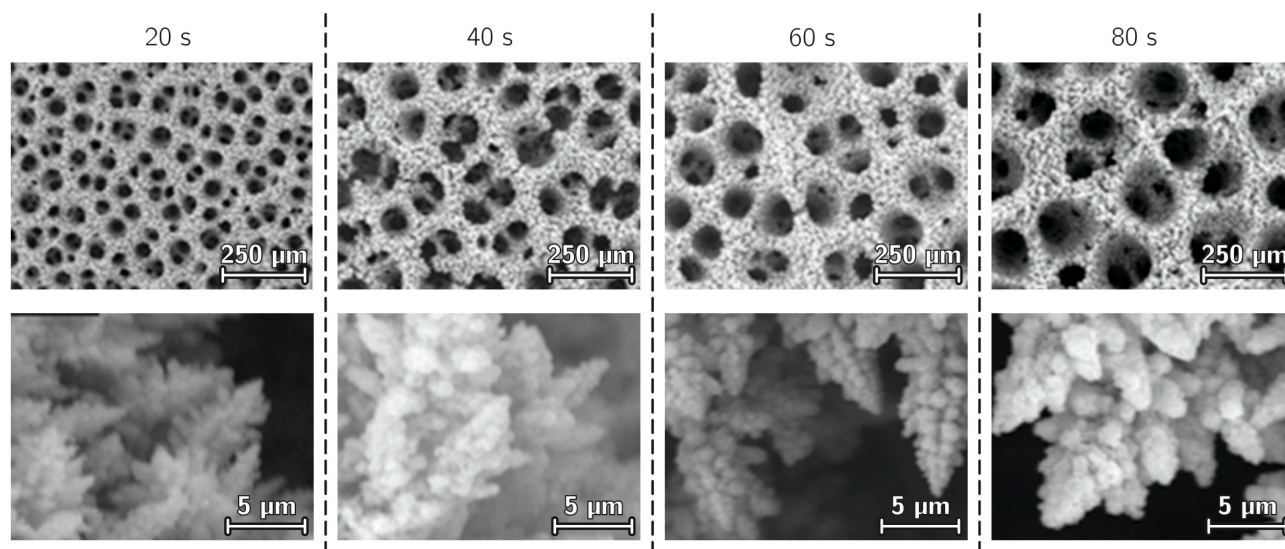

Figure 19. Scanning electron micrographs of Cu foams, deposited galvanostatically (nominal current density: $-3\ A\,cm^{-2}$) on a Cu wafer from a bath that contained $0.2\ mol\,dm^{-3}$ $CuSO_4$ and $1.5\ mol\,dm^{-3}$ H_2SO_4. Deposits obtained with different electrolysis times are shown. Reproduced from Ref. 75, with permission of the American Chemical Society.
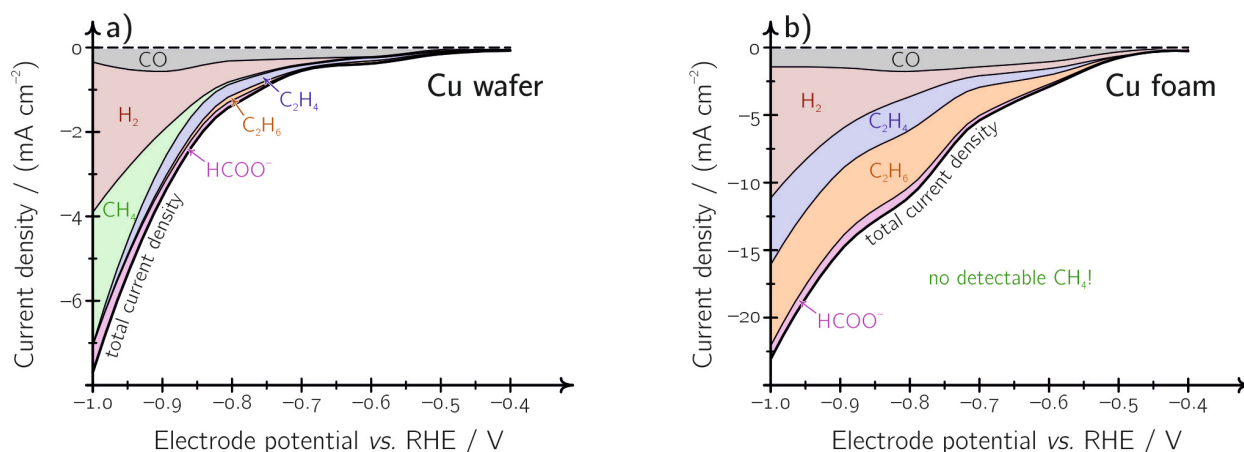
Figure 20. Polarization curves (interpolated) of a) a copper wafer and b) the copper foam shown in Figure 14 with the deposition time of 20 s. Electrolyses were carried out at distinct potentials in a CO_2-saturated 0.5 mol dm^{-3} NaHCO$_3$ solution, and the product distribution was determined by online gas, as well as post-electrolysis ionic liquid chromatography. Colour-shaded areas show the distribution of reaction products. Currents were normalized to the geometric (nominal) surface area of the electrodes. The graphs were prepared using data from Ref. 75.

disappearance (reduction) of surface copper oxides on Cu foam catalysts was recently proven by a combined operando X-ray diffraction (XRD), X-ray absorption spectroscopy (XAS) and Raman spectroscopy study.[76]

3.7. Ag–Cu Bimetallic Foams

By the combination of (primarily, CO forming) silver and (primarily, C$_2$ hydrocarbons forming) copper sites in the form of one bimetallic metal foam, it seems possible to direct the electroreduction of CO_2 towards the formation of products even

Figure 21. The distribution of CO_2 reduction products depend on the surface pore size of the Cu foam catalyst. Potentiostatic electrolyses lasting 1 hour were conducted at a potential of −0.8 V vs. RHE in a CO_2-saturated 0.5 mol dm^{-3} NaHCO$_3$ solution, and main gaseous products were analysed by means of online gas chromatography. Colour-shaded areas show the distribution of reaction products. The graph was prepared using data from Ref. 75.

more desired than either CO or hydrocarbons: ethyl- or even propylalcohol.[86]

The DHBT co-deposition of Ag–Cu bimetallic foams were first reported by Najdovski et al.,[46] who applied galvanostatic | j | > 1 A cm^{-2} co-depositions in H$_2$SO$_4$-acidified baths that contained both CuSO$_4$ and AgNO$_3$. As expected,[109] no alloy formation was observed and Najdovski et al. showed that the Ag–Cu bimetallic foam consists of small segregates of silver and copper phases.[46]

They observed that the surface pore size obtained during codeposition increases with increasing the c_{Ag+}:c_{Cu2+} ratio of the depositing bath. They argued that the increase of surface pore diameters, as well as the appearance of surface crack lines at higher silver contents is due to Ag exhibiting less catalytic activity towards HER than Cu (Figure 2), which favours the coalescence of H$_2$ bubbles.

The recipe of Najdovski et al.[46] was later applied by Kottakkat et al.[85] in order to create bimetallic Ag–Cu foams for purposes of CO_2 electroreduction. They used constant current (−1 A cm^{-2}, 10 s) co-deposition from baths containing 0.2 mol dm^{-3} CuSO$_4$, 1.5 mol dm^{-3} H$_2$SO$_4$ and 0.01–0.05 mol dm^{-3} AgNO$_3$. Kottakkat et al.[85] observed an improved CO selectivity and suppression of hydrogen evolution at low overpotentials, when comparing their bimetallic Ag–Cu foams to a plain Ag foil, and, similarly, a decrease of the Faradaic efficiency of formate production, compared to Cu foams.[85] The overall increase of the CO selectivity of bimetallic Ag–Cu foams was explained by an increased bonding strength of adsorbed CO, that Kottakkat et al.[85] verified by operando Raman spectroscopy. Although for other Ag–Cu bimetallic systems an enhanced selectivity towards multi-carbon oxygenate products was detected,[110] and it was attributed to near-surface alloying due to mechanical strain,[111] the formation of C$_2$ products, especially that of alcohols, was not observed by Kottakkat et al. on their Ag–Cu foams.[85]
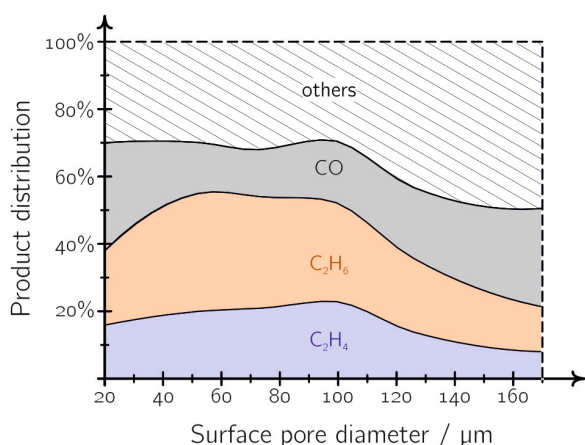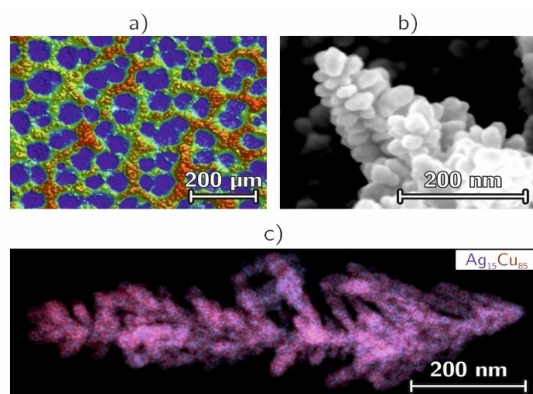
Figure 22. An Ag–Cu bimetallic foam deposited galvanostatically

In Ref. 86 we modified the original bath formulation of Najdovski et al.[46] by the inclusion of sodium citrate that, acting both as an adsorbent and a local chelating agent, changed the deposition mechanism,[86] resulting in honeycomb-like macropores and a fine dendritic microscopic structure. This is shown in Figure 22 for an $Ag_{15}Cu_{85}$ bimetallic foam deposited galvanostatically ($j = -3\ A\ cm^{-2}$, $t = 20\ s$) on a Cu foil substrate from a bath containing $1.5\ mol\ dm^{-3}\ H_2SO_4$, $0.02\ mol\ dm^{-3}$ $CuSO_4$, $0.002\ mol\ dm^{-3}\ AgNO_3$ and $0.1\ mol\ dm^{-3}$ sodium citrate.

Note that the notation $Ag_{15}Cu_{85}$ is based on an ICP–OES determination of the (bulk) atomic composition and by no means reflects compound formation. The white-light interferometric image of the Ag–Cu foam in Figure 22a reveals a near-surface pore diameter of ~25 μm; note, however, that the pore diameter is expected to vary also in this case along the surface normal, as was shown for other foams before (Figure 7). The side-walls of the macropores reveal dendrites with dimensions $< 50\ nm$, as shown in the electron micrograph of Figure 22b.

The dendrites themselves are composed of small, individual Ag and Cu phases, as revealed by the energy-dispersive X-ray map in Figure 22c.

The electrocatalytic performance of $Ag_{15}Cu_{85}$ bimetallic foams was investigated in Ref. 86 by 1 hour long electrolysis experiments carried out at certain potentials in CO_2-saturated $0.5\ mol\ dm^{-3}\ KHCO_3$ solutions. Results of these electrolysis experiments are shown in Figure 23.a.

It can be seen in Figure 23a that within the range of low overpotentials ($-0.7\ V < E < -0.3\ V$ vs. RHE) the predominant CO_2 reduction product is CO, assumed to take place preferentially on the Ag sites of the bimetallic catalyst. Accordingly, the Faradaic efficiency of formate production is suppressed, especially when compared to Cu foams, and in agreement with the observations of Kottakkat et al.[85] made on other bimetallic Ag–Cu foams. At potentials more cathodic than $-0.5\ V$ vs. RHE, hydrogen formation sets on, and along with it, pathways for the production of methane, ethylene and some small amounts ($<$ 1%) of ethane are opened.[86] At $E < -0.7\ V$, the product distribution of CO_2 reduction is already obviously dominated by the Cu component, as C–C coupling reactions are enabled. It can be assumed, that the C–C coupling reaction benefits from the high abundance of CO inside the porous catalyst. Due to the small domain sizes of the metallic components of the as-deposited $Ag_{15}Cu_{85}$ foam, the CO intermediate is rapidly transported from the Ag (CO producer) to the Cu domains (C–C coupler), either by surface diffusion ("spill-over") or by diffusion through the liquid electrolyte phase inside the pores of the bimetallic foam (as depicted in Figure 16b). As shown in Figure 23a, CO_2 reduction already results in the formation of some little amount of ethanol at this potential range, while only traces of n-propanol are detected.

The product distribution becomes remarkably different if we make subject the deposited $Ag_{15}Cu_{85}$ foam to thermal annealing before it is used as an electrocatalyst of CO_2
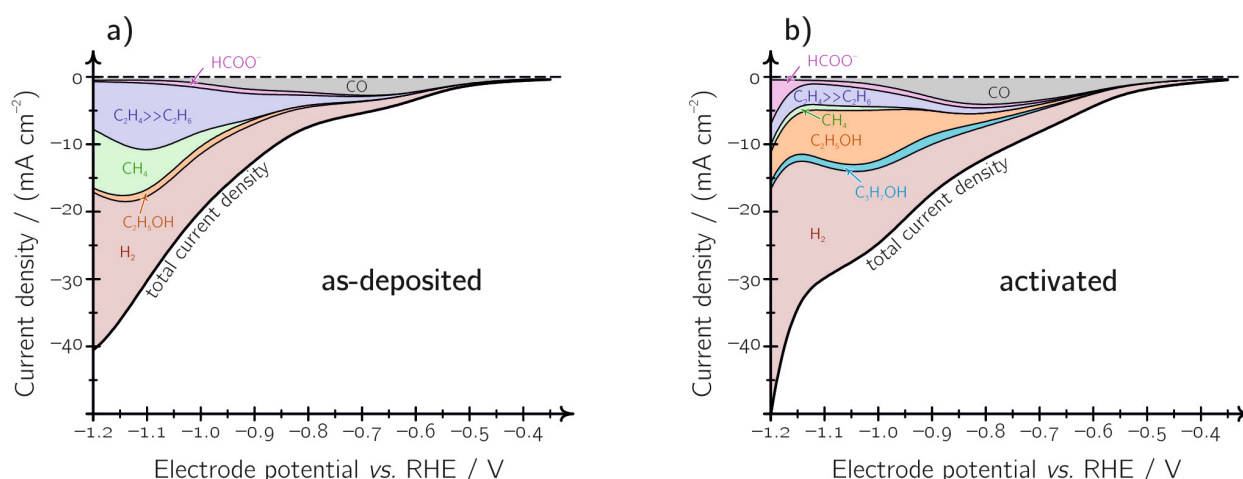

Figure 23. Polarization curves (interpolated) of CO_2 reduction recorded on a) an as-deposited $Ag_{15}Cu_{85}$ bimetallic foam and b) on the same foam following activation by mild thermal annealing in air (200 °C, 12 hours). Electrolyses were carried out at distinct potentials in a CO_2-saturated $0.5\ mol\ dm^{-3}\ KHCO_3$ solution, and the product distribution was determined by online gas, as well as by post-electrolysis ionic liquid chromatography. Colour-shaded areas show the distribution of reaction products. Currents were normalized to the geometric (nominal) surface area of the electrodes. The graphs were prepared using data from Ref. 86.
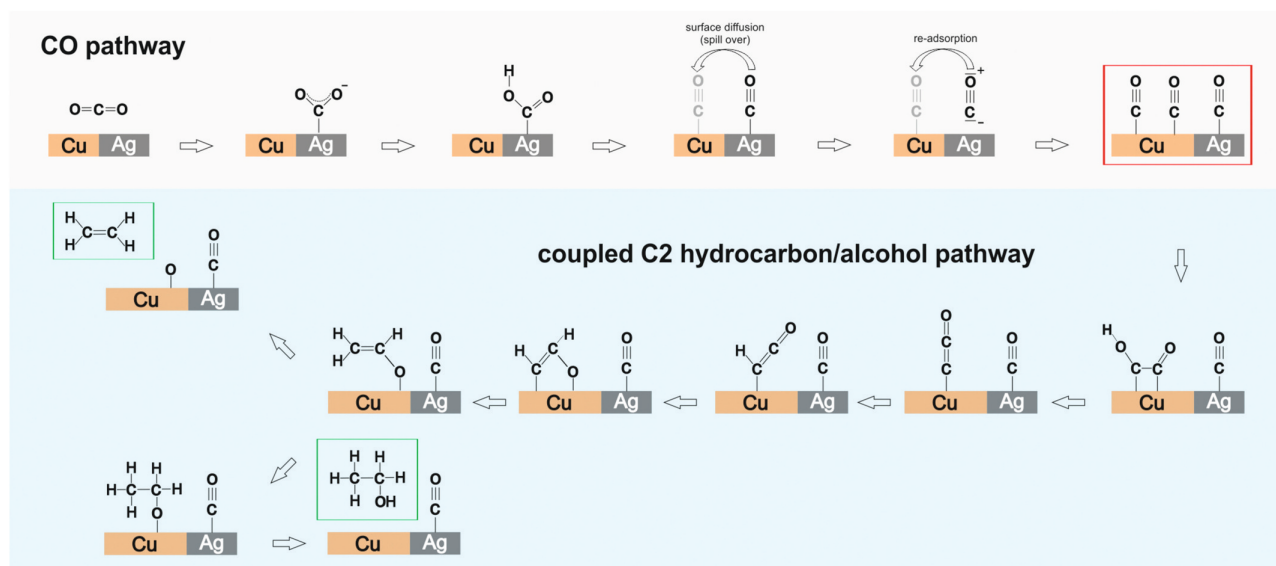
ChemCatChem

Reviews
doi.org/10.1002/cctc.202001145

Chemistry Europe
European Chemical
Societies Publishing

Figure 24. Proposed reaction scheme illustrating the coupling of the CO pathway and the C_2 hydrocarbon/alcohol reaction pathways on oxide-derived $Ag_{15}Cu_{85}$ bimetallic foams. Reproduced from Ref. 86 with the permission of Elsevier.

reduction (Figure 23b). It was shown in Ref. 86 that thermal annealing under mild conditions (200 °C for 12 hours) transforms the Cu in the bimetallic system into a mixture of crystalline Cu_2O and amorphous CuO, whereas the Ag islands remain in a metallic state due to the thermal instability of Ag_2O above temperatures of 180 °C. The selective oxidation of Cu in the bimetallic $Ag_{15}Cu_{85}$ catalyst goes along with an enrichment of Cu oxides on the surface of the formed mixed $AgCu_xO$ foam. Although both *operando* X-ray diffraction and *operando* Raman spectroscopy confirm that the cuprous/cupric oxide content of the catalyst is reduced back to the metallic state at potentials applied for CO_2 electrolysis, the formed oxide-derived bimetallic Ag–Cu foam was found to exhibit high selectivity towards alcohol formation (Figure 23b), with Faradaic efficiencies of about 34% and 7% for ethanol and *n*-propanol formation, respectively.

Extended electrolysis experiments (100 h) indicated a superior degradation resistance of the oxide-derived bimetallic catalyst, which was ascribed to the effective suppression of the C_1 hydrocarbon reaction pathway, assuring that irreversible carbon contaminations, appearing in particular during methane production, can be avoided.

The suggested mechanism of alcohol formation on the oxide derived, bimetallic Ag–Cu foam catalyst surface is shown in Figure 24. This mechanism is consistent with published models on alcohol formation on Cu,[112] with the addition that on the bimetallic foam CO forms selectively on the Ag domains, and is subsequently transported to the Cu domains via surface diffusion ("spillover") or alternatively via CO transport through the solution phase (desorption/readsorption). Besides the increased abundance of CO intermediates, it is the stabilization of the chemisorbed CO on the catalyst surface which further directs CO_2 reduction towards C–C coupling and alcohol formation, as confirmed by *operando* Raman experiments.[86]

3.8. Multimetallic Foams

The combination of multiple (more than two) metals in one foam structure has recently emerged as a new possibility of electrocatalyst design. In 2019 Lee *et al.*[113] described a Cu–In–Ag foam that was created by the deposition of a Cu foam that was electroplated by In and further modified by partial galvanic replacement of In with Ag (Figure 25). The preparation method is described briefly in Table 1, details can be found in Ref. 113. By the use of this trimetallic foam, Lee *et al.* achieved high Faradaic efficiency of CO production already at low overpotentials that, as they argued, was a result of synergistic effects arising from the high surface area of the Cu foam, the HER suppressing effect of In, and by Ag as a CO
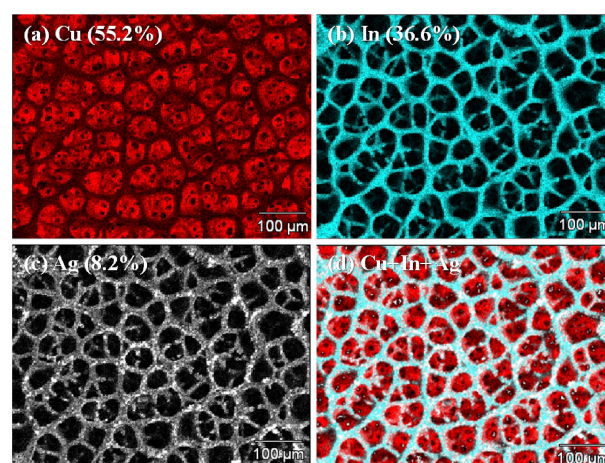

Figure 25. Elemental energy dispersive spectroscopy maps of the Ag–In–Cu foam prepared by Lee *et al.*[113] (a) Cu, (b) In, (c) Ag, and (d) Cu + In + Ag. Reproduced from Ref. 113, with the permission of Elsevier.

ChemCatChem

Reviews
doi.org/10.1002/cctc.202001145

Chemistry
Europe
European Chemical
Societies Publishing

Table 1. Overview of the metal foams (preparation and CO_2 reduction characteristics) discussed in Section 3.

Metal (featured CO_2 reduction product)	Preparation using the DHBT technique	CO_2 reduction characteristics
Sn, pure (formate)[67]	0.15 mol dm^{-3} SnSO$_4$, 1.5 mol dm^{-3} H$_2$SO$_4$., galvanostatic deposition on Sn foil, typ. current density: −3 A cm^{-2}, typ. deposition time: 5 to 20 s.	In CO_2-sat. 0.1 mol dm^{-3} NaHCO$_3$, at $E = -1.9$ V vs. SCE $j \approx -23.5$ mA cm^{-2}; > 90% *FE* for formate production.
Sn@Cu (formate)[81]	0.1 mol dm^{-3} SnCl$_2$, 0.1 mol dm^{-3} sodium citrate, 1.2 mol dm^{-3} HCl, galvanostatic deposition on electro-polished Cu foil, typ. current density: −2 A cm^{-2}, typ. deposition time: 2 min.	In CO_2-sat. 0.1 mol dm^{-3} KHCO$_3$, at $E = -1.2$ V vs. RHE $j \approx -6.5$ mA cm^{-2}; > 90% FE for formate production.
Pb (formate)[68]	0.01 mol dm^{-3} PbClO$_4$, 0.01 mol dm^{-3} sodium citrate, 1.0 mol dm^{-3} HClO$_4$, galvanostatic deposition on Pb plate, typ. current density: −0.5 to −8 A cm^{-2}, typ. deposition time: 10 to 20 s.	In CO_2-sat. 0.5 mol dm^{-3} KHCO$_3$, at $E = -1.7$ V vs. SCE $j \approx -10$ mA cm^{-2}; > 97% FE for formate production at 5 °C.
Zn (CO)[69]	0.1 mol dm^{-3} ZnSO$_4$, 1.5 mol dm^{-3} (NH$_4$)$_2$SO$_4$, galvanostatic deposition on a Cu mesh, typ. current density: −1 A cm^{-2}, typ. deposition time: 30 s.	In CO_2-sat. 0.1 mol dm^{-3} KHCO$_3$, at $E = -0.95$ V vs. SCE $j \approx -27$ mA cm^{-2}; > 95% FE for CO formation.
Ag (CO)[72]	0.02 mol dm^{-3} Ag$_2$SO$_4$, 0.1 mol dm^{-3} sodium citrate, 1.5 mol dm^{-3} H$_2$SO$_4$, galvanostatic deposition on an Ag foil, typ. current density: −3 A cm^{-2}, typ. deposition time: 20 s.	In CO_2-sat. 0.5 mol dm^{-3} KHCO$_3$, at $E = -0.8$ V vs. RHE about −8 mA cm^{-2}; > 99% FE for CO formation. At $E = -1.5$ V vs. RHE $j \approx -36$ mA cm^{-2}; FEs: 15% CO, 25% H$_2$, 55% CH$_4$, 5% C$_2$H$_4$.
Cu (C$_2$ hydrocarbons)[75]	0.2 mol dm^{-3} CuSO$_4$, 1.5 mol dm^{-3} H$_2$SO$_4$, galvanostatic deposition on a Cu wafer, typ. current density: −3 A cm^{-2}, typ. deposition time: 20 s. See Ref..	In CO_2-sat. 0.5 mol dm^{-3} KHCO$_3$, at $E = -0.8$ V vs. RHE $j \approx -12$ mA cm^{-2}; FEs: 37% C$_2$H$_6$, 22% C$_2$H$_4$, 16% CO, 7% HCOOH, 17% H$_2$. See Ref. 75.
CuAg bimetallic (C$_{\geq 2}$ alcohols)[86]	0.02 mol dm^{-3} CuSO$_4$, 0.002 mol dm^{-3} AgNO$_3$, 1.5 mol dm^{-3} H$_2$SO$_4$, galvanostatic deposition on a Cu foil, typ. current density: −3 A cm^{-2}, typ. deposition time: 20 s, activated by annealing in air at 200 °C, 12 hours.	In CO_2-sat. 0.5 mol dm^{-3} KHCO$_3$, at $E = -1.05$ V vs. RHE $j \approx -27$ mA cm^{-2}; FEs: 28% C$_2$H$_5$OH, 4% C$_3$H$_7$OH, 10% C$_2$ hydrocarbons, 2.5% formate, 2.5% CH$_4$, 3% CO, 50% H$_2$.
AgInCu trimetallic (CO)[113]	Cu foam substrate is prepared from 0.12 mol dm^{-3} CuSO$_4$, 0.5 mol dm^{-3} H$_2$SO$_4$, 1.2 mol dm^{-3} (NH$_4$)$_2$SO$_4$ and 40 μmol dm^{-3} benzotriazole on a Ti foil, galvanostaticaly, at a current density of −1.2 A cm^{-2} for 40 s. In deposition then takes place on the Cu foam at a current density of −50 mA cm^{-2} for 900 s, in a 0.1 mol dm^{-3} InCl$_3$ and 0.5 mol dm^{-3} HClO$_4$ solution. Galvanic replacement by Ag follows by immersion into a solution of 10 mmol dm^{-3} AgNO$_3$ and 2 mmol dm^{-3} 2-nitrobenzoic acid.	In CO_2-sat. 0.5 mol dm^{-3} KHCO$_3$, at $E = -0.53$ V vs. RHE $j \approx -2$ mA cm^{-2}; > 74% FE for CO formation.

producer. Apart from minor amounts of formate produced, Lee *et al.* did not detect any products other than CO and H$_2$ on this trimetallic foam.

4. Summary and Outlook

In this review we attempted to provide an oversight on the current state-of-the-art of DHBT-based deposition of metal foams, and on the application of these materials as promising new catalysts of the electroreduction of CO_2.

We gave an introduction to the phenomenology and mechanism of DHBT-based deposition of metal foams, addressing the most important factors affecting the structure and surface morphology of the prepared foams. It was shown that by a careful selection of appropriate experimental parameters, foams of hierarchical structure can be created from various types of noble, intermediate and normal metals. The success of DHBT-based foam deposition depends on a set of parameters, and appropriate selection of the applied (potentiostatic/galvanostatic) mode of deposition, the value of the electrode potential or current at which the deposition is carried out, as well as the proper formulation of the depositing bath have a key impact on the deposited foam structure. With respect to bath formulation, most emphasis is laid on the concentration of the used metal salt and of the acid component, as well as on

the concentration of buffering or complexing agents, and that of surfactants.

The review contains a brief description of several recipes, originating from works of our own or that of other groups, for the deposition of some metal foams, including pure metals such as Sn, Pb, Zn, Ag, Cu, as well as two-component systems like Sn foams deposited on Cu and the mixed Ag–Cu bimetallic foam. The reason why these metal foams and not some others like Pt, Pd, or Au were made subject of this study, is that the mentioned metals are the most promising candidates to be used as catalyst materials in electrochemical CO_2 reduction.

Accordingly, foams prepared by the DHBT technique from the above metals were also discussed from the point of view of CO_2 reduction, by placing special emphasis on the product distribution of this versatile process. While it is usually noted that on metal foams, mostly due to their increased surface area, electrocatalytic processes can occur at a higher rate compared to plain electrodes of the same metal, we found that hierarchical metal foams prepared by the DHBT technique often have a lot more to offer.

As it was pointed out especially in the cases of Ag, Cu and Ag–Cu bimetallic foams, the pores of these hierarchical three-dimensional structures can harbour reactions which would otherwise be unavailable on open surfaces due to the confinement (entrapping) of key reaction intermediates. In case of CO_2 electroreduction, confinement allows desorbed CO and H$_2$ to remain close and potentially re-adsorb on the electrode surface,

ChemCatChem

Reviews
doi.org/10.1002/cctc.202001145

Chemistry
Europe
European Chemical
Societies Publishing

ultimately leading to the formation of reaction products of a lower oxidation state (such as hydrocarbons and alcohols). Moreover, by the application of post-deposition, pre-electrolysis treatments (such as the oxidation of Cu-containing foams by annealing in air), the microstructure of the foams may further be fine-tuned towards the formation of certain, desired, CO_2 reduction products. Although most metal oxides never survive the reductive conditions of CO_2 electrolysis, oxide-derived surfaces have a different (usually, more open) structure, which opens a pathway before the formation of C_2 and even of C_3 products.

To conclude, the DHBT technique of metal foams preparation has the key advantage of meeting the most important structural and electronic factors that are considered essential for the electrocatalysis of CO_2 reduction. Processes fundamental to the technique, such as bubble nucleation, growth and detachment mechanisms, as well as the kinetics of metal deposition and dendrite formation are now understood at a level which will allow the rational design of mono- or multi-metallic foams that can act as new catalysts of CO_2 reduction. As it was shown, research on some metal foam catalysts is now ready to move in the direction of industrial upscaling (cf. to Figure 18), as foams with good structural qualities can even be deposited on gas diffusion electrodes. It is thus expected that in the coming years, metal foams will provide a viable alternative to, and may even outperform supported nanoparticle based (ink-like) catalysts in terms of yield, selectivity and, especially, stability.

Acknowledgements

Conflict of Interest

The authors declare no conflict of interest.

[1] S. J. Davis, K. Caldeira, H. D. Matthews, *Science* **2010**, *329*, 1330–1333.
[2] B. Khezri, A. C. Fisher, M. Pumera, *J. Mater. Chem. A* **2017**, *5*, 8230–8246.
[3] F. D. Meylan, V. Moreau, S. Erkman, *J. CO₂ Util.* **2015**, *12*, 101–108.
[4] W. Luc, F. Jiao, *ACS Catal.* **2017**, *7*, 5856–5861.
[5] P. Liu, G. Chen, *Porous Materials*, Butterworth-Heinemann, Oxford, **2014**, pp. 189–220.
[6] W. Zhu, R. Zhang, F. Qu, A. M. Asiri, X. Sun, *ChemCatChem* **2017**, *9*, 1721–1743.
[7] H. Zhao, Y.-P. Zhu, Z.-Y. Yuan, *Eur. J. Inorg. Chem.* **2016**, *2016*, 1916–1923.
[8] *IUPAC Compendium of Chemical Terminology* (Eds.: A. D. Mc-Naught, A. Wilkinson), Blackwell Scientific Publications, Oxford, 2ⁿᵈ ed, **1997**.
[9] R. Du, X. Jin, R. Hübner, X. Fan, Y. Hu, A. Eychmüller, *Adv. Energy Mater.* **2020**, *10*, 1901945.
[10] M. F. Ashby, T. Evans, N. A. Fleck, J. W. Hutchinson, H. N. G. Wadley, *Metal Foams: A Design Guide*, Butterworth-Heinemann, **2000**.
[11] H. W. Pickering, P. R. Swann, *Corrosion* **1963**, *19*, 373–389.
[12] K. Hashimoto, T. Goto, W. Suëtaka, S. Shimodaira, *Trans. Jpn. Inst. Met.* **1965**, *6*, 107–112.
[13] A. J. Forty, *Nature* **1979**, *282*, 597–598.
[14] J. Erlebacher, M. J. Aziz, A. Karma, N. Dimitrov, K. Sieradzki, *Nature* **2001**, *410*, 450–453.
[15] D. Walsh, L. Arcelli, T. Ikoma, J. Tanaka, S. Mann, *Nat. Mater.* **2003**, *2*, 386–390.
[16] H.-L. Gao, L. Xu, F. Long, Z. Pan, Y.-X. Du, Y. Lu, J. Ge, S.-H. Yu, *Angew. Chem. Int. Ed.* **2014**, *53*, 4561–4566; *Angew. Chem.* **2014**, *126*, 4649–4654.
[17] B. C. Tappan, M. H. Huynh, M. A. Hiskey, D. E. Chavez, E. P. Luther, J. T. Mang, S. F. Son, *J. Am. Chem. Soc.* **2006**, *128*, 6589–6594.
[18] B. C. Tappan, S. A. Steiner, E. P. Luther, *Angew. Chem. Int. Ed.* **2010**, *49*, 4544–4565; *Angew. Chem.* **2010**, *122*, 4648–4669.
[19] N. C. Bigall, A.-K. Herrmann, M. Vogel, M. Rose, P. Simon, W. Carrillo-Cabrera, D. Dorfs, S. Kaskel, N. Gaponik, A. Eychmüller, *Angew. Chem. Int. Ed.* **2009**, *48*, 9731–9734; *Angew. Chem.* **2009**, *121*, 9911–9915.
[20] W. Liu, A.-K. Herrmann, N. C. Bigall, P. Rodriguez, D. Wen, M. Oezaslan, T. J. Schmidt, N. Gaponik, A. Eychmüller, *Acc. Chem. Res.* **2015**, *48*, 154–162.
[21] S. Tang, S. Vongehr, Y. Wang, J. Cui, X. Wang, X. Meng, *J. Mater. Chem. A* **2014**, *2*, 3648–3660.
[22] B. J. Plowman, L. A. Jones, S. K. Bhargava, *Chem. Commun.* **2015**, *51*, 4331–4346.
[23] O. Lummer, F. Kurlbaum, *Ann. Phys. Chem.* **1892**, *282*, 204–224.
[24] F. Kohlrausch, *Ann. Phys. Chem.* **1897**, *299*, 423–430.
[25] S. E. Stanca, F. Hänschke, A. Ihring, G. Zieger, J. Dellith, E. Kessler, H.-G. Meyer, *Sci. Rep.* **2017**, *7*, 1074.
[26] *Modern Electroplating* (Eds.: M. Schlesinger, M. Paunovic), Wiley, New York, 5ᵗʰ ed, **2010**.
[27] C. Marozzi, A. Chialvo, *Electrochim. Acta* **2000**, *45*, 2111–2120.
[28] C. Marozzi, A. Chialvo, *Electrochim. Acta* **2001**, *46*, 861–866.
[29] H.-C. Shin, J. Dong, M. Liu, *Adv. Mater.* **2003**, *15*, 1610–1614.
[30] H.-C. Shin, M. Liu, *Chem. Mater.* **2004**, *16*, 5460–5464.
[31] N. D. Nikolić, K. I. Popov, Lj. J. Pavlović, M. G. Pavlović, *J. Electroanal. Chem.* **2006**, *588*, 88–98.
[32] N. Nikolić, K. Popov, Lj. Pavlović, M. Pavlović, *Sensors* **2007**, *7*, 1–15.
[33] N. Nikolić, G. Branković, M. Pavlović, K. Popov, *J. Electroanal. Chem.* **2008**, *621*, 13–21.
[34] N. D. Nikolić, K. I. Popov, *Mod. Aspects Electrochem.*, Springer, New York, **2010**, pp. 1–70.
[35] N. D. Nikolić, *Morphology of Electrochemically and Chemically Deposited Metals*, Springer, Cham, **2016**, pp. 171–203.
[36] N. D. Nikolić, *J. Electrochem. Sci. Eng.* **2020**, *10*, 111–126.
[37] S. Cherevko, X. Xing, C.-H. Chung, *Electrochem. Commun.* **2010**, *12*, 467–470.
[38] S. Cherevko, C.-H. Chung, *Electrochim. Acta* **2010**, *55*, 6383–6390.
[39] S. Cherevko, C.-H. Chung, *Talanta* **2010**, *80*, 1371–1377.
[40] S. Cherevko, C.-H. Chung, *Electrochem. Commun.* **2011**, *13*, 16–19.
[41] S. Cherevko, X. Xing, C.-H. Chung, *Appl. Surf. Sci.* **2011**, *257*, 8054–8061.
[42] S. Cherevko, N. Kulyk, C.-H. Chung, *Nanoscale* **2012**, *4*, 568–575.
[43] S. Cherevko, N. Kulyk, C.-H. Chung, *Nanoscale* **2012**, *4*, 103–105.
[44] I. Najdovski, P. R. Selvakannan, A. P. O'Mullane, S. K. Bhargava, *Chem. Eur. J.* **2011**, *17*, 10058–10063.
[45] A. Ott, L. A. Jones, S. K. Bhargava, *Electrochem. Commun.* **2011**, *13*, 1248–1251.
[46] I. Najdovski, P. R. Selvakannan, A. P. O'Mullane, *RSC Adv.* **2014**, *4*, 7207.
[47] V. E. Coyle, D. K. J. Oppedisano, L. A. Jones, A. E. Kandjani, Y. M. Sabri, S. K. Bhargava, *J. Electrochem. Soc.* **2016**, *163*, B689–B695.
[48] M. de J. Gálvez-Vázquez, V. Grozovski, N. Kovács, P. Broekmann, S. Vesztergom, *J. Phys. Chem. C* **2020**, *124*, 3988–4000.
[49] R. Winand, *Electrochim. Acta* **1994**, *39*, 1091–1105.
[50] S. Trasatti, *J. Electroanal. Chem. Interfacial Electrochem.* **1972**, *39*, 163–184.
[51] Y. Li, Y.-Y. Song, C. Yang, X.-H. Xia, *Electrochem. Commun.* **2007**, *9*, 981–988.
[52] H. Zhang, Y. Ye, R. Shen, C. Ru, Y. Hu, *J. Electrochem. Soc.* **2013**, *160*, D441–D445.

ChemCatChem

Reviews
doi.org/10.1002/cctc.202001145

Chemistry Europe
European Chemical
Societies Publishing

[53] K. Popov, S. S. Djokić, B. Grgur, *Fundamental Aspects of Electrometallurgy*, Springer, New York, **2013**.

[54] N. Ibl, *Chem. Ing. Tech.* **1961**, *33*, 69–74.

[55] P. Chandran, S. Bakshi, D. Chatterjee, *Chem. Eng. Sci.* **2015**, *138*, 99–109.

[56] L. J. J. Janssen, J. G. Hoogland, *Electrochim. Acta* **1970**, *15*, 1013–1023.

[57] H. Vogt, R. J. Balzer, *Electrochim. Acta* **2005**, *50*, 2073–2079.

[58] N. Kovács, V. Grozovski, P. Moreno-García, P. Broekmann, S. Vesztergom, *J. Electrochem. Soc.* **2020**, *167*, 102510.

[59] D. Fernández, P. Maurer, M. Martine, J. M. D. Coey, M. E. Möbius, *Langmuir* **2014**, *30*, 13065–13074.

[60] W. Fritz, *Phys. Z.* **1935**, *36*, 379–384.

[61] G. G. Láng, C. A. Barbero, *Laser Techniques for the Study of Electrode Processes*, Springer, Berlin, **2012**, pp. 41–73.

[62] S. A. Amadi, D. R. Gabe, M. Goodenough, *J. Appl. Electrochem.* **1991**, *21*, 1114–1119.

[63] H. Yang, X. Hao, J. Tang, W. Jin, C. Liu, H. Hou, X. Ji, J. Hu, *Appl. Surf. Sci.* **2019**, *494*, 731–739.

[64] Y. Li, W.-Z. Jia, Y.-Y. Song, X.-H. Xia, *Chem. Mater.* **2007**, *19*, 5758–5764.

[65] N. L. Ritzert, T. P. Moffat, *J. Phys. Chem. C* **2016**, *120*, 27478–27489.

[66] D. H. Won, C. H. Choi, J. Chung, M. W. Chung, E.-H. Kim, S. I. Woo, *ChemSusChem* **2015**, *8*, 3092–3098.

[67] D. Du, R. Lan, J. Humphreys, S. Sengodan, K. Xie, H. Wang, S. Tao, *ChemistrySelect* **2016**, *1*, 1711–1715.

[68] J. Wang, H. Wang, Z. Han, J. Han, *Front. Chem.* **2015**, *9*, 57–63.

[69] W. Luo, J. Zhang, M. Li, A. Züttel, *ACS Catal.* **2019**, *9*, 3783–3791.

[70] P. Moreno-García, N. Schlegel, A. Zanetti, A. C. López, A. de Jesús Gálvez-Vázquez, A. Dutta, M. Rahaman, P. Broekmann, *ACS Appl. Mater. Interfaces* **2018**, *10*, 31355–31365.

[71] M. Fan, S. Prabhudev, S. Garbarino, J. Qiao, G. A. Botton, D. A. Harrington, A. C. Tavares, D. Guay, *Appl. Catal. B* **2020**, *274*, 119031.

[72] A. Dutta, C. E. Morstein, M. Rahaman, A. Cedeño López, P. Broekmann, *ACS Catal.* **2018**, *8*, 8357–8368.

[73] H. Wang, Z. Han, L. Zhang, C. Cui, X. Zhu, X. Liu, J. Han, Q. Ge, *J. CO₂ Util.* **2016**, *15*, 41–49.

[74] Y. Yu, N. Zhong, J. Fang, S. Tang, X. Ye, Z. He, S. Song, *Catal.* **2019**, *9*, 57.

[75] A. Dutta, M. Rahaman, N. C. Luedi, M. Mohos, P. Broekmann, *ACS Catal.* **2016**, *6*, 3804–3814.

[76] A. Dutta, M. Rahaman, B. Hecker, J. Drnec, K. Kiran, I. Z. Montiel, D. J. Weber, A. Zanetti, A. C. López, I. Martens, P. Broekmann, M. Oezaslan, *J. Catal.* **2020**.

[77] S. Sen, D. Liu, G. T. R. Palmore, *ACS Catal.* **2014**, *4*, 3091–3095.

[78] S. Min, X. Yang, A.-Y. Lu, C.-C. Tseng, M. N. Hedhili, L.-J. Li, K.-W. Huang, *Nano Energy* **2016**, *27*, 121–129.

[79] Y. Wang, J. Zhou, W. Lv, H. Fang, W. Wang, *Appl. Surf. Sci.* **2016**, *362*, 394–398.

[80] W. Lv, J. Zhou, F. Kong, H. Fang, W. Wang, *Int. J. Hydrogen Energy* **2016**, *41*, 1585–1591.

[81] B. Qin, H. Wang, F. Peng, H. Yu, Y. Cao, *J. CO₂ Util.* **2017**, *21*, 219–223.

[82] C. Chen, Y. Pang, F. Zhang, J. Zhong, B. Zhang, Z. Cheng, *J. Mater. Chem. A* **2018**, *6*, 19621–19630.

[83] J. Zeng, K. Bejtka, W. Ju, M. Castellino, A. Chiodoni, A. Sacco, M. A. Farkhondehfal, S. Hernández, D. Rentsch, C. Battagliaand, C. F. Pirri, *Appl. Catal. B* **2018**, *236*, 475–482.

[84] Q. Li, M. Li, S. Zhang, X. Liu, X. Zhu, Q. Ge, H. Wang, *Catalysts* **2019**, *9*, 476.

[85] T. Kottakkat, K. Klingan, S. Jiang, Z. P. Jovanov, V. H. Davies, G. A. M. El-Nagar, H. Dau, C. Roth, *ACS Appl. Mater. Interfaces* **2019**, *11*, 14734–14744.

[86] A. Dutta, I. Z. Montiel, R. Erni, K. Kiran, M. Rahaman, J. Drnec, P. Broekmann, *Nano Energy* **2020**, *68*, 104331.

[87] Y. Chen, M. W. Kanan, *J. Am. Chem. Soc.* **2012**, *134*, 1986–1989.

[88] A. Dutta, A. Kuzume, M. Rahaman, S. Vesztergom, P. Broekmann, *ACS Catal.* **2015**, *5*, 7498–7502.

[89] A. Dutta, A. Kuzume, V. Kaliginedi, M. Rahaman, I. Sinev, M. Ahmadi, B. R. Cuenya, S. Vesztergom, P. Broekmann, *Nano Energy* **2018**, *53*, 828–840.

[90] M. Fan, S. Garbarino, G. A. Botton, A. C. Tavares, D. Guay, *J. Mater. Chem. A*, **2017**, *5*, 20747–20756.

[91] A. Rudnev in *Encyclopedia of Interfacial Chemistry* (Ed.: K. Wandelt), Elsevier, Amsterdam, **2018**, pp. 321–325.

[92] Y. Hori, *Modern Aspects of Electrochemistry, Vol. 42*, Springer, New York, **2008**, pp. 89–189.

[93] W. Zhu, Y.-J. Zhang, H. Zhang, H. Lv, Q. Li, R. Michalsky, A. Peterson, S. Sun, *J. Am. Chem. Soc.* **2014**, *136*, 16132–16135.

[94] R. Kortlever, J. Shen, K. J. P. Schouten, F. Calle-Vallejo, M. T. M. Koper, *J. Phys. Chem. Lett.* **2015**, *6*, 4073–4082.

[95] A. M. Berezhkovskii, A. V. Barzykin, V. Y. Zitserman, *J. Chem. Phys.* **2009**, *130*, 245104.

[96] I. V. Grigoriev, Y. A. Makhnovskii, A. M. Berezhkovskii, V. Y. Zitserman, *J. Chem. Phys.* **2002**, *116*, 9574–9577.

[97] N. G. van Kampen, *Stochastic Processes in Physics and Chemistry*, Elsevier, Amsterdam **2007**.

[98] T.-T. Zhuang, Y. Pang, Z.-Q. Liang, Z. Wang, Y. Li, C.-S. Tan, J. Li, C. T. Dinh, P. D. Luna, P.-L. Hsieh, T. Burdyny, H.-H. Li, M. Liu, Y. Wang, F. Li, A. Proppe, A. Johnston, D.-H. Nam, Z.-Y. Wu, Y.-R. Zheng, A. H. Ip, H. Tan, L.-J. Chen, S.-H. Yu, S. O. Kelley, D. Sinton, E. H. Sargent, *Nat. Can.* **2018**, *1*, 946–951.

[99] N. Hodnik, M. Zorko, M. Bele, S. Hočevar, M. Gaberšček, *J. Phys. Chem. C*, **2012**, *116*, 21326–21333.

[100] Y. Hori, I. Takahashi, O. Koga, N. Hoshi, *J. Mol. Catal. A* **2003**, *199*, 39–47.

[101] K. J. P. Schouten, Y. Kwon, C. J. M. van der Ham, Z. Qin, M. T. M. Koper, *Chem. Sci.* **2011**, *2*, 1902.

[102] K. P. Kuhl, E. R. Cave, D. N. Abram, T. F. Jaramillo, *Energy Environ. Sci.* **2012**, *5*, 7050.

[103] W. Tang, A. A. Peterson, A. S. Varela, Z. P. Jovanov, L. Bech, W. J. Durand, S. Dahl, J. K. Nørskov, I. Chorkendorff, *Phys. Chem. Chem. Phys.* **2012**, *14*, 76–81.

[104] J. H. Montoya, C. Shi, K. Chan, J. K. Nørskov, *J. Phys. Chem. Lett.* **2015**, *6*, 2032–2037.

[105] C. S. Chen, J. H. Wan, B. S. Yeo, *J. Phys. Chem. C* **2015**, *119*, 26875–26882.

[106] K. W. Frese, *J. Electrochem. Soc.* **1991**, *138*, 3338.

[107] C. W. Li, M. W. Kanan, *J. Am. Chem. Soc.* **2012**, *134*, 7231–7234.

[108] M. Le, M. Ren, Z. Zhang, P. T. Sprunger, R. L. Kurtz, J. C. Flake, *J. Electrochem. Soc.* **2011**, *158*, E45–E49.

[109] P. R. Subramanian, J. H. Perepezko, *J. Phase Equilib.* **1993**, *14*, 62–75.

[110] E. L. Clark, C. Hahn, T. F. Jaramillo, A. T. Bell, *J. Am. Chem. Soc.* **2017**, *139*, 15848–15857.

[111] J. L. Stevens, R. Q. Hwang, *Phys. Rev. Lett.* **1995**, *74*, 2078–2081.

[112] M. Rahaman, A. Dutta, A. Zanetti, P. Broekmann, *ACS Catal.* **2017**, *7*, 7946–7956.

[113] H. Lee, H. Kim, I. Choi, S. H. Ahn, *Electrochim. Acta* **2019**, *323*, 133102.

5.8. A Tandem (Bi₂O₃ → Biₘₑₜ) Catalyst for Highly Efficient ec-CO₂ Conversion into Formate: Operando Raman Spectroscopic Evidence for a Reaction Pathway Change

Reprinted with permissions from ACS Catal. 2021, 11, 4988−5003, Copyright ©2021 American Chemical Society

Authors: Abhijit Dutta, Iván Zelocualtecatl Montiel, Kiran Kiran, Alain Rieder, Vitali Grozovski, Lukas Gut, and Peter Broekmann

Highlights: Bismuth oxide with interconnected open cell structure demonstrated to exhibit electrocatalytic selectivity towards formate maintaining an efficiency of 90% within an extended potential window of ca. 1100 mV, reaching a maximum efficiency of $FE_{formate}$ = 100% at −0.6 V vs RHE. Two distinct reaction pathways i) sub-carbonate pathway on partially reduced Bi_2O_3 foam at low overpotentials, ii) Bi-O pathway on Bi_{met} at medium and high overpotentials were shown as to be origin of this promising electrocatalytic characteristics. *Operating* Raman spectroscopy as a function of electrolytic time and voltage monitors the progressive translation of the carbonate/oxide composite catalyst into their completely metallic state. The observed structural and compositional variations correspond with variations in faradaic efficiency and partial current density of formate production ($PCD_{formate}$), which achieves a maximum of $PCD_{formate}$ = −84.1 mA cm^{-2} at −1.5 V versus RHE.

Contributions: I assisted in the electrochemical experiments and characterization (by SEM) of the catalyst. I performed the cross section analysis for the thickness of the sample. I was involved in the final preparation of manuscript.

A Tandem (Bi$_2$O$_3$ → Bi$_{met}$) Catalyst for Highly Efficient *ec*-CO$_2$ Conversion into Formate: *Operando* Raman Spectroscopic Evidence for a Reaction Pathway Change

Abhijit Dutta,* Iván Zelocualtecatl Montiel, Kiran Kiran, Alain Rieder, Vitali Grozovski, Lukas Gut, and Peter Broekmann*

Read Online

ACCESS | Metrics & More | Article Recommendations | SI Supporting Information

ABSTRACT: A novel bismuth oxide nanofoam, produced by means of the dynamic hydrogen bubble template (DHBT) electrodeposition approach followed by thermal annealing at 300 °C for 12 h, demonstrates excellent electrocatalytic selectivity toward formate production with faradaic efficiencies (FEs) never falling below 90% within an extended potential window of ~1100 mV (max. FE$_{formate}$ = 100% at −0.6 V vs RHE). These promising electrocatalytic characteristics result from the coupling of two distinct reaction pathways of formate formation in the aqueous CO$_2$-sat. 0.5 M KHCO$_3$ electrolyte, which are active on (i) the partly reduced Bi$_2$O$_3$ foam at low overpotentials (sub-carbonate pathway) and (ii) on the corresponding metallic Bi$_{met}$ foam catalyst at medium and high overpotentials (Bi−O pathway). For the first time, *operando* Raman spectroscopy provides experimental evidence for the embedment of CO$_2$ into the oxidic Bi$_2$O$_3$ matrix (sub-carbonate formation) at low overpotentials prior to and during the CO$_2$ reduction reaction (CO$_2$RR). The gradual transition of the formed carbonate/oxide composite catalyst into its fully metallic state is monitored by *operando* Raman spectroscopy as a function of electrolysis time and applied potential. The observed structural and compositional alterations correlate with changes in the faradaic efficiency and partial current density of formate production (PCD$_{formate}$), which reaches a maximum value of PCD$_{formate}$ = −84.1 mA cm^{-2} at −1.5 V vs RHE. The so-called identical location scanning electron microscopy technique was applied to monitor morphological changes that take place on the nanometer length scale upon sub-carbonate formation and partial electro-reduction of the oxidic precursor during the CO$_2$RR. However, the macroporous structure of the foam catalyst remains unaffected by the (oxide/carbonate → metal) transition and the catalytic CO$_2$RR.

KEYWORDS: ec-CO$_2$ reduction, operando Raman spectroscopy, identical location (IL) SEM, formate production, carbon fiber cloth, (BiO)$_2$CO$_3$, Bi$_2$O$_3$ nanofoam

INTRODUCTION

Societal, economic, and technological advancements over the last several decades have led to the extensive use of fossil fuels and, consequently, to substantially enhanced emissions of the greenhouse gas carbon dioxide (CO$_2$), which is the primary origin of global climate change.[1,2] Furthermore, alternative energy sources need to be explored due to the limited supply of fossil fuels. In principle, synthetic fuels (e.g., oxygenates[3] and hydrocarbons[3,4]) and other valuable platform chemicals (e.g., formate[5]) can be produced by means of the electrochemical reduction of CO$_2$ (denoted hereinafter CO$_2$RR), a process that has significant potential to contribute in the future to the necessary closing of the anthropogenic CO$_2$ cycle.[6] It is the use of renewable energy sources as the input for the highly endergonic CO$_2$RR that will render the overall CO$_2$ conversion process truly sustainable.[7−10]

Formate, one of the targeted liquid CO$_2$RR products, is currently synthesized in the industry on a large scale from CO.[11] The "green" electrochemical approach of formate production via the CO$_2$RR (electrochemical synthesis route) can be considered a promising alternative to the mature but environmentally unfriendly process of formate production (CO synthesis route).

It is known that electrocatalysts are essential not only to accelerate the inherently slow CO$_2$RR process but also to direct the reaction selectivity toward the targeted product.

Early studies by Azuma et al.[12] and Hori et al.[13] focused primarily on the CO_2RR in an aqueous reaction environment and mono-metallic "bulk" materials as the catalysts. Based on their pioneering work, CO_2RR catalysts were classified into three major groups depending on the resulting product distribution: (i) carbon monoxide (CO) forming catalysts (e.g., Ag, Au, and Zn), (ii) hydrocarbon and oxygenate producing catalysts (Cu), and (iii) formate producing metals (e.g., Pb, Sn, Tl, Hg, and In).[12,14]

Recently, several more complex CO_2RR catalysts for formate production have been developed, such as nitrogen- and sulfur-doped reduced graphene oxide,[15] molecular catalysts,[16] nanocomposite materials,[17] and Pd-based composites.[5] Intriguingly, transition metal oxides, such as Co_3O_4,[18,19] SnO_2,[20] ZnO,[21] and In_2O_3,[22] have also been identified as promising candidates for the electrosynthesis of formate from CO_2.

Among the formate-producing catalysts studied thus far, Bi and Bi-based materials stand out, in particular because of their ability to stabilize the adsorbed $CO_2^{\cdot-}$ radical anion, which is considered to be a key intermediate in the reaction pathway of formate production.[23−25]

Previous studies have focused on two-dimensional (2D) Bi materials, e.g., foils,[26] nanosheets,[23,24,27] thin layers of Bi,[28] and dendritic Bi catalysts.[29] However, in most of these cases, an excellent formate efficiency was achieved only within a rather narrow potential window (e.g., a faradaic efficiency of ~86% and $PCD_{formate}$ of approximately −13.33 mA cm^{-2} at −1.1 V vs RHE[27] and on a comparably short electrolysis time scale of a few hours.[24,27,30−32] The latter suggests substantial catalyst degradation over more extended electrolysis times.[23,24,27,31,33]

In the present work, we apply the additive-assisted dynamic hydrogen bubble template (denoted hereinafter DHBT)[34,35] approach for the electrosynthesis of three-dimensional (3D) dendritic Bi foams. As substrates of choice, we chose carbon fiber cloths, which often find use as gas diffusion electrodes (GDEs, see Figure S1) in electrolyzer systems. The results obtained on the GDE are further compared to Bi foams deposited on ideal planar support electrodes (e.g., Cu and C foils). Herein, we demonstrate that the combination of a GDE support material with the DHBT approach for catalyst preparation results in electrodes of particularly high electrochemically active surface area (ECSA), thus leading to excellent partial current densities of formate production ($PCD_{formate}$) that reach values of ~−84.1 mA cm^{-2} (normalized to the geometric surface area of the support material).

From previous electrochemical and *operando* spectroscopic studies, e.g., on SnO_2-based precursor materials, it is known that (transient) intermediate oxide species can play a crucial role in the catalytic mechanism of formate formation.[36,37] Similar to Sn, Bi and Bi-based materials are also highly oxophilic and therefore prone to rapid surface oxidation after their (electro) synthesis. The specific role of oxygen and oxidic species in the CO_2RR mechanism on Bi-based electrocatalysts has, however, not yet been addressed. For this purpose, we compare the as-prepared Bi foams with foams that were treated by a further thermal annealing step at 300 °C, thus transforming the pristine and largely metallic Bi foams into well-defined Bi_2O_3 oxide foams.
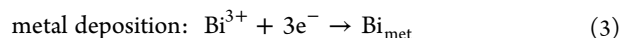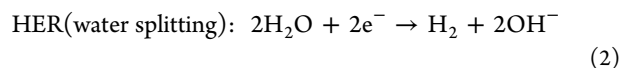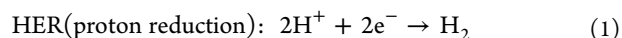
By analyzing the CO_2RR product distribution in combination with *operando* Raman spectroscopy, we demonstrate that both the oxidic Bi_2O_3 and the metallic Bi are highly selective catalyst materials toward formate production. However, the underlying CO_2RR mechanisms on the Bi_2O_3 and Bi catalyst are found to be substantially different. Herein, we present for the first time *operando* spectroscopic evidence for the so-called bismuth sub-carbonate[30] reaction pathway of formate production involving the absorptive embedment of CO_2 into the oxide matrix prior to its electro-conversion into formate.

RESULT AND DISCUSSION

Synthesis and *Ex Situ* Structural Characterization of Bi/Bi$_x$O$_y$ and Bi$_2$O$_3$ Foams. Using the dynamic hydrogen bubble template (DHBT) electrodeposition approach, Bi foams were first deposited on planar copper (Cu) and carbon (C) foil supports. This process was subsequently transferred to a porous carbon fiber cloth that often finds use as a gas diffusion electrode (GDE) in electrolyzer systems.

When applying high current densities of $j = −3$ A cm^{-2} in a highly acidic environment (1.5 M H_2SO_4), the actual metal deposition is inevitably superimposed on the hydrogen evolution reaction (HER). Under the applied harsh experimental conditions, the HER relies on the superposition of (i) proton reduction and (ii) water splitting according to

$$\text{HER(proton reduction):} \quad 2H^+ + 2e^- \rightarrow H_2 \qquad (1)$$

$$\text{HER(water splitting):} \quad 2H_2O + 2e^- \rightarrow H_2 + 2OH^- \qquad (2)$$

$$\text{metal deposition:} \quad Bi^{3+} + 3e^- \rightarrow Bi_{met} \qquad (3)$$

At these high current densities, proton reduction is mass transport-limited, thus further activating the HER reaction pathway through water splitting.[38,39] Hydrogen gas bubbles, which temporarily form on the cathode, function as a transient geometric template for the actual metal foaming process.[34,35,40−42] In the course of the metal deposition process, smaller H_2 bubbles tend to coalesce into larger bubbles, thus introducing dynamics into the templated metal deposition process.[38,43] Importantly, the local pH close to the electrode surface significantly changes as a consequence of the massive H^+ consumption (eq 1) and OH^- formation (eq 2). The basic principle of the additive and DHBT-assisted metal foaming process is illustrated in Figure 1 for a carbon fiber cloth (gas diffusion electrode, GDE, see also Figure S1) serving as the support electrode. In this work, a citrate-based salt (ammonium bismuth citrate) was used as the Bi precursor to avoid undesirable hydrolysis processes, which are typical of most inorganic Bi salts (e.g., $Bi_2(SO_4)_3$ and $Bi(NO_3)_3$) during solution preparation in aqueous media. Although citrate anions transform almost completely into citric acid in the highly acidic environment of the bulk electrolyte solution, nonetheless anionic citrate forms in the interfacial boundary layer under vigorous HER conditions due to local pH changes (Figure 1).[34] Therefore, it can be assumed that the actual metal foaming process occurs from a complexed bismuth solution because citrate readily forms chelating complexes with Bi^{3+} ions.[40] These complexing ligands are released from the reduced Bi and remain temporarily chemisorbed on the metallic surface during metal electrodeposition, which might further alter the nucleation and growth characteristics of the Bi.[34] Note that, due to their oxophilicity and high surface area, metallic Bi foams readily undergo surface oxidation immediately after their emersion from the plating bath (see discussion
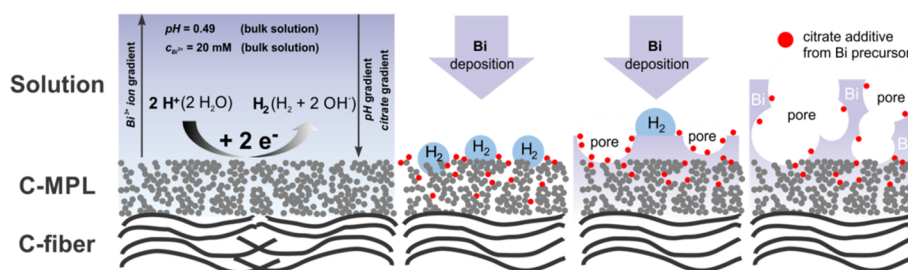
Figure 1. Scheme illustrating the additive-assisted dynamic hydrogen bubble template (DHBT) electrodeposition approach carried out on the carbon fiber cloth support (gas diffusion electrode, GDE).
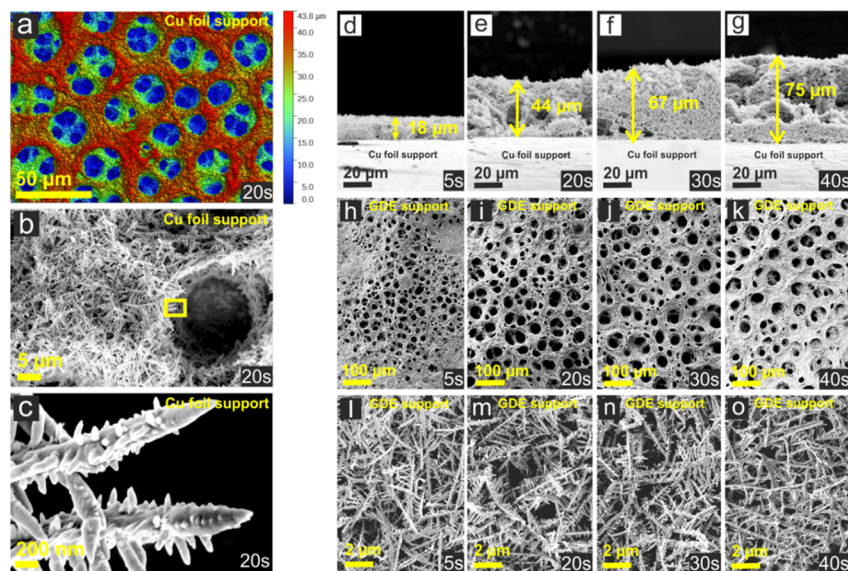

Figure 2. Morphology of the as-prepared (ap) Bi/Bi$_x$O$_y$ foam. (a) White light interferometry image of the ap Bi/Bi$_x$O$_y$ foam deposited on a Cu foil support (denoted ap Bi/Bi$_x$O$_y$@Cu). (b, c) Corresponding SEM images. (d−g) Side view of the ap Bi/Bi$_x$O$_y$@Cu foams, foam thickness as a function of the deposition time. (h−o) ap Bi/Bi$_x$O$_y$ foam deposited on a carbon fiber cloth support (denoted Bi/Bi$_x$O$_y$@GDE).

of the XPS results below). For this reason, we denote them in the following "as-prepared" (ap) "Bi/Bi$_x$O$_y$" foams.

Figure 2 depicts white light interferometry (WLI) (panel a) and SEM images (panels b and c) of the ap Bi/Bi$_x$O$_y$ foam deposited on the planar Cu foil substrate. Similar to the morphologies of the related Cu, Ag, Sn, and Zn systems,[34,35,42,44,45] the obtained Bi/Bi$_x$O$_y$ foams also show a distinct gradient in the pore diameters along the surface normal, with the smallest pores near the support electrode (Cu foil) and the largest pores at the outermost surface of the foam material. Two distinct levels of interconnected open-cell pores are visible with surface pore diameters ranging from 15 to 25 μm, thus representing the "primary" macroscale porosity of the formed ap Bi/Bi$_x$O$_y$ foam (Figure 2a). The pore side-walls consist of more loosely packed Bi dendrites, thus introducing a "secondary" nanoscale porosity to the ap Bi/Bi$_x$O$_y$ foam (Figure 2b,c). Dendritic metal growth results from the applied harsh experimental conditions ($j = -3$ A cm^{-2}), in which the rate of metal deposition is limited by mass transport of Bi^{3+} ions along with the decreased mobility of the formed adatoms on the emerging electrode surface. Both the thickness of the ap foams and the respective size distribution of the surface pores increase with elapsed deposition time, at least in the initial time period of metal foaming (Figure 2d−g, Figures S2 and S3). Figure 2h−o depicts top-down SEM images of four selected ap Bi/Bi$_x$O$_y$@GDE samples differing in the thickness of the

covering Bi foams. Obviously, the dendritic nature of the pore side-walls does not depend on the chosen support material. However, the primary macroporosity (e.g., pore size distribution) experiences certain alterations when changing the support material. This can in principle be due to the ratio of faradaic efficiencies (FE$_{H2}$/FE$_{Bi}$) and the so-called "bubble break-off diameter", both of which depend on the chemical nature and the surface morphology of the support material.[34,35,38,44−46] In general, the pore size distribution of the Bi foams is broader and less well defined on the porous GDE support compared to the planar Cu and C foil substrates (see Figure S5). However, the gravimetric analysis of the deposits suggests that the amount of Bi material is similar for all three support materials used (Figure S6).

Obviously, the formed hydrogen bubbles are more stable on the rough GDE support and tend further to coalesce during the concerted metal deposition/HER processes, thus explaining the bigger surface pores in case of the GDE support compared to the Cu and C foils substrates (Figure S5).

Note that both sides of the carbon fiber cloths used in this work were coated with a microporous carbon layer (denoted C-MPL, Figure S1). Due to the porous nature of this support material, it can be assumed that Bi is also deposited to some extent inside the outermost C-MPL (Figure 1). For the electrochemical catalyst performance testing, discussed below, we restrict our study to foams obtained by 20 s of deposition
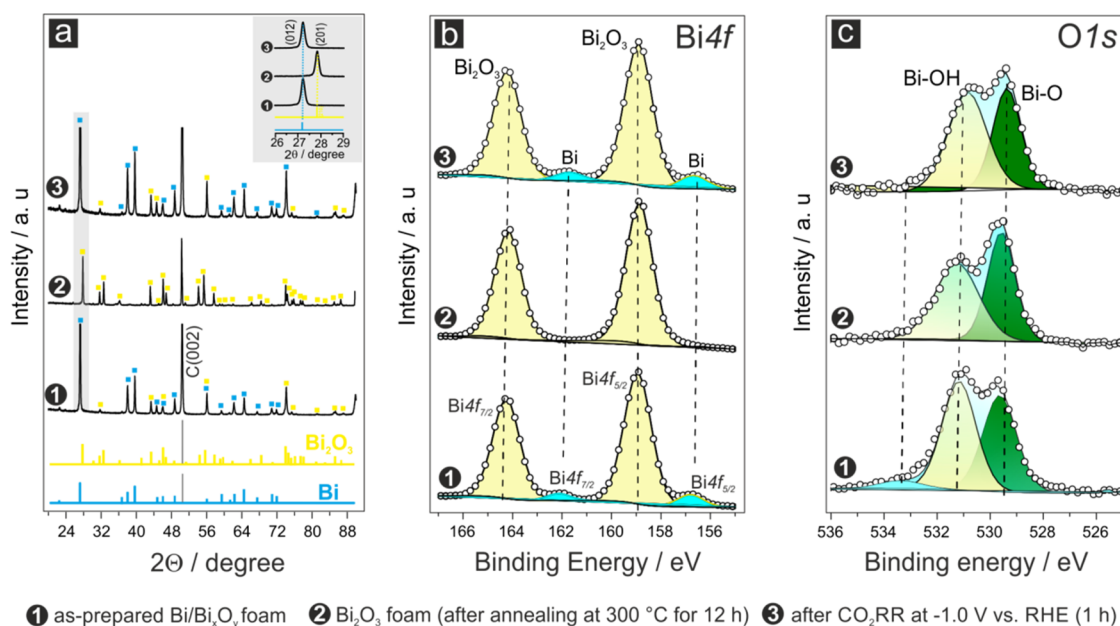
❶ as-prepared Bi/Bi$_x$O$_y$ foam   ❷ Bi$_2$O$_3$ foam (after annealing at 300 °C for 12 h)   ❸ after CO$_2$RR at -1.0 V vs. RHE (1 h)

Figure 3. (a) X-ray diffraction (XRD) inspection of the Bi foams depending on their stage of preparation, as indicated by the numbers. The foams were deposited on a carbon foil support; for comparison purposes, the references for metallic Bi (blue) and Bi$_2$O$_3$ (yellow) are also provided. (b) Corresponding Bi4f X-ray photo-emission spectra. (c) Corresponding O1s X-ray photo-emission spectra. Note that for the 1 h CO$_2$RR, the Bi$_2$O$_3$ foam was used as the catalyst.

time, yielding on the Cu foil support a thickness of the active catalyst materials of ∼44 μm (Figure 2e and Figure S4). Thicker catalyst films often become mechanically instable under harsh CO$_2$RR conditions in particular when gases evolve as reaction products (e.g., hydrogen gas bubbles at higher overpotentials).

The *ap* Bi/Bi$_x$O$_y$ foams were further subjected to thermal annealing at 300 °C for 12 h in air, thus transforming the catalyst material into a fully oxidized Bi$_2$O$_3$ foam. This assumption is confirmed by TEM analyses of the *ap* Bi/Bi$_x$O$_y$ and the Bi$_2$O$_3$ foams (see Figure S7). The overall morphology of the foams remains preserved upon thermal annealing, as evidenced by SEM inspection (Figure S8). It should be noted that the thermal treatment leads to a pronounced color change of the foam from black (*ap* Bi/Bi$_x$O$_y$) to yellowish (Bi$_2$O$_3$, Figure S9).

In the corresponding X-ray diffraction (XRD) analysis (Figure 3a, Table S1) the diffraction patterns of three Bi foams in distinct preparation stages are compared. The *ap* sample yields a diffraction pattern that is dominated by features of polycrystalline Bi (rhombohedral crystal structure, space group *P*21/c).[47−49] These are superimposed by minor contributions from α-Bi$_2$O$_3$ that likely forms on the surface of the foam following its immersion in the plating bath and exposure to air. The diffractogram of the thermally annealed sample, by contrast, exclusively shows contributions from the monoclinic α-Bi$_2$O$_3$ phase. Post-electrolysis XRD inspection (after 1 h at −1.0 V vs RHE in CO$_2$-sat. 0.5 M KHCO$_3$) suggests an electro-reduction of the α-Bi$_2$O$_3$ bulk phase back into metallic Bi. Again, the minor contributions of α-Bi$_2$O$_3$ to the XRD patterns most likely result from post-electrolysis surface oxidation of the oxophilic Bi under ambient conditions. Also, trace residuals of the formed Bi$_2$O$_3$, which were not in proper contact to the support during electrolysis, might add to the observed minor oxide features visible in the XRD patterns after

the electrolysis (Figure 3a). Similar effects have recently been discussed for SnO$_2$-based CO$_2$RR catalysts.[36]

Whereas XRD is sensitive only to the "bulk" of the catalyst material exhibiting long-range transitional order, XPS selectively probes the chemical composition of the catalyst surface, which does not necessarily exhibit a lateral order. Panels b and c in Figure 3 show the spin-orbit split (5.3 eV) Bi4f and the O1s photoemissions of the Bi foams depending on their preparation state (see also Figures S10 and S11). It is noteworthy that, even for the as-prepared sample, Bi(III) species (BE (Bi4f$_{5/2}$) = 162.1 eV) govern the Bi4f emission (Figure 3b-1) superimposed by minor contributions from metallic Bi(0), which appear as a satellite peak at BE (Bi4f$_{5/2}$) = 156.8 eV. This particular feature can be assigned to photoemissions from the near-surface "bulk" of the metallic Bi foam. The ratio of integrated intensities (I$_{Bi(III)}$/I$_{Bi(o)}$ = 6.92), derived from the quantitative analysis of the Bi4f$_{5/2}$ emissions, confirms a largely oxidized Bi foam surface. The corresponding O1s spectrum, shown in panel c, indicates the presence of two different oxygen components, which are attributed to Bi−OH (BE (O1s) = 530.7 eV) and oxidic Bi−O species (BE (O1s) = 529.5 eV); the latter can be assigned to the surface-confined α-Bi$_2$O$_3$ phase, which has already been observed in the respective XRD analysis of the as-prepared foam sample (panel a-1). Bi−OH species most likely originate from the partial hydrolysis of the oxide on the outermost surface of the foam when exposed, even for a short time, to (humid) air prior to the XPS inspection.

Annealing the foam sample for 12 h at 300 °C transforms the mixed Bi/Bi$_x$O$_y$ foam into its fully oxidized α-Bi$_2$O$_3$ state (panel a-2) and lets the Bi(0) contribution completely disappear from the respective Bi4f photoemission spectrum (panel b-2). However, the corresponding O1s emission is only marginally affected by the thermal treatment (panel c-2). The presence of hydroxy species on the surface of the foam even after the annealing treatment is again supportive of a mixed
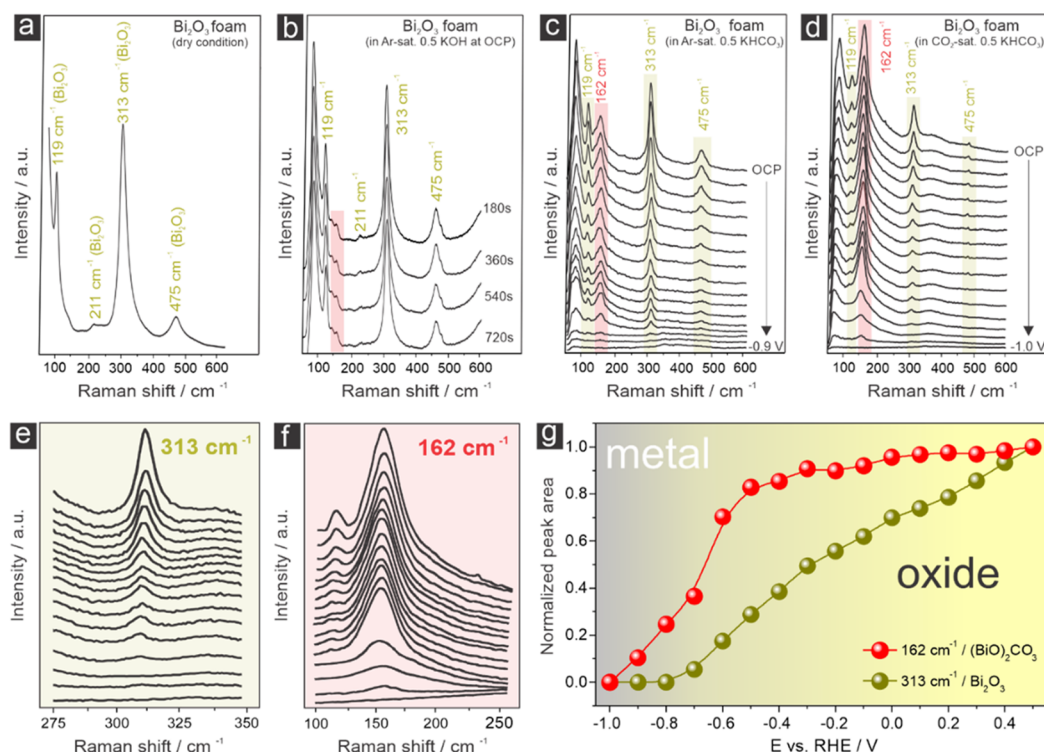
Figure 4. (a) *Ex situ* Raman spectrum of the Bi_2O_3 foam under dry conditions after annealing the *ap* Bi/Bi_2O_3 foam at 300 °C for 12 h. (b) Time-resolved Raman spectra of the Bi_2O_3 foam at the open-circuit potential (OCP) in the Ar-sat. 0.5 M KOH solution. (c) Series of potential-dependent Raman spectra showing the (oxide → metal) transition of the Bi_2O_3 foam in the Ar-sat. 0.5 M $KHCO_3$ solution; the holding time at each potential was 3 min. (d) Series of potential-dependent Raman spectra showing the respective (oxide/carbonate → metal) transition in the CO_2-sat. 0.5 M $KHCO_3$ solution; the holding time at each potential was 3 min. (e) Potential-dependent changes of the Raman peak at 313 cm^{-1} used as the fingerprint for the presence of Bi_2O_3 (enlarged section of spectra shown in panel (d)). (f) Potential-dependent changes of the Raman peak at 162 cm^{-1} used as the fingerprint for the presence of the sub-carbonate species on the catalyst (enlarged section of spectra shown in panel (d)). (g) Potential-dependent integrated intensities of the Raman peaks shown in panels (e) and (f).

hydroxy/oxide surface layer that instantaneously forms on the foam surface when exposed to air. Obviously, the presence of hydroxy species on the foam surface does not require any exposure to an aqueous electrolyte prior to XPS analysis.

Post-electrolysis XPS inspection of the foam sample shows the re-appearance of satellite peaks in the Bi4f$_{5/2}$ emissions assigned to the metallic Bi(0) (panel b-3), thus resembling the photoemission characteristics of the as-prepared sample, in full accordance with the XRD analysis. As expected, the corresponding O1s spectrum again shows the presence of both hydroxy and oxidic species on the foam surface (panel c-3), supporting our assumption of a surface chemical composition of the Bi foam, which is governed more by exposure to environmental air prior to XPS inspection than by the particular experimental history of the sample (e.g., thermal annealing or electrolysis).

These findings call for more advanced *in situ* (*operando*) investigations of the Bi foams to probe the chemical state of the catalyst under potential control prior to and during the CO_2RR.

Potential- and Time-Dependent *Operando* Raman Spectroscopy. The porous nature of the metallic or oxidic Bi foams facilitates the method of Raman spectroscopy.[50,51] Note that, due to the finite penetration depth of the laser light, Raman spectroscopy probes both the surface and to some extent also the bulk properties of the catalyst sample.[36,37] The Supporting Information contains several reference measure-

ments on the optimization of the Raman experiment in terms of laser light source and laser power (see Figures S12 and S13).

Figure 4a depicts a representative *ex situ* Raman spectrum of the dry Bi_2O_3 foam sample after 12 h of annealing at 300 °C in air (internal reference). Several prominent peaks are visible in the range between 100 and 700 cm^{-1}, which can be attributed to the vibrational modes of the α-Bi_2O_3 phase and its double refraction biaxial crystal structure, revealing a low symmetry of monoclinic geometry.[52−54] According to the literature,[46,47,55,56] the observed Raman bands can be grouped into three types of features: (i) strong Raman bands appearing at wavenumbers <120 cm^{-1}, which are typically assigned to displacements of cationic −Bi(III)− entities with regard to the surrounding oxide matrix (e.g., at 119 cm^{-1});[53] (ii) weaker bands appearing between 120 and 155 cm^{-1} that are due to the concerted vibrational motions of binuclear Bi−O entities;[47,55] and (iii) vibrational modes of mononuclear −O− entities that are typically found at wavenumbers >155 cm^{-1} (e.g., the Bi−O stretching mode at 313 cm^{-1}).[46,53,56] As expected from the *ex situ* XRD and XPS analysis (Figure 3), the Raman spectrum of the corresponding dry *ap* Bi/Bi_xO_y foam (*ex situ* characterization) shows qualitatively the same Raman features as the thermally annealed foam (see Figure S14). However, the oxide-related Raman features are broader, less well defined, and weaker in intensity in the case of the surface oxides on the *ap* sample.

Figure 4b displays a time-dependent series of Raman spectra of the Bi_2O_3 foam exposed to an Ar-saturated 0.5 M KOH

solution at the open-circuit potential (pH = 13.5, OCP ≈ +0.79 V vs RHE, Figure S15a). A CO_2/bicarbonate-free potassium hydroxide electrolyte was chosen for this measurement to selectively study the effect of the exposure of the foam to an alkaline electrolyte on its surface composition, independent of the additional alteration resulting from CO_2/ bicarbonate adsorption phenomena (see discussion below). The Raman characteristics of the dry Bi_2O_3 foam sample (panel a) are, in principle, preserved in the alkaline aqueous electrolyte of pH = 13.5. Very minor alterations appear at the OCP in the range from 120 to 170 cm^{-1} and are due to a more extended surface hydrolysis in the aqueous electrolyte involving the exchange of Bi−O by Bi−OH species. Further alterations concern the less intense Raman band at 475 cm^{-1}, which shows a small satellite feature in the alkaline electrolyte environment. These minor changes in the Raman characteristics that are visible in the first spectrum of the time-resolved series are already completed after 180 s of exposure. There are no further alterations observed in the subsequently recorded spectra at exposure times >180 s, thus proving the stability of the Bi_2O_3 foam at OCP and pH of 13.5 in full accordance with the thermodynamic predictions represented in the respective Pourbaix diagram.[57] This observation is full in agreement with the corresponding OCP measurement which reaches a plateau value at exposure times >200 s (Figure S15a). The Raman spectra acquired in the CO_2 and bicarbonate-free 0.5 M KOH electrolyte serve as further reference for the potential-dependent Raman experiments of the Bi_2O_3 foam carried out in an Ar-saturated aqueous 0.5 M $KHCO_3$ electrolyte (Figure 4c). Again, all main Raman features at 119, 313, and 475 cm^{-1} attributed the Bi_2O_3 phase are preserved in the Ar-saturated bicarbonate solution even at the OCP of ca. +0.60 V vs RHE (see Figures S15b and S16a). However, a new strong Raman feature appears at 162 cm^{-1} (highlighted red in panel c), which can be assigned to the so-called sub-carbonate species[58] that forms in the Ar-sat. bicarbonate solution even at the OCP through the partial surface exchange of oxidic Bi−O or Bi−OH species by Bi−CO_3−Bi ensembles according to

$$Bi_2O_3 + CO_2 \rightarrow (BiO)_2CO_3 \qquad (4)$$
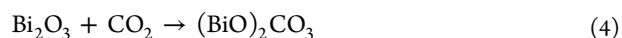
This assignment could be further corroborated by *ex situ* Raman measurements using a commercial $(BiO)_2CO_2$ powder sample as the reference material. Clearly visible in Figure S17 is the strong Raman feature at 162 cm^{-1}. Less intense vibrational modes at 366 and 574 cm^{-1}, visible in the reference spectra (Figure S17), are typically not detected in the *in situ* (e.g., at OCP) and *operando* Raman experiments under CO_2RR conditions. These observations (Figure 4c) imply a direct adsorptive interaction of either dissolved CO_2 or the bicarbonate anion with the Bi_2O_3 foam even in the Ar-saturated 0.5 M $KHCO_3$ electrolyte under non-reactive conditions at the OCP (Figure S16a). Note that traces of gaseous CO_2 are present even in the Ar-saturated bicarbonate solution. Both the oxide-related Raman features at 119, 313, and 475 cm^{-1}, and the new sub-carbonate vibrational mode at 162 cm^{-1} gradually disappear when changing the potential from the OCP to −0.9 V vs RHE (Figure 4c). A quantitative analysis of this (oxide/sub-carbonate → metal) transition is provided in the Supporting Information (see Figures S18 and S19). Note that the derived integrated intensities do not exactly correlate with the abundance of a certain Raman active species on the electrode. Integrated intensities also depend on other factors, e.g., the surface roughness or changes thereof

(e.g., during the oxide → metal transition). Plots of the integrated Raman intensity versus the applied electrode potential (e.g., Figure S18) provide, however, valuable qualitative trends in the stability of the oxidic and carbonate phases present on the electrode.

Hereinafter, we restrict the discussion to analogue Raman experiments carried out in the CO_2-saturated 0.5 $KHCO_3$ electrolyte solution (Figure 4d and Figure S15c), which served as the working electrolyte for mechanistic studies and the actual catalyst performance testing (discussed below). The main difference to the Raman spectra acquired in the Ar-saturated bicarbonate solution (panel c) is the intensity of the sub-carbonate Raman band at 162 cm^{-1}, which becomes the dominant Raman feature in the CO_2−sat. (~35 mM)[59] electrolyte. Our *operando* spectroscopic results strongly suggest substantial "non-reactive" CO_2 adsorption on the Bi_2O_3 prior to the actual CO_2RR onset (see also Figure S16b). These results also imply a (partial) displacement of the oxide and surface hydroxide features by the sub-carbonate at the OCP, which is not restricted to the outermost catalyst surface but extends further into deeper layers and the near-surface bulk of the Bi_2O_3 foam catalyst. This hypothesis is further supported by Figure S20, comparing the integrated intensities of the Raman spectra acquired from the *ap* Bi/Bi_xO_y foam and the corresponding thermally annealed Bi_2O_3 foam at the OCP. Interesting to note is that, in the case of the largely metallic *ap* Bi/Bi_xO_y foam, which is covered only by a thin oxidic skin, the oxide-related Raman features instantaneously disappear when brought into contact with the CO_2-sat 0.5 M $KHCO_3$ electrolyte (Figure S21). As a result, a thin bismuth sub-carbonate skin is formed on the otherwise *ap* metallic Bi foam. Note that, for the sub-carbonate formation under non-reactive conditions (at OCP), also the electrolyte pH is of importance (see discussion of Figure S22).

Formed sub-carbonate species can be regarded as precursors of CO_2 electroreduction at low overpotentials in the initial stage of the CO_2RR. A quantitative analysis of the potential-dependent (oxide/sub-carbonate → metal) transition is based on the integrated intensities of the Raman features at 313 cm^{-1} (Bi_2O_3 fingerprint, Figure 4e) and 162 cm^{-1} (sub-carbonate fingerprint; Figure 4f). The results of this analysis are presented in Figure 4g. Both the oxide and the sub-carbonate features follow the same qualitative trend of decreasing intensities with increasing CO_2RR overpotentials (decreasing applied potentials). The potential-dependent Raman data suggest that the (oxide → metal) transition of the Bi_2O_3 foam is completed at approximately −0.8 V vs RHE. By using Bi_2O_3 microsphere particles as the CO_2RR catalyst, Deng et al. have recently demonstrated that the Bi−O Raman mode at 313 cm^{-1} can persist, at least to an extent, even to applied potentials beyond −0.9 V vs RHE.[60] Sub-carbonate-related Raman features were, however, not discussed in that study. On the Bi_2O_3 foam, these sub-carbonate species appear to be even more stable than the corresponding oxides. This can be concluded from the quasi-plateau behavior of the 162 cm^{-1} features in the intensity vs potential plot at potentials ranging from the OCP to −0.6 V vs RHE (Figure 4g). The significant decrease in intensity at potentials less than −0.6 V vs RHE spectra is completed only at −1.0 V vs RHE. We do consider the formed metallic Bi foam catalyst present at potentials less than −1.0 V vs RHE as oxide/sub-carbonate derived (denoted hereinafter as *oc-d*).

Note that the data shown in Figure 4d−g do not necessarily present steady-state conditions; the holding time at each applied potential was 3 min (see the Experimental Section). The exchange of the oxide (surface hydroxide) species by the sub-carbonate might therefore further proceed even during an ongoing CO_2RR in the low overpotential regime. This is demonstrated by the series of time-dependent Raman spectra in Figure 5, which further support our working hypothesis that the oxide/sub-carbonate exchange is not restricted to the outermost surface but proceeds deeper into the bulk of the foam catalyst with time. Note that the observed Raman feature at 1017 cm^{-1} is due to bicarbonate in the solution phase, as evidenced by the additional control experiments depicted in Figure S23.

The transition from the oxidic Bi_2O_3 foam to the oxide/sub-carbonate/Bi_{met} composite at low applied overpotentials can be monitored as a function of time and applied potential by using visual inspection. Figure 6 depicts representative optical photographs of the oxidic Bi_2O_3 foam exposed to the CO_2-sat. 0.5 M $KHCO_3$ electrolyte. The yellowish color gradually disappears with time and turns into black, which is characteristic not only of the *ap* Bi/Bi_xO_y foam (see Figure S9 and the corresponding multimedia file) but also for the corresponding oxide/sub-carbonate/Bi_{met} composite formed in this potential regime (see Figure 4g). As expected, this compositional transition is faster at −0.6 V vs RHE than at −0.3 vs RHE.

ICP-MS Analysis of the Electrolyte during the CO_2RR. *Operando* Raman spectroscopy is sensitive to the composi-

Figure 6. *Operando* optical inspection of the time-dependent (oxide → sub-carbonate/metal) transition in the CO_2-sat. 0.5 M $KHCO_3$ solution at low overpotentials.

Figure 5. (a) Series of time-resolved Raman spectra acquired over 120 min at $E = -0.6$ V vs RHE. (b) Integrated intensities of the Raman peaks at 162 cm^{-1} (sub-carbonate) and 313 cm^{-1} (Bi_2O_3) as functions of time. This experiment confirms the non-steady-state characteristics of the Raman measurements shown in Figure 4.
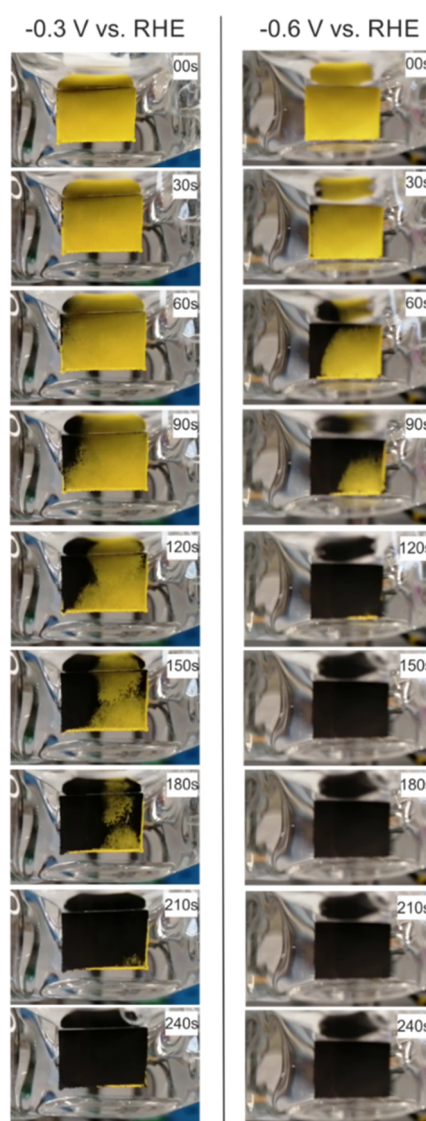
tional and structural alterations that the oxidic catalyst undergoes upon sub-carbonate formation and potential-induced oxide/sub-carbonate reduction. As known from the work by Mayrhofer et al.,[61−63] the electroreduction of oxidic species can lead to the release of metal ions into the electrolyte. Under the harsh cathodic conditions typically applied for the CO_2RR, these metal ions might be re-deposited on the catalyst surface during the ongoing CO_2 electrolysis reaction. To probe these effects, a series of potentiostatic electrolysis reactions was carried out in CO_2-saturated 0.5 M $KHCO_3$ solution using freshly prepared Bi_2O_3 foams as the catalysts. Aliquots of the bicarbonate electrolyte were analyzed by means of ICP-MS as a function of electrolysis time in the range of applied potentials between −0.3 and −1.8 V vs RHE. The results of this analysis are presented in Figure 7 and Table S2.

Clearly, the amount of Bi ions released into the electrolyte upon oxide reduction strongly depends on the applied electrolysis potential. Interestingly, we find the highest amount of Bi ions in the electrolyte at the lowest applied electrolysis potentials (−0.3 V vs RHE), reaching a maximum Bi content
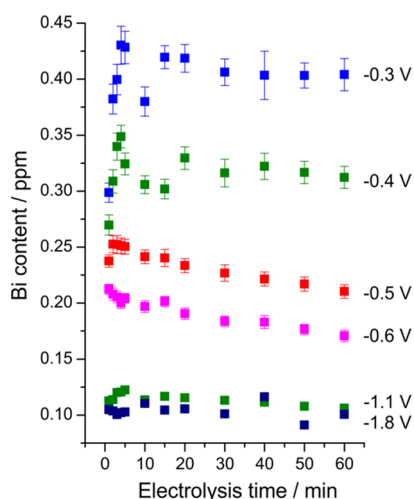
Figure 7. Time evolution of the Bi content in the CO_2-sat. 0.5 M $KHCO_3$ electrolyte solution under potentiostatic conditions determined by ICP-MS. The potentials applied during potentiostatic electrolysis are indicated in the graph. Freshly prepared Bi_2O_3 foams (20 s deposition time, annealing at 300 °C for 12 h in air) were used as the catalyst (single catalyst approach).

of 0.430 ppm after 4 min followed by a slow drop-down in concentration. In this potential regime, we observed the (partial) displacement of the oxidic bismuth species by the respective sub-carbonate (see Figures 4 and 5). Apparently, it is this oxide/sub-carbonate displacement at low overpotentials that provokes the massive release of Bi ions into the electrolyte, as observed by ICP-MS.

Note that, due to the CO_2 purging of the electrolyte during electrolysis, the released metal ions are homogeneously distributed in the electrolyte solution after their release from the electrode surface. A similar peak-like behavior in the Bi content evolution can be observed for the electrolyses at −0.4 and −0.5 V vs RHE, respectively. The maximum detected Bi content decreases to 0.100 ppm at −1.8 V vs RHE, suggesting that rapid oxide reduction and rapid metal ion deposition at the lowest potentials applied effectively prevented the massive release of Bi into the solution.

CO_2 Electrolysis. The results of the electrochemical catalyst performance testing, carried out in a broad potential range from −0.3 V down to −2.0 vs RHE, are presented in Figure 8a,b for the *ap* Bi/Bi_xO_y foam and the thermally annealed foam. In both cases, carbon cloths (GDE, Figure S1) served as the support material for the initial catalyst preparation. For comparison purposes, also the electrolysis results obtained for a planar Bi foil are presented (reference). Panel a in Figure 8 depicts the resulting CO_2RR product distribution in the form of a FE vs E plot (faradaic efficiency versus applied electrolysis potential), whereas in panel b, the corresponding partial current densities (PCDs) are considered. The only electrolysis products are gaseous hydrogen (H_2) and non-volatile formate. Within the entire potential range studied in this work, the faradaic efficiencies of formate and H_2 production sum up to ~100% (see Table S3). For the sake of clarity, in Figure 8, we present only the respective formate data.

In the FE vs E plot (panel a), the Bi foil shows a characteristic peak-like behavior in the product distribution with a maximum formate efficiency of $FE_{formate}$ = 55.0% ($PCD_{formate}$ = −2.92 mA cm^{-2}) at −0.8 V vs RHE. This is in

agreement with the results recently reported by Zhang et al., using a sulfide-derived Bi catalyst.[64]

A significant improvement in the formate efficiency is achieved when using the foam-type Bi catalyst. Both *ap* Bi/Bi_xO_y and Bi_2O_3/oc-*d* Bi exhibit faradaic efficiencies of formate production that reach ~100% (Table S3). Quite intriguingly, this excellent product selectivity is observed not only within a narrow potential regime, as typical, e.g., for 2D systems like Bi foil, but within a rather broad range of applied electrolysis potentials ("plateau" regime), that is substantially broader in the case of the Bi_2O_3/oc-*d* Bi foam (~1100 mV) compared to the *ap* Bi/Bi_xO_y catalyst (~800 mV). Only marginal differences between both foam catalysts are noted for electrolysis potentials less than −0.9 V, whereas substantial differences in their product distributions appear at low overpotentials in the range from −0.3 to −0.7 V vs RHE. Under these electrolysis conditions, the product distribution of the *ap* Bi/Bi_xO_y foam better resembles the Bi foil with negligible formate production. It can safely be assumed that the metallic Bi foil is partly oxidized on its surface prior to the CO_2RR, thus rationalizing the qualitative similarity to the *ap* Bi/Bi_xO_y foam. However, a high level of formate efficiency is observed for the fully oxidized Bi_2O_3 foam catalyst, which also reaches almost 100% in this low-overpotential regime (Figure 8a and Table S3). This observation is indicative of the opening of a second reaction pathway of formate formation on the oxide/sub-carbonate/Bi_{met} composite at these low overpotentials that is not active on the *ap* Bi/Bi_xO_y catalyst. The thin surface oxide layer of the latter catalyst is obviously not sufficient to mimic the catalytic properties of the fully oxidized Bi foam in the electrochemical screening experiment at low overpotentials. The most prominent difference between the *ap* Bi/Bi_xO_y and the fully oxidized Bi_2O_3 foam concerns the capability of the Bi_2O_3 to adsorb/absorb dissolved CO_2 from the electrolyte phase,[65] giving rise to the appearance of prominent features in the Raman spectra assigned to sub-carbonate species (Figure 4d and Figure S20).

Based on the presented Raman data, it can be concluded that the near-surface oxide phase is partially converted into a mixed oxide/carbonate phase, even under non-reactive conditions, prior to the actual CO_2RR onset (Figure 4d). The Raman data further suggest a partial reduction of the mixed $(BiO)_2CO_3$-Bi_2O_3 at the CO_2RR onset (−0.4 V to −0.8 V vs RHE; Figure 4g) to metallic Bi, thus leading to a complex oxide/sub-carbonate/Bi_{met} composite on which the CO_2RR takes place in the low-overpotential regime. Figure 8d depicts the proposed "sub-carbonate" reaction pathway of formate production on the composite material assuming that the Bi oxide/carbonate species play an active role in the CO_2 conversion at these low overpotentials.[30] The overall reaction rates and the $PCD_{formate}$ remain at low levels within this low overpotential regime (Figure 8b and Table S4), also likely due to the limited conductivity of the oxide/sub-carbonate/Bi_{met} composite. Local pH changes at the catalyst/electrolyte interface as the driving force for the observed sub-carbonate formation at low overpotentials (Figures 4d−g and 5) can therefore be excluded due to the low overall reaction rates (Table S3) and in particular due to negligible faradaic efficiencies for hydrogen production at low overpotentials (Table S3).

It is the compositional transformation from the mixed oxide/carbonate composite to a fully metallic Bi state, evidenced by the *operando* Raman data (Figure 4), that allows
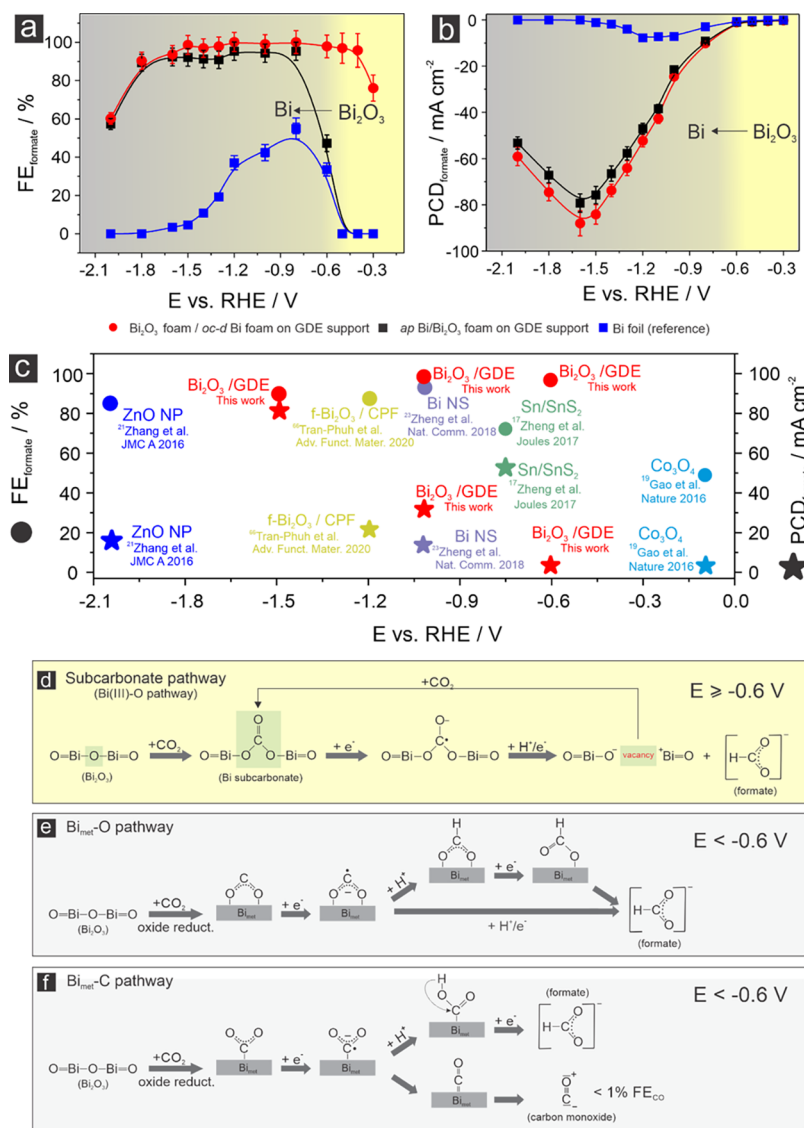
Figure 8. (a) CO_2RR product distribution represented as FE vs E plot (single catalyst approach); results of the Bi_2O_3/oc-d Bi foam are compared with the *ap* Bi/Bi_xO_y foam and a Bi foil catalyst (reference). (b) CO_2RR product distribution represented as $PCD_{formate}$ vs E plot; note that the potential-dependent product distributions shown in panels (a) and (b) are averaged over three individual electrolysis experiments per potential applied. (c) Performance overview for formate-producing CO_2RR catalysts (for detailed discussion in terms of long-term electrolysis, see text and Table 1). (d) Proposed CO_2RR mechanism at low overpotentials, $E \geq -0.6$ V vs RHE (Bi_2O_3 catalyst). (e) Dominant CO_2RR mechanism at high overpotentials, $E < -0.6$ V vs RHE (Bi_{met} catalyst; Bi_{met}–O pathway). (f) Alternative CO_2RR mechanism at high overpotentials (Bi_{met} catalyst; Bi_{met}–C pathway).

the partial current densities of formate production to substantially increase (Figure 8b). In the following, we denote the activated metallic Bi catalyst as "oxide/carbonate-derived" (*oc-d*). Note that the observed PCDs are systematically higher for the *oc-d* Bi foam compared to the *ap* Bi/Bi_xO_y (Figure 8b). This trend is due to the increased electrochemically active surface area (ECSA) after the reduction of the "bulk" oxide phases (see also Figure S24). Similar trends of increasing ECSA were reported for other oxide-derived CO_2RR catalysts, e.g., Cu-based materials.[35,44] Particularly noteworthy are the maximum PCDs of formate production for the *ap* Bi/Bi_xO_y and the *oc-d* Bi, reaching values of $PCD_{formate} = -75.8$ mA cm^{-2} and $PCD_{formate} = -84.1$ mA cm^{-2} at -1.5 V vs RHE, respectively. At potentials less than -1.5 V vs RHE, both the $FE_{formate}$ and $PCD_{formate}$ values decrease, and the HER becomes the dominant electrolysis process (see Table S4). This peak-

like behavior in the CO_2RR efficiency plot is typically rationalized by the onset of CO_2 mass transport limitations appearing at elevated total reaction rates and high overpotentials as the CO_2 concentration is limited to only ∼35 mM in the aqueous electrolyte.[59] In contrast, the competing water splitting reaction (HER) does not become diffusion-limited.

It should be emphasized that both foam catalysts outperform other Bi-based electrocatalysts in terms of faradaic efficiency and with regard to the maximum partial current densities ($PCD_{formate}$) when considering classical half-cell measurements. Figures of merit for the Bi_2O_3 foam catalyst are presented in Figure 8c along with the performance data of recently reported benchmark catalysts for formate formation in the half-cell configuration, e.g., partially oxidized/ultrathin Co_3O_4,[18,19] Sn/SnS_2,[17] fractal-Bi_2O_3,[66] Au–Bi_2O_3[67] and ultrathin Bi-NS,[23] and ZnO.[21] Partial current densities of formate formation, higher

than those reported herein, were only achieved when using gas/liquid flow electrolyzer systems.[68] In this context, Gong et al. have recently reported a PCD$_{formate}$ of −288 mA cm^{-2} using a high concentration of KOH in combination with an oxidic Bi double-wall nanotube catalyst.[69]

The most striking characteristic of the Bi$_2$O$_3$ foam catalyst, reported herein, is clearly the extraordinarily broad potential window of ~1100 mV in which the faradaic efficiency of formate formation never falls below 90%. This unique feature is the direct result of the coupling of the two formate reaction pathways operative either on the oxidic catalyst ("sub-carbonate" pathway, low overpotentials, Figure 8d) or on its metallic form (Bi$_{met}$−O pathway; high overpotentials, Figure 8e). Note that, for the metallic Bi catalyst, also an alternative reaction pathway has also been proposed that involves Bi−C bond formation and the appearance of *COOH intermediates (Figure 8f).[29,70,71] However, in light of the high oxophilicity of Bi and the presented Raman data, proving Bi−O bond formation, we consider the Bi−O reaction pathway (Figure 8e) to be the dominant one at high overpotentials where the oxide/carbonates are fully reduced. This conclusion becomes further supported by the absence of significant amounts of CO as a CO$_2$RR byproduct (< 1%) that enables formate production through the Bi$_{met}$−O pathway.[29,70,71]

It should be noted that the choice of the support material (e.g., Cu foil or carbon fiber cloth) and related to the fact that differences in the macroporosity have only a marginal impact on the resulting product distribution (ratio of FE$_{HE}$ and FE$_{formate}$, see Figure S5, Figure S25, Figure S26, Table S5, and Table S6). This is a major difference to other foam-type catalysts, e.g., copper-based systems, in which changes of the macroporosity lead to severe alterations in the respective CO$_2$RR product distribution. The latter effect was rationalized by Dutta et al.[35] by particular "trapping" phenomena of CO$_2$RR intermediates (e.g., CO or C$_2$H$_4$) inside the porous foam catalyst, thus facilitating the re-adsorption and further coupling and hydrogenation of trapped intermediates.[35] In the present case, there are no significant amount of electrolysis products observed other than formate and hydrogen. Morphology-induced "trapping" effects are therefore not relevant for the catalysts and reaction pathways discussed herein. The beneficial role of the porous foam structure remains restricted in the present case to the increase of the electrochemically active surface area (ECSA) and the resulting increased partial current densities whereas the reaction pathways remain unaltered.

Electrochemical Durability and Morphological (In)-Stability of the Bi$_2$O$_3$ Foam Catalyst. Not only are the resulting product distribution and the observed activity/product selectivity of importance for the overall catalyst performance evaluation but also the catalyst durability over more extended electrolysis times than typically applied in the standard catalyst screening approach (Figure 8). To demonstrate the excellent stability of the Bi$_2$O$_3$ foam catalyst, two extended potentiostatic electrolysis experiments were carried out under experimental conditions where either the "sub-carbonate" pathway (Figure 8d) or the Bi$_{met}$−O pathway (Figure 8e) was dominant at applied potentials of −0.6 V vs RHE and −1.0 V vs RHE, respectively.

The corresponding current vs time traces (Figure 9a) suggest quasi-steady-state conditions after passing an initial cathodic event indicating the partial or even complete reduction of the oxidic precursor. Due to the varying applied
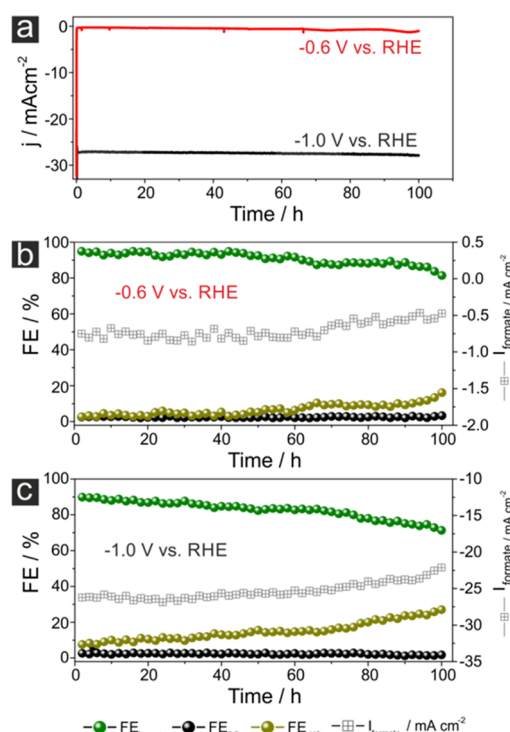

Figure 9. (a) Current transient curves representing the potentiostatic CO$_2$RR at −0.6 V and −1.0 V vs RHE, respectively. (b) FE/PCD vs t plot of the CO$_2$RR at −0.6 V vs RHE. (c) FE/PCD vs t plot of the CO$_2$RR at −1.0 V vs RHE. Bi$_2$O$_3$ foams (20 s deposition time, annealing at 300 °C for 12 h in air) were used as catalysts for the extended electrolysis experiments.

electrolysis potentials, also the resulting quasi-steady-state current densities are different and reach values of j_{mean} = −0.88 ± 0.2 mA cm^{-2} (−0.6 V vs RHE) and j_{mean} = −26.2 ± 2.1 mA cm^{-2} (−1.0 V vs RHE). However, a slight trend toward higher total current densities over time can be noted for both cases (see also discussion of the IL inspection below).

In particular, for the electrolysis at −0.6 V vs RHE (Figure 9b), the FE$_{formate}$ values decrease by only <10% within 100 h of electrolysis time (from an initial 97.3% to a final 89.1%), thus indicating the excellent stability of the mixed oxide/sub-carbonate/Bi$_{met}$ composite catalyst (sub-carbonate pathway). Note that trends in the time-dependent FE$_{H2}$ and FE$_{formate}$ changes are anti-correlated to each other.

More substantial is the catalyst degradation, however, when the electrolysis is carried out at −1.0 V vs RHE (Figure 9c). In this case, we observe a decrease from the initial FE$_{formate}$ = 91.7% to final FE$_{formate}$ = 79.1% after 100 h of electrolysis. Accordingly, the corresponding partial current density decreases from $j_{formate}$ = −28.67 mA cm^{-2} to a final $j_{formate}$ = −21.06 mA cm^{-2}. Table 1 summarizes the stability characteristics of various Bi catalysts. It demonstrates that the foams, presented in this work, reveal an excellent stability in the electrochemical electrolysis experiment over other Bi-based electrocatalysts.

Although the extended electrolysis experiments (Figure 9b) suggest reaching stable quasi-steady-state conditions, at least on the scale of a few hours, the Raman data have already indicated substantial compositional changes of the foam catalyst in particular in the initial phase of the CO$_2$RR. Under these conditions, the CO$_2$RR is obviously superimposed by a continued exchange of oxide by the carbonate (Figure 5).

Table 1. Comparison of Some Representative Studies Conducted in Recent Years for the Electrochemical Reduction of CO_2 to Formate or Formic Acid

catalysts	Pot. vs RHE (V)	partial current density$_{formate}$ (mA cm^{-2})	FEs of formate (%)	FEs (over extended electrolysis period of time in hour)	references
Bi_2O_3 NF @GDE	−0.60	−00.88	97.3	100 h (dropped to 91% after 80 h)	this work
Bi_2O_3 NF @GDE	−1.00	−26.11	91.7	100 h (dropped to 80% after 80 h)	this work
f-Bi_2O_3 @ CFP	−1.20	−24.0	87.0	16 h	Tran-Phu et al.[66]
Bi_2O_3NSs@ MCCM	−0.96	−05.58	77.3	12 h	Liu et al.[31]
ultra-thin Bi NS	−1.74	−24.00	89.8	10 h	Han et al.[23]
ultra-thin Bi NS	−1.10	−16.5	95.5	10 h	Zhang et al.[27]
ultra-thin Bi_2O_3 NS	−1.00	−12.3	95.1	05 h	Su et al.[24]
Bi nanostructure	−0.90	−13.33	92.3	30 h	Lu et al.[32]
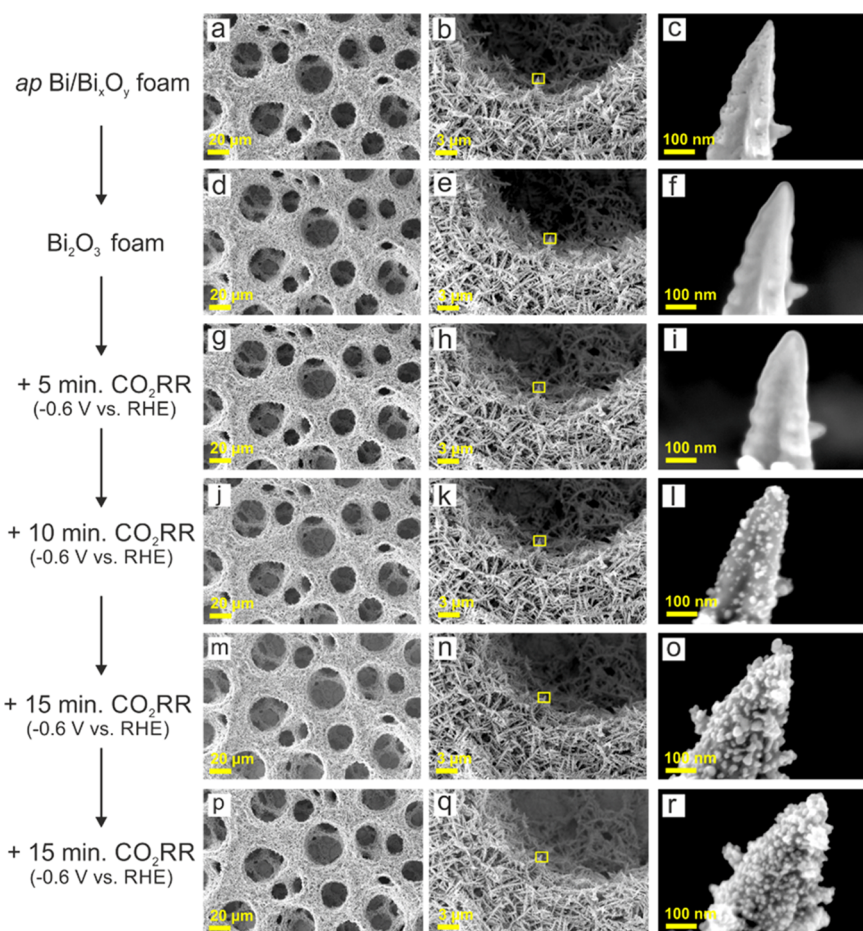
Figure 10. (a−r) Identical location (IL) SEM inspection of morphological changes associated to the thermal annealing of the *ap* Bi/Bi$_x$O$_y$ foam and subsequent potentiostatic CO_2 electrolysis in the CO_2-sat. 0.5 M KHCO$_3$ solution at −0.6 V vs RHE.

These results prove that stable current vs time and the corresponding FE vs time traces (Figure 9) alone are not conclusive for monitoring the actual catalyst stability.

The *operando* Raman results are therefore further complemented by so-called identical location (IL) SEM investigations. Figure 10 displays the changes in the catalyst morphology due to the thermal annealing of the *ap* Bi/Bi$_x$O$_y$ foam and, within the first 45 min of electrolysis, a time scale that is comparable to the Raman experiment shown in Figure 5. For this purpose, the CO_2RR was interrupted at defined electrolysis times (after 15, 30, and 45 min total electrolysis

time) and then subjected to *ex situ* SEM inspection, focusing on the same spot on the catalyst surface.

On a larger μm length scale (panel a, d, g, j, m, and p), severe morphological alterations are neither observed for the thermal annealing nor for the electrolysis itself. Both the "primary" macropore structure and the dendritic nature of the pore sidewalls are clearly preserved even after 45 min of electrolysis at −0.6 V vs RHE.

Substantial changes occur, however, on the nanometer length scale, as evidenced by the SEM images shown in panels c, f, i, l, o, and r. One characteristic feature of these morphological changes under CO_2RR conditions is the

appearance of smaller nanoparticles (<10 nm) on the surface of the dendrite. In addition, it seems that the apparent volume of the dendrite increases, which is indicative of increased porosity. Note that the ECSA is further increased upon oxide reduction. Nanoparticle growth and surface roughening effects are reported for the activation for foam-type and dendritic Cu catalysts by Cu_xO precursor reduction.[35,44] In the present case, a further process needs to be considered, which might also contribute to the nanoscale changes in the catalyst morphology. The *operando* Raman shows the continued embedment of CO_2 into the oxidic Bi_2O_3 precursor material (Figure 5), forming sub-carbonate species at the expense of oxidic Bi−O. Note that this process also involves an inward (CO_2) and outward (e.g., oxygen species) mass transport, which might further roughen the catalyst. These microscopic data support our working hypothesis that the observed sub-carbonate formation (Figure 5) is not restricted to the outermost surface of the oxidic precursor but also affects the near-surface bulk of the catalyst material.

The SEM image in Figure 10r represents the oxide/sub-carbonate/Bi_{met} composite (see also Figure 4g), which is considered the active catalyst in the low overpotential regime.

A similar IL-SEM analysis but comparing the initial oxidic catalyst morphology and the one after 100 h of electrolysis (Figure S27) confirm the morphological changes already observed on a shorter time scale, suggesting that the most severe changes occur in the initial stage of the CO_2RR (approximately the first hour).

◼ CONCLUSIONS

By means of *operando* Raman spectroscopy combined with electrochemical performance testing, we have demonstrated that three-dimensional Bi_2O_3 foams, produced by an additive-assisted dynamic hydrogen bubble template approach and thermal annealing (12 h at 300 °C), show a "tandem" electrocatalytic activity toward formate formation. The (partly) oxidic Bi_2O_3 foam and the reduced metallic Bi_{met} foam reveal both a high selectivity toward formate, reaching faradaic efficiencies close of 100%. It is the porous nature of the foam catalyst in combination with the use of a carbon fiber cloth (GDE) as the support material that leads to a particularly high electrochemically active surface area and, accordingly, to excellent partial current densities $PCD_{formate}$ of approximately −90 mA cm^{-2} (normalized to the geometric surface area) in the CO_2 electrolysis. However, what makes this catalyst unique is the extraordinarily broad potential window of astonishing ~1100 mV in which the $FE_{formate}$ values do not fall below 90%. This was proven herein to be directly related to the coupling of two different formate reaction pathways, being operative either at low overpotentials (sub-carbonate pathway) and medium/high overpotentials (Bi_{met}−O pathway). For the first time, experimental evidence was provided to demonstrate the displacement of oxidic species by carbonate species, which is not only restricted to the outermost surface but further extends into the near surface bulk of the foam material. The formed sub-carbonate serves as the reactant in the course of the CO_2RR, at least at low overpotentials. The so-called identical location (IL) SEM inspection proves severe morphological alterations upon sub-carbonate formation and partial oxide-reduction during an ongoing CO_2RR at low overpotentials.

In our future studies, we will apply synchrotron-based *operando* X-ray absorption and X-ray diffraction techniques in combination with Raman spectroscopy to reveal in more detail the mechanism of sub-carbonate formation during the CO_2RR.

◼ EXPERIMENTAL SECTION

Chemicals and Materials. For metal foaming the following support materials have been used: (i) a 20 cm × 20 cm carbon fiber cloth (gas diffusion electrode, GDE) was purchased from Fuel Cell (USA). This carbon fiber cloth is covered on both sides with an extra mesoporous carbon layer (C-MPL, see Figure S1) facilitating the adhesion of the electrodeposited metallic foam to the support. The total thickness of the carbon cloth is ~385 μm. The carbon fiber cloths were used as received. (ii) Cu foils were purchased from Alfa Aesar (thickness 0.25 mm, 200 × 200 mm, purity ≥99.95%) and subjected to an electropolishing treatment in ortho-phosphoric acid (50 w%, ACS grade, Sigma Aldrich) to remove the native oxide layer prior their use. A graphite foil thereby served as the counter (cathode) electrode and the Cu foil as the working electrode (anode). A constant potential difference of 2.0 V was applied between both electrodes for the duration of 2 min. (iii) Graphitic carbon foils were purchased from Alfa Aesar (0.25 mm thickness) and activated by annealing in air at 550 °C for 12 h in a tube furnace prior to the Bi electrodeposition.

Electrolyte Solutions. The standard plating bath for the Bi foam deposition was composed of 1.5 M H_2SO_4 (prepared from 96% H_2SO_4, ACS grade, Sigma-Aldrich) serving as the supporting electrolyte and 20 mM bismuth ammonium citrate ($C_{12}H_{22}BiN_3O_{14}$, Sigma Aldrich, purity ≥99.5%). The CO_2RR experiments were carried out in 0.5 M $KHCO_3$ (ACS grade, Sigma-Aldrich) electrolyte solutions saturated with CO_2 gas (99.999%, Carbagas, Switzerland). For blank experiments, the same electrolyte was saturated with inert Ar gas (99.999%, Carbagas, Switzerland). Ar saturated potassium hydroxide (KOH, ACS grade, Sigma Aldrich) is also used for performing blank experiments.

Electrochemical Experiments. The galvanostatic Bi foam deposition was carried out in a 100 mL glass beaker by applying a current density of $j = -3.0$ A cm^{-2} (referred to the geometric surface area of the support electrode). The three-electrode arrangement consisted of a leakless Ag/AgCl$_{3M}$ reference electrode (EDAQ), a bright Pt foil (15 mm × 5 mm) serving as the anode, and the support electrode (GDE, Cu foil, and C foil) as the cathode. The electrodeposition was performed in a face-to-face configuration (distance between the anode and cathode: 3.5 mm) similar to the Ag foam electrodeposition process described elsewhere.[34] Important to note is that the deposited Bi foam is thick enough to avoid any undesired contribution from the support material (carbon and copper) to the resulting CO_2RR product distribution (see discussion of Figure S26). All voltammetric and CO_2RR electrolysis experiments were carried out in a custom-built, air-tight glass-cell (H-type) described elsewhere.[35] Possible chloride ion cross-contaminations in the working electrolytes originating from the Ag/AgCl$_{3M}$ reference electrode were monitored and excluded by ion exchange (IC) chromatography (Metrohm). All potentials given herein are *iR*-corrected (~85% of the cell resistance). The cell resistance was determined by means of the current interrupt method (Autolab NOVA 2.1 software).

For comparison purposes, all potentials measured versus the Ag/AgCl$_{3M}$ reference are referenced to the reversible hydrogen electrode (RHE) and calculated according to

$$E_{\mathrm{RHE}}(\mathrm{V}) = E_{\mathrm{Ag/AgCl(3M)}}(\mathrm{V}) + 0.210\ \mathrm{V} + (0.059\ \mathrm{V} \times \mathrm{pH}) \tag{5}$$

A reversible redox probe (dimethyl viologen (DMV^{2+})) was used for the determination of the electrochemically active surface area (ECSA) by means of cyclic voltammetric (CV) measurements (Figure S24). Scan-rate dependent CVs were measured in an H-type glass cell containing aqueous 1 M Na_2SO_4 (ACS grade, Sigma-Aldrich) solution and 10 mM $DMVCl_2$ (Sigma-Aldrich). The ECSA was determined on the basis of the Randles− Ševčík equation according to

$$i_{\mathrm{p}} = 2.69 \times 10^5 n^{3/2} A c D^{1/2} \nu^{1/2} \tag{6}$$

with i_{p} representing the peak current, n is the number of transferred electrons ($n = 1$), c is the concentration of the redox-active DMV^{2+} species, D is the DMV^{2+} diffusion coefficient, and ν is the potential sweep rate. ^{1}H DOSY NMR measurements were carried to estimate the diffusion coefficient of dimethyl viologen ($D = 5.5 \times 10^{-10}\ \mathrm{m^2\ s^{-1}}$). We note that the Randles−Ševčík equation was originally derived for planar macroelectrodes (e.g., discs) and not for highly porous electrode materials. The ECSA was derived from the linear regression of the respective i_{p} vs $\nu^{1/2}$ plots with A (ECSA) serving as a free fit parameter (see discussion of Figure S24 in the Supporting Information).

Annealing Treatment. Electrodeposited Bi metal foams were further activated by thermal annealing in air at 300 °C for 12 h using a tube furnace (GERO Hochtemperaturofen GmbH, Germany).

Structural and Compositional Characterization. *X-ray Diffraction (XRD) Analysis.* STOE Stadi system with a Cu Kα radiation source ($\lambda = 0.1540$ nm, 40 mA) operated at 40 keV was used for XRD analysis. Diffractograms were recorded in reflection mode (Bragg−Brentano geometry) in steps of 1° min^{-1} with 2θ values ranging from 0 to 90°. For the XRD analysis of the Bi foams, a carbon foil substrate was used. The obtained XRD patterns were analyzed and compared to JCPDS (Joint Committee on Powder Diffraction standards) data of polycrystalline Bi and Bi_2O_3 (file nos. 44-1246 and 41-1449).

Elemental Analysis. Elemental analysis of the electrolytes after the electrolysis was carried out by means of inductively coupled plasma mass spectrometry (ICP-MS, Perkin Elmer NexION 2000 instrument). For the ICP-MS analysis, aliquots of 20 μL of electrolyte (CO_2-sat. 0.5 M $KHCO_3$ solution) were diluted in 3% nitric acid solutions (501 times dilution). Each ICP-measurement was repeated four times by default; these repetitive measurements served as the basis for the determination of the sample-specific values of the relative standard deviation (RSD). ICP-MS-related RSD values are typically between 1 and 2%. An extra measuring error of ca. 1.5% needs to be taken into account and is due to the dilution treatment required for certain samples. Error bars in Figure 7 include both the instrumental error (ICP-MS) and the additional error resulting from the dilution procedure.

X-ray Photoelectron Spectroscopy (XPS). XPS measurements were carried out using a PHI VersaProbeII scanning XPS micro-probe (Physical Instruments AG, Germany) equipped with a monochromatic Al Kα X-ray source operated at 24.8 W with a spot size of 100 μm. The spherical capacitor analyzer was set at 45° take-off angle with respect to the sample surface. The pass energy was 46.95 eV. Peak positions were referenced to the carbon C1s peak at 285.5 eV. The curve fitting was performed using the Casa-XPS software.

SEM, EDX, and TEM. The morphology of the alloy foams was characterized by means of scanning electron microscopy (SEM) and energy-dispersive X-ray spectroscopy (EDX) using a Hitachi S-3000 N scanning electron microscope and a Noran SIX NSS200 energy-dispersive X-ray spectrometer. For the high-resolution (HR) identical location (IL) SEM imaging, a Zeiss DSM 982 instrument was used. For HR-TEM imaging, a FEI Tecnai G^2 F20 instrument equipped with a thermal (Schottky) field-emission source was used and operated at a 200 kV accelerating voltage. The microscope objective lens was a FEI Tecnai "Twin" lens type. A spherical aberration coefficient of Cs = 2.2 mm permitted a point resolution of 2.7 Å and a line resolution of 1.44 Å. The images were taken on a CETA CCD camera.

White Light Interferometry Analysis. The mesoscopic surface morphology of the foam electrodes was analyzed by means of white light interferometry (Contour GT, Bruker). Vision64 software (Bruker) was used for operating the instrument and the data analysis.

Quantification of Gaseous Electrolysis Products. During electrolysis, CO_2 was continuously purged through the catholyte at a flow rate of 13 mL min^{-1}. The headspace of the electrolysis cell was directly connected to the gas sampling loop of the gas chromatograph (GC 8610C, SRI Instruments). GC measurements were conducted in intervals of 20 min. The GC was equipped with both (i) a packed Hayesep D column and (ii) a packed Molesieve 5A column. Argon (99.9999%, Carba Gas) was used as the carrier gas. A thermal conductivity detector (TCD) was applied for the quantification of the formed H_2. Partial current (I_i) of each gaseous product, formed during the electrochemical CO_2 reduction, was determined according to

$$I_i = \frac{c_i \cdot \nu \cdot F \cdot z}{10^6 \cdot V_{\mathrm{m}}} \tag{7}$$

where I_i is the partial current for a given product i, c_i refers to the amount of product in ppm, z represents the number of electrons transferred during the electron transfer reaction, F is the Faraday constant in C mol^{-1}, ν is the flow rate in L s^{-1}, and V_{m} represents the molar volume of gas at 1 atm and room temperature in L mol^{-1}.

The faradaic efficiency (FE) for a given gaseous product was calculated by dividing its partial current density by the total current density (I_{total}), derived from the respective current vs time traces.

$$\mathrm{FE} = \frac{I_i}{I_{\mathrm{total}}} \cdot 100\% \tag{8}$$

Quantification of Liquid Products. In order to determine the yield of the non-volatile products (formate), aliquots were taken from the known volume of the catholyte after (see, e.g., Figures 8a and 8b) or during the electrolysis (see, e.g., Figure 9). The concentration of the liquid product was determined by an ion exchange chromatograph (Metrohm 940 Professional IC Vario) equipped with a Metrosep A Supp 7 column and controlled by the MagicNet 3.1 software. A 3 mM Na_2CO_3/0.1 M H_2SO_4 solution served as the eluent and suppressor, respectively. The instrument was calibrated by injecting known std. concentrations in the range from 2 to 10 ppm formate solution (see Figure S28). The standard solution was prepared by dilution of 1000 ppm ICstd. solution (Sigma Aldrich). The electrolysis samples were diluted 20 times by the

eluent prior to the analysis in order to reduce solvent effects by the bicarbonate solution.

The faradaic efficiency for the non-volatile products was derived on the basis of the integrated partial (Q_i) and total charges (Q_{total}) of the electrolysis reaction according to

$$Q_i = \frac{V_{cath} \cdot F \cdot z}{10^3 \cdot M} \cdot c_i \qquad (9)$$

$$FE = \frac{Q_i}{Q_{total}} \cdot 100\% \qquad (10)$$

where Q_i is the partial charge involved for the formation of a certain product i, V_{cath} is the total volume of the catholyte in L, c_i is the amount of the product i in ppm, M refers to the molar mass of the product, F is the Faraday constant, and z is the number of electron transferred to form the product. Q_{total} is the total charge transferred during the electrolysis experiment (see Figure S29).

Note that, for all potential-dependent CO$_2$RR experiments, a single catalyst approach was used (e.g., Figures 7, 8a, and 8b). A freshly prepared catalyst was used for each electrolysis experiment.

***Operando* Raman Spectroscopy.** Raman spectroscopic analyses were conducted using a LabRAM HR800 confocal microscope (Horiba Jobin Yvon). Spectral data were collected with the Raman spectrometer coupled to a confocal microscope (Horiba Jobin Yvon) and operated by the Lab Space 3.0 software. The calibration was carried out using a silicon wafer standard (520.6 cm^{-1}). A large working distance objective lens (50 × magnification, 8 mm focal length) has been applied with a numerical aperture of 0.1 in order to focus a diode-pumped solid-state (DPSS) laser beam (excitation wavelength of 532 nm; laser power of 3 mW for standard Raman measurements) on the sample and to collect both the incident and scattered laser light. For comparison purposes, also a He-Ne laser (excitation wave length of 633 nm) was used (see Figure S13).

A home-made spectro-electrochemical cell made of Kel-F was used for spectroscopic analysis.[46] The spectro-electrochemical cell consisted of a Ag/AgCl reference (EDAQ) electrode and an Au wire and the Bi foam (*ap* Bi/Bi$_x$O$_y$ or Bi$_2$O$_3$) as the counter and working electrode, respectively.

A μ-Autolab III (EcoChemie) potentiostat was used for the electrochemical Raman measurements. The ohmic resistances of about 17 Ω were determined by the current interrupt method and compensated (~85%) during the measurement via GPES 4.0 software. Unless otherwise stated, Raman spectra were collected in the spectral range from 100 to 1200 cm^{-1} at a 3 mW laser power and an excitation wavelength of 532 nm (DPSS laser). For the data acquisition in the potentiostatic experiments (Figure 4c−g), the holding time was 180 s at each applied electrolysis potential. The actual Raman spectroscopic measurements were started only after 2 min holding the potential in order to reach (quasi) steady-state conditions after the potential step (see also discussion of Figure 5). To improve the signal-to-noise ratio, 10 individual spectra (10 s recording time each) were recorded at a given potential, averaged, and displayed (e.g., in Figures 4c and 4d). Time-resolved Raman spectroscopy experiments under OCP conditions were performed with an interval time of ca. 90 s (e.g., in Figure 4b and Figure S16). For the data acquisition, 10 spectra were recorded (10 s recording time each), averaged, and displayed (e.g. in Figure 4b).

All Raman spectra were baseline corrected in the Lab Space 3.0 software using a polynomial fit function. The normalization of the integrated peak intensities (Figure 4g and Figure S18) was carried out using the integrated intensity data at the OCP as the reference point.

■ ASSOCIATED CONTENT

Ⓢ Supporting Information

The Supporting Information is available free of charge at https://pubs.acs.org/doi/10.1021/acscatal.0c05317.

SEM images, reference measurements on the optimization of the Raman experiment in terms of laser light source and laser power, quantitative analysis of this (oxide/sub-carbonate → metal) transition, and additional supporting results and discussion (PDF)

Corresponding media file of Figure S9 (MP4)

■ AUTHOR INFORMATION

Corresponding Authors

Abhijit Dutta − *Department of Chemistry and Biochemistry, University of Bern, Bern 3012, Switzerland;* ⓘ orcid.org/0000-0002-3054-0492; Email: abhijit.dutta@dcb.unibe.ch

Peter Broekmann − *Department of Chemistry and Biochemistry, University of Bern, Bern 3012, Switzerland;* ⓘ orcid.org/0000-0002-6287-1042; Email: peter.broekmann@dcb.unibe.ch

Authors

Iván Zelocualtecatl Montiel − *Department of Chemistry and Biochemistry, University of Bern, Bern 3012, Switzerland*

Kiran Kiran − *Department of Chemistry and Biochemistry, University of Bern, Bern 3012, Switzerland*

Alain Rieder − *Department of Chemistry and Biochemistry, University of Bern, Bern 3012, Switzerland*

Vitali Grozovski − *Department of Chemistry and Biochemistry, University of Bern, Bern 3012, Switzerland*

Lukas Gut − *Department of Chemistry and Biochemistry, University of Bern, Bern 3012, Switzerland*

Complete contact information is available at:
https://pubs.acs.org/10.1021/acscatal.0c05317

Notes

The authors declare no competing financial interest.

■ ACKNOWLEDGMENTS

■ REFERENCES

(1) Wang, W.-H.; Himeda, Y.; Muckerman, J. T.; Manbeck, G. F.; Fujita, E. CO$_2$ Hydrogenation to Formate and Methanol as an Alternative to Photo- and Electrochemical CO$_2$ Reduction. *Chem. Rev.* **2015**, *115*, 12936−12973.

(2) Karl, T. R.; Trenberth, K. E. Modern Global Climate Change. *Science* **2003**, *302*, 1719.

(3) Gurudayal; Bullock, J.; Srankó, D. F.; Towle, C. M.; Lum, Y.; Hettick, M.; Scott, M. C.; Javey, A.; Ager, J. Efficient solar-driven electrochemical CO$_2$ reduction to hydrocarbons and oxygenates. *Energy Environ. Sci.* **2017**, *10*, 2222−2230.

(4) Peterson, A. A.; Abild-Pedersen, F.; Studt, F.; Rossmeisl, J.; Nørskov, J. K. How copper catalyzes the electroreduction of carbon dioxide into hydrocarbon fuels. *Energy Environ. Sci.* **2010**, *3*, 1311−1315.

(5) Rahaman, M.; Dutta, A.; Broekmann, P. Size-Dependent Activity of Palladium Nanoparticles: Efficient Conversion of CO_2 into Formate at Low Overpotentials. *ChemSusChem* **2017**, *10*, 1733−1741.

(6) Daggash, H. A.; Patzschke, C. F.; Heuberger, C. F.; Zhu, L.; Hellgardt, K.; Fennell, P. S.; Bhave, A. N.; Bardow, A.; Mac Dowell, N. Closing the carbon cycle to maximise climate change mitigation: power-to-methanol vs. power-to-direct air capture. *Sustain. Energy Fuels* **2018**, *2*, 1153−1169.

(7) Seh, Z. W.; Kibsgaard, J.; Dickens, C. F.; Chorkendorff, I.; Nørskov, J. K.; Jaramillo, T. F. Combining theory and experiment in electrocatalysis: Insights into materials design. *Science* **2017**, *355*, No. eaad4998.

(8) García de Arquer, F. P.; Dinh, C.-T.; Ozden, A.; Wicks, J.; McCallum, C.; Kirmani, A. R.; Nam, D.-H.; Gabardo, C.; Seifitokaldani, A.; Wang, X.; Li, Y. C.; Li, F.; Edwards, J.; Richter, L. J.; Thorpe, S. J.; Sinton, D.; Sargent, E. H. CO_2 electrolysis to multicarbon products at activities greater than 1 A cm^{-2}. *Science* **2020**, *367*, 661.

(9) Liu, C.; Colón, B. C.; Ziesack, M.; Silver, P. A.; Nocera, D. G. Water splitting−biosynthetic system with CO_2 reduction efficiencies exceeding photosynthesis. *Science* **2016**, *352*, 1210.

(10) Pan, F.; Yang, Y. Designing CO_2 reduction electrode materials by morphology and interface engineering. *Energy Environ. Sci.* **2020**, 2275.

(11) Qiao, J.; Liu, Y.; Hong, F.; Zhang, J. A review of catalysts for the electroreduction of carbon dioxide to produce low-carbon fuels. *Chem. Soc. Rev.* **2014**, *43*, 631−675.

(12) Azuma, M.; Hashimoto, K.; Hiramoto, M.; Watanabe, M.; Sakata, T. Electrochemical Reduction of Carbon Dioxide on Various Metal Electrodes in Low-Temperature Aqueous $KHCO_3$ Media. *J. Electrochem. Soc.* **1990**, *137*, 1772−1778.

(13) Hori, Y.; Kikuchi, K.; Suzuki, S. Production of CO and CH_4 in electrochemical reduction of CO_2 at metal electrodes in aqueous hydrogencarbonate solution. *Chem. Lett.* **1985**, *14*, 1695−1698.

(14) Hori, Y.; Wakebe, H.; Tsukamoto, T.; Koga, O. Electrocatalytic process of CO selectivity in electrochemical reduction of CO_2 at metal electrodes in aqueous media. *Electrochim. Acta* **1994**, *39*, 1833−1839.

(15) Chai, G.-L.; Guo, Z.-X. Highly effective sites and selectivity of nitrogen-doped graphene/CNT catalysts for CO_2 electrochemical reduction. *Chem. Sci.* **2016**, *7*, 1268−1275.

(16) Sun, Z.; Ma, T.; Tao, H.; Fan, Q.; Han, B. Fundamentals and Challenges of Electrochemical CO_2 Reduction Using Two-Dimensional Materials. *Chem* **2017**, *3*, 560−587.

(17) Zheng, X.; De Luna, P.; García de Arquer, F. P.; Zhang, B.; Becknell, N.; Ross, M. B.; Li, Y.; Banis, M. N.; Li, Y.; Liu, M.; Voznyy, O.; Dinh, C. T.; Zhuang, T.; Stadler, P.; Cui, Y.; Du, X.; Yang, P.; Sargent, E. H. Sulfur-Modulated Tin Sites Enable Highly Selective Electrochemical Reduction of CO_2 to Formate. *Joule* **2017**, *1*, 794−805.

(18) Gao, S.; Jiao, X.; Sun, Z.; Zhang, W.; Sun, Y.; Wang, C.; Hu, Q.; Zu, X.; Yang, F.; Yang, S.; Liang, L.; Wu, J.; Xie, Y. Ultrathin Co_3O_4 Layers Realizing Optimized CO_2 Electroreduction to Formate. *Angew. Chem., Int. Ed.* **2015**, *128*, 708−712.

(19) Gao, S.; Lin, Y.; Jiao, X.; Sun, Y.; Luo, Q.; Zhang, W.; Li, D.; Yang, J.; Xie, Y. Partially oxidized atomic cobalt layers for carbon dioxide electroreduction to liquid fuel. *Nature* **2016**, *529*, 68.

(20) Fu, Y.; Li, Y.; Zhang, X.; Liu, Y.; Qiao, J.; Zhang, J.; Wilkinson, D. P. Novel hierarchical SnO_2 microsphere catalyst coated on gas diffusion electrode for enhancing energy efficiency of CO_2 reduction to formate fuel. *Appl. Energy* **2016**, *175*, 536−544.

(21) Zhang, T.; Zhong, H.; Qiu, Y.; Li, X.; Zhang, H. Zn electrode with a layer of nanoparticles for selective electroreduction of CO_2 to formate in aqueous solutions. *J. Mater. Chem. A* **2016**, *4*, 16670−16676.

(22) Zha, B.; Li, C.; Li, J. Efficient electrochemical reduction of CO_2 into formate and acetate in polyoxometalate catholyte with indium catalyst. *J. Catal.* **2020**, *382*, 69−76.

(23) Han, N.; Wang, Y.; Yang, H.; Deng, J.; Wu, J.; Li, Y.; Li, Y. Ultrathin bismuth nanosheets from in situ topotactic transformation for selective electrocatalytic CO_2 reduction to formate. *Nat. Commun.* **2018**, *9*, 1320.

(24) Su, P.; Xu, W.; Qiu, Y.; Zhang, T.; Li, X.; Zhang, H. Ultrathin Bismuth Nanosheets as a Highly Efficient CO_2 Reduction Electrocatalyst. *ChemSusChem* **2018**, *11*, 848−853.

(25) Zhang, H.; Ma, Y.; Quan, F.; Huang, J.; Jia, F.; Zhang, L. Selective electro-reduction of CO_2 to formate on nanostructured Bi from reduction of BiOCl nanosheets. *Electrochem. Commun.* **2014**, *46*, 63−66.

(26) Rudnev, A. V.; Kiran, K.; Broekmann, P. Specific Cation Adsorption: Exploring Synergistic Effects on CO_2 Electroreduction in Ionic Liquids. *ChemElectroChem* **2020**, *7*, 1897−1903.

(27) Zhang, W.; Hu, Y.; Ma, L.; Zhu, G.; Zhao, P.; Xue, X.; Chen, R.; Yang, S.; Ma, J.; Liu, J.; Jin, Z. Liquid-phase exfoliated ultrathin Bi nanosheets: Uncovering the origins of enhanced electrocatalytic CO_2 reduction on two-dimensional metal nanostructure. *Nano Energy* **2018**, *53*, 808−816.

(28) Yang, F.; Elnabawy, A. O.; Schimmenti, R.; Song, P.; Wang, J.; Peng, Z.; Yao, S.; Deng, R.; Song, S.; Lin, Y.; Mavrikakis, M.; Xu, W. Bismuthene for highly efficient carbon dioxide electroreduction reaction. *Nat. Commun.* **2020**, *11*, 1088.

(29) Koh, J. H.; Won, D. H.; Eom, T.; Kim, N.-K.; Jung, K. D.; Kim, H.; Hwang, Y. J.; Min, B. K. Facile CO_2 Electro-Reduction to Formate via Oxygen Bidentate Intermediate Stabilized by High-Index Planes of Bi Dendrite Catalyst. *ACS Catal.* **2017**, *7*, 5071−5077.

(30) Zhang, Y.; Zhang, X.; Ling, Y.; Li, F.; Bond, A. M.; Zhang, J. Controllable Synthesis of Few-Layer Bismuth Subcarbonate by Electrochemical Exfoliation for Enhanced CO_2 Reduction Performance. *Angew. Chem., Int. Ed.* **2018**, *57*, 13283−13287.

(31) Liu, S.; Lu, X. F.; Xiao, J.; Wang, X.; Lou, X. W. Bi_2O_3 Nanosheets Grown on Multi-Channel Carbon Matrix to Catalyze Efficient CO_2 Electroreduction to HCOOH. *Angew. Chem., Int. Ed.* **2019**, *58*, 13828−13833.

(32) Lu, P.; Gao, D.; He, H.; Wang, Q.; Liu, Z.; Dipazir, S.; Yuan, M.; Zu, W.; Zhang, G. Facile synthesis of a bismuth nanostructure with enhanced selectivity for electrochemical conversion of CO_2 to formate. *Nanoscale* **2019**, *11*, 7805−7812.

(33) Li, L.; Ma, D.-K.; Qi, F.; Chen, W.; Huang, S. Bi nanoparticles/ Bi_2O_3 nanosheets with abundant grain boundaries for efficient electrocatalytic CO_2 reduction. *Electrochim. Acta* **2019**, *298*, 580−586.

(34) Dutta, A.; Morstein, C. E.; Rahaman, M.; Cedeño López, A.; Broekmann, P. Beyond Copper in CO_2 Electrolysis: Effective Hydrocarbon Production on Silver-Nanofoam Catalysts. *ACS Catal.* **2018**, *8*, 8357−8368.

(35) Dutta, A.; Rahaman, M.; Luedi, N. C.; Mohos, M.; Broekmann, P. Morphology Matters: Tuning the Product Distribution of CO_2 Electroreduction on Oxide-Derived Cu Foam Catalysts. *ACS Catal.* **2016**, *6*, 3804−3814.

(36) Dutta, A.; Kuzume, A.; Kaliginedi, V.; Rahaman, M.; Sinev, I.; Ahmadi, M.; Roldán Cuenya, B.; Vesztergom, S.; Broekmann, P. Probing the chemical state of tin oxide NP catalysts during CO_2 electroreduction: A complementary operando approach. *Nano Energy* **2018**, *53*, 828−840.

(37) Dutta, A.; Kuzume, A.; Rahaman, M.; Vesztergom, S.; Broekmann, P. Monitoring the Chemical State of Catalysts for CO_2 Electroreduction: An In Operando Study. *ACS Catal.* **2015**, *5*, 7498−7502.

(38) Plowman, B. J.; Jones, L. A.; Bhargava, S. K. Building with bubbles: the formation of high surface area honeycomb-like films via hydrogen bubble templated electrodeposition. *Chem. Commun.* **2015**, *51*, 4331−4346.

(39) Gálvez-Vázquez, M. D. J.; Grozovski, V.; Kovács, N.; Broekmann, P.; Vesztergom, S. Full Model for the Two-Step

Polarization Curves of Hydrogen Evolution, Measured on RDEs in Dilute Acid Solutions. *J. Phys. Chem. C* **2020**, *124*, 3988−4000.

(40) Asato, E.; Katsura, K.; Mikuriya, M.; Turpeinen, U.; Mutikainen, I.; Reedijk, J. Synthesis, Structure, and Spectroscopic Properties of Bismuth Citrate Compounds and the Bismuth-Containing Ulcer-Healing Agent Colloidal Bismuth Subcitrate (CBS). 4. Crystal Structure and Solution Behavior of a Unique Dodecanuclear Cluster $(NH_4)_{12}[Bi_{12}O_8(cit)_8](H_2O)_{10}$. *Inorg. Chem.* **1995**, *34*, 2447−2454.

(41) Vesztergom, S.; Dutta, A.; Rahaman, M.; Kiran, K.; Zelocualtecatl Montiel, I.; Broekmann, P. Hydrogen Bubble Templated Metal Foams as Efficient Catalysts of CO_2 Electro-reduction. *ChemCatChem* **2021**, *13*, 1039−1058.

(42) Dutta, A.; Rahaman, M.; Mohos, M.; Zanetti, A.; Broekmann, P. Electrochemical CO_2 Conversion Using Skeleton (Sponge) Type of Cu Catalysts. *ACS Catal.* **2017**, *7*, 5431−5437.

(43) Zhang, H.; Ye, Y.; Shen, R.; Ru, C.; Hu, Y. Effect of Bubble Behavior on the Morphology of Foamed Porous Copper Prepared via Electrodeposition. *J. Electrochem. Soc.* **2013**, *160*, D441−D445.

(44) Sen, S.; Liu, D.; Palmore, G. T. R. Electrochemical Reduction of CO_2 at Copper Nanofoams. *ACS Catal.* **2014**, *4*, 3091−3095.

(45) Shin, H.-C.; Liu, M. Copper Foam Structures with Highly Porous Nanostructured Walls. *Chem. Mater.* **2004**, *16*, 5460−5464.

(46) Dutta, A.; Montiel, I. Z.; Erni, R.; Kiran, K.; Rahaman, M.; Drnec, J.; Broekmann, P. Activation of bimetallic AgCu foam electrocatalysts for ethanol formation from CO_2 by selective Cu oxidation/reduction. *Nano Energy* **2020**, *68*, 104331.

(47) Harwig, H. A. On the Structure of Bismuthsesquioxide: The α, β, γ, and δ-phase. *Z. Anorg. Allg. Chem.* **1978**, *444*, 151−166.

(48) Kumar, P.; Singh, J.; Pandey, A. C. Rational low temperature synthesis and structural investigations of ultrathin bismuth nano-sheets. *RSC Adv.* **2013**, *3*, 2313−2317.

(49) Pereira, A. L. J.; Errandonea, D.; Beltrán, A.; Gracia, L.; Gomis, O.; Sans, J. A.; García-Domene, B.; Miquel-Veyrat, A.; Manjón, F. J.; Muñoz, A.; Popescu, C. Structural study of α-Bi_2O_3 under pressure. *J. Phys.: Condens. Matter* **2013**, *25*, 475402.

(50) Jiang, S.; Klingan, K.; Pasquini, C.; Dau, H. New aspects of operando Raman spectroscopy applied to electrochemical CO_2 reduction on Cu foams. *J. Chem. Phys.* **2018**, *150*, No. 041718.

(51) Dutta, A.; Rahaman, M.; Hecker, B.; Drnec, J.; Kiran, K.; Zelocualtecatl Montiel, I.; Jochen Weber, D.; Zanetti, A.; Cedeño López, A.; Martens, I.; Broekmann, P.; Oezaslan, M. CO_2 electrolysis − Complementary operando XRD, XAS and Raman spectroscopy study on the stability of Cu_xO foam catalysts. *J. Catal.* **2020**, *389*, 592−603.

(52) Denisov, V. N.; Ivlev, A. N.; Lipin, A. S.; Mavrin, B. N.; Orlov, V. G. Raman spectra and lattice dynamics of single-crystal. *J. Phys.: Condens. Matter* **1997**, *9*, 4967−4978.

(53) Betsch, R. J.; White, W. B. Vibrational spectra of bismuth oxide and the sillenite-structure bismuth oxide derivatives. *Spectrochim. Acta, Part A* **1978**, *34*, 505−514.

(54) Schröder, F.; Bagdassarov, N.; Ritter, F.; Bayarjargal, L. Temperature dependence of Bi_2O_3 structural parameters close to the α−δ phase transition. *Phase Transitions* **2010**, *83*, 311−325.

(55) Ho, C.-H.; Chan, C.-H.; Huang, Y.-S.; Tien, L.-C.; Chao, L.-C. The study of optical band edge property of bismuth oxide nanowires α-Bi_2O_3. *Opt. Express* **2013**, *21*, 11965−11972.

(56) Steele, J. A.; Lewis, R. A. In situ micro-Raman studies of laser-induced bismuth oxidation reveals metastability of β-Bi_2O_3 microis-lands. *Opt. Mater. Express* **2014**, *4*, 2133−2142.

(57) Ibl, N. Atlas d'équilibres électrochimiques à 25 °C. Von M. Pourbaix, unter Mitwirkung zahlreicher Fachgelehrter. Verlag: Gauthier-Villars & Cie., Paris 1963. 1. Aufl., 644 S., zahlr. Abb., geb. NF 140.—. *Angew. Chem., Int. Ed.* **1964**, *76*, 444−444.

(58) Taylor, P.; Sunder, S.; Lopata, V. J. Structure, spectra, and stability of solid bismuth carbonates. *Can. J. Chem.* **1984**, *62*, 2863−2873.

(59) Wiebe, R.; Gaddy, V. L. The Solubility of Carbon Dioxide in Water at Various Temperatures from 12 to 40° and at Pressures to

500 Atmospheres. Critical Phenomena*. *J. Am. Chem. Soc.* **1940**, *62*, 815−817.

(60) Deng, P.; Wang, H.; Qi, R.; Zhu, J.; Chen, S.; Yang, F.; Zhou, L.; Qi, K.; Liu, H.; Xia, B. Y. Bismuth Oxides with Enhanced Bismuth−Oxygen Structure for Efficient Electrochemical Reduction of Carbon Dioxide to Formate. *ACS Catal.* **2020**, *10*, 743−750.

(61) Cherevko, S.; Reier, T.; Zeradjanin, A. R.; Pawolek, Z.; Strasser, P.; Mayrhofer, K. J. J. Stability of nanostructured iridium oxide electrocatalysts during oxygen evolution reaction in acidic environ-ment. *Electrochem. Commun.* **2014**, *48*, 81−85.

(62) Cherevko, S.; Mayrhofer, K. J. J., On-Line Inductively Coupled Plasma Spectrometry in Electrochemistry: Basic Principles and Applications. In *Encyclopedia of Interfacial Chemistry*; Wandelt, K., Ed. Elsevier: Oxford, 2018; pp 326−335, DOI: 10.1016/B978-0-12-409547-2.13292-5.

(63) Löffler, M.; Khanipour, P.; Kulyk, N.; Mayrhofer, K. J. J.; Katsounaros, I. Insights into Liquid Product Formation during Carbon Dioxide Reduction on Copper and Oxide-Derived Copper from Quantitative Real-Time Measurements. *ACS Catal.* **2020**, *10*, 6735−6740.

(64) Zhang, Y.; Li, F.; Zhang, X.; Williams, T.; Easton, C. D.; Bond, A. M.; Zhang, J. Electrochemical reduction of CO_2 on defect-rich Bi derived from Bi_2S_3 with enhanced formate selectivity. *J. Mater. Chem. A* **2018**, *6*, 4714−4720.

(65) Ortiz-Quiñonez, J. L.; Vega-Verduga, C.; Díaz, D.; Zumeta-Dubé, I. Transformation of Bismuth and β-Bi_2O_3 Nanoparticles into $(BiO)_2CO_3$ and $(BiO)_4(OH)_2CO_3$ by Capturing CO_2: The Role of Halloysite Nanotubes and "Sunlight" on the Crystal Shape and Size. *Cryst. Growth Des.* **2018**, *18*, 4334−4346.

(66) Tran-Phu, T.; Daiyan, R.; Fusco, Z.; Ma, Z.; Amal, R.; Tricoli, A. Nanostructured β-Bi2O3 Fractals on Carbon Fibers for Highly Selective CO_2 Electroreduction to Formate. *Adv. Funct. Mater.* **2020**, *30*, 1906478.

(67) Tran-Phu, T.; Daiyan, R.; Fusco, Z.; Ma, Z.; Rahim, L. R. A.; Kiy, A.; Kluth, P.; Guo, X.; Zhu, Y.; Chen, H.; Amal, R.; Tricoli, A. Multifunctional nanostructures of Au−Bi_2O_3 fractals for CO_2 reduction and optical sensing. *J. Mater. Chem. A* **2020**, *8*, 11233−11245.

(68) Del Castillo, A.; Alvarez-Guerra, M.; Solla-Gullón, J.; Sáez, A.; Montiel, V.; Irabien, A. Sn nanoparticles on gas diffusion electrodes: Synthesis, characterization and use for continuous CO_2 electro-reduction to formate. *J. CO2 Util.* **2017**, *18*, 222−228.

(69) Gong, Q.; Ding, P.; Xu, M.; Zhu, X.; Wang, M.; Deng, J.; Ma, Q.; Han, N.; Zhu, Y.; Lu, J.; Feng, Z.; Li, Y.; Zhou, W.; Li, Y. Structural defects on converted bismuth oxide nanotubes enable highly active electrocatalysis of carbon dioxide reduction. *Nat. Commun.* **2019**, *10*, 2807.

(70) Liu, M.; Pang, Y.; Zhang, B.; De Luna, P.; Voznyy, O.; Xu, J.; Zheng, X.; Dinh, C. T.; Fan, F.; Cao, C.; de Arquer, F. P. G.; Safaei, T. S.; Mepham, A.; Klinkova, A.; Kumacheva, E.; Filleter, T.; Sinton, D.; Kelley, S. O.; Sargent, E. H. Enhanced electrocatalytic CO_2 reduction via field-induced reagent concentration. *Nature* **2016**, *537*, 382−386.

(71) Yoo, J. S.; Christensen, R.; Vegge, T.; Nørskov, J. K.; Studt, F. Theoretical Insight into the Trends that Guide the Electrochemical Reduction of Carbon Dioxide to Formic Acid. *ChemSusChem* **2016**, *9*, 358−363.

5.9. Suppression of the Hydrogen Evolution Reaction is the Key: Selective Electrosynthesis of Formate from CO_2 over Porous $In_{55}Cu_{45}$ Catalysts

Authors: Motiar Rahaman[Δ*], Kiran Kiran[Δ*], Ivan Zelocualtecatl Montiel, Abhijit Dutta, and Peter Broekmann[*]

Δ These authors contributed equally to this work.
* Corresponding authors

Highlights: Formate is the key product achieved in this study. $In_{55}Cu_{45}$ was used as an efficient electrocatalyst for selective formate formation with faradaic efficiencies ($FE_{formate}$) never falling below 90% within a relatively broad potential of ca. 400 mV, ranging from – 0.8 V to – 1.2 V vs. the reversible hydrogen electrode (RHE). A maximum $FE_{formate}$ of 96.8 % was achieved at −1.0 V vs. RHE, corresponding to a partial current density, $j_{formate} = -8.9\ mA\ cm^{-2}$. The durability of the catalyst against deterioration and chemical poisoning was investigated by an extended electrolysis experiment for 30 h, revealing high stability with a efficiency of ca. 94%. On the contrary, pure In film catalysts (the reference system) exhibited a significant reduction in formate efficiency from 82% to 50% under identical experimental circumstances. Morphological alternation of the catalyst were monitored by identical location (IL)-SEM analysis, demonstrating the structural stability at various length scales.

Contribution: I performed all the electrochemical characterization and the catalyst development. I performed the identical location (IL)-SEM analysis of the $In_{55}Cu_{45}$ before and after 30 h of electrolysis. Catalyst was successfully transferred to 3d substrate, depicting the similar efficiency as to the planar foil (Cu). I was also involved in data analysis and writing of the manuscript.

Suppression of the Hydrogen Evolution Reaction Is the Key: Selective Electrosynthesis of Formate from CO_2 over Porous $In_{55}Cu_{45}$ Catalysts

Motiar Rahaman,*,§ Kiran Kiran,*,§ Ivan Zelocualtecatl Montiel, Abhijit Dutta, and Peter Broekmann*

ACCESS | Metrics & More | Article Recommendations | SI Supporting Information

ABSTRACT: Direct electrosynthesis of formate through CO_2 electroreduction (denoted CO_2RR) is currently attracting great attention because formate is a highly valuable commodity chemical that is already used in a wide range of applications (e.g., formic acid fuel cells, tanning, rubber production, preservatives, and antibacterial agents). Herein, we demonstrate highly selective production of formate through CO_2RR from a CO_2-saturated aqueous bicarbonate solution using a porous $In_{55}Cu_{45}$ alloy as the electrocatalyst. This novel high-surface-area material was produced by means of an electrodeposition process utilizing the dynamic hydrogen bubble template approach. Faradaic efficiencies (FEs) of formate production ($FE_{formate}$) never fell below 90% within a relatively broad potential window of approximately 400 mV, ranging from −0.8 to −1.2 V vs the reversible hydrogen electrode (RHE). A maximum $FE_{formate}$ of 96.8%, corresponding to a partial current density of $j_{formate}$ = −8.9 mA cm^{-2}, was yielded at −1.0 V vs RHE. The experimental findings suggested a CO_2RR mechanism involving stabilization of the HCOO* intermediate on the $In_{55}Cu_{45}$ alloy surface in combination with effective suppression of the parasitic hydrogen evolution reaction. What makes this CO_2RR alloy catalyst particularly valuable is its stability against degradation and chemical poisoning. An almost constant formate efficiency of ∼94% was maintained in an extended 30 h electrolysis experiment, whereas pure In film catalysts (the reference benchmark system) showed a pronounced decrease in formate efficiency from 82% to 50% under similar experimental conditions. The identical location scanning electron microscopy approach was applied to demonstrate the structural stability of the applied $In_{55}Cu_{45}$ alloy foam catalysts at various length scales. We demonstrate that the proposed catalyst concept could be transferred to technically relevant support materials (e.g., carbon cloth gas diffusion electrode) without altering its excellent figures of merit.

KEYWORDS: CO_2 conversion, formate electrosynthesis, indium−copper alloy, hydrogen evolution reaction (HER) suppression, technical support
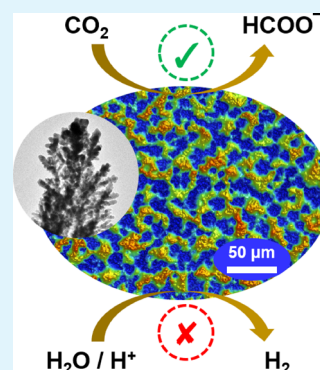
1. INTRODUCTION

The electrochemical reduction of CO_2 (hereafter, CO_2RR) is considered a feasible approach to mitigate the constantly raising levels of CO_2 in the atmosphere and its harmful impact on the global climate.[1−4] CO_2RR provides a means of producing value-added platform chemicals from CO_2 in a highly sustainable manner, particularly when a surplus of renewables from solar, wind, and hydro energy sources is used to power the highly endergonic CO_2 conversion process.

Formate is regarded a valuable CO_2RR product that has utility in various sectors. Its potential as a future energy carrier in advanced fuel-cell technologies is currently being explored.[5,6] In the chemical industry, it finds wide use as a solvent and reactant for neutralization reactions. In the textile industry, it is used as a tanning agent in the production of leather goods.[7−9] In many products of our daily life, formate and formic acid serve as preserving agents.[10] Current efforts to use CO_2RR for the electrosynthesis of formate are further motivated by analyses suggesting that from an economic

standpoint, the electrochemical approach might be competitive with existing mature synthesis routes.[11−15]

A key aspect of designing an efficient CO_2RR process concerns the catalyst material, which is essential not only to accelerate the inherently slow CO_2RR process but also to increase its energy efficiency by lowering the required overpotentials. In addition, the chemical nature and morphological characteristics of the catalyst material ultimately dictate the resulting CO_2RR product distribution.[16−19] In their pioneering work, Hori et al. grouped monometallic catalysts into three categories according to the observed main product of the CO_2RR process.[20] The first category of catalysts was
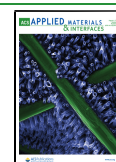
found to predominantly produce formate (e.g., Sn, Pb, Hg, Cd, and Tl); the post-transition metal indium (In) also belongs to this formate-producing group of catalysts. The second category of metallic CO_2RR catalysts, which included but was not restricted to Ag and Au, showed a high product selectivity toward CO. Copper stands out as a unique material because it was identified as the only catalyst that can form hydrocarbons and alcohols from CO_2RR by allowing C—C coupling reactions.[20−28]

Combining two metallic catalysts from different groups of Hori et al.'s classification scheme has demonstrated promise in various aspects.[29−31] Among these, one benefit of such a two-component catalyst system could be the increase in CO_2RR selectivity toward a certain target product that is predominantly or exclusively formed on one of the catalyst constituents. The role of the secondary (nondominant) constituent is to further promote one particular CO_2RR pathway on the primary (dominant) catalyst component. A prime example is the combination of a CO former (e.g., Ag or Pd, nondominant constituent) with Cu (C—C coupler; dominant constituent), where spillover effects of CO intermediates from the nondominant constituent (Ag or Pd) to the Cu sites are discussed as the mechanistic origin of the improved faradaic yields toward higher alcohols (ethanol and 1-propanol).[32−36]

Another outcome of combining two metallic catalysts from different groups of Hori et al.'s classification scheme could be to alter the CO_2RR product selectivity in such a way that it becomes atypical for the respective two pure monometallic constituents of the mixed system. Examples are co-alloyed In_xCu_y systems, which often demonstrate high CO_2RR selectivities toward CO.[37−40] This is atypical in particular for the In component, which, in its monometallic form, belongs to the group of formate-producing catalysts.[20,41−44] In principle, CO forms on Cu but mainly as an intermediate that is typically converted further into hydrocarbons or higher alcohols, particularly at higher negative overpotentials. For the reported CO-forming In_xCu_y systems, Cu can be considered as the dominant catalyst component and In correspondingly as the nondominant (auxiliary) component. Its mechanistic role in the course of the multistep CO_2 conversion is to weaken the Cu—CO bond. This concept of weakening the metal—CO (M—CO) binding strength by a co-alloyed metal is well known from other two-component catalyst systems, for example, from binary Au_xCu_y, Ag_xCu_y, and Pd_xCu_y alloys.[45−47] This weakening of the Cu—CO bond, mediated by In, gives rise to the facile release of CO from the Cu sites of the alloy catalyst surface, thereby preventing any further reaction of intermediates in terms of C—C coupling or multicarbon formation. For monometallic systems, Kuhl et al. identified M—CO binding strength as a key descriptor for the resulting CO_2RR product distribution, demonstrating a volcano-like behavior, with (pure) Cu being located on the side of a high M—CO binding strength close to the volcano peak.[48] According to this consideration, the reported In_xCu_y alloys[37−40] need to be placed on the "low-binding" side of the volcano (compared with pure Cu), where catalysts such as Au and Ag are found to demonstrate lower M—CO binding strengths and facile release of CO as the main CO_2RR product.

In this study, we report a novel dendritic $In_{55}Cu_{45}$ alloy catalyst that differs substantially from those reported so far in the literature. In this $In_{55}Cu_{45}$ alloy, In is the dominant catalyst component governing CO_2RR product distribution, with a clear preference toward formate formation, whereas the electrocatalytic characteristics of Cu in terms of (intermediate) CO, hydrocarbon, and alcohol formation remain fully suppressed. Note that when brought into a highly dendritic form, a pure Cu catalyst also demonstrates a high formate selectivity of ∼50%, particularly at moderate overpotentials (at −0.7 V vs RHE).[28] Herein, we will demonstrate that the presence of Cu in the dendritic $In_{55}Cu_{45}$ alloy further boosts faradaic efficiency ($FE_{formate}$) values to 96.8% at −1.0 V vs RHE, yielding a partial current density ($PCD_{formate}$) of −8.9 mA cm^{-2}, which is considered excellent for electrolyses in H-type cells.

The most beneficial effect of co-alloying In and Cu on catalytic performance concerns, however, is its long-term stability. The $In_{55}Cu_{45}$ catalyst shows remarkable catalytic stability at −1.0 V vs RHE for 30 h with a constant production rate of formate ($FE_{formate}$ = 94.2 ± 2.1%). On the other hand, pure In electrocatalysts undergo severe degradation during extended CO_2 electrolysis, which typically results in a drastic increase in the parasitic hydrogen evolution reaction (HER) at the expense of formate yields.

2. EXPERIMENTAL METHODS

2.1. Materials and Chemicals. The Cu foil (99.9% pure), serving as the support material for the alloy foam electrodeposition, was purchased from Alfa Aesar and cut into pieces of 8 mm × 30 mm. For X-ray diffraction (XRD) analysis, alloy foam was deposited on a graphite foil substrate (0.25 mm thick, 99.8%, Alfa Aesar) to omit the contribution from the Cu foil support to the XRD pattern.

$In_2(SO_4)_3·xH_2O$ (Sigma-Aldrich, 99.99%) and $CuSO_4·5H_2O$ (Sigma-Aldrich, 99.99%) were used as metal precursors for the metal foam electrodeposition. ACS-grade H_2SO_4 (Sigma-Aldrich) was used to prepare the plating bath. $KHCO_3$ (99.7%) was purchased from Sigma-Aldrich and used to prepare the electrolyte for the CO_2 electrolyses. All chemicals were used as received without further purification.

Milli-Q water (18.2 MΩ cm, 4 ppb of total organic carbon content; Millipore) was used to prepare all the solutions.

2.2. Catalyst Preparation. The Cu foil substrate was first electropolished in 50% orthophosphoric acid (ACS grade, Sigma-Aldrich) to remove contamination and the native oxide layer from its surface. For this purpose, a two-electrode arrangement was used, with graphite and Cu foil serving as a cathode and anode, respectively. For the electropolishing treatment, a potential difference of 2 V was applied for ∼2 min. The Cu foil was then thoroughly rinsed with Milli-Q water, sonicated for 15 min in absolute ethanol (Merck, Germany), and finally dried in air before using it as the support for the foam electrodeposition. Before electrodeposition, the Cu support was masked with insulating PTFE tape, defining a geometrical surface area (A_{geo}) of 1 cm^2. The $In_{55}Cu_{45}$ alloy electrodeposition was carried out from a 1.5 M H_2SO_4 electrolyte (pH ≈ 0.5) containing 20 mM indium sulfate and 5 mM copper sulfate precursor salts (25 mM total metal ion concentration). For the electrodeposition, a three-electrode arrangement was used, consisting of the electropolished and masked Cu foil, a Pt foil (4 cm × 3 cm), and an Ag/AgCl$_{3M}$ electrode (Metrohm) acting as the working electrode (WE), counter electrode (CE), and reference electrode (RE), respectively. The electrodeposition was carried out in galvanostatic mode (Metrohm Autolab 128N potentiostat; Autolab 10 A current booster; Metrohm Autolab, Utrecht, the Netherlands) by applying a constant current density of −3 A cm^{-2} for 30 s. The resulting catalyst film was denoted $In_xCu_y@$Cu. After the electrodeposition process, the alloyed In_xCu_y metal foams were carefully rinsed with Milli-Q water to remove residuals of the plating bath from the surface and interior of the porous catalyst material. The electrochemically active surface areas (ECSAs) of the alloy foam catalysts were determined by means of a cyclic voltammetry approach using dimethyl viologen as a reversible redox

probe. The ECSA determination procedure and possible short-comings have been described in detail elsewhere.[27]

The same deposition protocol was transferred to graphite and carbon (fiber) cloth (gas diffusion electrode, GDE) supports; the resulting catalyst films were denoted In_xCu_y@C and In_xCu_y@GDE, respectively. Before electrodeposition, the graphite foil (Alfa Aesar, 99.8%) was activated by annealing at 500 °C for 6 h, washing in a 1:1 acetone:water mixture, and finally drying at 100 °C for 1 h.

A 20 cm × 20 cm carbon cloth (GDE) was purchased from Fuel Cell (USA). This carbon cloth is covered on both sides with an extra mesoporous carbon layer (C-MPL, see the Supporting Information), facilitating the adhesion of the electrodeposited metallic foam to the support. The total thickness of the carbon cloth is ∼385 μm. The carbon fiber cloths were used as received.

2.3. CO_2 Electrolysis Experiments. A 128N potentiostat/galvanostat (Metrohm Autolab) was used for all electrochemical measurements. Cell resistance was measured by means of impedance spectroscopy before each CO_2 electrolysis experiment. A custom-made H-type glass cell was used for the CO_2RR experiments, where the cathode and anode compartments were separated by a proton exchange Nafion membrane (Nafion 117, Electrochem, USA). All experiments were performed at room temperature under ambient conditions. CO_2RR experiments were performed in a three-electrode configuration using aqueous 0.5 M KHCO_3 solution as the electrolyte. The dendritic In_xCu_y catalyst served as the WE, a leakless Ag/AgCl_{3M} (EDAQ) electrode served as the RE, and a Pt foil (20 mm × 5 mm, 99.9%, Alfa Aesar) was used as the CE, where the water oxidation (counter reaction) took place. All potentials reported herein are iR-corrected. Prior to the CO_2 electrolysis, both the anode and cathode compartments (containing 0.5 M KHCO_3 electrolyte) were purged with CO_2 (99.9999%, Carbagas, Switzerland) for at least for 30 min to obtain a CO_2-saturated (sat.) 0.5 M KHCO_3 buffer electrolyte (pH = 7.2). The cathode compartment, having a headspace of approximately 12 mL, was constantly purged with CO_2 during the electrolysis.

Keeping pH dependency in mind, all the measured potentials vs the Ag/AgCl_{3M} electrode were converted into RHE using the equation below:

$$E_{RHE}(V) = E_{Ag/AgCl}3M(V) + 0.210\ V + (0.0591\ V \times pH)$$

(1)

Quantification of gaseous and liquid products by gas chromatography and ion-exchange chromatography is described in detail elsewhere.[28]

From the X-ray photoelectron spectroscopy (XPS) and post-electrolysis inductively coupled plasma optical emission spectroscopy (ICP-OES) measurements, no traces of Pt were detected on the catalyst surface or in the electrolyte. Any Pt cross-contamination originating from the anode during electrodeposition or during the CO_2 electrolysis experiments can thus be excluded.

2.4. Scanning Electron Microscopy (SEM) and Energy-Dispersive X-ray Spectroscopy (EDX). An FE Zeiss DSM 982 and a Zeiss Gemini 450 scanning electron microscopy (SEM) instrument were used to analyze the catalyst morphology. The composition was studied by using a Noran SIX NSS200 energy-dispersive X-ray (EDX) spectrometer.

2.5. X-ray Diffraction (XRD) Analysis. XRD was carried out by means of powder XRD (Bruker D8) using Cu Kα radiation (λ = 0.1540 nm, 40 mA) at 40 keV. A range of 2θ value from 30° to 80° was recorded at a 1° min⁻¹ scan rate. Joint Committee on Powder Diffraction (JCPD) standards for pure Cu and In metals, as well as for the bimetallic alloy, were used for comparison purposes to analyze the measured XRD patterns of the In_xCu_y material. To avoid undesired contributions from the Cu foil substrate to the measured XRD pattern, an activated graphite foil was used as the support for all XRD analyses.

2.6. X-ray Photoelectron (XPS) Spectroscopy. XPS analyses were carried out with an Escalab 250Xi ultrahigh-vacuum photoemission instrument equipped with a monochromatic Al Kα X-ray source (spot size, 100 μm). CasaXPS software was used for the peak fitting and the peak positions were referenced to the carbon C1s peak

at 285.5 eV. It is important to note that the sample specimens were not subjected to any further modification (e.g., metal sputtering) before XPS analysis.

2.7. High-Resolution Transmission Electron Microscopy (HR-TEM) and High-Angle Annular Dark-Field Scanning Transmission Electron Microscopy (HAADF-STEM). A Talos F200X G2 TEM (FEI, operating voltage 200 kV; Thermo Scientific) electron microscope was used for high-resolution transmission electron microscopy (HR-TEM) and high-angle annular dark-field scanning transmission electron microscopy (HAADF-STEM) analyses. The sample was prepared by dispersing the electrodeposited catalyst material in ethanol using a bath sonicator and drop-casted on a carbon-coated Ni grid (300 mesh) that served as the support for the HR-TEM and HAADF-STEM analyses.

2.8. Inductively Coupled Plasma Optical Emission Spectrometry (ICP-OES) and Inductively Coupled Plasma Mass Spectrometry (ICP-MS). To determine the nominal bulk composition of the electrodeposited In_xCu_y catalyst material, ICP-OES analysis was performed using an iCAP 7400 ICP-OES DUO instrument (Thermo Scientific). Before the ICP-OES measurement, the bimetallic In_xCu_y alloy was chemically dissolved in 30% HNO_3 solution. To monitor the time-dependent changes in the metal content in the electrolyte solution (CO_2-sat. 0.5 M KHCO_3) during electrolysis, the ICP-MS technique was applied. For the ICP-MS analysis, aliquots of 20 μL of electrolyte (CO_2-sat. 0.5 M KHCO_3 solution) were taken from the electrolysis cell as a function of electrolysis time and diluted in 3% nitric acid solution (501 times dilution). Each ICP measurement was repeated five times by default, these repetitive measurements served as the basis for the determination of the sample-specific values of the relative standard deviation (RSD), and ICP-MS-related RSD values are typically between 1 and 2%. An extra measuring error of ∼1.5% needs to be taken into account and is caused by the dilution treatment required for certain samples. Error bars in Figure 4 include both the instrumental error (ICP-MS) and the additional error resulting from the dilution procedure.

3. RESULTS AND DISCUSSION

3.1. Physical Characterization of the ap-In_{55}Cu_{45} Catalyst. The In_xCu_y alloy discussed herein was produced using the dynamic hydrogen bubble template (DHBT) approach of metal foaming[49−54] adjusted to the needs of alloy deposition and specifically optimized toward efficient formate production from CO_2. Figure 1a shows a schematic diagram of the DHBT-assisted alloy deposition. In the following, we denote the catalyst used herein as ap-In_{55}Cu_{45} (as-prepared) according to its bulk composition determined by the quantitative ICP-OES analysis of the alloy after its oxidative dissolution into a dilute nitric acid solution (for details, see Section 2). Note that the complementary EDX analysis of the bimetallic catalyst revealed a slightly different chemical composition of 59 at % In and 41 at % Cu (Figure S1). Semiquantitative EDX has, however, only a limited probing depth and does not, therefore, necessarily represent the true bulk composition of the respective catalyst material.[32,36]

A top-down SEM inspection revealed a highly porous appearance of the ap-In_{55}Cu_{45} catalyst material deposited on a planar Cu foil support (ap-In_{55}Cu_{45}@Cu; Figure 1b,c and Figure S2). Although the experimental conditions applied were common for the DHBT approach,[27,51] for example, in terms of applied current density (−3 A cm⁻²), no typical foam morphology developed during the InCu co-deposition. The ratio of the concentration-dependent exchange current density of metal deposition (j^0_{depo}) and of the competing hydrogen evolution reaction (j^0_{HER}) governs actual metal foaming and, thus, the resulting film morphology.[49] Clearly, the presence of
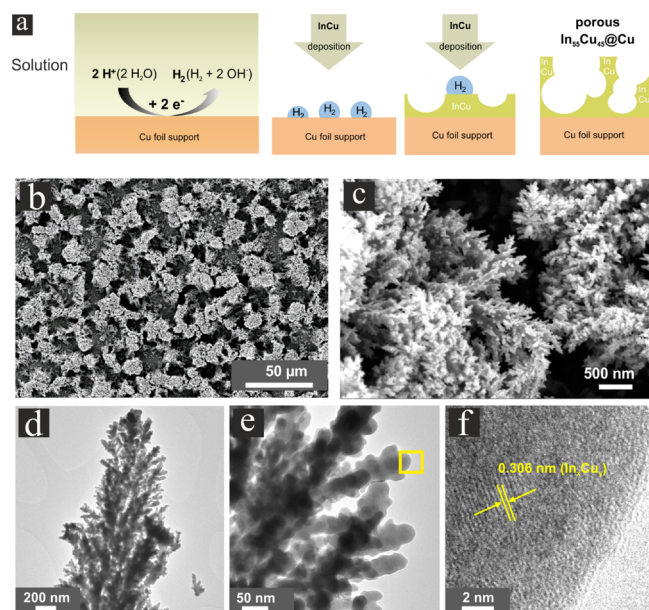
Figure 1. (a) Scheme demonstrating the principle of the dynamic hydrogen bubble template (DHBT) approach of metal foam electrodeposition using a planar Cu foil as the support. (b, c) Top-down SEM inspection of the *ap*-In$_{55}$Cu$_{45}$@Cu deposit. (d–f) Representative TEM and HR-TEM analysis of an isolated dendrite of the *ap*-In$_{55}$Cu$_{45}$@Cu sample.

Figure 2. (a) HAADF and (b–d) STEM-EDX mapping of an isolated dendrite of the *ap*-In$_{55}$Cu$_{45}$ foam. This analysis confirms the homogeneous distribution of Cu and In in the bimetallic alloy material.

In had a substantial impact on the nucleation, growth, and the so-called break-off diameter of hydrogen bubbles formed on the emerging porous alloy during electrodeposition. Further support for this conclusion came from a comparative survey of morphologies showing pure Cu, pure In, and *ap*-In$_{55}$Cu$_{45}$ films after 30 s of deposition at an applied current density of −3 A cm^{-2} (Figure S3). Only the pure Cu deposit showed a well-developed multilevel foam morphology with interconnected open macropores,[27,51] whereas the electrodeposition of In on the Cu foil support, carried out under the same experimental conditions, resulted in a comparably smooth polycrystalline film composed of In grains with diameters in the micrometer range (In@Cu, Figure S3). In addition to their (primary) macroporosity, the *ap*-In$_{55}$Cu$_{45}$ deposit and the *ap*-Cu foam showed smaller dendritic features on the submicrometer length scale (Figure S3), thus introducing secondary porosity to both electrodeposits and further increasing their electrochemically active surface area (ECSA, Figure S4), which grow in the following sequence: In@Cu (1.5 cm^2) < In$_{55}$Cu$_{45}$@Cu (2.7 cm^2) < and Cu-foam@Cu (3.6 cm^2). The geometric surface area of the Cu foil support was identical in all three cases (A_{geo} = 1 cm^2).

White light interferometry (WLI) analysis of the *ap*-In$_{55}$Cu$_{45}$ deposit revealed an apparent thickness of ∼19 μm (Figure S2a,b), whereas the corresponding cross-sectional SEM inspection showed a slightly increased catalyst film thickness in the range of 20 to 23 μm (Figure S2c,d). This is because the WLI does not completely probe the porous catalyst film down to the Cu foil support.

TEM analysis showed the branch-like (dendritic) nanostructures of the In$_{55}$Cu$_{45}$ material (Figure 1d). A high-resolution TEM inspection (Figure 1e,f) of individual dendrites of the *ap*-In$_{55}$Cu$_{45}$ deposit confirmed the InCu co-alloying, resulting in the In$_x$Cu$_y$ fringe pattern corresponding neither to pure Cu nor to pure In (Figure 1f). The high degree
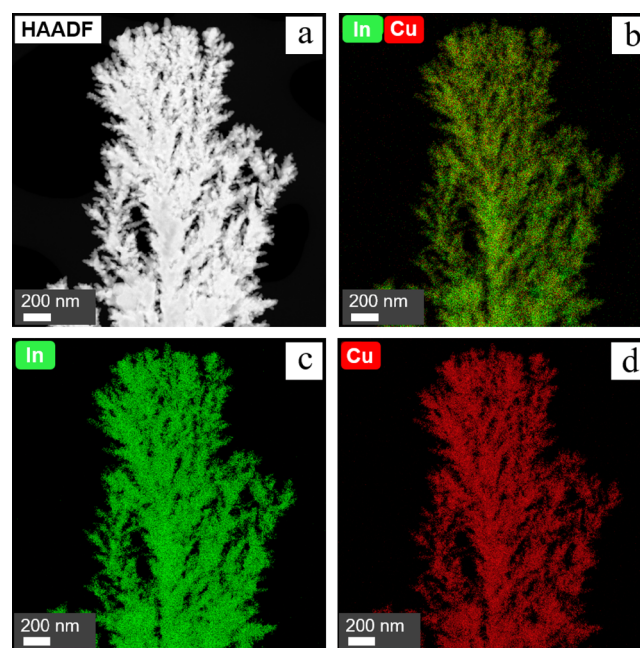
of co-alloying was further supported by the spatially and chemically resolved STEM-EDX mapping of a representative dendrite feature demonstrating the homogeneous intermixing of Cu and In in the *ap*-In$_{55}$Cu$_{45}$ deposit (Figure 2). An XRD analysis of the *ap*-In$_{55}$Cu$_{45}$ material suggested the presence of well-defined intermetallic phases having an elemental composition close to an In-to-Cu ratio of 1:1 (Figure 3). Most prominent were the intermetallic InCu and In$_9$Cu$_{11}$ phases (for a detailed analysis of the XRD patterns, see Table S1). Only minor contributions were visible in the diffractogram

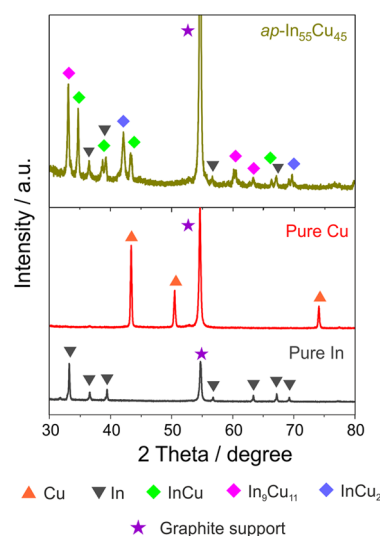**Figure 3.** X-ray diffraction (XRD) pattern of the *ap*-In$_{55}$Cu$_{45}$ foam deposited on a graphite support. For comparison purposes, XRD patterns of pure (polycrystalline) Cu and In samples (deposited on graphite support) are also presented. For a detailed analysis based on JCPDS references, see Table S1.

originating from InCu$_2$ and metallic In. All of these experimental observations were in full agreement with the phase diagram of the binary InCu system (Figure S5).[55] It is interesting to note that there is no indication in the diffractograms of the presence of (surface) oxides that are reported for pure (as-prepared) Cu foams.[27] This observation is remarkable insofar as the deposit certainly becomes more oxophilic when co-alloying Cu with In. The standard enthalpy changes of formation ($\Delta_f H^\ominus$) for the pure oxides might serve as a hint for the affinity of In and Cu toward (surface) oxide formation:

$$|(\Delta_f H^\ominus_{In_2O_3} = -923.5 \text{ kJ mol}^{-1}|$$
$$\gg |(\Delta_f H^\ominus_{Cu_2O} = -170 \text{ kJ mol}^{-1}|$$
$$> |(\Delta_f H^\ominus_{CuO} = -156 \text{ kJ mol}^{-1}|$$

The presence of a thin oxidic skin on the *ap*-In$_{55}$Cu$_{45}$ alloy, however, could be concluded from a more surface-sensitive XPS analysis (Figure S6). The spin-orbit split In3d photo-emission, shown in Figure S6b, is deconvoluted by assuming two In species with a binding energies of BE(In3d$_{5/2}$) = 443.9 eV and BE(In3d$_{5/2}$) = 444.9 eV assigned to metallic In(0) and In(III), respectively. The dominance of the In(III) species in the In3d photoemission clearly indicates the presence of a thin oxide layer, whereas the In(0)-related photoemission most likely results from contributions of the metallic In$_{55}$Cu$_{45}$ bulk. The corresponding Cu2p$_{3/2}$ emission (Figure S6c) showed a prominent peak at BE(Cu2p$_{3/2}$) = 932.7 eV and a smaller satellite feature at BE(Cu2p$_{3/2}$) = 933.5 eV. The latter can be ascribed to traces of Cu(II) species. It is important to note that the *ex situ* XPS cannot discriminate between cuprous Cu(I) and metallic Cu(0).[56,57] The dominant emission at BE-(Cu2p$_{3/2}$) = 932.7 eV might be assigned to a mixture of both Cu(I) and Cu(0) species.[58]

3.2. Structural Alterations of the *ap*-In$_{55}$Cu$_{45}$ Catalyst under Potential Control.
Note that the partially oxidized catalyst surface experiences further alterations when exposed to the electrolyte at open-circuit potential (OCP) and subsequently set under potential control. Oxides are readily reduced, in particular under the harsh experimental conditions required to operate the CO$_2$RR.[56] Such oxide reduction is typically considered as an inherent part of the catalyst activation. From online ICP-MS studies on model electrodes, it is well known that metal ions are preferentially released into an electrolyte solution upon reduction of the formed (surface) oxides.[59−61] Similar observations have recently been made for the *in situ* activation of thermally annealed Pd$_x$Cu$_y$ alloy foam catalysts under CO$_2$ electrolysis conditions.[36] Time-dependent ICP-MS analysis of the electrolyte composition revealed, in that case, partial dissolution of the less precious Cu (E^0(Cu^{2+}/Cu^0) = +0.34 V vs standard hydrogen electrode (SHE)) in the very initial stage of the electrolysis, whereas the more precious Pd (E^0(Pd^{2+}/Pd^0) = +0.85 V vs SHE) was not released into the electrolyte solution at all and remained in a (metallic) state on the catalyst surface upon oxide reduction. One consequence of this corrosive behavior during the *in situ* catalyst activation via oxide precursor reduction is a slow (mass transport-limited) metal deposition process superimposed on the actual CO$_2$RR, even with an extended electrolysis time.[36] Similar dissolution processes are expected for the *ap*-In$_{55}$Cu$_{45}$ alloy catalyst discussed herein. Figure 4 depicts the time-dependent evolution of In and Cu ion content in the electrolyte for two
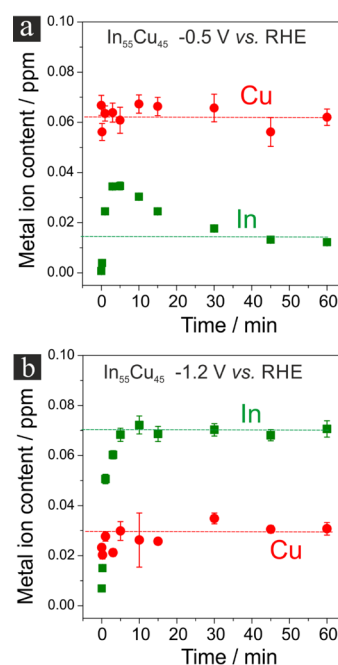

Figure 4. (a) Time-dependent ICP-MS analysis of the metal ion content (In and Cu) in the CO$_2$-sat. 0.5 M KHCO$_3$ electrolyte when −0.5 V vs RHE was applied for 1 h. (b) Corresponding ICP-MS data for an applied potential of −1.2 V vs RHE.

extreme potentials of −0.5 V and −1.2 V vs RHE referring to the lower and upper limits of the potential window considered herein (see also Figure 5 below). All traces of the metal ion concentration vs time showed a rapid increase in the metal ion concentration within the initial 5 to 10 min of exposure to the electrolyte before a (quasi)plateau was reached. Note that due to the continuous bubbling of CO$_2$ gas through the catholyte during electrolysis, the released metal ions are readily distributed (diluted) in the entire electrolyte volume after
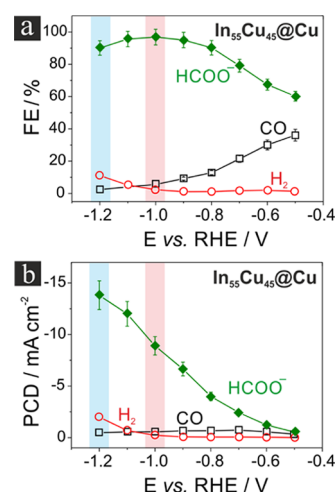

Figure 5. (a) Product distribution represented as the plot of the faradaic efficiency (FE) vs the electrolysis potential (E). The 1 h electrolysis was carried out using the CO$_2$-sat. 0.5 M KHCO$_3$ electrolyte. (b) Corresponding plot of the partial current densities (PCDs) vs E. Note that the current density is normalized to the geometric surface area of the support. Highlighted in red and blue are the data for the maximum FE$_{formate}$ and PCD$_{formate}$, respectively. FE and PCD data are listed in Tables S2 and S3.

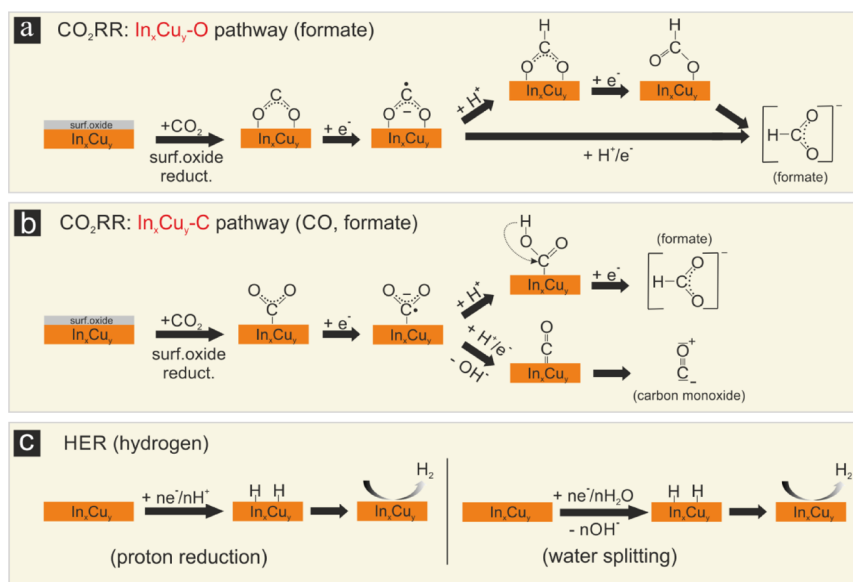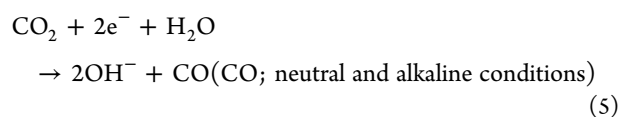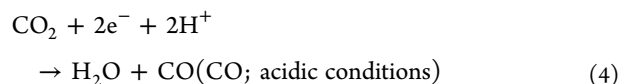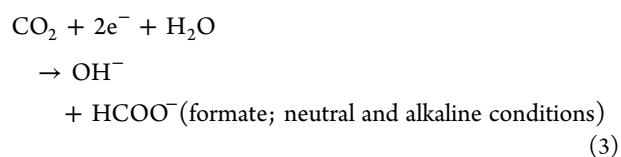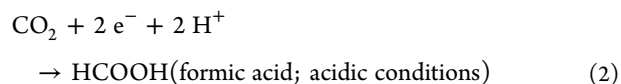**Figure 6.** (a) Proposed In_xCu_y-O pathway of formate production (oxophilic case) and (b) In_xCu_y-C pathway of CO and formate production (carbophilic case). (c) Different reaction pathways of hydrogen evolution (proton reduction and water splitting).

completion of the oxide reduction. Figure 4 reveals that the dissolution characteristics depended on the applied electrolysis potential. At the lowest applied overpotentials (−0.5 V *vs* RHE, Figure 4a), it is the Cu component of the oxidic skin that gets preferentially dissolved into the electrolyte, whereas the In content of the electrolyte remains at a comparably low level. This is likely due to the more negative standard potential of the In(III)/In(0) redox transition $(E^0(In^{3+}/In^0) = -0.34$ V *vs* SHE). The reduction of indium oxide is assumed to be much slower and eventually not fully completed under these experimental conditions. Interestingly, the situation was reversed at the highest applied potentials (−1.2 V *vs* RHE, Figure 4b). It is now In that gets preferentially dissolved upon surface oxide reduction, whereas the Cu content in solution remains at a comparably low concentration. Obviously, the release of Cu ions into the electrolyte was more suppressed at higher overpotentials. It rapidly transformed into metallic Cu upon applying a potential of −1.2 V *vs* RHE. These ICP-MS analysis results demonstrate that activation of the catalyst by (surface) oxide reduction might lead to slightly different surface compositions when applying different electrolysis potentials.

3.3. Electrocatalytic Performance. The *ap*-$In_{55}Cu_{45}$ alloy samples were subjected to a series of potentiostatic electrolysis reactions (1 h each) within a broad range of applied electrode potentials (−0.5 to −1.2 V *vs* RHE). The electrolyses were carried out in a classical H-cell configuration using CO_2-sat. 0.5 M $KHCO_3$ as the electrolyte (pH = 7.2). For each electrolysis experiment, a freshly prepared catalyst was applied (multi-catalyst approach). Figure 5a,b depicts the resulting product distribution as plots of the faradaic efficiency (FE) *vs* the applied electrolysis potential (E) and the partial current densities (PCDs) *vs* E, respectively (Tables S2 and S3). The most striking observation is that the parasitic HER remains almost fully suppressed within the entire range of electrolysis potentials studied herein. Only below −1.0 V *vs* RHE did the FE_{H2} value start to rise, reaching 11.1% at −1.2 V *vs* RHE $(PCD_{H2} = -1.99$ mA cm^{-2}). The exclusive CO_2RR products

are CO and formate, both involving a coupled two-electron/two-proton transfer reaction as follows:

$$CO_2 + 2\,e^- + 2\,H^+$$
$$\rightarrow HCOOH(\text{formic acid; acidic conditions}) \quad (2)$$

$$CO_2 + 2e^- + H_2O$$
$$\rightarrow OH^-$$
$$\quad + HCOO^-(\text{formate; neutral and alkaline conditions}) \quad (3)$$

$$CO_2 + 2e^- + 2H^+$$
$$\rightarrow H_2O + CO(\text{CO; acidic conditions}) \quad (4)$$

$$CO_2 + 2e^- + H_2O$$
$$\rightarrow 2OH^- + CO(\text{CO; neutral and alkaline conditions}) \quad (5)$$

Under neutral and alkaline conditions, water (solvent) itself serves as the proton source for the coupled electron-proton transfer reaction. The parasitic HER, typically superimposed on the CO_2RR, is fed by reductive water splitting rather than by proton reduction at an electrolyte pH of 7.3.[49]

$$2H^+ + 2e^- \rightarrow H_2(\text{proton reduction}) \quad (6)$$

$$2H_2O + 2e^- \rightarrow 2OH^- + H_2(\text{reductive water splitting}) \quad (7)$$
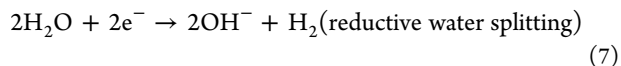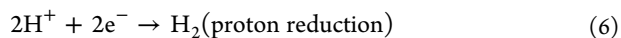
From the plot in Figure 5a, it is evident that the FEs of CO and formate formation are anticorrelated with each other. At the lowest applied overpotentials (−0.5 V *vs* RHE), the formate efficiency amounted to $FE_{formate}$ = 60.2% ($PCD_{formate}$ = −0.54 mA cm^{-2}), increasing to a maximum of 96.8% at −1.0 V *vs* RHE ($PCD_{formate}$ = −8.9 mA cm^{-2}). A remarkable characteristic of the novel $In_{55}Cu_{45}$ catalyst is that $FE_{formate}$ values did not fall below 90% within a rather broad potential window of ~400 mV (−0.8 to −1.2 V *vs* RHE). The reaction selectivities toward CO were only substantial at the lowest
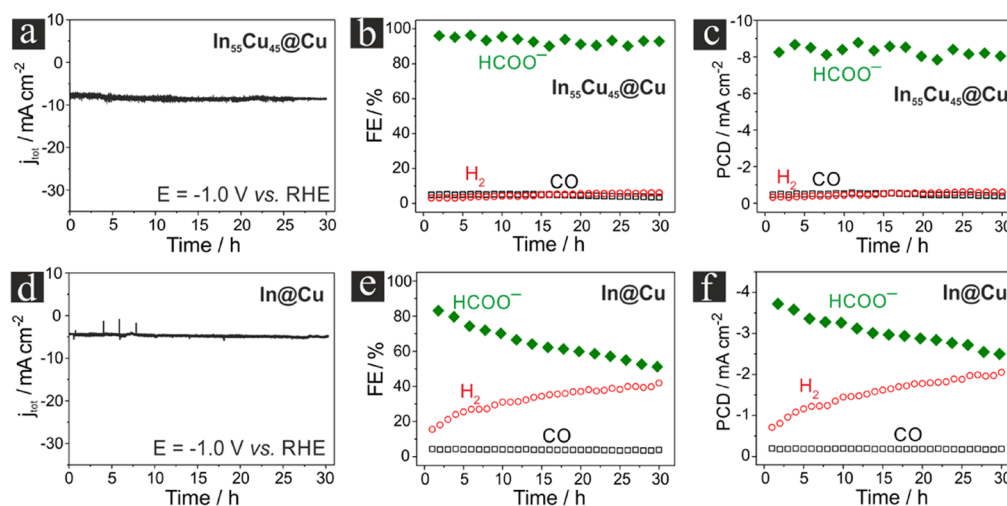
Figure 7. (a) Plot of the total (electrolysis) current density (j_{tot}) as a function of time using ap-In$_{55}$Cu$_{45}$@Cu as the catalyst. The extended electrolysis was carried out at $E = -1.0$ V vs RHE for 30 h; (b) plot of the faradaic efficiencies (FEs) as a function of electrolysis time; (c) plot of the partial current densities (PCDs) as a function of electrolysis time; (d–f) corresponding reference data of an extended electrolysis reaction carried out over an electrodeposited In@Cu (pure In deposit on Cu foil) catalyst (see also Figure S9). Note that the PCD values are normalized to the geometrical surface area of the support.

applied potentials (e.g., FE$_{CO}$ = 36.1% at -0.5 V vs RHE) and gradually decreased with increasing overpotentials. The resulting PCDs in this low overpotential regime, however, remained low (PCD$_{CO}$ = -0.34 mA cm^{-2} at -0.5 V vs RHE).

The absence of any hydrocarbons (e.g., CH$_4$, C$_2$H$_4$, and C$_2$H$_6$) or alcohols in the CO$_2$RR product distribution, in particular at higher negative overpotentials (<-0.7 V vs RHE), is indicative of effective suppression of the electrocatalytic characteristics of pure Cu in the binary In$_{55}$Cu$_{45}$ alloy. For a wide potential range, formate (HCOO$^-$) is the main CO$_2$RR product, proving that In (formate producer[20,41−44]) is the dominant catalyst component in the binary alloy governing the overall CO$_2$RR product distribution; Cu can be considered as a "modifier", amplifying the intrinsic catalytic characteristics of In in the In$_{55}$Cu$_{45}$ catalyst and further improving the degradation stability of the formed alloy (see discussion below). Only a few studies in the literature report increased product selectivities for formate when pure Cu is used as the CO$_2$RR catalyst. As an example, Rahaman et al. report on a dendritic Cu catalyst electrodeposited on a Cu mesh support that demonstrated an anomalously high selectivity toward formate, reaching FE$_{formate}$ = 49.2% at -0.7 V vs RHE.[28] This high formate efficiency, however, goes along with the production of hydrogen and decreases to FE$_{formate}$ = 5% at -1.2 V vs RHE. Note that the opposite trend in potential-dependent product distribution was observed for the porous In$_{55}$Cu$_{45}$ alloy catalyst discussed herein (Figure 5a).

In particular, oxophilic (post-transition) metals (e.g., Sn and In) favor CO$_2$RR reaction pathways involving reductive CO$_2$ adsorption through metal−oxygen (M−O) coordination via HCOO* intermediates (where * represents an adsorption state), denoted herein as the M−O pathway (Figure 6a). In some cases, the partially oxidized and oxygen-containing catalyst surface (e.g., SnO$_2$/SnO nanoparticles) is considered as the active catalyst species. For the M−O pathway, Feaster et al. proposed the HCOO* species as a key intermediate for the production of formate.[62] Its stabilization on the catalyst surface and, consequently, an increased abundance of HCOO* species are assumed to direct the CO$_2$RR product selectivity toward formate, thereby hindering the competitive adsorption of

*COOH and *H species, which are considered key intermediates for the M−C pathway of the CO$_2$RR and the HER, respectively (see Figure 6b,c).[63]

For a number of transition metals, Yoo et al. described a scaling relationship between the Gibbs free energies of adsorption for *COOH (carboxyl intermediate, M−C pathway) and *H.[63] This consideration suggests that formate production via the M−C pathway is typically accompanied by the parasitic HER, as observed for some Cu catalysts. However, this scaling relation is a bit less pronounced for the post-transition metals (e.g., In and Sn).[63]

The effective suppression of the HER within the potential range studied herein (Figure 5a) is, based on the argument above, indicative of the prevalence of the M−O pathway (HCOO* intermediate) of formate formation on the porous In$_{55}$Cu$_{45}$ catalyst (Figure 6a). What makes this bimetallic In$_{55}$Cu$_{45}$ catalyst unique, however, is the fact that both CO and formate are formed as CO$_2$RR products over the porous bimetallic alloy. CO formation typically requires a carbophilic catalyst (the term "carbophilic" refers to CO$_2$RR pathways where the initial CO$_2$ adsorption occurs via M−C bonding and carboxyl intermediates (*COOH, Figure 6b)).[64−66]

From the physical characterization of the ap-In$_{55}$Cu$_{45}$ material, there is no indication of any phase separation into (nanometer-sized) domains of the pure components, as described for a bifunctional AgCu foam catalyst composed of a CO-forming component (pure Ag domains) and a C−C coupler (pure Cu domains).[32] Instead, all experimental observations suggested a rather homogeneous dispersion of Cu into In (or vice versa) in the ap-In$_{55}$Cu$_{45}$ material (e.g., Figure 2). These considerations suggest a "hybrid" characteristic of the bimetallic In$_{55}$Cu$_{45}$ catalyst that allows for M−C bonding or CO production at lower (negative) overpotentials and dominant M−O bonding or formate production at higher applied overpotentials.

In-depth mechanistic studies on the underlying CO$_2$RR pathway (e.g., by $operando$ Raman spectroscopy that has successfully been applied to Cu and CuAg foam catalysts[32,56]) are impeded in the present case by the extraordinarily low
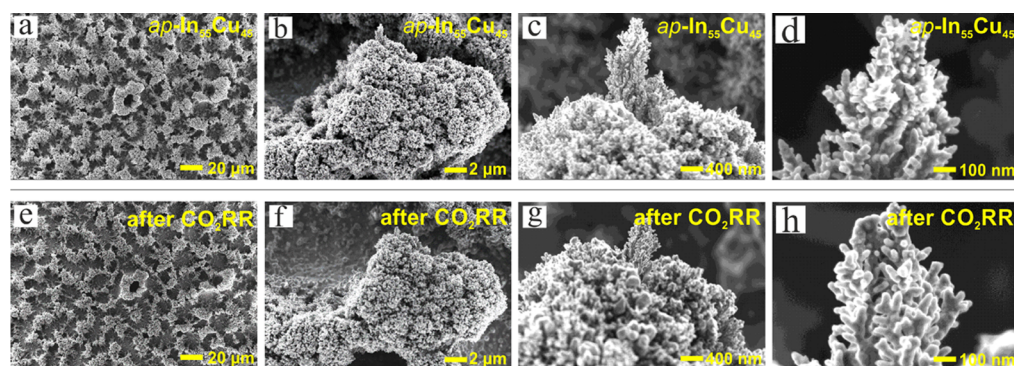
Figure 8. Identical location (IL) SEM analysis of the ap-In$_{55}$Cu$_{45}$@Cu alloy catalyst (a−d) before and (e−h) after the electrolysis. The CO$_2$ electrolysis experiment was carried out for 30 h at −1.0 V vs RHE in the CO$_2$-sat. 0.5 M KHCO$_3$ electrolyte.
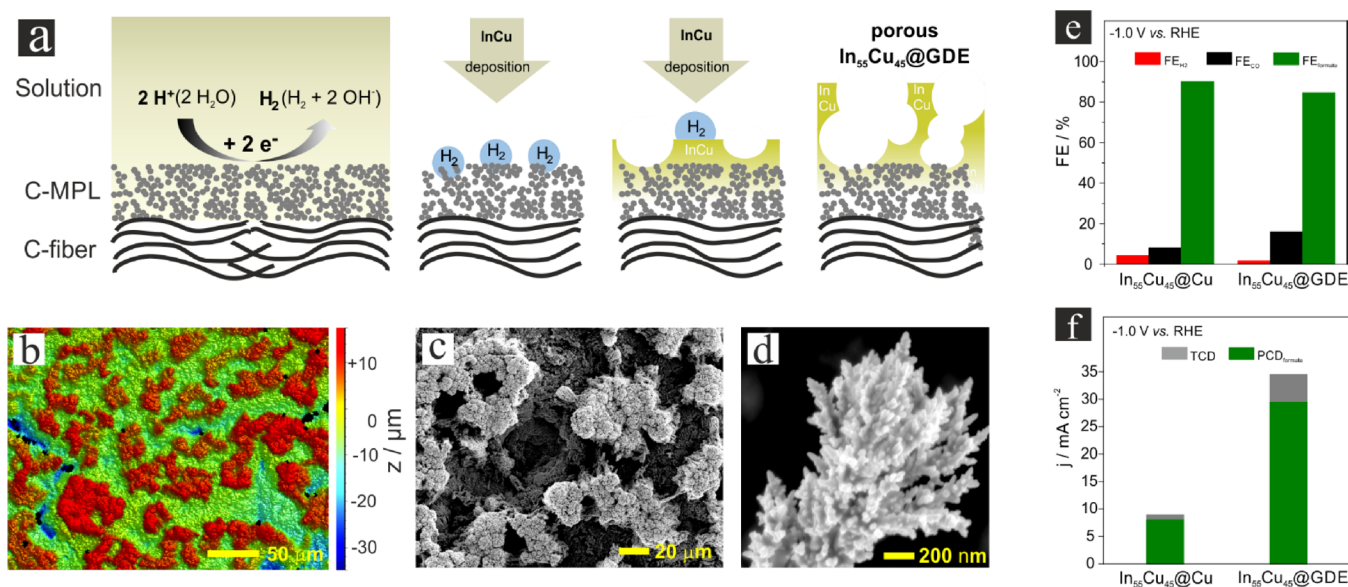

Figure 9. (a) Scheme demonstrating the DHBT approach of alloy deposition transferred to a carbon cloth support (GDE); (b) WLI image of the ap-In$_{55}$Cu$_{45}$@GDE catalyst; (c, d) top-down SEM inspection of the ap-In$_{55}$Cu$_{45}$@GDE catalyst. (e) Comparison of the product distribution using In$_{55}$Cu$_{45}$@Cu and In$_{55}$Cu$_{45}$@GDE as catalysts. (f) Corresponding total (TCD) and partial (PCD) current densities. The electrolyses were carried out for 1 h at −1.0 V vs RHE in CO$_2$-sat. 0.5 M KHCO$_3$ solution.

Raman intensities on the porous In$_{55}$Cu$_{45}$ material due to the alloying effect (see Figure S7).

The chemical composition of the In$_{55}$Cu$_{45}$ catalyst is optimized particularly for formate production and extended catalyst stability. A gradual increase in the Cu content in the deposit leads to an increase in CO yields at the expense of formate efficiencies. A survey of catalyst morphologies and resulting product distributions for In$_{55}$Cu$_{45}$, In$_{26}$Cu$_{74}$, and In$_2$Cu$_{98}$ catalysts are presented in Figure S8. Cu foams containing only 2 at % In outperformed in terms of CO production, reaching a CO efficiency of almost 100% in the potential range from −0.4 to −0.6 V vs RHE. The production of hydrocarbons and alcohols remained suppressed at higher overpotentials, suggesting that a trace amount of In was already sufficient to substantially reduce the M−CO binding strength. This is why release of the formed CO is favored over C−C coupling and further transformations of the chemisorbed *CO intermediate into hydrocarbons/alcohols as reported for numerous Cu-based CO$_2$RR catalysts.[21,22,37,39]

What makes the bimetallic In$_{55}$Cu$_{45}$ catalyst outstanding, however, is its long-term stability during extended CO$_2$ electrolysis. Results of a representative 30 h potentiostatic

CO$_2$RR carried out at −1.0 V vs RHE are presented in Figure 7a−c (Table S4). Corresponding reference experiments using an electrodeposited polycrystalline In film as the catalyst are shown in Figure 7d−f (Table S5). In both cases, the current density vs time traces (panels a and d) remained stable during the 30 h lasting electrolysis. The product distribution, however, underwent severe alterations in the case of the pure In catalyst (Figure 7e,f). This suggests that the current densities or changes thereof (panels a and d) cannot be considered suitable measures to probe the stability of the catalyst against chemical or structural degradation, both of which affect the resulting product distribution. The decrease in FE$_{formate}$ values from initially 82.1% (PCD$_{formate}$ = −3.67 mA cm^{-2}) to ultimately 50.2% (PCD$_{formate}$ = −2.45 mA cm^{-2}) after 30 h of continuous electrolysis was anticorrelated with the increase in FE$_{H2}$ from 15.5% (PCD$_{H2}$ = −0.71 mA cm^{-2}) to 41.9% (PCD$_{H2}$ = −2.05 mA cm^{-2}). In contrast, both the faradaic efficiency (FE$_{formate}$ = 94.2 ± 2.1%) and the corresponding partial current density (PCD$_{formate}$ = −8.2 ± 0.4 mA cm^{-2}) remained stable during the electrolysis when the porous In$_{55}$Cu$_{45}$ material was used as the catalyst (see also Figure S9). These results strongly suggest that it is HER (Figure 6c) that causes an irreversible

transformation of the comparatively planar In catalyst surface, thereby creating more of those (catalytic) surface sites that are active toward the HER. In this respect, we can consider the HER as a "self-accelerating" process that becomes increasingly dominant at the expense of other (competitive) reactions (e.g., the CO_2RR) with time. On the other hand, a 3D dendritic $In_{55}Cu_{45}$ alloy surface, with a higher ECSA, is capable to stabilize the CO_2RR intermediates (HCOO*), thereby suppressing the HER during the long-term electrolysis. This emphasizes the importance of complete suppression of HER right from the beginning of the electrolysis reaction as a crucial prerequisite for the long-term stability of the catalyst. A performance comparison based on the existing literature for InCu-based systems is presented in Table S6 and indicates the high performance of the $In_{55}Cu_{45}$ material studied herein. Further support for the excellent stability of the $In_{55}Cu_{45}$ catalyst comes from the identical location scanning electron microscopy (IL-SEM) analysis performed prior to and after 30 h of continuous electrolysis at −1.0 V *vs* RHE (Figure 8). The macroporosity on the micrometer-length scale remained unaffected by the extended electrolysis (Figure 8a,b,e,f). Minor morphological changes concern, however, the dendritic fine structure of the porous catalyst on the nanometer-length scale (Figure 8d,h).

3.4. Transfer of the Catalyst Concept to Technical GDE Substrates. The preparation of the bimetallic $In_{55}Cu_{45}$ catalyst has so far been restricted to DHBT-assisted alloy deposition on planar Cu foil supports. Future applications of the CO_2RR will apply gas-fed electrolyzer systems in which the gaseous CO_2 reactant is transported toward the actual catalyst layer through a porous (carbon cloth) support electrode.[26,40] By this approach, it is possible to substantially reduce CO_2 mass transport limitations, which are severe when the CO_2RR is carried from an aqueous electrolyte at high overpotentials. The actual CO_2 concentration in aqueous electrolytes is limited to ~35 mM only.[67] It is therefore vital that the newly developed catalyst material can be transferred to a technical carbon cloth support that might serve as a gas diffusion electrode (GDE). The principle of DHBT-assisted alloy deposition on the GDE support is depicted in Figure 9a. Note that the electrolyte, when brought into contact with the carbon cloth, will penetrate to some extent into the topmost layers of the carbon microporous layer (C-MPL) of the GDE support. Catalyst deposition in the outermost part of the MPL is considered beneficial because it improves the overall adhesion (wetting) of the porous metallic catalyst deposit onto the carbon support. Figure S10a provides insights into the structure of the carbon cloth support, which consists of carbon fibers in its core that is further covered by a carbon MPL (panels b−d of Figure S10) on which the actual catalyst electrodeposition takes place. The macromorphology on the micrometer (μm)-length scale observed for ap-$In_{55}Cu_{45}$@Cu (Figure 1) is largely conserved on the GDE support (Figure 9b,c). Also, the dendritic features of the porous $In_{55}Cu_{45}$ catalyst are visible on the nanometer (nm)-length scale (Figure 9d). To exemplarily test the performance of the $In_{55}Cu_{45}$@GDE catalyst, a 1 h electrolysis was carried out from CO_2-saturated 0.5 M $KHCO_3$ solution at −1.0 V *vs* RHE and compared with data derived for the $In_{55}Cu_{45}$@Cu catalyst. In general, the excellent selectivity toward formate observed for $In_{55}Cu_{45}$@Cu is reproduced on the GDE support ($FE_{formate} \approx$ 86%); also, hydrogen production remained largely suppressed ($FE_{H_2} \approx 1\%$, Figure 9e). Compared with $In_{55}Cu_{45}$@Cu,

however, FE_{CO} was slightly increased (~15%). These slight changes in the catalytic activity of $In_{55}Cu_{45}$@GDE can be attributed to the minor morphological irregularity of the catalyst that could arise during the electrodeposition using the porous carbon network substrate unlike the planar Cu foil model substrate. It can be further assumed, however, that the ratio of formate/CO efficiencies can be further improved for the GDE support by optimizing the plating conditions (e.g., current density and deposition time).

Note that the GDE support had an intrinsically higher surface area compared to the Cu foil. This increased roughness is transferred during electrodeposition to the layer of the $In_{55}Cu_{45}$ catalyst. One consequence of this was improved total and partial CO_2RR current densities. For formate production, a partial current density of $PCD_{formate} \approx$ −30 mA cm^{-2} was reached when using the carbon cloth as the support (Figure 9f).

4. CONCLUSIONS

A novel porous $In_{55}Cu_{45}$ alloy catalyst was produced on a Cu foil support by means of the DHBT deposition approach, which showed excellent electrocatalytic performance toward formate production, with $FE_{formate}$ values never falling below 90% within an extended (400 mV) potential window (−0.8 to −1.2 V *vs* RHE). Structural and compositional analysis of the as-prepared $In_{55}Cu_{45}$@Cu catalyst revealed homogeneous dispersion of Cu in In. The absence of pure domains of Cu in the bimetallic $In_{55}Cu_{45}$ alloy catalyst explains the complete suppression of CO_2RR pathways, which involve hydrocarbon/alcohol formation via C−C coupling. The most prominent characteristic of the $In_{55}Cu_{45}$@Cu catalyst is its high stability during extended CO_2 electrolysis reactions (30 h at −1.0 V *vs* RHE). Both the faradaic efficiency ($FE_{formate}$ = 94.2 ± 2.1%) and the partial current density ($PCD_{formate}$ = −8.2 ± 0.4 mA cm^{-2}) were unaltered during the continuous CO_2 electrolysis. Essential for this long-term stability is a low rate of hydrogen formation. In the case of the In@Cu reference system, the HER has been identified as the source for severe degradation phenomena in terms of a self-amplifying process, creating further sites during the continued electrolysis reaction that are specifically active toward HER, thus reducing the CO_2RR yields.

The concept of DHBT-assisted alloy deposition could be transferred to technically relevant porous GDE supports. The CO_2RR product distribution experienced only marginal alterations, whereas the resulting PCDs were substantially increased (e.g., $PCD_{formate}$ = −30 mA cm^{-2} at −1.0 V *vs* RHE). This was due to the intrinsic roughness of the support, which was substantially higher for the porous GDE compared with the plane Cu foil. Future work will focus on the transfer of this $In_{55}Cu_{45}$@GDE to gas-fed electrolyzer systems, where even higher PCDs are expected.

■ ASSOCIATED CONTENT

ⓢ Supporting Information

The Supporting Information is available free of charge at https://pubs.acs.org/doi/10.1021/acsami.1c07829.

> Physical characterizations of the catalyst by SEM, WLI, and XPS analyses; electrochemically active surface area (ECSA) analysis; *operando* Raman spectroscopy, phase diagram of binary InCu systems, composition-dependent

activity, formate production rate, and supplementary tables (PDF)

■ AUTHOR INFORMATION

Corresponding Authors

Motiar Rahaman − *Department of Chemistry, Biochemistry and Pharmaceutical Sciences, University of Bern, Bern 3012, Switzerland*; Present Address: Yusuf Hamied Department of Chemistry, University of Cambridge, Lensfield Road, CB2 1EW Cambridge, United Kingdom (M.R.);
  orcid.org/0000-0002-8422-0566; Email: mr820@cam.ac.uk

Kiran Kiran − *Department of Chemistry, Biochemistry and Pharmaceutical Sciences, University of Bern, Bern 3012, Switzerland*; Email: kiran.kiran@dcb.unibe.ch

Peter Broekmann − *Department of Chemistry, Biochemistry and Pharmaceutical Sciences, University of Bern, Bern 3012, Switzerland*;   orcid.org/0000-0002-6287-1042; Email: peter.broekmann@dcb.unibe.ch

Authors

Ivan Zelocualtecatl Montiel − *Department of Chemistry, Biochemistry and Pharmaceutical Sciences, University of Bern, Bern 3012, Switzerland*

Abhijit Dutta − *Department of Chemistry, Biochemistry and Pharmaceutical Sciences, University of Bern, Bern 3012, Switzerland*;   orcid.org/0000-0002-3054-0492

Complete contact information is available at:
https://pubs.acs.org/10.1021/acsami.1c07829

Author Contributions

§M.R. and K.K. contributed equally to this work. M.R. and P.B. conceived the idea and designed the project. M.R. and K.K. prepared and characterized the catalysts and performed the electrochemical experiments. I.Z.M. and K.K. conducted the ICP-MS analysis. A.D. and I.Z.M. performed the *operando* Raman experiments. M.R. prepared the figures and drafted the manuscript. P.B. revised and finalized the manuscript with inputs from all authors. M.R. and P.B. supervised the work.

Notes

The authors declare no competing financial interest.

■ ACKNOWLEDGMENTS

■ REFERENCES

(1) Whipple, D. T.; Kenis, P. J. A. Prospects of CO_2 Utilization via Direct Heterogeneous Electrochemical Reduction. *J. Phys. Chem. Lett.* **2010**, *1*, 3451−3458.

(2) Jhong, H.-R. M.; Ma, S.; Kenis, P. J. A. Electrochemical Conversion of CO_2 to Useful Chemicals: Current Status, Remaining Challenges, and Future Opportunities. *Curr. Opin. Chem. Eng.* **2013**, *2*, 191−199.

(3) Peter, S. C. Reduction of CO_2 to Chemicals and Fuels: A Solution to Global Warming and Energy Crisis. *ACS Energy Lett.* **2018**, *3*, 1557−1561.

(4) Kibria, M. G.; Edwards, J. P.; Gabardo, C. M.; Dinh, C.-T.; Seifitokaldani, A.; Sinton, D.; Sargent, E. H. Electrochemical CO_2 Reduction into Chemical Feedstocks: From Mechanistic Electrocatalysis Models to System Design. *Adv. Mater.* **2019**, *31*, 1807166.

(5) Jiang, J.; Wieckowski, A. Prospective direct formate fuel cell. *Electrochem. Commun.* **2012**, *18*, 41−43.

(6) Bartrom, A. M.; Ta, J.; Nguyen, T. Q.; Her, J.; Donovan, A.; Haan, J. L. Optimization of an anode fabrication method for the alkaline Direct Formate Fuel Cell. *J. Power Sources* **2013**, *229*, 234−238.

(7) Supronowicz, W.; Ignatyev, I. A.; Lolli, G.; Wolf, A.; Zhao, L.; Mleczko, L. Formic acid: a future bridge between the power and chemical industries. *Green Chem.* **2015**, *17*, 2904−2911.

(8) Szatmári, I.; Papp, G.; Joó, F.; Kathó, Á. Unexpectedly fast catalytic transfer hydrogenation of aldehydes by formate in 2-propanol−water mixtures under mild conditions. *Catal. Today* **2015**, *247*, 14−19.

(9) Zhang, F.; You, X.; Dou, H.; Liu, Z.; Zuo, B.; Zhang, X. Facile Fabrication of Robust Silk Nanofibril Films via Direct Dissolution of Silk in $CaCl_2$−Formic Acid Solution. *ACS Appl. Mater. Interfaces* **2015**, *7*, 3352−3361.

(10) Derbyshire, J. C.; Gordon, C. H.; Waldo, D. R. Formic Acid as a Silage Preservative for Milking Cows. *J. Dairy Sci.* **1976**, *59*, 278−287.

(11) Durst, J.; Rudnev, A.; Dutta, A.; Fu, Y.; Herranz, J.; Kaliginedi, V.; Kuzume, A.; Permyakova, A. A.; Paratcha, Y.; Broekmann, P.; Schmidt, T. J. Electrochemical CO_2 Reduction—A critical View on Fundamentals. *Mater. Appl. Chim.* **2015**, *69*, 769−776.

(12) Daiyan, R.; Lovell, E. C.; Bedford, N. M.; Saputera, W. H.; Wu, K.-H.; Lim, S.; Horlyck, J.; Ng, Y. H.; Lu, X.; Amal, R. Modulating Activity through Defect Engineering of Tin Oxides for Electrochemical CO_2 Reduction. *Adv. Sci.* **2019**, *6*, 1900678.

(13) Dutta, A.; Zelocualtecatl Montiel, I.; Kiran, K.; Rieder, A.; Grozovski, V.; Gut, L.; Broekmann, P. A tandem ($Bi_2O_3{\rightarrow}Bi_{met}$) catalyst for highly efficient ec-CO_2 conversion into formate: Operando Raman spectroscopic evidence for a reaction pathway change. *ACS Catal.* **2021**, *11*, 4988−5003.

(14) Tran-Phu, T.; Daiyan, R.; Fusco, Z.; Ma, Z.; Amal, R.; Tricoli, A. Nanostructured β-Bi_2O_3 Fractals on Carbon Fibers for Highly Selective CO_2 Electroreduction to Formate. *Adv. Funct. Mater.* **2020**, *30*, 1906478.

(15) Rahaman, M.; Dutta, A.; Broekmann, P. Size-Dependent Activity of Palladium Nanoparticles: Efficient Conversion of CO_2 into Formate at Low Overpotentials. *ChemSusChem* **2017**, *10*, 1733−1741.

(16) Hori, Y. I. Electrochemical CO_2 Reduction on Metal Electrodes. In *Modern Aspects of Electrochemistry*; Springer: New York, 2008; pp. 89−189, .

(17) Kortlever, R.; Shen, J.; Schouten, K. J. P.; Calle-Vallejo, F.; Koper, M. T. M. Catalysts and Reaction Pathways for the Electrochemical Reduction of Carbon Dioxide. *J. Phys. Chem. Lett.* **2015**, *6*, 4073−4082.

(18) Qiao, J.; Liu, Y.; Hong, F.; Zhang, J. A Review of Catalysts for the Electroreduction of Carbon Dioxide to Produce Low-Carbon Fuels. *Chem. Soc. Rev.* **2014**, *43*, 631−675.

(19) Costentin, C.; Robert, M.; Savéant, J.-M. Catalysis of the electrochemical reduction of carbon dioxide. *Chem. Soc. Rev.* **2013**, *42*, 2423−2436.

(20) Hori, Y.; Wakebe, H.; Tsukamoto, T.; Koga, O. Electrocatalytic Process of CO Selectivity in Electrochemical Reduction of CO_2 at Metal Electrodes in Aqueous Media. *Electrochim. Acta* **1994**, *39*, 1833−1839.

(21) Kuhl, K. P.; Cave, E. R.; Abram, D. N.; Jaramillo, T. F. New Insights into the Electrochemical Reduction of Carbon Dioxide on Metallic Copper Surfaces. *Energy Environ. Sci.* **2012**, *5*, 7050−7059.

(22) Nitopi, S.; Bertheussen, E.; Scott, S. B.; Liu, X.; Engstfeld, A. K.; Horch, S.; Seger, B.; Stephens, I. E. L.; Chan, K.; Hahn, C.; Nørskov, J. K.; Jaramillo, T. F.; Chorkendorff, I. Progress and Perspectives of Electrochemical CO_2 Reduction on Copper in Aqueous Electrolyte. *Chem. Rev.* **2019**, *119*, 7610−7672.

(23) Peterson, A. A.; Abild-Pedersen, F.; Studt, F.; Rossmeisl, J.; Nørskov, J. K. How copper catalyzes the electroreduction of carbon dioxide into hydrocarbon fuels. *Energy Environ. Sci.* **2010**, *3*, 1311−1315.

(24) Nie, X.; Esopi, M. R.; Janik, M. J.; Asthagiri, A. Selectivity of CO$_2$ Reduction on Copper Electrodes: The Role of the Kinetics of Elementary Steps. *Angew. Chem., Int. Ed.* **2013**, *52*, 2459−2462.

(25) Luo, W.; Nie, X.; Janik, M. J.; Asthagiri, A. Facet Dependence of CO$_2$ Reduction Paths on Cu Electrodes. *ACS Catal.* **2016**, *6*, 219−229.

(26) Dinh, C.-T.; Burdyny, T.; Kibria, M. G.; Seifitokaldani, A.; Gabardo, C. M.; García de Arquer, F. P.; Kiani, A.; Edwards, J. P.; De Luna, P.; Bushuyev, O. S.; Zou, C.; Quintero-Bermudez, R.; Pang, Y.; Sinton, D.; Sargent, E. H. CO$_2$ electroreduction to ethylene via hydroxide-mediated copper catalysis at an abrupt interface. *Science* **2018**, *360*, 783−787.

(27) Dutta, A.; Rahaman, M.; Luedi, N. C.; Mohos, M.; Broekmann, P. Morphology Matters: Tuning the Product Distribution of CO$_2$ Electroreduction on Oxide-Derived Cu Foam Catalysts. *ACS Catal.* **2016**, *6*, 3804−3814.

(28) Rahaman, M.; Dutta, A.; Zanetti, A.; Broekmann, P. Electrochemical Reduction of CO$_2$ into Multicarbon Alcohols on Activated Cu Mesh Catalysts: An Identical Location (IL) Study. *ACS Catal.* **2017**, *7*, 7946−7956.

(29) Wang, Y.; Cao, L.; Libretto, N. J.; Li, X.; Li, C.; Wan, Y.; He, C.; Lee, J.; Gregg, J.; Zong, H.; Su, D.; Miller, J. T.; Mueller, T.; Wang, C. Ensemble Effect in Bimetallic Electrocatalysts for CO$_2$ Reduction. *J. Am. Chem. Soc.* **2019**, *141*, 16635−16642.

(30) Zhi, X.; Jiao, Y.; Zheng, Y.; Vasileff, A.; Qiao, S.-Z. Selectivity roadmap for electrochemical CO$_2$ reduction on copper-based alloy catalysts. *Nano Energy* **2020**, *71*, 104601.

(31) Vasileff, A.; Xu, C.; Jiao, Y.; Zheng, Y.; Qiao, S.-Z. Surface and Interface Engineering in Copper-Based Bimetallic Materials for Selective CO$_2$ Electroreduction. *Chem* **2018**, *4*, 1809−1831.

(32) Dutta, A.; Montiel, I. Z.; Erni, R.; Kiran, K.; Rahaman, M.; Drnec, J.; Broekmann, P. Activation of bimetallic AgCu foam electrocatalysts for ethanol formation from CO$_2$ by selective Cu oxidation/reduction. *Nano Energy* **2020**, *68*, 104331.

(33) Hoang, T. T. H.; Verma, S.; Ma, S.; Fister, T. T.; Timoshenko, J.; Frenkel, A. I.; Kenis, P. J. A.; Gewirth, A. A. Nanoporous Copper−Silver Alloys by Additive-Controlled Electrodeposition for the Selective Electroreduction of CO$_2$ to Ethylene and Ethanol. *J. Am. Chem. Soc.* **2018**, *140*, 5791−5797.

(34) Li, Y. C.; Wang, Z.; Yuan, T.; Nam, D.-H.; Luo, M.; Wicks, J.; Chen, B.; Li, J.; Li, F.; de Arquer, F. P. G.; Wang, Y.; Dinh, C.-T.; Voznyy, O.; Sinton, D.; Sargent, E. H. Binding Site Diversity Promotes CO$_2$ Electroreduction to Ethanol. *J. Am. Chem. Soc.* **2019**, *141*, 8584−8591.

(35) Clark, E. L.; Hahn, C.; Jaramillo, T. F.; Bell, A. T. Electrochemical CO$_2$ Reduction over Compressively Strained CuAg Surface Alloys with Enhanced Multi-Carbon Oxygenate Selectivity. *J. Am. Chem. Soc.* **2017**, *139*, 15848−15857.

(36) Rahaman, M.; Kiran, K.; Montiel, I. Z.; Grozovski, V.; Dutta, A.; Broekmann, P. Selective n-propanol formation from CO$_2$ over degradation-resistant activated PdCu alloy foam electrocatalysts. *Green Chem.* **2020**, *22*, 6497−6509.

(37) Rasul, S.; Anjum, D. H.; Jedidi, A.; Minenkov, Y.; Cavallo, L.; Takanabe, K. A Highly Selective Copper−Indium Bimetallic Electrocatalyst for the Electrochemical Reduction of Aqueous CO$_2$ to CO. *Angew. Chem.* **2015**, *54*, 2146−2150.

(38) Larrazábal, G. O.; Martín, A. J.; Mitchell, S.; Hauert, R.; Pérez-Ramírez, J. Enhanced Reduction of CO$_2$ to CO over Cu−In Electrocatalysts: Catalyst Evolution Is the Key. *ACS Catal.* **2016**, *6*, 6265−6274.

(39) Luo, W.; Xie, W.; Mutschler, R.; Oveisi, E.; De Gregorio, G. L.; Buonsanti, R.; Züttel, A. Selective and Stable Electroreduction of CO$_2$ to CO at the Copper/Indium Interface. *ACS Catal.* **2018**, *8*, 6571−6581.

(40) Xiang, H.; Rasul, S.; Hou, B.; Portoles, J.; Cumpson, P.; Yu, E. H. Copper−Indium Binary Catalyst on a Gas Diffusion Electrode for High-Performance CO$_2$ Electrochemical Reduction with Record CO Production Efficiency. *ACS Appl. Mater. Interfaces* **2020**, *12*, 601−608.

(41) Luo, W.; Xie, W.; Li, M.; Zhang, J.; Züttel, A. 3D hierarchical porous indium catalyst for highly efficient electroreduction of CO$_2$. *J. Mater. Chem. A* **2019**, *7*, 4505−4515.

(42) Hegner, R.; Rosa, L. F. M.; Harnisch, F. Electrochemical CO$_2$ reduction to formate at indium electrodes with high efficiency and selectivity in pH neutral electrolytes. *Appl. Catal., B* **2018**, *238*, 546−556.

(43) Bohlen, B.; Wastl, D.; Radomski, J.; Sieber, V.; Vieira, L. Electrochemical CO$_2$ reduction to formate on indium catalysts prepared by electrodeposition in deep eutectic solvents. *Electrochem. Commun.* **2020**, *110*, 106597.

(44) Ma, W.; Xie, S.; Zhang, X.-G.; Sun, F.; Kang, J.; Jiang, Z.; Zhang, Q.; Wu, D.-Y.; Wang, Y. Promoting electrocatalytic CO$_2$ reduction to formate via sulfur-boosting water activation on indium surfaces. *Nat. Commun.* **2019**, *10*, 892.

(45) Kim, D.; Resasco, J.; Yu, Y.; Asiri, A. M.; Yang, P. Synergistic geometric and electronic effects for electrochemical reduction of carbon dioxide using gold-copper bimetallic nanoparticles. *Nat. Commun.* **2014**, *5*, 4948.

(46) Kottakkat, T.; Klingan, K.; Jiang, S.; Jovanov, Z. P.; Davies, V. H.; El-Nagar, G. A. M.; Dau, H.; Roth, C. Electrodeposited AgCu Foam Catalysts for Enhanced Reduction of CO$_2$ to CO. *ACS Appl. Mater. Interfaces* **2019**, *11*, 14734−14744.

(47) Yin, Z.; Gao, D.; Yao, S.; Zhao, B.; Cai, F.; Lin, L.; Tang, P.; Zhai, P.; Wang, G.; Ma, D.; Bao, X. Highly selective palladium-copper bimetallic electrocatalysts for the electrochemical reduction of CO$_2$ to CO. *Nano Energy* **2016**, *27*, 35−43.

(48) Kuhl, K. P.; Hatsukade, T.; Cave, E. R.; Abram, D. N.; Kibsgaard, J.; Jaramillo, T. F. Electrocatalytic Conversion of Carbon Dioxide to Methane and Methanol on Transition Metal Surfaces. *J. Am. Chem. Soc.* **2014**, *136*, 14107−14113.

(49) Vesztergom, S.; Dutta, A.; Rahaman, M.; Kiran, K.; Zelocualtecatl Montiel, I.; Broekmann, P. Hydrogen Bubble Templated Metal Foams as Efficient Catalysts of CO$_2$ Electro-reduction. *ChemCatChem* **2021**, *13*, 1039−1058.

(50) Plowman, B. J.; Jones, L. A.; Bhargava, S. K. Building with bubbles: the formation of high surface area honeycomb-like films *via* hydrogen bubble templated electrodeposition. *Chem. Commun.* **2015**, *51*, 4331−4346.

(51) Shin, H.-C.; Liu, M. Copper foam structures with highly porous nanostructured walls. *Chem. Mater.* **2004**, *16*, 5460−5464.

(52) Popov, K. I., Djokić, S.S., Nikolić, N.D., Jović, V.D.: *Morphology of Electrochemically and Chemically Deposited Metals*; Springer, 2016, DOI: 10.1007/978-3-319-26073-0.

(53) Daiyan, R.; Lu, X.; Ng, Y. H.; Amal, R. Highly Selective Conversion of CO$_2$ to CO Achieved by a Three-Dimensional Porous Silver Electrocatalyst. *ChemistrySelect* **2017**, *2*, 879−884.

(54) Li, D.; Wu, J.; Liu, T.; Liu, J.; Yan, Z.; Zhen, L.; Feng, Y. Tuning the pore structure of porous tin foam electrodes for enhanced electrochemical reduction of carbon dioxide to formate. *Chem. Eng. J.* **2019**, *375*, 122024.

(55) Bahari, Z.; Dichi, E.; Legendre, B.; Dugué, J. The equilibrium phase diagram of the copper−indium system: a new investigation. *Thermochim. Acta* **2003**, *401*, 131−138.

(56) Dutta, A.; Rahaman, M.; Hecker, B.; Drnec, J.; Kiran, K.; Zelocualtecatl Montiel, I.; Jochen Weber, D.; Zanetti, A.; Cedeño López, A.; Martens, I.; Broekmann, P.; Oezaslan, M. CO$_2$ electrolysis − Complementary *operando* XRD, XAS and Raman spectroscopy study on the stability of Cu$_x$O foam catalysts. *J. Catal.* **2020**, *389*, 592−603.

(57) Biesinger, M. C.; Lau, L. W. M.; Gerson, A. R.; Smart, R. S. C. Resolving surface chemical states in XPS analysis of first row transition metals, oxides and hydroxides: Sc, Ti, V, Cu and Zn. *Appl. Surf. Sci.* **2010**, *257*, 887−898.

(58) Dutta, A.; Rahaman, M.; Mohos, M.; Zanetti, A.; Broekmann, P. Electrochemical CO_2 Conversion Using Skeleton (Sponge) Type of Cu Catalysts. *ACS Catal.* **2017**, *7*, 5431−5437.

(59) Cherevko, S.; Geiger, S.; Kasian, O.; Kulyk, N.; Grote, J.-P.; Savan, A.; Shrestha, B. R.; Merzlikin, S.; Breitbach, B.; Ludwig, A.; Mayrhofer, K. J. J. Oxygen and hydrogen evolution reactions on Ru, RuO_2, Ir, and IrO_2 thin film electrodes in acidic and alkaline electrolytes: A comparative study on activity and stability. *Catal. Today* **2016**, *262*, 170−180.

(60) Löffler, M.; Khanipour, P.; Kulyk, N.; Mayrhofer, K. J. J.; Katsounaros, I. Insights into Liquid Product Formation during Carbon Dioxide Reduction on Copper and Oxide-Derived Copper from Quantitative Real-Time Measurements. *ACS Catal.* **2020**, *10*, 6735−6740.

(61) Topalov, A. A.; Cherevko, S.; Zeradjanin, A. R.; Meier, J. C.; Katsounaros, I.; Mayrhofer, K. J. J. Towards a comprehensive understanding of platinum dissolution in acidic media. *Chem. Sci.* **2014**, *5*, 631−638.

(62) Feaster, J. T.; Shi, C.; Cave, E. R.; Hatsukade, T.; Abram, D. N.; Kuhl, K. P.; Hahn, C.; Nørskov, J. K.; Jaramillo, T. F. Understanding Selectivity for the Electrochemical Reduction of Carbon Dioxide to Formic Acid and Carbon Monoxide on Metal Electrodes. *ACS Catal.* **2017**, *7*, 4822−4827.

(63) Yoo, J. S.; Christensen, R.; Vegge, T.; Nørskov, J. K.; Studt, F. Theoretical Insight into the Trends that Guide the Electrochemical Reduction of Carbon Dioxide to Formic Acid. *ChemSusChem* **2016**, *9*, 358−363.

(64) Zhu, W.; Michalsky, R.; Metin, O.; Lv, H.; Guo, S.; Wright, C. J.; Sun, X.; Peterson, A. A.; Sun, S. Monodisperse Au Nanoparticles for Selective Electrocatalytic Reduction of CO_2 to CO. *J. Am. Chem. Soc.* **2013**, *135*, 16833−16836.

(65) Hansen, H. A.; Varley, J. B.; Peterson, A. A.; Nørskov, J. K. Understanding Trends in the Electrocatalytic Activity of Metals and Enzymes for CO_2 Reduction to CO. *J. Phys. Chem. Lett.* **2013**, *4*, 388−392.

(66) Gao, F.-Y.; Bao, R.-C.; Gao, M.-R.; Yu, S.-H. Electrochemical CO_2-to-CO conversion: electrocatalysts, electrolytes, and electrolyzers. *J. Mater. Chem. A* **2020**, *8*, 15458−15478.

(67) Lucile, F.; Cézac, P.; Contamine, F.; Serin, J.-P.; Houssin, D.; Arpentinier, P. Solubility of Carbon Dioxide in Water and Aqueous Solution Containing Sodium Hydroxide at Temperatures from (293.15 to 393.15) K and Pressure up to 5 MPa: Experimental Measurements. *J. Chem. Eng. Data* **2012**, *57*, 784−789.

5.10. Insights from operando and identical location (IL) techniques on the activation of electrocatalysts for the conversion of CO₂: a mini-review

Authors: Abhijit Dutta, Kiran Kiran, Motiar Rahamana, Ivan Zelocualtecatl Montiel, Pavel Moreno-García, Soma Vesztergoma, Jakub Drnec, Mehtap Oezaslan and Peter Broekmann

*Chimia 75 (2021) 733–743 , **DOI**:10.2533/chimia.2021.733*

Highlights: This mini-review encapsulates the *operando* and *identical location* techniques for electrocatalysts like Cu_xO and Bi_2O_3 metal foam obtained by DHBT assisted method. We evaluate two prototype metal foam electrocatalysts used for CO_2 conversion into value-added products (e.g. alcohols on Cu foams, formate on Bi foams). In case of oxidic Cu foam catalyst, the active catalyst is metallic Cu produced from the precursor by oxide electroreduction. On the contrary, in oxidized Bi foams, both metallic and the thermally derived oxidic Bi foams are highly active towards ec-CO_2RR (formate production).

Contribution: I was involved in the electrochemical measurements and physical characterization of the monometallic Cu foam, Bi foam catalysts for the CO_2 reduction process.

Insights from *Operando* and Identical Location (IL) Techniques on the Activation of Electrocatalysts for the Conversion of CO_2: A Mini-Review

Abhijit Dutta*[a], Kiran Kiran[a], Motiar Rahaman[a#], Ivan Zelocualtecatl Montiel[a], Pavel Moreno-García[a], Soma Vesztergom[a,b], Jakub Drnec[c], Mehtap Oezaslan[d], and Peter Broekmann*[a]

Abstract: In this mini-review we compare two prototypical metal foam electrocatalysts applied to the transformation of CO_2 into value-added products (*e.g.* alcohols on Cu foams and formate on Bi foams). A substantial improvement in the catalyst performance is typically achieved through thermal annealing of the as-deposited foam materials, followed by the electro-reduction of the pre-formed oxidic precursors prior or during the actual CO_2 electrolysis. Utilizing highly insightful and sensitive complementary *operando* analytical techniques (XAS, XRD, and Raman spectroscopy) we demonstrate that this catalyst pre-activation process is entirely accomplished in case of the oxidized Cu foams prior to the formation of hydrocarbons and alcohols from the CO_2. The actually active catalyst is therefore the metallic Cu derived from the precursor by means of oxide electro-reduction. Conversely, in their oxidic form, the Cu-based foam catalysts are inactive towards the CO_2 reduction reaction (denoted ec-CO_2RR). Oxidized Bi foams can be regarded as an excellent counter example to the above-mentioned Cu case as both metallic and the thermally derived oxidic Bi foams are highly active towards ec-CO_2RR (formate production). Indeed, *operando* Raman spectroscopy reveals that CO_2 electrolysis occurs upon its embedment into the oxidic Bi_2O_3 foam precursor, which itself undergoes partial transformation into an active sub-carbonate phase. The potential-dependent transition of sub-carbonates/oxides into the corresponding metallic Bi foam dictates the characteristic changes of the ec-CO_2RR pathway. Identical location (IL) microscopic inspection of the catalyst materials, *e.g.* by means of scanning electron microscopy, demonstrates substantial morphological alterations on the nm length scale on the material surface as consequence of the sub-carbonate formation and the potential-driven oxide reduction into the metallic Bi foam. The foam morphology on a mesoscopic length scale (macroporosity) remains, by contrast, fully unaffected by these phase transitions.

Keywords: Catalyst activation · CO_2 reduction reaction · Identical location (IL) technique · Metal foam · *Operando* spectroscopy

Dr. Abhijit Dutta obtained his PhD in chemistry from the Indian Institute of Engineering Science and Technology, Kolkata. During his PhD studies, his research mainly focused on the development of Pt and *non*-Pt based nanostructured materials for the application to fuel cells such as alcohol electro-oxidation, hydrogen oxidation, and the oxygen reduction reaction. He worked as a post-doctoral fellow at the National University of Singapore, Singapore. In 2015 he joined the interfacial electro-chemistry group of Prof. Peter Broekmann at the University of Bern, Switzerland, where he focuses on the development of various *operando* techniques (Raman, XAS, and XRD) to characterize novel electrocatalysts for the selective conversion of CO_2 into value-added products.

Kiran Kiran received her MSc in physics from Maharshi Dayanand University (M.D.U.) India in 2015. She is currently pursuing her PhD at the Department of Chemistry, Biochemistry and Pharmaceutical Sciences at the University of Bern under the supervision of Prof. Peter Broekmann. Her research interests are focused on the synthesis of novel electrocatalysts for CO_2RR applications.

Dr. Motiar Rahaman received his MSc in chemistry (2013) from the Indian Institute of Technology Madras, India. He obtained his PhD (2018) from the University of Bern (group of Peter Broekmann) on the topic of electrochemical conversion of CO_2 into value-added products. Currently he works as a post-doctoral fellow at the University of Cambridge (UK).

Correspondence: Prof. Dr. P. Broekmann[a], E-mail: peter.broekmann@dcb.uni-be.ch; Dr. A. Dutta[a], E-mail: abhijit.dutta@dcb.unibe.ch
[a]University of Bern, Department of Chemistry, Biochemistry and Pharmaceutical Sciences; [b]Eötvös Loránd University, Department of Physical Chemistry, H-1117 Budapest, Pázmány Péter sétány 1/A, Hungary; [c]European Synchrotron Radiation Facility, Grenoble, France; [d]Institute of Technical Chemistry, Technical University of Braunschweig, Braunschweig, Germany; #Current address: Department of Chemistry, University of Cambridge, Cambridge, United Kingdom

Ivan Zelocualtecatl Montiel received his BSc and MSc in chemistry from the Meritorious Autonomous University of Puebla (BUAP) in 2013 and 2016, respectively. He is currently a PhD candidate at the Department of Chemistry, Biochemistry and Pharmaceutical Sciences at the University of Bern under the supervision of Prof. Dr. Peter Broekmann. His research interest is focused on the development of novel catalysts for the electroreduction of CO_2.

Dr. Pavel Moreno-García received his PhD in chemistry and molecular science from the University of Bern in 2013, under the supervision of Prof. Dr. Thomas Wandlowski. At that time, his work was devoted to the study of electron transport through nano-objects at electrified interfaces by *in situ* STM. In 2013, he joined the group of Prof. Dr. Peter Broekmann, where he is involved in research activities on electrocatalysis, metal corrosion and laser ablation mass spectrometry.

Dr. Soma Vesztergom obtained his MSc (2010) and PhD (2014) degrees in chemistry, working with Prof. Dr. G. G. Láng at Eötvös Loránd University, Hungary. He was a post-doctoral researcher in Prof. Dr. Peter Broekmann's group at the University of Bern for one year (2014) and is a regular collaborator of this group since then. His research primarily focuses on instrumental developments in electrochemistry and on the modelling of electrocatalytic processes. Currently, he is an assistant professor at Eötvös Loránd University in Budapest.

Dr. Jakub Drnec obtained his PhD degree at University of Victoria, Canada, in the field of surface electrochemistry. He is currently beamline scientist at the European Synchrotron (ESRF) in Grenoble (France), developing new high energy X-rays experimental techniques to study materials for energy conversion and storage. His main goal is to probe materials in their working environment in order to better understand their functioning. His current projects involve *operando* investigations of fuel cells and batteries, fundamental studies of electrocatalyst's degradation and structure-activity relationships, and development of *operando* electrochemical cells and data analysis routines.

Prof. Dr. Mehtap Oezaslan obtained her PhD degree (2012) in electrochemistry from Technische Universität Berlin, Germany. After a post-doctoral stay at the Electrochemistry Laboratory Group, Paul Scherrer Institute, Switzerland, she was a Junior professor for Electrochemistry at Carl von Ossietzky University of Oldenburg from 2014–2019. Since June 2019, she holds a Full (W3) Professorship at the Institute of Technical Chemistry, Technische Universität Braunschweig. Her research is focused on the development and characterization of electrocatalysts for PEM fuel cells and electrolysis.

Prof. Dr. Peter Broekmann obtained his MSc in chemistry (1998) and a PhD (2000) from the University of Bonn. After a post-doctoral stay at the University of Twente (The Netherlands) in 2001, he became project leader at the Institute of Physical Chemistry in Bonn. Since 2008 he holds a lecturer position for electrochemistry at the University of Bern. His research focuses on metal deposition processes for semiconductor and electrocatalysis applications.

1. Introduction

The conversion of CO_2 into value-added products by means of electrolysis (denoted hereafter ec-CO_2RR) is considered a promising approach to mitigate the negative impact that CO_2 is exerting on the global climate.[1] The vision of converting this environmentally harmful molecule into chemical platform chemicals or synthetic fuels on large industrial scale even offers the unique chance of decreasing the existing atmospheric CO_2 concentration, which already exceeds a level of 400 ppm. For this purpose, the ec-CO_2RR has to be coupled in the future to advanced direct air capture technologies.[2–4] The products of CO_2 reduction – typically light-weight molecules such as carbon monoxide, formic acid or alcohols – could be used as either chemical feedstock and transformed further into products of higher value, *e.g. via* Fischer–Tropsch synthesis or biotechnological transformations,[5] or directly as 'green' fuels. The latter is considered vital for the so-called 'energy transition'.[6,7] In particular, if a surplus of renewable energies, originating from solar, wind, or hydroenergy sources, is used to operate the highly endergonic and energy demanding ec-CO_2RR, this conversion process might become truly sustainable and possibly a key element of a future circular economy. Without doubt, ec-CO_2RR has the highest potential of contributing to the closing of the anthropogenic CO_2 cycle (see Fig. 1).[8]
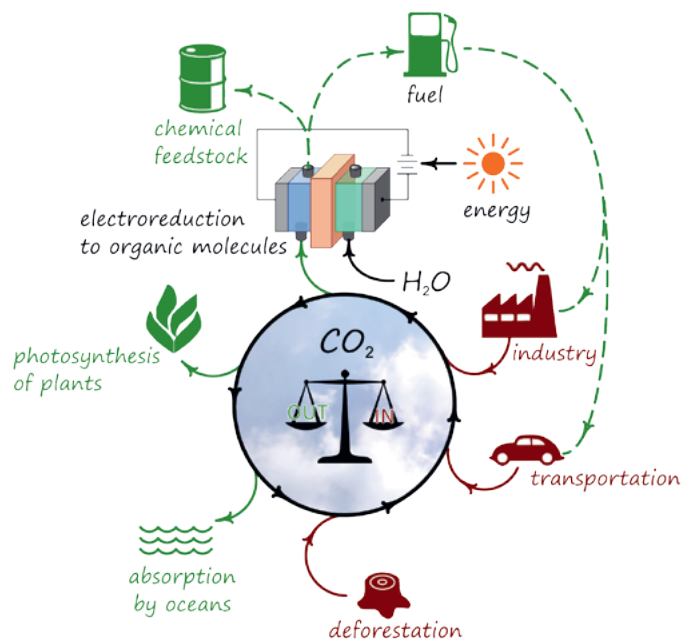

Fig. 1. Schematic depiction of the overall concept to close the anthropogenic carbon cycle by ec-CO_2RR: Towards sustainable conversion of CO_2 into synthetic fuels and chemical feedstock powered by solar energy. Adapted from ref. [8], with permission from John Wiley and Sons.

Most of the known electrochemical CO_2 transformations are, however, still immature and uneconomic.[9] One reason for this is related to electrocatalysts which still require substantial improve-
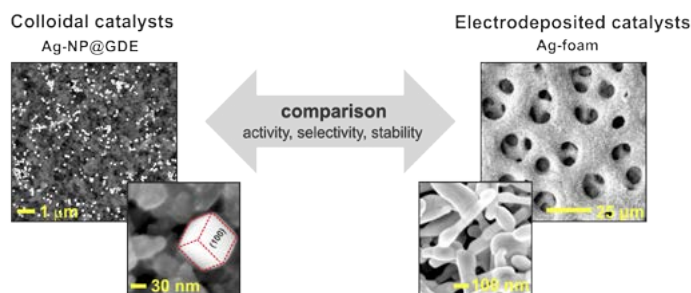
Fig. 2. Complementary catalyst concepts for the ec-CO$_2$RR: carbon-supported colloidal nanoparticles (left) *versus* electrodeposited metal foams (right) exemplified for Ag-based electrocatalysts. Adapted from refs [13,19], with permission of the American Chemical Society.

ments in terms of material costs, (energy) efficiency and catalyst reliability (stability).[8] Additionally, electrocatalysts are essential not only to accelerate the intrinsically slow ec-CO$_2$RR process but also to direct the electrolysis reaction towards the desired reaction products (selectivity).[10] It is, however, not only the chemical nature of the catalyst itself which governs the resulting ec-CO$_2$RR product distribution[10] but also its morphological characteristics on various length scales.[11] Some of the most common ec-CO$_2$RR catalyst concepts rely on the use of nanoparticulate materials.[12] A clear advantage of this classical approach of catalyst design is that the whole spectrum of (mature) colloid chemistry can be applied to synthesize nano-materials of various shapes, morphologies and size distributions. In addition, this approach offers a straightforward and well-established route to functionalize highly porous carbon supports (*e.g.* gas diffusion electrodes (GDEs), Fig. 2) that are used in gas-fed electrolyzer systems that can reach ec-CO$_2$RR current densities of technological relevance (> 200 mA × cm^{-2}). [13,14]

A relatively new and alternative concept of ec-CO$_2$RR catalyst design relies on the electrodeposition of foam-type materials[11,15–17] (Fig. 2), which, similar to their nanoparticulate counterparts, offer a large surface area that is not only accessible to reactants but also enables fast, multidimensional electron transport.[17] Moreover, self-standing foams can directly be employed as cathodes for the ec-CO$_2$RR often without the need for additional mechanical support, rendering the application of conductive binders unnecessary.[17]

Herein we review and compare the structural, compositional and performance characteristics of two prototypical foam electrocatalysts that are based on Cu and Bi systems published recently.[11,18–20] Among various materials studied so far, Cu stands out as the only known mono-metallic catalyst that can produce multiple hydrocarbons and alcohols of various chain lengths at elevated rates from the ec-CO$_2$RR.[10,21–26] In this context, C–C

coupled (liquid) alcohols are of particular interest due to their high volumetric energy density (*e.g.* n-propanol: 27.0 MJ L^{-1}).[27] Note that, prior to their use in operating electrolyzers, numerous as-synthesized/as-deposited ec-CO$_2$RR catalysts require further activation as an essential pre-requisite to attain a highly selective CO$_2$ conversion into the targeted product(s).[28–33] The terms 'as-synthesized' and 'as-deposited' refer to the stage of catalyst preparation right after the initial electrodeposition of the catalyst material and prior to its further activation. A common approach of such catalyst activation involves the partial or complete surface oxidation of the as-deposited metallic foams, *e.g.* by thermal annealing in air.[20,29,31] An ultimate activation step of such formed oxidic catalyst precursors is often only achieved *in situ* under reductive conditions prior to or during the actual CO$_2$ electrolysis.[19,31,34] Such oxidation/electro-reduction treatments not only lead to the further increase of the electrochemically active surface area of the catalyst but also often create those active sites on the foam surface which are required for highly selective ec-CO$_2$RR.[28] It should be emphasized that, at least in the case of copper-based materials, the oxidic precursors (Cu$_2$O or CuO) formed upon thermal annealing are thermodynamically instable at electrolysis potentials typically applied during ec-CO$_2$RR,[35] which in turn results into the formation of so-called oxide-derived (OD) catalysts.[31,36] In general, one possible complication of this catalyst activation approach lies in the reduced electric conductivity of the formed 'bulk' oxides. This can, in principle, lead to a 'kinetic' stabilization of the formed oxidic catalyst precursor phases even under the extremely cathodic potentials applied. In some rare cases one might therefore observe oxidic catalyst species even at potentials far beyond the stability regime predicted by thermodynamics. The specific role of oxides for the ec-CO$_2$RR mechanism and in particular the occurrence of oxygen species embedded inside the hosting metallic Cu matrix under reductive conditions are still the subject of highly controversial debates. To date, there is no ultimate consensus achieved in the literature on the potential-dependent stability of surface and sub-surface oxide/oxygen species and their specific role for the ec-CO$_2$RR.[19,20,33,37–42] To address these mechanistic questions of catalyst activation, a highly complementary approach utilizing several *operando* techniques is needed, which provides various means of deriving structural and chemical information of the catalyst state under reactive conditions.[28] When further combined with high-resolution imaging techniques, *e.g.* identical-location electron microscopy (*e.g.* IL-SEM[28] or IL-TEM[43]), this holistic approach even permits discriminating *transient* phenomena of catalyst precursor reduction (activation). Fig. 3 depicts the set of complementary *operando* analytical techniques described herein.[19]

X-ray absorption spectroscopy (XAS)[19] provides information on (i) the oxidation state (XANES: X-ray Absorption Near
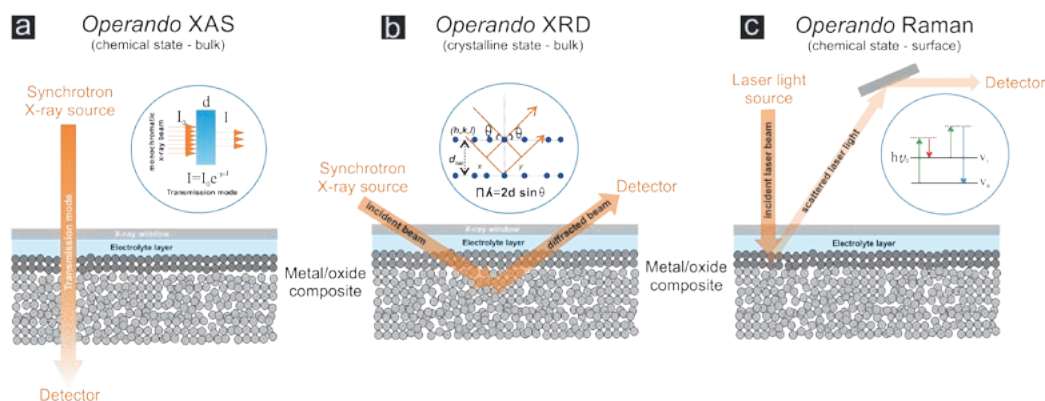

Fig. 3. Complementary *operando* analytical approaches to study the potential-dependent oxide precursor–metal conversion.
a) *Operando* X-ray absorption spectroscopy (XAS); b) *Operando* X-ray diffraction (XRD);
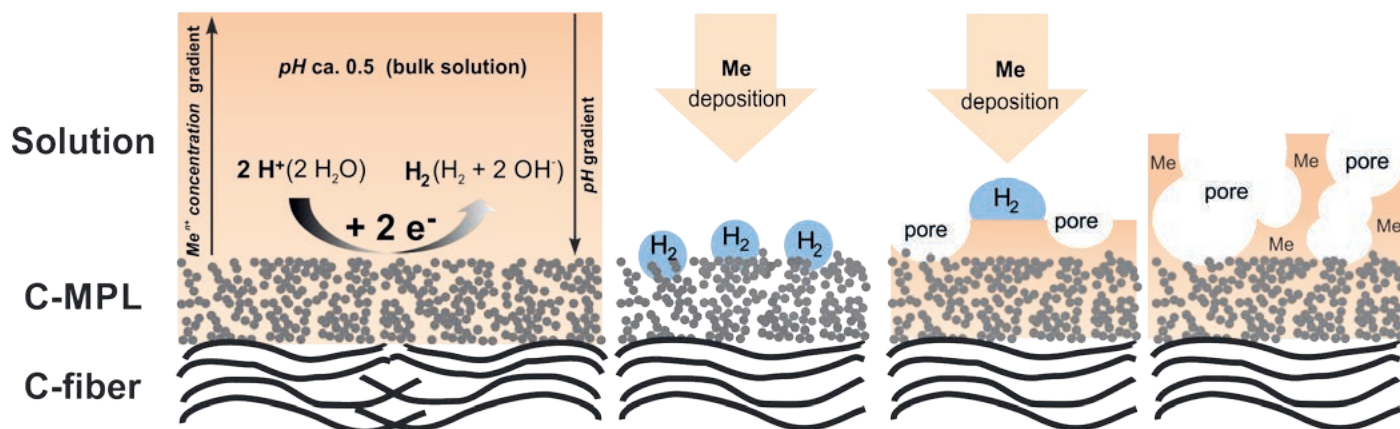c) *Operando* Raman spectroscopy. Adapted from ref. [19], with permission of Elsevier.

Fig. 4. Metal foam electrodeposition ('Me' deposition) by means of the dynamic hydrogen bubble template (DHBT) approach. The working principle is exemplified for a porous carbon support that finds use as gas-diffusion electrode (GDE). 'MPL' and 'Me' stand for microporous layer and metal, respectively. Adapted from ref. [18], with permission of the American Chemical Society.

Edge Structure) and (ii) the coordination number changes (EXAFS: Extended X-ray Absorption Fine Structure) that typically go along with the electro-reduction of the oxidic precursor materials. Compared to their nanoparticulate counterparts, metal foam electrocatalysts and their oxidic precursors exhibit a more unfavorable surface to volume (bulk) ratio (see *e.g.* Fig. 2). Therefore, information derived from XANES and EXAFS techniques originate predominantly from the 'bulk' of the foam material and comprise only marginal contributions from the respective catalyst surfaces. However, what makes the *operando* grazing-incidence X-ray absorption spectroscopy particularly valuable is its capability to probe these potential-dependent oxidation state transitions even when amorphous phases, lacking any long-range translational order, are involved. Note that the activation of Cu foam catalysts *via* thermal annealing and subsequent electroreduction often proceeds *via* amorphous Cu_xO phases.[19,20]

The *operando* X-ray diffraction (XRD) technique[19] is highly complementary to XAS as it permits probing changes in the crystal structure of the foam catalysts, which typically accompany the potential-driven oxidation state changes.

Raman spectroscopy[19] can be considered as the most surface sensitive *operando* technique among those employed herein. A particular strength of the *operando* Raman spectroscopy is that not only the potential-induced alterations of the catalyst themselves can be probed but, in addition, also the emergence of ec-CO_2RR intermediate species, which might be chemisorbed on the evolving 'active' metallic catalyst surface.[19,44]

Herein we introduce Cu foams and their oxidic precursors as prototypical model systems where the oxide–metal transition (catalyst activation) is completed prior to (or at the very onset of) the ec-CO_2RR.[19,20,28] The actual foam catalysts, being active towards alcohol and hydrocarbons, can therefore be considered as truly oxide-derived (OD).[19]

As a counter-example to that, we also discuss oxidized Bi foam catalysts[18] used for the highly selective production of formate. Our investigations reveal that both the oxidized as well as the corresponding metallic foams exhibit pronounced electrocatalytic activity towards the ec-CO_2RR. Finally, we hint at two ec-CO_2RR pathways that are distinctly active on oxide-derived Cu and Bi_2O_3/Bi foam electrocatalysts.[18]

2. Experimental[18,19]

Experimental details on the Cu and Bi foam preparation and the performed *operando*/IL investigations have already been detailed elsewhere.[11,18,19] We therefore restrict ourselves here to a brief description of the applied experimental approaches.

2.1 Preparation of the Cu/Cu$_x$O and Bi/Bi$_2$O$_3$ Foam Catalysts[11,19]

Metallic Cu foams were electrodeposited onto activated carbon foil substrates (0.25 mm thick, 99.8%, Alfa Aesar, Germany) using the dynamic hydrogen bubble template (DHBT)[15,16] approach (see Fig. 4). The carbon foil support was then immersed into a Cu plating bath containing 0.2 M $CuSO_4 \cdot 5H_2O$ and 1.5 M H_2SO_4. For the galvanostatic deposition process, a current density of $j = -3.0$ A $\times$ cm^{-2} (normalized to the geometric surface area of the carbon support) was applied for the duration of 5 seconds. The electrodeposited Cu foams were further subjected to thermal annealing in air for 12 h at a temperature of 300 °C using a tube furnace (GERO, GmbH, Germany).

For the *operando* Raman spectroscopy studies, metallic Bi foams were electrodeposited on graphitic carbon foils (Alfa Aesar) that were activated prior to the Bi deposition by annealing in air at 550 °C for 12 h in a tube furnace. To further increase the electrochemically active surface area Bi foams were deposited on highly porous carbon fiber cloths (gas diffusion electrodes, GDEs, Fuel Cell, USA) for the electrolysis experiments. The carbon fiber cloths were used as received. The standard plating bath for the Bi foam deposition was composed of 1.5 M H_2SO_4 (prepared from 96% H_2SO_4, ACS grade, Sigma-Aldrich) serving as the supporting electrolyte and 20 mM bismuth ammonium citrate ($C_{12}H_{22}BiN_3O_{14}$, purity $\geq$ 99.5 % Sigma Aldrich). The galvanostatic Bi foam deposition was carried by applying a current density of j = -3.0 A $\times$ cm^{-2} (referred to the geometric surface area of the support electrode) for 20 s. The as-prepared Bi foams were further subjected to thermal annealing in air at 300 °C for 12 h, thus transforming the metallic Bi into fully oxidized Bi_2O_3.

2.2 Operando X-ray Absorption Spectroscopy[19]

XAS experiments were carried out at the SuperXAS (X10DA) beamline at the Swiss Light Source (SLS) in Villigen, Switzerland. The storage ring was operated at 2.4 GeV and 400 mA. For the *operando* spectroscopic experiments a dedicated liquid flow-cell was used.[45] XAS experiments were carried out in CO_2-sat. 0.5 M $KHCO_3$ electrolyte solution (pH = 7.2) in the potential range from +0.8 V to –0.9 V vs. RHE. All potentials were iR-corrected.

2.3 Operando X-ray Diffraction[19]

Operando XRD experiments were performed at the high energy beamline ID31 of the European Synchrotron Radiation Facility (ESRF). The X-ray beam was mono-chromatized with a Laue-Laue monochromator to the energy of 69 keV and focused to the size of 5 $\times$ 20 µm^2 (vertical $\times$ horizontal) at the sample posi-

tion. The 2D XRD patterns were collected with a Dectris Pilatus 2M CdTe detector. A custom-made PEEK electrochemical flow cell was used for the experiments.[46] The measurements were performed in grazing incidence geometry (the incidence angle was less than 1 degree), in CO_2-sat. 0.5 M $KHCO_3$ electrolyte. A continuous flow of fresh CO_2-sat. electrolyte solution through the spectro-electrochemical cell prevented any undesired accumulation of soluble Cu species in the investigated X-ray window. All potentials were iR-corrected.

2.4 *Operando Raman Spectroscopy*[19]

Raman spectra were recorded using a LabRAM HR800 confocal microscope (Horiba Jobin Yvon) at a working distance of 8 mm between the objective lens (LMPLFLN from Olympus, 50X magnification) and the sample with a numerical aperture of 0.1 in order to focus a diode-pumped solid-state or He-NE laser beam (excitation wavelength of 532 or 633 nm, power of 3 mW) on the sample. The Raman signal was collected in a back-scattering geometry using a lab-made spectro-electrochemical cell made of Kel-F.[47,48] CO_2-sat. 0.5 M $KHCO_3$ solution was used as the electrolyte. The ohmic drop was determined using the positive feedback technique and compensated during the measurement.

2.5 *Identical Location Scanning Electron Microscopy (IL-SEM)*

For the high-resolution (HR) identical location (IL) SEM imaging a Zeiss DSM 982 instrument was used.

2.6 *Product Analysis of the ec-CO_2RR*[11,18]

All electrolysis experiments were carried out in CO_2-sat. 0.5 M $KHCO_3$ solution using a custom-built, air-tight glass-cell (H-type) described elsewhere.[11] During electrolysis CO_2 was continuously purged through the catholyte at a flow rate of 13 mL × min^{-1}. The headspace of the electrolysis cell was directly connected to the gas sampling loop of the gas chromatograph (GC 8610C, SRI Instruments). The GC was equipped with a packed Hayesep D column and a packed Molesieve 5A column. Argon (99.9999 %, Carbagas) was used as the carrier gas. A flame ionization detector (FID) coupled to a methanizer was used to quantify CO and volatile hydrocarbons. A thermal conductivity detector (TCD) was used for the H_2 detection. Non-volatile products (*e.g.* alcohols) were quantified by a second FID detector. After the electrolysis, a 2 μL aliquot of the electrolyte solution was injected into a second Haysep D column (post-electrolysis alcohol detection). Other liquid products (*e.g.* formate) were analyzed by means of ion exchange chromatography (IC, Metrohm Advanced Modular Ion Chromatograph: L-7100 pump, Metrosep A Supp 7-250 column, conductivity detector).

3. Results and Discussion

3.1 *Activation of Cu Foam Electrocatalysts*[19]

Fig. 5 displays a prime example of Cu foams fabricated by means of the DHBT-assisted electrodeposition method.[11] The basic concept of this approach was adapted from the work by Shin *et al.*[15,16] As the Cu electrodeposition takes place under rather harsh hydrogen evolution reaction (HER) conditions (*e.g.* at current densities of $j = -3$ A × cm^{-2}, see Fig. 4), gas bubbles rapidly evolve on the support electrode and serve as geometric template for the actual metal plating process which is superimposed on the HER. Cu is deposited only in the bubble-free areas of the support and the emerging porous film. The process of hydrogen bubble
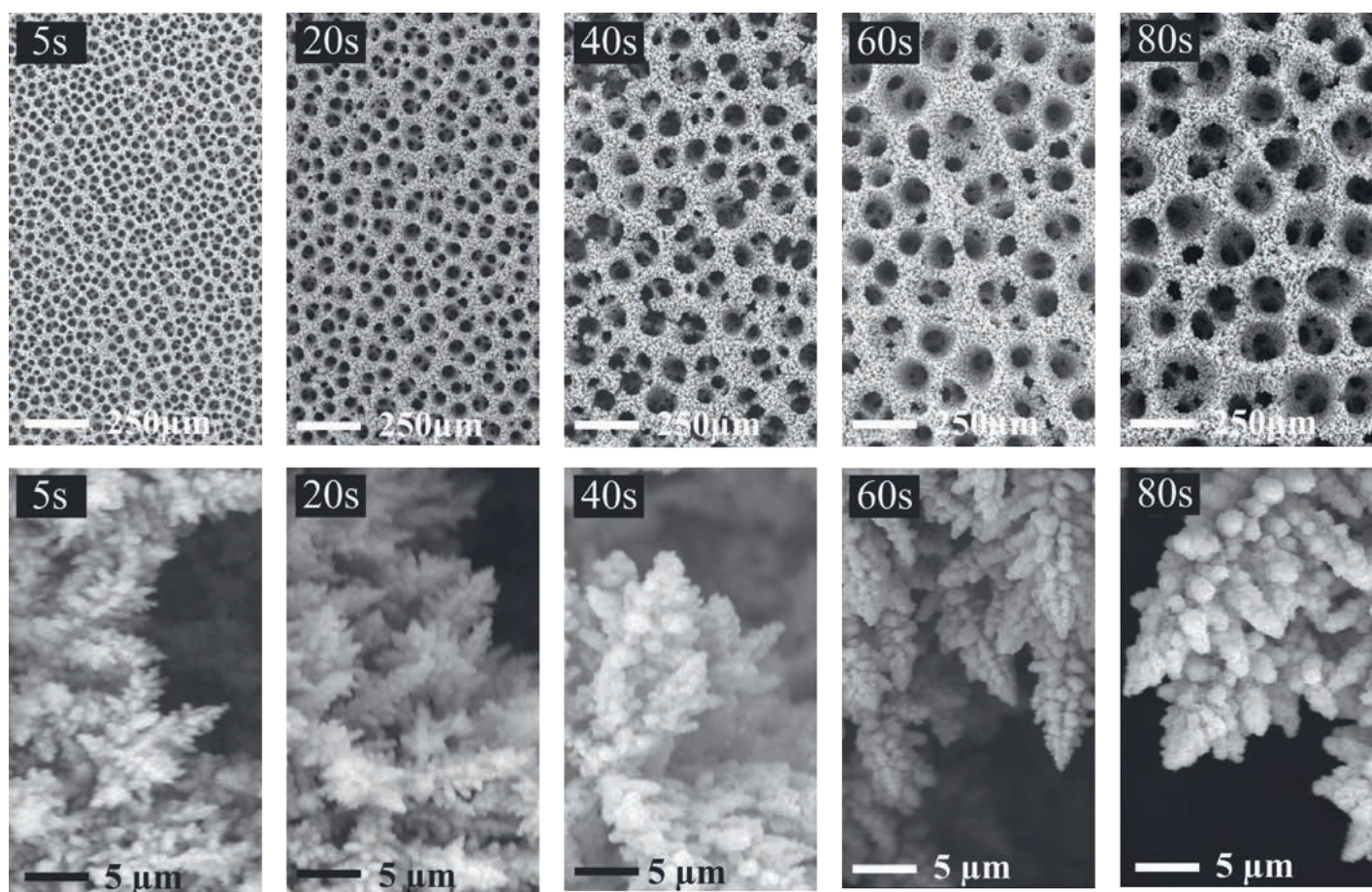
Fig. 5. Top-down SEM analysis showing the surface pore size (upper row) and dendrite size (lower row) evolution as function of the deposition time (exemplified for a Cu foam catalyst). Adapted from ref. [11], with permission of the American Chemical Society.

nucleation, growth and coalescence is continuous. This is why the average surface pore size increases as function of the deposition time and film thickness (Fig. 5).[11] A characteristic feature of the formed metal foams is a gradient in the pore sizes along the surface normal. Smallest pores are typically created close to the support electrode whereas the biggest ones are found at the outermost surface of the foam material which is exposed to the (liquid) electrolyte during the CO_2 electrolysis reaction.[11]

In addition to this primary macro-porosity (µm length scale), originated by the gaseous H_2-template during the metal deposition, the scaffold of the formed 3D foam itself is porous, too.[11,20,49] The macro-pore sidewalls are composed of randomly distributed Cu dendrites thus introducing a secondary porosity to the catalyst (nm length scale).[15] Such a dendritic growth mode originates from the applied experimental conditions that impose a deposition rate limited by mass transport of the metal ions and a reduced mobility of the deposited atoms on the emerging foam surface.[11]

In particular when alcohols are targeted as products, the electrodeposited catalysts often require further activation prior to the ec-CO_2RR, *e.g.* by thermal annealing in air.[28,50] Fig. 6 displays representative SEM micrographs of an 'as-deposited' Cu foam and its morphological evolution induced by thermal annealing at 300 °C for 12 h in air, and a subsequent 1 h CO_2 electrolysis in CO_2-sat. 0.5 M bicarbonate solution carried out at –0.67 V vs. RHE. Obviously, the macro-porous morphology of the Cu foam remains completely unaffected by both the thermal annealing in air (Cu oxidation) and the subsequent ec-CO_2RR, the latter involving the electro-reduction of the formed oxides.[19,20] However, the Cu foam undergoes substantial morphological alterations on the nm length scale particularly induced by the thermal treatment (see Fig. 6e–h). Following the 12 h annealing step at 300 °C, the surface of the pristine metallic Cu foam is completely transformed into a composite material consisting of cuprous (Cu_2O) and cupric (CuO) oxides[19,20,28] (denoted Cu_xO). This transformation requires substantial mass transport of oxygen and Cu species. A combination of *ex situ* (post-deposition, post-electrolysis) XRD and XPS analysis

confirms the composite nature of the oxidic foam.[19,20] It should be noted that the applied annealing temperature of 300 °C is sufficient to form a crystalline Cu_2O phase whereas the cupric CuO remains largely in an amorphous state lacking any long range transitional order.[19,20] Consequently, Cu(II) species are detected in the XPS but not in the corresponding XRD analysis.[19,20] It should be noted here that, in full agreement with previous studies, the thermal annealing activates the Cu catalyst for C2 and C3 alcohol production.[19] For instance, the partial current density for ethanol formation increases from $j_{EtOH} = -0.86$ mA $\times$ cm^{-2} ($FE_{EtOH} = 5\%$) at –0.77 V vs. RHE to $j_{EtOH} = -1.61$ mA $\times$ cm^{-2} ($FE_{EtOH} = 6.7\%$) at –0.87 V vs. RHE. Similarly, the partial current density for n-propanol formation reaches a value of $j_{PrOH} = -1.72$ mA $\times$ cm^{-2} ($FE_{PrOH} = 7.1\%$) at –0.87 V.[19] A full description of the electrocatalytic performance of the annealed Cu foam can be found in ref. [19].

More sophisticated *operando* analytical techniques are required to ultimately address how important oxide species are in particular for the alcohol electrosynthesis *via* the ec-CO_2RR on these Cu foams. Fig. 7 provides an overview on the results of the highly complementary XAS, XRD, and Raman spectroscopic investigations discussed by Dutta *et al*.[19] Changes in the potential-dependent Cu K-edge XANES spectra of the Cu_xO foam could be attributed to potential-dependent redox state changes of Cu species (Fig. 7, panel a; selected data set). Panel b in Fig. 7 shows the result of a linear combination fitting (LCF) that was applied to the obtained XANES data using Cu K-edge XANES spectra of a Cu foil, Cu_2O and CuO as reference materials. The plot displays the relative concentrations of the Cu(0), Cu(I), and Cu(II) species present in the Cu_xO foam as a function of the potential applied.[19] The LCF analysis suggests that the Cu_xO foam at +0.6 V vs. RHE predominantly consists of CuO, whereas only a lower Cu_2O content was observed (25–35 wt.%). Upon potential excursion from +0.6 down to 0 V vs. RHE, the relative abundances of Cu(II) and Cu(I) anti-correlate and further negative polarization leads to the onset of oxide reduction to metallic Cu(0). At potentials below 0 V vs. RHE the Cu(II) abundance
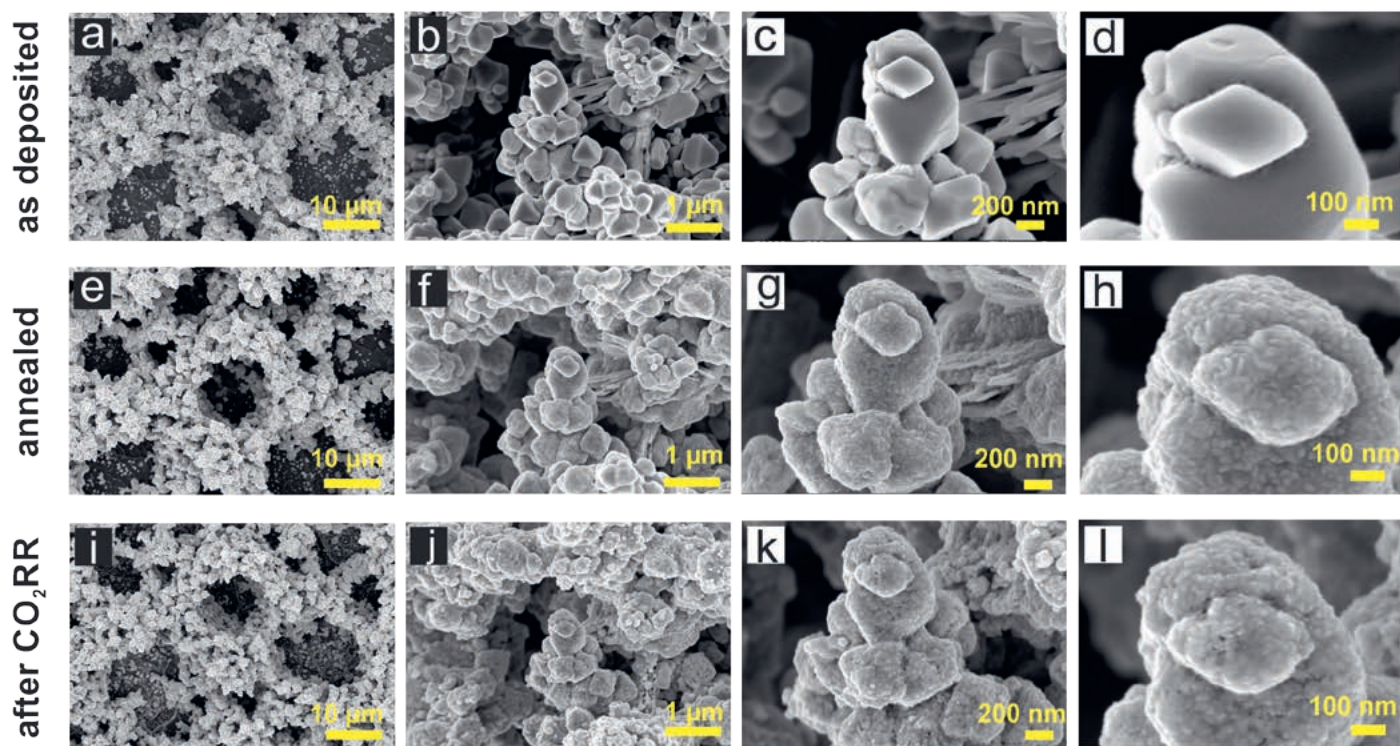

Fig. 6. Identical location (IL) SEM inspection of the Cu foam catalyst. (a–d) As-deposited Cu foam (5 s deposition at -3 A $\times$ cm^{-2}); (e–h) Thermally annealed Cu foam (300 °C for 12 h in air, denoted Cu_xO foam); (i–l) Oxide-derived (OD) Cu foam after 1 h CO_2RR in CO_2-sat. 0.5 M KHCO$_3$ solution at –0.67 V vs. RHE. Adapted from ref. [19], with permission of Elsevier.
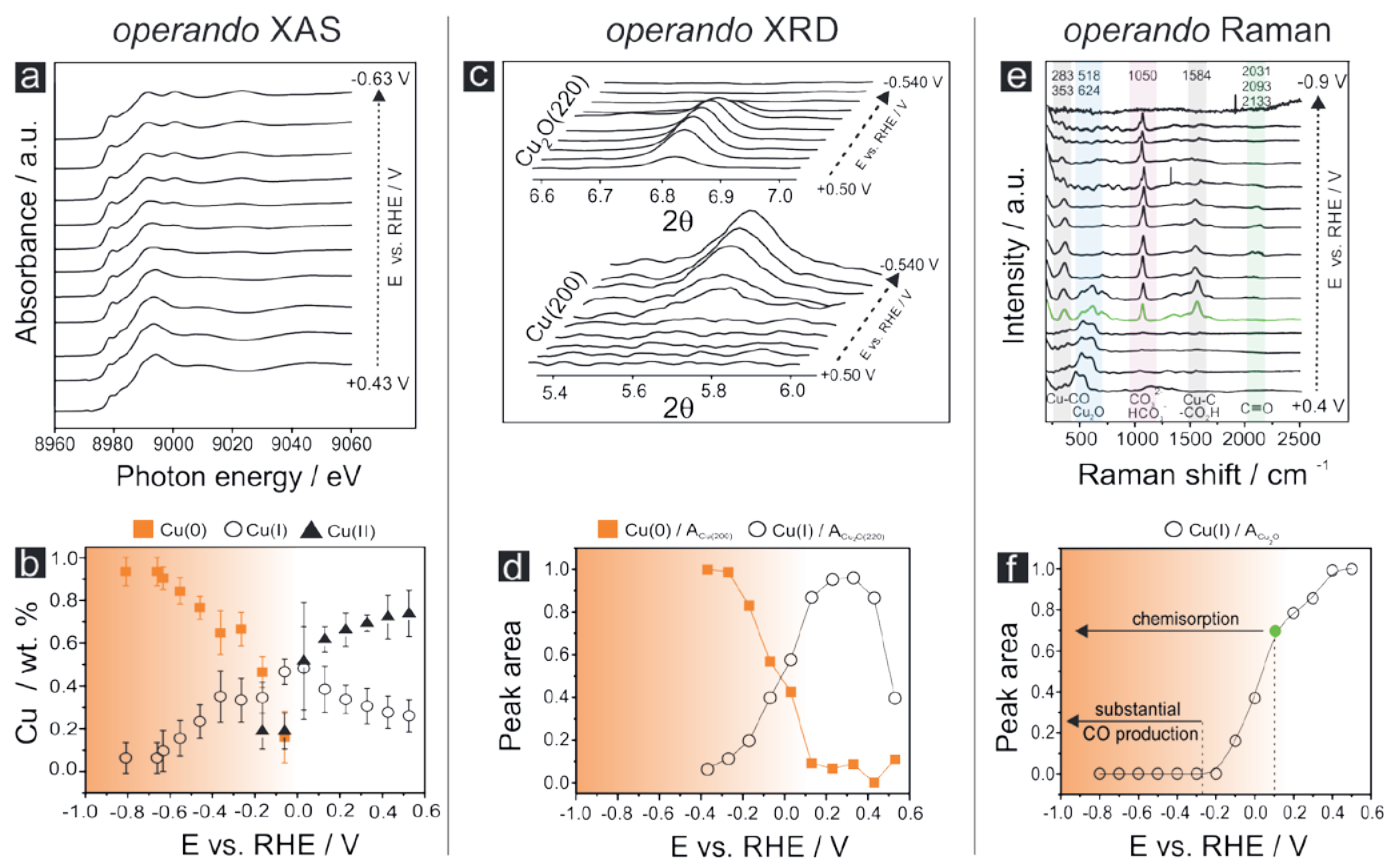
Fig. 7. Survey of experimental *operando* results demonstrating the potential-dependent oxide–metal transition of the oxidic catalyst precursor (Cu$_x$O foam). (a) Potential-dependent *operando* XANES spectra (Cu K-edge) of the thermally annealed Cu foam (Cu$_x$O) in CO$_2$-sat. 0.5 M KHCO$_3$ solution; (b) Potential-dependent composition of the Cu$_x$O foam (relative content of Cu species: Cu(0), Cu(I), and Cu(II) derived from a linear combination fitting (LCF) of the XANES spectra shown in (a)); (c) Potential-dependent *operando* grazing-incidence X-ray diffractograms of the Cu$_2$O(220) and Cu(200) reflections; (d) Integrated and normalized peak intensities of the diffractograms shown in (c); (e) Corresponding potential-dependent *operando* Raman spectra; (f) Integrated and normalized peak intensities of the Cu$_2$O-related Raman peaks (518 cm^{-1} and 624 cm^{-1}) shown in (e). The peak areas were normalized with respect to the most intense peaks at most positive electrode potentials. The grey and orange areas in panel b, d, and f indicate the stability windows of the oxidic and metallic state of Cu, respectively. Adapted from ref. [19], with permission of Elsevier.

drops down to zero, whereas Cu(I) species are present in the bulk material down to potentials of -0.5V vs. RHE.[19] The potential-dependent decrease of the Cu(I) content below 0 V vs. RHE is clearly anti-correlated to the increase of the Cu(0) abundance. The transition from the oxidic precursor to metallic Cu in the bulk is completed at about –0.7 V vs. RHE.[19]

Operando XRD experiments basically confirm the XAS investigations (panel c and d in Fig. 7). As hypothesized on the basis of the XAS results the integrated intensity of the Cu$_2$O(220) diffraction peak first increases when sweeping the cathode potential from +0.5 V to +0.2 V vs. RHE. This trend is consistent with the assumption of an intermediate crystalline Cu$_2$O phase which accumulates in the initial stage of the oxide–metal transition in the foam material at the expense of the amorphous CuO phase.[19] Interestingly, the disappearance of the Cu$_2$O related diffraction pattern with negative going potentials is already completed at –0.4 V vs. RHE, whereas the XAS experiment indicates the presence of Cu(I) species for potentials down to –0.8 V vs. RHE. These deviations in the particular potential-dependence of the Cu(I)(XAS)/Cu$_2$O(XRD) stability regime are related to the intrinsic characteristics of both *operando* techniques. The ultimate reduction of the Cu(I) to Cu(0) proceeds most likely *via* an intermediate amorphous Cu(I) phase.[19]

Among the *operando* techniques applied Raman spectroscopy is the most surface sensitive one.[19] Raman features observed at 148 cm^{-1}, 518 cm^{-1}, and 624 cm^{-1} can be ascribed to cuprous oxide species (Cu$_2$O), whereas vibrational modes at

298 cm^{-1} and 346 cm^{-1} originate from cupric oxides (panel e and f in Fig. 7).[19] Interesting to note is that after exposure to the 0.5 M KHCO$_3$ electrolyte at the open circuit potential, the CuO related vibrational modes have completely disappeared from the Raman spectra.[19] Only vibrational modes of the cuprous oxide (Cu$_2$O) are left which indicates that the initial catalyst surface is terminated exclusively by Cu(I) species when exposed to the electrolyte. Both XRD and XAS typically do not show these effects when the oxidic foam is exposed to the electrolyte at OCP.[19] This is due to the dominance of 'bulk' contributions to the data with only minor contributions from the foam surface. Integrated intensities of the Cu$_2$O specific Raman features (panel f) follow qualitatively the same trend as observed in the XAS and XRD. However, the 'surface oxide reduction' proceeds apparently faster than the corresponding transition of the oxidic 'bulk phases' probed by *operando* XAS and XRD and is therefore completed at less negative applied potentials.[19]

Operando Raman spectroscopy provides additional information on intermediate species associated to the ec-CO$_2$RR. Raman modes observed at 283 cm^{-1}/253 cm^{-1}, 1050 cm^{-1}, 1584 cm^{-1} and 2031 cm^{-1}/2093 cm^{-1}/2133 cm^{-1} are attributed to adsorbed CO, HCO$_3^-$, and HCOOH respectively. These intermediates appear only after partial reduction of the oxide to the metallic Cu.[19]

The 'holistic view' on the potential-dependent oxide–metal transition using different complementary *operando* techniques let us safely conclude that the surface and bulk Cu oxide reduction is completed at potentials more positive than the onset of hydrocar-

Fig. 8. (a,b) *ap* Bi/Bi$_x$O$_y$ foam deposited on a carbon cloth support (denoted Bi/Bi$_x$O$_y$@GDE); (c) CO$_2$RR product distribution represented as *FE*$_{formate}$ vs. E plot (*FE*: Faradaic efficiency). The annealed foam (denoted Bi$_2$O$_3$@GDE) was used as the catalyst; (d) Corresponding CO$_2$RR reaction rate represented as PCD$_{formate}$ vs. E plot (PCD: partial current density). Note that the only side-product of the CO$_2$RR is hydrogen; (e–h) *Operando* Raman spectroscopy results showing the potential-dependent oxide/sub-carbonate reduction. Raman bands at 313 cm^{-1} and 162 cm^{-1} were used to probe the presence of oxide and sub-carbonate species, respectively; (i) *Operando* optical inspection of the time-dependent oxide/sub-carbonate/metal transition in CO$_2$-sat. 0.5 M KHCO$_3$ solution at -0.6 V vs. RHE; (j,k) Proposed reaction mechanisms of formate formation. Adapted from ref. [18], with permission of the American Chemical Society.
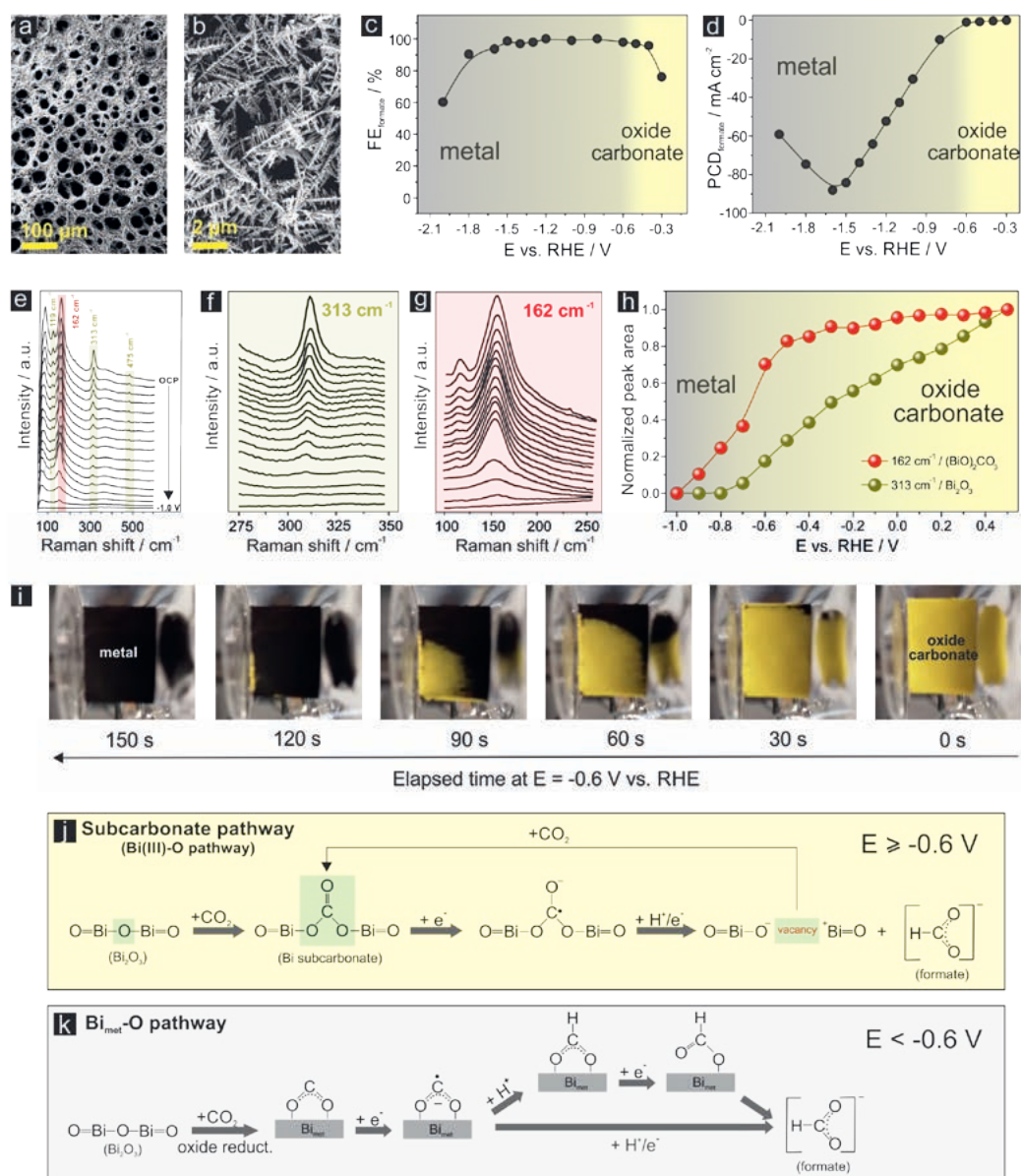
bon and alcohol formation. Obviously, oxidic species do not play any significant role for the ec-CO$_2$RR on Cu in general and for the alcohol production in particular.

3.2 Activation of Bi/Bi$_2$O$_3$ Foam Electrocatalysts[18]

A novel bismuth oxide (Bi$_2$O$_3$) foam-type of catalyst (precursor) material has been produced by means of an additive-assisted DHBT electrodeposition followed by thermal annealing at 300 °C for 12 h.[18] This DHBT approach could successfully be applied to functionalize technical supports, *e.g.* gas diffusion electrodes (GDEs). This transfer of the foam catalyst from planar substrates (*e.g.* Cu foils[11]) to highly porous carbon supports is considered a crucial technical pre-requisite for any future application of this novel catalyst concept in gas-fed (CO$_2$) electrolyzer systems. The latter will be vital to achieve ec-CO$_2$RR current densities which are of technological relevance ($j_{CO2RR} > 200$ mA × cm^{-2}). It should be noted that the resulting (surface) pore sizes are altered when changing the support material.[18] In general, the pore size distribution is substantially broader when the foam materials are electrodeposited on porous carbon supports compared to respective metal foaming processes on planar metal foil supports. Fig. 8a,b shows representative top-down SEM images of the as-prepared Bi foam on the technical carbon support denoted hereafter *ap* Bi/

Bi$_2$O$_3$@GDE. Note that the as-prepared oxophilic Bi foam is typically covered by an ultrathin Bi$_2$O$_3$ layer after its emersion from the Bi plating bath.[18]

The thermal treatment at 300 °C for 12 h in air leaves the macroporosity of *ap* Bi/Bi$_2$O$_3$ foam fully unaffected (see also Fig. 9), similar to the Cu case (Fig. 6). This annealing yields a fully oxidized Bi$_2$O$_3$ foam which shows a characteristic yellow color (Fig. 8i at 0 s).

The formed oxidic Bi foam exhibits a superior electrocatalytic selectivity toward formate production with Faradaic efficiencies (FEs) never falling below 90 % within an extraordinarily huge potential window of ~ 1100 mV (max. *FE*$_{formate}$ = 100% at –0.8 V vs. RHE).[18] Panel c and d of Fig. 8 depict the potential-dependent Faradaic efficiencies (c) and partial current densities (d) of formate production when the electrolysis is carried out from aqueous CO$_2$-sat. 0.5 M KHCO$_3$ solution.

For the first time, *operando* Raman spectroscopy provided clear experimental evidence for the embedment of CO$_2$ into an oxidic matrix (so-called 'sub-carbonate' formation) at low overpotentials prior to and during the CO$_2$ reduction reaction (Fig. 8e–h). We used the Raman bands at 313 cm^{-1} and 162 cm^{-1} as characteristic 'fingerprints' for the presence of Bi oxide and Bi subcarbonate species, respectively.[18] Note that
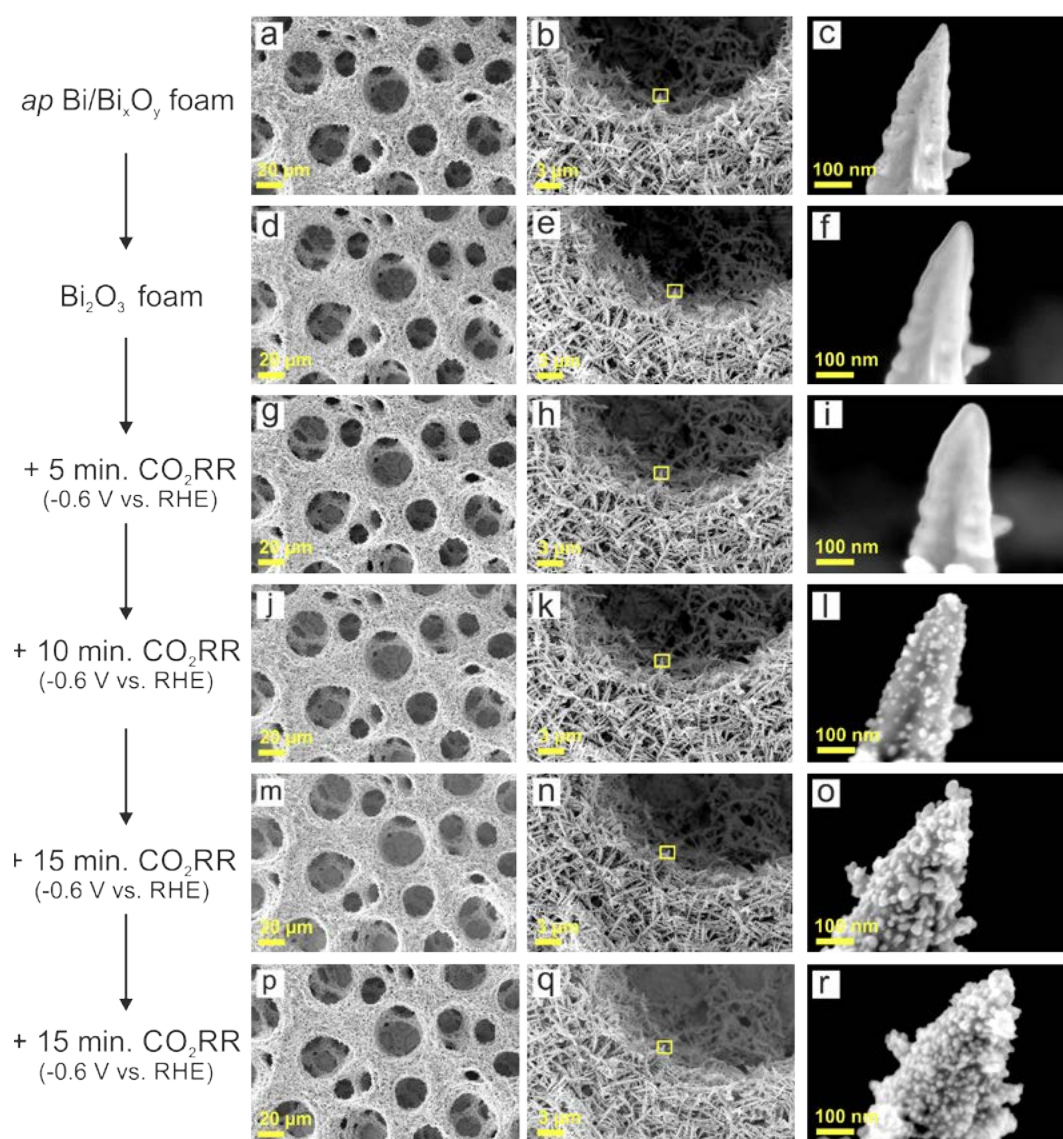
Fig. 9. (a-r) Identical location (IL) SEM inspection of morphological changes associated to the thermal annealing of the *ap* Bi/Bi$_x$O$_y$ foam, the sub-carbonate formation and subsequent potentiostatic CO$_2$ electrolysis in CO$_2$-sat. 0.5 M KHCO$_3$ solution at –0.6 V vs. RHE. Adapted from ref. [18] with permission of the American Chemical Society.

the exchange of the oxide by the sub-carbonate is a spontaneous and rather fast process which takes place in the CO$_2$-sat. 0.5 M KHCO$_3$ solution even at the open circuit potential without initiating the ec-CO$_2$RR. Indeed, the potential-dependent integrated intensities of the Raman bands at 313 cm^{-1} and 162 cm^{-1} suggest that formed sub-carbonate species are more stable than the corresponding oxides (Fig. 8h). As shown in Fig. 8i, this transition from the oxide/sub-carbonate to the metallic Bi state is accompanied by a characteristic color change from yellow (oxide) to black (metal).

These excellent electrocatalytic characteristics of the novel Bi foam catalysts result from the coupling of two distinct reaction pathways of formate formation which are active (i) in the presence of the (partly-reduced) Bi$_2$O$_3$ foam at low overpotentials (sub-carbonate pathway) and (ii) on the corresponding metallic Bi foam catalyst at medium and high overpotentials (Bi-O pathway). The reaction mechanisms, proposed also on the basis of the *operando* Raman results, are displayed in Fig. 8j,k. To probe in more detail the structural and morphological changes which take place on the nanometer length scale upon sub-carbonate formation and partial electro-reduction of the oxidic precursor during ec-CO$_2$RR we further applied the identical location (IL) scanning electron microscopy (SEM) technique

by sequentially imaging the same single spot on the catalyst surface after the initial electrodeposition (as prepared), after the thermal annealing treatment, and after a series of dedicated CO$_2$ electrolyses. The results of this IL-SEM analysis are depicted in Fig. 9 and demonstrate severe morphological changes on the nm length scale which go along with (i) the oxidation upon thermal annealing, (ii) the sub-carbonate formation when exposed to the CO$_2$-sat. bicarbonate solution, and (iii) the ensuing catalyst electro-reduction into the metallic state at higher applied overpotentials.

These microscopic results impressively demonstrate that the actually active catalyst forms only under reactive conditions.

4. Conclusions

Herein we have demonstrated the usefulness of advanced *operando* analytical techniques to probe the (chemical) state evolution of foam-type catalysts under reactive conditions, *e.g.* in the course of CO$_2$ electrolysis. In particular for the case of Cu foams and their oxidic precursors it could be shown that a complementary *operando* analysis approach is mandatory to derive a full understanding of the catalyst activation process which involves the potential-driven electro-reduction of the oxidic precursors. Due to intrinsic technical limitations associated with

each applied *operando* technique (*e.g.* XAS, XRD, and Raman spectroscopy) the probed potential dependence of the observed structural and compositional alterations is slightly different in all cases. However, from all applied *operando* techniques it can be concluded that the oxide–metal transition is completed prior to the onset of hydrocarbon or alcohol formation. The active Cu catalyst can be indeed considered as metallic (oxide-derived).

The understanding of the catalyst activation process is, however, much more complex in case of Bi foams and their oxidic counterparts. As evidenced by the comparison of *operando* Raman spectroscopy results and corresponding electrochemical performance testing, both the oxidic and the metallic foams are active towards ec-CO$_2$RR (formate production). The scenario becomes even more complex due to the rapid exchange of oxidic species by sub-carbonates in the presence of (dissolved) CO$_2$ in the electrolyte solution. It is the coupling of two distinct reaction pathways of formate production (sub-carbonate pathway at low overpotentials; Bi-O pathway at high overpotentials) that leads to the extraordinarily broad potential window of ~1100 mV in which the Faradaic efficiency of formate production does not fall below 90%.

[1] E. V. Kondratenko, G. Mul, J. Baltrusaitis, G. O. Larrazabal, J. Perez-Ramirez, *Energy Environ. Sci.* **2013**, *6*, 3112, https://doi.org/10.1039/C3EE41272E

[2] M. Fasihi, O. Efimova, C. Breyer, *J. Clean. Prod.* **2019**, *224*, 957, https://doi.org/10.1016/j.jclepro.2019.03.086

[3] S. Fujikawa, R. Selyanchyn, T. Kunitake, *Polym. J.* **2021**, *53*, 111, https://doi.org/10.1038/s41428-020-00429-z

[4] N. McQueen, K. V. Gomes, C. McCormick, K. Blumanthal, M. Pisciotta, J. Wilcox, *Prog. Energy* **2021**, *3*, 032001, https://doi.org/10.1088/2516-1083/abf1ce

[5] T. Haas, R. Krause, R. Weber, M. Demler, G. Schmid, *Nat. Catal.* **2018**, *1*, 32, https://doi.org/10.1038/s41929-017-0005-1

[6] N. Kittner, F. Lill, D. M. Kammen, *Nat. Energy* **2017**, *2*, 17125, https://doi.org/10.1038/nenergy.2017.125

[7] B. D. Solomon, K. Krishna, *Energy Policy* **2011**, *39*, 7422, https://doi.org/10.1016/j.enpol.2011.09.009

[8] A. V. Rudnev, Y.-C. Fu, I. Gjuroski, F. Stricker, J. Furrer, N. Kovács, S. Vesztergom, P. Broekmann, *ChemPhysChem* **2017**, *18*, 3153, https://doi.org/10.1002/cphc.201700737

[9] J. Durst, A. Rudnev, A. Dutta, Y. Fu, J. Herranz, V. Kaliginedi, A. Kuzume, A. A. Permyakova, Y. Paratcha, P. Broekmann, T. J. Schmidt, *Chimia* **2015**, *69*, 769, https://doi.org/10.2533/chimia.2015.769

[10] Y. Hori, in 'Modern Aspects of Electrochemistry', Springer, New York, **2008**, 89, https://doi.org/10.1007/978-0-387-49489-0_3.

[11] A. Dutta, M. Rahaman, N. C. Luedi, M. Mohos, P. Broekmann, *ACS Catal.* **2016**, *6*, 3804, https://doi.org/10.1021/acscatal.6b00770

[12] J. Quinson, S. Neumann, T. Wannmacher, L. Kacenauskaite, M. Inaba, J. Bucher, F. Bizzotto, S. B. Simonsen, L. T. Kuhn, D. Bujak, A. Zana, M. Arenz, S. Kunz, *Angew. Chem. Int. Ed.* **2018**, *57*, 12338, https://doi.org/10.1002/anie.201807450

[13] M. de Jesus Gálvez-Vázquez, P. Moreno-García, H. Xu, Y. Hou, H. Hu, I. Z. Montiel, A. V. Rudnev, S. Alinejad, V. Grozovski, B. J. Wiley, M. Arenz, P. Broekmann, *ACS Catal.* **2020**, *10*, 13096, https://doi.org/10.1021/acscatal.0c03609

[14] M. d. J. Gálvez-Vázquez, S. Alinejad, H. Hu, Y. Hou, P. Moreno-García, A. Zana, G. K. H. Wiberg, P. Broekmann, M. Arenz, *Chimia* **2019**, *73*, 922, https://doi.org/10.2533/chimia.2019.922

[15] H. C. Shin, M. Liu, *Chem. Mater.* **2004**, *16*, 5460, https://doi.org/10.1021/cm048887b

[16] H. C. Shin, J. Dong, M. Liu, *Adv. Mater.* **2004**, *16*, 237, https://doi.org/10.1002/adma.200305660

[17] S. Vesztergom, A. Dutta, M. Rahaman, K. Kiran, I. Zelocualtecatl Montiel, P. Broekmann, *ChemCatChem* **2021**, *13*, 1039, https://doi.org/10.1002/cctc.202001145

[18] A. Dutta, I. Zelocualtecatl Montiel, K. Kiran, A. Rieder, V. Grozovski, L. Gut, P. Broekmann, *ACS Catal.* **2021**, *11*, 4988, https://doi.org/10.1021/acscatal.0c05317

[19] A. Dutta, M. Rahaman, B. Hecker, J. Drnec, K. Kiran, I. Zelocualtecatl Montiel, D. Jochen Weber, A. Zanetti, A. Cedeño López, I. Martens, P. Broekmann, M. Oezaslan, *J. Catal.* **2020**, *389*, 592, https://doi.org/10.1016/j.jcat.2020.06.024

[20] A. Dutta, M. Rahaman, M. Mohos, A. Zanetti, P. Broekmann, *ACS Catal.* **2017**, *7*, 5431, https://doi.org/10.1021/acscatal.7b01548

[21] M. G. Kibria, C.-T. Dinh, A. Seifitokaldani, P. De Luna, T. Burdyny, R. Quintero-Bermudez, M. B. Ross, O. S. Bushuyev, F. P. García de Arquer, P. Yang, D. Sinton, E. H. Sargent, *Adv. Mater.* **2018**, *30*, 1804867, https://doi.org/10.1002/adma.201804867

[22] Y. Hori, A. Murata, R. Takahashi, *J. Chem. Soc., Faraday Trans. 1* **1989**, *85*, 2309, https://doi.org/10.1039/F19898502309

[23] Y. Hori, I. Takahashi, O. Koga, N. Hoshi, *J. Phys. Chem. B* **2002**, *106*, 15, https://doi.org/10.1021/jp013478d

[24] S. Ma, M. Sadakiyo, R. Luo, M. Heima, M. Yamauchi, P. J. A. Kenis, *J. Power Sources* **2016**, *301*, 219, https://doi.org/10.1016/j.jpowsour.2015.09.124

[25] J. J. Kim, D. P. Summers, K. W. Frese, *J. Electroanal. Chem.* **1988**, *245*, 223, https://doi.org/10.1016/0022-0728(88)80071-8

[26] K. P. Kuhl, T. Hatsukade, E. R. Cave, D. N. Abram, J. Kibsgaard, T. F. Jaramillo, *J. Am. Chem. Soc.* **2014**, *136*, 14107, https://doi.org/10.1021/ja505791r

[27] M. Rahaman, K. Kiran, I. Z. Montiel, V. Grozovski, A. Dutta, P. Broekmann, *Green Chem.* **2020**, *22*, 6497, https://doi.org/10.1039/D0GC01636E

[28] M. Rahaman, A. Dutta, A. Zanetti, P. Broekmann, *ACS Catal.* **2017**, *7*, 7946, https://doi.org/10.1021/acscatal.7b02234

[29] R. Kas, R. Kortlever, A. Milbrat, M. T. M. Koper, G. Mul, J. Baltrusaitis, *Phys. Chem. Chem. Phys.* **2014**, *16*, 12194, https://doi.org/10.1039/C4CP01520G

[30] C. W. Li, J. Ciston, M. W. Kanan, *Nature* **2014**, *508*, 504, https://doi.org/10.1038/nature13249

[31] K. W. Frese, *J. Electrochem. Soc.* **1991**, *138*, 3338, https://doi.org/10.1149/1.2085411

[32] M. Ma, K. Djanashvili, W. A. Smith, *Phys. Chem. Chem. Phys.* **2015**, *17*, 20861, https://doi.org/10.1039/C5CP03559G

[33] D. Gao, I. Zegkinoglou, N. J. Divins, F. Scholten, I. Sinev, P. Grosse, B. Roldan Cuenya, *ACS Nano* **2017**, *11*, 4825, https://doi.org/10.1021/acsnano.7b01257

[34] C. W. Li, M. W. Kanan, *J. Am. Chem. Soc.* **2012**, *134*, 7231, https://doi.org/10.1021/ja3010978

[35] B. Beverskog, I. Puigdomenech, *J. Electrochem. Soc.* **1997**, *144*, 3476, https://doi.org/10.1149/1.1838036

[36] A. Verdaguer-Casadevall, C. W. Li, T. P. Johansson, S. B. Scott, J. T. McKeown, M. Kumar, I. E. L. Stephens, M. W. Kanan, I. Chorkendorff, *J. Am. Chem. Soc.* **2015**, *137*, 9808, https://doi.org/10.1021/jacs.5b06227

[37] H. Mistry, A. S. Varela, C. S. Bonifacio, I. Zegkinoglou, I. Sinev, Y. W. Choi, K. Kisslinger, E. A. Stach, J. C. Yang, P. Strasser, B. R. Cuenya, *Nat. Commun.* **2016**, *7*, https://doi.org/10.1038/ncomms12123

[38] A. Eilert, F. Cavalca, F. S. Roberts, J. Osterwalder, C. Liu, M. Favaro, E. J. Crumlin, H. Ogasawara, D. Friebel, L. G. M. Pettersson, A. Nilsson, *J. Phys. Chem. Lett.* **2017**, *8*, 285, https://doi.org/10.1021/acs.jpclett.6b02273

[39] F. Cavalca, R. Ferragut, S. Aghion, A. Eilert, O. Diaz-Morales, C. Liu, A. L. Koh, T. W. Hansen, L. G. M. Pettersson, A. Nilsson, *J. Phys. Chem. C* **2017**, *121*, 25003, https://doi.org/10.1021/acs.jpcc.7b08278

[40] M. Fields, X. Hong, J. K. Nørskov, K. Chan, *J. Phys. Chem. C* **2018**, *122*, 16209, https://doi.org/10.1021/acs.jpcc.8b04983

[41] A. J. Garza, A. T. Bell, M. Head-Gordon, *J. Phys. Chem. Lett.* **2018**, *9*, 601, https://doi.org/10.1021/acs.jpclett.7b03180

[42] P. Grosse, D. Gao, F. Scholten, I. Sinev, H. Mistry, B. Roldan Cuenya, *Angew. Chem. Int. Ed.* **2018**, *57*, 6192, https://doi.org/10.1002/anie.201802083

[43] K. J. J. Mayrhofer, S. J. Ashton, J. C. Meier, G. K. H. Wiberg, M. Hanzlik, M. Arenz, *J. Power Sources* **2008**, *185*, 734, https://doi.org/10.1016/j.jpowsour.2008.08.003

[44] T. Kottakkat, K. Klingan, S. Jiang, Z. P. Jovanov, V. H. Davies, G. A. M. El-Nagar, H. Dau, C. Roth, *ACS Appl. Mater. Interfaces* **2019**, *11*, 14734, https://doi.org/10.1021/acsami.8b22071

[45] M. R. Antonio, L. Soderholm, I Song, *J. Appl. Electrochem.* **1997**, *27*, 784, https://doi.org/10.1023/A:1018464526864

[46] I. Martens, R. Chattot, M. Rasola, M. V. Blanco, V. Honkimäki, D. Bizzotto, D. P. Wilkinson, J. Drnec, *ACS Appl. Energy Mater.* **2019**, *2*, 7772, https://doi.org/10.1021/acsaem.9b00982

[47] A. Dutta, A. Kuzume, M. Rahaman, S. Vesztergom, P. Broekmann, *ACS Catal.* **2015**, *5*, 7498, https://doi.org/10.1021/acscatal.5b02322

[48] A. Dutta, A. Kuzume, V. Kaliginedi, M. Rahaman, I. Sinev, M. Ahmadi, B. R. Cuenya, S. Vesztergom, P. Broekmann, *Nano energy* **2018**, *53*, 828, https://doi.org/10.1016/j.nanoen.2018.09.033
[49] A. Dutta, C. E. Morstein, M. Rahaman, A. Cedeño López, P. Broekmann, *ACS Catal.* **2018**, *8*, 8357, https://doi.org/10.1021/acscatal.8b01738
[50] A. Dutta, I. Z. Montiel, R. Erni, K. Kiran, M. Rahaman, J. Drnec, P. Broekmann, *Nano Energy* **2020**, *68*, 104331, https://doi.org/10.1016/j.nanoen.2019.104331

Appendix

I.   List of Figures, Tables, and Acronyms

List of Figures

List of Tables

Acronyms

GHG	Greenhouse gases
GHE	Greenhouse effect
DAC	Direct air capture
CCS	Carbon capture and sequestration
TRL	Technological readiness level
RWGS	Reverse water-gas shift
SNG	Synthetic natural gas
CO_2RR	Carbon dioxide reduction reaction
WE	Working electrode
RE	Reference electrode
CE	Counter electrode
OER	Oxygen evolution reaction
HER	Hydrogen evolution reaction
GDE	Gas diffusion electrodes
XAS	X-ray absorption spectroscopy
XRD	X-ray diffraction
FCC	Face-centred cubic
PCD	Partial current density
XANES	X-ray Absorption Near Edge Spectroscopy
EXAFS	Extended X-ray absorption fine structure
LCF	Linear combination fitting
RHE	Reversible hydrogen electrode
DHBT	Dynamic hydrogen bubble template
AP	As prepared
MD	Metal deposition
MPL	Microporous carbon layer
XPS	X-ray photoelectron spectroscopy
OCP	Open circuit potential
FE	Faradic efficiency
WLI	White light interferometer
SEM	Scanning electron microscopy
TEM	Transmission electron microscopy
SERS	Surface-enhanced Raman spectroscopy
GC	Gas chromatography
IC	Ion chromatography
ECSA	Electrochemical active surface area
IL	Identical location
OD	Oxide derived
SHE	Standard hydrogen electrode
TCD	Total current density
ILs	Ionic Liquids
RTIL	Room temperature ionic liquid
[EMIm][BF$_4$]	1-ethyl-3-methyl-imidazoliumtetra fluoroborate
[BMIm][BF4]	1-butyl-3-methylimidazolium tetrafluoroborate
IRDE	Inverted Rotating disk electrode

II. Publication List during P.hD.

1. **<u>Kiran K</u>** et al., (In preperation)
   An operando study: selectively CO formation on CuO/SnO material over gas diffusion electrodes

2. Dutta A, **<u>Kiran K</u>**, Rahaman M, Montiel IZ, Moreno-García P, Vesztergom S, and Broekmann P (submitted)
   Insights from operando and identical location (IL) techniques on the activation of electrocatalysts for the conversion of CO_2: a mini-review.
   Chimia (under review)

3. Rahaman M$^{\Delta\dagger}$, **<u>Kiran K</u>**$^{\Delta\dagger}$, Montiel IZ, Dutta A, Broekmann P†.
   Supperession of HER is the key: Selective Electrosynthesis of Formate from CO_2 over Porous InCu Catalysts.
   ACS Appl. Mater.& Inter., Accepted, **Joint first author and corresponding author**

4. Dutta A, Montiel IZ, **<u>Kiran K</u>**, Rieder A, Grozovski V, Gut L, Broekmann P
   A tandem catalyst ($Bi_2O_3 \rightarrow Bi_{met}$) for highly efficient ec-CO_2 conversion into formate: Operando Raman spectroscopic evidence for a reaction pathway change.
   ACS Catal., 2021; DOI: 10.1021/acscatal.0c05317

5. Vesztergom S, Dutta A, Rahaman M, **<u>Kiran K</u>**, Zelocualtecatl Montiel I, Broekmann P. *Hydrogen Bubble Templated Metal Foams as Efficient Catalysts of CO_2 Electroreduction.*
   ChemCatChem. 2020; DOI: https://doi.org/10.1002/cctc.202001145

6. Rahaman M$^{\Delta}$, **<u>Kiran K</u>**$^{\Delta}$, Montiel IZ, Grozovski V, Dutta A, Broekmann P.
   Selective n-propanol formation from CO_2 over degradation-resistant activated PdCu alloy foam electrocatalysts.
   Green Chem.2020;22(19):6497-6509, **Joint first author**; DOI: 10.1039/D0GC01636E

7. Dutta A, Rahaman M, Hecker B, Drnec J, **<u>Kiran K,</u>** Montiel IZ, Jochen DW, Zanetti A, López AC, Martens I, Broekmann P, Oezaslan M.
   CO_2 electrolysis – Complementary operando XRD, XAS and Raman spectroscopy study on the stability of Cu_xO foam catalysts.
   J. Catal. 2020; 389: 592-603; DOI:https://doi.org/10.1016/j.jcat.2020.06.024

8. Rudnev AV, **<u>Kiran K</u>**, Broekmann P.
   Specific Cation Adsorption: Exploring Synergistic Effects on CO_2 Electroreduction in Ionic Liquids.
   ChemElectroChem. 2020; 7 (8):1897-1903, https://doi.org/10.1002/celc.202000223

9. Moreno-García P, Grozovski V, Vázquez MdJG, Mysuru N, **<u>Kiran K</u>**, Kovács N, Hou Y, Vesztergom S, Broekmann P.
   Inverted RDE (iRDE) as Novel Test Bed for Studies on Additive-Assisted Metal Deposition under Gas-Evolution Conditions.

J. Electrochem. Soc. 2020; 167(4):042503,   DOI: 10.1149/1945- 7111/ab7984

10. Dutta A, Montiel IZ, Erni R, **Kiran K,** Rahaman M, Drnec J, Broekmann P.
    Activation of bimetallic AgCu foam electrocatalysts for ethanol formation from CO_2 by selective Cu oxidation/reduction.
    Nano Energy. 2020; 68: 104331, DOI: https://doi.org/10.1016/j.nanoen.2019.104331

11. Rudnev AV, **Kiran K**, Cedeño López A, Dutta A, Gjuroski I Furrer J Broekmann P
    Enhanced electrocatalytic CO formation from CO_2 on nanostructured silver foam electrodes in ionic liquid/water mixtures.
    Electrochim. Acta. 2019;306:245-253,
    DOI:https://doi.org/10.1016/j.electacta.2019.03.102

12. Rudnev AV, Gjuroski I, **Kiran K**, Vasilyev D, Dyson P, Furrer J Broekmann P *Mass Transport Effects in Electrochemical CO_2 Conversion from Ionic Liquids (in Preparation)*

III. Conference presentations and talk

SCS fall meeting- 2018

- Poster presentation titled 'Enhanced electrocatalytic CO_2 conversion on nanostructured silver electrodes in ionic liquids.'

- Mass transport in Ionic Liquids for CO_2 reduction

International Summer School on power to value, Villars- 2018

- Poster presentation titled 'Enhanced electrocatalytic CO_2 conversion on nanostructured silver electrodes in ionic liquids.'

Internal SCCER meeting, Villars, Switzerland- 2019

- Talk on Mass Transport Effects in Electrochemical CO_2 Conversion from Ionic Liquids

8 th Symposium SCCER HaE, Empa, Dübendorf- 2019

- Towards selective C3 alcohol formation: Efficient CO_2 conversion on activated Cu-Pd catalysts

- Towards Deeper Understanding of Electrochemical CO_2 Reduction in Ionic Liquids

IV. Acknowledgements

As an interdisciplinary research center, the University of Bern has long been an interesting and inspirational place to do research. I consider myself fortunate to work in such a nice, cosmopolitan, and stimulating workplace. First and foremost, I would like to convey my heartfelt gratitude to my thesis supervisor, Prof. Dr. Peter Broekmann. I am thankful to him for giving me the chance to work in his group and for giving me the flexibility to conduct research work, as well as for providing valuable feedback on areas of my work. I thank him immensely for the continuous support and encouragement throughout the whole Ph.D.

I am really thankful to Prof. Dr. Christina Roth (University of Bayreuth, Germany) for accepting the request to serve as a referee for my thesis. I am also grateful to Prof. Dr. Andreas Türler (University of Bern) for kindly accepting the invitation to act as the chair and referee of my Ph.D dissertation.

I would like to thank Dr. Alexander Rudnev for introducing me to electrochemistry and teaching me many elements of the discipline throughout first year of my Ph.D thesis. He showed me how to work with ionic liquids, glovebox, and gas chromatography in the context of electrocatalysis. I am really thankful to Dr. Abhijit Dutta, an exceedingly competent researcher, who helped and encouraged me. It was a joy to work with him and have scholarly conversations about many issues concerning my project.

It has been a joy to work with Dr. Motiar Rahaman. We worked together on two projects, and I got to learn a lot from him. Dr. Pavel Moreno Garcia's valuable suggestions are highly appreciated. He constantly lifted my spirits and led me to the solutions to my questions. I'd also want to thank Dr. Yuhui Hou, who joined the group at the same time as me. She has been a continual source of support for me since then.

It is rightly said that one needs a pleasant environment for better results. I am really thankful to my other colleagues; Dr. Soma Vesztergom, Dr. Noèmi Kovacs, Dr. Maria, future doctors: Ivan (good friend who always jokes around), Huifang Hu, Ying kong, Menglong liu, Changzhe Sun, Alain Rieder, Anna Larchuck; members from other projects Mike Liechti, Sven Hadorn, Denis Flury, Nicola Lüdi for creating a friendly and healthy working environment. I was lucky enough to know many people who left the DCB for their future endeavours; Dr. Valentine &

V. Statement of Work- Art. 18 PromR Phil.-nat. 19

Declaration of consent

on the basis of Article 18 of the PromR Phil.-nat. 19

Name/First Name: Kiran, Kiran

Registration Number: 17-121-484

Study program: Chemistry and Molecular Sciences

Bachelor ☐   Master ☐   Dissertation ☑

Title of the thesis: CO2 to X: Electrochemical CO2 Reduction on Metal Foam Catalysts

Supervisor: Prof. Dr. Peter Broekmann

I declare herewith that this thesis is my own work and that I have not used any sources other than those stated. I have indicated the adoption of quotations as well as thoughts taken from other authors as such in the thesis. I am aware that the Senate pursuant to Article 36 paragraph 1 litera r of the University Act of September 5th, 1996 and Article 69 of the University Statute of June 7th, 2011 is authorized to revoke the doctoral degree awarded on the basis of this thesis.

For the purposes of evaluation and verification of compliance with the declaration of originality and the regulations governing plagiarism, I hereby grant the University of Bern the right to process my personal data and to perform the acts of use this requires, in particular, to reproduce the written thesis and to store it permanently in a database, and to use said database, or to make said database available, to enable comparison with theses submitted by others.

Bern/8.11.2021

Place/Date

Signature